DISS. ETH NO. 30192

CHARACTERIZING LIQUID–SOLID PHASE TRANSITIONS FOR MECHANISTIC MODEL-BASED PROCESS DESIGN

A thesis submitted to attain the degree of
DOCTOR OF SCIENCES
(Dr. sc. ETH Zurich)

presented by
LEIF-THORE DECK
MSc in Chemical and Bioengineering, ETH Zurich

born on 28.05.1997

accepted on the recommendation of

Prof. Dr. Marco Mazzotti, examiner
Prof. Dr. Mark W. Tibbitt, co-examiner
Prof. Dr. Richard D. Braatz, co-examiner

2024

The work presented in this document was performed at the Institute of Energy and Process Engineering, ETH Zurich, 8092 Zurich, Switzerland.

This document was typeset in LaTeX using the typographical look-and-feel classicthesis. The figures in this thesis were generated using MATLAB and Python. The bibliography was typeset using biblatex.

ACKNOWLEDGEMENTS

Many people have supported me during the past years and contributed to this thesis. First and foremost, I express my sincere gratitude to Prof. Dr. Marco Mazzotti, my *Doktorvater*, for your continuous support throughout my doctorate. Your firm believe in the power of mechanistic modeling and your passion for rigorous, elegant and always crystal-clear derivations have been inspirational. You gave me the freedom to follow my creativity and to pursue whatever research questions I found worth exploring. Thank you, Marco. I am looking forward to seeing what more we can do together.

Special thanks go to my co-examiners Prof. Dr. Mark Tibbitt and Prof. Dr. Richard Braatz for their interest in my work as well as the many engaging and fruitful discussions at ETH and elsewhere over the past years.

For initiating the collaboration with Janssen, for introducing me to the topic of freezing, and for teaching me so many of the things needed to make it through the doctorate, I am immensely grateful to Dr. David Ochsenbein. Thanks for all your support, both personally and professionally.

I would like to thank the entire research group for the great working environment. I am particularly grateful to the senior members who supported me during the early stages of my doctorate. Thank you to Dr. Pietro Binel for all the time spent together on the SOWA project and to Dr. Brigitta Bodák for fueling my interest in PBE modeling. Further thanks go to Dr. Luca Bosetti and to Dr. Viktoria Wiedmeyer for the very warm welcome to G 16 and for all the scientific and non-scientific discussions. Learning how to ski with Brigitta and Viktoria has been a great experience.

For all the time spent together on deracemization and on the distillation course, I am very grateful to my colleague Mercedeh Sadat Hosseinalipour. Working with you has been very rewarding and enjoyable. I also owe many thanks to Daniel Trottmann for being a magician in building new setups and fixing broken ones. Special thanks go to Janina Müller-Herrlitz for taking care of all the administrative matters that arose during the doctorate and the deep discussions we had.

I am very thankful to Daniel Biri. We know each other since we started our studies at ETH, and being in the office with you has been one of the best things that happened during my doctorate. I am very happy how we were able to share everything, both in good and bad times.

Many thanks go to all my collaborators in academia and industry. I am very grateful to Dr. Juan Carlos Araque and Dr. Ryan Wall at Janssen for their continuous guidance, insights, and discussions. Further thanks to everyone who made the micro-droplet project possible: to Prof. Dr. Nadia Shardt for initiating the project with me, for sharing my interest in nucleation and for the countless discussions on whatever topic; to Prof. Dr. Andrew deMello and Dr. Florin Isenrich in Chemical Engineering and Prof. Dr. Ulrike Lohmann and Dr. Claudia Marcolli in the Atmospheric Sciences for providing their expertise and for bridging the disciplines.

I am immensely grateful to all the students and interns I supervised, whose efforts contributed to many of the results reported in this thesis. I owe special thanks to Andraž Košir, Imad El-Bakouri, and Nicole Ferru for carrying out their Master's theses with me, to Vasiliki (Celia) Deligianni and Shina Roshanfekr who worked with me as IAESTE interns, and to Lisanne Wittenberg, Christine Fux, Nikita Gusev, and Gaia Pivari for pursuing shorter projects under my supervision. I am particularly thankful to Andraž for continuing the work on freezing during his doctorate and I am very excited to follow this project in the future.

Finally, I thank my family for their supporting unconditional love; my friends for the encouraging words and for sticking together. My flatmate Henry Lindner for always being there whenever I needed support. To everyone else, who are not on the list but supported me during my doctoral studies.

ABSTRACT

Freezing, freeze-drying and crystallization are central to the manufacture of pharmaceuticals and fine chemicals. They all involve a phase transition from the liquid to the solid, and it is the inherent complexity of this transition that renders process design challenging. This thesis aims to deepen the mechanistic understanding of the liquid–solid phase transition and to utilize the knowledge gained for rational process design. It has been motivated by unexpected challenges encountered in the commercial freezing process of the Janssen COVID-19 vaccine, where no ice formed in vials filled with the drug product despite being stored at −20°C for multiple days. This observation served as the starting point for extensive studies on freezing, aimed both at elucidating the role of fundamental phenomena such as crystal nucleation and growth as reported in Part I, and at understanding the process at industrially-relevant scales as reported in Part II. The ensuing insights inspired investigations into complex systems in crystallization from solution, which are reported in Part III of this thesis.

Part I focuses on the phenomenon of ice nucleation, which denotes the onset of the phase transition. Its slow kinetics were the main reason for the aforementioned issue related to the Janssen COVID-19 vaccine. To study ice nucleation, I first developed a methodology for measuring its rate in aqueous solutions filled in vials. I then used this method to assess the effects of solution composition and of particulate impurities on the nucleation rate. A key finding was that ice nucleation is slower in samples prepared under particulate-free conditions compared to less clean conditions, because it is driven by the availability of so-called heterogeneous nucleation sites. To further assess the effect of volume on ice nucleation, I studied the freezing process of aqueous solutions in micro-droplets in collaboration with the research groups of Prof. Dr. Andrew deMello and of Prof. Dr. Ulrike Lohmann.

Part II discusses the development of mechanistic models for freezing processes and their validation with experimental data. In particular, I developed a suite of three freezing models that all consider the stochastic nature of nucleation, and I made them openly available in the form of a Python package termed *SNOW: Stochastic Nucleation Of Water*. The first model simulates the freezing stage in a freeze-drying process, where a large number of vials is densely packed in two dimensions on a shelf. The predictions of this model have been validated experimentally with a newly developed experimental setup for the batch-scale online monitoring of freeze-drying using infrared

thermography. The second model simulates the commercial freezing process of the Janssen COVID-19 vaccines, where tens of thousands of vials have been stacked in three dimensions on a pallet; the model correctly predicted all relevant experimental trends that were observed in engineering runs. The third model simulates freezing in a single container with spatial resolution. It was validated using the data generated in Part I and revealed that thermal gradients within a vessel may affect the time at which ice nucleation happens.

Inspired by the experimental studies on ice nucleation in Part I and the modeling efforts in Part II, I investigated three complex systems in crystallization from solution, as reported in Part III. Crystallization is characterized by the occurrence of two types of nucleation, called primary and secondary nucleation, whereby the latter refers to the nucleation of new crystals promoted by existing crystals. I theoretically assessed two challenges related to secondary nucleation: first I studied the interplay of primary and secondary nucleation and how it affects the accuracy of methods for the measurement of nucleation rates. Second, I analyzed the stability of the steady state in a continuous crystallizer in which crystal growth and secondary nucleation take place. The resulting mathematical framework is particularly useful for describing the crystallization of systems with multiple solid forms – such as polymorphic or chiral compounds. A specific crystallization process of chiral compounds – solid-state deracemization – has been assessed in more detail, whereby I could elucidate its governing mechanism through a rigorous theoretical analysis supported by experiments.

In conclusion, the results obtained in this thesis have aided the understanding and design of industrially relevant processes that involve liquid–solid phase transitions. The quantitative description of the ice nucleation rate, the suite of openly available mechanistic freezing models, and the theoretical results achieved in describing complex crystallization systems promise to be of broad interest both to fundamental scientists and to practitioners in industry.

ZUSAMMENFASSUNG

Das Einfrieren, die Gefriertrocknung und die Kristallisation spielen eine zentrale Rolle bei der Herstellung von Arzneimitteln und Feinchemikalien. Diese drei Prozesse beinhalten einen Phasenübergang vom flüssigen in den festen Aggregatzustand, und es ist die inhärente Komplexität dieses Übergangs, die zu Herausforderungen bei der Prozessgestaltung führt. Ziel dieser Arbeit ist es, das mechanistische Verständnis dieses Phasenübergangs zu vertiefen und die gewonnenen Erkenntnisse für die Prozessgestaltung zu nutzen. Sie wurde motiviert durch eine Beobachtung beim Gefrierprozess des Janssen COVID-19 Impfstoffs: in vielen mit dem Arzneimittel gefüllten Fläschchen bildete sich kein Eis, obwohl sie mehrere Tage lang bei $-20°C$ gelagert wurden. Dieses Verhalten diente als Ausgangspunkt für umfangreiche Studien zum Gefrieren, die sowohl die Rolle grundlegender Phänomene wie Kristallkeimbildung und -wachstum (siehe Teil I) als auch das Prozessverhalten in industriell relevanten Grössenordnungen (siehe Teil II) aufklären sollten. Die sich daraus ergebenden Erkenntnisse inspirierten weitere Untersuchungen komplexer Systeme im Kontext der Kristallisation, die in Teil III dieser Arbeit beschrieben werden.

Teil I befasst sich mit dem Phänomen der Eiskeimbildung, die den Beginn der Eisbildung beim Gefrieren darstellt. Seine langsame Kinetik ist der Hauptgrund für das oben erwähnte Einfrierverhalten des COVID-19 Impfstoffs. Um die Eiskeimbildung quantitativ zu untersuchen, entwickelte ich eine Methode zur Messung ihrer Rate in wässrigen Lösungen. Diese Methode ermöglichte detaillierte Studien zu den Effekten von Lösungszusammensetzung und Verunreinigungen auf die Keimbildungsrate. Eine wichtige Erkenntnis dieser Studien ist, dass die Eiskeimbildung in Proben, die unter partikelfreien Bedingungen hergestellt wurden, langsamer ist als in Proben hergestellt unter weniger sauberen Bedingungen. Das kommt daher, dass die Keimbildungsrate durch die Verfügbarkeit so genannter heterogener Keimbildungsstellen bestimmt wird. Um den Einfluss des Volumens auf die Keimbildung zu untersuchen, habe ich in Kollaboration mit den Forschungsgruppen von Prof. Dr. Andrew deMello und Prof. Dr. Ulrike Lohmann das Gefrieren wässriger Lösungen in mikroskopisch kleinen Tröpfchen untersucht.

Teil II beschreibt die Entwicklung mechanistischer Modelle für Gefrierprozesse und deren Validierung mit experimentellen Daten. Im Rahmen dieser Arbeit entwickelte ich drei solcher Modelle und veröffentlichte sie als Python-Paket unter dem Namen *SNOW: Stochastic Nucleation Of Water*. Das erste Modell simuliert die Gefrierphase in einem Gefriertrocknungsprozess, bei

dem eine grosse Anzahl an Fläschchen dicht gepackt auf einer gekühlten Metallplatte stehen. Die Vorhersagen dieses Modells wurden experimentell mit einem neu entwickelten Versuchsaufbau für die Echtzeitbeobachtung der Gefriertrocknung mittels Infrarot-Thermografie validiert. Das zweite Modell simuliert den kommerziellen Gefrierprozess des COVID-19-Impfstoffs von Janssen, bei dem zehntausende Fläschchen dreidimensional auf einer Palette gestapelt wurden; das Modell sagte alle relevanten experimentellen Trends korrekt voraus. Das dritte Modell simuliert das Einfrieren in einem einzelnen Behälter mit räumlicher Auflösung. Es wurde anhand der in Teil I gewonnenen Daten validiert und zeigte, dass Temperaturgradienten innerhalb eines Behälters den Zeitpunkt der Keimbildung beeinflussen.

Die Studien zur Eiskeimbildung in Teil I und den Prozessmodellen in Teil II inspirierten weitere Arbeiten im Bereich der Kristallisation organischer Moleküle, die in Teil III erörtert werden. Kristallisation unterschiedet sich vom Gefrieren dadurch, dass zwei Arten der Keimbildung auftreten, nämlich primäre und sekundäre Keimbildung. Letztere bezeichnet das Phänomenon, dass neu Kristalle schneller gebildet werden, wenn bereits andere Kristalle in der Lösung vorliegen. Ich bearbeitete zwei Fragestellungen im Zusammenhang mit der sekundären Keimbildung: Zunächst untersuchte ich das Zusammenspiel von primärer und sekundärer Keimbildung und quantifizierte die Genauigkeit von Methoden zur Messung der Keimbildungsraten. Weiterhin analysierte ich die Stabilität der stationären Zustände in einem kontinuierlichen Kristallisator, in dem Kristallwachstum und sekundäre Keimbildung stattfinden. Die sich daraus ergebenden mathematischen Werkzeuge sind besonders nützlich, um die Kristallisation von Systemen mit mehreren festen Phasen – wie polymorphe oder chirale Verbindungen – zu beschreiben. Ein spezifischer Kristallisationsprozess chiraler Verbindungen – die Festphasenderacemisierung – wurde genauer untersucht, wobei ich den zugrunde liegenden Mechanismus durch eine theoretische Analyse, die durch Experimente unterstützt wurde, aufklären konnte.

Abschliessend ist festzuhalten, dass die in dieser Arbeit erzielten Ergebnisse beigetragen haben zum Verständnis und zur Gestaltung industrieller Prozesse, in denen flüssig–fest Phasenübergänge stattfinden. Die quantitative Beschreibung der Eiskeimbildungsrate, die öffentlich verfügbaren mechanistischen Gefriermodelle und die theoretischen Ergebnisse, die bei der Beschreibung komplexer Kristallisationssysteme erzielt wurden, versprechen, von grossem Interesse für Wissenschaft und Industrie zu sein.

CONTENTS

LIST OF FIGURES

LIST OF TABLES

1 INTRODUCTION

1.1 MOTIVATION AND AIM OF THE THESIS

In 2020, people all over the world stayed in isolation to slow down the spread of the COVID-19 pandemic, while scientists and engineers at pharma companies and research institutes joined the race to develop vaccines against the virus. Even though the development of new drug products traditionally takes multiple years, multiple companies succeeded in developing vaccines and assessing their performance in clinical trials within less than one year. This tremendous speed represents a truly extraordinary and unprecedented achievement in the history of pharmaceuticals.

Such an accelerated timeline posed major challenges for the manufacture and distribution of the COVID-19 vaccines.[1,2] In particular, there was little time for stability studies that in normal circumstances are carried out to identify optimal storage conditions, so that the COVID-19 vaccines were distributed in the frozen state following conservative best-practices. The requirement for ultra-cold storage capabilities at -80°C for the vaccines based on mRNA heavily impacted the distribution of the vaccines of Pfizer/BioNtech and Moderna, particularly in developing countries.[3–5] In contrast, earlier vaccines based on adenoviral vectors developed by The Janssen Pharmaceutical Companies of Johnson & Johnson (Janssen in short) had been shown to be stable in the long-term when frozen at higher temperatures and even as refrigerated liquid at 2–8°C,[6,7] so that their COVID-19 vaccine initially was distributed in the frozen state at -20°C. While such a higher storage temperature simplified the distribution of the vaccine, it also caused an unexpected issue: when freezing vials filled with the drug product at -20°C for several days, in many of them no ice formed. This had to be accounted for in the design of the freezing process, and initially led to the loss of vaccine doses. And it was this behavior that became the starting point for this thesis.

The freezing process of a vaccine, like of any aqueous solution, involves a liquid–solid phase transition where the newly-formed solid phase comprises pure ice crystals. The research group of my doctoral advisor, Prof. Dr. Marco Mazzotti, at ETH Zurich studied liquid–solid phase transitions in the context of pharmaceuticals since the early 2000's, however with a focus on crystallization

from solution, not on freezing. In Fall 2020, Janssen and ETH Zurich initiated a collaboration to expand these research activities to the freezing process of vaccines, with the objective to elucidate the issues encountered in the commercial freezing process. During the past three and a half years, I have been leading this research project at ETH Zurich, with close support from several senior scientists at Janssen.

As I quickly realized, understanding the behavior of such a complex manufacturing process is rather challenging. On the one hand, there were no quantitative information available on the relevant physical phenomena that happen during freezing – in particular, on ice nucleation, which denotes the onset of ice formation in a solution, and which apparently occurred at a rate slow enough that no ice would form in some vials during the freezing process. On the other hand, the freezing process was designed in an empirical manner, using a large number of experimental engineering runs. There was no mechanistic model available that could have guided process design.

To tackle these challenges, I carried out fundamental studies to elucidate the phenomenon of ice nucleation and utilized the ensuing insights to develop mechanistic process-scale models of freezing. Realizing the similarities in the underlying phenomena of freezing and of crystallization, I further expanded my research to the study of complex crystallization systems. Similar to freezing, crystallization is widely employed in the pharmaceutical industry, yet the mechanistic understanding of the associated industrial processes is rather limited, which severely impacts their design and optimization. In Section 1.4, I discuss the structure of this thesis in more detail. In Sections 1.2 and 1.3, I introduce relevant concepts regarding freezing and crystallization processes in the pharmaceutical industry, and regarding the fundamentals of the liquid–solid phase transition.

1.2 FREEZING AND CRYSTALLIZATION OF PHARMACEUTICALS

Most biopharmaceutical drug products, including vaccines, are distributed as so-called parenteral formulations, which are aqueous solutions or suspensions that are delivered by injection. To facilitate their handling, a single dose or a few doses of the drug product are stored in a vial with a fill volume on the order of a few milli-liters. Generally, bio-pharmaceuticals comprise water, a number of excipients (additives such as sugars or salts), and the active pharmaceutical ingredient (for example a protein, an RNA molecule, or a viral vector). As many active ingredients exhibit limited stability in aqueous solution, two processes are commonly employed to extend the shelf life of these products: freezing, as discussed in Section 1.2.1, and freeze-drying,

where freezing is followed by drying under vacuum to remove water from the drug product by sublimation and desorption, as discussed in Section 1.2.2.

Drug products where the active ingredient is a small organic molecule, in contrast, are predominantly administered as tablets that contain a compressed powder. Such powder comprises numerous (e.g., billions of) typically micrometer-sized crystalline particles, and many of the powder's practically-relevant properties such as bio-availability or compressibility depend on the particle size and its distribution. For this reason, the design of crystallization processes that provide products with well-controlled particle size distributions is a long-standing topic of great interest not only to the pharmaceutical industry, but also to related fields such as agro-chemicals and food. Crystallization is discussed in detail in Section 1.2.3.

1.2.1 Freezing

Freezing is well-known to enhance the stability of active pharmaceutical ingredients and hence to extend the shelf life of biopharmaceuticals compared to storage in the liquid state.[8–13] The prediction and quantification of this effect, and therefore the selection of optimal freezing process conditions and long-term storage conditions, is not trivial.[14,15] Both the formulation, i.e., the composition of the drug product, and the freezing process conditions are known to affect the shelf life.[9,14,16–18] This thesis focuses on the freezing process itself because the rational design of various industrial processes is a core area of expertise of my doctoral advisor's research group, and hence I could greatly benefit from this experience. Identifying optimal formulations for freezing represents a very interesting (and active) avenue of research in its own right, however, it is outside the scope of the thesis.

A freezing process in the most general sense comprises two stages, namely a cooling stage, during which the formulation is in the liquid, and a solidification stage, during which ice is formed.[19–21] At the onset of solidification, an ice nucleus forms, which is a stochastic phenomenon.[19,20,22–27] This is of practical relevance because when multiple vials are frozen together, nucleation takes place at different times, even when they contain identical formulations and experience similar heat transfer.[19,21,25,27–29] This implies that certain quantities linked to freezing such as the temperature at which nucleation happens, or the time required between nucleation and complete freezing, vary among the vials in a batch. These quantities have been linked to numerous degradation mechanisms, so that a broad distribution in these quantities may translate into a distribution in the residual activity of a drug product. For example, the solidification time is connected to the phenomenon of freeze-concentration, which denotes the spatial transfer of material from regions

in a vessel that are frozen early toward those that freeze later. This affects buffer concentrations and thus the stability of the active pharmaceutical ingredient.[30–33] The nucleation temperature, in contrast, is widely interpreted as a predictor for the ice crystal morphology in the frozen product,[21,34] which in turn controls the rate of deactivation mechanisms at the ice-water interface, as observed for a number of proteins.[12] Therefore, the freezing process of pharmaceuticals should be designed such that all vials in a batch meet qualified target ranges for nucleation and solidification with sufficient probability.

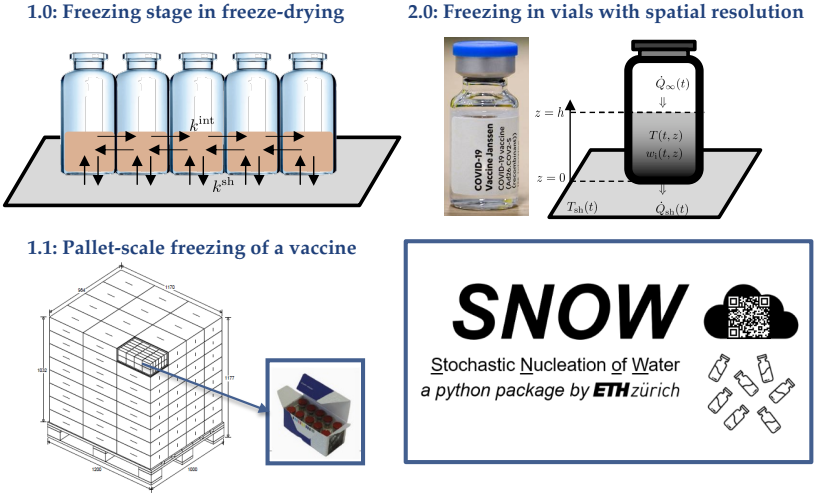

Figure 1.1 Schematic of the three types of freezing processes studied in this thesis. The models have been made available in the form of the Python package *SNOW: Stochastic Nucleation Of Water*. Version 1.0: Model of the freezing-stage in freeze-drying. Version 1.1: Model of the pallet freezing process as used in the manufacture of the Janssen COVID-19 vaccine. Version 2.0: Model of freezing within a single container with spatial resolution.

Doing so is challenging for several reasons. At the scale of commercial manufacturing, there are very few means for process control, as tens of thousands of vials are typically packed together in a pallet and frozen by storing the pallet in a cold storage room. Such a setup is shown in the bottom left panel of Figure 1.1. Because heat transfer depends on the position of a vial within the pallet, it is not realistic to expect that all vials nucleate and solidify similarly. The inherent stochasticity of ice nucleation further enhances this batch heterogeneity. Even worse, there are only few means for

process monitoring, which relies on the insertion of thermocouples into the pallet and on manual visual inspection to detect frozen and non-frozen vials. Therefore, it is a major objective of this thesis to enhance the understanding of such a commercial freezing process, in line with the general trend in the pharmaceutical industry to move towards more more rational process design.[35,36]

Freezing has been a topic of intense research in the past.[19,28,37–40] Studies reported in the literature have established links between properties of the frozen drug product, such as its mean ice crystal size or the extent of freeze concentration, and the process conditions during freezing. Yet, the design of commercial freezing processes still is performed mostly in an empirical fashion, which is largely because the literature predominantly focuses on the single-vial scale. This observation has motivated me to model freezing specifically on the process-scale.

To do so, I developed a suite of three freezing models targeted not only at the simulation of pallet freezing, but also at the freezing stage in freeze-drying (see Section 1.2.2), and at the spatial evolution of freezing in a single vessel (for the validation of the process-scale models). A main feature of these models is that they describe nucleation as a stochastic phenomenon (see Section 1.3.2). In contrast, existing freezing models used in the field consider nucleation in a simplified manner in the sense that they assume that ice starts to form either as soon as the solution reaches its melting point or as soon as it reaches a predetermined deterministic nucleation temperature.[19,28,40] Motivated by the success in the application of the model to explain experimental trends of the freezing process of the Janssen COVID-19 vaccine, I decided in collaboration with Dr. David Ochsenbein from Janssen to provide open source access to these models in the form of a Python package, as shown in Figure 1.1. This package is termed *SNOW: Stochastic Nucleation Of Water*, and comprises the aforementioned three models as versions 1.0, 1.1, and 2.0.

1.2.2 Freeze-drying

Freezing not only extends the shelf life of drug products, but also causes substantial logistical challenges due to the required cold chain. Another process that enables the stable long-term storage of biopharmaceuticals is freeze-drying, also called lyophilization. Freeze-dried products can be stored at higher temperatures than frozen ones, sometimes even at ambient temperatures.[1,41] As of 2020, about 650 drug products were distributed in the freeze-dried state, with hundreds more in development,[8] which corresponds to about 40-50% of all biopharmaceuticals.

A freeze-drying process consists of three stages, namely freezing, primary drying, and secondary drying.[41] During freezing, most of the liquid water in the product turns into ice crystals, while the solutes and the remaining water form either an amorphous (vitrified) freeze-concentrate or a crystalline phase engulfed among the ice crystals. During primary drying, the ice crystals are removed via sublimation under vacuum at low temperature, which typically requires multiple days and is the most time-consuming stage. What is left at the end of sublimation is the highly porous vitrified or crystalline micro-structure, as shown in Figure 1.2; the water that is still part of this structure is removed by means of desorption at elevated temperature under vacuum. This is called secondary drying.[21,41]

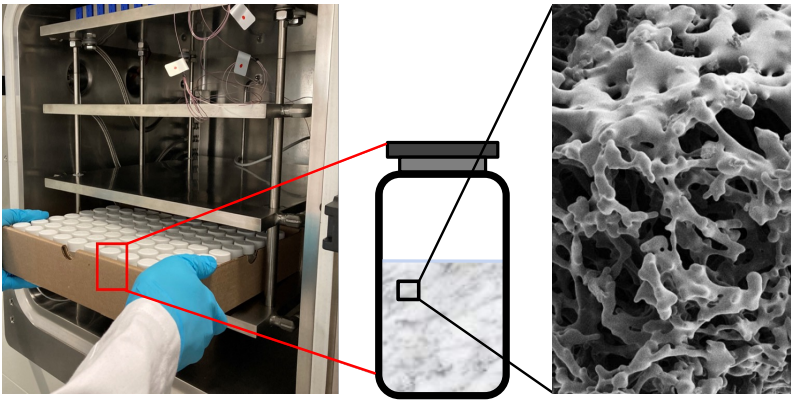

Figure 1.2 Photo of a tray packed with vials that is loaded into the chamber of a laboratory-scale freeze-dryer. The zoom-in shows a scanning electron microscopy (SEM) image of the micro-structure of a freeze-dried product.

Freeze-drying is a batch process whereby a single batch may comprise hundreds of thousands of vials that are densely packed on a temperature-controlled shelf. When designing such a process, the objective is to identify suitable process conditions that yield dry and *acceptable* products in the shortest time possible. The definition of what is acceptable is not straightforward and is an active area of research (see Patel et al.[42] for a comprehensive recent review on quality guidelines regarding freeze-dried products). The main parameters for process design are the thermal evolution of the shelf on which the vials are placed and the pressure levels during the drying stages. A higher temperature of the shelf during drying increases the rates of both sublimation and of desorption.[41] It also increases the temperature in the product itself, which may result in its structural collapse, an outcome that is

not acceptable. Therefore, the drying temperature must be chosen high enough to allow for fast drying, but low enough to prevent collapse. Such collapse is linked to the glass transition temperature of the freeze-concentrated phase in the product, because if this temperature is surpassed, the viscosity decreases by orders of magnitude, which affects the mechanical stability. The measurement of this temperature therefore is a routine step in process design, and is typically carried out using differential scanning calorimetry or freeze-dry microscopy;[20,21] in Chapter 5, I introduce a new measurement technique based on droplet microfluidics that may complement the existing ones.

Given that the physical properties of the freeze-concentrate are defined by the formulation, there are only limited opportunities for process optimization during drying. Instead, in a seminal paper published about twenty years ago, Searles et al.[43] suggested that the ice nucleation temperature during freezing indirectly governs the rate of drying, whereby higher nucleation temperatures allow for faster drying. This effect has been traced back to the observation that high nucleation temperatures promote the formation of micro-structures with large ice crystals that are beneficial for fast sublimation. In contrast, low nucleation temperatures result in micro-structures with a large number of small ice crystals, which provide a relevant mass transfer resistance for sublimation, hence slowing down sublimation.[19,20] For this reason, the identification of the optimal freezing protocol that minimizes the duration of the drying stages has become a major theme in the current freeze-drying literature.[20,44]

The link between freezing conditions, micro-structure formation, and drying rates is not entirely understood (yet) in the sense that it is currently not possible to predict with quantitative accuracy how a change in freezing conditions affects the drying rates. On a higher level, one can however postulate the following: if properties related to freezing – such as the nucleation temperature or the solidification time – affect drying, then it is beneficial that these properties are similar in all vials, because broad distributions would result in batch heterogeneity in the dried product. This raises two questions, both of which I aim to address within this thesis. The first one is this: how does one measure or monitor the freezing and drying behavior of a large number of individual vials in a batch inside a freeze-dryer? This is not trivial, and I have developed a new shelf-scale monitoring technique based on infrared thermography (see Chapter 4) for this purpose. The second question is how to predict or simulate the freezing behavior of densely packed vials on a shelf, to identify suitable freezing process conditions that minimize batch heterogeneity. I have developed such a shelf-scale mechanistic freezing model (see Chapter 6), as mentioned in the earlier discussion on freezing, and confirmed

its predictive capabilities using laboratory-scale freeze-drying experiments monitored with the infrared thermography setup.

1.2.3 Crystallization

This section introduces concepts in crystallization that are relevant to this thesis. Even though freezing also represents a crystallization process, there are major differences between freezing, where water – the solvent – crystallizes, and processes where a solute crystallizes, as outlined in the following.

The product of a crystallization process typically is a powder that consists of billions of crystalline particles, and many of its practically-relevant properties such as bio-availability or compressibility depend on the particle size and its distribution.[45,46] These particulate products must therefore be manufactured such that they have a specific particle size distribution. This is challenging due to the complex interplay of, on the one hand, several poorly understood phenomena such as nucleation and crystal growth, and on the other hand, transport phenomena at the scale of the crystallizer. Additional complexity arises because crystals exhibit multiple facets each of which has its own growth kinetics.[47] For this reason, not only the size but also the shape of crystals depends on the operating conditions of the process, which renders its design even more challenging. Crystallization process design in the industry therefore largely relies on trial and error, and it involves extensive experimental campaigns.

A key topic of interest to the pharmaceutical industry is the crystallization of compounds with multiple solid forms, such as polymorphic or chiral species. Polymorphism denotes the phenomenon that a compound forms several solid phases, each of which with a distinct crystal lattice, and therefore, distinct thermodynamic and kinetic properties. This means that different polymorphs exhibit differences in properties relevant to pharmaceuticals, such as mechanical properties linked to flowability and compressibility, or the dissolution rate linked to bio-availability.[48] Given that a majority of active ingredients used in pharmaceuticals are polymorphic,[49] it is a key aspect of crystallization process design to ensure that only a single polymorph forms, and that this outcome is robust. To this end, Chapter 11 introduces a general mathematical framework to predict the polymorphic outcome in crystallization processes that are operated continuously. It is worth noting that the manufacture of pharmaceuticals still predominantly relies on batch operation, and that the understanding and design of continuous crystallization processes is a focus of current research.[50]

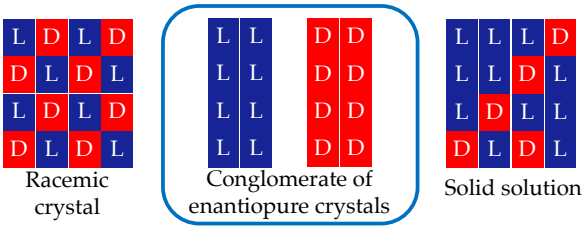

Figure 1.3 Schematic of the three types of solid forms into which chiral species crystallize.

The majority of small molecules used as active pharmaceutical ingredients are chiral species.[51] This means that they occur in two enantiomeric forms, which may differ in their pharmacological effects, as is exemplified in the disastrous case of Thalidomide, where the desired effect of preventing morning sickness in pregnant women was attributed to one enantiomer, whereas the second one was found to cause birth defects.[52] The resolution, i.e., the separation, of the two enantiomers of a chiral compound therefore is of paramount interest, but it is practically challenging, because enantiomers exhibit identical physical and chemical properties in non-chiral environments.[53]

A peculiar property of chiral species is that they crystallize in three different ways, as shown in Figure 1.3: they may form a conglomerate of enantiopure crystals (about 10% to 20% of cases), a solid solution with irregular crystal lattice (rare), or racemic crystals that comprise both enantiomers in a 1:1 ratio in a regular lattice (about 80% to 90% of cases).[53] In a landmark contribution in 1848, Pasteur [54] demonstrated the chiral resolution of conglomerate crystals by mechanically separating those made up of one enantiomer from the others using tweezers. This experiment forms the basis for a large family of chiral resolution methods based on crystallization that resolve conglomerate crystals by various technical means including grinding and temperature-cycling.[55–57] The mechanism of one such process, called solid-state deracemization, is elucidated in Chapter 12 through a combination of theory, simulations, and experiments.

1.3 FUNDAMENTALS OF THE LIQUID–SOLID PHASE TRANSITION

This section introduces fundamental concepts related to liquid–solid phase transitions. A phase in its most general sense is defined as a region in

space with uniform physical and chemical properties (such as density and composition). The stability of a phase j is quantified by its chemical potential μ_j, which is a function of the state of the system, i.e., of temperature, pressure and composition. A transition from one phase into another may proceed if the chemical potential of the new phase is lower than that of the old phase. This is discussed in more detail in Section 1.3.1. Section 1.3.2 explains the phenomenon of nucleation, i.e., the onset of the formation of a new phase.

1.3.1 Thermodynamics

The driving force of a phase transition is quantified by the difference in chemical potential between the old phase and the new phase. The driving force of freezing, for instance, is the difference in chemical potential between ice and the water in solution, termed $\Delta\mu$:

$$\Delta\mu = RT\ln\left(\frac{a_\mathrm{w}}{a_\mathrm{w}^\mathrm{eq}}\right) \tag{1.1}$$

where R denotes the universal gas constant. Water activity is a convenient quantity to express the driving force of freezing, because it is experimentally accessible and because it provides a general means to account for the effect of solution composition.[58–60] It is defined through the Schröder van Laar (SvL) equation, which gives the equilibrium water activity $a_\mathrm{w}^\mathrm{eq}(T)$ as a function of temperature, or conversely, the equilibrium freezing temperature $T^\mathrm{eq}(a_\mathrm{w})$ as a function of the solution's water activity a_w:[61]

$$\ln\left(a_\mathrm{w}^\mathrm{eq}\right) = \frac{\Delta H}{R}\left(\frac{1}{T^\mathrm{m}} - \frac{1}{T}\right) - \frac{\Delta c_\mathrm{p}}{R}\left(\ln\left(\frac{T^\mathrm{m}}{T}\right) + 1 - \frac{T^\mathrm{m}}{T}\right) \tag{1.2}$$

where ΔH is the latent heat of fusion of pure ice, Δc_p is the difference in heat capacity between liquid water and ice, and T^m is the freezing point of pure water, all to be evaluated at the relevant pressure level.

While the chemical potential difference provides the *exact* value of the driving force, it is beneficial for practical applications to work with estimates that are simpler to compute. Intuitively, the distance of the solution's state to the equilibrium can be expressed either (i) as difference of the activities, i.e., $\Delta a_\mathrm{w} = a_\mathrm{w} - a_\mathrm{w}^\mathrm{eq}(T)$, as typically used in the atmospheric sciences;[58–60] or (ii) as difference of temperatures, i.e., $\Delta T = T^\mathrm{eq} - T$, which is also called degree of supercooling and is preferred in pharmaceutical applications.[19,62] The expression for the chemical potential can be rewritten in terms of these quantities when taking the appropriate simplifications:

$$\Delta\mu = RT\ln\left(\frac{a_\mathrm{w}}{a_\mathrm{w}^\mathrm{eq}}\right) \approx \frac{RT}{a_\mathrm{w}^\mathrm{eq}}(a_\mathrm{w} - a_\mathrm{w}^\mathrm{eq}) = \alpha(T)\Delta a \tag{1.3}$$

$$\Delta\mu = RT\ln\left(\frac{a_w}{a_w^{eq}}\right) \approx \frac{\Delta H}{T^{eq}}(T^{eq} - T) = \beta\Delta T \tag{1.4}$$

As it can be seen, interpreting $\Delta\mu$ as a function solely of Δa requires (i) linearization of the logarithm, and (2) neglecting the temperature-dependency of the pre-factor α. In contrast, to arrive at the expression for ΔT, no linearization is required, but the Δc_p term in the Schröder van Laar equation is neglected. Hence, neither ΔT nor Δa provide an exact quantification of the driving force, however, their use may be justified by the fact that the temperature of a system and the water activity in a solution can be easily measured.

Notably, the derivation carried out so far applies not only to freezing, but also to crystallization from solution, if one replaces the properties of water with those of the solute. A key concept used in crystallization is that of the *saturation ratio* S, defined as the ratio of the solute's activity in solution, a, and the equilibrium value, a^{eq}.[45,46]

$$S = \frac{a}{a^{eq}} = \frac{c\gamma}{c^{eq}\gamma^{eq}} \approx \frac{c}{c^{eq}} \tag{1.5}$$

whereby the second equality relies on the concept that an activity can be written as product of an activity coefficient γ, and of a concentration c. The quantity c^{eq} denotes the concentration at equilibrium, also called solubility. The last equality follows when assuming that the ratio of the activity coefficients at the solution's state and at equilibrium is about one. If $S > 1$, the solution is *super-saturated* and the crystalline phase is stable, so that crystal nucleation and growth take place. If $S < 1$, the solution is *under-saturated* and the crystalline phase dissolves over time.

From a process perspective, it is important to keep in mind that the chemical potential difference must be generated by technical means – in the case of freezing this typically requires cooling. In the case of crystallization, cooling is just one out of many options, and indeed not always the preferred one, because the solubility of some compounds depends only weakly on temperature (consider e.g., sodium chloride).[63] Alternative means to generate supersaturated solutions are evaporation of the solvent (increasing the concentration of the solute), or the addition of an anti-solvent (decreasing the solubility of the solute).[45,46] This thesis, however, focuses on freezing and crystallization processes that involve phase transitions by cooling.

1.3.2 Kinetics of nucleation

Nucleation denotes the onset of the formation of a new phase from a parent phase. It is an activated process, which means that an energy barrier must

be overcome to form a nucleus.[45,64] As a consequence, nucleation is an intrinsically stochastic phenomenon, and this stochastic nature represents a major theme in this thesis. The expected number of nuclei that form per unit time in a system of finite size is given by the *nucleation frequency*, which can be written as the product of three terms

$$K = \begin{pmatrix} \text{number of} \\ \text{sites} \end{pmatrix} \begin{pmatrix} \text{frequency of} \\ \text{attempts per site} \end{pmatrix} \begin{pmatrix} \text{probability of success} \\ \text{per attempt} \end{pmatrix} \tag{1.6}$$

whereby the first term, the number of sites, scales with the size of the system. The other two terms are defined by the state of the system, i.e., temperature, pressure, and composition. In particular, they are strong functions of the thermodynamic driving force. To decouple the effects of system size and state, one defines a *nucleation rate* J, which quantifies the expected number of nuclei that form per unit time and per unit volume

$$K = \int_V J(\mathbf{x}) \, \mathrm{d}^3\mathbf{x} \approx JV \tag{1.7}$$

where one integrates the value of J over all positions $\mathbf{x}$ in the volume of interest V to obtain K, which in case of a homogeneous system simplifies to $K = JV$. In reality, where systems never are perfectly homogeneous, $K = JV$ is only an approximation, the accuracy of which has been studied in detail in Chapter 9 in the context of freezing. The Classical Nucleation Theory (CNT) provides a family of kinetic rate expressions for $J(S, T)$ as a function of super-saturation and temperature based on the notion that nuclei are formed by the attachment and detachment of molecules to molecular clusters, namely

$$J(S, T) = A(T)S \exp\left\{-\frac{B(T)}{\ln(S)^2}\right\} \tag{1.8}$$

where A and B are temperature-dependent parameters with physical meaning as discussed elsewhere.[45,65] In practice, the values of these parameters are challenging to predict and therefore often fitted to experimental data. It is worth noting that CNT is deterministic, i.e., it does not consider the stochastic nature of nucleation, and scale-independent, i.e., it does not consider that nuclei form as discrete entities. The latter is important, because intuitively, a system can only contain an integer number of crystals/nuclei; for instance, it may contain zero, one, or two nuclei, but not a fraction of one.

To account for these properties in a physically consistent manner, nucleation is interpreted as a stochastic process, where the *expected* number of nuclei $E(N)$ formed in a time interval $[t, t + \Delta t]$ is given as[22,66]

$$E(N) = \int_t^{t+\Delta t} K(t')\mathrm{d}t'. \tag{1.9}$$

If a set of conditions hold (see Chapter 10 for a detailed discussion), the probability that k nuclei form during the time interval follows a Poisson distribution and is given as

$$P^{(\mathrm{k})} = \frac{\mathrm{E}(N)^{\mathrm{k}}}{k!} \exp\left\{-\mathrm{E}(N)\right\}. \tag{1.10}$$

This equation applies independent of the choice of rate expression for J in the computation of K and $\mathrm{E}(N)$. In this thesis, I use the expression predicted by CNT in studies on crystallization from solution. In the context of freezing I instead rely on power law expressions of the thermodynamic driving force. As demonstrated in Chapters 2 and 3, these expressions accurately describe all relevant experimental trends, but come with lower computational costs, which is useful for the process-scale freezing models described in Chapters 6 and 8.

In some scenarios, e.g., when freezing in vials or when measuring crystal nucleation rates, one is particularly interested in the formation of the first nucleus during an experiment. Such nucleus forms at the time t_{n1}, which is a continuous random variable. Its cumulative distribution function $F(t_{\mathrm{n1}})$ is obtained as

$$F(t_{\mathrm{n1}}) = 1 - \exp\left\{-\int_0^{t_{\mathrm{n1}}} K(t')\mathrm{d}t'\right\} = 1 - \exp\left\{-Kt_{\mathrm{n1}}\right\} \tag{1.11}$$

where the second equality applies for stationary conditions, i.e., for constant temperature and supersaturation. In physical terms, $F(t)$ denotes the fraction of experiments in which the first nucleation event has happened between the beginning of the experiment and a time t. If the first nucleation time is measured in a large number of experiments, an empirical distribution can be constructed and be used to estimate the value of K at the given experimental conditions.[67,68] This approach relies on the notion that the formation of the first nucleus is immediately detected, which is true in the case of freezing in vials or in smaller volumes, where the ensuing ice crystal growth after nucleation is rapid.[69]

For crystallization from solution, the situation is more complex, and it was found beneficial to account for a delay between first nucleation and detection.[67,68] This is done by introducing the detection time t_{det} as the sum of the first nucleation time t_{n1} and of a growth time t_{g}, as shown in Figure 1.4. Hence, one obtains for stationary conditions (T, S)

$$F(t_{\mathrm{det}}) = 1 - \exp\left\{-K(t_{\mathrm{det}} - t_{\mathrm{g}})\right\}. \tag{1.12}$$

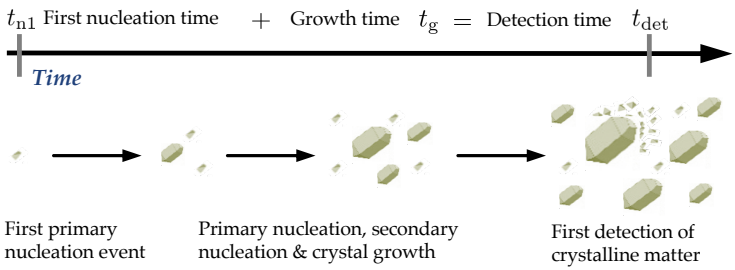

Figure 1.4 Schematic of the steps from a clear solution to the detection of a crystalline suspension.

In this case both K and t_g have to be estimated from experimental data. It is important to note that only the value of K can be estimated using such a method, but one does not obtain any direct information on the nucleation rate J. While one may choose to use the relation $K = JV$, this may not be accurate, as discussed before.

I conclude this section with a comment on the different *types* of nucleation phenomena. Up to this point, nucleation was characterized by a nucleation frequency that scales with the volume of a system. This holds for *homogeneous primary* nucleation, and for *heterogeneous primary* nucleation where the nucleation sites are distributed evenly in the system. The term homogeneous indicates that nucleation takes place in the absence of external surfaces such as dust particles, whereas the term heterogeneous implies that nucleation sites are located on external surfaces. Under standard laboratory conditions (i.e., not particulate-free), heterogeneous nucleation is considered to be dominant at the milli-liter scale and above, with some ambiguity in smaller volumes.[70] Because in principle all types of surfaces may promote heterogeneous nucleation, including the walls of the crystallizer, it is difficult to predict how sensitive the nucleation frequency is to changes in volume.[70] Furthermore, one distinguishes between *primary* and *secondary* nucleation, whereby primary nucleation describes the formation of nuclei from clear solution, which is what was discussed until now.[71] Secondary nucleation, in contrast, denotes the formation of new nuclei promoted by existing crystals, i.e., due to their attrition or due to interparticle energies.[72] Such secondary nucleation plays a key role in crystallization from solution, particularly in continuous crystallization processes, where the supersaturation level is too low for primary nucleation to take place.[45,50] Chapter 11 discusses in detail how secondary nucleation in continuous crystallizers can be described mathematically.

1.4 STRUCTURE OF THE THESIS

This thesis aims to deepen the mechanistic understanding of complex manufacturing processes in the pharmaceutical industry that involve liquid–solid phase transitions. It is divided into three parts, which represent three lines of research that are closely linked to each other. **Part I: Nucleation of ice** consists of four chapters that contain detailed investigations on the rate of ice nucleation in the context of the freezing of aqueous solutions. The findings from these studies are used to inform mechanistic models of pharmaceutical freezing processes. The development of these models as well as their validation with experimental data is outlined in **Part II: Freezing of pharmaceuticals**, which also consists of four chapters. While these two parts are centered on freezing and have been the focus during the early stages of my doctorate, the underlying fundamental phenomena and modeling methodology are of immediate relevance to crystallization from solution as well. **Part III: Crystallization systems** hence reports three contributions related to the design and understanding of crystallization processes that I made throughout of my doctorate.

Part I: Nucleation of ice, comprises Chapters 2–5 that focus on the phenomenon of ice nucleation. In Chapter 2, I report a methodology for measuring the rate of ice nucleation in aqueous solutions on the milli-liter scale, which was applied in Chapters 3 and 4 to elucidate the effects of solution composition and of particulate impurities on the nucleation rate. The key accomplishment of these three chapters lies in the validation of the first quantitative and mechanistic model that predicts the rate of ice nucleation in milli-liter volumes as a function of both solution composition and temperature. To further elucidate the effect of volume on ice nucleation, I initiated a collaboration with the research groups of Prof. Andrew deMello and Prof. Ulrike Lohmann, both at ETH Zurich, where we assessed the freezing process of aqueous solutions using droplet microfluidics; the results of this collaboration are reported in Chapter 5. Intriguingly, droplet microfluidics enabled the measurement not only of nucleation temperatures, but also of melting points, glass transition temperatures, and crystal growth rates, all of which are properties of interest to the freezing of pharmaceuticals.

Part II: Freezing of pharmaceuticals, comprises Chapters 6–9, in which I studied freezing and freeze-drying at process-scale. In particular, I have developed a suite of mechanistic freezing models that consider both heat transfer and the stochastic nature of ice nucleation. These models have been made available to the public in the form of a python package termed *SNOW*, short for *Stochastic Nucleation of Water*.[73] SNOW comprises three distinct models. The first, presented in Chapter 6 is dedicated to shelf-scale simulations

of the freezing stage in freeze-drying. The second model enables simulations of vials stacked in three dimensions on a pallet and was used to investigate the commercial freezing process of the Janssen COVID-19 vaccine, as reported in Chapter 8. The third model, reported in Chapter 9, enables simulations of the freezing process within a single container with spatial resolution; its predictions were validated experimentally using the nucleation data reported in Chapter 2. This model was used to identify process conditions under which thermal gradients are negligible, hence verifying key assumptions made in deriving the first two models. In addition to these models, I developed an experimental setup to monitor a freeze-drying process on the shelf-scale using an infrared camera, as outlined in Chapter 7; this setup was used to confirm the predictive capabilities of the shelf-scale freezing model.

Part III: Crystallization systems, comprises Chapters 10–12 that report three contributions related to crystallization. Inspired by the studies on ice nucleation reported in Part I, I assessed the accuracy of two classes of experimental methods for the estimation of crystal nucleation rates through the means of a novel modeling methodology, as discussed in Chapter 10. Knowledge of nucleation rates is a prerequisite for the mechanistic design of industrial crystallization processes: in Chapter 11, I conceived and formulated a mathematical framework to describe the stability of steady states in a continuous crystallizer based on a compound's crystal growth, nucleation, and withdrawal behavior. This framework is particularly useful to describe the crystallization of systems with multiple solid forms – such as polymorphic or chiral compounds, which are of great relevance to the manufacture of pharmaceuticals. Chapter 12, finally, provides a detailed analysis of a specific chiral crystallization process. This process, termed solid-state deracemization, describes the phenomenon that a crystalline suspension of a chiral molecule experiences an increase in enantiomeric excess over time up to an enantiopure final state, caused by various technical means such as stirring or temperature fluctuations. Through a rigorous theoretical analysis supported by experiments I could prove an exact condition for deracemization; suspensions deracemize when the kinetics of crystal dissolution are faster than those of crystal growth, which is true in general terms, hence explaining the ubiquitous nature of this process.

The research presented in Parts I and II was carried out in the framework of an industrial collaboration with *The Janssen Pharmaceutical Companies of Johnson & Johnson*, as mentioned in Chapter 1.1. The industrial collaborators provided me with engineering run data from the freezing process of the Janssen COVID-19 vaccine, which supported the development the model presented in Chapter 8. They further contributed to the study reported in Chapter 4 by providing me with more than one thousand vials containing

solutions of various compositions that were prepared under particulate-free conditions. The research on crystallization presented in Part III has been funded through the ERC Advanced Grant *SNICC: Secondary Nucleation for the Intensification of Continuous Crystallization* that aims to elucidate the role of nucleation phenomena in industrial crystallization processes.

The results reported in Chapters 2–12 have been published in peer-reviewed journals,[74–81] with the exceptions of Chapter 4, where the associated article is currently in preparation, and of Chapter 7, where the article is currently under review and where a pre-print is available. A footnote at the beginning of each chapter provides additional information on the corresponding publications. The individual chapters are written as standalone works, i.e., they comprise distinct introduction, methodology, results, discussion, and conclusion sections. Chapter 13 closes this thesis with a summary of the main research findings and an indication of potential avenues for future work.

Part I

NUCLEATION OF ICE

2 CHARACTERIZING AND MEASURING THE ICE NUCLEATION KINETICS OF AQUEOUS SOLUTIONS IN VIALS

The stochastic nature of ice nucleation presents a major challenge in freezing and freeze-drying processes of biopharmaceuticals in vials. During freezing, nucleation events occur in the vials of a batch at different times and temperature, which has to be accounted for in process design. This work paves the way towards model-based freezing process design, by presenting a method to estimate nucleation kinetic parameters and their uncertainty from experimental data generated in a parallelized mid-throughput batch-crystallizer. The methodology extends the conventional stochastic description of ice nucleation by considering both the inherent stochasticity, and the variability in heterogeneous nucleation sites among vials. Model validation revealed a nearly quantitative agreement for the predictions of the extended model with experimental data, and only a qualitative one for the conventional model. While this work focuses on ice nucleation kinetics, the rigorous analysis of the experimental uncertainty may also be of relevance for nucleation studies in related fields, such as industrial crystallization.

2.1 INTRODUCTION

Biopharmaceuticals commonly exhibit limited stability in aqueous solution and require freezing or freeze-drying to meet shelf life targets.[41] Pharmaceutical freezing and freeze-drying at commercial scale is carried out following good manufacturing practice (GMP) in batches of vials that contain a single or up to a few doses of a drug product.[20,41,74] A typical example for such manufacturing process is the freezing of the Janssen COVID-19 vaccine, which is carried out in pallets comprising tens of thousands of vials.[75]. Under these conditions – low particulate content and vial fill volume on the millilitre scale

The work presented in this chapter has been reported in: Deck, L.-T.; Mazzotti, M. Characterizing and measuring the ice nucleation kinetics of aqueous solutions in vials. *Chem. Eng. Sci.*. **2023**, 272, 118531.

– aqueous solutions generally experience pronounced supercooling before the onset of ice formation.[19,21,41,43,75]

Freezing generally comprises two phases; first a cooling phase, during which the material is liquid, and second a solidification phase, during which ice is formed.[19–21,74] The first ice is formed via nucleation, which initiates the ensuing solidification process within the entire vial. Ice nucleation is a stochastic process,[19,25,26,82,83] implying that nucleation occurs at different times and temperatures (i.e., levels of supercooling) when the freezing process is repeated under identical conditions. The nucleation behavior of a drug product is of great interest, since it affects both process and product design as follows.

First, the ice crystal morphology in the frozen product is related to the nucleation temperature, whereby lower nucleation temperatures lead to smaller mean ice crystal sizes.[21,28,34,43] This is of importance in the case of pharmaceutical freeze-drying, where the drying kinetics depends on the ice crystal morphology; smaller ice crystals lead to slower sublimation, thus prolonging the process duration.[20,21,28,43] Since vials of the same batch may nucleate at different temperatures, drying times vary across the batch as well; the process duration, however, has to be chosen to ensure sufficient drying in all vials.[28,41]

Similarly, the ice nucleation kinetics governs both process duration and batch heterogeneity in the case of pallet freezing,[75] i.e., the freezing of a large number of vials packed together in a pallet. If nucleation occurs at lower temperatures, the process requires more time and may even fail to complete at all for certain process temperatures.[75]

Finally, the stochastic occurrence of nucleation in a batch induces variability in the thermal evolution of the vials in the neighborhood of the nucleation event, due to the release of heat upon nucleation. This implies that the freezing behavior of a vial depends on the random sequence of nucleation events of other vials in the batch; a batch-scale modeling framework that takes into account both the nucleation kinetics and the interaction among vials is thus required to fully understand such a process.[74,75,84] The relevant modeling approaches have recently been developed by us.[73–75]

Stochastic nucleation has been studied intensely in several research fields; of special relevance for pharmaceutical freezing are works in the field of primary nucleation of solutes and of melts in the context of crystallization,[66,68,85] works on ice nucleation in microdroplets in the context of atmospheric physics,[27,86,87] and works on ice nucleation in cryopreservation.[88,89] In crystallization research, commercial devices are available for mid-throughput measurements of nucleation kinetics in vials.[23,68] A customized version of

such device is used in this work, building on our experience in the field of crystallization.[22–24,90]

In the field of pharmaceutical freezing and freeze-drying, however, a quantitative characterization of ice nucleation kinetics in vials has not yet been achieved, and only few works are dedicated to this topic.[40,62] This is likely due to the large number of nucleation events that must be monitored for such endeavor - in the field of primary crystallization of solutes a standard of about one hundred data points has been established.[23,24,91] Furthermore, it has to be ensured that the heat transfer in all monitored vials is identical and reproducible across repetitions, which is inherently challenging in typical freezing and freeze-drying equipment.[84,92]

In this work, we address the knowledge gap in pharmaceutical freezing with respect to ice nucleation. We develop a novel approach to experimentally measure nucleation temperatures in vials and to estimate kinetic parameters based on the generated data. In Section 2.2, we present the experimental methodology as well as the statistical approach towards parameter estimation. In Section 2.3, we present our results. Finally, in Section 2.4, we discuss and generalize our findings, and we draw the relevant conclusions.

2.2 METHODS

2.2.1 Phenomenology of stochastic ice nucleation

The stochastic nature of nucleation is widely acknowledged in the literature, and of relevance for a variety of research fields and applications. In the context of freezing in vials, one observes a rapid rise in temperature at the end of the cooling phase, which is due to the latent heat released by ice formation upon nucleation.[20,93] The time and temperature, at which this rise occurs, vary upon repetitions of the process at identical conditions within the same vial, and among different vials, indicating stochasticity.

Figure 2.1 reports a representative temperature curve from a cooling experiment carried out in this work: the black line denotes the thermal evolution measured by a thermocouple, while the blue line indicates the set-point temperature. The nucleation event is identified through the sharp rise in temperature. After nucleation, the temperature remains for some time close to the equilibrium freezing temperature T_ℓ^{eq}. This denotes the period of *solidification*, during which most of the liquid water turns into ice, thus releasing latent heat.[74,75] Under the given experimental conditions, i.e., for a vial containing 1 mL of 20 wt.% sucrose solution, the temperature rise was observed to take

place in 1–2 s. This is in line with literature that reports growth rates of supercooled pure water on the order of 0.1 ms^{-1} at the typical range of nucleation temperatures.[69] The experimental behavior is interpreted as single, primary ice nucleation event followed by rapid crystal growth. This directly follows from the observation that the vial spends several minutes (about 20 min for the vial shown here) in a supercooled state, before crystal growth depletes the supercooling within about a second. It is unlikely that further nucleation events happen during the very short growth phase; the same holds for the longer solidification phase, which takes place close to the equilibrium freezing temperature. This phenomenon may also be verified visually: direct imaging shows that freezing is initiated from a single point within the vial, from which a *cloud* of rapidly growing ice expands.[20,28] The stochastic formation of the first and single nucleus thus is responsible for the subsequent depletion of supercooling via rapid growth, and for the observed variability in nucleation time and temperature among vials and repetitions.

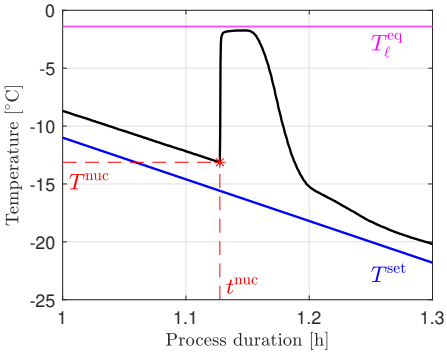

Figure 2.1 Thermal evolution during cooling of a single vial containing 1 mL of 20 wt.% sucrose solution. Thermocouple readout is presented in black, the setpoint temperature in blue. Equilibrium freezing temperature (magenta) and nucleation event (red) are indicated. The nucleation event is followed by a rapid rise in temperature to its equilibrium value, which corresponds to the release of latent heat during solidification.

Importantly, this manifestation of nucleation, where only a single nucleus is formed, is a prerequisite to explain the observed stochasticity: the stochastic nature of nucleation only induces an observable variability in process attributes in case nucleation is a *rare event*.[68] Thus, whenever variability in connection with stochastic nucleation is reported in literature, the underlying mechanism involves either the formation of a single nucleus, or of a few nuclei; such behavior was observed independently in the fields of solute nucleation

in crystallization, in ice nucleation in microdroplets, in melt crystallization, and eventually, in pharmaceutical freezing.[23,25,68,82,83,86,94]

2.2.2 Quantifying the frequency of nucleation events

Nucleation is characterized by the nucleation frequency K, which denotes the expected number of nuclei formed per unit time in the system of interest,[22,74] in this case a vial containing an aqueous solution. While we refer in this work generally to aqueous *solutions*, the methodology is agnostic to the type of mixture studied. The approach presented here may be applied to suspensions and emulsions as well. The cumulative probability $F(t)$ that a vial in the liquid state experiences nucleation in a time interval $[0, t]$ follows an inhomogeneous Poisson distribution and is defined as

$$F(t) = 1 - \exp\left\{-\int_0^t K(t')\mathrm{d}t'\right\} \tag{2.1}$$

whereby K varies over time: K depends on temperature, which is set to decrease during freezing. Since nucleation is an activated process,[22,82,83] i.e., an energy barrier has to be overcome to form a nucleus, the expression for K comprises three contributions, namely

$$K = \begin{pmatrix}\text{number of}\\ \text{sites}\end{pmatrix}\begin{pmatrix}\text{frequency of}\\ \text{attempts per site}\end{pmatrix}\begin{pmatrix}\text{probability of success}\\ \text{per attempt}\end{pmatrix} \tag{2.2}$$

The number of nucleation sites depends on the type of nucleation that dominates the process. Nucleation may be either homogeneous, where nuclei are formed without interaction with any surface, or heterogeneous, i.e., induced by the presence of surfaces. In the case of homogeneous nucleation, the number of sites scales with volume, since every water molecule conceptually represents a site.[83] For heterogeneous nucleation, the relevant type of surface is not known *a priori*. In case of solute crystallization, it is commonly found that in vials at the millilitre scale nucleation is slowed down when filtering.[95,96] This indicates that under these conditions nucleation occurs heterogeneously, specifically on surfaces provided by impurities within the solution. Similarly, Searles et al.[43] reported lower ice nucleation temperatures for solutions prepared in a laminar flow hood, compared to standard laboratory conditions. Assuming a uniform spatial distribution of impurities within the fill volume, the number of nucleation sites scales with volume also for heterogeneous nucleation.[74,95,96]

The frequency of attempts per site corresponds to a kinetic factor that scales with the diffusivity of the molecules of the substance that nucleates.[83] The probability of success, on the other hand is a function of the thermodynamic

driving force $T^{eq} - T$. The term $T^{eq} - T$ is commonly referred to as supercooling, whereby T^{eq} denotes the equilibrium freezing temperature of the solution to be frozen.

Nucleation is commonly described in the framework of the classical nucleation theory (CNT), which links the aforementioned terms with physicochemical properties of the solution, such as the interfacial tension between the nuclei to be formed and the solution.[82,83] In the field of pharmaceutical freezing, however, power law expressions are commonly applied.[40,62,74] We thus use a power law expression in this work as well, and we note that the presented methodology is applicable to any arbitrary functional form for K. K is defined as

$$K(t) = VJ(t) = Vk_b(T^{eq} - T(t))^b \tag{2.3}$$

where k_b and b are two empirical and temperature-independent parameters, which have to be inferred from experimental data. Eq. 2.3 assumes a uniform temperature within the entire vial. If thermal gradients are present, they locally affect the nucleation frequency. Given that solutions in freezing processes are not stirred, such gradients are likely to form and potentially to affect the observed nucleation temperatures. In case the temperature field $T(\mathbf{x}, t)$ at all positions $\mathbf{x}$ within the vial is known, the value of $K(t)$ may be obtained by integrating the nucleation rate per unit volume $J(\mathbf{x}, t)$ over the fill volume:

$$K(t) = \int_V J(\mathbf{x}, t) \mathrm{d}^3\mathbf{x} = \int_V k_b(T^{eq} - T(\mathbf{x}, t))^b \, \mathrm{d}^3\mathbf{x} \tag{2.4}$$

2.2.3 Experimental setup

In the field of crystallization, stochastic nucleation is commonly studied in parallelized batch crystallizers.[23,70,95,97] These devices enable highly automated mid-throughput measurements under comparably consistent and reproducible process conditions. A commercial device used in the literature for such studies is the Crystal16 (Technobis Crystallization Systems); the experiments presented in this work were carried out in such instrument, which was customized to our specifications. Photos of the experimental setup are provided in Section 2.5.1. The device comprises 16 reactors arranged in four blocks (labeled A,B,C,D), whereby each reactor may hold a vial of 11.6 mm outer diameter that allows for fill volumes of up to 1.5 mL. Each reactor block comprises an internal temperature sensor that is used to control the temperature profile during experiments. The temperature sensors were recalibrated by the manufacturer before the start of the experimental work. In addition, each vial is independently equipped with a thermocouple (K-type,

Inconel 600, certified by Picolog, sampling interval 1s) and a transmissivity sensor. For a more detailed description of the sensing equipment, we refer to earlier work of the group.[23] Here, we emphasize that both thermocouple and transmissivity sensor enable the detection of nucleation events. While the thermocouple data is used throughout the main body of the work, the use of transmissivity sensors as non-invasive alternative is discussed in Section 2.3.5.

The customizations of the Crystal16 device include the integration of a chilled cooling system. The cooling system enables operation down to −25°C in all four reactor blocks in parallel. To do so, a thermostat (Huber unistat 430, set to −10°C) has been directly connected to the Crystal16. A lower setpoint temperature in the thermostat would enable a lower minimum temperature in the Crystal16, however this was not required for the experimental campaign presented in this work. An important feature of the chilled cooling system is that its cooling capacity is sufficiently large to remove the latent heat of ice formation without heating up the neighboring vials. It is worth noting that preliminary experiments without additional cooling system revealed that freezing in one vial of the reactor block would heat up the neighboring vials, since the standard cooling system was unable to sufficiently remove the latent heat of solidification. This phenomenon was studied recently,[74] and it was found to significantly affect the thermal evolution profiles under a broad range of conditions. The capability to remove the latent heat of solidification in short time thus must be considered a necessary prerequisite of any parallelized experimental setup for ice nucleation studies.

2.2.4 Experimental campaign

The experimental campaign aims to establish and to assess a methodology for the estimation of ice nucleation kinetics in the context of pharmaceutical freezing and freeze-drying. In line with typical solutions used in the field,[40,74,93] 1 mL aqueous sucrose solution was selected as model system. Preliminary experiments revealed that the concentration range from pure water to 40 wt.% sucrose is experimentally accessible, so we focus here on the center of this range, i.e., on 20 wt.% sucrose solution. All experiments comprise freeze-thaw cycles, whereby the temperature is firstly decreased from +20°C to −25°C at a constant cooling rate, and then increased again to +20°C as fast as possible. Before initiating a new cycle, the temperature is held at +20°C for 10 minutes. Each experiment comprises twelve freeze-thaw cycles and sixteen vials, of which fifteen (Vials A1 to D3) are equipped with thermocouples. The remaining thermocouple was used to record the ambient temperature. We note that preliminary experiments revealed the minimum achievable temperature to be a function of the ambient temperature. Measure-

ments of the ambient temperature thus were used to rationalize variabilities in minimum temperature. For the experiments reported in this work, the cooling capacity was set sufficiently high to ensure that this variability does not affect the nucleation temperature measurements. The chosen number of cycles ensures that every experiment comprises enough nucleation events to be statistically relevant, in line with typical data set sizes in the crystallization literature.[23,24,91] Every experiment was carried out at least three times, whereby we refer to a single repetition of an experiment as *Series*. The campaign comprises the following experiments:

1. Series 1–4: Cooling rate of 0.6 $Kmin^{-1}$; discussed in Sections 2.3.1, 2.3.2, 2.3.3 and 2.3.5 .
2. Series 5–7: Alternating cycles (12 each) with cooling rates of 0.6 $Kmin^{-1}$ and of 0.2 $Kmin^{-1}$; discussed in Section 2.3.4.
3. Series 8–10: Cooling rate of 0.6 $Kmin^{-1}$, without thermocouples inserted; discussed in Section 2.5.3.
4. Series 11–13: Cooling rate of 0.6 $Kmin^{-1}$, without thermocouples inserted and with plastic vials instead of glass vials; discussed in Section 2.5.3.

The cooling rate of 0.6 $Kmin^{-1}$ was chosen to reflect typical values in pharmaceutical freeze-drying, which are in the range of 0.1-1.0 $Kmin^{-1}$.[41] For all experiments, the same experimental protocol was applied: before use, all glassware and thermocouples were cleaned with deionized water (Millipore, Milli-Q Advantage A10 system), then with acetone, then three times again with deionized water. Fresh sucrose stock solutions were prepared for every experiment by weighing 10 g of sucrose (Sigma-Aldrich, BioXtra grade, $>$ 99.5% purity) and filling with deionized water to a total mass of 50 g. The stock solution was filtered (0.22 μm hydrophilic PTFE syringe filter) and filled into glass vials (Lab Logistics Group GmbH, 1.5 mL) via a 100-1000 μL pipette (Socorex Acura 825). In some experiments, plastic vials (Thermo Fischer Scientific, 1.5 mL, polypropylene) were used instead of glass vials. All sample preparation steps were carried out under standard laboratory conditions, i.e., not under sterile conditions. This is important, because preliminary experiments indicated that aged sucrose solutions exhibit higher nucleation temperatures. We attribute this to the formation of biomass following bacterial growth. After overnight resting at ambient temperature, sucrose solution contained visible biomass. Thus, freshly prepared solutions were used in all experiments. If sterile conditions are required, one may carry out the sample preparation in a laminar flow hood, which may affect the nucleation behavior.[43]

2.2.5 Parameter estimation and statistical data analysis

A main objective of this work is the estimation of nucleation parameters using the method described in this section. The relationship for the nucleation frequency provided in Eqn. 2.3 is used as starting point for parameter estimation. A more complex version of Eqn. 2.3 that considers a variability in heterogeneous nucleation sites among vials will be derived as well. With respect to the temperature evolution within the vials, we assume that the temperature profile in the supercooled regime follows precisely the predefined cooling rate γ:

$$T(t) = T^{\mathrm{eq}} - \gamma t \tag{2.5}$$

whereby T^{eq} denotes the equilibrium freezing temperature of the solution, which may be computed using the expression derived by Blagden in 1788:[98]

$$T^{\mathrm{eq}} = T_{\mathrm{m}} - \frac{k_{\mathrm{f}}}{M_{\mathrm{s}}} \left(\frac{m_{\mathrm{s}}}{m_{\mathrm{w}}} \right) \tag{2.6}$$

where M_{s} is the molar mass of the solute, m_{s} its mass in solution, k_{f} the cryoscopic constant of water, T_{m} its melting point, and m_{w} its mass in solution. This equation provides a value $T^{\mathrm{eq}} = -1.35°\mathrm{C}$ for the studied 20 wt.% sucrose solution. For the thermal evolution given by Eqn. 2.5, the integral in Eqn. 2.1 can be calculated explicitly as

$$F(T) = 1 - \exp\left\{ -\frac{k_{\mathrm{b}} V}{\gamma(b+1)} (T^{\mathrm{eq}} - T)^{b+1} \right\} \tag{2.7}$$

where $F(T)$ denotes the cumulative probability (CDF) that a vial nucleates between the equilibrium freezing temperature and an arbitrary temperature T during cooling. Equation 2.7 links the set of kinetic parameters (b, k_{b}) with the distribution of nucleation temperatures. It may be applied in a stochastic manner to simulate random sets of nucleation temperatures for comparison with the experimental data. To do so, stochastic values of $F(T)$ are generated by drawing random numbers from the uniform distribution in [0,1]. The corresponding nucleation temperatures may then be computed via Eqn. 2.7. Similar approaches were recently implemented by Maggioni and Mazzotti[22] to simulate the stochastic formation of primary nuclei in crystallization processes, and by Deck et al.[74,75] to simulate the freezing process of biopharmaceuticals. With respect to the experimental data, we define an empirical cumulative distribution function (eCDF) $F^*(T)$ as follows

$$F^*(T) = \frac{\hat{N}_{\mathrm{tot}}(T)}{N_{\mathrm{tot}} + 1} \tag{2.8}$$

for an experimental data set that comprises N_{tot} nucleation temperatures. We note that $N_{tot} = N_c N_v$, since the chosen experimental strategy ensures that nucleation occurs in all N_v vials in all N_c cycles. $\hat{N}_{tot}(T)$ denotes the number of nucleation events that experimentally occurred within the temperature interval $[T^{eq}, T]$ out of the N_{tot} measured events. We underline that this definition of $F^*(T)$ differs from those provided in literature in one aspect, i.e., it contains a division by $N_{tot} + 1$, while literature expressions generally involve a division by N_{tot}.[23,24,68,97] To appreciate the difference between the two approaches, let us consider an eCDF comprising just one data point. The definition in Eqn. 2.8 attributes this data point a probability of 0.5, while the literature approach results in a probability of 1. Considering Eqn. 2.7, a probability of 1 is only achievable in case the exponential term approaches zero, which corresponds to an infinitely low value of the nucleation temperature. To avoid this non-physical behavior, we rely on the definition provided in Eqn. 2.8. It should be noted that this consideration is of general validity; we recommend to use this definition also in works related to nucleation of solutes in crystallization, for both isothermal and polythermal experiments.[78] Given the large data sets applied in these literature studies,[23,24,68,97] we posit that this non-physical behavior simply has been overlooked so far.

Parameter estimation in the context of stochastic nucleation is typically carried out by minimizing the difference between theoretical CDF and eCDF,[23,24] i.e., by identifying the set of parameters (b,k_b) that minimizes an objective function of the form

$$\min_{b,k_b} \sum_{j=1}^{N_{tot}} (F^*(T_j) - F(T_j))^2. \tag{2.9}$$

where T_j indicates the temperature at which the j-th nucleation event has been measured when arranging all experimental nucleation temperatures in descending order. This approach is based on the Glivenko-Cantelli theorem which states that the eCDF approaches the theoretical CDF in the limit of an infinitely large sample size:[99]

$$\lim_{N_{tot}\to\infty} \left(\sup_{1\leq j\leq N_{tot}} (F^*(T_j) - F(T_j)) \right) = 0 \tag{2.10}$$

Consequently, one expects an ideal agreement between model predictions and experimental data, if N_{tot} is sufficiently large. In previous works of our research group, this approach was applied to estimate the number of experiments that are required to compute the nucleation kinetics with a certain accuracy.[23,24] Here, we emphasize one of the underlying assumptions of this approach, namely that the N_{tot} measured nucleation temperatures are identically and independently distributed. As discussed in Sections 2.3.2 and

2.3.3, this assumption was found to be invalid in this work, since the measured nucleation temperatures exhibited a statistically significant variability among vials. When the eCDF is subject to such additional variability, which is not caused by the inherent stochasticity of nucleation, the agreement between CDF and eCDF is no useful criterion for parameter estimation. For this reason, an alternative approach to parameter estimation was developed in this work, derived from the method of moments estimator. For a model with M parameters to optimize, we define an objective function based on M characteristic quantities of the distribution. For the 2-parameter model described here, we base the optimization on the mean nucleation temperature $\bar{T}_{\mathrm{tot}}$ and the total variance σ^2_{tot}, which is defined as

$$\sigma^2_{\mathrm{tot}} = \frac{1}{N_{\mathrm{tot}} - 1} \sum_{j=1}^{N_{\mathrm{tot}}} (T_{\mathrm{j}} - \bar{T}_{\mathrm{tot}})^2 \tag{2.11}$$

The objective function then is

$$\min_{a,b} \left[\left(\frac{\bar{T}_{\mathrm{tot,exp}} - \bar{T}_{\mathrm{tot,sim}}}{\bar{T}_{\mathrm{tot,exp}}} \right)^2 + \left(\frac{\sigma^2_{\mathrm{tot,exp}} - \sigma^2_{\mathrm{tot,sim}}}{\sigma^2_{\mathrm{tot,exp}}} \right)^2 \right] \tag{2.12}$$

whereby a and b are the chosen response variables, with $a = -\log_{10}(k_{\mathrm{b}})$. Building on previous experience,[22] we apply the derivative-free MATLAB routine *fminsearch* to minimize the objective function; *fminsearch* is based on the Nelder-Mead Simplex method.[100]

When estimating model parameters from experimental data, an assessment of their uncertainty is of utmost interest in order to ensure that conclusions are drawn with statistical significance. Literature works on ice nucleation in the context of pharmaceutical freezing do not yet provide such information,[40,62] thus necessitating the development of a novel method to do so. We developed the following procedure to infer confidence intervals of the parameters subject to a significance level α via stochastic simulations:

1. Computation of the optimal parameter values for an experimental data set with N_{v} times N_{c} data points.
2. Stochastic simulation of a large number of data sets (i.e., 1,000 times) with N_{v} times N_{c} data points.
3. Computation of the value of the objective function for these data sets.
4. Exclusion of the fraction α of data sets that correspond to the highest values of the objective function.
5. Computation of the optimal parameter values for the remaining data sets.

6. Identification of the smallest and largest values for each parameters; these values correspond to the boundaries of the confidence interval.

In this work, a significance level of $\alpha = 0.1$ is used. In general, a smaller value of α leads to broader confidence intervals. Values of 0.05 and 0.2 were considered as well, but are not shown explicitly, since they did not affect any of the conclusions.

2.2.6 Accounting for additional experimental variability

Experimental variability that goes beyond the one induced by the inherent stochasticity of nucleation is commonly observed in studies on nucleation rate measurements. However, it is rarely investigated in detail due to numerous potential sources of experimental error.[23,24,97] One may classify the main sources of experimental variability as follows:

1. Variability in operating conditions: This comprises variability in temperature and concentration among vials and among repetitions.
2. Variability in growth time (period between nucleation and detection) among vials and among repetitions.
3. Variability in nucleation frequency: K is governed by both volume and nucleation rate, thus differences in these two quantities may contribute to variability in nucleation temperatures among vials.

Their relevance is discussed in the following for freezing in vials. Regarding variability in operating conditions, some differences in absolute temperatures were indeed observed among vials during cooling, as illustrated in Figure 2.2(b). These differences were on the order of 1 K, and they were found not to affect the effective cooling rate in the supercooled region; this is, all vials precisely followed the pre-defined cooling profile, but they did so with different lag times. A variability among vials in temperature only impacts nucleation if the effective cooling rate differs among vials (see e.g., Equation 2.7), whereas a mere delay of the cooling ramp is irrelevant. Hence, the observed temperature differences are of no concern for this study, as long as the temperature is measured accurately. We thus consider the accuracy of the thermocouples: when comparing the maximum temperature in a vial after nucleation, which is considered deterministic, all fifteen thermocouples reported values within a range of 0.3 K. This is smaller than the observed differences among vials, indicating that alternative factors such as minor position-dependencies in heat transfer contribute to them.

With respect to concentration, no relevant effects on the nucleation behavior are expected; solute concentration affects the ice nucleation behavior via its effect on the equilibrium freezing temperature. For the studied solution,

a deviation of for example 0.1 wt.% would be connected to a change in equilibrium temperature on the order of 0.01 K, i.e., it is of no practical relevance.

Regarding variability in growth time, the post-nucleation temperature rise was found to take place for the model system over the course of 1–2 s; the contribution of the growth rate towards the observed variability thus is to be considered negligible. This is in contrast to studies on solute nucleation in the field of crystallization, where growth may be considerably slower.[22,24,68,95]

What remains is the variability in nucleation kinetics among vials. Vials were filled with a pipette with a precision of $\pm$ 0.5 μL, amounting to a relative error in fill volume of 0.05%. Variability in fill volume thus may be considered negligible as well. For smaller volumes, as typically used in microfluidic crystallizers, such contribution may be more relevant. The theoretical framework to take into account such variability in volume was derived recently.[90,101]

In this work, we apply a similar approach to a variability in the nucleation rate. Such variability may stem from a variability in number and in activity of heterogeneous nucleation sites among vials; it is widely reported with respect to ice nucleation in the literature, however, mainly for freezing experiments in micro-droplets.[25,82,86,94] To the best of our knowledge, such effect has not yet been investigated in detail at the vial-scale, neither with respect to freezing, nor in the context of solute nucleation in crystallization.

We rely on the following assumptions to model the variability in nucleation rate, in line with the relevant literature:[25,43,82,86,94–96]

1. Ice nucleation occurs heterogeneously in all vials for all repetitions.
2. All nucleation sites have the same activity. Their number may vary among vials, but not among freeze-thaw cycles.
3. The nucleation frequency of a vial comprises the contributions of all its nucleation sites.

Let us apply these assumptions to the selected functional form of K (Eqn. 2.3): the pre-factor k_b is expected to vary among vials due to the variability in number of sites. The power parameter b, however, is vial-independent, since it depends only on the activity of the individual nucleation sites. Following literature on ice nucleation in microdroplets,[82,86] we impose a log-norm distribution for the pre-factor:

$$\log_{10}(k_{b,v}) = -(a + \xi_v c) \tag{2.13}$$

whereby $k_{b,v}$ is the vial-dependent pre-factor, which comprises a part that is independent of the vial, characterized by parameter a, and a vial-dependent

one, given by c; ξ_v is a number randomly drawn from the standard normal distribution. Note that the previously discussed vial-independent model is obtained by setting $\xi_\mathrm{v} c = 0$. The vial-dependent model thus may be interpreted as the generalized form of the vial-independent model. Indeed, in case only a single vial is studied, the two models are equivalent.

The more complex functional form of the vial-dependent model necessitates an adjustment to the parameter estimation approach. To quantify both the inherent stochasticity and the vial-to-vial variability, we interpret the total variance as combination of two contributions: the internal variance σ^2_int (i.e. variability within a vial) and the external variance σ^2_ext (i.e. variability among vials). The objective function for the parameter estimation thus is given as

$$\min_{a,b,c} \left[\left(\frac{\bar{T}_\mathrm{tot,exp} - \bar{T}_\mathrm{tot,sim}}{\bar{T}_\mathrm{tot,exp}} \right)^2 + \left(\frac{\sigma^2_\mathrm{ext,exp} - \sigma^2_\mathrm{ext,sim}}{\sigma^2_\mathrm{ext,exp}} \right)^2 + \left(\frac{\sigma^2_\mathrm{int,exp} - \sigma^2_\mathrm{int,sim}}{\sigma^2_\mathrm{int,exp}} \right)^2 \right] \tag{2.14}$$

whereby the internal variance $\sigma^2_{\mathrm{int},v}$ for an individual vial v is defined as:

$$\sigma^2_{\mathrm{int},v} = \frac{1}{N_\mathrm{c} - 1} \sum_{j=1}^{N_\mathrm{c}} (T_{\mathrm{v},j} - \bar{T}_\mathrm{v})^2 \tag{2.15}$$

The internal variance for the entire data set is then obtained via

$$\sigma^2_\mathrm{int} = \frac{1}{N_\mathrm{tot} - 1} \sum_{v=1}^{N_\mathrm{v}} \sum_{j=1}^{N_\mathrm{c}} (T_{v,j} - \bar{T}_v)^2. \tag{2.16}$$

The external variance σ^2_ext, on the other hand, denotes the variance in the vial mean nucleation temperatures $\bar{T}_v$ across the set of N_v vials in an experiment. It is thus defined accordingly as

$$\sigma^2_\mathrm{ext} = \frac{1}{N_\mathrm{v} - 1} \sum_{v=1}^{N_\mathrm{v}} (\bar{T}_v - \bar{T}_\mathrm{tot})^2. \tag{2.17}$$

2.3 RESULTS

We present experimental results for freeze-thaw cycling of 1 mL 20 wt.% sucrose solutions as well as for the related nucleation parameter estimation. In Section 2.3.1 we study the phenomenology of the observed thermal evolution profiles, and of the obtained nucleation temperatures. We estimate kinetic parameters from the experimental data in Section 2.3.2 based on the vial-independent model and in Section 2.3.3 based on the vial-dependent model;

for both models we critically assess the validity of the underlying assumptions. The models are further validated by comparing their predictions for experiments at various cooling rates with experimental data in Section 2.3.4. Finally, Section 2.3.5 presents and discusses an alternative method to detect nucleation events in a non-invasive manner via transmissivity measurements. This method is used to conduct a root cause analysis into the dominant type of the heterogeneous nucleation sites.

2.3.1 Phenomenology of freezing

Figure 2.2 presents the results for one out of four experimental series (i.e., Series 4) at a cooling rate of 0.6 K min^{-1} involving 15 vials and 12 cycles. Panel (a) shows the thermal evolution of the vial in position A1 during the experiment; the magenta line indicates the equilibrium freezing temperature and the red markers visualize the time and temperature of the nucleation events. Nucleation is identified based on the *thermal spikes* up to the equilibrium freezing temperature. This is shown in more detail in panel (b), which highlights the thermal evolution of the four vials in the A-block during the first cycle: upon nucleation, the temperature remains close to the equilibrium value for several minutes, until most of the water is solidified. Furthermore, nucleation occurred at different times and temperatures for the four vials, thus illustrating the variability of the process.

With respect to variability, panels (c,d) present scatter plots of all nucleation events (i.e., of all 15 vials and of all 12 cycles) measured during the experimental Series 4; they are shown in panel (c) grouped by vial, and in panel (d) grouped by cycle. As seen in panel (c), significant variability in nucleation temperatures is observed among vials. The vial in position A1, for example, nucleated consistently at lower temperatures than vial B3. When analyzing a larger body of experimental data, this variability among vials was found to be independent of reactor block, and of vial position in general. Such finding is of great relevance, since the conventional, vial-independent modeling framework does not consider such variability (cf. Section 2.2). With respect to variability among cycles (panel (d)), no significant cycle-to-cycle variability could be observed. This was found for all experiments carried out in this work. The absence of cycle-to-cycle variability implies that the number and activity of heterogeneous nucleation sites remains constant over time, which is a prerequisite for applying the stochastic models. Keeping in mind potential issues and limitations due to vial-to-vial variability, we proceed with parameter estimation.

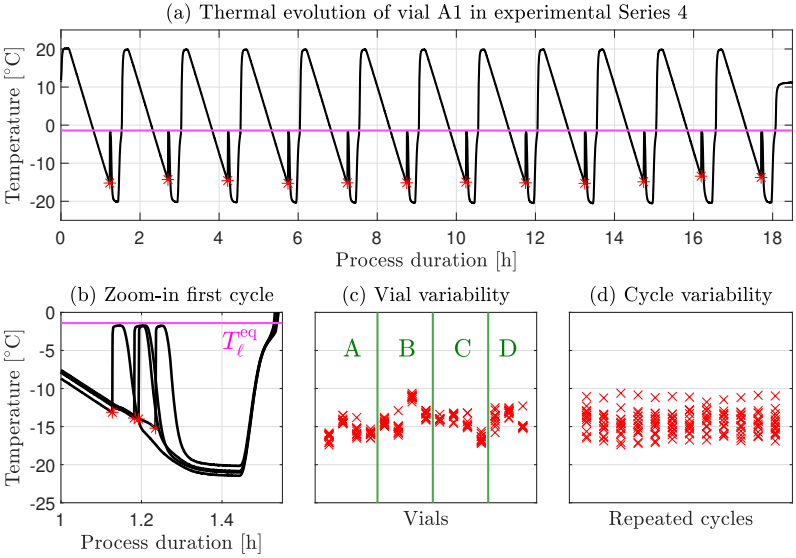

Figure 2.2 Experiment with constant cooling rate (Series 4). (a) Thermal evolution for the vial in position A1 during the entire experiment comprising 12 freeze-thaw cycles. (b) Zoom-in into the first cycle. The thermal evolution of the four vials in reactor block A is shown. (c) Scatter plot of nucleation temperatures (red), sorted by vial. The green letters indicate the reactor block. In each block, vials are sorted in ascending order, i.e., starting with the vial in position 1. Note that the vial in position D4 was not equipped with a thermocouple. (d) Scatter plot of nucleation temperatures, sorted by cycle.

2.3.2 Vial-independent parameter estimation

Parameter estimation is based on four repetitions of the experiment at 0.6 Kmin^{-1}, referred to as Series 1–4. Figure 2.3 presents the empirical cumulative distributions, both for the individual series (panel (a)), and for the combined set (panel (b)). Nucleation parameters were estimated (cf. top part of Table 2.1), and the simulated CDF for the combined data set is shown in panel (b); simulation and experiments are in quantitative agreement. A similar agreement was observed when fitting the individual Series (not explicitly shown).

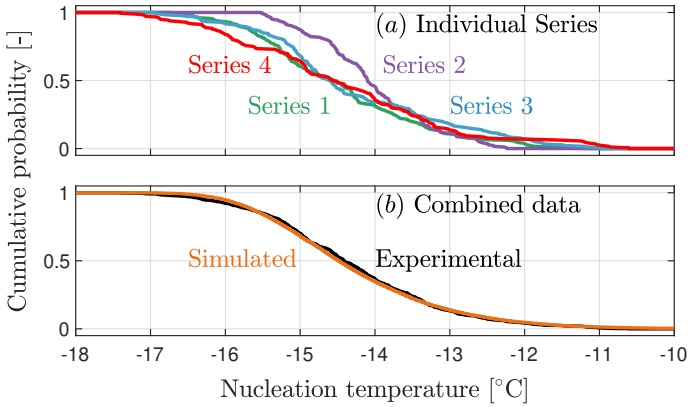

Figure 2.3 Empirical and simulated cumulative distributions for the studied sucrose solution. (a) Cumulative distributions of the individual Series. Each experiment comprises 15 vials with 12 cycles. Series 4, indicated in red, is presented in detail in Figure 2.2. (b) Combined data set comprising the four series, i.e., a total of 60 vials with 12 cycles. The black line indicates the experimental data, while the orange line shows the model predictions for the optimized set of parameters.

A closer investigation of Figure 2.3(a) reveals some variability among the individual series that may warrant further analysis. This is especially true for Series 2 (violet), for which nucleation events in average occurred earlier. Figure 2.4 presents all experimentally measured nucleation temperatures of the four series, and it shows that Series 2 experienced fewer nucleation events at extreme temperatures than the other series. Series 4, on the other hand, contains both the vial with the highest mean nucleation temperature, and the one with the lowest. In general, and in line with the observations in Section 2.3.1, statistically significant variability among vials is observed in the experimental data.

Consequently, further analysis is required to determine whether this variability among vials goes beyond the inherent stochasticity of nucleation. We do this in two ways. First, we consider the uncertainty in the optimized parameter values for the four individual series (see top part of Table 2.1); the confidence intervals for three of the four experimental series overlap, however, this is not the case for Series 2 (violet, cf. Figures 2.3(a) and 2.4). This implies that the empirical distribution of this experiment is statistically unlikely to be drawn from the same underlying distribution as the other series. This implies either that the experimental measures to ensure reproducibility were

insufficient, or that there is an additional source of variability that is not (yet) considered in the stochastic model.

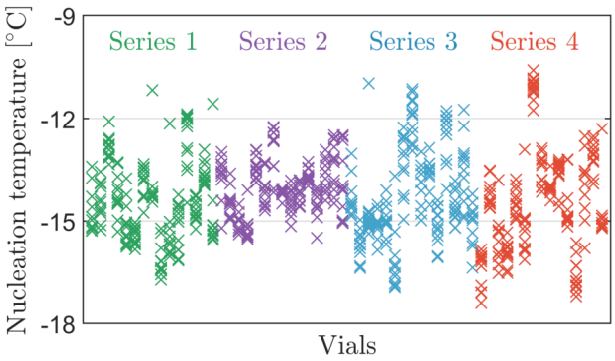

Figure 2.4 Experimental nucleation temperature data for Series 1–4, grouped by vial. The color-coding refers to the individual experimental Series. Series 4, in red, is presented in detail in Figure 2.2.

To test the latter hypothesis, we quantified the internal (within-vial) and external (vial-to-vial) variabilities of the entire data set, as introduced in Section 2.2.6. To this end, Figure 2.5 reports three distributions for both model predictions (red and blue) and experimental data (black). Panel (a) shows the distribution of nucleation temperatures, while panel (b) illustrates the distributions of vial mean nucleation temperatures, as a measure of variability among vials. Panel (c) reports the within-vial variance, as a measure of variability within vials.

Let us first consider the external variability in panel (b). As it can be seen, the vial-independent model considered here predicts a more narrow distribution compared to the experimental data. In fact, the experimental distribution is significantly broader than the simulated one: a total of one million vials with 12 cycles were simulated to generate the curve for the vial-independent model, whereby the highest simulated vial mean nucleation temperature was -12.4°C; however, 3 out of 60 vials in the experiments nucleated in average at even higher temperatures. This implies that an additional source of experimental variability is present that induces vial-to-vial variability, independent of and in addition to the inherent stochasticity of nucleation.

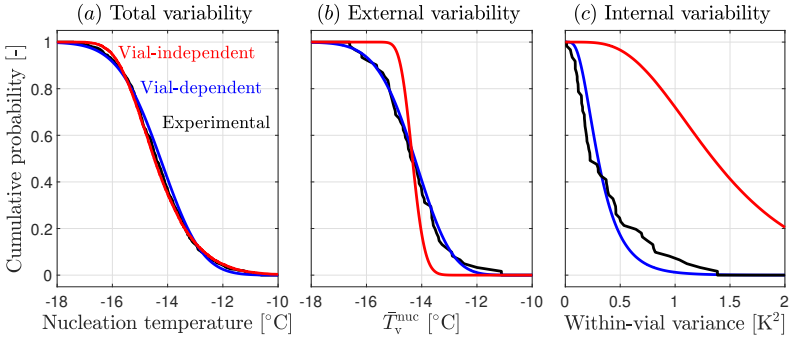

Figure 2.5 Agreement between experimental data (black) and the vial-independent (red) as well as vial-dependent (blue) model predictions. (a) Total variability, i.e., the cumulative distributions. (b) External variability, i.e., variability in mean nucleation temperature among vials. (c) Internal variability, i.e., variability in nucleation temperatures within individual vials.

Next, we consider the internal variability in panel (c). The simulated within-vial variance is significantly larger than the experimental one: 47% of the simulated vials exhibit a variability larger than the highest experimentally measured value. This again implies that the vial-independent stochastic model is unable to describe the variability observed in the experimental data. To this end, we introduce the notion of vial-dependency in Section 2.3.3.

2.3.3 Vial-dependent parameter estimation

The vial-independent model was found to over-predict the within-vial variance, while under-predicting the variability among vials. This implies that part of the total variability in nucleation temperatures stems from a vial-dependence of the nucleation frequency. To quantify such effect, we apply the vial-dependent modeling framework that was proposed in Section 2.2.6. The computed kinetic parameters and their uncertainty are provided in the top part of Table 2.1.

Series & Method	a	b	c
1 (TC, green), indep.	10.4 (8.5, 12.7)	12.7 (11.1, 14.8)	-
1 (TC, green), dep.	22.1 (16.6, 27.8)	23.5 (18.5, 28.5)	0.80 (0.43, 1.22)
2 (TC, violet), indep.	16.6 (13.9, 20.0)	18.6 (16.3, 21.7)	-
2 (TC, violet), dep.	29.4 (23.1, 36.8)	30.5 (24.9, 36.9)	0.69 (0.35, 1.06)
3 (TC, blue), indep.	8.2 (6.6, 10.2)	9.3 (10.7, 12.5)	-
3 (TC, blue), dep.	20.9 (15.7, 27.3)	22.4 (17.8, 27.8)	0.93 (0.51, 1.37)
4 (TC, red), indep.	6.8 (5.4, 8.5)	9.4 (8.2, 10.9)	-
4 (TC, red), dep.	26.9 (20.7, 34.7)	27.8 (22.6, 34.2)	1.39 (0.67, 2.28)
1–4 (TC), indep.	9.5 (8.6, 10.5)	12.0 (11.2, 12.8)	-
1–4 (TC), dep.	24.2 (21.2, 28.0)	25.5 (23.0, 28.8)	0.96 (0.67, 1.24)
1–4 (TM), indep.	10.3 (9.4, 11.4)	12.1 (11.3, 13.0)	-
1–4 (TM), dep.	29.0 (25.7, 33.4)	28.6 (25.8, 32.4)	1.08 (0.77, 1.43)
1–4 (TM, corr), indep.	8.2 (7.4, 9.1)	10.8 (10.0, 11.5)	-
1–4 (TM, corr), dep.	24.3 (21.3, 28.2)	25.6 (23.0, 28.9)	1.08 (0.80, 1.36)
5–7 (TC, fast), indep.	10.3 (9.3, 11.6)	12.7 (11.8, 13.8)	-
5–7 (TC, fast), dep.	23.0 (18.5, 26.5)	24.3 (20.3, 27.4)	0.83 (0.53, 1.11)
5–7 (TC, slow), indep.	11.5 (10.4, 12.8)	13.3 (12.4, 14.5)	-
5–7 (TC, slow), dep.	29.0 (25.2, 33.2)	29.3 (25.9, 33.2)	1.00 (0.64, 1.37)

Table 2.1 Computed model parameters for the seven experimental series discussed in the main body of this work. Parameters were estimated for both vial-independent (indep.) and vial-dependent (dep.) modeling methodologies. They correspond to the power law provided in Equation 2.3, i.e. $K = V k_b (T^{eq} - T)^b$. We note that $\log_{10}(k_{b,v}) = -(a + \xi_v c)$, as discussed in Equation 2.13. Nucleation was detected either via thermocouples (TC) or via transmissivity sensor (TM). All experiments involved a cooling rate of $\gamma = 0.6$ Kmin^{-1}, except for Series 5–7 with slow cooling ($\gamma = 0.2$ Kmin^{-1}). All confidence intervals are based on 1000 stochastic simulations and a significance level of 10%.

Let us first consider Figure 2.5, where the blue lines show the predictions of the vial-dependent model. When considering only the total variability (panel (a)), both the vial-dependent and the vial-independent modeling approaches provide a quantitative agreement. This implies that the cumulative distribution of nucleation temperatures alone is not a proper measure to validate the stochastic model and to estimate kinetic parameters, since the values of the optimized parameters are very different for the two models. While the vial-independent model fails to describe both external and internal variability (panels (b,c)), the vial-dependent model quantitatively agrees with the experimental data in terms of external variability. With respect to internal variability, we find a rather satisfactory agreement, which represents a significant improvement compared to the vial-independent model. These findings confirm that the vial-dependent model provides a superior description of the experimental variability.

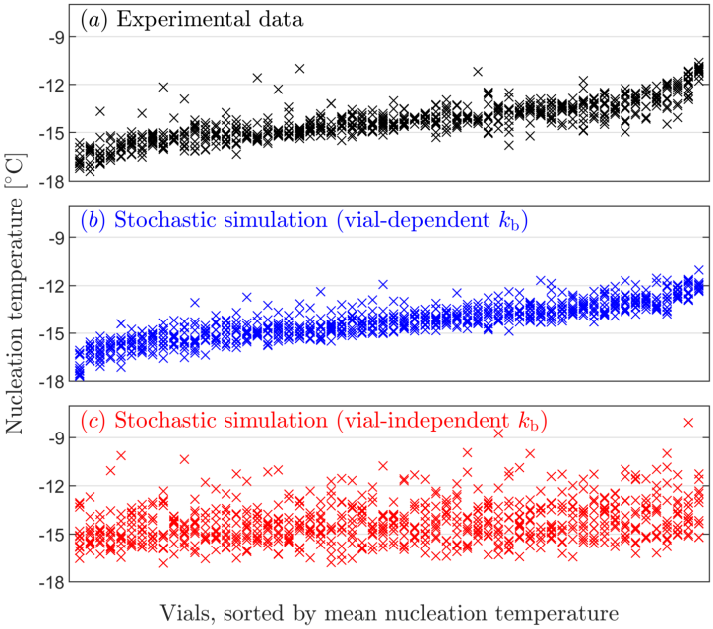

Figure 2.6 Comparison of experimental and simulated nucleation temperatures. Vials are sorted in the order of ascending mean nucleation temperature. (a) Experimental observation. (b) Stochastic simulation using the vial-dependent approach. The vial-dependency was simulated by sampling equidistant quantiles from the standard normal distribution when computing ξ_v. (c) Stochastic simulation using the vial-independent approach.

To appreciate the differences between the two models, let us directly compare the experimentally measured nucleation temperatures with simulated data. Figure 2.6 reports the combined experimental data of Series 1–4 (black) and stochastic simulations based on the optimized parameters for both vial-dependent (blue) and vial-independent (red) models. For the stochastic simulations, a data set of 60 vials with 12 cycles was simulated with both models, corresponding to the size of the experimental data set. The data sets are grouped by vials and arranged in the order of ascending vial mean nucleation temperature. As it can be observed with the naked eye, the vial-dependent approach (panel (b)) agrees more closely with the experimental data (panel (a)): it accurately captures the presence of both internal and external variabilities. The simulations by means of the vial-independent model (panel (c)), however,

only exhibit very little variability among vials, and overestimate the internal variability; this is in line with the findings reported in Figure 2.5.

While the analysis so far has been focused on the combined data set of Series 1–4, it is worth highlighting that the vial-dependent model also provides additional insights with respect to the individual experimental series. When considering the value of parameter c (cf. Table 2.1), which quantifies the extent of the vial-to-vial variability, we observe the largest value for Series 4 and the smallest one for Series 2. This is in line with visual observation of Figure 2.4 and indicates that the parameter c is physically meaningful. Furthermore, the vial-independent model discussed in Section 2.3.2 predicted with statistical significance that the four series are unlikely to exhibit the same nucleation kinetics. For the vial-dependent model, however, the confidence intervals of the optimized parameter values overlap for all series (cf. Table 2.1). This indicates that the observed variability among Series 1-4 indeed can be explained via the description provided by the vial-dependent model. Since the vial-dependent model considers two sources of uncertainty, the confidence intervals are naturally broader compared to the vial-independent model. We interpret this behavior as another indicator of the consistency and of the accuracy of the vial-dependent model.

2.3.4 Validation based on alternating cooling rates

As discussed in Section 2.3.3, accounting for a variability in nucleation sites among vials leads to a closer agreement between stochastic model predictions and experimental data. In order to understand the applicability of the computed parameters, it is essential not only to fit them to experimental data, but also to assess the predictive power of the model. Such validation is generally carried out by generating experimental data under different sets of operating conditions: the data from one set of conditions is used to compute parameter values, which then are applied to predict the outcome of the experiment carried out at the second set of conditions. To do so, we carried out a set of experiments (i.e., Series 5–7) with alternating cycles at cooling rates of 0.2 K min^{-1} and of 0.6 K min^{-1}. In this way, two sets of nucleation temperatures are obtained per experiment, namely one per cooling rate. Given that both cooling rates are studied within the same experiment, i.e., with the same vials, the number of nucleation sites is expected to be independent of cooling rate. Three series were carried out, and the computed parameter values of the combined data set (i.e. $3 \times 15 \times 12$ nucleation events per cooling rate) are reported in the lower part of Table 2.1. Figure 2.7 illustrates the outcome of experimental Series 5: it presents the applied thermal evolution profile (panel

(a)); the measured nucleation temperatures, grouped by vial (panel (b)); and the corresponding eCDFs of the nucleation temperatures (panel (c)).

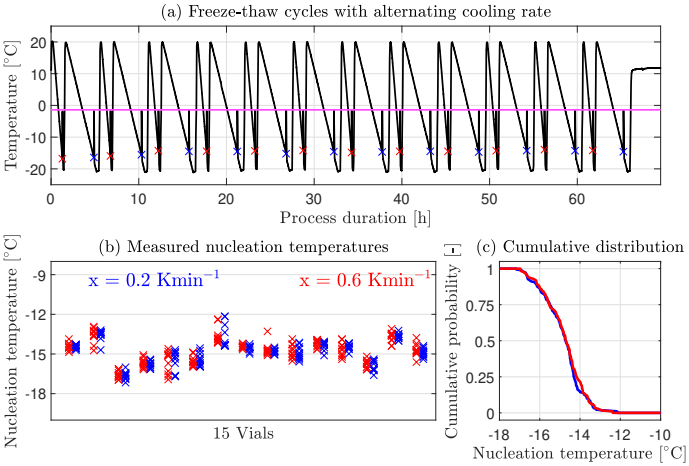

Figure 2.7 Experiment with alternating cooling rate (series 5). (a) Thermal evolution for twelve freeze-thaw cycles. The nucleation events are indicated with a colored cross; red indicates the faster cooling rate of 0.6 $Kmin^{-1}$, and blue the slower rate of 0.2 $Kmin^{-1}$. (b) Observed nucleation temperatures, shown per vial. (c) Corresponding empirical cumulative distributions.

Figure 2.7(b,c) shows that the nucleation temperature distributions are essentially independent of the cooling rate. To be precise, vials experiencing the slower cooling rate nucleated in average at 0.1 K lower temperatures. Such behavior appears counter-intuitive at first sight, given that literature generally indicates that slower cooling is correlated to higher nucleation temperatures, for both ice nucleation and for solute nucleation in crystallization.[22,74] In any case, we investigate whether the two models can predict this behavior. To this end, Figure 2.8 presents the empirical cumulative distributions for both cooling rates and compares them with model predictions. In panel (a), model parameters were computed from the nucleation temperatures at 0.2 K min^{-1} and the model then was applied to predict the behavior at a cooling rate of 0.6 K min^{-1}; panel (b) illustrates the outcome of the opposite procedure.

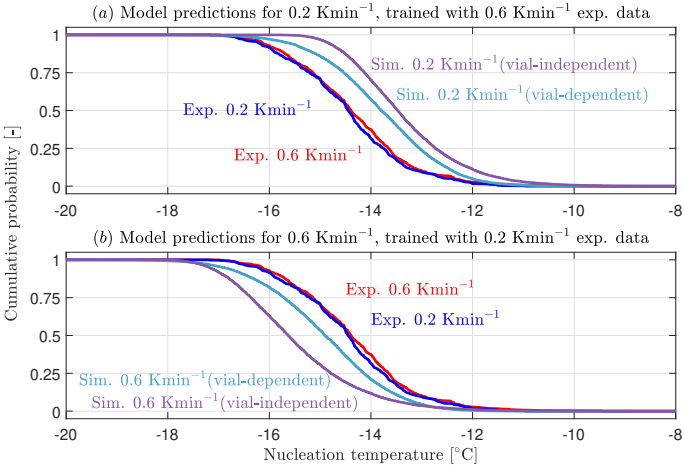

Figure 2.8 Comparison between experiments and model predictions for alternating cooling rates. Experimental distributions comprise the entire data set, i.e. three repetitions with 15 vials each. (a) Model predictions for 0.6 Kmin^{-1} after training with the 0.2 Kmin^{-1} experimental data. (b) Model predictions for 0.2 Kmin^{-1} after training with the 0.6 Kmin^{-1} experimental data. The used kinetic parameter values are summarized in Table 2.1.

Considering panel (a), both models predict too high a median nucleation temperature for the cooling rate of 0.2 K min^{-1}; 0.7 K too high in the case of the vial-dependent model, and 1.0 K too high in the case of the vial-independent model. Still, in terms of absolute numbers, both fits are sufficiently accurate for the use of the model in practical applications. The same view emerges from panel (b). Here, both models predict too low nucleation temperatures for the cooling rate of 0.6 K min^{-1}; too low by 0.5 K in the case of the vial-dependent model, and too low by 1.1 K in the case of the vial-independent one. Importantly, in both cases the vial-dependent model provides a superior predictive performance, which confirms that the vial-to-vial variability in nucleation sites is an essential element of the experimental variability.

We attribute the remaining, minor difference between experimental observation and vial-dependent model predictions to the presence of thermal gradients. Since vials are not stirred, thermal gradients within the vial form during cooling, and their extent depends on the cooling rate. As discussed in Section 2.2, spatial differences in temperature directly affect the nucleation frequency, whereby nucleation is more likely in colder regions of the vial. The thermocouples are positioned in the center of the vial's cross-section, close

to the top of the liquid. They measure the temperature at the warmest spot in the vial; this measurement becomes less representative for the entire vial volume in the case of larger gradients.

To quantify this effect, we derived an analytical expression for the steady-state temperature temperature profile during cooling with a constant cooling rate. The derivation is presented in Section 2.5.2. The predicted temperature differences between vial wall and thermocouple were of the same order of magnitude as the difference between the vial-dependent model predictions and the experimental validation data set. This implies that the vial-dependent model may indeed provide a quantitatively accurate description of the system, if one were to account for the thermal gradients.

With respect to the experimental methodology, we thus postulate that nucleation kinetics should be computed from experiments with slow cooling rates, where thermal gradients are negligible. For this work, this implies that the kinetic parameters computed from the 0.2 K min^{-1} data are more accurate than those obtained from the 0.6 K min^{-1} data. With respect to future work, we recommend choosing suitable cooling rates based on both accuracy and throughput considerations: while being more accurate, slow cooling rates are also linked to longer processing times, thus reducing the experimental throughput and increasing the risk of cycle-to-cycle variability.

2.3.5 Non-invasive sensing as alternative detection method

The methodology presented so far relied on invasive sensing, i.e., on the measurement of the thermal evolution by means of thermocouples (TC) placed within the vials. Such insertion may be counter-indicated in some settings; for example, in sterile manufacturing conditions in industry, where the content of a vial may be contaminated due to the insertion of a thermocouple.[43,102] Furthermore, the presence of thermocouples may affect the heat transfer within the vials, potentially leading to differences in process behavior among vials with thermocouples inserted and those without thermocouples; thus, process monitoring in the context of pharmaceutical freeze-drying in vials increasingly employs non-invasive sensing methods.[103]

For these reasons we developed a second method to detect nucleation events based on non-invasive transmissivity sensors (TM). The Crystal16 instrument is equipped with one transmissivity sensor per reactor, i.e., per vial. When nucleation occurs, ice grows rapidly and the solution turns into a non-transparent suspension; the TM sensor thus is capable to detect the *time* of the nucleation event in a non-invasive manner. However, it does not provide information regarding the *temperature* at the time of the nucleation

event. This temperature has to be inferred from readouts of the instrument's internal temperature probes, of which there is only one per reactor block, i.e. one per four vials. As shown for experimental Series 4 in Figure 2.2(b) in Section 2.3.1, these four vials may experience minor position-dependent temperature differences, which may affect the accuracy of the measurements.

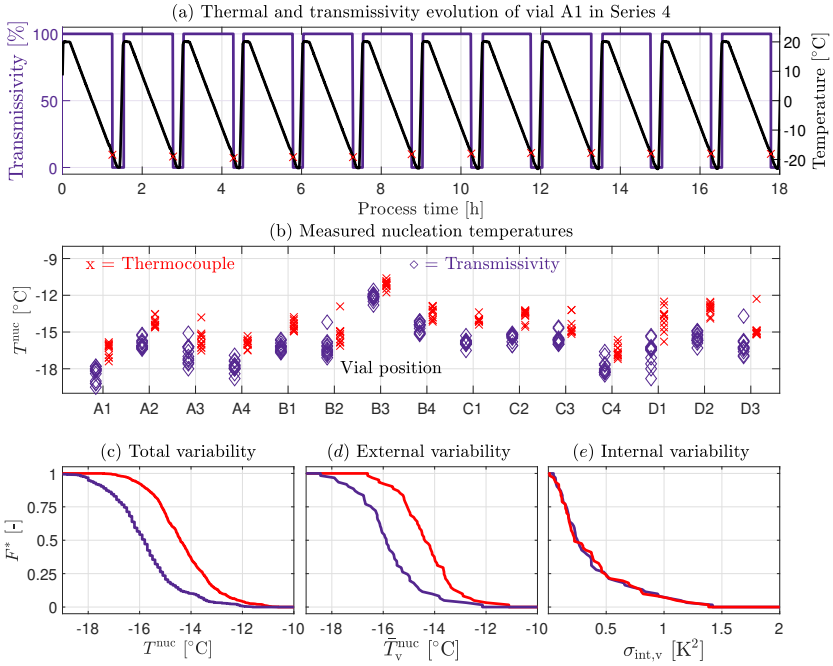

Figure 2.9 Comparison between invasive (thermocouple within vial, TC) and non-invasive (transmissivity) sensing. (a) Evolution of temperature and of transmissivity for a single vial (A1) during the entire experiment comprising 12 freeze-thaw cycles. (b) Measured nucleation temperatures, computed via thermocouple readouts and via transmissivity measurements. (c-e) Statistical analysis of the observed variability in nucleation temperatures. (c) Total variability. (d) Variability among vials, quantified based on vial mean nucleation temperatures. (e) Variability within vials, quantified based on the within-vial variance. Note that vial D4 was excluded from both measurements, since no thermocouple was inserted into this vial.

Figure 2.9(a) presents the thermal and trasmissivity evolution for Series 4 (see also Figure 2.2 for comparison with TC readouts). In each cycle, the transmissivity remains constant at 100 %, until a sharp drop occurs when ice

grows upon nucleation. We note that thermocouples were inserted during this experiment, which enables a direct comparison of both methods. Figure 2.9(b) shows the nucleation temperatures obtained from transmissivity readouts (violet) as well as those obtained from thermocouple readouts (red): the mean nucleation temperature for the transmissivity readouts is about 1.5 K colder, and the entire nucleation temperature distribution is shifted towards colder values, as indicated by Figure 2.9(c). Considering the external variability (panel (d)), both methods provide a similar shape for the profile of the vial mean nucleation temperature. The measured internal variabilities (panel (e)) for both methods were practically identical. Such behavior is expected: the temperature sensors used together with the transmissivity readouts measure not the temperature within the vials, but that of the surrounding reactor block. During cooling, there is a temperature gradient between the probe's position and the interior of the vial (where the thermocouple is). At the time of nucleation, the reactor block is slightly colder than the interior of the vials, which explains the lower nucleation temperatures obtained through the transmissivity method. Since internal and external variabilities are nearly unaffected by this effect, only minor differences in the computed kinetic parameters are observed between the two methods, as shown in Table 2.1(TC and TM). If the TM nucleation temperatures are corrected for the temperature gradient (TM, corr), the nucleation parameters (a, b) quantitatively match those obtained from the thermocouple readouts for the vial-dependent model. This is of great relevance, as it indicates that the parameter values are robust towards the choice of measurement method; hence, both methods may be used for parameter estimation.

For parameter c, both methods provide similar values as well, although not identical ones (0.96 for TC and 1.08 for both TM and TM,corr). The reason for this is that the TM method uses one temperature sensor per four vials; since the actual temperatures of these four vials may differ slightly (see Figure 2.2), this leads to additional uncertainty. While this effect is of minor relevance for the setup we use here, we recommend that future transmissivity-based methods rely on more temperature sensors, ideally one per vial.

As a final note, we applied the transmissivity method in this work to study the effect of thermocouple presence and of vial material on nucleation. This study is presented in Section 2.5.3; for the given model system, neither for the presence of a thermocouple nor for the material of the vial was the collected evidence strong enough to indicate a dominant role of the corresponding surfaces in nucleation. We conclude that the dominant nucleation sites likely are neither located on the thermocouple surface nor on the vial wall. Impurities within the solution thus are the most plausible candidate for the dominant nucleation sites. This is in line with findings in the literature, in the

context of ice nucleation in microdroplets,[94] of primary nucleation of solutes in vials,[95,96] and of ice nucleation in pharmaceutical freezing.[34,43]

2.4 DISCUSSION AND CONCLUSIONS

In the following, the implications of this work will be discussed in detail. First, we discuss the applicability of the presented method for pharmaceutical freezing and freeze-drying in Section 2.4.1. We further generalize this work and elaborate on its relevance for nucleation studies in the context of crystallization in Section 2.4.2, before drawing concluding remarks in Section 2.4.3.

2.4.1 Applications in pharmaceutical freezing and freeze-drying

This section highlights potential use cases for computed ice nucleation parameters in pharmaceutical manufacturing. We recently developed mechanistic models for the vial freezing process at commercial scale.[73–75] If the nucleation kinetics of the formulation to be frozen is known, these models predict the nucleation and solidification behavior of all vials in the batch and enable an estimate of the process duration and variability; the information provided by these models may be used as well to infer the subsequent drying rates in case of freeze-drying.[19,28,43,74]

An in-depth study of ice nucleation is useful to validate some theories commonly employed in the freeze-drying literature. For example, the literature reports that faster cooling leads to a smaller mean ice crystal size in the frozen product, which is hypothesized to be because nucleation temperatures are lower when cooling faster.[20,21] However, in this work we find that the cooling rate has little effect on nucleation under conditions relevant to pharmaceutical freeze-drying. Hence, there is a need to revisit how the nucleation temperature is linked to the mean ice crystal size (this is also discussed in our earlier work[74]).

2.4.2 Relevance for nucleation studies in the context of crystallization

While the presented parameter estimation approach has been developed specifically for freezing, the underlying principles are applicable to the field of crystallization and, specifically, to solute nucleation. Importantly, variability in nucleation sites among vials to our knowledge has not yet been considered

in solute nucleation studies. As we show in this work, the pre-factor k_b of the nucleation rate expression may differ by 10–20 orders of magnitude between vial-dependent and vial-independent stochastic models. Given that both solute nucleation and ice nucleation are generally considered to occur heterogeneously, we see merits in generalizing this concept to solute nucleation. Indeed, a variety of works on solute nucleation report significant disagreements between the stochastic predictions and the observed experimental data when using the conventional vial-independent modeling approach.[70,97]

It is unclear if heterogeneous nucleation *inherently* implies the presence of vial-to-vial variability, in which case it should be considered as an essential part of any stochastic description, or if it is of relevance only to specific systems. We thus deem a detailed statistical analysis of vial-to-vial variability in the context of solute nucleation to be an important avenue for future work. The modeling framework presented here may form the basis for such analysis.

As our findings indicate, quantifying vial-to-vial variability requires experiments involving both a large number of vials, and a large number of cycles. Being unaware of vial-to-vial variability, crystallization studies typically focus on the total number of experimental data points to characterize the inherent uncertainty,[23,68] and commonly employ experimental protocols with a large number of vials, and only few cycles. Indeed, a number of studies involve only a single experimental cycle per vial,[104,105] in which case no assessment of vial-to-vial variability is possible.

2.4.3 Concluding remarks

To conclude, we have developed and validated a novel methodology to measure the ice nucleation kinetics of aqueous solutions in vials based on parallelized experiments at mid-throughput and on a refined stochastic modeling framework. The study revealed two additional sources of experimental variability which induce variability in nucleation temperatures beyond the one created by the inherent stochasticity of nucleation. These are, first, the variability in nucleation sites among vials, and second, the occurrence of temperature gradients during cooling. We discussed the role of nucleation sites in detail and integrated it into a multi-component stochastic description of nucleation with vial-dependent nucleation parameters. Doing so led to a closer agreement between experimental data and model predictions, as was validated in experiments with alternating cooling rates. Importantly, this vial-dependent model predicted the experimental behavior significantly better than the vial-independent model. Similarly, the magnitude of the thermal gradients during cooling was computed and it was found to be large enough

to explain the remaining, minor difference between experiments and model prediction.

In order to suit the needs of the pharmaceutical industry, where sterile manufacturing conditions may not allow for invasive sensing, we developed a second experimental method to detect nucleation events. This method relies on transmissivity sensors that were found to reliably detect the time of nucleation; the corresponding temperature at this time is to be inferred from external temperature sensors. In this work, we have used this non-invasive method to investigate whether the presence of a thermocouple in the vial or the vial material affects nucleation. In both cases no statistically significant effect could be identified, likely due to the high particulate content in standard laboratory conditions. Furthermore, we confirmed that invasive and non-invasive methods predict similar nucleation parameters.

Finally, we envision that the ice nucleation kinetics is explicitly taken into account in the process and formulation design for a variety of biopharmaceuticals in the long-term. This ultimately may enable more efficient freezing process design, with potential positive implications for residual drug activity. The methodology presented in this work may form the basis for such endeavor.

2.5 SUPPLEMENTARY INFORMATION

2.5.1 Photos of the experimental setup

This section aims to visualize the used experimental setup. Figure 2.10 shows the entire setup, comprising Crystal16 instrument (left), desktop computer (center) and thermostat (right). Figure 2.11 shows a zoom-in into the Crystal16 instrument. The Crystal16 is connected with the thermostat via the black, insulated tubing at the bottom right of the device. Internally, the tubing is linked to a heat exchanger, which dissipates heat from the heat sink of the instrument.

Figure 2.10 Ice nucleation setup, comprising Crystal16 instrument (left), desktop computer (center) and thermostat (right).

Furthermore, the sixteen thermocouples can be seen, fifteen of which are inserted into the device. The black aluminum blocks ensure that the position of the vials and thermocouples stays constant during the experiment; this addition is necessary, since the caps of the reactor blocks (blue, behind the thermocouple wires) cannot be closed when the thermocouples are inserted. The final thermocouple is found in the back, on the left side, measuring the ambient temperature. Note that while reactor D4 does not contain a thermocouple, it is filled with a vial containing the same solution as the other fifteen; this ensures that the heat transfer conditions in all four blocks are as similar as possible.

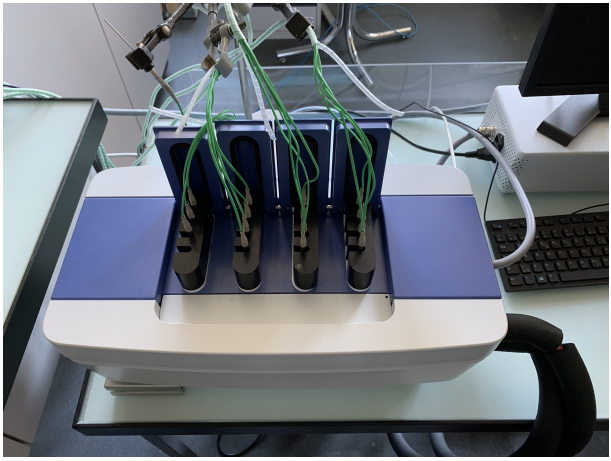

Figure 2.11 Crystal16 instrument during an experimental run with all vials loaded.

2.5.2 Modeling thermal gradients

In order to quantify the thermal gradients within a vial during cooling, we may formulate an enthalpy balance subject to the following assumptions:

1. The vial is of cylindrical geometry with radial coordinate r and radius R.
2. All positions within the vial cool down with the same, constant cooling rate γ.
3. Thermal gradients are dominated by the radial direction, neglecting vertical contributions.

The balance then reads

$$\frac{\rho c_\mathrm{p}}{\lambda}\frac{\partial T}{\partial t} = \frac{\partial^2 T}{\partial r^2} + \frac{1}{r}\frac{\partial T}{\partial r} \tag{2.18}$$

Considering that $\dfrac{\partial T}{\partial t} = -\gamma$, the balance simplifies to

$$\frac{-\gamma \rho c_\mathrm{p}}{\lambda} = \frac{\partial^2 T}{\partial r^2} + \frac{1}{r}\frac{\partial T}{\partial r} \tag{2.19}$$

This balance is subject to the boundary conditions $\frac{\partial T}{\partial r}(r = 0, t) = 0$ and $T(r = R, t) = T_0(t)$, where $T_0(t)$ is the temperature at the walls of the vial; during cooling this corresponds to the coldest point. Note that the absolute

value of $T_0(t)$ is not of interest, given that this analysis solely focuses on quantifying the temperature differences within the vial. Solving the differential equation subject to the presented boundary conditions yields

$$T(r) - T_0 = (R^2 - r^2)\frac{\rho c_p \gamma}{4\lambda_v} \tag{2.20}$$

Let us apply this equation to compute the difference in temperature between the thermocouple positioned in the center (at $r = 0$) and the vial walls. The vial has an inner radius of $R = 5.0$ mm, while the physicochemical parameters of the solution are assumed to be linear combinations of those for pure water and pure sucrose. Densities, heat capacities and thermal conductivities for the pure substances were sourced from the literature.[40] Cooling rates of 0.6 K min^{-1} and of 0.2 K min^{-1} yield temperature differences between vial wall and center of 0.46 K and of 0.16 K, respectively. These differences should be interpreted as lower bound for thermal gradients within the vial, as we do not consider vertical gradients here.

2.5.3 Investigating the dominant type of heterogeneous nucleation sites

The results presented in Sections 2.3.3 and 2.3.4 indicate that the observed vial-to-vial variability in nucleation behavior stems from a difference in heterogeneous nucleation sites among vials. This finding motivates the question which type of surface is dominating the nucleation rate in the studied system. This section addresses this question by comparing the results of three experimental studies:

1. Glass vials with thermocouples inserted (i.e., Series 1–4)
2. Glass vials without thermocouples (i.e., Series 8–10)
3. Plastic (polypropylene) vials without thermocouples (i.e., Series 11–13)

This comparison enables the quantification of effects of thermocouples and of vial material on nucleation. Thermocouple effects, for example, are commonly reported in the literature related to pharmaceutical freeze-drying, as discussed in the main body of this work. Figure 2.12 presents the experimental results for three experimental series, i.e. glass vials with thermocouples inserted (blue and violet), glass vials without thermocouple (green) and plastic vials without thermocouple (red).

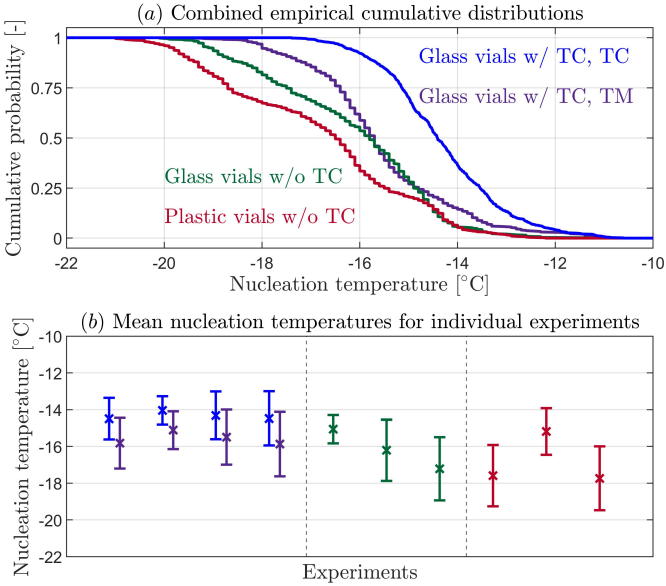

Figure 2.12 Single cooling rate experiments for various measurement and preparation methods. (a) Combined eCDFs for the experiments in glass vials with thermocouples (4 experiments with 15 vials each), without thermocouples (3 experiments with 16 vials each), as well as in plastic vials without thermocouples (3 experiments with 16 vials each). TM indicates that the measurement was carried out via the transmissivity sensor. Due to the limited thermal resolution of the internal sensors used for the transmissivity method (0.1 K), the corresponding eCDFs appear more step-like than those generated directly from thermocouple readouts (resolution 0.01 K). (b) Corresponding comparison of mean nucleation temperatures and their variability across the experiments. The error bars indicate one standard deviation.

With respect to the experiments in glass vials with thermocouples, all measurements via transmissivity are linearly shifted towards lower temperatures, compared to the thermocouple readouts; this is in line with the findings discussed before. When comparing the three sets of transmissivity measurements, the glass vials with inserted nucleation temperatures nucleate in average at slightly higher temperatures than those without thermocouple. However, only a single experiment is responsible for this difference, making it hardly statistically significant. Plastic vials were found to nucleate at even lower temperatures in average, with two out of three series having the lowest mean nucleation temperatures across all presented studies. It must be noted, how-

ever, that it was observed experimentally that the plastic vials were of slightly smaller diameter than the glass vials, despite specifications indicating the same outer diameter. This minor difference in geometry led to the formation of a small air gap between plastic vial and reactor. This gap may slow down heat transfer and thus increases the external temperature gradient. In consequence, the lower nucleation temperatures may be caused either by the change in nucleation sites on the vial surface, or by the change in external temperature gradient.

Given this additional uncertainty (and the high nucleation temperatures in the second experiment), we may not conclude that plastic vials statistically lead to lower nucleation kinetics. To enable such statement, a more precise characterization of the transmissivity method would be required for the plastic vials, i.e. a direct comparison with the invasive method. However, this could not be carried out within this work, since the neck type of the plastic vials did not allow for connection with the thermocouples. Here, we conclude that the transmissivity method provides a useful alternative method to measure nucleation temperatures, that is especially beneficial in order to understand the effects of heterogeneous nucleation sites. It may be used for measurements under realistic, sterile manufacturing conditions in the pharmaceutical industry. However, the technical specifications of the setup have to be studied in detail in order to characterize the accuracy of the method. Based on the presented experimental studies, neither the presence of thermocouples, nor the vial material could be confirmed to influence the mean nucleation temperatures significantly.

3 THERMODYNAMICS EXPLAINS HOW SOLUTION COMPOSITION AFFECTS THE KINETICS OF STOCHASTIC ICE NUCLEATION

The freezing of aqueous solutions is of great relevance to multiple fields, yet the kinetics of ice nucleation, its first step, remains poorly understood. The literature focuses on the freezing of micrometer-sized droplets, and it is unclear if those findings can be generalized and extended to larger volumes, such as those used in the freezing of biopharmaceuticals. To this end, we study ice nucleation from aqueous solutions of ten different compositions in vials at the millilitre scale. The statistical analysis of the about 6,000 measured nucleation events reveals that the stochastic ice nucleation kinetics is independent of the nature and concentration of the solute. We demonstrate this by estimating the values of the kinetic parameters in the nucleation rate expression for the selected solution compositions, and we find that a single set of parameters is able to describe quantitatively the nucleation behavior in all solutions. This holds regardless of whether the nucleation rate is expressed as a function of the chemical potential difference, of the water activity difference or of the supercooling. While the chemical potential difference is the thermodynamically correct driving force for nucleation and hence more accurate from a theoretical point of view, the other two expressions allow for an easier implementation in mechanistic freezing models in pharmaceutical manufacturing.

3.1 MAIN SECTION

Despite a long history of research on the freezing of aqueous solutions, the nature of some underlying phenomena remains elusive. This is especially true for ice nucleation, which denotes the formation of the first ice crystal from a clear solution.[20,45,64] Its kinetics is of great relevance to multiple fields, from

The work presented in this chapter has been reported in: Deck, L.-T.; Wittenberg, L.; Mazzotti, M. Thermodynamics Explains How Solution Composition Affects the Kinetics of Stochastic Ice Nucleation. *J. Phys. Chem. Lett.* **2023**, 14, 26, 5993–6000.

cloud microphysics[27,86,106], to cryobiology[88,107], to pharmaceutical manufacturing[20,21]. The formation of a nucleus is a stochastic event,[66,94] so that solutions of identical composition that are stored under identical conditions nucleate at different, randomly distributed times.[19,74] Such behavior is highly undesirable in pharmaceutical manufacturing, because of its strict quality control regulations for the freezing of biopharmaceutical drug products.[62,108] The majority of biopharmaceuticals, including most commercially available vaccines against COVID-19, is formulated and distributed in a frozen or freeze-dried state in vials of millilitre scale.[1,4,75] Still, mechanistic descriptions of ice nucleation in models for the freezing of these products have become available only recently.[74–76]

This is largely because research on ice nucleation has traditionally been driven by the atmospheric sciences.[58,60,82,83] To mimic the properties of cloud droplets, freezing experiments have been predominantly carried out in micro-droplets.[27,109–111] In such small volumes, ice nucleation may occur homogeneously, i.e., independent of the so-called heterogeneous nucleation sites;[27,58] this is because these sites are located for instance on dust particles, whose concentration is low enough that a sufficiently small droplet contains none of them. For the freezing of biopharmaceuticals in vials, however, nucleation has been shown to be governed by heterogeneous nucleation sites.[43,76,102] Heterogeneous nucleation has been studied at the micro-scale as well, by inserting ice-nucleation agents such as mineral dust particles in a controlled manner.[59,112–114] Such insertion of foreign materials to control the nucleation rate, however, is unlikely to find acceptance in pharmaceutical manufacturing due to product quality considerations.[43,102] For these reasons, the large body of literature on ice nucleation has received little attention from researchers and practitioners working on the design and optimization of pharmaceutical freezing processes.

In this contribution, we address this gap by studying ice nucleation in aqueous solutions in vials of millilitre scale, that is, under conditions relevant to pharmaceutical manufacturing. We carried out a large experimental campaign comprising about 6,000 freezing events to accurately capture the stochastic nature of ice nucleation by exploiting a methodology developed recently.[76] In short, vials were filled with 1 mL of solution and were cooled down at a constant cooling rate of 0.6 K min^{-1} to a temperature of -25°C. The time and temperature when ice nucleation occurred were measured by means of thermocouples inserted into each vial. To generate data sets of statistical relevance, three to four experiments were carried out, each comprising twelve freeze-thaw cycles and fifteen vials; this yields 540 to 720 nucleation temperatures for each solution composition (further information about the methodology is provided in Section 3.2). Ten different solutions were studied, which contain

sucrose, trehalose and sodium chloride at different concentrations. The three solutes represent commonly used excipients in biopharmaceutical formulations,[21,41] and their physicochemical properties are sufficiently different to allow contending that the findings presented here are of general relevance. That is, we show first that the solution composition affects the nucleation behavior predominantly through the solution's thermodynamic properties. Second, we demonstrate that the nucleation rate can be expressed with comparable quantitative accuracy through a driving force given in terms of a difference either in chemical potential, in water activity, or in temperature.

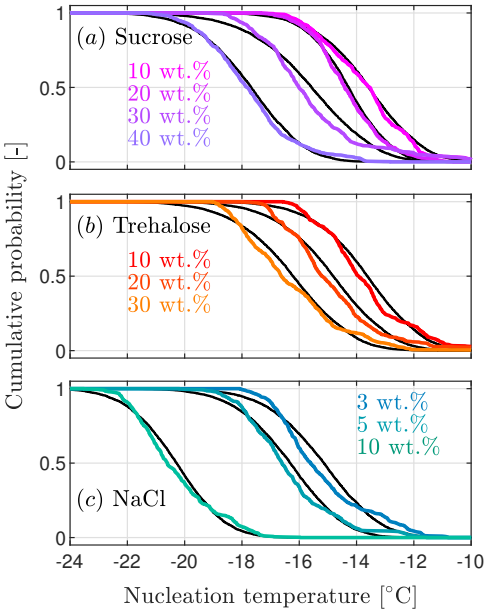

Figure 3.1 Cumulative distributions of the experimentally measured nucleation temperatures, i.e., the fraction of instances where nucleation has occurred when cooling down the solution to a specific temperature. The colored lines represent the experimental data, while the black lines show the optimal model fit for the supercooling-based parameterization of nucleation. (a) Sucrose solutions of four concentration levels. (b) Trehalose solutions of three concentration levels. 40 wt.% solutions were not studied due to the lower solubility of trehalose compared to sucrose. (c) Sodium chloride solutions of three concentration levels.

Figure 3.1 shows all the measurements of nucleation temperatures during a cooling ramp for the ten aqueous solutions considered. Each colored symbol (point) gives the fraction of vials (vertical coordinate) already nucleated at the corresponding temperature (horizontal coordinate); obviously, such fraction increases monotonically as the temperature decreases, until it reaches one at a temperature low enough where all vials have nucleated. The resulting curve is called the empirical cumulative distribution function (the CDF of nucleation temperatures in this case), and can also be calculated using a nucleation model (these are the black solid lines in Figure 3.1 that will be discussed below). Considering that the nucleation temperature is measured with an accuracy of $\pm$ 0.15 K, that the experimental conditions are the same for all points on a curve (same solute concentration and cooling rate), and that the first and the last nucleation temperature differ in all ten cases by 5–7 K, one can safely conclude that nucleation is the main source of the observed variability.

However, Figure 3.1 does not show *how* nucleation induces this variability, i.e., whether it is due to its inherent stochasticity or it is due to random differences in heterogeneous nucleation sites among vials. In earlier work we have observed that both effects are relevant,[76] and this is the case here as well. To demonstrate this, we plot in Figure 3.2 all the 6,000 measured nucleation temperatures. Each panel reports the data for one solution composition; the twelve nucleation temperatures measured per vial are arranged in columns sorted by ascending vial mean nucleation temperature. The horizontal lines indicate the equilibrium freezing temperature, i.e., the melting point. Independent of solution composition, the nucleation temperatures within most vials vary by 2–3 K. As no significant variability among cycles has been observed (not shown explicitly), it is safe to assume that the nucleation sites within each vial remain unchanged throughout an experiment. Hence, the variability in nucleation temperatures within vials is due to the inherent stochasticity of nucleation. In addition to this inherent stochasticity, the vials with the lowest nucleation temperatures (on the left of each panel), nucleate in average at about 5 K lower temperature levels than those with the highest nucleation temperatures (on the right of each panel). This phenomenon is due to differences in the nucleation sites among vials: the vials that nucleate earlier must contain either more numerous or more active sites than the late-nucleating ones.

Further, it is worth noting that for the same solute, increasing concentration shifts nucleation towards lower temperatures, which is consistent with the fact that the equilibrium freezing temperature T^{eq} of the solution also decreases with increasing solute concentration (see Figure 3.2).[98,115,116]

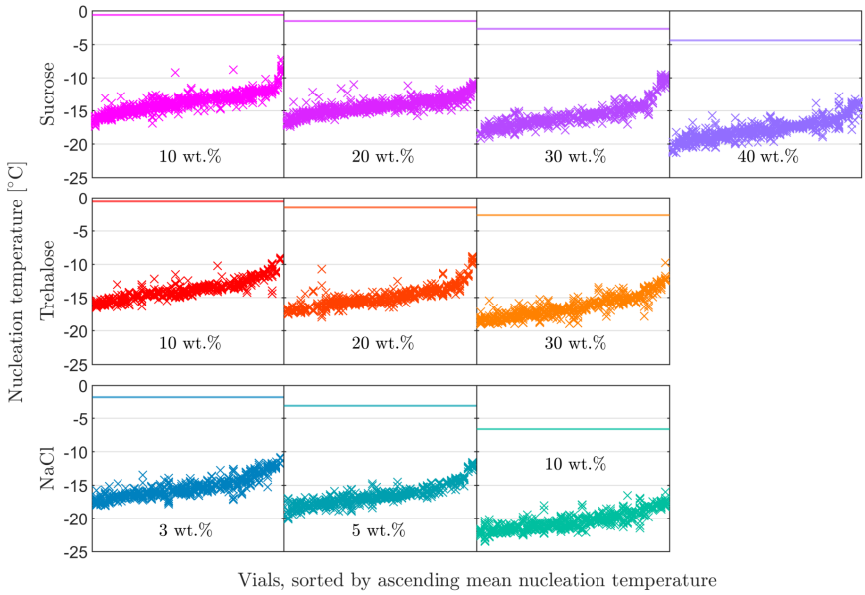

Figure 3.2 Overview over all measured nucleation temperatures. Each panel shows the data for one solution composition: the twelve nucleation temperatures measured per vial are arranged in columns sorted by ascending mean nucleation temperature. The horizontal lines indicate the equilibrium freezing temperature. Top row: sucrose. Center row: trehalose. Bottom row: sodium chloride.

Figure 3.3(a) illustrates a nucleation experiment within the binary water-solute phase diagram, with coordinates water activity, a_w, and temperature, T. Water activity is a convenient quantity to express the driving force for nucleation, because - though it depends on the solute concentration - its temperature-dependence is negligible.[58–60] The black solid line denotes the solid-liquid equilibrium between ice and solution. It is defined through the Schröder van Laar (SvL) equation, which gives the equilibrium water activity $a_w^{eq}(T)$ as a function of temperature, or conversely, the equilibrium freezing temperature $T^{eq}(a_w^0)$ as a function of the solution's water activity a_w^0:[61]

$$\ln\left(a_w^{eq}\right) = \frac{\Delta H}{R}\left(\frac{1}{T^m} - \frac{1}{T}\right) - \frac{\Delta c_p}{R}\left(\ln\left(\frac{T^m}{T}\right) + 1 - \frac{T^m}{T}\right) \tag{3.1}$$

where $\Delta H = 6002\ \mathrm{J\ mol^{-1}}$ is the latent heat of fusion of pure ice, $\Delta c_p = 38.03\ \mathrm{J\ mol^{-1}\ K^{-1}}$ is the difference in heat capacity between liquid water and ice, and

$T^{\mathrm{m}} = 273.15$ K is the freezing point of pure water, all evaluated at ambient pressure. Thus, with reference to Figure 3.3(a), the cooling experiment starts from a point of coordinates (a_{w}^0, T^0), and the solution's state evolves along a vertical line, whose points have coordinates (a_{w}^0, T). For $T > T^{\mathrm{eq}}$, the solution is in a thermodynamically stable state; for $T < T^{\mathrm{eq}}$ it enters a metastable state that persists until the phase transition is triggered by nucleation.

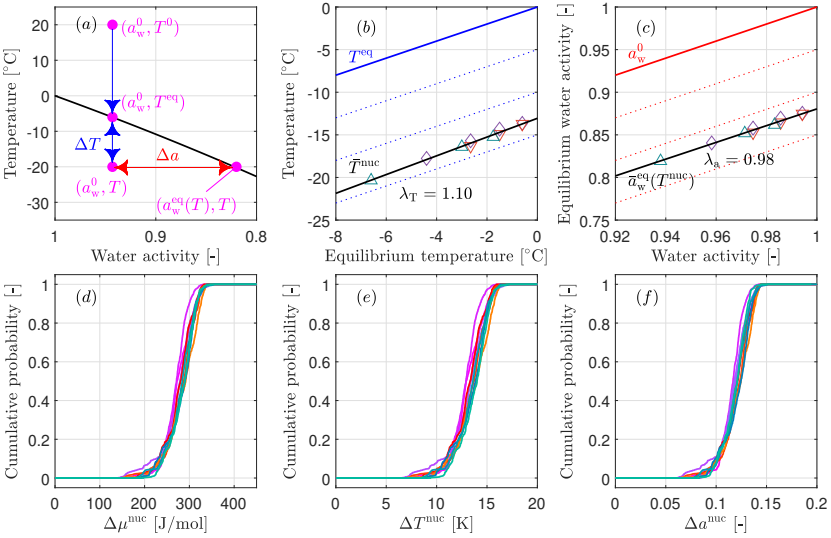

Figure 3.3 (a) Temperature-water activity diagram for the freezing process of aqueous solutions. The black line indicates the solution's equilibrium properties, while the blue line shows the change in temperature during the process. (b,c) Mean nucleation temperatures $\bar{T}^{\mathrm{nuc}}$ and mean nucleation activities $\bar{a}_{\mathrm{w}}^{\mathrm{eq}}(T^{\mathrm{nuc}})$ for the ten studied solution compositions. The data points are arranged by equilibrium freezing point or by the corresponding water activity of the solution. The black line indicates the linear relationships between the solution's equilibrium properties and the mean nucleation behavior. The dashed lines denote the iso-supercooling (blue) or the iso-activity difference (red) curves. Red indicates the activity difference Δa to the equilibrium. (d,e,f) Rescaled nucleation temperature distributions in terms of chemical potential difference $\Delta\mu^{\mathrm{nuc}}$, of supercooling ΔT^{nuc} and of water activity difference Δa^{nuc}. The color-coding for the solution compositions is the same as the one used in Figure 3.1.

The thermodynamic driving force for nucleation is the difference in chemical potential between ice and the solution, termed $\Delta\mu$:

$$\Delta\mu = RT\ln\left(\frac{f_\ell}{f_\mathrm{i}}\right) = RT\ln\left(\frac{f_\ell}{f_\ell^\mathrm{eq}}\right) = RT\ln\left(\frac{a_\mathrm{w}}{a_\mathrm{w}^\mathrm{eq}}\right) \tag{3.2}$$

where f_i and f_ℓ are the fugacities of ice and of water in solution, respectively, and f_i equals the fugacity of water in solution when at equilibrium with ice crystals, i.e., f_ℓ^eq. The last expression follows when considering that fugacity is the product of a reference fugacity and the activity of water. With reference to the schematic in Figure 3.3(a), we note that the distance of the solution's state to the equilibirum can be expressed either (i) as difference of the activities, i.e., $\Delta a_\mathrm{w} = a_\mathrm{w}^0 - a_\mathrm{w}^\mathrm{eq}(T)$, as typically used in the atmospheric sciences;[58–60] or (ii) as difference of temperatures, i.e., $\Delta T = T^\mathrm{eq} - T$, which is also called degree of supercooling and is preferred in pharmaceutical applications due to its experimental accessibility.[19,62,75] The expression for the chemical potential can be rewritten in terms of these quantities when taking the appropriate simplifications:

$$\Delta\mu = RT\ln\left(\frac{a_\mathrm{w}}{a_\mathrm{w}^\mathrm{eq}}\right) \approx \frac{RT}{a_\mathrm{w}^\mathrm{eq}}(a_\mathrm{w} - a_\mathrm{w}^\mathrm{eq}) = \alpha(T)\Delta a \tag{3.3}$$

$$\Delta\mu = RT\ln\left(\frac{a_\mathrm{w}}{a_\mathrm{w}^\mathrm{eq}}\right) \approx \frac{\Delta H}{T^\mathrm{eq}}(T^\mathrm{eq} - T) = \beta\Delta T \tag{3.4}$$

As it can be seen, interpreting $\Delta\mu$ as a function solely of Δa requires (i) linearization of the logarithm, and (2) neglecting the temperature-dependency of the pre-factor α. In contrast, to arrive at the expression for ΔT, no linearization is required, however, the Δc_p term in the Schröder-van Laar equation is neglected.

Our working hypothesis is that $\Delta\mu$, Δa and ΔT can all quantify the driving force for nucleation, even though likely with different accuracy. Moreover, we conjecture that the nucleation rate is given by a power law expression, and that it can be calculated using either of the three, once the relevant parameters are estimated from experimental measurements:

$$J_\mu(T) = k_\mu(\Delta\mu(T))^{b_\mu} \tag{3.5}$$

$$J_\mathrm{a}(T) = k_\mathrm{a}(\Delta a(T))^{b_\mathrm{a}} \tag{3.6}$$

$$J_\mathrm{T}(T) = k_\mathrm{T}(\Delta T(T))^{b_\mathrm{T}} \tag{3.7}$$

where J_μ, J_a and J_T denote the expected number of nucleation events per unit time and unit volume, and b_μ, b_a and b_T are constant exponents. The temperature-independent pre-factors k_μ, k_a and k_T are vial-specific constants

with values that are log-norm distributed across vials; their negative decadic logarithm assumes a mean value of a_μ, a_a, or a_T, and a standard deviation of c_μ,c_a, or c_T, respectively. Such distributed parameter is required to account for the experimentally observed variability in nucleation sites among vials.[76,82,86,94,117]. To keep the notation simple, subscripts for J and the associated kinetic parameters are only used when referring to a specific rate expression. While more complex rate expressions could be used to describe the nucleation kinetics, such as those based on the classical nucleation theory (CNT),[45,60,118] we refrained from doing so: as we discuss below, all three power law expressions well describe the experimental data, so that more complex models would provide little benefit. To describe the variability in nucleation temperatures, we introduce the cumulative distribution function (CDF), $F_v(t)$, which denotes the probability that nucleation occurs in a specific vial v with fill volume V in the time interval $[0, t]$. The CDF is obtained by assuming that nucleation occurs through an inhomogeneous Poisson process (it would be homogeneous, if temperature were constant) in terms of the nucleation rate defined above, i.e., of the rate $J(T)$:[22,66,106]

$$F_v(t) = 1 - \exp\left\{-\int_0^t VJ(t')\mathrm{d}t'\right\} \tag{3.8}$$

The cumulative probability for nucleation to occur within the interval $[0, t]$ for a *set of N vials*, termed $F(t)$, is the mean of the CDFs of the individual vials:

$$F(t) = \frac{1}{N}\sum_{v=1}^{N} F_v(t) \tag{3.9}$$

When computing $F(t)$, we consider the log-norm distribution of the pre-factor k in the expressions for $J(T)$: every vial v is assigned a unique value of k, namely $-\log_{10}(k) = a + \xi_v c$ with $\xi_v = \mathrm{probit}(\frac{v}{N+1})$, whereby the probit function denotes the quantile function of the standard normal distribution.

The link among (i) the CDF $F(t)$ as a function of time, (ii) the temperature-dependent nucleation rate $J(T)$, and (iii) the distributions shown in Figure 3.1, follows from the nature of the freezing process: it is the temperature that changes over time during freezing, in our case in a pre-determined manner, and it is this change that eventually triggers nucleation. To analyse whether $\Delta\mu$, Δa and ΔT allow for an accurate quantitative description of nucleation, we follow a two-pronged approach: (i) first, the re-evaluation of the experimental results shown in Figure 3.1; (ii) second, the estimation of the model parameters in Equations 3.5, 3.6 and 3.7, and the assessment of the quality of the fit thus obtained between experimental measurements and model results.

First, with reference to Figure 3.3(a), we notice that when a vial nucleates at T^nuc, then the driving forces for nucleation, to be used in Equations 3.6 and 3.7,

can be either $\Delta T^{\mathrm{nuc}} = T^{\mathrm{eq}} - T^{\mathrm{nuc}}$ or $\Delta a^{\mathrm{nuc}} = a_{\mathrm{w}}^{0} - a_{\mathrm{w}}^{\mathrm{eq}}(T^{\mathrm{nuc}})$. When plotting the CDFs for the ten different solution compositions (originally shown in Figure 3.1) as a function either of $\Delta\mu^{\mathrm{nuc}}$ in Figure 3.3(d), or of ΔT^{nuc} in Figure 3.3(e) or of Δa^{nuc} in Figure 3.3(f), the ten curves overlap almost perfectly. They exhibit an average $\Delta\mu^{\mathrm{nuc}}$ of 278 J mol^{-1}, an average ΔT^{nuc} of 13.3 K and an average Δa^{nuc} of 0.119. This demonstrates that the three quantities indeed represent the driving force for nucleation, irrespective of the absolute temperature level, of the water activity (i.e., of solute concentration), and even of the nature of the solute. Furthermore, from the ten empirical cumulative distribution functions of the nucleation temperatures one can calculate the average nucleation temperature, and at that temperature the corresponding equilibrium water activity. These two quantities are plotted as a function of the equilibrium temperature (Figure 3.3(b)) and of the initial water activity (Figure 3.3(c)), respectively. In these panels, isolines of the driving force are plotted as blue and red dotted lines (the equilibrium isolines are solid). The black solid lines were obtained through linear regression of the experimental data (symbols). For the temperature-based driving force the slope of the regression line is $\lambda_{\mathrm{T}} = 1.10$, whereas it is $\lambda_{\mathrm{a}} = 0.98$ in the case of the activity-based driving force. A slope of one would imply that the mean value of the driving force is independent of solution composition, so that the driving force quantitatively captures the effect of solution composition on nucleation. We hence conclude that both expressions accurately describe nucleation across the ten compositions investigated in this study, and that the activity-based driving force is slightly more accurate than the temperature-based one. This is also suggested by the fact that the overlap of the cumulative distribution functions in Figure 3.3(f) is visually better than in Figure 3.3(e).

Second, by optimally fitting each empirical cumulative distribution with that calculated by Equation 3.9 using the methodology developed recently,[76] we have estimated the three model parameters, namely a, b, c, in the three nucleation rate expressions (Equations 3.5, 3.6 and 3.7). Their values are shown for all ten solution compositions in Figure 3.4 (symbols; the rows correspond to the three rate expressions, respectively), together with their confidence intervals (error bars, significance level $\alpha = 0.05$, obtained by carrying out 500 Monte Carlo simulations each). In addition, we have estimated the nucleation parameters for the concatenated data set comprising all compositions; these parameter values are shown as thin black lines, with their confidence intervals given by the grey-shaded band. The cumulative distribution functions measured experimentally have been simulated with the estimated parameters, and plotted as black solid lines in Figure 3.1 (where for the sake of clarity, only the lines calculated using J_{T} are shown, as those obtained using J_{a} and J_{μ} mostly overlap); the agreement is rather satisfactory, in both average nucleation temperature and shape of the distribution.

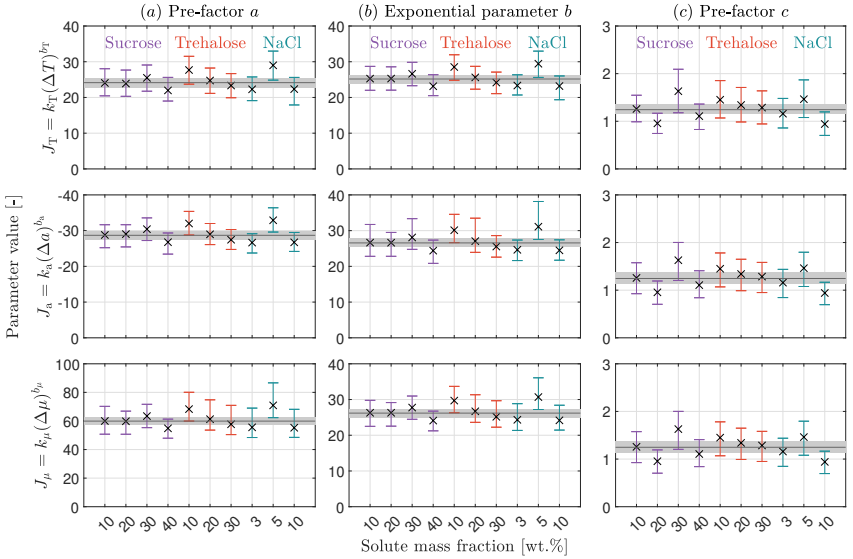

Figure 3.4 Estimated values for the three kinetic parameters a, b, c as well as their confidence intervals (error bars) for the three expressions of the nucleation rate: temperature-based (top row), activity-based (center row), and chemical potential-based (bottom row). The black line surrounded by the grey region denotes the optimum parameter values and their confidence interval estimated from a concatenated data set comprising all ten solution compositions. The colors indicate the three different solutes used.

When comparing the estimated parameter values for the three rate expressions in Figure 3.4, we notice that $b_\mu \approx b_\mathrm{a} \approx b_\mathrm{T}$ and $c_\mu \approx c_\mathrm{a} \approx c_\mathrm{T}$, whereas $a_\mathrm{a} \ll a_\mathrm{T} \ll a_\mu$. The similarity in the parameters b and c reflects the fact that they determine the shape of the nucleation temperature distributions, whereas parameter a acts as a scaling factor. Its order of magnitude is determined by the ratio between average values of the nucleation rate and of the driving force, the latter being very different when expressed as $\Delta\mu^\mathrm{nuc}$, ΔT^nuc or as Δa^nuc, since $\Delta\mu^\mathrm{nuc} \gg \Delta T^\mathrm{nuc} \gg \Delta a^\mathrm{nuc}$. When comparing the estimated values across compositions, we do not observe any significant trend; the confidence intervals are similar in size in all cases, and for all ten solution compositions, they overlap with those of the concatenated set. These observations lead to the conclusion that all three descriptions are sufficiently accurate to describe nucleation from millilitre-scale solution, and that a single set of parameters accurately quantifies the nucleation rate across solution compositions. This is a finding of great interest for both researchers and practitioners in this field.

Let us contextualize this finding. Experimental studies on ice nucleation in small volumes have established that the effect of solution composition on mean nucleation temperature quantitatively matches the one on the solution's water activity.[58,59,112,113] Our study complements and extends this observation in multiple ways.

First, we extend it to larger volumes at the millilitre-scale, where we generated an extensive data set of 6,000 nucleation events. Second, we show that not only water activity, but also supercooling and chemical potential quantitatively describe the effect of solution composition on nucleation; for the chemical potential, to the best of our knowledge, this has not yet been shown. Concerning supercooling, the literature reports that the mean nucleation temperature decreases more strongly with solute concentration than the equilibrium freezing temperature (i.e., $\lambda_T > 1$).[112,119,120] Our value of $\lambda_T = 1.10$ is smaller than most of those reported in the literature, which typically rely on experiments in micro-droplets, but it quantitatively agrees with a recent study that considered millilitre-scale solutions.[88] This suggests that the supercooling provides an accurate description of the nucleation rate in sufficiently large volumes; for smaller volumes, the use of either water activity or chemical potential may be more appropriate. Third, we underline that the nucleation rate is expressed as a power law of the thermodynamic driving force in this study. Alternative rate expressions such as those based on the classical nucleation theory, which consider additional kinetic effects, are commonly used in the literature.[60,86] As our experimental data shows, however, the rate is accurately quantified by considering thermodynamic effects only: more complex models are not required to describe ice nucleation at the millilitre-scale. Fourth and finally, we emphasize that the statistical analysis goes beyond assessing trends about the dependence of the mean nucleation temperature on solution composition: we explicitly studied whether there are significant effects of solution composition on the parameters in the nucleation rate expression. Despite carrying out large numbers of experiments, hence obtaining small confidence intervals, no significant differences were observed. The underlying modeling approach considers both the inherent stochasticity of nucleation (a Poisson process) and the variability in nucleation sites among vials (a log-norm distribution). This has been possible, because the experimental data comprises multiple nucleation temperatures per vial, so that one can distinguish between the variability in nucleation temperatures within vials and the one among vials. To conclude, the analysis presented here provides a deeper understanding of ice nucleation and of its controlling driving force, which can be of immediate value to the different fields where freezing processes play a major role.

3.2 METHODOLOGY

The experimental methodology used to generate the nucleation temperature data reported in this contribution has been developed and explained in detail in our earlier work.[76] Here, we provide a summary focusing on those aspects that are relevant to this work. All experiments were carried out in a second generation Crystal16 instrument (Technobis Crystallization Systems) that was customized to extend the attainable temperature range down to −30°C. To ensure a sufficient cooling capacity, the instrument was connected to a thermostat (Huber unistat 430, set to −10°C). For the solutions comprising 10 wt.%, 20 wt.% and 40 wt.% sucrose, four experiments were conducted, and for the remaining ones three; the data for 20 wt.% sucrose was already analysed earlier (see Series 1 − 4 in Deck and Mazzotti[76]). Each experiment comprised twelve freeze-thaw cycles in fifteen vials, amounting to a total of 540 or 720 nucleation events per solution composition, and a total number of 495 monitored vials, i.e., 5940 nucleation events, across compositions.

All experiments were carried out using the same experimental protocol: during each cycle, the temperature was decreased from +20°C to −25°C with a constant cooling rate of 0.6 K min^{-1}. The vials with 11.6 mm outer diameter were filled with 1 mL of aqueous solution using a micropipette (Socorex Acura 825). For each experiment, a fresh stock solution was prepared using deionized water (Millipore, Milli-Q Advantage A10 system) and solute. Sucrose (Sigma-Aldrich, BioXtra grade, > 99.5% purity), trehalose (Sigma-Aldrich, dihydrate, from starch, > 99% purity), and sodium chloride (Sigma-Aldrich, puriss. p.a. > 99.5%) were used as solutes in this work. All stock solutions were filtered (0.22 μm hydrophilic PTFE syringe filter) before insertion into the glass vials (Lab Logistics Group GmbH, 1.5 mL). The time and temperature of nucleation in a vial was detected based on the rapid rise in temperature due to the fast crystal growth that follows nucleation. A thermocouple (K-type, Inconel 600, certified by Picolog, sampling interval 1s) was inserted into each vial for online temperature monitoring.

It is worth underlining two experimental challenges that are associated to the measurement of the nucleation kinetics. First, freezing experiments have to be carried out under well-controlled conditions to ensure that the experimentally observed variability in nucleation temperatures is indeed dominated by the stochastic nature of nucleation, and not by experimental error. Doing so is challenging at all scales;[27,76] the instrument we use here allows for highly-automated, long-term freeze-thaw experiments in fifteen vials in parallel. We achieve a temperature accuracy of about ± 0.15 K that we consider sufficient compared to the width of the measured nucleation temperature distributions, which is on the order of 5–7 K. Second, the experimental data set must

comprise nucleation temperatures both from a large number of vials, and from a large number of freeze-thaw cycles: a single experiment hence comprises twelve freeze-thaw cycles in fifteen vials, amounting to 180 nucleation events. Such a large data set is essential, because different types of variabilities may be observed when considering the distributions of nucleation temperatures within vials, across vials, and across experiments; the stochastic description of ice nucleation has to account for this, as in the methodology we presented earlier,[76] and as it has been done with respect to micro-droplets in the atmospheric sciences.[82,86,94]

To estimate the parameters in the rate expressions as well as their uncertainty, we have utilized the approach presented in our earlier work.[76] When analysing the thermal evolution curves of the 495 vials that were monitored, we encountered technical issues with the inserted thermocouples in four vials. Hence, these four vials were excluded from the data analysis (1 vial each for 3 wt.% NaCl and 10 wt.% sucrose, 2 for 40 wt.% sucrose). The equilibrium freezing point data required for the computation of the supercooling has been obtained from experimental contributions in the literature for sodium chloride,[116] and for sucrose and trehalose.[115] Relevant properties for all solution compositions are summarized in Table 3.1.

Composition	T^{eq} [°C]	a_w^0	$\bar{\Delta T}^{nuc}$ [K]	$\bar{\Delta a}^{nuc}$	$\bar{\Delta \mu}^{nuc}$ [Jmol^{-1}]
Suc., 10 wt.%	−0.6	0.994	13.1	0.119	275
Suc., 20 wt.%	−1.5	0.986	12.8	0.116	269
Suc., 30 wt.%	−2.65	0.974	13.0	0.117	273
Suc., 40 wt.%	−4.4	0.958	13.4	0.118	278
Tre., 10 wt.%	−0.6	0.994	13.1	0.119	276
Tre., 20 wt.%	−1.5	0.986	13.4	0.121	281
Tre., 30 wt.%	−2.65	0.974	13.7	0.122	285
NaCl, 3 wt.%	−1.75	0.983	13.5	0.121	283
NaCl, 5 wt.%	−3.0	0.971	13.4	0.120	280
NaCl, 10 wt.%	−6.6	0.938	13.7	0.119	284

Table 3.1 Relevant data for the ten selected solution compositions. Suc: Sucrose. Tre: Trehalose. The equilibrium freezing temperatures T^{eq} have been sourced from the literature, with a precision of 0.05 K.[115,116] The corresponding water activity $a_w(T^{eq})$ was computed through Eq. 3.1. The mean values of the thermodynamic driving force, namely $\bar{\Delta T}^{nuc}$, $\bar{\Delta a}^{nuc}$ and $\bar{\Delta \mu}^{nuc}$, were computed from the experimental data set generated in this work.

4 FROM THE DIRTY LAB TO THE CLEAN MANUFACTURING OF PHARMACEUTICALS: HOW PARTICULATE IMPURITIES AFFECT ICE NUCLEATION

Numerous commercially available biopharmaceuticals are frozen or freeze-dried in vials. The temperature at which ice nucleates and its distribution across vials in a batch is critical to the design of both freezing and freeze-drying processes. This work reports a large data set of nucleation temperatures measured in vials filled with different concentrations of sucrose and prepared with different levels of particulate impurities. Independent of sucrose concentration, the spiking of solutions with silver iodide resulted in significantly higher and less variable nucleation temperatures compared to the reference solutions. Samples prepared under particulate-free conditions, in contrast, nucleated at significantly lower temperatures and with more variability among vials. These findings confirm that the level of particulates has a significant effect on the distribution of nucleation temperatures under conditions of industrial relevance.

The work reported in this chapter is in preparation for submission to a peer-reviewed journal: Deck, L.-T.; Gusev, N.; Deligianni, V.; Mazzotti, M. From the dirty lab to the clean manufacturing of pharmaceuticals: how particulate impurities affect ice nucleation.

4.1 MAIN SECTION

Ice nucleation denotes the onset of ice formation and is of immediate relevance to various fields, including cryobiology,[88,107] food preservation,[121,122] cloud formation and precipitation,[27,106] and the manufacture of biopharmaceuticals[21,43]. The formation of a nucleus is a stochastic event, whereby an accurate description of this stochasticity is essential to predict how long a solution remains in a metastable state below its melting point before ice is formed.[20,45,64,94] In biopharmaceutical manufacturing, drug products commonly are filled into vials with fill volumes of a few milli-liters and are frozen or freeze-dried in batches containing tens of thousands of vials.[41,75] The time and temperature of nucleation and their distribution across vials are relevant in this context because they affect both the dynamics of the freezing/freeze-drying process and the properties of the drug products.[1,14,28,123] Understanding how to quantify the stochasticity of nucleation and how it contributes to heterogeneity among vials hence is a topic of recent research.[74,84,124]

In large volumes such as vials, ice nucleates in a *heterogeneous* manner, which means that its rate is controlled by the availability of surfaces such as vial walls and particulate impurities.[59,76,102,114,125] *Homogeneous* nucleation, in contrast, occurs in the absence of surfaces and its rate is too low to explain nucleation events at the temperatures observed in vials; it is observed mainly in sufficiently small micro-droplets that are free of impurities.[27,43,83,126] While both types of nucleation are stochastic, the dependence on particulate impurities represents an additional source of variability for heterogeneous nucleation. For example, different samples (i.e., vials) in a batch may contain different numbers and types of particulates, and hence nucleate at a different rate, resulting in a broader distribution of nucleation temperatures.[76,88] Further, samples prepared under particulate-free conditions require lower temperatures to nucleate compared to those prepared under less clean conditions, which represents a major challenge when scaling-up pharmaceutical freezing and freeze-drying processes from lab to manufacturing conditions.[20,41,43,127]

This contribution aims to deepen the understanding of heterogeneous ice nucleation in vials with a focus on the two aspects mentioned above. The nucleation behavior of aqueous sucrose solutions that were prepared under three different conditions, as schematized in Figure 4.1, was assessed in an extensive experimental campaign. First, nucleation temperatures were measured in vials prepared under standard laboratory conditions, i.e., without any means of lowering the concentration of particulate impurities, and following the method developed earlier.[76,79] Second, samples were spiked with silver iodide (50.0 ± 0.1 mg per vial), which is known for its ability to promote ice nucleation.[128–130] Therefore, when adding AgI particles to a

vial, nucleation is expected to predominantly takes place on their surface. Third, particulate-free samples prepared by our industrial collaborators at The Janssen Pharmaceutical Companies of Johnson & Johnson (Janssen in short) were studied to quantify the effect of clean conditions on nucleation. To assess effects of solution composition on nucleation, solutions containing 10 wt%, 20 wt%, 30 wt%, and 40 wt% sucrose were investigated.

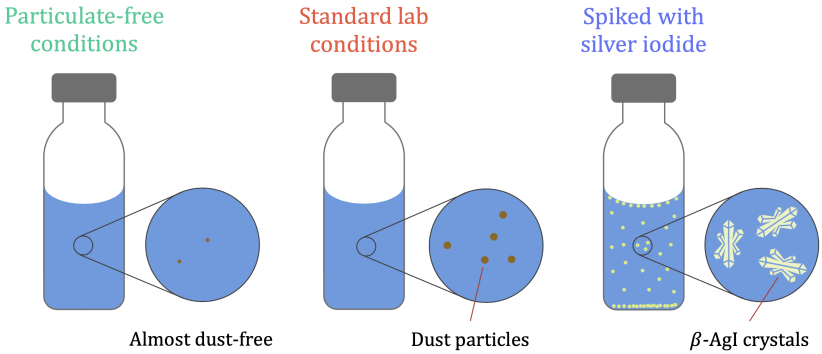

Figure 4.1 Schematic of the three sample preparation conditions studied. Left: Particulate-free samples that were filled at Janssen. Center: Samples prepared under standard laboratory conditions. Right: Samples prepared under standard laboratory conditions that were spiked with 50.0 mg silver iodide (AgI) each.

In all experiments, vials filled with 1 mL solution were cooled down at a constant cooling rate of 0.6 K min^{-1} from ambient temperature to a temperature low enough that nucleation happened in all vials. Nucleation *times* were identified using non-invasive transmissivity sensors and converted into nucleation *temperatures* using the temperature measurements of the jacket that surrounds the vials (precision of ± 0.05 K), as explained in an earlier contribution.[76] A detailed description of the experimental methodology is provided in Section 4.2. 576 nucleation events were monitored per solution composition and level of particulates. This corresponds to three experiments that each comprise twelve freeze-thaw cycles and sixteen vials. Fewer data points (i.e., 384 nucleation events) were obtained for the particulate-free 10 wt% sucrose samples, where only two experiments could be carried out due to vial breakage during transport. Such large data sets are required to accurately characterize the statistics of nucleation, considering both its inherent stochasticity and the phenomenon that it may occur at different rates in different vials.

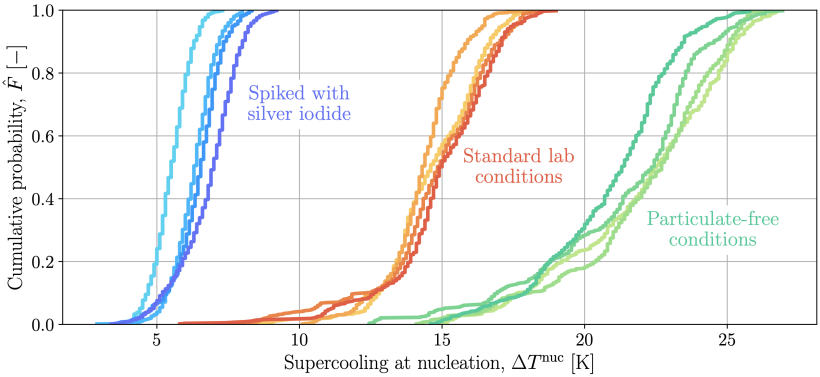

Figure 4.2 Cumulative distributions of the experimentally measured nucleation temperatures, i.e., the fraction of instances where nucleation has occurred when cooling down the solution to a specific temperature. The colored lines represent the experimental data, whereby each line represent a total of 576 measured nucleation temperatures. Darker lines correspond to more concentrated solutions. Sucrose concentrations of 10 wt%, 20 wt%, 30 wt%, and 40 wt% were studied.

Figure 4.2 reports all measured nucleation temperatures in the form of cumulative distribution functions (CDFs), which denote the fraction of instances in which nucleation happened between the beginning of the cooling ramp and cooling to a given temperature. To facilitate the comparison between solutions of different compositions, the distributions are plotted in terms of the supercooling at nucleation, ΔT^{nuc}, which is the difference between the solution's nucleation temperature and its melting point. The colors represent the three sample preparation conditions, and their shades the concentration level, whereby darker lines correspond to more concentrated solutions.

Several trends are worth discussing. First, the nucleation temperatures are distributed at all conditions, which is in line with the notion that nucleation is stochastic. Second, the nucleation temperatures are lower (i.e., the supercooling is larger) the cleaner the samples: the median supercooling at nucleation is about 7 K for the AgI samples, about 14 K for the standard ones, and about 22 K for the particulate-free ones. This confirms that the rate of heterogeneous nucleation scales with the availability of particulates. Third, no major differences in supercooling at nucleation are observed among the different concentrations of sucrose studied here. This absence of relevant concentration effects on the supercooling at nucleation is in line with recent literature on freezing in milli-liter volumes.[79,88] Fourth and finally, the nucleation temperatures are more variable the cleaner the samples are. They vary by about 3–4 K for the AgI samples, by about 6–8 K for the standard ones,

and by about 10–11 K for the particulate-free ones. Understanding this trend requires a more detailed analysis of the experimental data.

To this end, Figure 4.3 reports all 3×576 nucleation temperatures measured for the 20 wt% sucrose solution. Panel (a) shows the nucleation temperatures grouped by vial, and arranged in order of ascending mean vial nucleation temperature, whereas panel (b) shows the same data grouped by freeze-thaw cycles. The trends discussed in the following apply to all concentration levels, and similar figures for the other levels are provided in the SI.

As is evident from Figure 4.3(a), the variability in the nucleation temperatures within a vial is similar, i.e., 2–3 K, for all three conditions of sample preparation. What is different is the variability *among* the vials: the mean nucleation temperatures of the lowest and the highest nucleating vial differ by 2.5 K for the AgI samples, by 6.3 K for standard ones, and by 10.9 K for the particulate-free ones. While there is no direct control over the ubiquitous dust particles that may enter the vials during sample preparation, spiking vials with similar amounts of AgI (50.0 ± 0.1 mg per vial) is expected to ensure that all vials nucleate at similar temperatures. This is indeed confirmed by the experiments. When decreasing the number of dust particles by preparing samples under particulate-free conditions, the nucleation rate decreases as well and it becomes even more variable among vials.

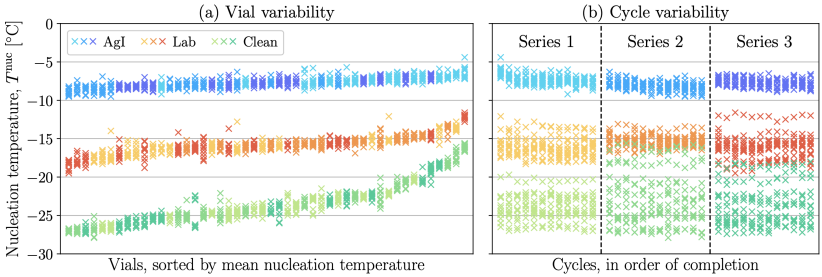

Figure 4.3 Experimental nucleation temperature results for 20 wt% sucrose solutions. The colors denote the conditions of sample preparation and their shades the three independent series per experimental conditions. Blue: Samples spiked with silver iodide. Orange: Samples prepared under standard laboratory conditions. Green: Samples prepared under particulate-free conditions. (a) Scatter plot of nucleation temperatures, sorted by vial in the order of ascending mean nucleation temperature. (b) Scatter plot of nucleation temperatures, sorted by cycles in order of completion.

On another note, Figure 4.3(b) indicates that there are little to no long-term trends of the nucleation temperature with freeze–thaw cycles, at least for samples prepared under standard and particulate-free conditions. This implies

that the nucleation rate does not depend on the history of a solution, which is in line with the relevant literature, and which facilitates the mathematical modeling of nucleation.[66,76,126] In contrast, the samples spiked with silver iodide exhibit a minor decrease in nucleation temperatures over the first few cycles, which is more prominent in higher concentrations (see the complementary figures in the SI); this may be because silver iodide particles slowly sediment over the course of several freeze–thaw cycles and form a densely packed layer at the vial bottom. The water-AgI interfacial area is expected to decrease due to this process, hence lowering the nucleation rate. While such an effect qualitatively explains the observed behavior, a quantitative assessment is outside the scope of this work.

In conclusion, this work highlights the importance of particulates for ice nucleation under conditions of relevance to the manufacturing of pharmaceuticals. The finding that samples prepared under cleaner conditions nucleate with more variability presents a dilemma to the design of pharmaceutical freezing processes, because particulate-free conditions are necessary to avoid contamination of drug products with undesired substances. However, both low absolute values of the nucleation temperature as well as a broad variability are undesired.[19,20,28,43] To clarify the role of vial-to-vial variability when freezing drug products and to account for it in process design, we recommend to integrate nucleation measurements into standard operating procedures. The effort to do so is rather modest because these measurements can be carried out using the methodology we report here, that is, with commercially available equipment, and with little amount of sample. Experimental nucleation temperatures provide practically useful insights into the dynamics of freezing and may be used to estimate nucleation rates.[76,79] The knowledge of nucleation rates enables the informed use of mechanistic freezing models in process design and optimization.[74,75,77]

4.2 METHODOLOGY

This section explains the experimental methodology used to measure nucleation temperatures in vials. In earlier work, this methodology was applied to measure the nucleation behavior of samples prepared under standard laboratory conditions and was explained in detail,[76,79] hence this section is limited to a summary of the main elements. All experiments were conducted in a second generation Crystal16 instrument (Technobis Crystallization Systems). The hardware of this instrument had been modified earlier[76] to extend its attainable temperature range down to $-35°C$, and it is connected to a thermostat (Huber unistat 430, set to $-10°C$). For each solution, that is for each

composition and particulate level, three experiments were carried out, each of which consists of twelve freeze-thaw cycles and sixteen vials, amounting to a total of 576 detected nucleation events each. For particulate-free 10 wt% sucrose solution, only two experiments were carried out because some vials broke during transport and hence had to be discarded. Each experiment involves cooling down from ambient temperature to a temperature low enough that nucleation happened in all vials at a constant cooling rate of 0.6 K min^{-1}.

The samples that were prepared under standard conditions as well as those that were spiked with silver iodide (AgI) were prepared at ETH Zurich; those prepared under particulate-free conditions were prepared at Janssen, frozen, and shipped on dry ice to ETH Zurich for measurement. Given geometrical constraints of the Crystal16 apparatus, all samples were filled into vials with 11.6 mm outer diameter to a volume of 1 mL. The sample preparation at ETH Zurich included the following steps: for each experiment, a fresh stock solution was prepared using deionized water (Millipore, Milli-Q Advantage A10 system) and solute. Sucrose (Sigma-Aldrich, BioXtra grade, $>$ 99.5% purity), trehalose (Sigma-Aldrich, dihydrate, from starch, $>$ 99% purity), and sodium chloride (Sigma-Aldrich, puriss. p.a. $>$ 99.5%) were used as solutes in this work. All stock solutions were filtered (0.22 μm hydrophilic PTFE syringe filter) before insertion into the glass vials (Lab Logistics Group GmbH, 1.5 mL). For the samples spiked with silver iodide, 50.0 mg of silver iodide was weighted using a precision balance and inserted into each vial before filling it with the solution. The time of nucleation in a vial was detected based on the readout of pre-installed transmissivity sensors that detect the transition from a transparent state to a non-transparent state of the vial upon nucleation. The nucleation times were converted into temperatures using the temperature measurements of the jacket that surrounds the vials (one sensor per set of four vials, precision of $\pm$0.05 K). A thermocouple (K-type, Inconel 600, certified by Picolog, sampling interval 1s) was inserted into each vial for online temperature monitoring (but not used to detect the time of nucleation). Note that the experimental data corresponding to the sucrose experiments under standard conditions has been reported earlier.[79]

The preparation of the particulate-free samples at Janssen included the following step: washing and autoclaving of the glass vials, which were provided by ETH Zurich to ensure that the same type of vials is used in all studies. The vials were filled with 1 mL sucrose solution in a laminar flow hood, sealed, and frozen on dry ice. They were shipped to ETH Zurich on dry ice, and stored in the frozen state until their measurement in the Crystal16 apparatus. Note that no thermocouples were inserted for the measurements to avoid contamination: the vials remained closed at all time between filling and the end of the experiment.

When computing the supercooling at nucleation, melting points of the sucrose solutions were taken from the literature.[115]

4.3 SUPPLEMENTARY FIGURES

This section contains additional figures that show all experimental nucleation temperature data that were generated within this chapter. Similar to Figure 4.3, which reported the data for the 20 wt% sucrose solution, Figures 4.4, 4.5, and 4.6 report the data for sucrose solutions of 10 wt%, 30 wt%, and 40 wt%, respectively. For the 10 wt% sucrose solution, only two independent experimental series were carried out, instead of three, as done for all other conditions. This is because a large number of vials broke during the transport from Janssen to ETH Zurich and hence were not suitable for experimental measurements.

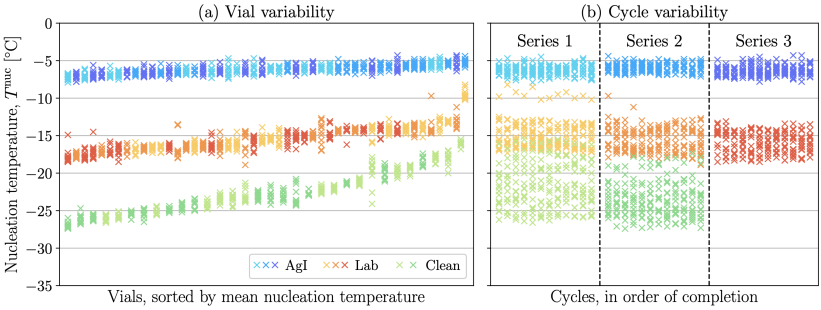

Figure 4.4 Experimental nucleation temperature results for 10 wt% sucrose solutions. The colors denote the conditions of sample preparation and their shades the three independent series per experimental conditions. Blue: Samples spiked with silver iodide. Orange: Samples prepared under standard laboratory conditions. Green: Samples prepared under particulate-free conditions. (a) Scatter plot of nucleation temperatures, sorted by vial in the order of ascending mean nucleation temperature. (b) Scatter plot of nucleation temperatures, sorted by cycles in order of completion.

Considering the sucrose samples, the experimental trends discussed in the main body apply to all concentration levels: that is, cleaner samples nucleate at lower temperatures and with more variability. The variability in nucleation temperatures among cycles is similar for the three conditions of sample preparation, however, the variability among vials increases the cleaner the samples are. The samples spiked with AgI and a concentration of at least 20 wt% sucrose exhibit a decrease in nucleation temperature over time; this effect is not evident in the 10 wt% sucrose samples.

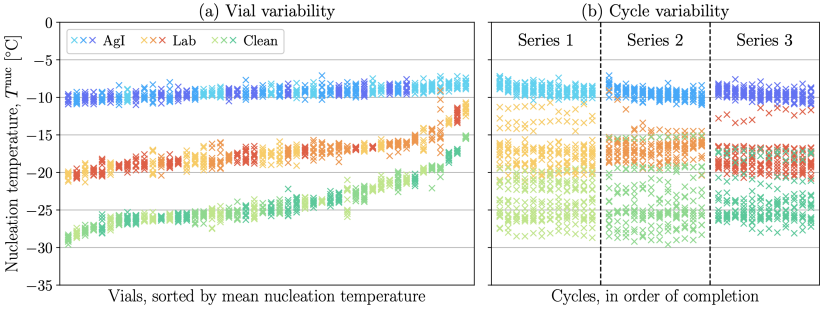

Figure 4.5 Experimental nucleation temperature results for 30 wt% sucrose solutions. The colors denote the conditions of sample preparation and their shades the three independent series per experimental conditions. Blue: Samples spiked with silver iodide. Orange: Samples prepared under standard laboratory conditions. Green: Samples prepared under particulate-free conditions. (a) Scatter plot of nucleation temperatures, sorted by vial in the order of ascending mean nucleation temperature. (b) Scatter plot of nucleation temperatures, sorted by cycles in order of completion.

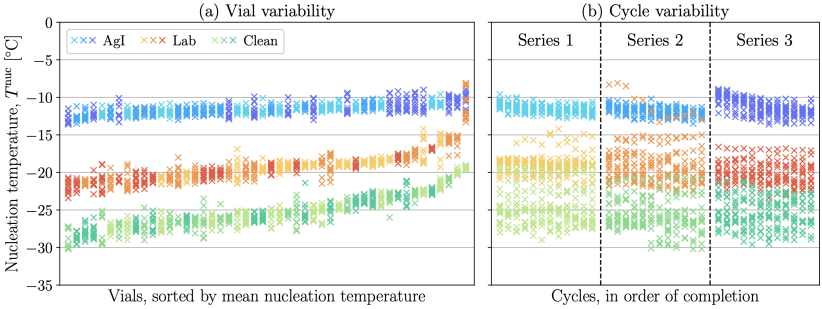

Figure 4.6 Experimental nucleation temperature results for 40 wt% sucrose solutions. The colors denote the conditions of sample preparation and their shades the three independent series per experimental conditions. Blue: Samples spiked with silver iodide. Orange: Samples prepared under standard laboratory conditions. Green: Samples prepared under particulate-free conditions. (a) Scatter plot of nucleation temperatures, sorted by vial in the order of ascending mean nucleation temperature. (b) Scatter plot of nucleation temperatures, sorted by cycles in order of completion.

5 MONITORING AQUEOUS SUCROSE SOLUTIONS USING DROPLET MICROFLUIDICS: ICE NUCLEATION, GROWTH, GLASS TRANSITION, AND MELTING

Freezing and freeze-drying processes are commonly used to extend the shelf life of drug products and to ensure their safety and efficacy upon use. When designing a freezing process, it is beneficial to characterize multiple physicochemical properties of the formulation, such as nucleation rate, crystal growth rate, temperature and concentration of the maximally freeze concentrated solution, and melting point. Differential scanning calorimetry has predominantly been used in this context, but it can have practical challenges and is unable to quantify the kinetics of crystal growth and nucleation. In this work, we introduce a microfluidic technique capable of quantifying the properties of interest, and we use it to investigate aqueous sucrose solutions of varying concentration. Three freeze–thaw cycles were performed on droplets with 75-µm diameters at cooling and warming rates of 1 °C/min. During each cycle, the visual appearance of the droplets was optically monitored as they experienced nucleation, crystal growth, the formation of the maximally freeze-concentrated solution, and melting. Nucleation and crystal growth manifested as increases in droplet brightness during the cooling phase. Heating was associated with a further increase as the temperature associated with the maximally freeze concentrated solution was approached. Heating beyond the melting point corresponded to a decrease in brightness. Comparison with the literature confirmed the accuracy of the new technique, while offering new visual data on the freeze concentrate. Thus, the microfluidic technique presented here may serve as a complement to differential scanning calorimetry in the context of freeze-drying. In the future, it could be applied to a plethora of mixtures that undergo such processing, whether in pharmaceutics or food production or beyond.

The work presented in this chapter has been reported in: Deck*, L.-T.; Shardt*, N.; El-Bakouri, I.; Isenrich, F.N.; Marcolli, C.; deMello, A.J.; Mazzotti, M. Monitoring aqueous sucrose solutions using droplet microfluidics: ice nucleation, growth, glass transition, and melting. *Langmuir* **2024**, 40, 12, 6304–6316. This article has been published with a shared first authorship between Nadia Shardt and myself.

5.1 INTRODUCTION

The freezing behavior of aqueous solutions is of broad interest to multiple disciplines, ranging from the atmospheric sciences[58,60,82,131–134] and cryobiology[107,135–139] to the manufacturing of pharmaceuticals[21,41] and food.[121,122] In all these fields, it is important to measure and predict the equilibrium state expected at certain conditions (temperature, pressure, composition, etc.) and to assimilate this information in the form of a phase diagram.[140] Due to the energy barrier required to form an ice nucleus,[20,64] metastable supercooled water may persist for prolonged periods of time under relevant conditions, e.g., in cloud droplets in the atmosphere[82,86,141] or in vials filled with ultra-pure, particulate-free aqueous solutions of biopharmaceutical formulations.[43,74] The temperature at which nucleation is actually observed depends on parameters such as the volume of the bulk solution, the cooling rate, and the mode of nucleation (whether homogeneous or heterogeneous). Thus, knowledge about the relevant kinetic parameters is required, including the rates at which ice crystals nucleate and grow, to understand and design processes of relevance to, for example, the pharmaceutical industry.

For the storage and distribution of biopharmaceuticals, processes such as freezing and freeze-drying are implemented to remove the water from the active ingredients to extend the shelf life of the drug product.[21,41] Designing such processes necessitates detailed knowledge of how the solution containing the active ingredients undergoes phase transitions. For instance, the size and morphology of the ice crystals that form influences the drying rate and, in the end, the physical characteristics of the freeze-dried formulation.[19,20,43,142] Empirical guidelines suggest that larger ice crystals enable faster drying times and that higher nucleation temperatures are correlated to larger crystals.[19,43] Hence, process conditions are chosen to promote higher nucleation temperatures, e.g., by using slow cooling rates.[21,41] After freezing is completed, the drying stage in freeze-drying must be designed such that the frozen drug product remains below a certain critical temperature, so as to avoid the collapse of its delicate micro-structure.[21,41]

Differential scanning calorimetry (DSC) is used to detect key thermal events (and temperatures) across the liquid–solid phase diagram. That is, DSC detects phase changes, including glass transitions, one of which is related to the critical temperature in freeze-drying. For some solutions, such as those containing proteins,[143] the accurate identification of glass transitions can be practically challenging due to weak signal strength.[144,145] For this reason, alternative technologies such as freeze-dry microscopy have been developed which enable the screening of process conditions for collapse phenomena in a microscopic sample.[146,147] However, neither DSC nor freeze-dry microscopy

allow for the measurement of kinetic parameters such as nucleation rate and crystal growth rate.

Herein, we demonstrate the use of microdroplets to access important phase transitions and temperatures on the isobaric phase diagram of sucrose–water mixtures that have not otherwise been possible to quantify using bulk volumes (µL–mL). Specifically, populations of microdroplets were generated in a microfluidic device and stored in perfluoroalkoxy alkane (PFA) tubing using an instrument named the Microfluidic Ice Nuclei Counter Zurich (MINCZ).[27,87] The droplets then were cooled and warmed, during which changes in droplet brightness were observed, corresponding to changes in the phase(s) present. This experimental tool could be used in the future for other mixtures that undergo detectable changes in brightness as the temperature range between freezing and melting is traversed. In addition, for highly concentrated sucrose solutions, we quantified the linear crystal growth rate at significantly lower temperatures than previously reported.[148] Thus, both thermodynamic and kinetic properties of a solution could be determined in a single experimental setup.

5.2 QUALITATIVE TRENDS IN DROPLET BRIGHTNESS

Fig. 5.1 outlines a qualitative extended phase diagram as a function of temperature and sucrose mass fraction. It is an *extended* phase diagram, because it shows features in addition to those derived from equilibrium thermodynamics that are relevant to the freezing process. First, the equilibrium melting line is extended beyond the eutectic concentration (shown as a dashed line), where the solution is supersaturated with respect to the solute, sucrose. This is because during freezing, pure ice crystals are formed, increasing the solute concentration in the unfrozen solution, and this increase continues beyond the eutectic point, at which point crystallization of the solute may eventually occur. Some solutes such as mannitol commonly nucleate during the freezing process.[41,149] For sucrose, however, such behavior has neither been reported nor been observed here.

Fig. 5.1 features two pieces of information related to glass transitions. The first is the glass transition temperature of the metastable solution in which neither ice nor sucrose has nucleated. This temperature depends on solution composition, and it is referred to as T_g. The second is a point highlighted by the coordinates (w', T'_g), which represents the glass transition temperature of the maximally freeze-concentrated solution at a sucrose mass fraction of w'. Freeze-concentration refers to the increase in concentration of the solute in solution as pure ice crystals form during the freezing process. As a result of

this concentration process, the viscosity of the solution gradually increases until it becomes high enough to inhibit further crystal growth.

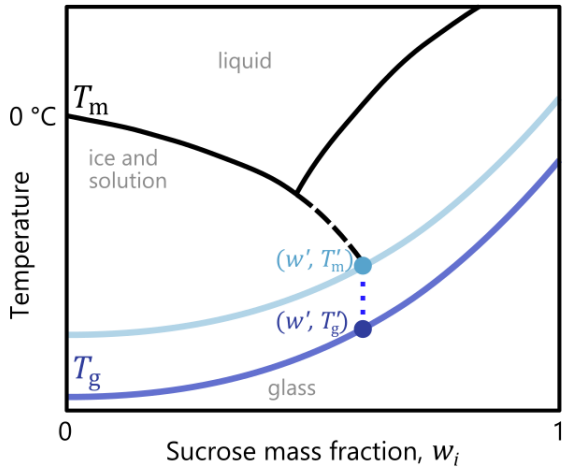

Figure 5.1 A qualitative, extended phase diagram of sucrose–water mixtures showing the melting temperature T_m, the composition-dependent glass transition temperature T_g, and the temperature of the maximally freeze concentrated solution T'_m with corresponding composition w'. The point (w', T'_m) lies on an iso-viscosity line at which the viscosity is sufficiently high to arrest further ice growth from the highly-concentrated solution. The glass transition temperature at the composition w' is denoted by T'_g.

While T_g is associated with the ultra-high viscosity of a glassy state (1×10^{12} Pa s),[150] there is a higher temperature where ice growth in the sucrose – water freeze-concentrate is inhibited – at a lower viscosity (approx. 1×10^8 Pa s)[150], shown by the *iso-viscosity line* in Fig. 5.1. Qualitatively, this iso-viscosity line is a vertical translation of the T_g curve. The point (w', T'_m) is the intersection of the iso-viscosity line and the melting line. w' represents the highest concentration level attainable in the freeze-concentrate, and the solution with this concentration is referred to as *maximally freeze-concentrated*. The value of w' is independent of the solution's initial composition, which only determines the relative amounts of the two phases that form upon freezing, i.e., the pure ice crystals and the freeze-concentrate. Both the physical interpretation and the name of the temperature associated with the point (w', T'_m) are inconsistently used in the literature (see Sacha and Nail[151] for a comprehensive discussion), with the terms *glass transition temperature of the freeze-concentrate*[143,152] and *antemelting temperature*[153] both in use.

The maximally freeze-concentrated solution (w', T'_m) is of immediate interest to the freezing and freeze-drying of biopharmaceuticals, whereas T'_g is not. This is because the primary drying stage of the freeze-drying process must be designed such that the frozen product remains at a temperature below a critical value (termed T_c) to avoid the collapse of the delicate micro-structure. A large number of studies have revealed that for formulations where the solutes do not crystallize during freezing (as is the case for sucrose-based formulations) this critical temperature lies close to the value of T'_m, so that the measurement of T'_m has become a standard practice in the field.[20,21,143,154] The associated concentration w' is of relevance to the storage of frozen biopharmaceutical drug products, as it governs the long-term stability of the active ingredients in the freeze-concentrated solution.[8,154] For the case of sucrose solutions, T'_m is reported to lie at about −33 °C independent of concentration, whereas T'_g lies between −49 °C to −45 °C, as measured by DSC.[143,151] While DSC can be used to provide both temperatures,[153,154] the microfluidic technique introduced here allows for the measurement of T'_m only.

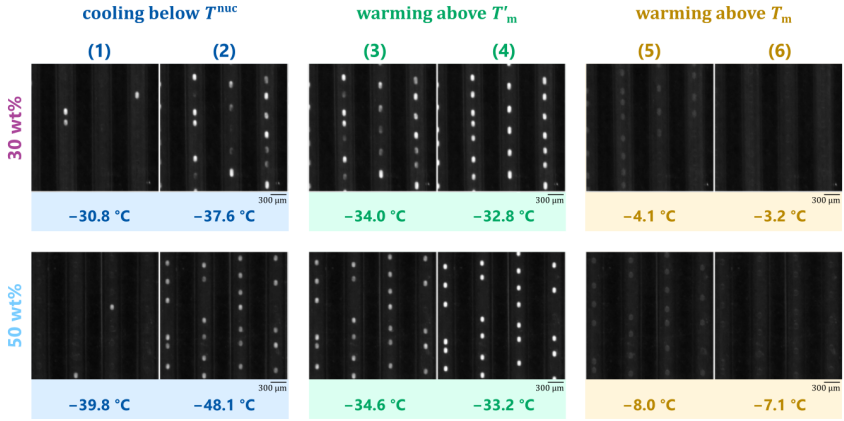

Figure 5.2 Sequence of images during the first cycle of the series depicted in Figs. 5.3 and 5.5 (triangle) for the 30 wt%(T_m = −3.1°C) and 50 wt% (T_m = −7.2°C) sucrose mixtures corresponding to the processes depicted by arrows in the schematic on the left. (1) to (2) shows the progression of droplets freezing as temperature decreased below the droplet nucleation temperatures T^{nuc}; (3) to (4) shows the onset and end of the region associated with T'_m that lies at about −33°C; and (5) to (6) shows the onset and end of melting (T_m). All images are cropped areas of size 2.4×2.4 mm at the center of the full image. Onsets and ends of the T'_m and T_m region are the temperatures at which vertical bars are drawn in Fig. 5.5(b).

Phase transitions in droplets upon temperature change can be observed optically by changes in how the droplet interacts with light, as illustrated in Fig. 5.2 for droplets of two aqueous sucrose concentrations (30 wt% upper row, and 50 wt% lower row). Aqueous sucrose solutions are optically transparent to visible light, as seen for the majority of droplets in panel (1). When ice formation occurs, the crystals reflect and scatter light, increasing the brightness of the phase against the dark background (bright spots in column (1)). The temperature at which ice is first detected, is called the nucleation temperature, T^{nuc}, and it varies among droplets due to the stochastic nature of nucleation. Upon further cooling, ice forms in more and more droplets, as can be seen in column (2), and intriguingly, frozen droplets differ in their brightness. As we will see later, this effect is related to the temperature at which nucleation in the droplets takes place. After reaching the pre-defined minimum temperature, the droplets were heated back to the initial temperature, as shown in columns (3) to (6). As long as the droplet temperature remained significantly below T'_{m} (around -33°C, column (3)), droplet brightness did not change. As T approached T'_{m} (column (4)), droplet brightness visibly increased, and all droplets eventually exhibited a similar level of brightness.

Upon further heating, the temperature eventually approaches the melting point where the brightness of the frozen droplets decreased (columns (5) to (6)) as the proportion of ice in the droplets decreased. The pixel intensity continued to decrease until the melting point was surpassed, at which fully liquid droplets were again observed (column (6)). Experiments were conducted for multiple sucrose concentrations between 1 wt% and 60 wt%, hence covering the entire concentration range below the eutectic composition.

5.3 QUANTITATIVE ANALYSIS OF FREEZING

5.3.1 Nucleation temperatures

Nucleation is a stochastic process;[64,94] hence, a quantitative analysis of a solution's nucleation behavior requires the measurement of a large number of nucleation events. Given that only a single nucleation event takes place in each droplet (see the Section 5.3.5), a large number of droplets must be observed to generate statistically-relevant nucleation data sets. We evaluate such data by computing the cumulative distribution function, i.e., the fraction of droplets frozen as a function of time over the course of an experiment. Since the thermal evolution during the experiment is recorded, it is possible to express such a distribution in terms of temperature. In general, the addition of a solute is expected to lower the temperature at which nucleation occurs.

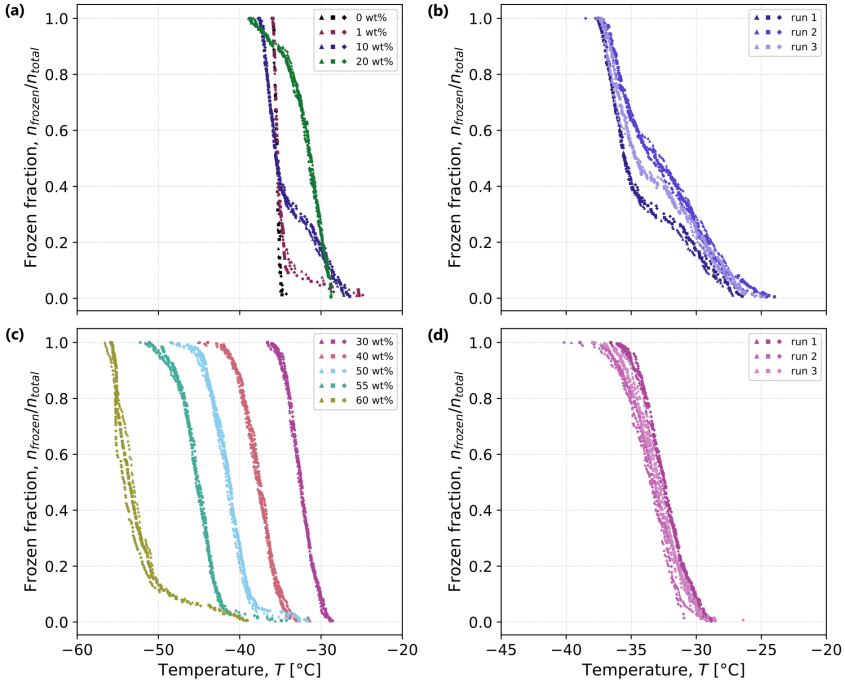

Figure 5.3 Frozen fraction of droplets ($n_{\text{frozen}}/n_{\text{total}}$) as a function of temperature and sucrose concentration observed in MINCZ. In panel (a), one droplet population (75 μ in diameter) was generated from a stock solution at each listed concentration and underwent three consecutive freeze–thaw cycles at a rate of 1 K min^{-1}. Each cycle is depicted with a different symbol (cycle 1: triangle; 2: square; 3: diamond). The thermocouple accuracy is estimated to be $\pm$ 0.2°C.[87] In panels (b) and (d), results from (a) and (b) are repeated for concentrations of 10 wt% and 30 wt% (labelled as run 1) with results from two additional independent droplet populations undergoing three freeze–thaw cycles (labelled as runs 2 and 3).

This is because a solute lowers the water activity, and hence lower absolute temperatures are required to achieve the same value of the thermodynamic driving force for ice nucleation to occur.[45,58,64] We have studied this effect recently for aqueous solutions containing sucrose, trehalose, and sodium chloride at different concentrations at the millilitre scale,[79] and here we aim to assess how such an effect manifests at the micro-scale. Fig. 5.3 depicts the cumulative fraction of droplets frozen at each temperature for each studied sucrose concentration, summarized in two panels ((a) and (c)) to facilitate the visual analysis. As was observed for the larger volumes in our earlier study,[79] nucleation temperatures decrease with increasing concentration for high sucrose concentrations above 20 wt%, as shown in panel (c).

For the lower concentrations shown in panel (a), namely 1 wt%, 10 wt%, and 20 wt%, the nucleation temperatures partially lie above those measured for pure water, contrary to expectation. All three distributions are bimodal, i.e., they exhibit a turning point (an abrupt change in the slope of the frozen fraction), at a frozen fraction of about 10 % for the 1 wt% solution, at 30 % for the 10 wt% solution and at about 90 % for the 20 wt% solution. The fraction at which the turning point is positioned is reproducible across the three freeze–thaw cycles (different symbols) for all concentrations. In addition, Fig. 5.3(b) shows that for three independent droplet populations each undergoing freeze–thaw cycles, the turning point also remains at the same temperature, and only the fraction of droplets freezing varies. At the higher concentration levels shown in panel (c), in contrast, the distributions are generally unimodal, with only slight variation in nucleation temperatures between different droplet populations and between consecutive freeze–thaw cycles within the same droplet population. At the highest studied concentration (60 wt%), the distribution becomes bimodal again, with almost 10 % of droplets freezing prior to the steepest increase in frozen fraction.

We propose the following explanation for these observations based on the concept that nucleation may occur either homogeneously (i.e., in the bulk volume) or heterogeneously (i.e., on surfaces of, e.g., impurities). The experiment for pure water is considered to feature homogeneous nucleation, supported by the fact that a large number of studies have observed similar nucleation temperatures for micrometer-sized droplets of ultra-pure water in different setups.[155,156] The increase in nucleation temperature in sucrose solutions with low concentration levels compared to pure water hence must be due to the presence of heterogeneous nucleation sites. If the number of heterogeneous nucleation sites is small, they are randomly distributed across droplets, and some droplets are expected to contain none, i.e., they nucleate homogeneously. This therefore explains the bimodal shape of the distributions. Given that the only difference between the experiments involving pure water and those

involving sucrose solutions is the presence of sucrose, one must conclude that the heterogeneous nucleation sites are located on impurity particles present in the sucrose used in the experiments. Hence, a higher sucrose concentration implies that more nucleation sites are present, so that eventually heterogeneous nucleation takes place in virtually all droplets for concentrations of 30 wt% and higher. Similarly, the bimodal distribution of the 60 wt% solution may be due to heterogeneous nucleation sites not present at the lower concentrations; to confirm this conjecture, experiments at higher concentration levels are required, which were not carried out due to the experimental challenges in dealing with highly viscous solutions. An experimental approach to directly investigate whether heterogeneous nucleation is present would be to measure nucleation temperatures in droplets of different sizes, since smaller droplets are less likely to contain an impurity particle on which nucleation sites may be located. Doing so is indeed feasible with the microfluidic setup used here,[87] but outside the scope of the work. Considering the literature, Miyata and Kanno[157] reported only homogeneous nucleation of sucrose solutions using an emulsion-based DSC, in which the emulsion comprises microdroplets with diameters of a few µm,[26] i.e., volumes more than three orders of magnitude smaller than the droplets measured here.

The presence of heterogeneous nucleation further explains the broadness of the measured nucleation temperature distributions on the order of 10 K, which is significantly wider than those for pure water of less than 3 K[87]. Heterogeneous nucleation sites vary in the characteristic temperature at which they catalyse nucleation,[158] leading to a droplet-to-droplet variability in nucleation temperature in addition to the inherent stochasticity. Such additional variability has been widely reported in the literature, both in micro-droplets[26,82,86] and at the millilitre scale.[76,79,159] Its quantitative study would require knowledge of droplet-specific mean nucleation temperatures, obtained by consecutively measuring nucleation temperatures for individual droplets over multiple freeze–thaw cycles. Given that our experiments comprise only three freeze–thaw cycles, we refrain from doing such an analysis; however, we point out that the setup presented here may indeed be capable of carrying out experiments with additional freeze–thaw cycles dedicated to the study of droplet-to-droplet variability.

Finally, it is worth comparing the monitored nucleation temperatures with those measured previously in vials filled with 1 mL sucrose solution prepared under the same condition;[76,79] in these studies, nucleation was found to take place at an average supercooling of 13 K, with no significant dependence on sucrose concentration. That nucleation in the micro-droplets takes place at significantly lower temperatures is explained by their smaller volume, which implies that each individual droplet contains only a few or no impurity

particles, as discussed before, whereas volumes at the scale of vials contain many more impurities.

5.3.2 Interplay between nucleation temperature and the freeze-concentrate

The visual appearance of the droplets after nucleation warrants further study, as their brightness was found to depend on the nucleation temperature. As an example, Fig. 5.4(a) shows a cropped image of each droplet after nucleation as a function of temperature, binned in intervals of 0.5 °C for the first freezing ramp of the 30 wt% sucrose droplets. Qualitatively, the pixel intensity of droplets that nucleated at higher temperatures was significantly greater than those that nucleated at lower temperatures. Quantitatively, Fig. 5.4(b) shows that the ratio between the intensities of the brightest and dimmest droplets is on the order of a factor of two. Let us further recall from Fig. 5.2 that upon reheating all droplets brighten to the same value of the pixel intensity. Physically, this behavior is due to the interplay between the temperature of ice nucleation (and the ensuing crystal growth) and whether the maximally freeze-concentrated solution is attained.

To elucidate this effect, one must consider the physical processes that take place during freezing within the droplets. We recall that the point (w', T'_m) is defined by the magnitude of viscosity that inhibits the kinetic process of crystal growth (cf. Fig. 5.1). Viscosity, in turn, is a function of temperature and composition, and the intersection of the melting curve with the iso-viscosity line yields the point (w', T'_m). If freezing is carried out in sufficiently large volumes (consider e.g., vials at the millilitre scale) where nucleation occurs above T'_m, the composition of the solution after nucleation follows the melting line until it approaches a concentration of w' corresponding to the temperature T'_m. This process is visualized by the blue line in Fig. 5.4(c).

In the micro-droplets studied here, however, nucleation occurs predominantly at temperatures below T'_m. In this case (the red line in Fig. 5.4(c)), the freeze-concentrated solution cannot attain the concentration level w', as the viscosity of the hypothetical state (w', T^{nuc}) is greater than the viscosity at which ice crystal growth is inhibited (see light blue iso-viscosity line). The droplet instead attains the final state $(w(T^{nuc}), T^{nuc})$ that correspond to the viscosity level at which crystal growth is inhibited. Since viscosity increases with decreasing temperature, it must hold that $w(T^{nuc}) < w'$ when $T^{nuc} < T'_m$. A smaller sucrose concentration in the freeze-concentrate implies that less water is turned into ice, which may be linked to differences in brightness of the frozen droplets. Naturally, when the droplets are heated, viscosity decreases, and the differences between the droplets vanish as all droplets

assume states on the melting line. We use this optical effect in the following section to quantify the value of T'_m.

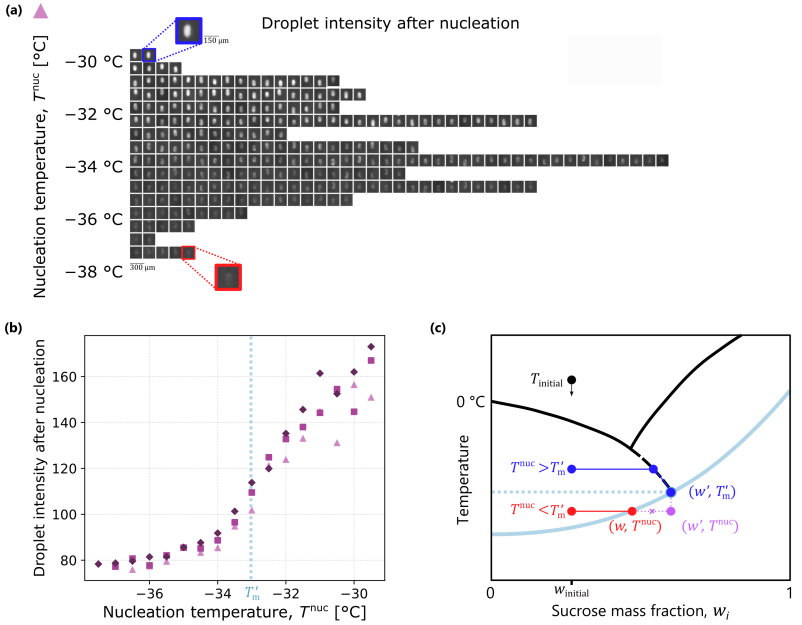

Figure 5.4 (a) Cropped images of frozen droplets with a sucrose concentration of 30 wt% as a function of their nucleation temperature binned in intervals of 0.5 °C for the first freeze–thaw cycle shown in Fig. 5.3(c). (b) Pixel intensity (monochrome scale between 0 (black) and 255 (white)) of a circle with 9-pixel radius at the center of each identified droplet averaged over all droplets in the same bin for all three freeze–thaw cycles of 30 wt% droplets (cycle 1: triangle; 2: square; 3: diamond) in Fig. 5.3(c). (c) Schematic phase diagram illustrating the hypothesis for the change in droplet intensity when $T^{nuc} < T'_m$: it is not possible to reach (w', T^{nuc}), because as ice grows, the iso-viscosity line is intersected at a lower concentration, and further ice growth ceases. T'_m is obtained from the analysis shown in Figs. 5.5 and 5.6.

5.3.3 Freeze-concentrate and melting temperatures

While nucleation is a stochastic process and each droplet experiences a distinct nucleation event, both T'_m and T_m are deterministic and therefore experienced simultaneously by all droplets. As a result, to facilitate image analysis, the region of interest for the image analysis was expanded from

individual droplets to the columns of the image that contained PFA tubing (the exact procedure for identifying the tubing is explained in the *Methods*5.5.2). Variability between droplets was confirmed to be less than the accuracy of the thermocouple (0.2 °C), and therefore the columns of pixels where PFA tubing was present was considered to be a suitable region of interest for quantitative analyses of pixel intensity.

Fig. 5.5(a) illustrates an example of the procedure for identifying important features of the normalized average intensity (I_n) of pixel columns as a function of temperature for the warming portion of the first freeze–thaw cycle for 30 wt% sucrose droplets (warming rate of 1 °C/min). As previously shown in Fig. 5.2, heating beyond T'_m is accompanied by an increase in brightness, and heating beyond T_m by a decrease in brightness. For a quantitative analysis it is beneficial to consider the derivatives as well: pertinent features of the intensity evolution were extracted from corresponding extrema in the first and second derivatives (I'_n and I''_n, respectively). The midpoint temperature of the transition was defined as the one where the maximum in the first derivative was reached (shown by the triangle symbols in Fig. 5.5(a)); the onset temperature as the first extremum in the second derivative before the midpoint; and the endpoint temperature as the first extremum in the second derivative after the midpoint. In Fig. 5.5(b), the normalized intensity evolution is shown for all concentrations and all freeze–thaw cycles, with the midpoints identified by symbols outlined in black, and onset and endpoint temperatures indicated by vertical segments. To reduce the size of the ensuing data sets, not all images taken during the warming period were saved, but only those around the expected glass transition and melting points, hence leading to gaps in the plotted thermal intensity evolution.

It is worth mentioning that T'_m (but not T_m) may also be obtained by monitoring the droplet brightness after nucleation during the freezing ramp, as demonstrated in Fig. 5.4. We chose the method described here (intensity change upon warming) for the quantitative analysis, because it allows for the measurement of both T'_m and T_m.

Fig. 5.6 and Table 5.1 summarize the observed values for T_m (gold symbols) and T'_m (green symbols) of sucrose solutions as a function of composition obtained from the analysis of Fig. 5.5. The melting point was defined as the midpoint of the decrease in the pixel intensity averaged over the columns of pixels where tubing was present, and the obtained values are in close agreement with other measurements reported in the literature.[115,153,160] T'_m was taken to be the midpoint of the identified temperature range over which an increase in average pixel intensity was observed. This choice of midpoint is similar to the methodology for interpreting differential scanning calorimetry experiments, where the midpoint temperature of a change in heat flow is taken

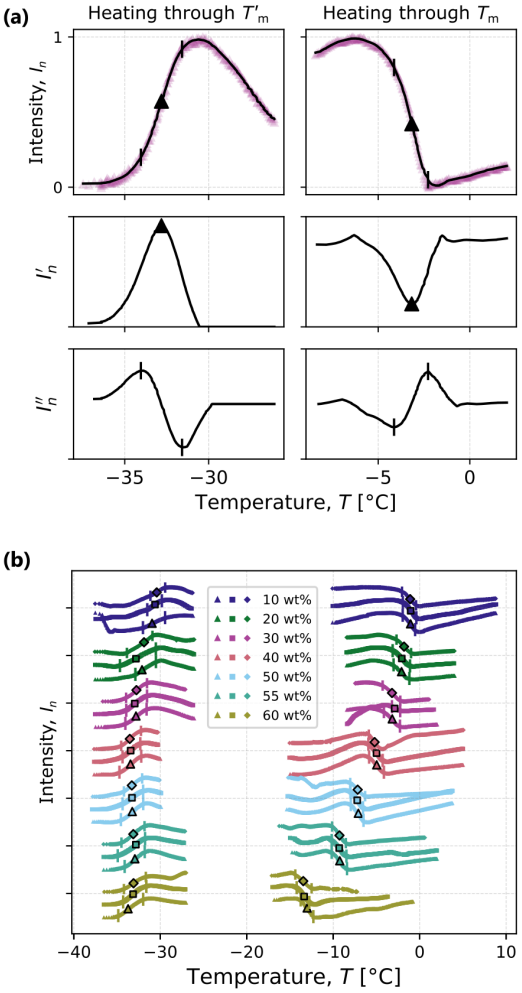

Figure 5.5 (a) Normalized average column pixel intensity ($I_n \in [0, 1]$) as a function of temperature for the warming portion of the first freeze–thaw cycle of 30 wt% droplets. In the first row, purple triangles are raw data, and the black line is the smoothed data. The midpoint (denoted by a filled triangle) is defined as the temperature at which the first derivative of intensity (I'_n, as shown in the second row) reached its maximum (steepest change). (b) Summary of intensity as a function of temperature for all concentrations. Symbols outlined in black indicate the temperatures at the midpoint of the two transitions, corresponding to T'_m and T_m. For a single experiment, moving upwards on the y-axis indicates an increase in intensity after cooling, and all experiments are simply offset from each other on the y-axis to clearly show the individual trends.

Sucrose concentration (wt%)	T'_m (°C)	T_m (°C)
0	—	0.7 ± 0.02
1	—	0.2 ± 0.04
10	-30.7 ± 0.4	-1.1 ± 0.1
20	-32.3 ± 0.8	-2.0 ± 0.3
30	-32.8 ± 0.2	-3.1 ± 0.3
40	-33.5 ± 0.1	-5.1 ± 0.2
50	-33.3 ± 0.04	-7.2 ± 0.1
55	-33.0 ± 0.2	-9.3 ± 0.05
60	-33.3 ± 0.6	-13.3 ± 0.4

Table 5.1 Summary of the midpoint of the freeze-concentrated glass transition temperature (T'_m) and the midpoint melting temperature (T_m) as a function of sucrose concentration obtained from the data shown in Fig. 5.5. Each value is the average ($\pm$ two standard deviations) of the three freeze–thaw cycles at that concentration. Thermocouple accuracy is ± 0.2 K.[87]

to be the value of T'_m.[143,145] It can be seen that at the lowest sucrose mass fractions (10–20 wt%), the identified T'_m values are higher than those obtained at higher sucrose mass fractions. This may be attributed to the high nucleation temperatures observed for these solutions (see Fig. 5.3), where a large number of droplets nucleates at or above T'_m, and hence experiences only little or no increase in brightness upon heating. It is worth noting that DSC, the standard method for the measurement of T'_m, similarly suffers from weak signals in low-concentrated solutions.[143,145] In Fig. 5.5, the average grid intensity is seen to slowly increase at a temperature lower than the identified midpoint. This observation could suggest that the onset of the intensity increase may be a more consistent feature to extract T'_m from the intensity evolution at the lower sucrose mass fractions. For all concentrations greater than 30 wt%, however, the observed T'_m values are in close agreement within the standard deviation between freeze–thaw cycles at each concentration. Taking the average of T'_m across all concentrations excluding 10 wt% and 20 wt% yields a value of (-33.2 ± 0.2) °C, where the uncertainty is the standard deviation. This value is in agreement with the average of (-33.5 ± 0.5) °C calculated from the values reported by Seifert et al.[154] over the concentrations studied therein using DSC (shown by upside-down triangles in Fig. 5.6).

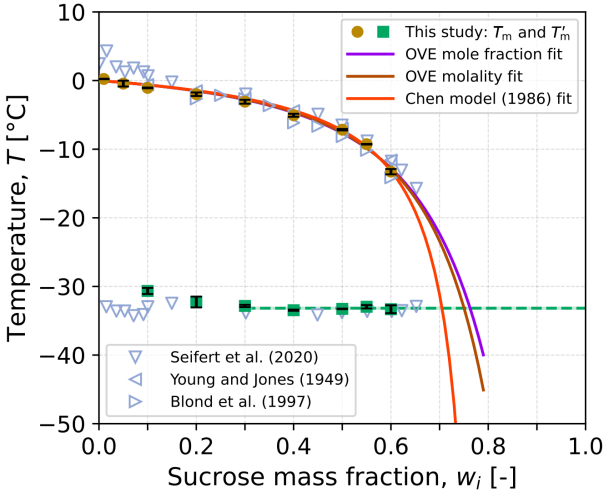

Figure 5.6 Temperatures in the maximally-freeze-concentrated region (T'_m) and the melting region (T_m) as a function of sucrose mass fraction. Each gold symbol corresponds to the average temperature over the three cycles for the midpoint of melting (Fig. 5.5), while each green symbol corresponds to the average temperature at the midpoint of the T'_m transition (Fig. 5.5). The error bars show two standard deviations over the three cycles. The horizontal dashed green line depicts this study's average $T'_m = -33.2\,°C$. The solid lines are fits to this study's T_m values using two forms of the osmotic virial equation (OVE)[161] and the Chen model[162]. Open symbols are experimental measurements of melting point from three literature sources[115,154,160] and a set of T'_m measurements from Seifert et al.[154]

5.3.4 Concentration of the freeze-concentrated solution

The concentration of sucrose in the maximally freeze-concentrated solution (w', T'_m) can be obtained by extrapolating the melting line beyond the measured melting points down to the temperature T'_m.[143,154] For fitting to the measured melting points, we investigate three theoretical models.

First, we combine the Gibbs–Duhem equation with a model that can describe the non-ideal solution behavior. We select the osmotic virial equation (OVE) due to its accuracy and rigorous derivation from principles in statistical mechanics[161,163,164], as well as for the possibility of using its regressed coefficients to accurately predict properties of solutions with three or more components in relevant applications.[138,161,165] There are two forms of the osmotic virial equation, yielding two distinct approaches for relating the

melting point to the solution composition when each is combined with the Gibbs–Duhem equation. One is based on the osmolality of the solution, π:[161]

$$T_{\mathrm{m}}^{\circ} - T_{\mathrm{m}} = \frac{RT_{\mathrm{m}}^{\circ}\pi M_{\mathrm{w}}/\Delta\overline{s_{\mathrm{f}}^{\circ}}}{1 + R\pi M_{\mathrm{w}}/\Delta\overline{s_{\mathrm{f}}^{\circ}}} \tag{5.1}$$

where T_{m}° is the melting point of pure water (273.15 K), R is the universal gas constant (8.314 J mol^{-1}), M_{w} is the molar mass of water (18.02 g mol^{-1}), and $\Delta\overline{s_{\mathrm{f}}^{\circ}}$ is the standard molar entropy change of fusion of water (22.00 J mol^{-1} K^{-1}). We truncate osmolality, π, to a polynomial of second-order: $\pi = m_i + B_{ii}m_i^2$ where m_i is the molality of solute i and B_{ii} is the molality-based second osmotic virial coefficient. The second approach is based on the osmole fraction, $\tilde{\pi}$:[161]

$$T_{\mathrm{m}}^{\circ} - T_{\mathrm{m}} = \frac{RT_{\mathrm{m}}^{\circ}\tilde{\pi}/\Delta\overline{s_{\mathrm{f}}^{\circ}}}{1 + R\tilde{\pi}/\Delta\overline{s_{\mathrm{f}}^{\circ}}} \tag{5.2}$$

where we truncate the osmole fraction to a second-order polynomial: $\tilde{\pi} = x_i + B_{ii}^{*}x_i^2$ where x_i is the mole fraction and B_{ii}^{*} is the mole-fraction-based second osmotic virial coefficient. Fitting Eq. 5.1 and Eq. 5.2 to the melting points reported in Table 5.1 yields values of $B_{ii} = 0.15 \pm 0.01$ molal^{-1} (brown line in Fig. 5.6) and $B_{ii}^{*} = 10.6 \pm 0.7$ (purple line in Fig. 5.6), respectively.

A commonly-used semi-empirical model in the literature on freeze-drying is the Chen model[162], which has the following form:

$$T_{\mathrm{m}}^{\circ} - T_{\mathrm{m}} = \frac{K_{\mathrm{w}}}{M_{\mathrm{w}}} \ln\left(\frac{1 - w_i - bw_i}{1 - w_i - bw_i + Ew_i}\right) \tag{5.3}$$

where b is a fitting parameter, $K_{\mathrm{w}} = 1.86\,\mathrm{kg\,K^{-1}\,mol^{-1}}$ for water, M_{w} is the molar mass of water, w_i is the mass fraction of the solute (sucrose), and $E = M_{\mathrm{w}}/M_{\mathrm{i}}$ where M_{i} is the molar mass of the solute. Fitting to our data of T_{m} in Table 5.1 yields $b = 0.30 \pm 0.01$ and the orange line in Fig. 5.6.

Finally, we set $T_{\mathrm{m}} = T_{\mathrm{m}}'$ in the obtained fitted models (Eqs. 5.1–5.3) to the temperature of T_{m}' to solve for the corresponding value of w' for the maximally freeze-concentrated solution. From the osmolality-based OVE model, we obtain a value of (75.0 ± 0.1) wt%, and from the osmole-fraction-based OVE, we obtain (76.3 ± 0.1) wt%. Both of these results are in close agreement with literature values that range between 72 wt% and 77 wt%.[166] On the other hand, the Chen et al.[162] fit to our measured data yields a value of (70.5 ± 0.1) wt%. The significant difference between the Gibbs–Duhem–OVE model and the Chen model highlights the sensitivity of the obtained value of w' to the model chosen for extrapolation.

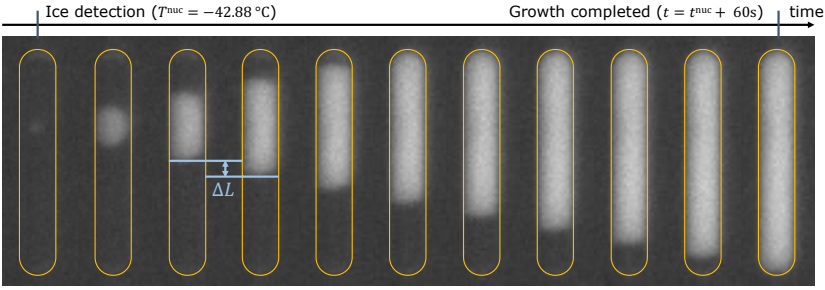

Figure 5.7 Observation of ice formation in a single slug containing 55 wt% sucrose solution. The slug is about 445 µm long, 75 µm in width, and crystal growth requires about 60 s to encompass its entire volume. A yellow outline representing the extent of complete crystal growth is overlaid at the same position in each frame to facilitate visual comparison. The nucleation time, t^{nuc}, is defined as the first point in time, i.e., the first image, where ice is detected; the nucleation temperature, T^{nuc}, is the temperature measured by the thermocouples at this time.

5.3.5 Ice crystal growth

Crystal growth is relevant in the scope of this work for at least the following two reasons. First, a nucleus upon its formation is extremely small and cannot be detected immediately. The new ice phase requires some time to grow to a detectable size; this detection delay must be considered when analysing nucleation data, as is commonly done in studies on nucleation from solution.[68,78] Second, when interpreting and modeling freezing processes, it is of importance to hypothesize how many nuclei form within a volume of interest. It is typically assumed that a single nucleus initiates growth that encompasses the entire volume before a second nucleus can form (this is plausible if crystal growth is very fast and the volume is small), which is consistent with the description of nucleation as a rare event. Such an assumption is commonly made when analysing the freezing behavior in microdroplets.[27,86] It has also been applied in previous studies focusing on larger volumes relevant to pharmaceutical applications,[76,79] where it was verified through visual observation that freezing in vials starts from a single point of origin, i.e., from a single nucleus.

These previous studies motivated us to carry out a detailed crystal growth analysis. Fig. 5.7 illustrates ice formation in a single slug (75 µm × 445 µm, yellow outline) containing 55 wt% sucrose solution; the use of elongated slugs instead of droplets allows for a monitoring of crystal growth over a longer period of time (see *Methods* for details on slug generation). The figure consists of a total of eleven cropped images of the same slug, taken every six

seconds, hence representing the evolution of the droplet over a total period of one minute. The leftmost image is the first image in which ice can be visually detected (bright spot); the rightmost image shows a slug that is nearly completely frozen, i.e., its entire volume appears bright.

Assuming that the maximally freeze-concentrated solution contains 75 wt% sucrose, this phase comprises 73.3 % of the slug's total mass, whereas the ice crystals comprise the remaining 26.7 %. Hence, even after ice formation is complete, ice crystals encompass only a minor mass (or volume) fraction of the slug. Even though the estimated amount of ice crystals is relatively minor, the rightmost image in Fig. 5.7 shows an evenly bright slug indicating the presence of ice throughout its entire volume. This is because there is no macroscopic separation of the two phases, and instead the ice phase and the freeze-concentrate form an intertwined network with contiguous regions having a length-scale on the order of micro-meters or below (see e.g., Först et al.[167] for images of such a crystalline network). The formation of such a network during freezing is in fact the reason why aqueous solutions can be freeze-dried. After the freezing phase of the process is complete, ice crystals sublimate during the primary drying phase under vacuum, leaving behind the highly porous network of the freeze-concentrated phase, which due to its large surface area, allows for a fast desorption of the water in the freeze-concentrate.[20,21] Given the resolution of 6.8 µm per pixel it is not possible to observe individual pockets of ice or freeze-concentrate, and instead the entire frozen region appears bright.

An image sequence as the one shown in Fig. 5.7 can be used to compute the velocity of the freezing front, i.e., of the interface between the region in which ice has already formed, and that where it has not. Because crystal growth is the only phenomenon that takes place in the slugs after nucleation (as in most cases only a single nucleus forms per slug), such velocity represents the crystal growth rate under the given conditions. The growth rate G is obtained by measuring the difference in length of the frozen region (ΔL) between two images and considering the time elapsed between them (Δt) as $G = \Delta L / \Delta t$.

The growth rate is a function of temperature and solution composition. To investigate this relationship, we report in Fig. 5.8 the growth rates measured in ten slugs each for three sucrose concentrations at different temperatures. Panel (a) shows the growth of ice as function of time in three slugs containing 55 wt% sucrose solution that represent the fastest-growing, the slowest-growing and an average-growing slug out of the ten measured in total. The markers denote experimental measurements, and lines the best fit for the growth rate obtained through linear regression. As can be seen, all slugs show a linear evolution of length grown with time, and the growth rate in the fastest-growing slug is about 20% higher than in the slowest-growing one.

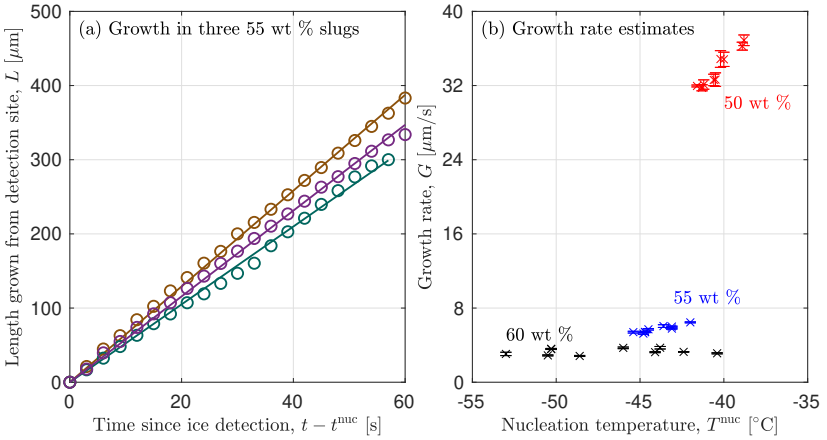

Figure 5.8 Growth rate estimates for slugs containing 50 wt%, 55 wt%, and 60 wt% sucrose solution. (a) Growth of ice in three slugs containing 55 wt% sucrose solution; they represent the fastest-growing, the slowest-growing and an average-growing slug out of the ten measured in total. The markers denote experimental measurements, and lines the best fit obtained through linear regression. (b) Growth rate measurements in ten slugs per solution composition, sorted by nucleation temperature. Error bars denote two standard deviations.

Panel (b) illustrates the regressed values of the growth rates and their uncertainty for all measured slugs, plotted in terms of their nucleation temperature. Average growth rates of $(33.4 \pm 4.4)\,\mu\mathrm{m\,s^{-1}}$, $(5.7 \pm 0.8)\,\mu\mathrm{m\,s^{-1}}$, and $(3.3 \pm 0.6)\,\mu\mathrm{m\,s^{-1}}$ were measured for 50 wt%, 55 wt%, and 60 wt%, respectively. Both the error bars and the uncertainty in the growth rates correspond to two standard deviations. A number of remarks are worth making.

First, the growth rate decreases significantly with increasing sucrose concentration. This is because with increasing sucrose concentration the viscosity level of the solution increases, and hence the molecular mobility of the water molecules decreases. In fact, at concentration levels below 50 wt%, crystal growth was too fast for it to be monitored adequately: the time elapsed between two images suffices for ice to grow into the entire volume of the slug. Hence, this analysis is limited to highly concentrated solutions where crystal growth is slow.

Second, at all concentration levels, growth is fast enough that there is no relevant delay in detection of nucleation, i.e., the time to grow to a detectable size is shorter than the time elapsed between two images (3 s). Third, the growth rate decreases with decreasing temperature, particularly for the 50 wt%

sucrose solution. The temperature-dependency of the growth rate stems from both the thermodynamic driving force (larger at lower temperature) and from kinetic effects related to the molecular mobility in the solution (lower at lower temperature). Hence, the growth rate is dominated by kinetic effects for the systems studied here.

Fourth and finally, all thirty slugs analysed in this study experienced only one single nucleation event. For 55 wt% and 60 wt% sucrose solutions, however, some slugs not included in the growth rate analysis exhibited a different freezing behavior; that is, two separate frozen regions were observed to form that eventually grew together. Such a scenario is expected for slugs in which two distinct nucleation events take place. It can be explained by considering Fig. 5.7 again, which shows that the time scale for growth in a 55 wt% slug is on the order of one minute. Slugs of this composition nucleate within a temperature interval of about 4 °C, as illustrated in Fig. 5.8(b), corresponding to a time interval of 4 min. Given that both times are on the same order of magnitude, it is indeed statistically reasonable to expect more than one nucleus to form in some slugs. For the droplets analysed in the nucleation temperature study, which are six times shorter in length than the slugs—and hence experience a six- times-shorter growth time—the single nucleus assumption is reasonable.

To conclude this section, we compare the estimated growth rates with literature values. It is worth noting that conventional growth rate experiments are typically carried out by monitoring seeded ice crystals at small supercooling (order of 1 °C), whereas the method presented here naturally operates at large supercooling, namely at that connected to the stochastic occurrence of nucleation. For example, Blanshard et al.[148] reported a growth rate of $(6.5 \pm 0.3)\,\mu m\,s^{-1}$ for a 58.6 wt% sucrose solution at a temperature of -16.2 °C. This value is of the same order of magnitude as those measured here for the 55 wt% and 60 wt% sucrose solutions, and it agrees well with the observation of a weak temperature-dependence. Since growth rates can be measured at relatively low temperature (high supercooling), the method presented here promises to complement existing techniques applicable to higher temperature (lower supercooling). For high supercooling levels, growth rates for droplets of pure water have been reported by Schremb et al.[168], which are significantly higher, namely on the order of $15\,cm\,s^{-1}$ for a supercooling of 20 °C. The same study reported an increase in crystal growth rate with increasing supercooling, i.e., the opposite trend that we observed here for concentrated sucrose solutions. This is not surprising, given the significant differences in viscosity and hence molecular mobility between pure water and concentrated sucrose solution.

5.4 CONCLUDING REMARKS

The importance of phase equilibrium predictions and of the kinetics of phase transitions is evident in the design and control of freezing and freeze-drying processes. Motivated by this, we investigated and demonstrated the use of droplet microfluidics to aid in mapping out the solid–liquid phase boundaries and the associated kinetics for a sucrose–water system at concentrations below the eutectic point. As a function of sucrose composition, three key temperatures were extracted based on an analysis of temporal changes in pixel intensity: the nucleation temperature distribution, the melting temperature (T_m), and the temperature of the maximally freeze-concentrated solution at (w', T'_m). Knowledge of the last two enabled the computation of the sucrose concentration in the maximally freeze-concentrated solution, another important design parameter for biopharmaceutical formulations.

Additionally, slugs (elongated droplets) were generated in separate experiments comprising highly-concentrated sucrose solutions, and the growth rate of ice crystals was quantified to yield insights into its dependence on both composition and temperature. The growth rate was observed to decrease at higher concentrations and lower temperatures likely due to the reduction in molecular mobility. Further, we assessed the commonly-made assumption that a single nucleating event occurs, confirming that it is valid for the spherical droplets, while occasionally two nuclei were observed for the slugs with the highest sucrose concentration.

Overall, we showed the ability of droplet microfluidics to characterize and quantify the freezing behaviour of aqueous sucrose solutions, both thermodynamically and kinetically. Future work can be pursued for other mixtures of interest to the broad range of applications in which controlling or understanding freezing is relevant—in industry (food, pharmaceutics, and cryobiology) and in the environment (the atmosphere).

5.5 METHODOLOGY

5.5.1 Experimental methods

The Microfluidic Ice Nuclei Counter Zurich (MINCZ) was used to generate and control the temperature of monodisperse populations of 75-µm droplets. The operating principle of MINCZ is described in detail by Isenrich et al.[87] First, microchannels were patterned onto an SU-8 coated silicon wafer, followed by standard soft lithography to transfer the channels to a

polydimethylsiloxane (PDMS, Elastosil RT 601 A/B, Ameba AG, Switzerland; mass ratio of 10:1 between the base and curing agent) device bonded to a glass slide (Menzler-Glaser, Germany) via plasma treatment. Second, immediately prior to droplet generation, a fresh sucrose solution with the desired concentration was prepared. Solution preparation entailed: (i) cleaning glassware with deionized water (Millipore, Milli-Q Advantage A10 system), acetone, and an additional three times with deionized water; (ii) weighing the desired mass of sucrose (Sigma-Aldrich, BioXtra grade, $> 99.5\,\%$ purity) and fully dissolving it in deionized water for a total solution mass of 50 g; (iii) filtering the sucrose solution (0.22 µm hydrophilic PTFE syringe filter); and (iv) transferring the solution to a glass vial (Lab Logistics Group GmbH, 1.5 mL) using a 100–1000 µL pipette (Socorex Acura 825). Third, to generate microfluidic droplets, three glass syringes (1 mL, Hamilton® syringe, Sigma-Aldrich) were placed in syringe pumps (Aladdin AL1000-220Z, World Precision Instruments, USA) to control the flowrates of the sucrose solution, fluorosurfactant (2 % v/v 008-FluoroSurfactant in HFE-7500 (RAN Biotechnologies, USA)), and fluorinated HFE-7500 oil (3M™ Novec™ 7500, Interelec Electronics AG, Switzerland) into the microfluidic device. Depending on the target droplet size, a different channel geometry was used: for small droplets of approx. 75 µm in diameter, the same channel geometry as described in Isenrich et al.[87]; and for elongated droplets (slugs), a T-junction channel geometry. Generated droplets exited the microfluidic device through an outlet connected to high-purity perfluoroalkoxy alkane (PFA) tubing (up to 50 cm in length; 360 µm o.d., 75 µm i.d.; IDEX Health & Science LLC, USA) held in a custom-milled polyether ether ketone (PEEK) structure. After droplets were generated, the PFA tubing was cut at the outlet of the microfluidic device with scissors, and the ends of the tubing were mechanically clogged with serrated forceps. Finally, the PFA tubing was placed in an ethanol bath, the temperature of which was regulated using a Peltier element (PKE 128A 0020 HR 150, Peltron GmbH, Germany) and recirculating chiller (Huber KISS K6, Huber Kältemaschinenbau AG, Germany) with a working fluid of aqueous 55 % v/v ethylene glycol (98 % technical grade, Sigma-Aldrich, USA). The polarity of the Peltier element was set by an Arduino UNO R3 (Arduino) with two single-pole double-throw (SPDT) switches (Grove 2-Channel SPDT Relay, Seeed Technology Co., Ltd) wired to create a double-pole double-throw (DPDT) switch. Temperature was measured with two K-type thermocouples (0.5 mm o.d., RS Components GmbH, Germany, and TC Direct, Germany) placed horizontally in the same plane as the droplets (see Isenrich et al.[87] and Shardt et al.[27] for more details). During both droplet generation and cooling, a stereoscope (Nikon SMZ1270 (0.5× objective lens) equipped with a fibre ring illuminator with LED light source) and CMOS camera (iDS UI-3060CP-M-GL Rev. 2) were used to observe the droplets.

Aqueous sucrose solutions with concentration levels of 0 wt%, 1 wt%, 10 wt%, 20 wt%, 30 wt%, 40 wt%, 50 wt%, 55 wt% and 60 wt% were studied with monodisperse droplet populations. Each droplet population underwent three freeze–thaw cycles that traversed three temperature regions of interest: the nucleation, maximally freeze-concentrated glass transition, and melting temperatures. The cycles were implemented with the recirculating chiller at either: (i) a constant setpoint temperature of −17 °C with the Peltier element controlling the ethanol bath temperature (necessitating a reversal of the Peltier element's polarity to reach the solutions' melting temperatures) or (ii) a dynamic temperature setpoint with an unchanged polarity for the Peltier element. A constant chiller temperature permits experiments that rapidly scan through the temperatures of interest. On the other hand, a dynamic chiller temperature permits constant cooling and warming rates to be maintained for all temperatures. Droplet size and cooling rate were selected to match the conditions used in an earlier study that focused on the monitoring of homogeneous ice nucleation in water droplets.[27]

5.5.2 Image analysis

Nucleation, maximal freeze-concentration, and melting temperatures were identified based on changes in the pixel intensity of the region of interest (implemented with OpenCV and SciPy in Python). For nucleation temperatures, the region of interest was each individual droplet, because nucleation is a stochastic process and each droplet nucleates at a different temperature. For the maximally freeze-concentrated and melting temperatures, the region of interest was the columns of pixels where PFA tubing was present, because these processes are deterministic, thus lending themselves to a simplified image processing approach.

Identifying which pixels contain tubing: To reduce computational time for image processing, only the regions of each image that contained tubing were used for further image analysis. These regions were found with the following procedure performed on the first image saved in the experiment: equalizing the histogram, applying Otsu's thresholding, calculating the mean pixel value of each pixel column in the image, smoothing the mean pixel value with a Savitzky–Golay filter, and identifying the regions with peaks in pixel intensity. The identified peaks in pixel intensity corresponded to the presence of a piece of tubing in the image.

Droplet nucleation temperature, T^{nuc}: Due to the stochasticity of nucleation, the average intensity of each droplet was tracked. To determine the droplets' locations, the following procedure was followed. The last image in the saved sequence was binarized and then morphological opening was

applied to remove extraneous bright pixels. The Hough circle transform was applied to find circular shapes (i.e., the droplets), and the average intensity of a 9-pixel radius circle at the identified center coordinate was calculated for each saved image.

To determine the temperature at which a droplet increased in brightness, the observed temporal evolution of the droplet intensity was analyzed. A Savitzky–Golay filter was applied to smooth the time series of average intensity, and the first derivative of intensity was calculated with respect to time for each consecutive pair of images. The temperature at which the first derivative reached its maximum was taken to be the temperature at the midpoint of the transition between liquid and solid. Next, the second derivative was calculated, and the temperatures where the second derivative reached extrema were identified (corresponding to the beginning and end of the phase transition, respectively). In Fig. 5.3, the temperature plotted on the x-axis is the one at the beginning of the transition. The results were reviewed manually to remove from consideration any droplets that were exceptionally large or had merged between freeze–thaw cycles.

T'_{m} and T_{m}: The average pixel value of the regions with tubing was calculated for each image. For both T'_{m} and T_{m}, the first and second derivatives were calculated. A maximum in the absolute value of the first derivative was assigned to be the midpoint of the transition in brightness. The extrema in the second derivative corresponded to the beginning and end of the transition regions. An increase in pixel intensity was observed as the temperature increased above the maximally freeze-concentrated temperature, while a decrease in pixel intensity was observed during melting (the solid-to-liquid phase transition).

Slug generation and crystal growth rate: For each experiment, ten slugs were selected for growth rate measurement based on the following criteria: (i) only a single nucleus formed in the slugs, (ii) the nucleus forms close to the top or bottom to allow for more time until growth is complete, (iii) the set of slugs represents the entire range of nucleation temperature. The grown length was measured in all images after nucleation based on the pixel intensity profile. A single pixel corresponded to a distance of 6.8 µm.

Part II

FREEZING OF PHARMACEUTICALS

6 STOCHASTIC SHELF-SCALE MODELING FRAMEWORK FOR THE FREEZING STAGE IN FREEZE-DRYING PROCESSES

Freezing and freeze-drying processes are commonly used to improve the stability and thus shelf life of pharmaceutical formulations. Despite strict product quality requirements, batch heterogeneity is widely observed in frozen products, thus potentially causing process failure. Such heterogeneity is the result of the stochasticity of ice nucleation and the variability in heat transfer among vials, which lead to unique freezing histories of individual vials.
We present for the first time a modeling framework for large-scale freezing processes of vials on a shelf. The model is based on first principles and couples heat transfer with ice nucleation kinetics, thus enabling studies on batch heterogeneity. Ice nucleation is assumed to be an inhomogeneous Poisson process and it is simulated using a Monte Carlo approach. We applied the model to understand the individual pathways leading to batch heterogeneity. Our simulations revealed a novel mechanism how ice nucleation leads to heterogeneity based on thermal interaction among vials. We investigated the effect of various cooling protocols, namely shelf-ramped cooling, holding steps and controlled nucleation, on the nucleation and solidification behavior across the shelf. We found that under rather general conditions holding schemes lead to similar solidification times, as in the case of controlled nucleation, thus identifying a potential pathway for freezing process optimization.

6.1 INTRODUCTION

Freezing and freeze-drying are widely used processes to improve the stability and thus the shelf life of pharmaceutical formulations.[21] The freeze-drying process of biopharmaceuticals is carried out in vials at large scale; a single

The work presented in this chapter has been reported in: Deck, L.-T.; Ochsenbein, D.R.; Mazzotti, M. Stochastic shelf-scale modeling framework for the freezing stage in freeze-drying processes. *Int. J. Pharm.* **2022**, 613, 121276.

batch may comprise ten to hundred thousands of vials. Freeze-drying consists of three stages, namely freezing, primary drying, and secondary drying. During freezing, most of the liquid water in the product transitions into ice crystals, while the solutes and the remaining water form either an amorphous or a crystalline phase engulfed among the ice crystals.[41] The ice crystal morphology of such a frozen product depends both on the formulation and on the freezing process itself and it has a profound impact on the duration of the subsequent drying steps.[34] Heterogeneity in morphology between vials will lead to heterogeneity in drying behavior, possible poor product quality and potential process failure.[169,170] Freezing process design and optimization is thus of great relevance for the overall process development and optimization in lyophilization.[44]

The freezing stage itself consists of at least three parts, namely ice nucleation, rapid unstable crystal growth upon nucleation, and directional solidification. Despite various experimental and theoretical studies in this field, predicting the ice crystal size distribution in the frozen product from process parameters remains challenging. A consensus exists about certain trends, e.g. that an increase in solute concentration generally results in smaller ice crystals.[43,167] Other trends are not accepted and considered general: Nakagawa et al.[19] found that higher cooling rates, too, lead to smaller particle size, but this could not be reproduced by others in a study with a lyo-microscope on a system where the fill height was lower.[167]

With observable phenomena in dispute, it is no surprise that also their rationalization remains a topic of intense research. Searles et al.[43] identified the ice nucleation temperature as the main predictor of the ice crystal morphology in a vial. Moreover, a number of empirical and semi-empirical models were developed that relate the average ice crystal size in a frozen product to freezing process parameters, i.e. to the rate of solidification and to the temperature gradient within the frozen zone.[19,28,171] Recently, Colucci et al.[40] developed a more mechanistic model based on a 1D population balance equation to describe the evolution of not only the mean, but also of the distribution of ice crystal sizes during freezing for the first time.

While all those studies focused on the freezing of individual vials, studies on batch heterogeneity and its causes are scarce. Such heterogeneity is undesired and of great practical relevance since operating conditions are generally chosen to accommodate the worst-performing vials.[41] Common explanations qualitatively depend on the stochasticity of ice nucleation and on the heterogeneity of heat transfer across the shelf. Mitigation tactics therefore revolve around addressing these sources of variation.[44,172,173] For example, to address the issue of ice nucleation stochasticity, controlled nucleation methods have been developed aiming at artificially triggering nucleation in all vials

at the same time. Such efforts are based on a number of physical mechanisms that promote nucleation; they include the ice-fog technique based on seeding all vials with small ice crystals from the air,[174] the vacuum-induced surface freezing mechanism based on evaporative cooling of the product surface,[175,176] and the depressurization method based on the formation of gas nuclei in the product.[177,178]

While these techniques have been shown to have positive effects,[175,179] a thorough analysis of the pros and cons of such approaches has not been carried out yet, also because of its difficulty. On the one hand, experimentally determining product attributes in a statistically significant number of vials to measure the improvements is difficult. On the other hand, the use of controlled nucleation adds significant complexity to the process design, which is intrinsically hard to quantify. For all these reasons, a shelf-scale model of the freezing process is required to deepen the understanding of batch heterogeneity and to optimize the process design. To the best of our knowledge, such model is not available in the literature, whose focus has been on single vials only.[19,28,40]

6.2 METHODS

We model the freezing process of vials on a shelf in a mechanistic way and take into account batch size and arrangement, heat transfer, composition of the formulation, and ice nucleation. We use a lumped capacitance approach, where each vial is considered as a lump. While spatial variability within a vial, i.e. in terms of temperature, may be present in practice, the lumped model is based on the mean values of the properties within the vial's volume. For the studied systems, i.e. vials with fill height of not more than 1 cm and heat transfer coefficients in the range of 20–60 $\frac{W}{m^2K}$, the accuracy of the approach allows for a qualitative understanding of freezing on the batch scale. During a simulation of the freezing process, each vial evolves from a liquid to an ice growth state. The governing equations account for the vial's physical state. Ice nucleation is described as an inhomogeneous Poisson process following existing literature on primary nucleation of solutes[22] and is simulated using a Monte Carlo approach.

6.2.1 Modeling framework

Balance equations

We start the model derivation with the balance equations for the freezing process in a single vial. As to the material balance, we can safely assume that the mass of the formulation in the vial, i.e. m_v, the mass of the solute, i.e. m_s, plus the total mass of water, i.e. m_w, remain constant during the freezing process:

$$m_\mathrm{v} = m_\mathrm{s} + m_\mathrm{w} = m_\mathrm{s} + m_\ell + m_\mathrm{i} \tag{6.1a}$$

$$\frac{\mathrm{d}m_\mathrm{v}}{\mathrm{d}t} = \frac{\mathrm{d}m_\mathrm{s}}{\mathrm{d}t} = 0 \tag{6.1b}$$

$$\frac{\mathrm{d}m_\mathrm{i}}{\mathrm{d}t} = -\frac{\mathrm{d}m_\ell}{\mathrm{d}t} \tag{6.1c}$$

The decrease in mass of liquid water, m_ℓ, during freezing equals the increase in mass of solid ice, m_i.

The total enthalpy of the formulation in a vial, H_v, is given by:

$$H_\mathrm{v} = m_\mathrm{s}h_\mathrm{s} + m_\ell h_\ell + m_\mathrm{i}h_\mathrm{i} \tag{6.2a}$$

$$= m_\mathrm{s}h_\mathrm{s} + m_\mathrm{w}h_\ell - m_\mathrm{i}\lambda_\mathrm{w} \tag{6.2b}$$

The latent heat of fusion λ_w is defined as $\lambda_\mathrm{w} = h_\ell - h_\mathrm{i}$, whereas the specific enthalpy h_k for component k is:

$$h_\mathrm{k} = \int_{T_\mathrm{ref}}^{T} c_{\mathrm{p,k}}(T')\mathrm{d}T' \tag{6.3}$$

Here, $c_{\mathrm{p,k}}$ denotes the specific heat capacity of component k, which generally depends on temperature. For the sake of simplicity, we neglect this temperature dependency in this work. Combining equations (6.1), (6.2), and (6.3) enables us to model the time evolution of the vial's enthalpy:

$$\frac{\mathrm{d}H_\mathrm{v}}{\mathrm{d}t} = \left(m_\mathrm{s}c_{\mathrm{p,s}} + m_\ell c_{\mathrm{p},\ell} + m_\mathrm{i}c_{\mathrm{p,i}}\right)\frac{\mathrm{d}T}{\mathrm{d}t} - \lambda_\mathrm{w}\frac{\mathrm{d}m_\mathrm{i}}{\mathrm{d}t} = \dot{Q} \tag{6.4}$$

where $\dot{Q}$ corresponds to the heat flow between the vial and its environment, i.e. the effect of the external cooling that is applied during the freezing process.

In the next step of model development, we consider the events that happen during freezing at the micro-scale, namely nucleation and growth of ice crystals. The rates of nucleation, J, and growth, G, which ultimately determine the rate of change of the ice mass, $\frac{\mathrm{d}m_\mathrm{i}}{\mathrm{d}t}$, may be expressed as power laws of the

thermodynamic driving force, which is defined as the temperature difference $T^{\mathrm{eq}} - T$, i.e. between the equilibrium and the actual temperature:

$$J = k_{\mathrm{b}}(T^{\mathrm{eq}} - T)^{b} \tag{6.5a}$$

$$G = k_{\mathrm{g}}(T^{\mathrm{eq}} - T)^{g} \tag{6.5b}$$

where k_{b} and k_{g} are temperature dependent coefficients and b and g are empirical constants. Importantly, the expression for the nucleation rate J is agnostic to the actual mechanism of primary nucleation, which may occur either homogeneously or heterogeneously, i.e. on the surface of dust particles in the solution. When estimating the nucleation parameters, one thus needs to consider the effect of the setup: It might be that values estimated under standard lab conditions are not applicable to describe nucleation under dust-free GxP conditions.

Let us consider freezing experiments in vials, whereby it is well known that the formation of the first ice nucleus initiates ice formation via rapid, recalescent growth in the entire volume of the system. In fact, a post-nucleation temperature rise from a supercooled state to the equilibrium freezing temperature is observed taking place in a matter of seconds or less.[20,180] Since primary nucleation is a rare event, we make the assumption that $k_{\mathrm{g}} \to \infty$ to simulate quantitatively such post-nucleation temperature rise. It follows that

$$T^{\mathrm{eq}} - T \to 0 \qquad \text{for } t \in [t^{\mathrm{nuc}}, \infty) \tag{6.6}$$

where t^{nuc} is the nucleation time, since the unstable, rapid growth of the first ice nucleus is assumed to instantly bring T to T^{eq}. Additional consequences of this assumption include first the fact that the first primary nucleus remains the only primary nucleus in the system, since the nucleation rate, too, drops to virtually zero. Secondly, the system enters a quasi-equilibrium-state, whereby the rate-limiting step of ice formation is the external removal of the heat of crystallization from the vial. Since heat transfer is the rate-limiting step, we may describe the subsequent evolution of the system without considering the micro-structure within the vial. In order to quantitatively predict this structure, i.e. the distribution of crystal sizes, in a mechanistic way, more knowledge on the rapid growth phase upon nucleation would be required. However, this phase remains the least understood part of the freezing process, which is why we do not consider it in detail within this model.

Freezing can thus be split into two distinct regimes, starting with a liquid state that lasts until the formation of the first primary nucleus, followed by an ice growth state. The energy balance for a vial in position (m, n) on a shelf with $(M \times N)$ vials in the former regime, where no ice is present, is then:

$$\dot{Q}_{(m,n)} = \left(m_{\mathrm{s}} c_{\mathrm{p,s}} + m_{\mathrm{w}} c_{\mathrm{p},\ell}\right) \frac{\mathrm{d}T_{(m,n)}}{\mathrm{d}t} = m_{\mathrm{v}} c_{\mathrm{p}} \frac{\mathrm{d}T_{(m,n)}}{\mathrm{d}t} \tag{6.7}$$

for $t \in [t_0, t^{\mathrm{nuc}}_{(m,n)})$ and where c_p is defined as the heat capacity of the solution. In the second regime, the ice growth phase, the thermal evolution is governed by $T^{\mathrm{eq}}_{(m,n)}$, which equals the temperature of the vial $T_{(m,n)}$:

$$\dot{Q}_{(m,n)} = \left(m_s c_{p,s} + m_{\ell,(m,n)} c_{p,\ell} + m_{i,(m,n)} c_{p,i} \right) \frac{\mathrm{d}T^{\mathrm{eq}}_{(m,n)}}{\mathrm{d}t} - \lambda_w \frac{\mathrm{d}m_{i,(m,n)}}{\mathrm{d}t} \quad (6.8)$$

for $t \in (t^{\mathrm{nuc}}_{(m,n)}, \infty)$. Note that we require a constitutive equation to describe $T^{\mathrm{eq}}_{(m,n)}$ as a function of the composition of the solution. We may consider for example the Schröder van Laar equation or the simplified law for freezing point depression given by Blagden.[98] In this work, the latter will be used, since it finds broad use in the general freezing literature:[181,182]

$$T^{\mathrm{eq}}_{(m,n)} = T_m - k_f b_{s,(m,n)} = T_m - \frac{k_f}{M_s} \left(\frac{m_s}{m_w - m_{i,(m,n)}} \right) \quad (6.9)$$

Here, b_s is the molality of the solute in the solution, M_s its molar mass, k_f its cryoscopic constant and T_m the melting point of water; we also introduce T^{eq}_{ℓ} as the equilibrium freezing temperature of the solution before the onset of ice formation, i.e. when $m_{i,(m,n)} = 0$. We note that the thermal evolution of the system is coupled with the evolution of the ice mass; the increase in mass of ice crystals is connected with an increase in solute concentration in the remaining solution that leads to a depression of the freezing point. Such concentration of the solution upon freezing is commonly referred to as freeze-concentration.

A direct consequence of it is that m_i approaches m_w only asymptotically. When m_i is small, at the beginning of the ice growth state, most of the heat that is removed from the vial is due to the growth of ice; if m_i is close to m_w, heat removal primarily leads to a decrease in temperature, theoretically towards infinitely low values. In practice, at very low temperatures, vitrification of the remaining water and solute or crystallization of the solute will occur, thus leading to a completely solidified product.[183] For the sake of simplicity and because these two phenomena occur at low temperatures, the model does not cover them and we assume that solidification is completed when $\frac{m_i}{m_w} = 0.9$ in order to compare solidification times between vials. The choice of such threshold is arbitrary; we tested values in the range of 0.9-0.95 and found no qualitative difference. Alternatively, one could define the endpoint of solidification based on temperature instead of formed ice and assume that solidification is complete when the formulation is cooled down to its glass transition temperature.

At the time of the nucleation event, it is necessary to identify the initial state of the vial in the ice growth state, i.e. the mass of ice formed immediately

after the unique nucleation event, $m_{\mathrm{i},(m,n)}(t^{\mathrm{nuc}})$, that led to the instantaneous depletion of the existing supercooling, and the corresponding temperature $T^{\mathrm{eq}}_{(m,n)}(t^{\mathrm{nuc}})$. We assume that the heat released upon nucleation equals the sensible heat associated to the rise in temperature from the nucleation temperature, $T^{\mathrm{nuc}}_{(m,n)}$, to the equilibrium freezing temperature of the now partially frozen solution, $T^{\mathrm{eq}}_{(m,n)}$:

$$\left(T^{\mathrm{eq}}_{(m,n)} - T^{\mathrm{nuc}}_{(m,n)}\right) c_{\mathrm{p}} m_{\mathrm{v}} = \lambda_{\mathrm{w}} m_{\mathrm{i},(m,n)} \qquad \text{for } t = t^{\mathrm{nuc}}_{(m,n)} \tag{6.10}$$

Eqn. 6.10 and the constitutive equation for the equilibrium freezing temperature, i.e. eqn. 6.9, form a system of two equations in two unknowns, namely $m_{\mathrm{i},(m,n)}$ and $T^{\mathrm{eq}}_{(m,n)}$, and are solved together.

Heat transfer for vials on a shelf

As derived in section 6.2.1, the rate of change of the enthalpy of a vial equals the heat flow with its surroundings, i.e. $\dot{Q}_{(m,n)}$. The computation of this heat flow requires knowledge of the system's heat transfer and geometry. For the sake of simplicity, we assume a cubic shape for the vials and a rectangular arrangement, so that each vial in the center of the batch has four neighbors and that the contact area between vial and shelf equals the area of one side of the vial, i.e. $A^{\mathrm{sh}} = A^{\mathrm{side}} = A$. In general the model may be applied to any arbitrary shape and arrangement, such as hexagonal arrangements which are also commonly used in practice. The heat flow $\dot{Q}_{(m,n)}$ comprises two contributions, firstly the heat transfer between vial bottom and shelf and the one through the vial top, $A^{\mathrm{sh}} q^{\mathrm{sh}}_{(m,n)}$ and secondly the heat transfer through the sides of the vial, $A^{\mathrm{side}} q^{\mathrm{side}}_{(m,n)}$:

$$\dot{Q}_{(m,n)} = A^{\mathrm{sh}} q^{\mathrm{sh}}_{(m,n)} + A^{\mathrm{side}} q^{\mathrm{side}}_{(m,n)} = A \left(q^{\mathrm{sh}}_{(m,n)} + q^{\mathrm{side}}_{(m,n)}\right) \tag{6.11}$$

Heat transfer within freezing and freeze-drying chambers is complex. It was shown that already for the shelf-to-vial heat transfer several mechanisms play a role, namely ranging from solid conduction, to radiation, to both gas conduction and convection.[92] We aim for a high-level understanding; investigations on the contributions of individual heat transfer mechanisms are beyond the scope of this work. We perform sensitivity analyses by modeling the freezing processes with a wide range of parameter values for the heat transfer coefficients to understand the process behavior under different conditions.

To ensure a qualitatively accurate description we use a 4-parameter approach: We define the vial-to-vial heat transfer coefficient k_{int} to model the

thermal interaction among vials, a vial-to-environment coefficient k_{ext}, and an (average) vial-to-shelf coefficient, k_{sh}. It has been shown in the literature[173] that the latter is not the same for all vials, but depends on their exact geometry. To account for this, we define a standard deviation for the vial-to-shelf heat transfer, s_{sh}, which can be used to add an isotropic source of variability via

$$k_{\text{sh},(m,n)} = k_{\text{sh},0} + s_{\text{sh}}\epsilon_{(m,n)}. \tag{6.12}$$

In equation (6.12), $\epsilon_{(m,n)}$ is a random scalar drawn from the standard normal distribution, and $k_{\text{sh},0}$ should be interpreted as a lumped coefficient for all related contributions, including radiative heat transfer from the top shelf. Similarly, k_{int} characterizes the *totality* of thermal interaction between the vials in this system. From a physical point of view, thermal interaction occurs both via direct heat transfer between the vials and indirectly via heat transfer with the base the vials are standing on, i.e. the shelf or the tray. A sudden temperature rise of one vial, as observed after nucleation, will heat up the immediate vicinity of said shelf and thus affect the heat transfer and the thermal evolution of the neighboring vials. These considerations lead to the following expressions for the heat fluxes:

$$q^{\text{sh}}_{(m,n)} = k_{\text{sh},(m,n)} \left(T_{\text{sh}} - T_{(m,n)} \right) \tag{6.13a}$$

$$q^{\text{side}}_{(m,n)} = q_{(m+1,n,m,n)} + q_{(m-1,n,m,n)} + q_{(m,n+1,m,n)} + q_{(m,n-1,m,n)} \tag{6.13b}$$

where

$$q(m',n',m,n) = \begin{cases} k_{\text{ext}} \left(T_{\text{ext}} - T_{(m,n)} \right) & \text{if } m' \in \{0, M+1\} \vee n' \in \{0, N+1\} \\ k_{\text{int}} \left(T_{(m',n')} - T_{(m,n)} \right) & \text{otherwise} \end{cases} \tag{6.14}$$

The heat flux $q^{\text{sh}}_{(m,n)}$ depends on the temperature of the shelf T_{sh}, while the quantity $q^{\text{side}}_{(m,n)}$ depends on the temperatures of the neighboring vials and/or of the environment, and thus on the vial's position. As eqn. (6.14) illustrates, we need to specify T_{ext}. We will focus in this work on the case where it equals the temperature of the shelf, i.e. $T_{\text{ext}} = T_{\text{sh}}$. In experimental works, the temperature distribution of the environment is often anisotropic. Especially in laboratory freeze-dryers, one commonly observes higher temperatures towards the chamber door due to limited thermal insulation. We could take into account such effect by introducing a position-dependency of T_{ext} or k_{ext}. Such approach would add another degree of freedom to the description of heat transfer and may be useful in validating the model in experimental studies. We also consider the case without any external heat transfer, i.e. where $k_{\text{ext}} = 0$ for all vials.

Transition from the liquid to the partially frozen state

During freezing, each vial transitions from the liquid state to a partially frozen state when the sole primary ice nucleus is formed. Since ice nucleation is stochastic, we expect the nucleation times $t^{\text{nuc}}_{(m,n)}$ to vary between vials on the shelf even in case they contain the same formulation and experience the same heat transfer.

We model ice nucleation as a Poisson process, i.e. the probability of nucleation depends on the current state of the vial, but not on its history.[22,23,66] The Poisson process provides an accurate description of primary nucleation, only requiring that nucleation is an activated process, i.e. that there is an energy barrier to overcome when forming a nucleus. This is the case not only for homogeneous nucleation, but also for heterogeneous nucleation, which is generally considered as the dominant mechanism of nucleation for freezing processes. The hypothetical effect of the thermal history of an aqueous solution on the freezing process is referred to as *Mpemba effect* in the crystallization literature. Despite extensive research on this effect over the past decades, no conclusive evidence for its existence has ever been found.[184] Indeed, such memory effects were only identified for the crystallization of a small number of components, which are prone to the formation of molecular assemblies upon dissolution, such as Fenoxycarb.[185] In the context of freezing, the assumption that ice nucleation only depends on the vial's temperature, thus may be considered as valid.

For a vial in position (m, n) on a shelf we define probabilities for being in the ice growth state, i.e. $P^{(1)}_{(m,n)}$, and in the liquid state, i.e. $P^{(0)}_{(m,n)}$. It must hold that $P^{(0)}_{(m,n)} + P^{(1)}_{(m,n)} = 1$ and $P^{(0)}_{(m,n)}(\mathrm{t}_0) = 1$, i.e. the initial state of the vial is liquid. The rate constant of the Poisson process, $K_{(m,n)}$, corresponds to the nucleation frequency in the vial, in units of nucleation events per unit time. Note that $K_{(m,n)} = J_{(m,n)}V$ for a lumped vial. $K_{(m,n)}$ is called homogeneous when it is time independent, e.g. because the temperature is kept constant, and inhomogeneous otherwise, e.g. because of cooling. We use the master equations to describe the time evolution of the probability that a vial is in the liquid state:

$$\frac{\mathrm{d}P^{(0)}_{(m,n)}}{\mathrm{d}t} = -K_{(m,n)}(t)P^{(0)}_{(m,n)} \tag{6.15}$$

the solution of which is:

$$P^{(0)}_{(m,n)}(t) = \exp\left\{-\int_{t_0}^{t} K_{(m,n)}(t')\mathrm{d}t'\right\} \tag{6.16}$$

hence:

$$P^{(1)}_{(m,n)}(t) = 1 - P^{(0)}_{(m,n)}(t) \tag{6.17}$$

As outlined in section 6.2.1, the thermal evolution of a vial, and thus its nucleation rate, may depend on the thermal evolution of the neighboring vials and in consequence also on the sequence of nucleation events across the shelf. The value of $K_{(m,n)}$ in such a system therefore depends not only on time, but also on the stochastic occurrence of prior nucleation events on the shelf. The type of stochastic process, where past stochastic events effect the future, is known as *self-exciting point process*, and may be interpreted as a step-wise inhomogeneous Poisson process.[22] We may express the probability $P^{(0)\to(1)}_{(m,n)}(t, t+\Delta t)$ that a nucleus is formed in a vial in the liquid state in the time interval $[t, t+\Delta t]$ as:

$$P^{(0)\to(1)}_{(m,n)}(t, t+\Delta t) = 1 - \exp\left\{-\int_t^{t+\Delta t} K_{(m,n)}(t')\mathrm{d}t'\right\} \tag{6.18a}$$

$$\approx K_{(m,n)}(t)\Delta t = V J_{(m,n)}(t)\Delta t \tag{6.18b}$$

We thus compute $P^{(0)\to(1)}_{(m,n)}$ step wise until nucleation occurred in all vials on the shelf. We use the power law outlined in equation 6.5a to compute $J_{(m,n)}$.

The nucleation rate parameters k_b and b were recently estimated by Colucci et al.[40] for 5 wt.% sucrose solution; we therefore investigate the same formulation in this work to make use of their estimations. However, it should be noted that their approach to model nucleation is different, i.e. they assumed the formation of multiple primary nuclei for the ice growth state. We accounted for this by adjusting the value of k_b. Due to the scarcity of literature data on ice nucleation kinetics in this liquid volume range we also conducted our own freezing experiments in a batch crystallizer to estimate the kinetic parameters for sucrose solutions. The detailed experimental study will be reported elsewhere, but the nucleation temperatures are in qualitative agreement with our simulations and literature results, which report nucleation events commonly in the range of -10°C to -15°C in laboratory freeze-dryers.[40] Given that ice nucleation is dominated by heterogeneous effects, the value of the nucleation parameters may depend on the specific setup of the process. For example, we expect slower nucleation under GxP conditions, where fewer dust particles are present that may drive heterogeneous nucleation compared to the lab.

In addition to primary ice nucleation we also study controlled ice nucleation. We model this technique by initiating nucleation in all non-nucleated, supercooled vials at a predefined time $t^\mathrm{nuc}_\mathrm{cont}$.

Numerical solution approach

In order to solve the coupled system of energy balances and stochastic ice nucleation equations described above, we have developed the following numerical algorithm. We discretize the balance equations in time and compute for each time step the thermal evolution of all vials, as well as the nucleation probability for those vials that are in a liquid, supercooled state. To identify nucleation events, we use a Monte Carlo approach: we compare the computed nucleation probabilities $P_{(m,n)}^{(0)\rightarrow(1)}$ with randomly generated numbers sampled from a uniform distribution in (0,1). We draw one number for each vial in the liquid, supercooled step per time step. By doing so, we ensure that the nucleation process is indeed stochastic; the randomly generated number for a specific vial at a given time step is independent of the numbers generated for other vials and for prior and later time steps.

The stochasticity of ice nucleation necessitates repetitive runs of the model to capture the variability of the process. The individual runs are completely independent from each other, thus enabling parallelization of the computations. To avoid obtaining repeated behavior in the parallelized program, we seed the random number generator for each run individually.

While the results generated for this work were computed using MATLAB, we have opted to provide an equivalent, open source implementation of our model in the form of a python package that we publish on pypi under the MIT license.[186] We have called this package "Stochastic Nucleation of Water", or SNOW for short.[73] It is our intention to integrate upcoming developments and potential contributions by third parties into future releases, hoping to foster a spirit of open collaboration among researchers in this field.

6.2.2 Cooling protocol

The control and reduction of batch heterogeneity is of special interest in process design and optimization. The number of process parameters in the freezing step of freeze-drying is small and optimization commonly reduces to the choice of a suitable cooling protocol. We investigate three aspects of it: the cooling rate, the holding steps, and the application of a controlled nucleation scheme. Figure 6.1 illustrates the thermal evolution of the shelf for four different cooling policies that will be analyzed and characterized in the following sections 6.2.2 and 6.2.2.

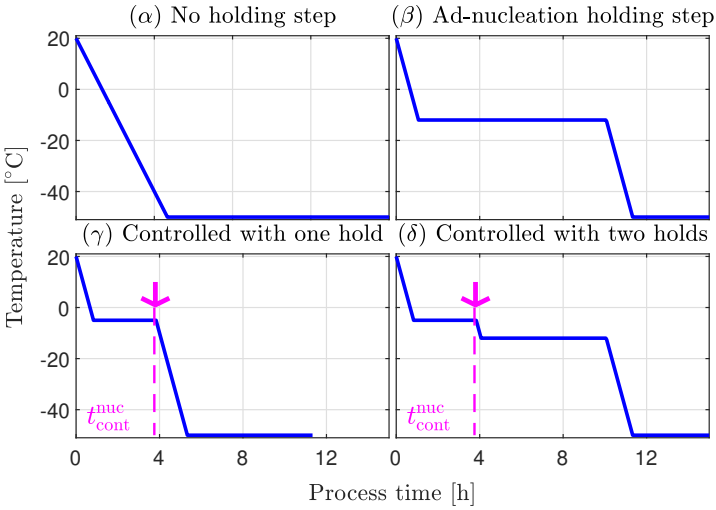

Figure 6.1 Temperature profiles of the shelf for (α) uncontrolled freezing without holding step, also known as shelf-ramped freezing, (β) uncontrolled freezing with ad-nucleation holding scheme, (γ) controlled nucleation without post nucleation hold and (δ) controlled nucleation with post-nucleation hold. The magenta arrow indicates the controlled nucleation event.

Cooling rate and holding step policies

Traditionally, freezing in lyophilization processes is carried out via shelf-ramped cooling, where the shelf temperature is reduced with a constant cooling rate γ from ambient temperature to a minimum temperature commonly around -50°C, as shown in figure 6.1(α). In such a setup, γ is the sole process parameter and is typically chosen in the range from 0.1 to 1.0 K min^{-1}.[41] Higher cooling rates are inaccessible in industrial freeze-dryers due to technical limitations; smaller cooling rates would lead to too long an overall process time.

Common strategies to reduce batch heterogeneity include the integration of holding steps at constant temperature into the cooling profile to equilibrate the temperatures of the vials across the shelf. In this study, we distinguish three types of holding steps that may be applied in cooling protocols:

1. Pre-Nucleation holding step (Figure 6.1(γ)): Holding at low temperature before the onset of nucleation, i.e. around 0°C, or in the supercooled region. The objective of such a step is to equilibrate the temperatures

across the batch in order to reduce heterogeneity, both within a vial and among vials before nucleation is triggered via either further cooling or controlled nucleation.[41,187]

2. Ad-Nucleation holding step (Figure 6.1 (β)): Holding at a temperature at which nucleation may occur in a viable timescale. This step aims at nucleating all vials close to the holding temperature, so as to achieve a narrower nucleation temperature distribution compared to cooling protocols without holding step.
3. Post-Nucleation holding step (Figure 6.1(δ)): This holding policy is implemented after nucleation occurred either randomly or in a controlled way. It typically is applied together with a pre-nucleation holding step in controlled nucleation schemes. It aims at steering the solidification time distribution towards higher values compared to cooling protocols with immediate cooling-down after the nucleation event and thus promotes the formation of larger ice crystals.[142]

For the design of both pre- and ad-nucleation holding steps, knowledge of the number of vials that nucleate spontaneously during the holding period is essential. Let us assume that all vials experience identical temperature profiles until nucleation and that the vials do not thermally interact with each other. This implies that $K_{(m,n)} = K$, hence one may express the expected number of non-nucleated vials $N^{(0)}$ and of nucleated vials $N^{(1)}$ on a shelf comprising n_v vials as:

$$N^{(0)}(t) = n_\mathrm{v} P^{(0)}(t) = n_\mathrm{v} \exp\left\{-\int_{t_0}^{t} K(t')\mathrm{d}t'\right\} \tag{6.19a}$$

$$N^{(1)}(t) = n_\mathrm{v} P^{(1)}(t) = n_\mathrm{v} \left(1 - \exp\left\{-\int_{t_0}^{t} K(t')\mathrm{d}t'\right\}\right) \tag{6.19b}$$

In the case of an isothermal system, which is the situation attained for the holding step after the vials reached the holding temperature, the nucleation frequency K is constant and eqn. 6.19 simplifies to:

$$N^{(0)}(t) = n_\mathrm{v} \exp\{-Kt\}\,. \tag{6.20a}$$

$$N^{(1)}(t) = n_\mathrm{v} \left(1 - \exp\{-Kt\}\right). \tag{6.20b}$$

We may use equation 6.20 to construct the design space for both types of holding steps. The main design parameter for both holding policies is the number of nucleated vials: During the pre-nucleation hold, virtually no vials should nucleate (i.e. $N^{(1)} \ll 1$), while virtually no non-nucleated vials should remain after completion of the ad-nucleation hold (i.e. $N^{(0)} \ll 1$). We thus introduce the design parameters $N^{(0)}_\mathrm{crit}$ for the ad-nucleation hold and $N^{(1)}_\mathrm{crit}$ for the pre-nucleation hold, that correspond to the expected value of

the number of vials in the undesired state at the end of the holding step. Importantly, these parameters denote an absolute number of (non)-nucleated vials and not a probability of nucleation; this definition may be appreciated by lyophilization practitioners aiming for processes that achieve complete nucleation independently of scale. While the nucleation process by itself does not depend on the scale of the system, ensuring that all vials without exception are nucleated becomes more challenging when more vials are present. By rearranging equation 6.20, we may express the duration of the holding steps t_h^{ad} as a function of the design parameter and of the holding step temperature T_h^{ad} for the ad-nucleation hold:

$$t_h^{ad}(T_h^{ad}) \geq \frac{1}{K(T_h^{ad})} \ln\left(\frac{n_v}{N_{crit}^{(0)}}\right) \tag{6.21}$$

and similarly for the pre-nucleation hold:

$$t_h^{pre}(T_h^{pre}) \leq \frac{1}{K(T_h^{pre})} \ln\left(\frac{n_v}{n_v - N_{crit}^{(1)}}\right) \tag{6.22}$$

It follows from equations 6.21 and 6.22 that the holding times depend on the ratio between number of vials and design parameter. For a given value of the design parameter, a larger number of vials makes the design more restrictive, i.e. shifts the pre-nucleation hold towards shorter times and higher temperatures and the ad-nucleation hold towards longer times and lower temperatures. To provide an example, when we set $N_{crit}^{(0)} = 0.1$, we demand that only in approximately 10% of the runs a non-nucleated vial remains at the end of the ad-nucleation holding step; in reality where we always have an integer number of nucleation events, one would find 0 non-nucleated vials in most batches, and 1 or more in a few. Eqn. 6.21 thus allows us to calculate the minimum time t_h^{ad} that fulfils the design criterion; it clearly follows from the equation that this time becomes longer when the number of vials increases.

Figure 6.2 shows the design curves for both pre-nucleation and ad-nucleation holding steps of the system with 7×7 vials; we use these curves as starting point for the design of the two holding schemes and the subsequent evaluation of their impact on the characteristic freezing quantities, as shown in Sections 6.3.4 and 6.3.4. The design curves idealize the holding scheme by assuming that the vials stay exactly at the holding temperature for the entire duration of the holding periods and by neglecting the time required for thermal equilibration. In order to understand the real behavior of the system, we have to compare the prediction of the design curves with the detailed simulations based on the freezing model derived in Section 6.2.1.

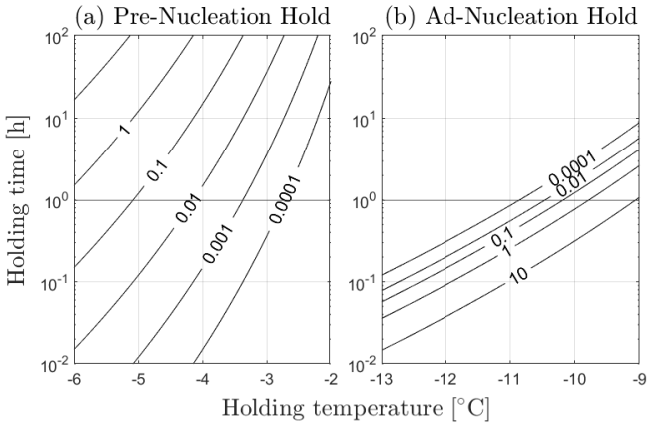

Figure 6.2 Holding step design curves for both the pre- (a) and ad-nucleation (b) approaches and a shelf size of 7×7 vials. For pre-nucleation, the numbers on the contour lines correspond to $N_{\text{crit}}^{(1)}$. For ad-nucleation, the numbers indicate $N_{\text{crit}}^{(0)}$, the number of vials that did not nucleate during the hold. The horizontal line indicates a holding time of one hour.

Controlled nucleation

Controlled nucleation, in which nucleation is initiated in all vials at the same predefined time, is used in freeze-dryers to reduce vial-to-vial variability and to increase the mean ice crystal size. Such process commonly involves holding steps, both before and after the forced nucleation event. The duration and temperature of these holds have been shown to greatly impact the performance of controlled nucleation strategies.[175] An important performance indicator of controlled nucleation techniques is the nucleation efficiency, i.e. the fraction of vials that actually nucleate at the predefined time. Vials that do not nucleate in a controlled way may nucleate later in a conventional manner, thus possibly generating heterogeneity between the two groups of vials[188]. Achieving close to 100% nucleation efficiency independent of the specific formulation is therefore one of the main requirements for effective controlled nucleation techniques. Due to limited research available on the dependence of the nucleation efficiency on process and formulation parameters, we will assume 100% efficiency in all simulations. However, we consider the effect of spontaneous nucleation occurring in individual vials *before* the controlled nucleation trigger, which may also lead to heterogeneity.[188]

6.2.3 Quantifying batch heterogeneity

A key motivation for the development of the model is its use for the quantification of batch heterogeneity. Heterogeneity in general poses one of the main design challenges of freezing and freeze-drying processes. Based on available works in literature and our own experience in crystallization, we classify three types of heterogeneity related to the freezing process. These include local heterogeneity, spatial heterogeneity (also referred to as intra-vial heterogeneity) and batch heterogeneity (also referred to as vial-to-vial variability and inter-vial heterogeneity).

The focus in literature has been on spatial heterogeneity,[19,171] with only one work available on local heterogeneity.[40] The aspect of batch heterogeneity remains the least studied, although literature[28] indeed confirmed the relationship between nucleation temperature of a vial and its mean pore size via experiments and modeling. However, as of today, we are not aware of any systematic model-guided assessment on the two main sources of batch heterogeneity, namely the stochasticity of primary ice nucleation and the variability in heat transfer among vials.

Experimental studies on batch heterogeneity are commonly based on measuring certain attributes in a large number of vials, including the morphology in frozen products,[189] the average pore size and the residual moisture in dried products,[188] or the estimated cake resistance during primary drying[190]. Alternatively, it may also be estimated from overall (integral) properties, e.g. via the time difference between the onset and offset of the Pirani-Baratron pressure ratio during primary drying.[175]

A variety of limitations for experimental quantification of batch heterogeneity persist, however. The most crucial of which is the difficulty in obtaining significantly large sample sizes to decouple the effects of different potential root causes of variability. To address this, we have developed a novel, systematic approach to quantify batch heterogeneity *in silico*. We define it based on three characteristic quantities of the process, namely the nucleation time t^{nuc}, the nucleation temperature T^{nuc}, and the solidification time t^{sol} as illustrated in Figure 6.3. We measure the nucleation time t^{nuc} and the freezing time t^{fr} from the beginning of the process. The solidification time t^{sol} then is the difference between these two quantities, i.e. it is the time the vial spends in a partially frozen ice growth state.

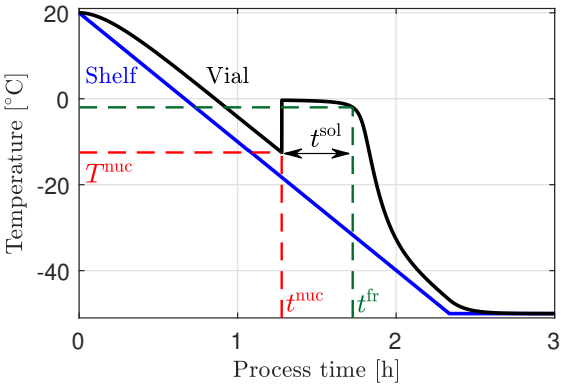

Figure 6.3 Thermal evolution of a single vial during the freezing process. The position of the nucleation event and the time when the vial is frozen, which corresponds to the predefined threshold for the ice mass formed, are indicated.

It follows from the stochasticity of ice nucleation that the values of these characteristic quantities are distributed across the vials, and for each vial across different realizations of the same freezing process. We compute these distributions by running the model repetitively and determining the corresponding probability density functions $f_{nt}(t)$, $f_{nT}(T)$ and $f_{sol}(t)$. Consequently, $f_{nt}(t^{nuc})dt$ provides the fraction of nucleation events that take place between t^{nuc} and $t^{nuc} + dt$; $f_{nT}(T^{nuc})dT$ the fraction that nucleates at temperatures between T^{nuc} and $T^{nuc} + dT$; $f_{sol}(t^{sol})dt$ is the fraction of freezing processes with solidification times between t^{sol} and $t^{sol} + dt$. In the same way we also define multivariate distributions of those characteristic quantities.

In general, batch heterogeneity in terms of product attributes such as the crystal size or product activity may only arise from variability in the freezing process among vials, assuming that all vials contain the same formulation. We express this variability as variability in nucleation time, in nucleation temperature and in solidification time and postulate that vials that nucleate and solidify identically, will also exhibit similar product attributes. The shape and especially the broadness of the three distributions may be interpreted as a measure of heterogeneity, where each characteristic quantity is related to different product attributes as outlined in the following.

Empirical models relate the local mean crystal diameter of frozen products d_p with the freezing front velocity and thus the solidification time t^{sol} such as the empirical relationship $d_p \propto (t^{sol})^{0.5}$.[191] By analyzing f_{sol}, we thus infer information about the variability of the mean ice crystal size. t^{sol} also plays a

role in deactivation mechanisms of biomolecules based on freeze concentration. The increase in solute concentration within the liquid phase may accelerate deactivation and denaturation reactions of molecules such as proteins.[192] Consequently, we may also expect heterogeneity in product activity in case f_{sol} is broad.

Nucleation temperatures, captured by f_{nT}, are of broad interest due to their relation to crystal morphology: Nakagawa et al.[19] presented a model that correlates lower nucleation temperatures with smaller crystal diameters. A similar model was applied later to quantify variability in mean crystal size among vials based on experimentally measured nucleation temperatures.[28] It must be noted that these works do not explicitly distinguish between nucleation and solidification effects on crystal morphology: they use the nucleation temperature together with heat transfer coefficients as input parameters to simulate the freezing process including solidification. In doing so, they are unable to provide insight into the dependence of the nucleation temperature distribution on the heat transfer and its variability. However, such knowledge is required to understand whether differences either in heat transfer or in nucleation temperature are the main source of batch heterogeneity. Our model does not require the nucleation temperature as input parameter, and only relies on formulation-dependent nucleation kinetics. In this way we can study for the first time the effects of different cooling schemes and of heat transfer variability on both nucleation temperatures and solidification times. Such study may also improve the knowledge about to which extent nucleation temperatures and solidification times may be interpreted as predictors for the mean ice crystal size.

The nucleation time distribution, f_{nt}, finally, provides us with the time vials spend in the liquid state. Broad distributions may be indicative of heterogeneity in for example denaturation effects caused by the liquid state. However, the time scale of freezing in freeze-drying is rather short compared to, e.g. freezing processes for the purpose of storage, where some vials may spend an extended period of time in a liquid, supercooled state due to slow heat transfer and slow ice nucleation kinetics. We thus expect that the nucleation time by itself has a minor effect on heterogeneity.

6.3 RESULTS

In this section the results of our study are reported and discussed. We present the simulation results for the freezing process of a shelf comprising 7×7 vials; 5000 simulations were carried out to capture the variability of the process. By studying a system comprising 70x70 vials, we have confirmed that

our conclusions are independent of shelf size. Since the computation time for the solution of the model equations scales linearly with the number of vials, the model is also suitable for the simulation of production-scale systems. If not stated otherwise, all simulations comprise vials containing 1 mL of 5 wt.% sucrose solution and follow a cooling protocol starting at 20°C, which is ramped down with a cooling rate of 0.5 Kmin^{-1} to -50°C (the overall duration of cooling is therefore 2 hours and 20 minutes). We have chosen a time step of Δt = 2 s in all simulations.

6.3.1 Thermally independent vials

We simulated the freezing process of vials that neither interact with their neighbors nor with the environment. Heat transfer in this case solely occurs via the shelf, i.e. via a constant value of k_{sh} in the range of 20 to 60 $\frac{\mathrm{W}}{\mathrm{m^2K}}$, while k_{ext} and k_{int} were set to zero. All vials evolve identically until nucleation occurs; the only variability lies in the stochasticity of the nucleation event as can be seen in Figure 6.4.

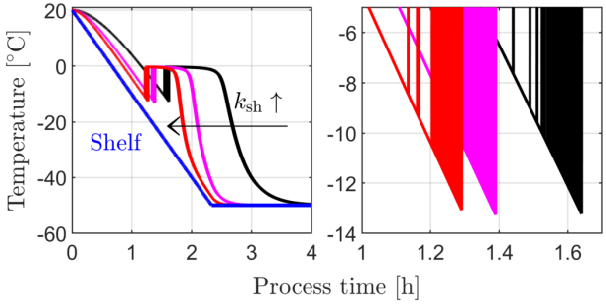

Figure 6.4 Thermal evolution of the simulated system, where all heat transfer coefficients except k_{sh} are set to zero. Left: Thermal evolution for the entire freezing process. Right: Focus on nucleation event. For each value of k_{sh}, the figure presents 50 randomly chosen temperature profiles out of the total 245'000 that were simulated.

The thermal evolution depends on the shelf-to-vial heat transfer; Figure 6.4 clearly demonstrates the connection between high values of k_{sh} and short nucleation and solidification times. However, for the nucleation temperatures we do not observe any dependency on k_{sh}. We confirm this observation by analysing the distributions of the characteristic quantities in Figure 6.5; they

provide us with the statistics of the freezing process, since they comprise all 245'000 (49 vials times 5000 simulations) freezing events.

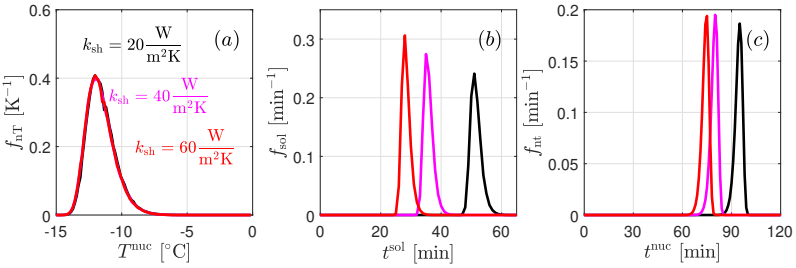

Figure 6.5 Marginal distributions of the three characteristic quantities for the system studied in figure 6.4: (a) Nucleation temperature distribution f_{nT}, (b) solidification time distribution f_{sol}, (c) nucleation time distribution f_{nt}. The figure summarizes the outcome of 5000 simulations for the system of 7×7 vials.

Figure 6.5 (a) confirms that the nucleation temperature distribution is indeed independent of k_{sh}. This behavior is a direct consequence of the fact that the nucleation rate J, as modeled, depends directly on temperature but not on the vial's history. As long as the thermal profile in the supercooled state is the same, we will observe the same nucleation temperature distribution. The temperature curves in Figure 6.4 are indeed equivalent, since they follow the shelf with different lags, but not different rates. The zoom-in of Figure 6.4 shows that the effective cooling rates of the vials are similar for the three studied values of k_{sh} in the relevant temperature range, where nucleation occurs. Only the temperature *difference* between shelf and vial is affected by k_{sh}; it decreases for increasing k_{sh}.

The distributions of nucleation times and of solidification times, on the other hand, are affected by the shelf-to-vial heat transfer. Vials that experience a higher value of k_{sh} nucleate earlier. In the limit of an infinitely fast heat transfer the temperature gradient between vial and shelf vanishes and the nucleation times are only governed by the thermal evolution of the shelf. As this situation is approached with increasing k_{sh}, the distributions tend to converge. The solidification times exhibit the strongest dependency on k_{sh}; we can observe a nearly inversely proportional relationship, because the removal of heat is the limiting step in the ice growth state. This implies that vials undergoing heat transfer with different k_{sh}, e.g. because they are frozen in different devices or due to variability across the shelf, may exhibit different product properties despite having experienced similar nucleation temperatures.

6.3.2 Thermally interacting vials

As second step, we studied the effect of thermal interaction among vials on the freezing process by running simulations with varying values of k_{int}, while keeping $k_{\text{ext}} = 0$. While Figure 6.6 shows the thermal evolution of such system, Figure 6.7 presents the univariate distributions of the three characteristic quantities and Figure 6.8 the bivariate distributions, which allow us to study the interaction effects in detail. Such interaction adds complexity to the freezing process, since the thermal evolution of a vial depends on the thermal evolution of the neighboring vials, as illustrated in Figure 6.6.

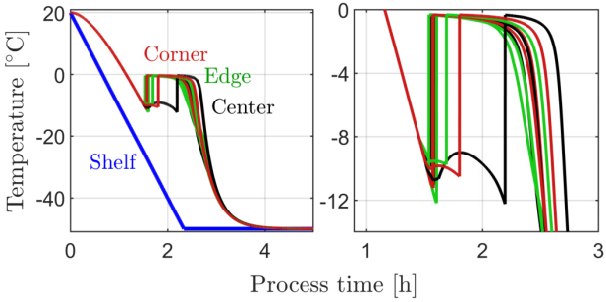

Figure 6.6 Thermal evolution of the simulated system for k_{sh}=k_{int}= 20 $\frac{\text{W}}{\text{m}^2\text{K}}$. Left: Thermal evolution for the entire freezing process. Right: Zoom-in on the nucleation event. For each vial position, i.e. center, edge and corner, the figure presents 5 randomly chosen simulated temperature curves.

Early nucleating vials act as local hot spots on the shelf during their solidification process. They dissipate heat into their neighbors and thus slow down their neighbors' further cooling process until they themselves are completely frozen and cool down again. We observe this effect also in the distributions of the characteristic quantities of freezing; thermal interaction leads to a broadening of the nucleation time distributions and, for sufficiently strong interaction, even to a bimodal distribution, as shown in Figure 6.7 (a-c).

Thermal interaction also broadens the distribution of solidification times and is thus a potential mechanism for batch heterogeneity. The formation of a bimodal nucleation time distribution in the presence of strong interaction among vials is connected to the formation of a broad, multi-modal solidification time distribution. This multi-modality is a consequence of multiple coupled effects. Thermally interacting neighbors accelerate solidification when they act as heat sinks for a solidifying vial or when they delay nucleation long

enough by dissipating their own heat of solidification that the shelf, now at a much lower temperature, allows for fast heat transfer. The result is a complex distribution whose characteristic attribute is a very large, highly undesirable broadness.

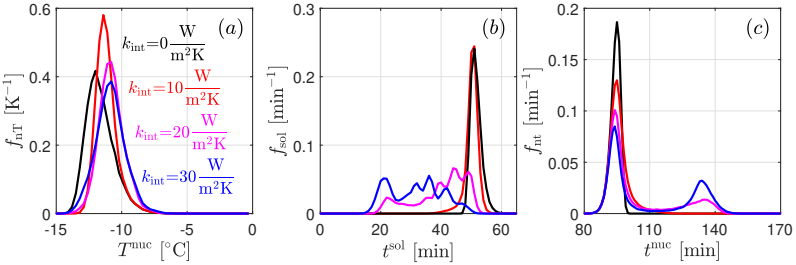

Figure 6.7 Marginal distributions of the three characteristic quantities for systems with varying strength of thermal interaction among vials and $k_{\text{sh}} = 20\ \frac{\text{W}}{\text{m}^2\text{K}}$: (a) Nucleation temperature distribution f_{nT}, (b) solidification time distribution f_{sol}, (c) nucleation time distribution f_{nt}. The figure summarizes the outcome of 5000 simulations for the system of 7×7 vials.

The effect of thermal interaction on the nucleation temperature distribution was smaller than for the other two quantities; we only identified a weak trend towards higher temperatures for increasing interaction as shown in Figure 6.7 (a). This trend is caused by the early nucleating vials that dissipate heat into their neighbors. The neighboring vials spend more time in a moderately supercooled state compared to the case without thermal interaction, leading to higher nucleation temperatures.

In summary, adding thermal interaction between vials yields a much more complex system than the one studied previously in Section 6.3.1. To better understand this complexity, we analyzed the bivariate distributions of the characteristic quantities, as shown in Figure 6.8. We first note that in the case, where $k_{\text{int}} = 0$, i.e. the system shown in Figures 6.4 and 6.5, the bivariate distributions assume the shape of lines as illustrated in the left column in Figure 6.8. These lines indicate that the three quantities are strongly correlated: lower nucleation temperatures correlate with longer nucleation times and shorter solidification times; the slopes of these lines depend on the applied cooling rate (not shown). Such strong correlation is expected, since the only variability in the freezing process is the nucleation event of the individual vial; this single event determines all three quantities as outlined in Section 6.3.1. The correlations become weaker when thermal interaction is present, where we observe more complex shapes of the bivariate distributions. This

again is expected, since it follows from thermal interaction that not only the nucleation event of an individual vial affects its freezing process, but also the nucleation events of its neighbors. In the case of strong thermal interaction, i.e. the right column of Figure 6.8, we observe the formation of individual populations of vials, corresponding to vials that nucleate during the initial cooling-down and those that nucleate delayed due to neighboring nucleation events. The early nucleating population is split further in sub-populations, since the solidification time of a vial depends on the number of its neighbors that nucleated earlier.

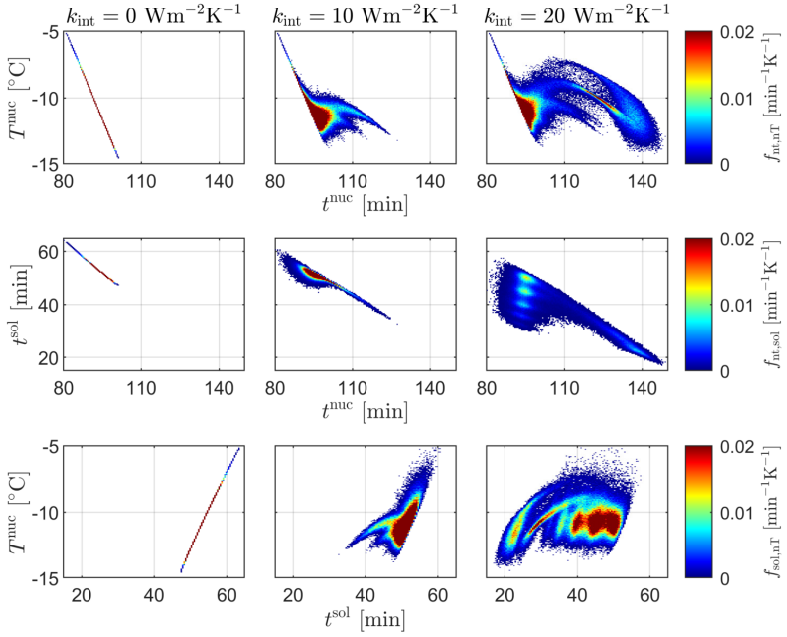

Figure 6.8 Bi-variate distributions of the three characteristic quantities of the freezing process. The color coding reflects the probability density of the marginal distribution. The figure summarizes the outcome of 5000 simulations for the system of 7×7 vials. A value of $k_{\mathrm{sh}} = 20\ \frac{\mathrm{W}}{\mathrm{m^2K}}$ was used in all simulations.

The observation that the three characteristic quantities behave differently is of particular importance in the context of process monitoring. In a recent study,[28] the distributions of nucleation times and nucleation temperatures were used interchangeably; nucleation times were detected with a camera and converted into temperatures using reference temperature measurements.

Based on our simulation results, we hypothesize that such approach may not be generally applicable. The direct measurement of both quantities, e.g. via infrared thermography, might be more appropriate.

In general, our simulations indicate that heterogeneity in nucleation and solidification times is not necessarily reflected in the distribution of nucleation temperatures. This clearly limits the applicability of the nucleation temperature distribution as indicator for batch heterogeneity. To accurately capture batch heterogeneity, e.g. in order to estimate heterogeneity in mean ice crystal sizes across the shelf, one requires direct knowledge of the solidification time distribution.

The effect of thermal interaction between vials during freezing is not yet well studied. A recent experimental study demonstrated that the presence of neighboring vials and their number affect the rate of drying during freeze-drying;[84] it was argued that this phenomenon may explain the difference in drying behavior between edge and center vials. This is in line with the outcome of our simulations that show similar trends for the freezing step. For the freezing step itself, we are not aware of any study that investigated the effect of thermal interaction on the nucleation and solidification behavior of vials. Another study recently investigated the thermal evolution of neighboring vials with an infrared camera during freezing and indeed observed "humps" in these profiles due to neighboring nucleation events similar to those we found in our simulations.[93] We thus recommend further experimental studies on interaction effects during freezing to better understand to what extent such interaction occurs in practice and how it depends on the setup.

6.3.3 Position-dependency

In this section we present the results on the position-dependency of the freezing process. We have identified both thermal interaction among vials and additional heat transfer with the environment as root causes for such dependency. To visualize these effects, we have generated tri-variate scatter plots comprising all three characteristic quantities, as shown in Figure 6.9. To simulate the heat transfer with the environment we varied the value of k_{ext} for freezing processes with and without thermal interaction among vials. The thermal evolution of the environment follows the cooling profile of the shelf, i.e. $T_{\text{ext}} = T_{\text{sh}}$; this means that vials in contact with the environment experience an additional cooling effect. Without thermal interaction between vials, this additional heat transfer affects only the outermost layer of vials. Corner, edge and center vials therefore freeze differently, forming three distinct populations. The nucleation temperatures, once again, are found to be independent of

position, for the same reasons that were outlined in section 6.3.1. Note that we may observe different effects in the case where $T_{ext} \neq T_{sh}$.

The case where thermal interaction among vials is present, but no additional heat transfer with the environment is illustrated in Figure 6.9(a). Vials in the interior of the system exhibit a bimodal distribution corresponding to populations of vials that nucleate either early or late because of delays induced by the nucleation of neighboring vials. The solidification times of the delayed population are the shortest overall; however, even the early nucleating inner vials solidify faster than most edge and corner vials. This is a direct consequence of the larger number of neighbors they have and thus of the higher capability to dissipate heat into their surroundings. Consequently, we observe higher solidification times for edge vials, and the highest for corner vials. The lower number of neighbors also prevent or reduce the formation of a population of delayed-nucleating vials for the corner and edge positions, respectively.

The case where both thermal interaction among vials and additional heat transfer with the environment are present, is illustrated in Figure 6.9(b). The additional heat removal from the environment leads to overall shorter nucleation and solidification times for all vials and especially for edge and corner vials, reversing the order for early-nucleating vials: edge and corner vials solidify faster than non-delayed center vials. For vials in the interior of the shelf we have observed a position-dependency, whereby vials nucleate in average the earlier the closer they are to the edge of the system.

We conclude that both thermal interaction between vials and additional heat transfer with the environment may play a relevant role in vial-to-vial variability. While thermal interaction affects the bulk of the system, heat transfer with the environment only occurs at the boundaries of the system and its relevance thus depends on the shelf size. The fraction of non-center vials decreases with increasing shelf size so that bulk effects based on thermal interaction may be more relevant at production scale. Still, it is generally desirable to have no or limited heat flow with the environment to reduce the heterogeneity between corner, edge and center vials.

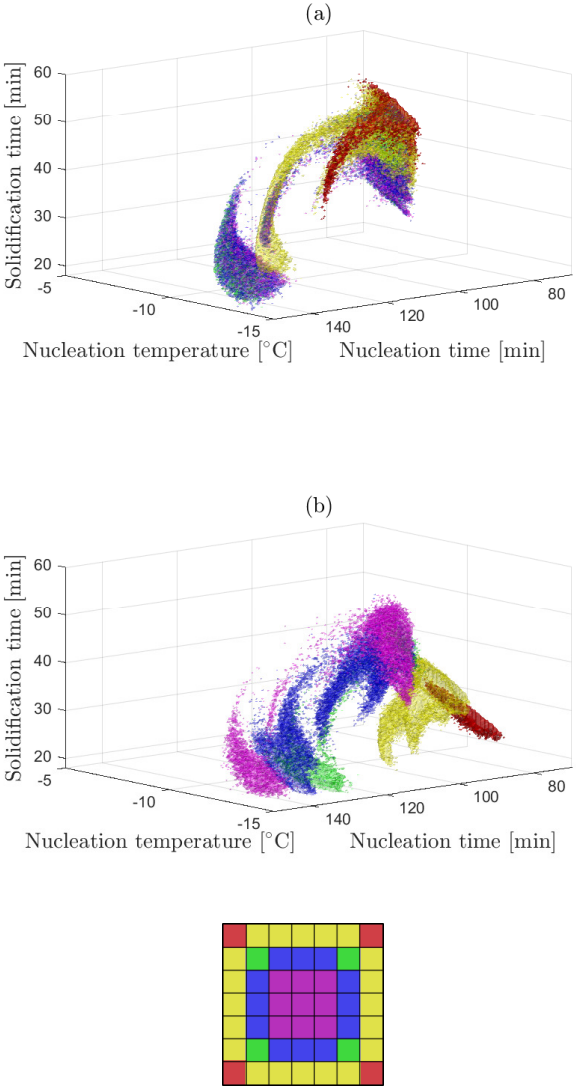

Figure 6.9 Position-dependent freezing behavior of the simulated system. (a) Thermal interaction between vials occurs, i.e. $k_{\text{int}} = 20\frac{\text{W}}{\text{m}^2\text{K}}$, but not with the environment, i.e. $k_{\text{ext}} = 0\frac{\text{W}}{\text{m}^2\text{K}}$. (b) Heat transfer occurs both between vials and with the environment, i.e. $k_{\text{int}} = k_{\text{ext}} = 20\frac{\text{W}}{\text{m}^2\text{K}}$. (c) Color-coding relative to shelf grid.

6.3.4 Cooling protocol

Cooling rate

In this section we present the results on the effect of the choice of the cooling rate on the freezing process. We simulated the freezing process for cooling rates γ in the range from 0.1 K min^{-1} to 2.0 K min^{-1}. Figure 6.10 shows the nucleation temperatures and solidification times obtained in the corresponding simulations.

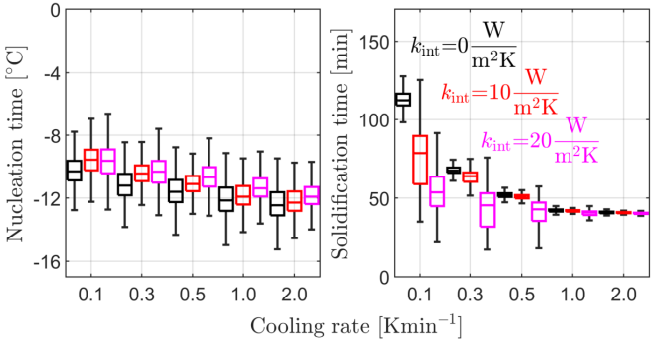

Figure 6.10 Dependency of (left) nucleation temperatures and (right) solidification times on cooling rate. The figure summarizes the outcome of 5000 model runs for the system of 7×7 vials. Values of $k_{sh} = 20 \frac{W}{m^2K}$ and $k_{sh} = 0$ were used.

We observe significantly longer process times in the case of smaller cooling rates; the median nucleation time decreases from 337.0 min to 40.0 min when increasing the cooling rate from 0.1 Kmin^{-1} to 2.0 Kmin^{-1} in the case of thermally independent vials (not shown). Faster cooling leads to lower nucleation temperatures on average; the difference in median nucleation temperatures between the cooling rates of 0.1 Kmin^{-1} and 2.0 Kmin^{-1} was only about 2°C, while the broadness of the distribution was not affected significantly. This is in line with the state of research suggesting that a change of cooling rate within the commonly applied range has only a weak impact on the nucleation temperature distribution.[43] It has to be noted, that as consequence of the lumped capacitance approach, the effect of thermal gradients within the vial on the nucleation frequency is not captured. Such gradients become more relevant for higher cooling rates and may affect the nucleation behavior especially for the highest rates studied, namely 1.0 Kmin^{-1} and 2.0 Kmin^{-1}.

We have observed a stronger sensitivity of the solidification time on the cooling rate: Not only did smaller cooling rates lead to slower solidification, but they also broadened the distribution. Slow cooling rates were also found to be more sensitive to thermal interaction, i.e. significant nucleation delay was already obtained for $k_{\text{int}} = 10\frac{\text{W}}{\text{m}^2\text{K}}$ when using cooling rates smaller than 0.5 Kmin^{-1}. Such behavior is in line with expectations, since slower cooling provides more time for thermal interaction effects to play a role. For faster cooling, on the other hand, the solidification time approaches a lower limit; the simulated values for 1.0 Kmin^{-1} (42.1 min) and 2.0 Kmin^{-1} (40.9 min) were nearly identical. This behavior is a consequence of the limited heat transfer within the system; for fast cooling, the lower boundary of the shelf temperature, i.e. -50°C, is reached early enough that most of the solidification process occurs at this constant temperature. A further increase in cooling rate thus does not affect the solidification process anymore.

The simulations confirm that faster cooling leads to faster solidification, which may result in smaller average crystal sizes. Larger ice crystals are generally preferred in freeze-drying, thus favoring slower cooling. Slow cooling, however, is also connected to broader solidification time distributions, thus leading to a more pronounced batch heterogeneity. As a consequence, the choice of the cooling rate should be based on a trade-off between the mean crystal size and the corresponding variability. To the best of our knowledge, the effect of increasing heterogeneity for slow cooling had not yet been studied in the literature.

Pre-nucleation holding step

In this section, we study the effect of integrating a pre-nucleation holding step in the cooling protocol on the freezing outcome. We have applied the approach outlined in section 6.2.2 for the design of such holding step and have investigated a pre-nucleation hold at -5°C with varying holding times. Figure 6.11 shows the thermal evolution of such system as well as the distributions of vial temperatures at the end of the holding step and of the nucleation temperature. In practice, there is a lower bound for the holding step duration, which is due to the requirement of thermal equilibration.

We present in detail four scenarios comprising different heat transfer regimes. The number of nucleated vials during the holding steps per simulation, $N^{(1)}$, has been found to correspond well with the expected number of nucleated vials $N^{(1)}_{\text{crit}}$, that was calculated based on eqn. 6.22. In fact, we have observed slightly fewer nucleation events in the simulations than predicted analytically, since the analytical expression does not take into account the time that is required for the vials to reach the holding temperature. We have

thus been able to confirm the usefulness of eqn. 6.22 to conservatively design pre-nucleation holding steps when nucleation kinetics are known, at least approximately. The findings for the scenario in which there is strong thermal interaction and a variable shelf-to-vial heat transfer coefficient, are illustrated in Figure 6.11.

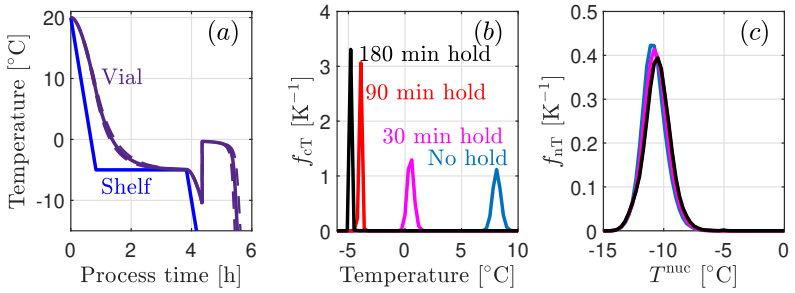

Figure 6.11 (a) Thermal evolution of a vial for a cooling profile including a 180 min pre-nucleation holding step at -5°C. A value of $k_{sh} = 20 \frac{W}{Km^2}$ was used and the dashed lines indicate the temperature profiles obtained with k_{sh} 10% smaller and larger to illustrate the effect of heat transfer on the profile. (b) Temperature distributions of the vials at the end of the holding step for various holding times at -5°C, corresponding to f_{cT} in the case of controlled nucleation. (c) Nucleation temperature distributions f_{nT} for various holding times at -5°C. Heat transfer coefficients of $k_{sh,0} = 20 \frac{W}{Km^2}$, $s_{sh} = 2 \frac{W}{Km^2}$ and $k_{int} = 20 \frac{W}{Km^2}$ were used.

The simulations have revealed only minor effects of the holding step on f_{nT} as shown in Figure 6.11 (c), irrespective of heat transfer parameters and holding time; as long as no nucleation events occur during the hold, the presence of the hold cannot have a major impact on the nucleation temperature distribution. We have also assessed the impact of the pre-nucleation holding step on the solidification time, and we have not found any significant effect either (not shown). We thus conclude that such a holding step is only of limited use in reducing batch heterogeneity resulting from ice nucleation and from the different types of heat transfer scenarios considered in this work. This is in contrast to practical guidelines on the freezing process design[41] that recommend such a step in order to improve homogeneity both within the batch and within the individual vials. Note that due to the lumped capacitance approach, the model is unable to investigate intra-vial heterogeneity and the effect of holding on this property; such a study would require the spatial freezing model reported in Chapter 9.

In the case of controlled nucleation, the situation changes. The forced nucleation event at the end of the holding step transforms the actual distribution of vial temperatures into the controlled nucleation temperature distribution f_{cT}. The broadness of f_{cT} decreases with increasing holding time in all studies, as is shown in Figure 6.11 (b). Additionally, for short holding times, the temperatures of the vials are significantly higher than the shelf temperature. In the case presented in Figure 6.11, more than 30 min of holding were required to ensure that all vials reached temperatures below T_ℓ^{eq}. If individual vials should experience temperatures above T_ℓ^{eq} at the time of the nucleation event, there may be a risk of failure, depending on the implemented method of nucleation. For example, we may hypothesize that an ice-fog method may be affected, because the seeded ice particles might melt when they reach vials that are not yet supercooled. Recently, nucleation efficiencies for the ice-fog technique were measured by means of frequency modulated spectroscopy, whereby a reduced efficiency at -3°C (87%) compared to -10°C (99.7%) was found.[188] Consequently, a controlled nucleation process requires a pre-nucleation holding step designed according to three criteria: (1) the holding temperature must be low enough so that all vials are (sufficiently) supercooled at the time of nucleation, (2) the holding step must be long enough to allow for equilibration of the vials, (3) it must be short enough so as the number of spontaneous nucleation events is low.

Ad-nucleation holding step

In this section, we study the effect of integrating an ad-nucleation holding step in the cooling protocol on the freezing outcome. Figure 6.12 (β) shows the thermal evolution of 25 vials during a cooling protocol whereby such holding step is simulated both with and without thermal interaction between vials. Figure 6.13 shows the bivariate distributions of nucleation temperatures and solidification times for six cooling protocols, showing both successful and unsuccessful holding steps. Figure 6.14 compares the complete nucleation times and complete freezing times for the studied system in the cases with and without thermal interaction with the analytical solution.

Following again the rationale outlined in Section 6.2.2, we have investigated the behavior for a 540 min holding step at -12°C, expecting it to be sufficient for complete freezing of all vials on the shelf, as shown in Figure 6.12 (β). Without thermal interaction, nucleation occurs in a narrow time window during the initial cooling-down towards the holding temperature; then a slow solidification process follows. With thermal interaction, the nucleation events occupy a longer time window, i.e. they are more distributed in time, whilst solidification is significantly faster. This behavior is a result of the dissipation

of heat from early nucleating vials towards their neighbors as discussed in Section 6.3.2. Thermal interaction thus increases the required holding time for complete nucleation, as also shown in Figure 6.14.

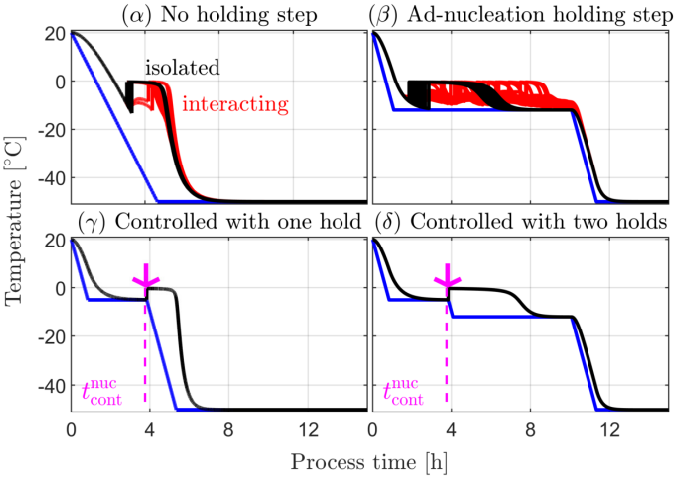

Figure 6.12 Temperature profiles for (α) uncontrolled freezing without holding step, (β) uncontrolled freezing with ad-nucleation holding step, (γ) controlled nucleation without post nucleation hold and (δ) controlled nucleation with post-nucleation hold. The magenta arrow indicates the controlled nucleation event. Heat transfer with the environment and variability in shelf-to-vial heat transfer were set to zero and the thermal interaction between vials is given by $k_{\text{int}} = 0 \frac{\text{W}}{\text{m}^2\text{K}}$ or $k_{\text{int}} = 20 \frac{\text{W}}{\text{m}^2\text{K}}$.

To understand the effects of holding time and holding temperature on the freezing outcome, in Figure 6.13 we compare six different policies, including one without any holding step (Figure 6.13(a)). The step design with -12°C and 540 min (Figure 6.13(d)) is just sufficient for all vials to nucleate during the hold; increasing the temperature slightly to -8°C (Figure 6.13(c)) or decreasing the holding time to 180 min (Figure 6.13(b)) leads to a situation where some vials nucleate during the hold and some afterwards. We observe distinct behaviors for the two groups, with the vials that nucleate after the hold exhibiting lower nucleation temperatures and solidification times and an increased overall variability. If the holding step is successful, i.e. cases (d) to (f), where all vials nucleate and solidify during the hold, the obtained solidification times are in average larger than for freezing without holding step, i.e. case (a). In the context of freeze-drying, this may be translated into

larger mean ice crystal size and thus shorter drying times. Consequently, such a holding step may provide a path for process optimization.

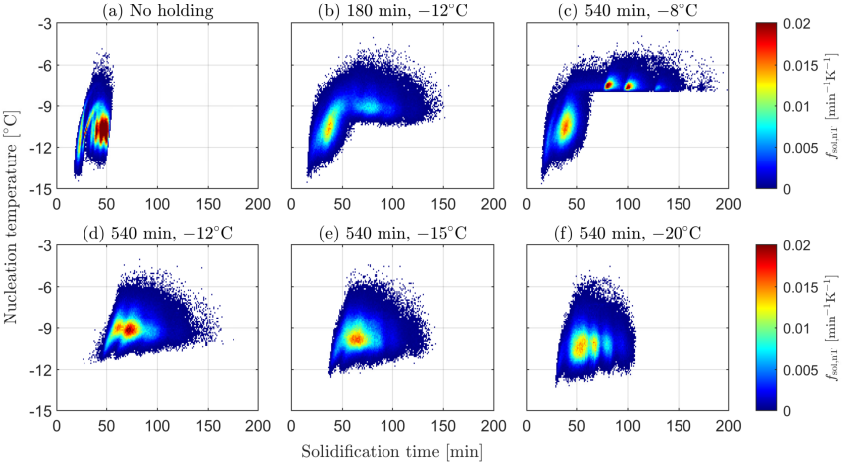

Figure 6.13 Simulated bi-variate distributions of nucleation temperatures and solidification times for five ad-nucleation holding policies (b to f) and freezing without holding step (a). The color coding represents the probability density of freezing outcomes for individual vials. A thermal interaction of $k_{\text{int}} = 20 \frac{\text{W}}{\text{m}^2\text{K}}$ was used for these six simulations. k_{ext} and s_{sh} were set to zero.

To implement such holding scheme in practice, we need to estimate the times required for complete nucleation $t_{\text{c}}^{\text{nuc}}$, i.e. when all vials on the shelf are nucleated, and for complete freezing t_{c}^{fr}, i.e. when all vials on the shelf are nucleated and solidified. We have obtained the distributions of these times, i.e. f_{nt}^{c} and f_{fr}^{c}, by simulating an ad-nucleation holding step of 200 hrs at temperatures ranging from -7°C to -15°C. Figure 6.14 illustrates the outcome; the curves correspond to the 50% quantiles of the distributions, while the error bars indicate the 10% and 90% quantiles. The analytical solution is based on eqn. 6.21 and was calculated for $N_{\text{crit}}^{(0)} = 0.5$, i.e. expecting 0.5 non-nucleated vials per batch at the end of the holding step. The error bars for the analytical solution correspond to the holding step times calculated for $N_{\text{crit}}^{(0)} = 0.1$ and $N_{\text{crit}}^{(0)} = 0.9$.

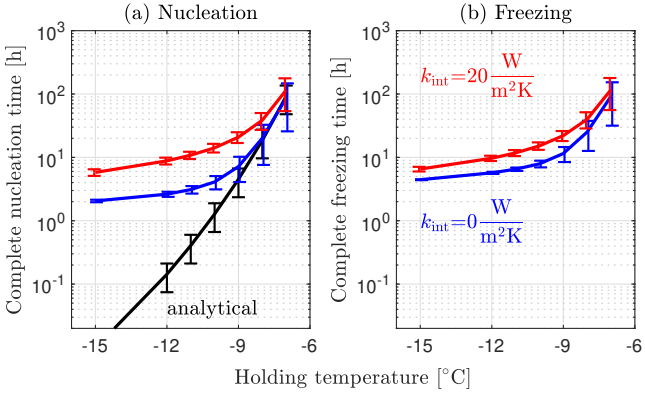

Figure 6.14 Simulated complete nucleation times t_c^{nuc} and complete freezing times t_c^{fr} in dependence of holding temperatures.

For both t_c^{nuc} and t_c^{fr}, we observe a non-linear dependency of the required holding times on temperature. Above around -10°C, the analytical solution becomes a good proxy for the simulations at $k_{int} = 0 \frac{W}{m^2K}$, as in these cases nucleation takes place primarily during the hold and not during the ramped cooling period towards the holding temperature. For lower holding temperatures, the analytical solution drastically underestimates the necessary holding times compared to the simulations, since it does not consider the time required to reach the holding temperature. The formation of the two freezing regimes is a direct consequence of the ice nucleation kinetics: At low shelf temperatures, nucleation would occur very fast, so that the nucleation times are governed by the time the vials need to reach the holding temperature. At higher shelf temperatures, nucleation rates are very low and nucleation requires a long time to take place in all vials. Consequently, the variability in complete nucleation and complete freezing times is higher in the nucleation-limited regime than in the heat-transfer-limited regime. In order to achieve complete freezing in a reasonable time frame and to avoid high variability one should not operate in the nucleation-limited regime.

On the other hand, the effect of the holding step on the nucleation temperature distribution will be less pronounced for lower holding temperatures. This behavior is visualized in Figures 6.13 (d) to (f), where a decrease in holding temperature from -12°C to -20°C strongly shifted the bi-variate distribution of nucleation temperatures and solidification times towards lower values, i.e. towards the behavior of the system without holding step. We thus recommend an ad-nucleation holding temperature close to the upper limit of the

heat-transfer-limited regime. For the studied system, this corresponds to the range between -12°C and -10°C.

We again observe that thermal interaction between vials slows down the freezing process. Compared to shelf-ramped cooling, such effect is more pronounced during a holding step, since each nucleation event slightly heats up the neighboring vials above the holding temperature and thus reduces their nucleation rate significantly. The analytical solution does not account for this effect; we recommend its use therefore especially in systems with weak or no thermal interaction between vials.

To conclude, an ad-nucleation hold is capable of shifting nucleation temperatures and solidification times towards more advantageous values in the context of freeze-drying. The model developed here and the simulations presented may aid lyophilization practitioners in designing such a cooling protocol in practice.

Controlled vs. uncontrolled nucleation

In this section, we compare freezing processes involving controlled nucleation with those relying on uncontrolled nucleation. Figure 6.12 (γ) and (δ) illustrate the thermal evolution of processes with controlled nucleation, while Figure 6.15 shows the simulated solidification time distributions for different heat transfer regimes. Freezing processes involving controlled nucleation commonly comprise two holding steps; namely a pre-nucleation and a post-nucleation holding step. Figure 6.12 (γ) illustrates a cooling protocol, where only a pre-nucleation hold is applied, while Figure 6.12 (δ) refers to a protocol with both holding steps. We have discussed the role of pre-nucleation holding steps and their importance for controlled nucleation in Section 6.3.4; nucleation-related heterogeneity in controlled nucleation is solely governed by the pre-nucleation holding scheme.

The second quantity of interest, i.e. the solidification time distribution and therefore the average crystal size, depends on the cooling protocol after nucleation. A post-nucleation holding step steers the system towards longer solidification times. We have compared the solidification time distributions for controlled nucleation with and without a post-nucleation holding step, as illustrated in Figures 6.15(d) and (c), respectively. As expected, the post-nucleation holding step leads to longer solidification times compared to the protocol without it. However, even in the absence of a post-nucleation holding step, controlled nucleation schemes always result in longer solidification times than uncontrolled shelf-ramped freezing, i.e. profile α, as is evident in all panels of Figure 6.15.

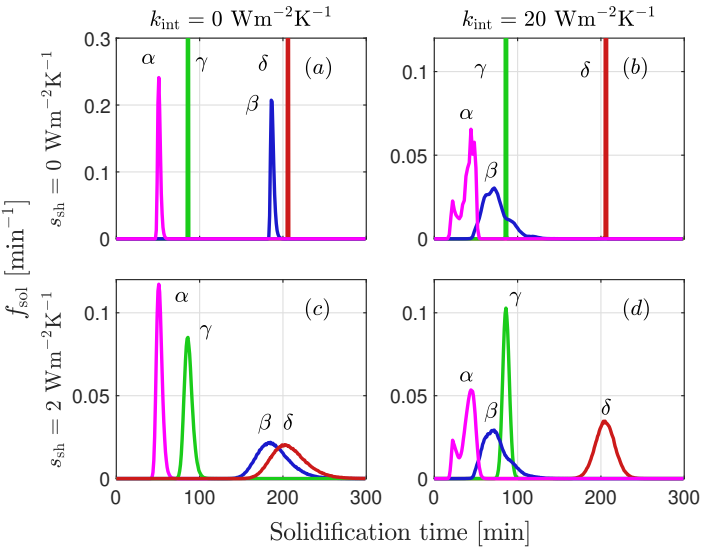

Figure 6.15 Simulated solidification time distributions for four different cooling protocols (shown in Figure 6.12) with and without thermal interaction between vials and with and without variability in shelf-to-vial heat transfer: (α) uncontrolled shelf-ramped freezing, (β) uncontrolled freezing with ad-nucleation hold, (γ) controlled nucleation without post nucleation hold and (δ) controlled nucleation with post-nucleation hold. Heat transfer with the environment was set to zero and the shelf-to-vial heat transfer is given by $k_{\mathrm{sh},0} = 20\ \frac{\mathrm{W}}{\mathrm{m^2K}}$.

We also note that with controlled nucleation, all vials require essentially the same time to solidify as long as they experience the same heat transfer (Figure 6.15(a) and (b)). However, for a variability in shelf-to-vial heat transfer of $s_{\mathrm{sh}} = 2\ \frac{\mathrm{W}}{\mathrm{m^2K}}$, we already found a solidification time distribution of similar broadness as with conventional nucleation (cf. panels α & γ in Figures 6.15(c) and (d)). The fact that minor differences in heat transfer among vials lead to pronounced variability in solidification time may explain why controlled nucleation schemes in practice only reduce, but not eliminate vial-to-vial variability.

We also find that controlled nucleation schemes are less affected by thermal interaction between vials than uncontrolled ones. Since nucleation is initiated in all vials at the same time, thermal interaction between vials is ineffective; therefore during solidification, there are no major temperature gradients between the vials on the shelf. This finding is in line with a recent experimental study,[93] which identified *humps* in the temperature profiles

of vials undergoing stochastic nucleation, but not of those experiencing controlled nucleation. For the uncontrolled freezing processes (α and β in Figure 6.15), thermal interaction leads to faster solidification and more vial-to-vial variability, particularly for the policy using the ad-nucleation step β.

Compared to the ad-nucleation holding scheme, controlled nucleation with post-nucleation hold δ provides comparable solidification times when no thermal interaction between vials is present. We thus hypothesize that such ad-nucleation holding schemes may be a potentially useful path for process optimization leading to frozen products with attributes between those of traditional shelf-ramped cooling and controlled nucleation. It may be especially advantageous in the case of weak or no thermal interaction among vials, i.e. in settings where k_{int} is kept low, either by choice of material or by adding insulating materials between vials.

6.4 CONCLUDING REMARKS

In this work, we have presented a modeling framework for the simulation of the freezing stage in freeze-drying processes. It is the first model that mechanistically covers the entire freezing process for an arbitrary number of vials on a shelf starting from a liquid. We model several aspects of the freezing process together for the first time, namely the stochasticity of ice nucleation, the variability in heat transfer with the shelf, and thermal interaction among vials. An important application lies in guiding the process design and optimization for freezing processes involving both controlled and uncontrolled nucleation. The model allows to quantify the impact of process parameters such as cooling rate and holding steps on the freezing behavior of vials at a shelf-scale and thus enables a rational process design. By providing open source access to the model in the form of a python package, we hope that this work will benefit researchers and lyophilization professionals alike.[73]

To demonstrate its usefulness, we applied the model to gain a better understanding of freezing-related batch heterogeneity and analyzed process strategies to reduce said heterogeneity. Our simulations revealed a novel mechanism how ice nucleation adds on the batch heterogeneity based on thermal interaction among vials: Early nucleating vials may act as local "hot spots" on the shelf and delay the nucleation events of their neighbors. Such effect may be of great relevance to the design of freeze-drying processes.

We identified and modeled thermal interaction between vials, heat transfer with the environment and a variable shelf-to-vial heat transfer all as potential

mechanisms for batch heterogeneity. All these effects led to a broadening of the solidification time distribution while only weakly affecting the nucleation temperature distribution; in fact, we observed that nucleation temperatures are inherently independent of heat transfer as long as the effective temperature profile in the supercooled regime remains similar. In practice, vials with similar nucleation temperatures may solidify differently due to variability in heat transfer. We conclude that the nucleation temperature distribution alone is *not* sufficient to characterize batch heterogeneity and we advise against using it as sole predictor of ice crystal morphology.

The simulation results confirmed the importance of both the choice of a suitable cooling rate and a careful design of holding steps. While controlled nucleation was shown to enable a more homogeneous freezing process, it requires a careful design of the pre-nucleation cooling profile to ensure a narrow nucleation temperature distribution. For uncontrolled nucleation, our results indicate that a pre-nucleation holding step does not reduce batch heterogeneity. With an ad-nucleation holding step, however, we were able to engineer the nucleation temperature and solidification time distributions successfully hence we recommend further studies on this type of holding step to investigate its potential for process optimization. Also, we showed that slow cooling rates, while leading to higher solidification times and nucleation temperatures, also increase batch heterogeneity; the existence of this trade-off constitutes a novel aspect to take into account when choosing the cooling rate.

While in this work we focus on quantifying the effects of stochasticity during the freezing process on a set of vials, the underlying methodology is not limited to freezing: Our work promises to benefit future efforts to develop a model comprising the entire freeze-drying process.

7 SHELF-SCALE ONLINE MONITORING OF VIAL FREEZE-DRYING USING INFRARED THERMOGRAPHY

Freeze-drying is widely used in the manufacture of biopharmaceuticals in vials and therefore its process design and optimization have received considerable attention. In this context, vial-to-vial heterogeneity, also known as batch heterogeneity, represents a major challenge that has been difficult to investigate to date due to the lack of adequate monitoring techniques that provide information on the nucleation, solidification, and sublimation behavior of all vials on a shelf. This contribution reports a novel experimental technique based on infrared thermography that is capable of doing so, hence enabling comprehensive studies of vial-to-vial heterogeneity. The technique was used to investigate the phenomenon of thermal interactions among vials, which had been identified earlier (see Chapter 6) as dominant mechanism of batch heterogeneity in the freezing stage of freeze-drying. The experimental measurements confirmed the relevance of thermal interactions and enabled their quantification; they revealed the use of high cooling rates and less dense vial arrangements on the shelf as two feasible ways of mitigating thermal interactions. This demonstrates the capability of this experimental technique to deepen the process understanding of freeze-drying, and to support practitioners in process design and optimization.

7.1 INTRODUCTION

The stability of most biopharmaceuticals in aqueous solution is limited. Their shelf life may be extended when storing them in the frozen state, which necessitates an expensive cold chain that comes with significant logistical challenges when distributing the drug products globally, particularly in developing countries.[1,2,4,194] To enable long-term storage at ambient conditions

The work reported in this chapter is under review at a peer-reviewed journal: Deck*, L.-T.; Ferru*, N.; Košir, A.; Mazzotti, M. Visualizing and understanding batch heterogeneity during freeze-drying using shelf-scale infrared thermography. A pre-print is available on ChemRxiv.[193] This article is to be published with a shared first authorship between Nicole Ferru, who carried out her Master's thesis research project under my supervision on this topic, and myself.

and thus facilitate the distribution of the drug products, freeze-drying (also called lyophilization) is commonly employed.[21,195,196] In freeze-drying, a formulation filled into vials is first frozen and then dried under vacuum, where most of the water is removed through sublimation (primary drying) followed by desorption (secondary drying).[21,41] The design of such a process is both challenging and time-consuming, which is why for instance the commercially available vaccines against COVID-19, that had to be developed at an unprecedented pace, were distributed as frozen products, despite the tremendous logistical challenges.[197,198]

The difficulty of designing freeze-drying processes stems from the complex interplay between the freezing and the drying stages.[21,43] Figure 7.1 provides a schematic overview of a freeze-drying process highlighting the fact that primary drying is the longest stage. Freezing conditions affect the dynamics of sublimation, and therefore freezing should be carried out such that the ensuing primary drying is as fast as possible. Two distinct phenomena occur during freezing, namely nucleation, which represents the onset of ice formation, and solidification, which denotes the crystal growth following nucleation. High nucleation temperatures and long solidification times have been correlated to fast sublimation,[19,43] because the micro-structure of the frozen product that forms under these conditions is expected to enable fast mass transfer of the sublimated water vapor out of the product.

At the shelf scale, the effect of freezing conditions such as the temperature profile in the freeze-dryer (gray line in Figure 7.1) on the micro-structure and its variability between vials is not yet entirely understood for multiple reasons. First, nucleation is stochastic, and therefore the formulation in different vials across the same batch experiences it at different points in time.[64,66,76] This means that a large data set is required to draw statistically relevant conclusions. Second, heat transfer may not be uniform across a shelf, which may lead to differences between vials at the edge and the core of the shelf.[41,92,169] Third, the temperature rise in a vial after nucleation affects the thermal evolution of the neighboring vials, which implies that parameters such as the vial packing configuration on the shelf (i.e., hexagonal or square arrangement) affect freezing.[74,84,199] These three effects lead to a pronounced batch heterogeneity, which must be considered in process design and which may potentially lead to process failure.[20,21,28,170] To achieve a mechanistic understanding of the freezing stage that can guide process design, one must therefore study it at the shelf–scale.

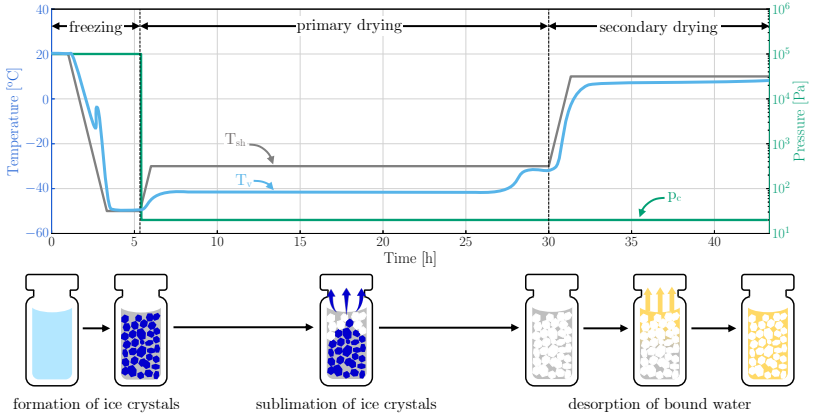

Figure 7.1 Schematic overview of the three phases of the freeze-drying process. Blue line: temperature in a vial. Gray line: temperature of the shelf on which the vials are placed. Green line: pressure inside the freeze-dryer. During the freezing phase, ice crystals are formed as the product is cooled at ambient pressure. Then, the ice crystals sublimate under vacuum during the primary drying phase which is followed by the secondary drying phase where the residual bound water is desorbed upon increasing the temperature.

To this end, we have developed an openly available shelf-scale model of the freezing stage that considers both the stochastic nature of nucleation and the thermal interaction among vials in the batch.[74] A variant of this model was used to simulate the commercial freezing process of the Janssen COVID-19 vaccine, and was found to correctly describe all relevant experimental trends that were observed in engineering runs.[75] For freeze-drying, model simulations revealed thermal interactions among vials as dominant mechanism of vial-to-vial heterogeneity under practically relevant conditions: some vials are expected to solidify more than twice as fast as others, even in cases where both vial position and heat transfer with the shelf are identical (see Figure 7b in Deck *et al.*[74]). Given that such heterogeneity poses a major challenge to the freeze-drying process in vials, it may be worthwhile to design these processes such that the extent of these interactions is limited. The model shows that this is the case for high cooling rates and low vial packing densities (as this reduces the heat transfer coefficient between neighboring vials).

However, it is important to note that the effect of thermal interactions on solidification times has not yet been reported experimentally. This is because there is no adequate monitoring technique available that provides information on the freezing (in particular solidification) behavior for all vials on a shelf. While the mechanistic character of the model ensures that the

simulated trends are qualitatively correct, experiments are required to validate the predictive performance of the model and quantitatively assess the extent of thermal interactions. This contribution introduces a shelf-scale monitoring technique based on infrared thermography for this purpose. We build on earlier techniques that have been employed to monitor the thermal evolution of a large number of vials at the same time during freeze-drying:[200–204] Emteborg *et al.*[200] cut a hole into the top of a freeze-dryer to install an infrared camera for the monitoring of the top-most shelf with 2D resolution. Lietta *et al.*[202] developed a camera module that fits inside a freeze-dryer and monitors the vials from the side, effectively measuring the temperature of the glass vial. However, due to its large size, the spacing between the shelves had to be increased significantly. Our technique combines the advantages of these two approaches and allows for direct 2D monitoring of the product temperature in a batch of vials without the need for any hardware modifications; it is explained in detail in Section 7.2. Its capabilities to monitor the thermal evolution of a set of vials are showcased in Section 7.3.1. We further utilize the setup to explore the influence of freezing process parameters on the freezing behavior and its variability in an extensive experimental campaign. In particular, we consider various packing configurations and cooling rates (Section 7.3.2) and compare the experimental measurements to simulation results (Section 7.3.3). We draw the relevant conclusions in Section 7.4.

7.2 EXPERIMENTAL METHODS

7.2.1 Experimental setup

The experimental setup developed in this work relies on infrared thermography as a non-invasive temperature measurement method for freeze-drying at the shelf scale. A schematic of the setup is shown in Figure 7.2(a): a set of 60 vials in a precise, but adaptable geometric configuration is placed in front of an infrared camera. An infrared mirror is installed at a 45° angle behind the vials. The infrared camera (FLIR A65 FOV 90, FLIR Systems Inc) is housed in a customized camera module (IMC Service S.r.l.), which also comprises an RGB camera, and a processing unit that manages all components and allows for wireless communication for real-time monitoring. The camera has a precision of $\pm 5\,^{\circ}\mathrm{C}$ and a resolution of 640×512 pixels, which corresponds to about 20 pixels per centimeter for the distances used in the experimental setup. The module is made of a thermally insulating, airtight plastic casing (Ertacetal C) that allows for the use of the camera module under vacuum, and protects the camera from humidity and extreme temperatures. With a height of 90 mm,

the module fits between the shelves of the laboratory-scale freeze-dryer used in this work (LyoBeta 3PS, Telstar), as shown in Figure 7.2(b). It is worth noting that an earlier version of such a camera module has been developed in collaboration between IMC Services and Politecnico di Torino.[202] This previous setup included a FLIR A35 infrared camera (FLIR Systems Inc) with a lower resolution encased in a larger housing that did not fit between shelves and did not feature the use of infrared mirrors to guide the optical path of the camera. The experience gained from this project from this initial model has been crucial in enhancing the design and functionality of the current system.

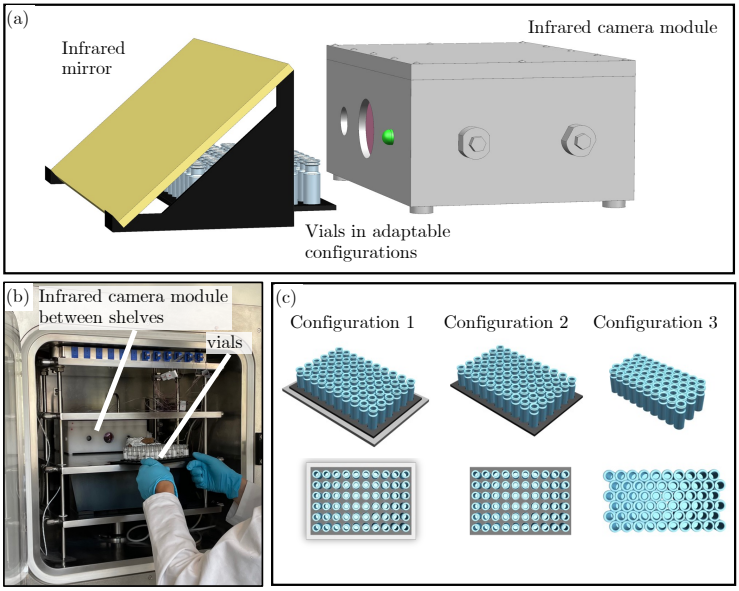

Figure 7.2 (a) Schematic of the experimental setup. The batch of 60 vials is monitored from the top, by guiding the optical path of the infrared camera through a mirror positioned in front of the camera and tilted at a 45°angle. (b) Photo of the setup in the lab-scale freeze dryer. (c) Schematic of the three packing configurations investigated in this work. Configuration 1: vials are placed on a plastic floor, i.e., they are not in direct contact with the shelf. Configuration 2: vials are placed directly on the shelf but separated by an air gap. Configuration 3: vials are placed directly on the shelf, but in a compact hexagonal arrangement.

The gold-coated metal substrate mirror (Edmund Optics Inc.) with a near-perfect infrared reflectance ($R_{700-2000\,\mathrm{nm}} > 96\%$) added in the current setup, is tilted at a 45° angle (see Figure 7.2(a)) to monitor a batch of vials from the top. Monitoring vials from the top as opposed to from the side yields three key

benefits: first, the geometry of top-down monitoring significantly increases the number of vials that can be monitored simultaneously. Second, it allows to monitor vials positioned at various locations of the shelf, i.e., both at the edges and in the core, which is required to identify spatial differences across the shelf. Finally, temperature measurements are obtained directly from the product's surface, whereas measurements from the side report the temperature of the vial wall and may not accurately indicate the vial's internal temperature. The custom-designed camera software accounts for (i) the transmittance of the Germanium lens of the module casing ($T_{700-2000\,\mathrm{nm}} = 82\%$), (ii) the reflectance of the mirror, and (iii) the emissivity of the sample (literature value for the emissivity of water:[205] $\epsilon = 0.96$) to convert the detected signal to temperature. Note that while ice has a slightly higher emissivity (literature value for the emissivity of ice:[205] $\epsilon = 0.97$), the difference is so small that the effect on the temperature measurement is negligible, allowing us to assume a constant emissivity during a freezing cycle. Preliminary experiments revealed considerable variability in absolute temperature readings, due to the camera's limited precision and ambient noise interference. We overcame these issues through the definition of a set of robust freezing characteristics, as discussed in Section 7.3.1. Additionally, a custom calibration pipeline was created in this work, whereby the raw temperature readout from the camera is corrected with a constant offset determined by the difference between the median temperature measured after nucleation and the equilibrium freezing temperature of the solution (which is close to the true temperature after nucleation). More information on the calibration pipeline and its validation are provided in Section 7.5.1.

The experimental setup allows to carry out sensitivity studies, exploring the effect of freezing process conditions on the thermal evolution across the batch. In this work, three different packing configurations of 60 vials in a 6×10 arrangement (see Figure 7.2(c)) using custom 3D-printed plastic holds were studied. In configuration 1, the vials are placed on a 4 mm thick plastic floor and separated from each other by a 3 mm air gap. In configuration 2, the vials are in direct contact with the freeze-dryer shelf, and separated from each other by a 3 mm air gap; for this configuration, we further assessed how the process behavior changes when increasing the cooling rate (configuration 2f). In configuration 3, the vials are in direct contact with the freeze-dryer shelf, and they touch each other in a hexagonal arrangement. The experiments and sample preparation steps were carried out under standard laboratory conditions, i.e., the samples were not sterilized and we did not operate in a particulate-free environment. In line with typical model solutions used in the field,[21,76,93,203] 1 mL aqueous sucrose solution with a concentration of 5 wt. % was selected as model system. A volume of 80 mL of fresh sucrose solution (deionized water: Millipore, Milli-Q Advantage A10 system; sucrose: Sigma–Aldrich,

BioXtra grade, 99.5% purity) was prepared for every experiment. Before use, the glassware where the solution was prepared in, was cleaned with acetone and deionized water. The vials were filled without a prior cleaning step. The bulk solution was mixed by manual shaking and filled into snap ring glass vials (APG Pharma, 1.5 mL), via a micro-pipette (Thermo Fisher Finnpipette F2), resulting in a fill height of 12 mm. Drying experiments were carried out with a 5 wt. % mannitol (Sigma-Aldrich, $\geq$98% purity) solution prepared in the same manner, as mannitol can be dried at higher temperatures resulting in shorter drying times.

7.2.2 Experimental protocol

The experimental campaign carried out in this work aims to demonstrate the capabilities of the infrared thermography setup proposed in this work. To this end, the freezing behavior of a set of vials was investigated by performing freeze-thaw cycle experiments. Each freezing experiment comprises 5–9 freeze–thaw cycles with thermal images being captured in 30 s intervals. Note that the number of cycles per experiment was constrained by the maximum number of 40 steps in a recipe allowed by the software of the freeze-dryer. We carry out freeze-thaw cycling experiments because they provide a large number of data points and hence ensure that enough measurements are collected in every experiment to be statistically relevant.[23,91] The full dataset for an exemplary freeze-thaw cycle is shown in Section 7.5.2. The experimental protocol was based on our earlier work:[76] The temperature of the shelf is first decreased from 20 °C to −50 °C at different constant cooling rates γ, held at −50 °C for 10–60 min, then increased again to 20 °C at a heating rate of 1 K min^{-1}, and finally held at 20 °C for 60–90 min before initiating a new cycle. The holding times were fine-tuned for each configuration based on the observed heat transfer rate to ensure that all vials have sufficient time to reach the minimum and maximum temperature respectively. An overview of the experiments is provided in Table 7.1. Each experiment was repeated three times.

#	Configuration	γ [K min^{-1}]	$t_{-50\,°C}$ [min]	$t_{20\,°C}$ [min]
1	Vials on plastic floor	−0.5	60	90
2	Vials on shelf	−0.5	10	60
2f	Vials on shelf, fast cooling	−1.2	30	60
3	Hexagonal arrangement	−0.5	10	60

Table 7.1 Process parameters of freeze-thaw cycles for each configuration.

7.3 RESULTS

This section reports and discusses the experimental data that was collected using the infrared camera setup. First, we discuss thermal evolution profiles that were extracted from the thermal images. Then, we leverage the ability of the setup to monitor the temperature of all vials to make a statistically relevant assessment of the freezing characteristics of a batch of 60 vials in different configurations. Finally, we compare the experimental measurements to simulation results obtained using the shelf-scale freezing model that was developed earlier.

7.3.1 Thermal evolution during freeze-drying

Figure 7.3(a) shows an example of a thermal image captured during a freezing experiment in configuration 1 (see Table 7.1) at the point in time when the shelf has reached $T_{sh} = -25\,°C$. The thermal image shows that the setup allows to identify the individual vials and to differentiate solidifying vials (bright, hot spots) from colder vials (dark spots), where nucleation either has not occurred yet or where solidification has already been completed. Hence, the spatial distribution of the nucleation events can be monitored and the temperature profiles of all vials can be extracted. Figure 7.3(b) shows the temperature profile of an exemplary vial, highlighted by the blue circle in panel (a): the vial temperature increases upon nucleation and remains close to the equilibrium value for several minutes while solidifying due to the release of latent heat. The shape of the thermal evolution profile is consistent with results obtained earlier using thermocouple readouts.[76]

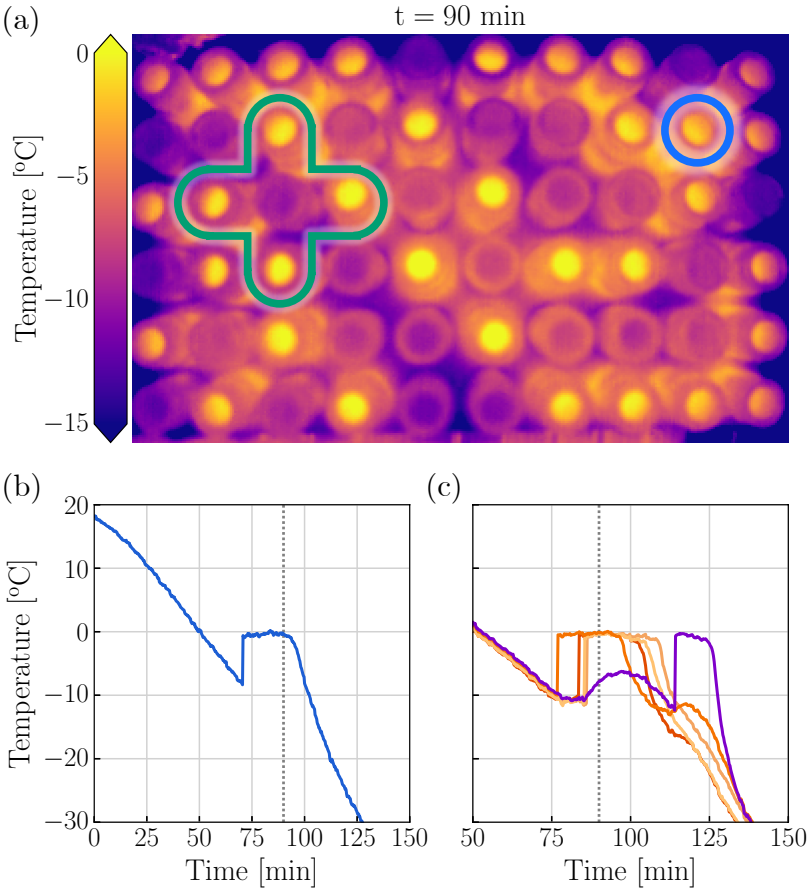

Figure 7.3 (a) Thermal image of a batch of vials during a freezing experiment after 90 min. Solidifying vials (yellow, $T \approx 0\,°C$) can be differentiated from colder vials (purple, $T < -10\,°C$), where nucleation either has not occurred yet or where solidification is already complete. (b) Thermal evolution of an early nucleating vial (see blue circle in panel (a)). The nucleation event is marked by the sharp rise in temperature followed by the solidification phase under constant temperature. (c) Thermal evolution for the five vials highlighted by the green outline in panel (a). The vial in the center (purple line) is heated up by the early nucleation of its neighboring vials (orange lines) and only nucleates once the neighboring vials are completely solidified.

The experimental setup hence enables the extraction of several relevant freezing characteristics, i.e., nucleation temperature, nucleation time, and solidification time, *for each vial on the shelf*. The nucleation time, t^{nuc}, is defined as the time between the onset of cooling and the nucleation event characterized by the thermal spike. The nucleation temperature, T^{nuc}, is the temperature measured at this time. In this work, it is computed by subtracting the temperature jump upon nucleation from the equilibrium freezing temperature T^{eq} (see also Figure 7.4)

$$T^{\mathrm{nuc}} = T^{\mathrm{eq}} - \Delta T^{\mathrm{nuc}}. \tag{7.1}$$

This method bypasses accuracy limitations in the absolute value of the temperature. The solidification time, t^{sol}, corresponds to the period after nucleation during which the temperature remains close to the melting point (see Section 7.5.1 for the exact definition).

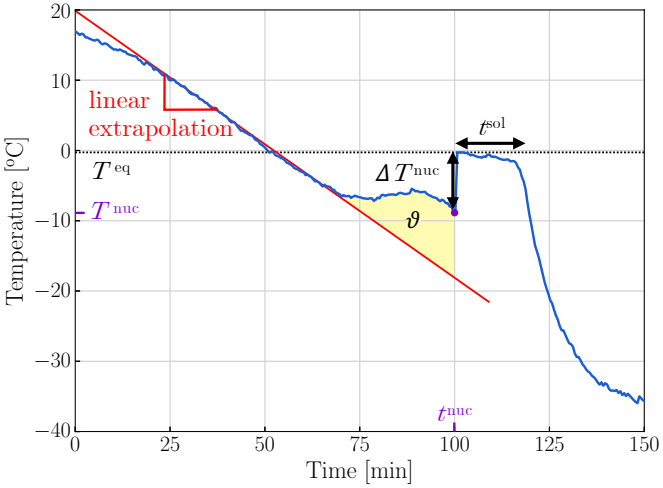

Figure 7.4 Freezing characteristics extracted from the thermal evolution of an exemplary vial. The temperature (T^{nuc}) and time (t^{nuc}) of the nucleation event (purple point) can be read right before the rapid rise in temperature. The solidification time (t^{sol}) is characterized by the phase where the vial temperature remains close to the equilibrium temperature. The thermal deviation (yellow area) is defined via the integral difference between the measured vial temperature and the extrapolated linear cooling curve (see Equation (7.2)).

To further demonstrate the capabilities of the setup, we plot the thermal evolution of a group of five neighboring vials, namely those highlighted by

the green frame in Figure 7.3(a). Panel (c) shows how the temperature of the vial in the center of the group (purple line) is affected by the thermal evolution of its four neighbors (orange lines): as the neighboring vials nucleate and solidify, their temperature increases and they act as hot spots. This interaction heats up the vial in the center and thus delays its nucleation: it only nucleates once its neighbors have completely solidified.

To study such thermal interaction in a quantitative manner, we define an indicator for the extent of interaction experienced by a vial, termed thermal deviation ϑ. This quantity is based on the observation that the thermal evolution of a late nucleating vial (e.g., the central vial in panel (c)) deviates from the linear profile imposed by the shelf during the cooling phase (i.e., before nucleation). We define ϑ as the integral difference between the measured vial temperature $T(t)$ and the extrapolated linear cooling curve $T_{\mathrm{lin}}(t)$. Since the thermal deviation is triggered by the nucleation of a neighboring vial, we anchor the integral at the time at which the first vial on the shelf nucleates, denoted by $t^{\mathrm{nuc}}_{\mathrm{min}}$:

$$\vartheta = \int_{t^{\mathrm{nuc}}_{\mathrm{min}}}^{t^{\mathrm{nuc}}} \left(T(t) - T_{\mathrm{lin}}(t)\right) \mathrm{d}t \tag{7.2}$$

The integral term is highlighted by the yellow area in Figure 7.4, and is given in units of K h. The setup allows extracting all four quantities shown in Figure 7.4 for all vials on the shelf. For a quantitative analysis of the shelf-scale freezing behavior, we introduce the probability density functions (PDFs) $f_{\mathrm{nt}}(t)$ for the nucleation time, t^{nuc}, $f_{\mathrm{sol}}(t)$ for the solidification time, t^{sol}, $f_{\mathrm{nT}}(T)$ for the nucleation temperature, T^{nuc}, and $f_{\mathrm{int}}(\vartheta)$ for the thermal deviation, ϑ. The quantity $f(x)\mathrm{d}x$ denotes the fraction of vials that have experienced nucleation, solidification, or thermal deviation respectively for a value of the independent variable x (i.e., t, T, or ϑ) between x and $x + \mathrm{d}x$. The corresponding cumulative distribution functions (CDFs), or cumulative probabilities, are called $F(x)$. CDFs and PDFs are related through the differential relationship $\mathrm{d}F = f(x)\mathrm{d}x$, where x denotes any of the independent variables above.

Figure 7.5 illustrates the cumulative probabilities obtained for all four freezing characteristics collected in 13 independent experiments (purple lines) carried out in configuration 2, as well as a concatenated distribution with all data points from the 13 experiments (red line). Each experiment (purple line) comprises the data from the 32 vials in the core of the set during 4–8 freezing cycles, corresponding to a total of 128–256 data points.

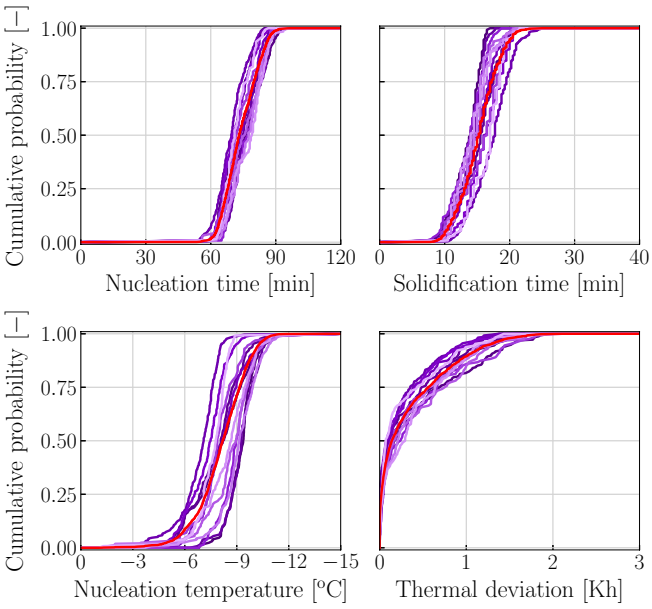

Figure 7.5 Cumulative probabilities of the nucleation times (top left), solidification times (top right), nucleation temperatures (bottom left), and thermal deviations (bottom right) over 13 repetitions (purple lines) of freezing cycle experiments in configuration 2. The red line denotes the sum over all experiments.

As readily observed, all freezing characteristics in all experiments exhibit a spread in their values across vials and freeze–thaw cycles (note that in the absence of any heterogeneity the lines would be rectangular steps). This is for several reasons, including the stochasticity of nucleation and the variability in heat transfer among the vials. Further, one observes variability among the experiments, as the individual purple lines do not overlap perfectly. This variability may be due to differences among sets of vials used in the individual experiments, and to differences in the solution inside these vials, e.g., in terms of particulate impurities levels.[76,79] Such observation points to the need to choose the experimental protocol carefully: in the experiments discussed in the next section, whenever comparing the effect of different operating conditions, the same vials filled with the same solution have been used. In doing so we ensure that the observed trends when changing the operating conditions are not affected by the factors mentioned before.

We close this section by emphasizing that the setup enables the shelf-scale monitoring not only of freezing but also of the primary drying stage. Even

though a quantitative study of primary drying is beyond the scope of this work, for the sake of illustration, Figure 7.6 shows thermal evolution data from an experiment that includes a primary drying step at a shelf temperature of −5 °C and a chamber pressure of 0.2 mbar. These preliminary results show that the setup can be used to monitor the distribution of the temperature of the vials across the shelf. Remarkably, the end point of primary drying – which traditionally is identified as the point in time when the pressure values measured through Pirani and Baratron probes approach each other[202,206] – coincides with the onset of a steady state in the vial temperature. Hence, the developed infrared thermography setup paves the way for future experimental studies aimed at elucidating the link between the freezing process conditions and the drying dynamics, for all vials on the shelf. Since primary drying may take multiple days to complete,[41] identifying process conditions that minimize its duration represents a main objective of freeze-drying process design and optimization. In addition, the setup allows to investigate the heterogeneity in drying behavior among vials, which is critical since the drying process needs to be designed to ensure complete sublimation of ice, even in the vial that dries the slowest.

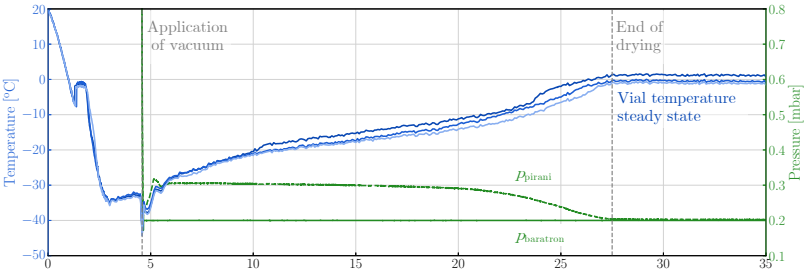

Figure 7.6 Overlay of the thermal evolution (blue lines) of three representative vials and the Pirani and Baratron pressure measurements (green lines) during a full freeze-drying experiment. The endpoint of drying of the entire batch as signaled by the steady state of the temperatures coincides with the endpoint of drying of the Pirani-Baratron readout. The three vials reach this endpoint at slightly different times, which indicates batch heterogeneity in drying that cannot be identified by the widely used Pirani-Baratron technique of endpoint determination.

7.3.2 Exploring freezing at the shelf scale

This section aims to elucidate the features of the nucleation, solidification, and thermal interaction properties on a shelf-scale. Figure 7.7 shows the measured nucleation times, nucleation temperatures, and solidification times

for three comparative experiments. The first pair of experiments (left column) addresses the effect of the cooling rate (slow in configuration 2 and fast in 2f); the second pair of experiments (center column) investigates the effect of the shelf-to-vial heat transfer (slow in configuration 1 and fast in 2); the third pair of experiments (right column) compares two vial configurations (square in configuration 2 and hexagonal in 3, as shown in Table 7.1). Every point in the scatter plots of Figure 7.7 represents a vial in one freezing cycle, and each plot reports the data for the 32 core vials across all 4–8 freezing cycles, i.e., comprises 128–256 data points per configuration. This analysis focuses on the core vials, and the behavior of the edge vials is discussed in more detail in Section 7.5.3. The top panels illustrate the correlation between nucleation times and nucleation temperatures, while the bottom panels show nucleation times and solidification times. The red dotted line indicates the temperature of the shelf as a function of time. The red arrow indicates the temperature difference between vial and shelf for the first nucleating core vial. The probability densities of the distributions are shown on the sides of the scatter plots.

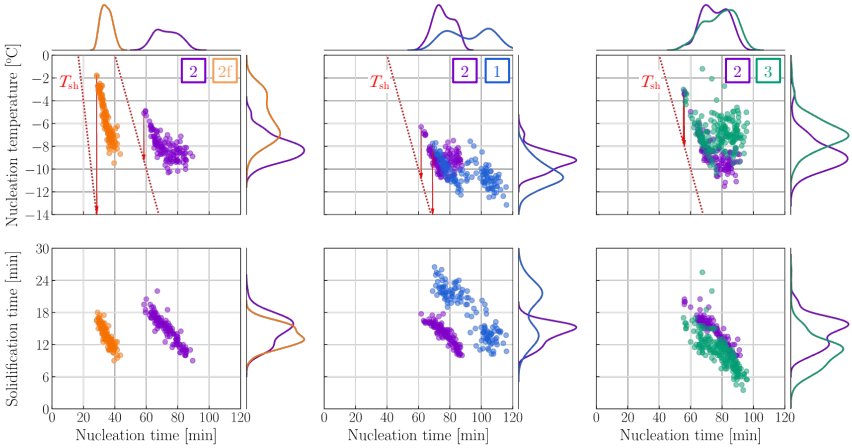

Figure 7.7 Shelf-scale analysis of the freezing behavior of core vials over a freezing experiment in configuration 1 (blue), configuration 2 (purple), configuration 2f (orange), and configuration 3 (green). Top: Correlation between nucleation times and temperatures. The red line indicates the temperature of the shelf *vs.* time. The red arrow indicates the temperature difference between vial and shelf for the first nucleating core vial. Bottom: Correlation between nucleation time and solidification times.

General remarks. Some trends and behaviors can be observed for all experiments. In particular, nucleation times are correlated with both nucleation temperatures and solidification times. The later a vial nucleates, the lower its nucleation temperature, and the shorter its solidification time. This is evident for all vials in configuration 2f and for early-nucleating vials in all other configurations. These correlations are an immediate consequence of the cooling protocol, whereby the shelf temperature decreases over time at a constant rate. The temperature of the vials follows the shelf temperature, which is the reason why late-nucleating vials are expected to nucleate at lower temperatures compared to those that nucleate earlier. Similarly, the later a vial nucleates, the colder the shelf and the faster the heat exchange between vial and shelf, and thus the shorter the solidification time.

Thermal interactions are the reason why this correlation weakens for late-nucleating vials in configurations 1, 2, and 3. To discuss this point, Figure 7.8 reports both the thermal deviation and the nucleation times for all core vials on the shelf, whereby the four panels correspond to the four configurations studied in this work. To enable an insightful comparison between configurations where the process has been operated different cooling rates, the nucleation times have been re-scaled with respect to the first nucleation event in the batch. In all configurations, vials thermally deviate more the later they nucleate. Such a behavior is expected because, by definition, thermal interactions only become relevant when a certain number of vials on the shelf has already nucleated, thus dissipating their heat into their neighbors and therefore slowing down their cooling. Configuration 2f stands out because it exhibits only small deviations – this can be attributed to the fast dynamics imposed by the fast cooling rate resulting in there not being enough time for the early-nucleating vials to heat up late-nucleating ones. Late-nucleating vials in configurations 1, 2, and 3, however, experience deviations on the order of 1 K h (configuration 2) or 5 K h (configurations 1 and 3). These deviations lead to a delay in the nucleation times and thus weaken the linear correlation between the nucleation times on the one hand, and the solidification times and nucleation temperatures on the other hand. Interactions are more pronounced in configurations 1 and 3 compared to configuration 2 because the heat transfer between neighboring vials is more relevant in relative terms: configurations 2 and 3 exhibit similar heat transfer between shelf and vials since the vials are placed directly on the shelf. However, the hexagonal arrangement of configuration 3 leads to a more dense packing of the vials and thus to faster vial-to-vial heat transfer. Configurations 1 and 2, in contrast, have the same geometrical arrangement of vials and therefore similar vial-to-vial heat transfer, but the plastic floor separating the vials from the shelf in configuration 1 effectively slows down the heat transfer with the shelf.

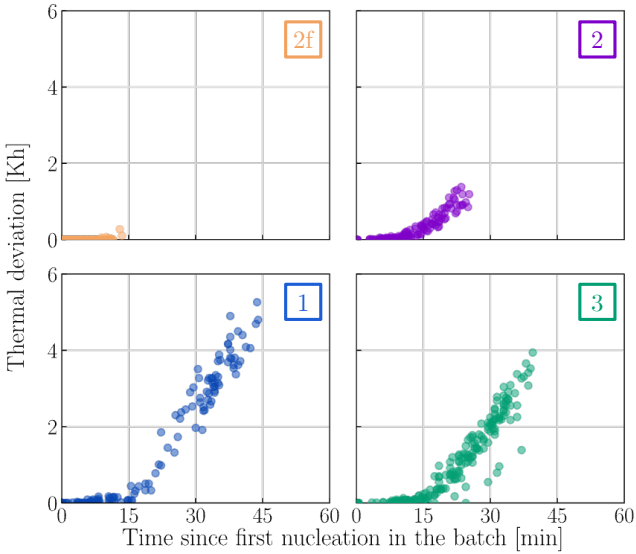

Figure 7.8 Effect of process conditions on thermal deviation in configuration 2f (top left, orange points), configuration 2 (top right, purple points), configuration 1 (bottom left, blue points), and configuration 3 (bottom right, green points).

Effect of cooling rate. For the same vial arrangement, in configurations 2 (purple) and 2f (orange), the shelf is cooled at $-0.5\,\mathrm{K\,min^{-1}}$ and at $-1.2\,\mathrm{K\,min^{-1}}$, respectively. The left column of Figure 7.7 shows that in configuration 2f all vials nucleate within 15 min, while nucleation takes place later and over a window of over 30 min in configuration 2. This is because under slow cooling more time is required to approach temperature levels at which the solution in the vials is supercooled and where nucleation can happen. Moreover, as mentioned before, thermal deviations are more pronounced in configuration 2 than in configuration 2f, which leads to a broader distribution of nucleation times. The solidification times, in contrast, are less affected by the cooling rate, with faster cooling leading to shorter solidification times. This is best evidenced when considering the PDFs plotted at the side of the panel. Such an effect is explained as follows: the rate of solidification is governed by how fast the latent heat can be removed from the solidifying vial. This scales with the difference in temperature between the solidifying vial (close to the equilibrium temperature) and the shelf temperature, amongst other things. At the time of the first nucleation event (see the red arrows),

the shelf is at a temperature of $-14\,°C$ in configuration 2f, and at $-6\,°C$ in configuration 2, which indicates that the shelf-to-vial heat transfer is faster in configuration 2f.

Considering nucleation temperatures, the PDF observed in configuration 2 is narrower and exhibits a lower median value than that of configuration 2f. The lower median value can be attributed to temperature gradients that form in the vials during cooling, which are more pronounced for faster cooling rates. As we have demonstrated earlier (see Figure 6 in Deck *et al.*[77]), nucleation predominantly takes place in the coldest part of the vial, which corresponds to the bottom of the vial when the vials are cooled from the shelf. The temperature at the bottom of the vial at nucleation depends only weakly on the cooling rate. However, with increasing cooling rates, the temperature gradients in the vial are more pronounced, meaning that the temperature at the surface of the vial at nucleation – monitored with the setup – is indeed dependent on the cooling rate. An investigation of the thermal gradients is provided in Section 7.5.1.

Effect of shelf-to-vial heat transfer. Configurations 1 and 2 use the same cooling rate ($-0.5\,K\,min^{-1}$) and vial arrangement (square), but differ in the rate of shelf-to-vial heat transfer which is slowed down in configuration 1 due to a plastic floor placed between vials and shelf. As is evidenced in the center column of Figure 7.7, doing so affects all characteristic quantities. In general, slowing down the heat transfer causes the vials to nucleate later. The first nucleation events in configuration 1 take place 8 min later than in configuration 2, and the temperature difference between vials and shelf at the time of such first nucleation is larger in configuration 1 (red arrows). Furthermore, the nucleation times exhibit a bimodal distribution for configuration 1, i.e., with the first peak corresponding to early-nucleating vials ($t^{nuc} < 80\,min$) and the second to late-nucleating vials ($t^{nuc} > 100\,min$). Such a bi-modality is also observed in the distribution of solidification times, whereby late-nucleating vials solidify significantly faster than early-nucleating ones. We attribute this behavior to the pronounced thermal interaction: the early-nucleating vials dissipate an amount of heat into the neighboring vials such that during their solidification period, almost no other vials nucleate, and the majority of late-nucleating vials start nucleating only after the early-nucleating vials have completely solidified and thus do not dissipate any further heat. In fact, the two peaks in the nucleation time distribution are separated by 30 min which corresponds to the solidification period of the early-nucleating vials which lasts about 30 min. This effect leads to a very broad distribution of solidification times in configuration 1, where early-nucleating vials solidify more than two times slower than late-nucleating ones. Given

that the solidification time is a key determinant of the properties of the frozen (or freeze-dried) product,[9,20,32] this heterogeneity is highly undesired.

While the nucleation window in configuration 1 is twice as wide (35 min) compared to the nucleation window of configuration 2 (17 min), the spread in nucleation temperatures is similar in both configurations. Considering the observations made in Figure 7.8, this re-iterates how strong thermal interactions weaken the correlation between nucleation temperatures and times.

Effect of vial arrangement. Here we assess how the geometrical arrangement of the vials on the shelf affects the freezing characteristics. In configuration 2, vials are arranged in a square array, while they are arranged in a hexagonal array in configuration 3. Conceptually, the denser hexagonal packing is expected to enhance the extent of thermal interactions compared to the square packing, which is confirmed by the data reported in Figure 7.8. The nucleation times, nucleation temperatures, and solidification times are shown in the right column of Figure 7.7.

Intriguingly, both configurations exhibit similar distributions of nucleation times (with a minor shift to longer times in configuration 3) but show significant differences in nucleation temperatures and solidification times. Given that in both configurations vials are placed directly on the shelf, the shelf-to-vial heat transfer rate is similar and indeed the temperature differences between the first vials that nucleate and the shelf are similar for both configurations (red arrow). Hence the differences in nucleation temperatures and solidification times between the configurations are due to the thermal interactions.

The shorter solidification times in configuration 3 are therefore explained by the fact that each vial that nucleates dissipates its heat into six neighboring vials, whereas in configuration 2 vials have only four neighbors. We can also see that the batch heterogeneity in terms of solidification times is more pronounced in the hexagonal arrangement compared to the square arrangement. In particular, the spread of solidification time relative to its median value is significantly larger in configuration 3 compared to configuration 2.

Closing remarks. The experimental data indicates that thermal interactions among vials broaden the distribution of both nucleation times and solidification times, which is considered undesirable due to the effect of these quantities on the ensuing drying behavior. When designing a freeze-drying process, one should therefore aim to minimize the extent of thermal interactions. The experimental measurements of the four configurations show that (i) fast cooling, (ii) fast heat transfer between shelf and vials, and (iii) slow heat transfer between vials achieved through a less dense packing all help to mitigate thermal interactions, and as a consequence batch heterogeneity.

These measures may be considered when designing a freeze-drying process, keeping in mind that they affect not only the extent of thermal interactions but also other relevant aspects: for instance, packing vials in a less dense arrangement lowers the total number of vials that fit into the freeze-dryer, whereas the cooling rate affects nucleation and solidification in numerous ways (e.g., fast cooling leads to substantial temperature gradients within the vials),[77] rendering its rational choice difficult.

7.3.3 Comparison to mechanistic model

The freezing process of a set of vials placed on a shelf in a square arrangement (configurations 1, 2, and 2f) can be simulated with the stochastic freezing model *SNOW*,[74] which provides the thermal evolution and therefore the freezing characteristics of all vials. Due to its mechanistic nature, this model requires knowledge of three classes of model parameters: (i) Physical properties of the formulation to be frozen, including its density and specific heat capacity, the molecular masses and mass fractions of all solutes (to compute the freezing point depression), and the nucleation kinetics; (ii) Operating conditions of the process, including vial volume and geometrical arrangement, the shelf temperature profile, and the number of vials on the shelf; (iii) heat transfer coefficients, whose values depend on the freeze-dryer hardware, materials, and vial configuration. In particular, the model distinguishes among heat transfer between neighboring vials (quantified by the heat transfer coefficient k_{int}), between edge vials and the environment (k_{ext}), and between shelf and vial (k_{sh}).

Previously,[74] we explored through comprehensive sensitivity studies the effect of the heat transfer parameters on the freezing behavior of a set of vials on a shelf. Model simulations revealed an inverse correlation between nucleation times and solidification times and predicted shorter freezing characteristics (nucleation times and solidification times) for increasing heat transfer between vials and shelf. We furthermore observed a shift from unimodal to bimodal or even multimodal distributions of nucleation and solidification times when increasing the value of the vial-to-vial heat transfer coefficient for constant shelf-to-vial heat transfer. These simulation results closely match the experimental findings that were presented and discussed in Section 7.3.2. It is worth noting that these simulations were carried out two years before we started the experimental campaign presented here, without precise knowledge of many of the parameter values and without any experimental evidence at hand that thermal interactions affect freezing at all (we introduced the concept of *thermal interactions* in our previous work[74]). The close agreement between experiments and simulations therefore provides strong evidence that

the *SNOW* model exhibits a strong predictive capability of the key features of freezing processes and that indeed thermal interactions play a major role in the freezing stage of freeze-drying.

These results clearly demonstrate the value of the *SNOW* model in enhancing the physical understanding of the freezing process. However, the model can also be used in a quantitative manner, in line with the current initiatives in pharmaceutical manufacturing toward model-based process design. In this context, we perform a parameter estimation for the heat transfer coefficients, in order to reproduce the specific behavior of the tested configurations 1 and 2. The heat transfer coefficients represent the only unknowns when using the model to simulate the freezing experiments carried out in this work (also consider our two recent studies[76,79] where we estimated the nucleation kinetics). The estimation of parameters requires an objective function that is to be minimized. Since the experimental data confirms that both nucleation and solidification properties are randomly distributed among vials, the objective function must consider the relevant probability distributions of both nucleation times and solidification times.

The objective function is based on the Chebyschev norm $D_{m,n}$,[23,24] which denotes the maximum difference between two cumulative probabilities, in this case between the simulated cumulative probability $F_{m,n}(t)$ and the empirical cumulative probability $\hat{F}_{m,n}(t)$ that is computed from the experimental data:

$$D_{m,n} = \max_t \left| F_{m,n}(t) - \hat{F}_{m,n}(t) \right| \tag{7.3}$$

where the subscript m indicates the type of distribution, i.e., $m = \{\mathrm{nt}, \mathrm{sol}\}$ for nucleation times and solidification times, respectively, and the subscript n the vial configuration. The parameter space includes six parameters, namely k_{ext}, k_{int} and k_{sh} for both configurations (denoted with subscripts 1 and 2). To reduce the search space, we focused the estimation on core vials: edge vials are not considered in computing the cumulative probabilities and the additional heat transfer between the edge vials and the environment is neglected in the simulations (i.e., $k_{\mathrm{ext}} = 0$). Further, we set $k_{\mathrm{int},1} = k_{\mathrm{int},2} = k_{\mathrm{int}}$, as the geometrical arrangement of the vials is identical in both configurations. The resulting system of equations therefore depends on three unknown heat transfer coefficients, namely k_{int}, $k_{\mathrm{sh},1}$, and $k_{\mathrm{sh},2}$. In line with earlier work,[24] we define the objective function as the Euclidean norm of the vector $\mathbf{D}$ that contains as entries the Chebyschev norms considered in the parameter estimation:

$$\min_{k_{\mathrm{int}},k_{\mathrm{sh},1},k_{\mathrm{sh},2}} \|\mathbf{D}\|_2 = \min_{k_{\mathrm{int}},k_{\mathrm{sh},1},k_{\mathrm{sh},2}} \sqrt{D_{\mathrm{nt},1}^2 + D_{\mathrm{sol},1}^2 + D_{\mathrm{nt},2}^2 + D_{\mathrm{sol},2}^2} \tag{7.4}$$

To find the optimal combination of parameter values $(k_{\mathrm{int}}, k_{\mathrm{sh},1}, k_{\mathrm{sh},2})$, we performed a gridsearch for all combinations of $k_{\mathrm{int}} \in [15, 45] \mathrm{W\,m^{-2}\,K^{-1}}$, and

$k_{sh,1}, k_{sh,2} \in [35, 110]\,\mathrm{W\,m^{-2}\,K^{-1}}$ in integer steps. Given the stochastic nature of the underlying phenomena, such a grid search – while computationally more expensive – enables a more robust identification of the global optimum compared to derivative-based algorithms.

Figure 7.9 compares the resulting simulated (dark gray lines) and empirical (colored lines) cumulative probabilities. A complete list of simulation parameters is provided in Section 7.5.4. The figure shows that the simulations correctly predict the absolute values as well as the bimodality in the distributions of the nucleation and solidification times for configuration 1 (blue lines). A larger value of k_{sh} was estimated for configuration 2 than for 1 which agrees well with the fact that the vials are placed directly on the shelf in configuration 2, whereas they are separated from the shelf with an insulating layer in configuration 1. Further, both shape and absolute values of the simulated cumulative probabilities match experiments of configuration 2 (purple line).

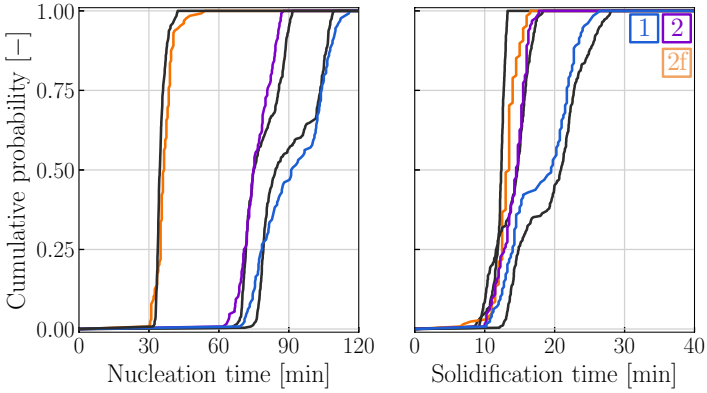

Figure 7.9 Comparison of the distributions of the simulated (dark gray lines) and measured nucleation times and solidification times (blue line: configuration 1, purple line: configuration 2, orange line: configuration 2f). The resulting heat transfer coefficients were $k_{int} = 20\,\mathrm{W\,m^{-2}\,K^{-1}}$, $k_{sh,1} = 51\,\mathrm{W\,m^{-2}\,K^{-1}}$ for configuration 1, and $k_{sh,2} = 110\,\mathrm{W\,m^{-2}\,K^{-1}}$ for configurations 2 and 2f.

To study the predictive capabilities of the model, we used the estimated parameters that were fitted to match configurations 1 and 2 to simulate the behavior of configuration 2f, which has the same geometrical arrangement of the vials as configuration 2 but exhibits a higher cooling rate. As is obvious from Figure 7.9, the model correctly predicts the relevant trends:

the simulated nucleation times in configuration 2f are shorter than those in configuration 2 and are narrowly distributed, in line with experiments (orange line). Similarly, the predicted solidification times for configuration 2f are shorter than those of configuration 2. These findings along with an additional qualitative comparison of the full simulated and measured thermal evolution profiles provided in Section 7.5.5 confirm that the model correctly reproduces the fundamental freezing behavior observed during experiments, which suggests that it can be used to guide the design and optimization of pharmaceutical freezing and freeze-drying processes.

7.4 CONCLUDING REMARKS

In this work, we introduced an experimental setup that utilizes infrared thermography as a reliable, non-invasive batch monitoring technique for freezing and freeze-drying processes. The setup allows to track the thermal evolution of 60 vials in parallel, hence facilitating a statistically relevant analysis of the process. From the resulting data set, several critical pieces of information have been extracted. These include the nucleation temperature, nucleation time, solidification time, and thermal deviation, which is a measure of the extent of thermal interactions among neighboring vials. To elucidate how freezing process conditions affect these features, we have measured them for various packing configurations and cooling rates. The experimental data furthermore allowed us to validate the stochastic shelf-scale modeling framework (SNOW) developed earlier;[74] the model correctly predicted all experimental trends and the simulated thermal evolution profiles closely matched the experimental ones.

It is worth putting these results in context, acknowledging that non-invasive monitoring techniques for freeze-drying have been introduced earlier in the literature. These include monochrome cameras[124] or optical fibers[207] for the detection of nucleation events at a batch scale, as well as the use of infrared thermography.[200,202] However, the use of monochrome cameras provides nucleation times only, and no information related to solidification or thermal interactions among vials. The existing infrared camera setups, in contrast, provide all this information (even though thermal interactions have not been studied explicitly), yet they require extensive alterations to freeze-drying systems, or they monitor vials from the side, which restricts the number of simultaneously monitored vials. The setup introduced here overcomes these limitations through the use of an infrared mirror and enables comprehensive shelf-scale studies of the freezing and primary drying stages in freeze-drying.

7.5 SUPPLEMENTARY INFORMATION

7.5.1 Validation of thermography data

The temperature readout of the infrared camera module was calibrated with a custom calibration pipeline: the raw data is corrected with a constant offset determined by the difference between the median temperature measured after nucleation and the melting point of the solution. As is well known in the literature and was observed in our experimental studies reported earlier,[76] the actual temperature of a partially frozen solution shortly after nucleation is very close to the solution's melting point. To create and validate the calibration pipeline, experiments were carried out to compare the temperature values measured by the infrared camera with those measured by a thermocouple. The thermocouple measurements were considered to be the true temperature of the vial at the position of the thermocouple.

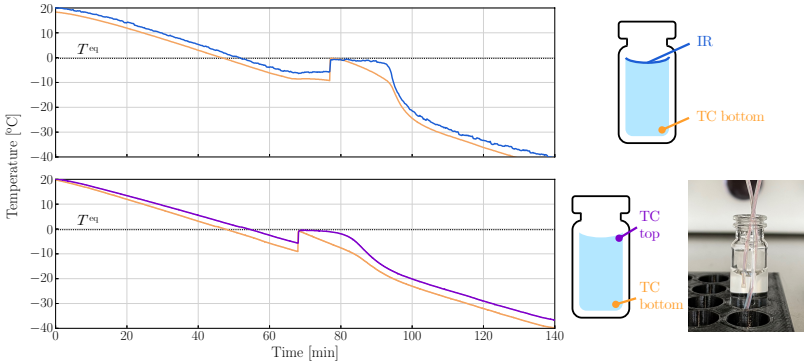

Figure 7.10 Calibration experiments. Top: Comparison of calibrated thermography measurement (blue) and thermocouple measurement (orange). The thermography measurement was calibrated with respect to the melting point of the solution (dashed line). The position of the measured temperature is shown in the schematic on the right. Bottom: Comparison of thermocouple measurement at the top (purple) and bottom (orange) of a vial. The respective locations of the thermocouples are shown in the schematic and the photograph on the right.

Identification of freezing characteristics: The top plot in Figure 7.10 compares the temperature evolution measured by a thermocouple placed at the bottom edge of the vial (orange line) to the calibrated temperature measured by the infrared camera (blue line). The figure shows that the temperature rise

caused by the nucleation event is simultaneously recorded by both measurement approaches. In the infrared data, the measured temperature remains close to the melting point during the entire solidification phase. During solidification, the fraction of ice in the vial continuously increases. Given that ice crystals contain water only, the concentration of the solute in the remaining unfrozen solution increases. This phenomenon is termed freeze-concentration. The increase in concentration is accompanied by a decrease in the solution's equilibrium freezing temperature due to freezing point depression. The equilibrium freezing temperature is a function of the composition of the formulation and can be described by a constitutive equation. To do so, we use the widely applied law for freezing point depression derived by Blagden:

$$T^{\mathrm{eq}} = T_{\mathrm{m}} - \frac{k_{\mathrm{f}}}{M_{\mathrm{s}}} \frac{m_{\mathrm{s}}}{m_{\mathrm{w}} - m_i} = T_{\mathrm{m}} - \frac{k_{\mathrm{f}}}{M_{\mathrm{s}}} \frac{m_{\mathrm{s}}}{(1-\sigma) m_{\mathrm{w}}} \tag{7.5}$$

whereby σ denotes the fraction of the total amount of water in the vial that has turned into ice. Solidification is considered complete when 90% of the water has turned into ice (i.e., when $\sigma = 0.9$). Experimentally, this point in time is detected when the vial cools down below the associated equilibrium freezing temperature (T^{eq}=−2.85 °C), as measured by the infrared camera. With this approach, the experimental setup can be used to accurately and automatically determine both nucleation times and solidification times.

Comparison to thermocouple: The two temperature curves differ in two aspects that are worth discussing. First, the infrared camera measures a higher temperature during the cooling phases before and after the nucleation event compared to the thermocouple. In particular, the nucleation temperature measured by the infrared camera is 3.5 °C higher than the nucleation temperature measured by the thermocouple. Second, the temperature measured by the infrared camera remains constant and equal to the equilibrium temperature throughout solidification, while the temperature measured by the thermocouple continuously decreases. These differences arise because the two sensors measure the temperature at different positions. The thermocouple measures the temperature at the bottom of the vial, while the thermography setup measures it at the top surface of the vial. During cooling, thermal gradients emerge within the vial, whereby the bottom of the vial will be colder than the top due to its proximity to the (cold) shelf. Further, solidification proceeds in a directional manner, whereby ice initially forms at the bottom of the vial. Over time, a solidification front moves upwards, and when it reaches the top, solidification is complete. Hence, during most of the solidification phase, the temperature at the top of the vial is expected to stay constant, whereas that at the bottom continuously decreases.

Thermal gradients: To demonstrate that the sensor location affects the measured values, we compare the temperature evolution measured by a

thermocouple placed at the top and by another one placed at the bottom of the same vial (see bottom panel in Figure 7.10). As is evident, the readouts of the thermocouple located at the top of the vial closely match those of the infrared camera shown in the top panel.

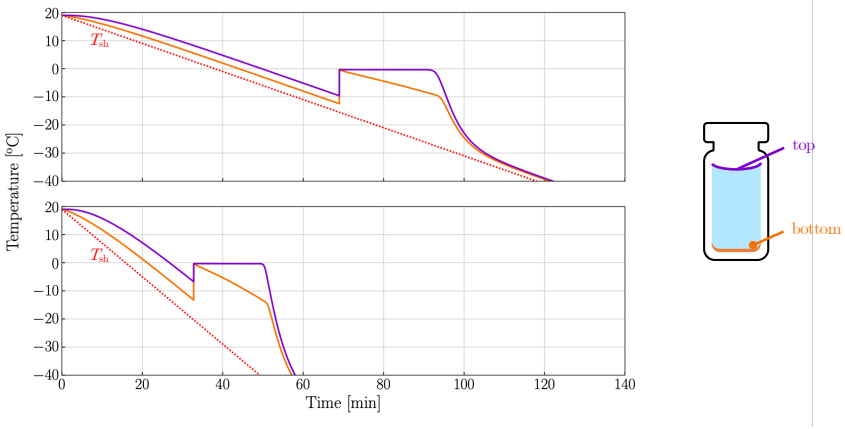

Figure 7.11 Effect of the cooling rate on thermal gradients as predicted by the SNOWing model. Both simulations consider a single vial placed directly on the shelf with $k_{sh} = 110\,W\,m^{-2}\,K^{-1}$. Top plot: simulated thermal evolution with $\gamma = -0.5\,K\,min^{-1}$ corresponding to configuration 2. Bottom plot: simulated thermal evolution with $\gamma = -1.2\,K\,min^{-1}$ corresponding to configuration 2f. The purple lines denote the temperature at the vial top surface, while the dark orange line denotes the temperature at the bottom of the vial, as shown by the schematic on the right. The red dotted line denotes the temperature of the shelf.

The temperature gradients at the time of nucleation affect the measured nucleation temperature. This is especially relevant for large cooling rates where the thermal gradients become more significant. The *SNOWing* model[77] considers thermal gradients during the cooling process of a single vial and is used to simulate the behavior of the experiment shown in the bottom panel in Figure 7.10. The top panel in Figure 7.11 shows how the difference between the temperature at the top and bottom of the surface steadily increases until it reaches 3 °C at nucleation. The model allows us to investigate how the thermal gradient changes for a higher cooling rate. The bottom panel in Figure 7.11 shows a simulation of the same vial, at an increased cooling rate (corresponding to configuration 2f). While the temperature at the bottom of the vial at nucleation (purple line) is rather independent of the cooling rate, thermal gradients are more pronounced for fast cooling, which results in a

significantly higher temperature at nucleation at the vial top (purple line). In particular, the temperature at the top is 7 °C higher than at the bottom of the vial for fast cooling. This supports the observations made in the experiment that the temperature at the surface of the vial at nucleation – monitored with the setup – is indeed sensitive to the cooling rate.

7.5.2 Experimental protocol

The freezing behavior of a set of vials was investigated by performing freeze–thaw cycle experiments. Each freezing experiment comprises 5–9 freeze–thaw cycles as shown in Figure 7.12. With the freeze–thaw cycling protocol, a large number of data points is collected for a single set of vials. The freezing characteristics of each cycle are concatenated in one dataset.

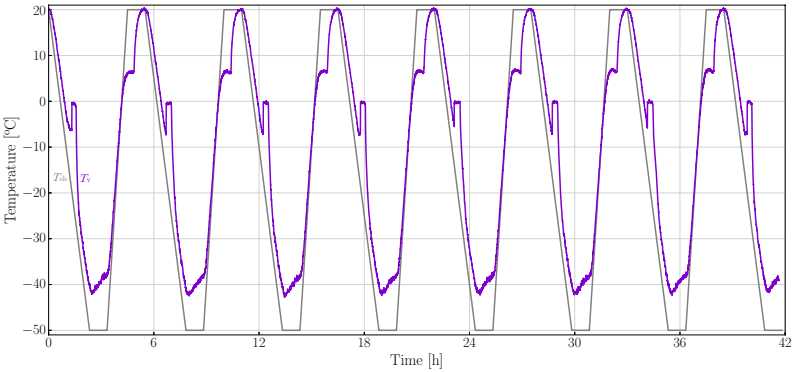

Figure 7.12 Experimental protocol of freeze-thaw cycle experiments. The gray line denotes the set point of the shelf temperature. The purple line shows the temperature of a typical core vial in configuration 2.

7.5.3 Edge effect

Edge vials are expected to display a different freezing behavior than core vials – termed *edge effect* in the literature – for two reasons. First, they are exposed to additional heat exchange with the walls of the freeze-dryer. Second, they are less affected by thermal interactions as they are in contact with fewer neighboring vials. To enable a quantitative study of the differences between the freezing behavior of edge and core vials, Figure 7.13 shows the characteristic quantities (nucleation times, nucleation temperatures, solidification

times) for both groups of vials. The columns correspond to the different vial configurations that were investigated.

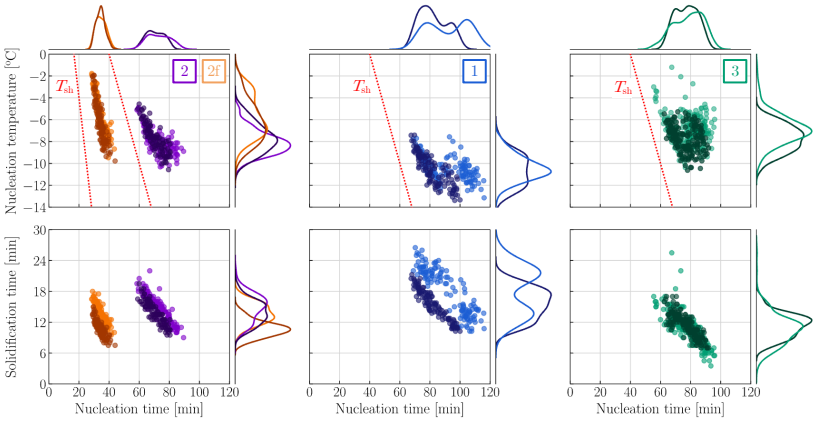

Figure 7.13 Comparison of the freezing behavior of edge (dark shades) and core (lighter shades) vials over a freezing experiment in configuration 1 (blue), configuration 2 (purple), configuration 2f (orange), and configuration 3 (green). Top row: Correlation between nucleation times and nucleation temperatures. The red dotted line indicates the temperature of the shelf as a function of time. Bottom row: Correlation between nucleation time and solidification times. The probability density functions for the three characteristics are shown on the sides of the scatter plots

General remarks: Some trends hold for all configurations and are discussed in the following. First, we see that there is no relevant difference in the nucleation temperatures of the edge and core vials in any configuration. In principle, such a difference could arise for two reasons: as nucleation kinetics are vial dependent, different vials in principle always exhibit different nucleation behaviors, or edge vials specifically may experience a different level of thermal gradients compared to core vials. As all vials were filled in the same way and both the number of vials at the edge (28 vials) and core (32 vials) of the group is large, a systematic difference in the nucleation kinetics between the two groups of vials would be unexpected. Similarly, as heat transfer is dominated by the shelf, additional heat transfer with the walls that acts at the sides of the edge vials only has a minor effect on the extent of the (vertical) thermal gradients. Therefore, the finding of negligible differences in nucleation temperatures between edge and core vials is indeed expected. Another general trend is observed during solidification: On average, edge vials tend to solidify faster than core vials. This effect is noticeable in all

configurations but to different extents. Edge vials solidify faster due to the additional cooling from the freeze-dryer walls (and the part of the shelf that lies in the view of the edge vials). It is worth emphasizing that such behavior is in line with shelf-scale simulations of freezing reported earlier.[74]

Low interaction configurations: In configurations 2 and 2f where the freezing behavior is only weakly affected by thermal interactions the nucleation event (i.e., nucleation temperature and time) is not affected by the edge effect at all. For fast cooling, the shortening of solidification times is the most pronounced.

Low shelf-to-vial heat transfer: The core vials in configuration 1 show a distinct bimodal distribution both in terms of nucleation and solidification times. The edge vials, however, do not: both the nucleation and solidification times follow uni-modal distributions, suggesting that the edge vials are only weakly affected by their (fewer) neighbors. In fact, the probability density function of the nucleation times shows that the bulk of the edge vials nucleates with the first group of core vials, and only very few edge vials experience a delay in nucleation.

High number of neighbors: The hexagonal arrangement of configuration 3 results in almost no difference between edge and core vials in terms of all freezing characteristics. Considering that the vial-to-vial heat transfer in the hexagonal arrangement is high – it is the most dense arrangement of vials studied in this work – and that edge vials in the hexagonal arrangement still have four neighbors, edge vials in configuration 3 are more strongly influenced by their neighbors than in other configurations.

7.5.4 Simulation parameters

Quantity	Symbol	Unit	Value
Vial volume	V	m^3	10^{-6}
Vial fill height	H	m	0.01
Vial width	w	m	0.01
Density	ρ	$kg\,m^{-3}$	1000
Sucrose mass fraction	w_s	%	5
Heat capacity water	$c_{p,w}$	$J\,K^{-1}\,kg^{-1}$	4187
Heat capacity ice	$c_{p,i}$	$J\,K^{-1}\,kg^{-1}$	2108
Heat capacity sucrose	$c_{p,s}$	$J\,K^{-1}\,kg^{-1}$	1240
Heat conductivity water	k_w	$W\,m^{-1}\,K^{-1}$	0.598
Heat conductivity ice	k_i	$W\,m^{-1}\,K^{-1}$	2.25
Heat conductivity sucrose	k_s	$W\,m^{-1}\,K^{-1}$	0.126
Molar mass sucrose	M_s	$kg\,mol^{-1}$	0.3423
Cryoscopic constant water	k_f	$K\,kg\,mol^{-1}$	1.853
Latent heat of fusion water	λ_w	$kJ\,kg^{-1}$	333.5
Melting point water	T_m	°C	0
Initial vial temperature	T_0	°C	20
Nucleation parameter	a	-	21.0
Nucleation parameter	b	-	24.3
Nucleation parameter	c	-	0.83
Batch size	MxN	-	$(10x6)$
Cooling rate	γ	$K\,min^{-1}$	-0.5, -1.2
Shelf–vial heat transfer coefficient	k_{sh}	$W\,m^{-2}\,K^{-1}$	35–110
Vial–vial heat transfer coefficient	k_{int}	$W\,m^{-2}\,K^{-1}$	15–45

Table 7.2 List of all parameters that were used in the simulations presented in this work.

7.5.5 Modeling thermal evolution

The *SNOW* freezing model provides the thermal evolution for each vial on the simulated shelf.[74] A qualitative comparison between the simulated and measured thermal evolution profiles is shown in Figure 7.14. The measured (left) and simulated (right) thermal evolution profiles are extracted from a group of five vials positioned at the top left of the batch, as highlighted in

Figure 7.3(a). Because nucleation is stochastic, the temperature profiles of the same group of vials are expected to vary between repetitions. To assess whether the model is able to capture this variability, we here show two representative experimental profiles collected in two independent experiments of the freezing experiments in configuration 1. In the top row, the vial at the center of the group (purple) nucleates last and its temperature strongly deviates from the linear cooling curve. In the bottom row, this vial nucleates first and delays the nucleation of its neighbors. The simulated profiles reproduce the experimental variability of the freezing process both in terms of thermal deviation and of nucleation sequence, i.e., by carrying out multiple simulations one observes that in some cases the center vial nucleates first, in other cases last, and in the remaining cases in between its neighboring vials. These findings confirm that the model correctly reproduces the fundamental freezing behavior observed during experiments.

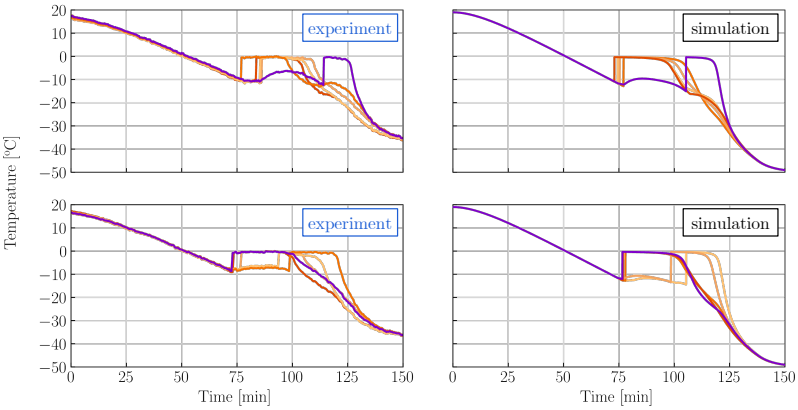

Figure 7.14 Comparison of the measured (left) and simulated (right) thermal evolution profiles of a group of neighboring vials located in the top left region of a set of vials as highlighted in Figure 7.3. The experimental data is taken from two independent repetitions of experiments in configuration 1. For the simulations, the estimated heat transfer parameters $k_{\mathrm{sh},1} = 51\,\mathrm{W\,m^{-2}\,K^{-1}}$ and $k_{\mathrm{int}} = 20\,\mathrm{W\,m^{-2}\,K^{-1}}$ were used. The model replicates the stochasticity observed in the experiments, and qualitatively predicts the effect of interactions in terms of thermal deviation and spread in nucleation times.

8 STOCHASTIC ICE NUCLEATION GOVERNS THE FREEZING PROCESS OF BIOPHARMACEUTICALS IN VIALS

Biopharmaceuticals commonly require freezing to ensure the stability of the active pharmaceutical ingredients (APIs). At commercial scale, freezing is typically carried out over the course of days in pallets comprising tens of thousands of vials. The selected process conditions have to ensure both complete freezing in all vials and a satisfactory manufacturing throughput. Current process design, however, is mainly experimental, since no mechanistic understanding of pallet freezing and its underlying phenomena has been achieved so far. Within this work, we derive a mechanistic modeling framework and compare the model predictions with engineering run data from the Janssen COVID-19 vaccine. The model qualitatively reproduced all observed trends and reveals that stochastic ice nucleation governs both process duration and batch heterogeneity. Knowledge on the ice nucleation kinetics of the formulation to be frozen thus is required to identify suitable freezing process conditions. The findings of this work pave the way towards a more rational design of pallet freezing, from which a plethora of frozen drug products may benefit. For this reason, we provide open source access to the model in the form of a python package.[73]

8.1 INTRODUCTION

The freezing of pharmaceuticals recently has garnered substantial public interest. Storage conditions of COVID-19 vaccines have received global news coverage, since they greatly impact the product's supply chain, with low temperature cold chains being costly or not even available depending on the market.[1,4,208] Although the stabilizing effect of freezing has been studied intensely,[8–13] its quantification and prediction remain challenging until today.[14,15]

The work presented in this chapter has been reported in: Deck, L.-T.; Ochsenbein, D.R.; Mazzotti, M. Stochastic ice nucleation governs the freezing process of biopharmaceuticals in vials. *Int. J. Pharm.* **2022**, 625, 122051.

Numerous studies have confirmed that the stabilization depends not only on the formulation, which includes the active pharmaceutical ingredient (API) and excipients, but also on the process conditions.[9,12,14,16–18] Freezing comprises two phases, namely a cooling phase, during which the formulation is in the liquid state, and a solidification phase, during which ice is formed.[19–21] Solidification is initiated by ice nucleation, which is a stochastic process,[19,20,22–27] leading to variability in freezing behavior among vials even if their thermal environment is identical.[19,21,25,27–29] Based on these considerations, freezing may be characterized by three quantities, which are conceptually linked to most of the known degradation mechanisms for frozen biopharmaceuticals:[10–13,21,30–34] These are the nucleation time, i.e. the duration of the liquid state; the nucleation temperature, which is interpreted as predictor for the ice crystal morphology in the frozen product;[21,34] and the solidification time, which is the duration of the solidification phase and connected to the phenomenon of freeze-concentration.[30–33] In case a drug product exhibits a relevant degradation mechanism related to freezing, these three quantities should be considered during development, implying that all vials meet qualified target ranges with sufficient probability.

At the same time, freezing in vials is inherently hard to control.[28,41] At commercial scale, tens of thousands of vials are typically packed together in a pallet and frozen slowly in a cold storage room. In addition to the inherent stochasticity of ice nucleation, spatial differences in heat transfer across the pallet imply that freezing depends on vial position.[74] Furthermore, the thermal evolution of a vial's neighborhood also shapes its own behavior due to thermal interactions resulting from the employed dense packing.[74,84] To complicate things further, the means for process monitoring are limited; in the case of the Janssen COVID-19 vaccine, a few thermocouples were inserted into a pallet to monitor its thermal evolution and to identify the endpoint of the process. Due to typical process times on the order of days, an optimization of the process duration is of great practical interest to maximize throughput while ensuring complete freezing in all vials. The observed thermal evolution profiles exhibited several trends, which were not entirely understood during process design, such as thermal spikes and a stationary phase at nearly constant temperature.

While pharmaceutical manufacturing is moving towards more rational process design as part of Quality by Design (QbD) initiatives,[35,36] pallet freezing process design is performed mostly in an empirical fashion and thus remains in the metaphorical dark ages. This is despite intense research related to freezing in the pharmaceutical context.[19,28,37–40] In particular, these research activities established links between properties of the frozen product, like its mean ice crystal size or the extent of freeze concentration, and the

freezing conditions. We posit that (part of) the reason why these valuable contributions have yet to reshape freezing process design in industry to a greater extent is because they are predominantly limited to the single-vial scale.

To bridge the existing freezing research at single-vial scale with process design at commercial scale, we recently introduced a batch-scale model for the freezing stage in freeze-drying.[74] The model simulates the evolution of temperature and ice mass for an arbitrary number of vials packed in two spatial dimensions, and thus predicts the nucleation and solidification behavior of all vials, as well as the process duration. It is entirely derived from first principles and explicitly takes into account the stochastic nature of ice nucleation.

In this work, we extend the model to batches comprising vials packed in three spatial dimensions, as is the case in pallet freezing. We simulated the process and compared the model predictions with engineering run data of the Janssen COVID-19 vaccine. The model qualitatively reproduced all experimentally observed trends; we thus apply it to characterize several freezing phenomena, such as the occurrence of thermal spikes and a stationary phase in the thermal evolution profiles. We further study how nucleation kinetics, storage temperature and batch size affect process duration. To promote the use and further development of the model, we provide open source access to it in the form of a python package.[73]

8.2 METHODS

The modeling framework used in this work is based on a shelf-scale model recently presented by the authors for the freezing stage of the vial freeze-drying process.[74] We refer to the original work for a detailed derivation of the model from first principles and present in Section 8.2.1 a summary of the relevant equations and of the underlying principles. In Section 8.2.2 we discuss how to interpret the model predictions and how to characterize freezing. Section 8.2.3, finally, outlines the experimental methods.

8.2.1 Modeling framework

We model the freezing process of densely packed vials in a mechanistic way and take into account number and arrangement of the vials, heat transfer, and ice nucleation and growth. A lumped capacitance approach is used, where each vial corresponds to a homogeneous lump characterized by its mean

temperature and ice mass. The formulation within the vials experiences both a cooling phase and an ice growth phase during freezing. Ice nucleation is the process that drives the vial's state from the liquid to the partially frozen state. It is described as an inhomogeneous Poisson process following existing literature on both ice nucleation and primary nucleation of solutes from solution,[22,23,25,29,66,70] and is simulated using a Monte Carlo approach.[74]

Single vial equations

For the derivation of the balance equations, let us consider a single vial containing a formulation of mass m_v, consisting of water and of solute, such that

$$m_\mathrm{v} = m_\mathrm{w} + m_\mathrm{s}. \tag{8.1}$$

All material is conserved within the vial during freezing, but the water in the formulation will undergo a phase transition from its initial liquid state to ice. Ice will be formed as soon as nucleation occurs. Given the above-mentioned mass conservation, this implies

$$m_\mathrm{w} = m_\ell + m_\mathrm{i} = \text{constant}. \tag{8.2}$$

In addition to the mass of the formulation, we consider its enthalpy, H_v. The evolution is governed by the heat exchange of the vial with its surroundings, characterized by the heat flow $\dot{Q}$:

$$\frac{\mathrm{d}H_\mathrm{v}}{\mathrm{d}t} = \dot{Q} = \left(m_\mathrm{s}c_{\mathrm{p,s}} + m_\ell c_{\mathrm{p},\ell} + m_\mathrm{i}c_{\mathrm{p,i}}\right)\frac{\mathrm{d}T}{\mathrm{d}t} - \lambda_\mathrm{w}\frac{\mathrm{d}m_\mathrm{i}}{\mathrm{d}t} \tag{8.3}$$

where $c_{\mathrm{p,k}}$ denotes the specific heat capacity of component $k \in \{\mathrm{s}, \ell, \mathrm{i}\}$, i.e., solute, liquid water, or ice, while the latent heat of fusion for water is given by λ_w. Assuming knowledge on $\dot{Q}$, we note that mass and enthalpy balance constitute a system of two equations in three unknowns, namely temperature T, mass of ice m_i and mass of liquid water m_ℓ. As long as no ice is present, the equation simplifies to

$$\frac{\mathrm{d}H_\mathrm{v}}{\mathrm{d}t} = \dot{Q} = \left(m_\mathrm{s}c_{\mathrm{p,s}} + m_\ell c_{\mathrm{p},\ell}\right)\frac{\mathrm{d}T}{\mathrm{d}t} = m_\mathrm{v}c_\mathrm{p}\frac{\mathrm{d}T}{\mathrm{d}t} \tag{8.4}$$

and can be solved readily, with $\mathrm{c_p}$ as the heat capacity of the solution. The missing constraint to determine the evolution of the freezing process in the presence of ice lies at the micro-scale, where one may characterize freezing as the process of nucleation and growth of ice crystals. The kinetics of nucleation and of growth, expressed by the corresponding rates of nucleation J, and of crystal growth, govern the rate of change of the ice mass. As

discussed earlier,[74] one commonly expresses these rates as a power law of the thermodynamic driving force $T^{\mathrm{eq}} - T$, which is the difference between the temperature of the formulation inside the vial and the equilibrium freezing temperature, T^{eq}. The equilibrium freezing temperature is governed by thermodynamics and depends on the composition of the formulation. It may be expressed using a constitutive equation, e.g., the widely applied law derived by Blagden:[98]

$$T^{\mathrm{eq}} = T_{\mathrm{m}} - k_{\mathrm{f}} b_{\mathrm{s}} = T_{\mathrm{m}} - \frac{k_{\mathrm{f}}}{M_{\mathrm{s}}} \left(\frac{m_{\mathrm{s}}}{m_{\mathrm{w}} - m_{\mathrm{i}}} \right) \tag{8.5}$$

where b_{s} is the molality of the solute in the solution, M_{s} its molar mass, k_{f} the cryoscopic constant and T_{m} the melting point of water; we also introduce T_{ℓ}^{eq} as the equilibrium freezing temperature of the solution before the formation of any ice, i.e. when $m_{\mathrm{i}} = 0$. The nucleation rate J then is expressed as

$$J = k_{\mathrm{b}} (T^{\mathrm{eq}} - T)^{b} \tag{8.6}$$

where k_{b} and b are empirical constants, which are assumed to be independent of temperature. Experimentally, one generally observes that freezing in vials starts from a single "point of origin of freezing",[20,180] from which the rapid, deterministic spread of a "slushy" phase is observed, which occurs together with a nearly instantaneous temperature rise to the equilibrium freezing temperature. We interpret such behavior as a single primary nucleation event at time t^{nuc} followed by rapid, recalescent growth of ice through the entire volume of the vial. As consequence of the rapid formation of ice, we consider the process of nucleation to be adiabatic with respect to the vial: the heat released upon ice formation equals the sensible heat associated to the rise in temperature from the nucleation temperature, T^{nuc}, to the equilibrium freezing temperature of the now partially frozen formulation, T^{eq}, i.e.:

$$(T^{\mathrm{eq}} - T^{\mathrm{nuc}})\, c_{\mathrm{p}} m_{\mathrm{v}} = \lambda_{\mathrm{w}} m_{\mathrm{i}}^{\mathrm{nuc}} \qquad \text{for } t = t^{\mathrm{nuc}} \tag{8.7}$$

where $m_{\mathrm{i}}^{\mathrm{nuc}}$ denotes the mass of ice formed immediately after the nucleation event, that led to the instantaneous depletion of the existing supercooling, and the corresponding equilibrium temperature $T^{\mathrm{eq}}(t^{\mathrm{nuc}})$. With the supercooling depleted, no further primary nucleation event may take place after t^{nuc}; the first primary nucleus thus remains the sole one. Crystal growth, on the other hand, is governed by heat transfer with the exterior, whereby

$$T^{\mathrm{eq}} - T = 0 \qquad \text{for } t \in [t^{\mathrm{nuc}}, \infty). \tag{8.8}$$

The enthalpy balance (Eqn. (8.3) and the constitutive equation for T^{eq} therefore form a system of two equations in two unknowns, subject to the initial condition in Eqn. 8.7.

Generalization to batch scale

We generalize the framework outlined in the previous section to an arbitrary number of vials arranged in three dimensions. The energy balance for a vial in position (m, n, p) in a densely packed system with $(M \times N \times P)$ vials is:

$$\dot{Q}_{(m,n,p)} = \left(m_\mathrm{s} c_{\mathrm{p,s}} + m_\mathrm{w} c_{\mathrm{p},\ell}\right) \frac{\mathrm{d}T_{(m,n,p)}}{\mathrm{d}t} = m_\mathrm{v} c_\mathrm{p} \frac{\mathrm{d}T_{(m,n,p)}}{\mathrm{d}t} \tag{8.9}$$

$$\dot{Q}_{(m,n,p)} = \left(m_\mathrm{s} c_{\mathrm{p,s}} + m_{\ell,(m,n,p)} c_{\mathrm{p},\ell} + m_{\mathrm{i},(m,n,p)} c_{\mathrm{p,i}}\right) \frac{\mathrm{d}T^\mathrm{eq}_{(m,n,p)}}{\mathrm{d}t} - \lambda_\mathrm{w} \frac{\mathrm{d}m_{\mathrm{i},(m,n,p)}}{\mathrm{d}t} \tag{8.10}$$

whereby the first equation holds for $t \in [t_0, t^\mathrm{nuc}_{(m,n,p)})$ and the second one for $t \in (t^\mathrm{nuc}_{(m,n,p)}, \infty)$. Before nucleation, no ice is present and the enthalpy balance simplifies accordingly. Importantly, the time at which nucleation occurs varies among vials. After nucleation, the enthalpy balance governs the evolution of both temperature and of ice mass, together with Eqn. 8.5, the constitutive equation for the equilibrium freezing temperature. As outlined in Section 8.2.1, the enthalpy balance for the this phase is subject to the initial condition:

$$\left(T^\mathrm{eq}_{(m,n,p)} - T^\mathrm{nuc}_{(m,n,p)}\right) c_\mathrm{p} m_\mathrm{v} = \lambda_\mathrm{w} m^\mathrm{nuc}_{\mathrm{i},(m,n,p)} \qquad \text{for } t = t^\mathrm{nuc}_{(m,n,p)} \tag{8.11}$$

Thus, the enthalpy balance (Eqn. 8.10) and Eqn. 8.5, the constitutive equation for $T^\mathrm{eq}_{(m,n,p)}$ form a system of two equations in two unknowns, subject to the initial condition in Eqn. 8.11. Since the evolution of the vial is subject to $\dot{Q}_{(m,n,p)}$, which may depend on the state of the neighboring vials, the evolution of all vials is coupled and a system of $(M \times N \times P)$ enthalpy balances has to be solved.

Heat transfer for vials in a batch

As derived in Section 8.2.1, the rate of change of the enthalpy of a vial equals the heat exchange with its surroundings, i.e. the heat flow $\dot{Q}_{(m,n,p)}$. In terms of arrangement and geometry, we assume that vials are of cubic shape and completely filled. They thus have six surfaces of equal size A and heat transfer occurs via all of them. We note, however, that this model is generally applicable for any arbitrary shape and arrangement. The heat flow for a vial in position (m, n, p) is given by

$$\dot{Q}_{(m,n,p)} = A \left(q^{(m,n,p)}_{(m+1,n,p)} + q^{(m,n,p)}_{(m-1,n,p)} + q^{(m,n,p)}_{(m,n+1,p)} + q^{(m,n,p)}_{(m,n-1,p)} + q^{(m,n,p)}_{(m,n,p+1)} + q^{(m,n,p)}_{(m,n,p-1)}\right) \tag{8.12}$$

whereby $q^{(m,n,p)}_{(m',n',p')}$ denotes the heat flux across a single side of the vial. While heat transfer in a cold storage room may be complex in practice, we consider

the least complex description that is still qualitatively accurate. Depending on position, each side of a vial is in contact with either another vial, or with the environment. We quantify the extent of heat transfer according to these two options with one lumped parameter each. These are the internal heat transfer coefficient k_{int}, which describes the heat transfer among neighboring vials, and the external heat transfer coefficient k_{ext}, which describes the heat transfer of vial surfaces facing the exterior of the system with the environment. These considerations lead to the following expressions for the heat fluxes:

$$q^{(m,n,p)}_{(m',n',p')} = \begin{cases} k_{\text{ext}} \left(T_{\text{ext}} - T_{(m,n,p)} \right) & \text{for external surfaces} \\ k_{\text{int}} \left(T_{(m',n',p')} - T_{(m,n,p)} \right) & \text{otherwise} \end{cases} \tag{8.13}$$

whereby a surface is considered as external if $m' \in \{0, M+1\} \vee n' \in \{0, N+1\} \vee p' \in \{0, P+1\}$. For a sufficiently large system of vials, such as a box or pallet, four types of vials are observed: corner vials with three sides exposed to the environment and thus three neighboring vials; edge vials with two sides exposed to the environment and four neighbors; side vials with one side exposed to the environment and five neighbors; and finally core vials that are not in contact with the environment and that have six neighbors. As Eqn. 8.13 indicates, T_{ext} is an additional parameter in the model to consider in process design. Pallets are typically frozen in cold storage rooms at constant temperature, motivating us to focus on the case where T_{ext} is constant during the process. As demonstrated in Chapter 6, the model can be used with a time-dependent definition of T_{ext} as well.

As a final note, a quantitative estimation of values for the heat transfer parameters k_{int} and k_{ext} is challenging due to the various mechanisms of heat transfer involved in freezing. In this work, we therefore focus on a sensitivity analysis and investigate how the freezing process behaves under various heat transfer conditions. Importantly, we do not fit the parameters to experimental data, and instead apply values that qualitatively correspond to conditions in a cold storage room, based on existing knowledge at Janssen.

Transition from liquid state to ice growth state

As discussed in Section 8.2.1, the formation of a single primary nucleus triggers the transition from the cooling phase to the ice growth phase due to the rapid growth of ice. Since ice nucleation is stochastic, the nucleation times $t^{\text{nuc}}_{(m,n,p)}$ vary among vials even when they experience identical freezing conditions and when repeating the process, e.g. in a temperature cycling experiment.

Ice nucleation is widely interpreted as a Poisson process, i.e. the probability of nucleation depends on the current state of the vial, but not on its history.[22,23,25,26,66] The rate constant of the Poisson process, $K_{(m,n,p)}$, corresponds to the nucleation frequency in the vial, in units of nucleation events per unit time, and is defined as

$$K = \int_0^V J(V')\mathrm{d}V' = \int_0^V k_\mathrm{b}(T^\mathrm{eq} - T(V'))^b \mathrm{d}V' \tag{8.14}$$

which simplifies to $K_{(m,n,p)} = J_{(m,n,p)}V$, in the case that the vial exhibits no relevant thermal gradients; a reasonable assumption for pallet freezing given the long duration of the process, which is typically on the order of several hours or even days. As outlined in Section 8.2.1, the thermal evolution of a vial, and thus its nucleation frequency, may also depend on the thermal evolution of the neighboring vials and as a consequence on the sequence of neighboring nucleation events. The value of $K_{(m,n,p)}$ in such a system therefore depends not only on time, but also on the stochastic occurrence of prior nucleation events. The type of stochastic process, where past stochastic events impact the future, is known as *self-exciting point process*, and may be interpreted as a step-wise inhomogeneous Poisson process.[22] We may express the probability $P^{(0)\to(1)}_{(m,n,p)}(t, t+\Delta t)$ that a nucleus is formed in a vial in the liquid state in the time interval $[t, t+\Delta t]$ as:

$$P^{(0)\to(1)}_{(m,n,p)}(t, t+\Delta t) = 1 - \exp\left\{-\int_t^{t+\Delta t} K_{(m,n,p)}(t')\mathrm{d}t'\right\} \tag{8.15a}$$

$$\approx K_{(m,n,p)}(t)\Delta t = V J_{(m,n,p)}(t)\Delta t \tag{8.15b}$$

We thus compute $P^{(0)\to(1)}_{(m,n,p)}$ step wise until nucleation occurred in all vials in the batch.

Numerical solution approach

In order to solve the coupled system of energy balances and stochastic ice nucleation equations described above, we have used an adapted version of the algorithm presented earlier.[73] Importantly, we note that repetitive simulations of the process are required to capture the variability resulting from the stochasticity of ice nucleation. The individual simulations are independent of each other, thus enabling parallelization of the computations.

While the results generated for this work were computed using MATLAB, we have opted to provide an equivalent, open source implementation of the model in the form of a python package that we published on pypi under the MIT license.[186] We have called this package *Stochastic Nucleation of Water*, or

SNOW for short.[73] It is our intention to integrate upcoming developments and potential contributions by third parties into future releases, thus hoping to foster a spirit of open collaboration among researchers in this field. All versions of the python package starting from v1.1.0 contain the implementation of the freezing model for densely packed vials presented herein.

8.2.2 Characterizing freezing

An important application of the presented modeling framework in this work is the quantification of properties of the frozen product and their variability among vials and among repetitions of the process, i.e. batch heterogeneity. Such heterogeneity is regarded as one of the main design challenges of freezing and of freeze-drying processes, since it may result in a variability in critical quality attributes.[28,37,41] Predicting and quantifying batch heterogeneity is therefore an essential step towards a rational design of the freezing process.

To the best of our knowledge there is no systematic, model-guided assessment available on batch heterogeneity in pallet freezing and on its root causes, namely stochasticity of ice nucleation, thermal interaction among vials, and position-dependency of heat transfer.[74] Compared to freeze-drying, in pallet freezing we expect an enhanced variability among vials due to the stacking in three instead of in two spatial dimensions: In freeze-drying, all vials are in direct contact with a shelf,[20,21,41] while in the case of pallet freezing most vials are not in direct contact with the exterior and heat transfer occurs through their neighbors only.

As discussed in Section 8.1, product stability and its variability may be related to the nucleation and solidification behavior of the frozen product. We define the nucleation time t^{nuc}, the nucleation temperature T^{nuc}, and the solidification time t^{sol} as characteristic quantities of the freezing process, and understand them as critical material attributes in the context of Quality by Design. Additional experimental studies are required when developing a novel drug to understand the ranges of values for these quantities that lead to acceptable critical quality attributes. Figure 8.1(a) shows the simulated thermal evolution of a single vial and illustrates the definition of these quantities, while Figure 8.1(b) provides complimentary information about the ice mass evolution. The solidification time of a vial, t^{sol}, denotes the elapsed time between the nucleation event at time t^{nuc} and the point in time when freezing is considered to be *complete* for this vial, denoted with t^{fr}. The definition for such completion is to some extent arbitrary; for this work we assume solidification to be complete when $m_{\mathrm{i}}/m_{\mathrm{w}} = 0.9$; however, the model is compatible with any definition based on temperature or ice mass fraction. In our prior work,[74] we studied the effect of the threshold on the characteristic

quantities, and we found that it did not affect the observed trends for values in the range of $m_{\mathrm{i}}/m_{\mathrm{w}} = 0.85 - 0.95$.[74] As it is apparent from Figure 8.1(b), higher values for the endpoint should be avoided, since the amount of ice that can be formed in the vial is ultimately limited by the freezing-point depression for a given storage temperature. This implies that some water will always remain in solution. Assuming sufficient knowledge of the specific formulation to be frozen, one could alternatively use the attainment of the glass transition temperature of the solution as indicator for completion of freezing. Indeed, there is no consensus in literature regarding the definition of complete freezing, with some authors relying on ice mass based definitions,[19,37] and some relying on the glass transition temperature.[32,39]

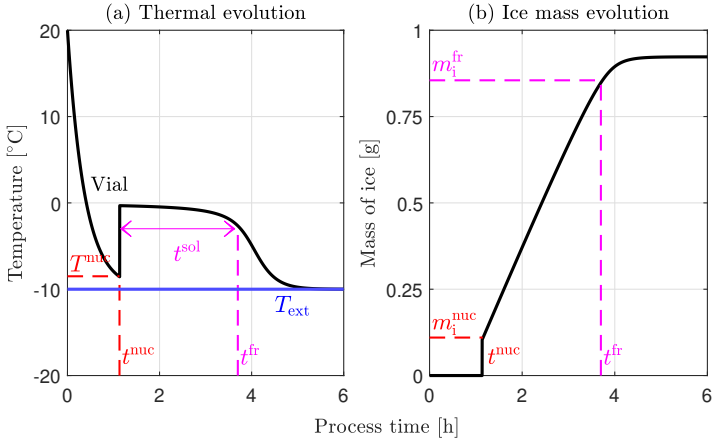

Figure 8.1 (a) Thermal evolution of a single vial during the freezing process. The position of the nucleation event and the time when the vial is frozen, which corresponds to the predefined threshold for the ice mass formed, are indicated. (b) Evolution of ice mass during freezing. The first ice forms at the time of nucleation.

We interpret the distribution of the characteristic quantities among vials as measure of batch heterogeneity: vials that nucleate and solidify differently, will presumably have different mean crystal sizes and different API activity levels,[9,28,37] even if the practical relevance of these differences cannot be known *a priori*. We compute these distributions by running a large number of independent simulations of the process and by determining the corresponding probability density functions $f_{\mathrm{nt}}(t)$, $f_{\mathrm{nT}}(T)$ and $f_{\mathrm{sol}}(t)$. By definition, $f_{\mathrm{nt}}(t)\mathrm{d}t$ provides the fraction of nucleation events that take place between t^{nuc} and $t^{\mathrm{nuc}} + \mathrm{d}t$; $f_{\mathrm{nT}}(T)\mathrm{d}T$ the fraction that nucleates at temperatures between T^{nuc}

and $T^{\mathrm{nuc}} + \mathrm{d}T$; $f_{\mathrm{sol}}(t)\mathrm{d}t$ is the fraction of freezing processes with solidification times between t^{sol} and $t^{\mathrm{sol}} + \mathrm{d}t$. In the same way we also define bi- and tri-variate distributions of the characteristic quantities. The broadness of the simulated probability density functions is gauged in this work by the difference between the 10% and 90% quantiles of the distribution.

In addition to the three characteristic quantities, which are defined per vial, the process duration Δt_{pt} is a quantity of key interest. We define the process duration as the time of complete nucleation for a batch, i.e., the duration from beginning of the cooling process until the nucleation of the last vial. This time will inherently vary due to the stochasticity of ice nucleation, and process design has to account for this variability.

Within this work, we assess the median values of these quantities and their variability in batches of various sizes and conduct sensitivity studies with respect to heat transfer rate, system size, and nucleation kinetics. Specifically, we investigate three sources of batch heterogeneity in four systems of increasing complexity. They comprise: a) the inherent stochasticity of ice nucleation that all systems exhibit; b) the thermal interaction among vials, which was recently shown to enhance the existing stochasticity in the case of freeze-drying;[74,84] and c) the batch geometry and the vials' position within the batch. Simulations of four systems allow us to gain insight and to reach a mechanistic understanding on all these phenomena.

8.2.3 Experimental

Freezing process design for the Janssen COVID-19 vaccine was carried out as per the governing standard operating procedures, i.e., by performing engineering runs at different storage temperatures in order to identify suitable operating conditions, coupled with extensive quality control testing to verify stability. After identifying supercooling as potential design challenge, constitutive experiments were carried out to characterize the supercooling in greater detail. Note that these experiments preceded the development of the model presented within this work.

Supercooling experiments

Qualitative experiments were carried out covering a total of about 300 vials to gain a high-level understanding of the supercooling phenomenon. The vials were either directly exposed to cold air or positioned in boxes in a cold storage room. It was found that a majority of vials containing the COVID-19 vaccine with thermocouples taped to the external side of the vial body would

nucleate in a temperature range of −15°C to −10°C; vials with thermocouples inside the vial were found to nucleate at temperatures anywhere from −15°C to the equilibrium freezing temperature. Since the thermal evolution of these vials was not tightly controlled, an estimation of the nucleation kinetics based on these data alone is not possible. However, these experiments indicate that a metastable zone for the COVID-19 vaccine extends down to at least −10°C.

Pallet freezing engineering runs

Engineering runs were carried out at pallet scale in three configurations with US standard size pallets (40″ × 48″) comprising either 32,400 vials (A-1 configuration, see Figure 8.11 in the supplementary information), 25,300 vials (A-2 configuration, similar to A-1, but with reduced box size) or 33,600 vials (B configuration, see Figure 8.12 in the supplementary information). The geometry chosen for the pallet freezing simulations is comparable to the A-2 configuration $(40 \times 36 \times 18)$ vials, in total 25,920 vials), and corresponds closely to the configuration presented in Figure 8.2. The geometry of the pallet used in the simulation is in some aspects simplified: Neither are multiple packaging layers considered, i.e. when vials are located in boxes that are stacked together, nor is the effect of spacers between boxes explicitly modeled. While these additional aspects may quantitatively affect the process outcome, their inclusion was not required to qualitatively explain all observed experimental trends, as discussed in Section 8.3. In other words, we present the *least complex* model that is able to describe the system adequately, which is the main task of any modeling effort.

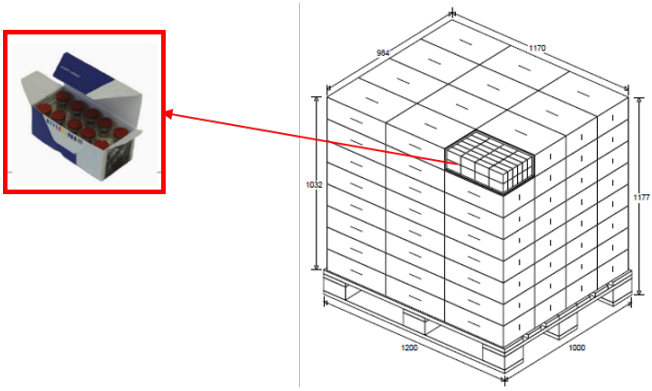

Figure 8.2 Typical packaging setup used for the pallet freezing process at Janssen. Vials are first packed together in small boxes, which then are stored in bigger boxes that are stacked together on the pallet. Shown geometry similar to configurations A-1 and A-2.

Engineering run material comprising the drug product at a concentration similar to that of the final formulation was filled in ISO 2R vials. The vials were packed together according to the aforementioned pallet configuration. A weight check was conducted to ensure homogeneity of fill volumes. The cooling process itself was initiated by moving the packed pallet into a cold storage room after filling; the pallets were positioned in the warmest part of the cold storage room to allow for a worst-case estimate of the process duration.

A total of five runs were carried out at three different storage temperatures of −20°C, −25°C and −40°C, and different duration, as outlined in Table 8.1. After process completion, manual visual inspection of the vials in the pallet was carried out for engineering run 4 and 5 at different points in time, and found no vials remaining in the liquid state at the final time. Because the effect of supercooling was initially not considered, freezing completion was not verified for runs 1 to 3. For the study at −20°C, three repetitions were carried out (i.e. runs 1,2 and 5), with varying freezing time and configuration.

Run	Temp.	Duration	Inspection	Configuration	# TC
1	−20°C	165h	not performed	A-1	5
2	−20°C	130h	not performed	A-1	5
3	−25°C	65h	not performed	A-1	5
4	−40°C	48h	all frozen	A-2	6
5	−20°C	264h	all frozen	B	12

Table 8.1 Summary of the five engineering runs performed to study the pallet freezing of the Janssen COVID-19 vaccine.

In all runs, the thermal evolution of the pallet was monitored for the entire duration of the process via thermocouples. These thermocouples were inserted at different positions in the pallet, with some of the sensors placed next to the center of the pallet, and some further away from it. Thermocouples were inserted directly into the vials. For such positioning, it is not possible to infer a nucleation temperature distribution from the temperature readouts. When thermocouples are positioned within vials, the nucleation kinetics may be affected due to the introduction of additional nucleation sites, thus rendering the observed nucleation behavior non-representative.[102] In the context of freeze-drying, non-invasive methods of temperature monitoring have been proposed recently,[209–211] which may help to overcome this issue. These monitoring instruments comprise thin film thermocouple arrays[209,210] and impedance spectroscopy[211], which both were unavailable at the time of the engineering runs.

Finally, it is worth underlining the scale of these engineering runs: The five runs that we analyze within this case study comprise about 160,000 vials in total, amounting to the equivalent of 800,000 vaccine doses. It is therefore of utmost interest not only to develop a safe and rational process design, but also to ensure that such design is identified in a small number of runs. Indeed, these five runs comprise only a subset of all engineering runs that were conducted during freezing process design.

8.3 RESULTS

We present simulation results for the freezing of a pallet comprising $40 \times 36 \times 18$ vials and compare it with engineering runs of the Janssen COVID-19 vaccine in Section 8.3.1; this analysis identified a number of complex freezing phenomena that are investigated in the following sections. To generalize our findings, we also studied the freezing of smaller systems, i.e. of single vials, of a set of $2 \times 2 \times 2$ vials, and of a box of $20 \times 12 \times 3$ vials; the corresponding studies are presented in Sections 8.5.3, 8.5.4 and 8.5.5. The packaging geometries for box and pallet resemble real-world geometries in use in the pharmaceutical industry. While the general findings are valid independent of geometry, we invite the interested readers to run simulations for arrangements of their interest via the open-source python package SNOW, as indicated in Section 8.2.1.

Unless stated otherwise, 1000 repetitions were carried out for each simulation study to accurately capture the variability of the process. Importantly, such high number of repetitions is not required for most applications, and was chosen in this work for being able to generate smooth plots of simulated distributions. For practical applications, already 16 repetitions were found to provide a sufficiently accurate estimate of the process variability. All simulations comprise vials containing 1 mL of 5 wt.% sucrose solution. The nucleation kinetics parameters used for the simulation of this solution lead to single-vial nucleation temperature distributions in the range of -5°C to -15°C. This range of temperatures is typically observed when freezing diluted aqueous solutions in laboratory freeze-dryers in non-sterile environments. A list of all simulation parameters is provided in Table 8.2.

8.3.1 Phenomenology of freezing

Within this section we study experimental data from engineering runs of the Janssen COVID-19 vaccine, and compare the thermal evolution profiles

with those from pallet freezing simulations. Figure 8.3 shows the readout of four to five thermocouples for three runs at temperatures from −20°C to −40°C. Figure 8.4 presents the simulated thermal profiles of one vial in the core (shades of green) of the pallet and one at its side (shades of red) for three repetitions of the freezing process, at storage temperatures of −8°C (8.4 (a)) and of −40°C (8.4 (b)). While the modeling framework provides the thermal evolution profiles for all 25,920 vials, we selected these two vials to present two extreme cases of particularly fast (side vial) and slow (core vial) freezing. We identify four characteristic phenomena in the experimental data, all of which were qualitatively reproduced by the simulations:

Thermal spikes: Two types of spikes are present in all profiles: First, every profile shows a single spike rising up to the equilibrium freezing temperature. For the experiments, these spikes occurred early on during the process, whereas in the simulations, more variability in terms of their time of occurrence was observed, with some spikes occurring close to the end of the process in the case of the simulation at −40°C. A second type of spikes, smaller but more frequent, was found to occur during most of the process. The number of spikes was found to increase with increasing storage temperature. We study the occurrence of these spikes in more detail in Section 8.3.2, where we reveal that the first type is connected to the nucleation event in the monitored vials, while the second type stems from nucleation events in neighboring vials.

Stationary phase: The stationary phase is where vials spend extended time at a nearly constant temperature during freezing. This is most distinct for the engineering run at −40°C (cf. Figure 8.3(c)) where the vials in the core of the pallet exhibit a stationary temperature of $T_{sp} \approx -15$°C. Similarly, the simulated profiles for vials in the core of the pallet comprise a stationary phase at $T_{sp} \approx -5$°C, nearly independent of storage temperature. In Section 8.3.3 we investigate this phenomenon, and find it to be an emerging property of freezing at pallet scale, linked to the nucleation kinetics of the formulation.

Process duration: When increasing the storage temperature from −40°C to −20°C for the engineering runs, a five-fold increase in process duration was observed. Similarly, simulations predict an increase in process duration of one order of magnitude when increasing the storage temperature from −40°C to −8°C for the studied sucrose solution. We study the process duration for systems at different scales in Section 8.3.4, and reveal that the strong increase in process duration at high storage temperatures is linked to kinetic limitations of the nucleation process. Given the great interest in obtaining estimates for the process duration, we derive and test a simplified model for its prediction in Section 8.3.5.

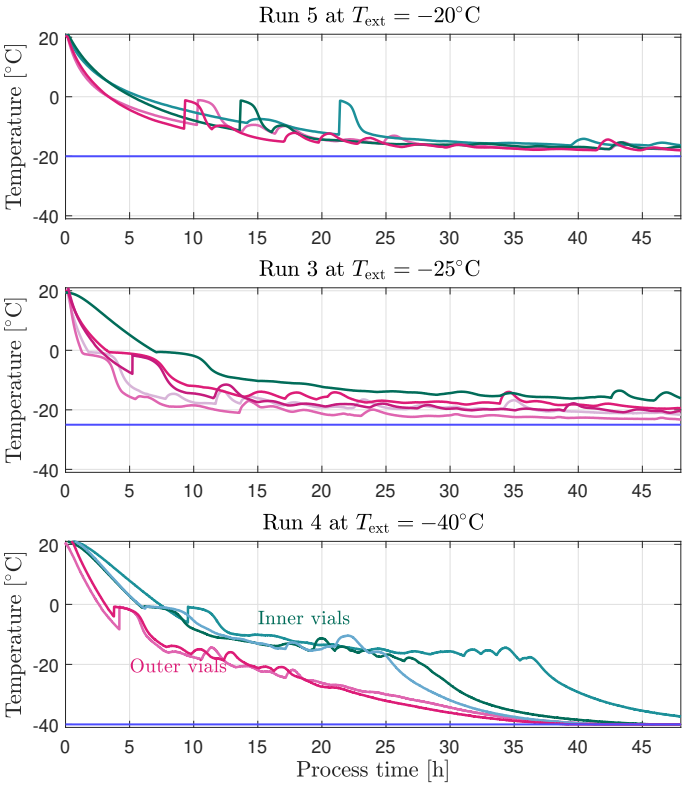

Figure 8.3 Thermal evolution for the first 48h of three engineering runs: Run 5 (−20°C), run 4 (−40°C) and run 3 (−25°C); the curves indicate the readouts of the thermocouples, while the blue lines denote the storage temperatures. Data points were recorded with a resolution of 5s. Complete freezing was only observed for run 4 within the shown time interval; complete freezing for run 5 was observed after about 200h, while run 3 was stopped after 65h without achieving complete freezing.

Variability in freezing behavior: For the engineering run at −40°C, vials close to the exterior cool down faster than their inner counterparts, and reach low temperatures already at times when core vials are still at the stationary temperature. At −20°C, all vials exhibited similar thermal evolution profiles, while for −25°C minor differences between the readouts were observed. Regarding the simulations, we find that the side vial nucleates generally earlier than the core vial and with less variability in time. We analyze variability

in freezing behavior among vials in Section 8.3.6, based not only on the thermal evolution profiles, but also on the nucleation and solidification behavior; this analysis reveals that significant variability is present at all storage temperatures, with potential impact on drug stability.

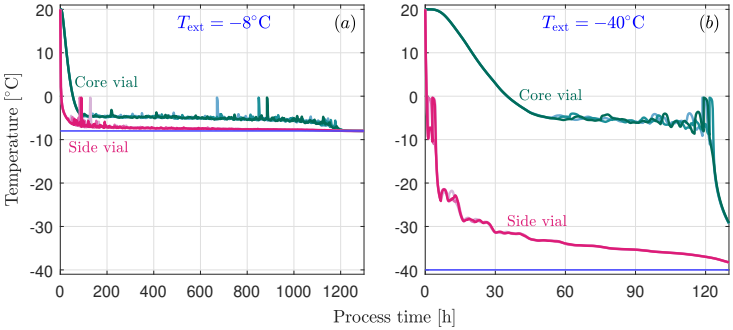

Figure 8.4 Thermal evolution for three repetitive simulations of the freezing process for the pallet with 25,920 vials. Curves for one side vial (in outermost layer, red) and one core vial (in innermost layer, green) are shown for storage temperatures of (a) −8°C and (b) −40°C. Repetitions are denoted by different shades of the used colors.

8.3.2 Thermal evolution: thermal spikes

We investigate the phenomenon of thermal spikes by simulating freezing at different scales. Figure 8.5 shows the thermal evolution of five single vials at (a) −5°C, (b) −10°C, and (c) −20°C. At −5°C, all vials remain in the liquid, supercooled state after 7h. At −10°C, all vials froze, albeit with significant variability in nucleation time. For −20°C, this variability reduced strongly. For all frozen vials, exactly one spike corresponding to a temperature rise to the equilibrium freezing temperature was observed. Even in the case of the pallet (as shown in Figures 8.3 and 8.4), one such rise was observed per vial, corresponding to its nucleation event. In the case of the experimental pallets, this rise took place early on, and at higher nucleation temperatures. This behavior indicates that the insertion of thermocouples into the vials affected the nucleation kinetics; i.e. additional nucleation sites enhanced the nucleation rate. Such behavior is commonly reported in literature with respect to pharmaceutical freeze-drying,[102] and is in line with the experimental findings from the single vial cooling studies, as reported in Section 8.2.3.

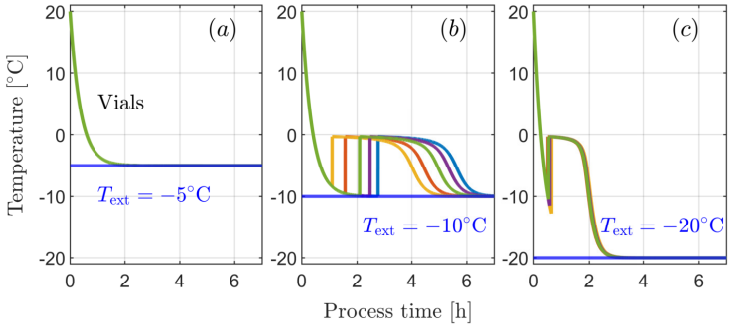

Figure 8.5 Thermal evolution of a single vial during the simulated freezing process. Five repetitions are shown for external temperatures at −5°C (a), at −10°C (b), and at −20°C (c). An initial vial temperature of 20°C is used in all simulations. Blue lines indicate the storage temperature.

A second type of spike emerges when moving towards larger systems of interacting vials. Figure 8.6 presents the thermal evolution for a system of $2 \times 2 \times 2$ vials at −10°C and at −20°C; in such system all vials are in equivalent positions. Heat transfer between neighboring vials is characterized through the thermal interaction coefficient k_{int}. We studied three values of k_{int}, resulting in thermal evolution profiles for weak (8.6(a,d)), intermediate 8.6((b,e)), and strong thermal interaction 8.6((c,f)). Thermal interaction causes additional variability in the thermal evolution, leading to the observation of spikes in the studies at −10°C (a,b,c) and to a lesser extent at −20°C in the case of intermediate and strong interaction (e,f).

To study this variability in detail, we investigate in Figure 8.6(g) the thermal evolution of one vial (green), while highlighting the nucleation events of the other vials: we find that all spikes in the thermal evolution profile are caused by nucleation events. The exothermic phase change affects neighboring vials that absorb this heat, which in turn either slows down their cooling or even heats them up temporarily. Thermal perturbations affect the thermal evolution profiles stronger at higher storage temperatures. This is in good agreement with the observations for the both the simulated and experimental pallets (cf. Figures 8.3 and 8.4), which exhibited more pronounced thermal spikes at higher temperature. Also, the effect of a nucleation event was found to become smaller with increasing distance, as can be seen explicitly in Figure 8.6(c): The thermal evolution of the direct neighbors (indicated in red) is more affected by the nucleation event of the *green* vial compared to the next nearest neighbors (magenta); the vial at the opposite side of the system (blue) is barely affected

at all. This is of practical importance, because it highlights that the number of neighboring nucleation events that can be observed may be limited to a few layers beyond the point of measurement. The detection of all nucleation events in a pallet would therefore require a large number of thermocouples. These findings confirm that thermal interaction is the responsible mechanism for the formation of the second type of spikes. A detailed analysis on how the nucleation and solidification behavior is affected by different levels of thermal interaction is provided in Section 8.5.4.

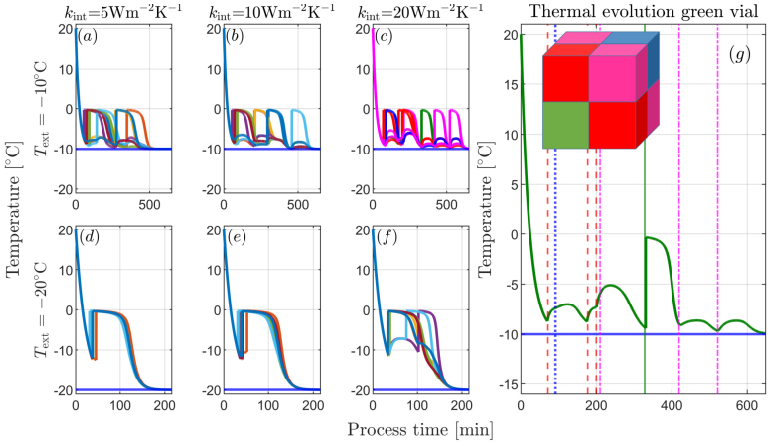

Figure 8.6 (a-f): Thermal evolution of all eight vials in the $(2 \times 2 \times 2)$ system for one simulation of the freezing process each at a storage temperature of -10°C (a,b,c) and of -20°C (d,e,f). External heat transfer for all studies is characterized by $k_{ext} = 10$ Wm^{-2}K^{-1}. Internal heat transfer is $k_{int} = 5$ Wm^{-2}K^{-1} for (a,d), $k_{int} = 10$ Wm^{-2}K^{-1} for (b,e) and $k_{int} = 20$ Wm^{-2}K^{-1} for (c,f). (g): Thermal evolution for one vial in study (c), with nucleation events of other vials indicated. Red dashed lines - nearest neighbors, magenta dash-dotted lines - next nearest neighbors, blue dotted line - most distant vial. The same color coding is applied in figure (c).

8.3.3 Thermal evolution: stationary phase

In the context of freezing, a change in temperature may be induced by either removal of heat due to external cooling, i.e. ΔQ_c, or by the latent heat released upon ice formation, ΔQ_{gen}. A stationary temperature within the pallet thus indicates that the two terms are in balance with each other. To formulate analytical expressions for these terms, we consider two simplifications: (1) All vials in the pallet exhibit the same stationary temperature T_{sp}, until freezing is

completed. (2) Heat transfer of the pallet with the exterior is characterized by a single, lumped coefficient K_c. For a time interval Δt, ΔQ_c is then given as:

$$\Delta Q_c = A_{pt} K_c (T_{sp} - T_{ext}) \Delta t \tag{8.16}$$

where A_{pt} is the outer surface area of the pallet. ΔQ_{gen} is linked to the number of nucleating vials. Since nucleation induces solidification within an entire vial, it implicitly generates heat on the order of $m_w \lambda_w$. The probability for a vial to nucleate was derived in Eqn. 8.15 as $JV\Delta t$; for a pallet comprising n_v vials at temperature T_{sp}, the expected number of nucleation events becomes $n_v JV\Delta t$. ΔQ_{gen} thus is:

$$\Delta Q_{gen} = (m_w \lambda_w)(n_v JV\Delta t) \tag{8.17}$$

To understand how ΔQ_{gen} and thus the stationary phase depend on nucleation, we introduce a second set of *slow* kinetic parameters, for which vials nucleate at lower temperatures, in line with values observed in vial freeze-drying under GMP conditions.[41,102,169] We also study the limiting case of *instantaneous* nucleation, where ice is formed as soon as the vial reaches the equilibrium freezing temperature. Figure 8.7(a) illustrates the values for five heat flows as function of the stationary pallet temperature T_{sp}: heat removed by external cooling at storage temperatures of -8°C and of -40°C, and heat generated subject to (our standard) *fast* and newly introduced *slow* and *instantaneous* kinetics. A total of six stable states are identified; for the "fast" kinetics, the heats balance at temperatures of about -5.5°C for $T_{ext} = -40$°C and of -4.5°C for $T_{ext} = -8$°C. With respect to the *slow* kinetics, this value shifted to -13°C for $T_{ext} = -40$°C. For -8°C, the stable state corresponds to a system which does practically not transfer any heat; this indicates that the vials will stay very long in the supercooled, liquid state before they eventually nucleate. For the *instantaneous* kinetics, the stationary phase by nature is confined to the equilibrium freezing temperature.

Figure 8.7(b) shows the thermal evolution for a core vial subject to the three sets of parameters at $T_{ext} = -40$°C. A stationary phase is observed in all cases and the values of T_{sp} indeed correspond to those predicted; since no supercooling occurs in the case of instantaneous nucleation, no thermal spikes are observed in the corresponding profiles either. For comparison, Figure 8.7(c) presents the profiles for $T_{ext} = -8$°C; as expected, the thermal evolution for the *slow* kinetics confirms that the core vials spend the entire simulated process duration in the supercooled liquid. When comparing the process duration for *fast* and *instantaneous* kinetics, one notices that the predicted values are qualitatively similar for $T_{ext} = -40$°C, but differ by about a factor of three for $T_{ext} = -8$°C. This clearly demonstrates the important role of stochastic nucleation on process duration, manifested for pallet freezing in the form of

the stationary phase. We thus study the behavior of the process duration in more detail in Section 8.3.4.

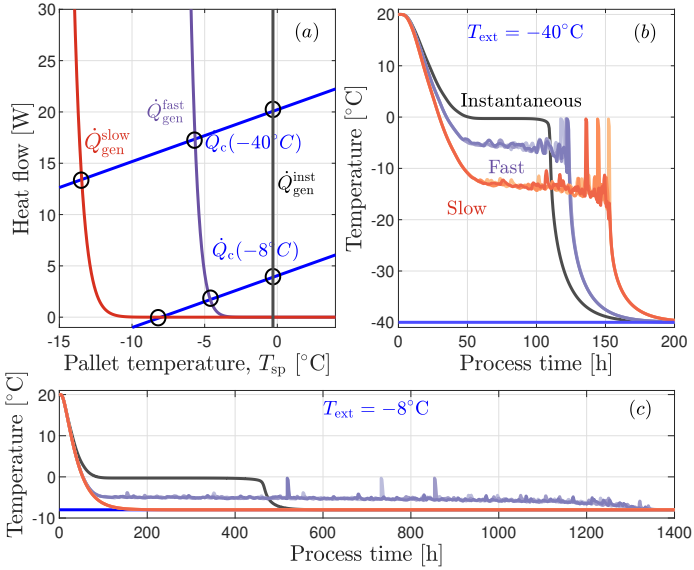

Figure 8.7 (a) Heat flows $\dot{Q} = \Delta Q/\Delta t$ for external cooling (blue, for storage temperatures of −8°C and −40°C) and ice crystal formation (orange, subject to *fast* and *slow* nucleation kinetics). A value of K_c = 0.90 $Wm^{-2}K^{-1}$ was used, based on the procedure outlined in section 8.3.5. (b) Thermal evolution for three repetitions of the freezing process for the pallet with 25,920 vials. Curves for the same core vial are shown at a storage temperature of −40°C for three sets of nucleation kinetics. The corresponding median complete nucleation times were found to be 153h (*slow*) and 122h (*fast*). (c) Complementary figure to (b), generated for a storage temperature of −8°C. Note that the freezing process for the *slow* kinetics is not completed at the end of the simulation.

These findings confirm that the stationary phase stems from a balance of external cooling and heat generated by ice formation. The stochastic nature of nucleation implies that the pallet does not assume a constant temperature T_{sp}, but that the temperature oscillates around T_{sp}, since nucleation events release a considerable amount of heat in short time into their neighborhood. Each nucleation event leads to a local rise in temperature, and thus reduces the likelihood of nearby nucleation events, until solidification is mostly complete and the temperature decreases again. The establishment of such balance requires

a certain minimum number of vials, which explains why the stationary phase was observed for neither the single vial nor the system of $2 \times 2 \times 2$ vials.

8.3.4 Process duration and freezing regimes

The relationship between process duration and storage temperature is of great practical interest, since it has to be well-understood in order to identify suitable freezing conditions. Regarding stability, having vials remain in the liquid state at the end of freezing was considered a relevant type of batch heterogeneity that should be avoided if possible. An inspection of all vials in densely packed pallets is undesirable due to the sheer number of vials involved.

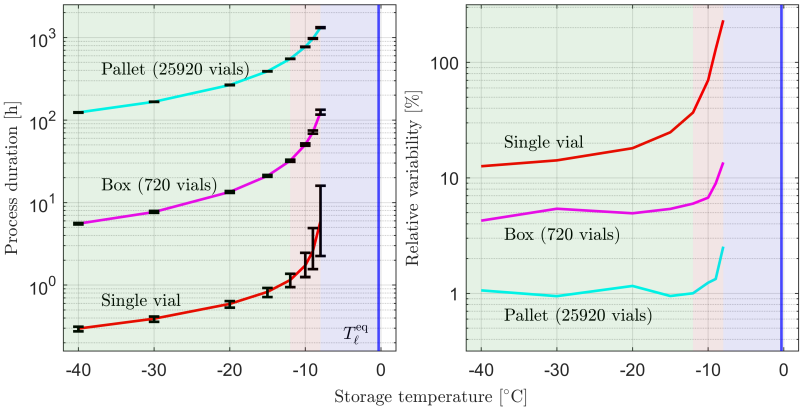

Figure 8.8 Left: Process duration for the single vial (red), the box with 720 vials (magenta) and the pallet with 25,920 vials (cyan) subject to the *fast* nucleation kinetics. The lines indicate the median of the distribution of the complete nucleation time, while the error bars denote the 10% and 90% quantiles. 80,000 repetitions of the freezing process were simulated for the single vial, 1,000 repetitions for the box and all pallet simulations up to −12°C. For pallet simulations at −10°C and at higher temperatures, 128 repetitions were simulated. Right: Relative variability in process duration for the same studies, measured as difference among the 90% and 10% quantiles divided by the median value. The shaded regions in both figures indicate the boundaries of the three regimes: Cooling-limited (green), nucleation-limited (red), metastable (blue).

To this end, we simulated the freezing process at different scales, subject to storage temperatures of −8°C to −40°C, as shown in Figure 8.8. Due to the stochasticity of nucleation, the process duration varies among repetitive

simulations, whereby Figure 8.8(a) shows the median duration, while Figure 8.8(b) illustrates the relative variability. Based on the model predictions, we identified three distinct *freezing regimes* dependent on storage temperatures, but independent of scale. Their boundaries are governed by the nucleation kinetics, as our discussion in Section 8.3.3 illustrates. Importantly, we recognize that the *emergence* of these three regimes is a direct consequence of nucleation itself and therefore scale-independent. The three regimes are defined as follows:

1. A **metastable regime** (-8°C to T_ℓ^{eq}, blue), in which nucleation does not take place in a reasonable timescale (weeks or shorter). The reason is that the supercooling is not sufficient to overcome the energy barrier required to form a primary ice nucleus. Freezing therefore has to be carried out at lower temperatures.
2. A **nucleation-limited regime** (-8°C to -12°C, red), in which a highly non-linear increase in nucleation times with increasing storage temperature is observed. The duration of the process is affected by the kinetics of nucleation which are slow compared to the capacity of the system to remove heat.
3. A **cooling-limited regime** (below -12°C, green), in which nucleation for a single vial predominantly occurs during the initial cooling phase from the initial temperature towards the storage temperature. Thus, the regime is connected with short process times and low variability.

A decision on suitable process temperatures requires knowledge on these regimes, and thus the nucleation kinetics of a formulation. This implies that lab-scale work should be carried out with vials that are filled under realistic, GMP conditions. To ensure short process duration, one may operate the process in the cooling-limited regime at temperatures as low as practically feasible. However, the choice of the storage temperature is not trivial and may need to consider factors beyond process duration, such as freezer availability. Additional constraints may be related to nucleation temperatures and solidification times, as both quantities may be linked to stability and depend on storage temperature, as discussed in Section 8.3.6.

Figure 8.8(b) indicates that the variability in process duration increases with storage temperatures, especially in the nucleation-limited regime, and decreases with scale. Such behavior results from the fact that the variability is governed by the nucleation behavior of the last-nucleating vial. Its stochasticity results only in small variations in nucleation time at low storage temperatures (cf. Figure 8.5), and is overall less relevant at larger scales with overall longer process durations.

In addition to the choice of storage temperature, the model predicts the effect of the packaging configuration on process duration. For example, Figure 8.8(a) shows that, because of the more favorable surface to volume ratio, the freezing of a box is about one order of magnitude faster than that of a pallet. Thus, for the same storage temperature faster processes can be achieved by freezing a larger number of individual boxes in parallel.

8.3.5 Simplified model of pallet freezing

Practitioners typically desire guidelines and approximations that are easy to implement into development procedures, motivating us to introduce a simplified approach to estimate the process duration for pallet freezing, Δt_{pt}. Based on Eqns. 8.16 and 8.17 in Section 8.3.3, we formulate the total heat transferred during the freezing process, ΔQ^{pt}:

$$\Delta Q^{\mathrm{pt}}_{\mathrm{gen}} = n_{\mathrm{v}} m_{\mathrm{w}} \lambda_{\mathrm{w}} \tag{8.18}$$

$$\Delta Q^{\mathrm{pt}}_{\mathrm{c}} = A_{\mathrm{pt}} K_{\mathrm{c}} (T_{\mathrm{sp}} - T_{\mathrm{ext}}) \Delta t_{\mathrm{pt}} \tag{8.19}$$

Since the generated heat $\Delta Q^{\mathrm{pt}}_{\mathrm{gen}}$ equals the removed heat $\Delta Q^{\mathrm{pt}}_{\mathrm{c}}$, the process duration reads

$$\Delta t_{\mathrm{pt}} = \frac{n_{\mathrm{v}} m_{\mathrm{w}} \lambda_{\mathrm{w}}}{A_{\mathrm{pt}} K_{\mathrm{c}} (T_{\mathrm{sp}} - T_{\mathrm{ext}})} \tag{8.20}$$

Given that T_{sp} is tied to the nucleation behavior of the formulation, it may be determined either by simulations using known nucleation kinetics or inferred directly from thermal evolution profiles of engineering runs. K_{c}, the lumped system-scale heat transfer coefficient, remains the only hitherto unknown quantity. It may be computed from the remaining quantities, either from experiments or simulations. We computed K_{c} for the simulated pallet (T_{sp} assumed to be -4.5°C for all T_{ext}) at storage temperatures of -40°C (K_{c} = 0.93 $\mathrm{Wm^{-2}K^{-1}}$) and -8°C (K_{c} = 0.88 $\mathrm{Wm^{-2}K^{-1}}$): a nearly temperature-independent value of K_{c} implies that the simplified model may be useful to estimate the process duration at a broad range of temperatures. In practice, one may conduct one engineering run or pallet simulation at one storage temperature to obtain the value of K_{c}, and use this value to predict the process duration at different storage temperatures.

Process duration is governed not only by the storage temperature, but also by the nucleation kinetics. We may apply the model to compute the

relative change in process duration with nucleation kinetics and with storage temperature directly, i.e. without estimating K_c, via

$$\frac{\Delta t_{pt}^{(a)}}{\Delta t_{pt}^{(b)}} = \frac{T_{sp}^{(b)} - T_{ext}^{(b)}}{T_{sp}^{(a)} - T_{ext}^{(a)}} \tag{8.21}$$

for two arbitrary systems "(a)" and "(b)" with the corresponding temperatures. Figure 8.7(b) in Section 8.3.3 shows a 25% increase in process duration for the slower set of nucleation kinetics compared to the "fast" one for $T_{ext} = -40°C$. For the same system, Eqn. 8.21 predicted a similar increase of 31%.

We further tested the simplified model with the experimental data presented in section 8.3.1. We use the data from run 4 (duration of about 40h at $-40°C$ and $T_{sp} = -15°C$) to predict the duration at higher storage temperature. Eqn. 8.21 predicts a five-fold increase in process duration when increasing the storage temperature to $-20°C$, in agreement with the experimentally observed trend (duration of about 200h at $-20°C$). It also correctly predicts incomplete freezing for run 3 at $-25°C$. We thus confirm that the simplified model may be a useful practical tool to predict the effect of both storage temperature and nucleation kinetics on process duration.

8.3.6 Variability and control of freezing

The control of the freezing outcome and the characterization of its variability represents a major aspect of process design. For a system of pallet size, the effect of vial position within the batch has to be studied in detail, since we observed differences in thermal evolution among core and side vials in both simulations and experiments (cf. Figures 8.3 and 8.4). To achieve a system-scale understanding of the process, we report the temperature of all vials within vertical layers of the pallet at a few points in time in the form of heatmap snapshots.

Figure 8.9 shows the temperature distribution for the pallet at three points in time, selected based on the fraction of nucleated vials, for a storage temperature of $-40°C$; Figures 8.19 and 8.20 in the supplementary information showcase the process at storage temperatures of $-20°C$ and $-8°C$. We notice both a layer-wise progression of freezing at low storage temperatures and a stationary temperature for vials in the core, whereby the spatial extent of this stationary region shrinks with time. Furthermore, we identify individual vials at higher temperatures than their neighbors: they correspond to vials that are solidifying at the corresponding point in time.

The pronounced position-dependency of freezing necessitates a more detailed investigation based on the characteristic quantities, i.e. the nucleation

time, the nucleation temperature, and the solidification time. To do so, we define position-dependent populations of vials with different distance to the side of the pallet. The simulated pallet comprises 18 vertical layers, which may be categorized into nine populations based on their location along the vertical axis. The outermost population, referred to as layer 1, comprises vials in the top-most and bottom-most layers, which exhibit the same thermal environment. To exclude edge and corner effects (which are studied in detail in Section 8.5.5 in the supplementary information), only the 36 vials in the center of each layer are included in the populations. The relevant subset of vials is contained in a rectangle, as visualized for layers 1, 5 and 9 in the left column of Figure 8.9.

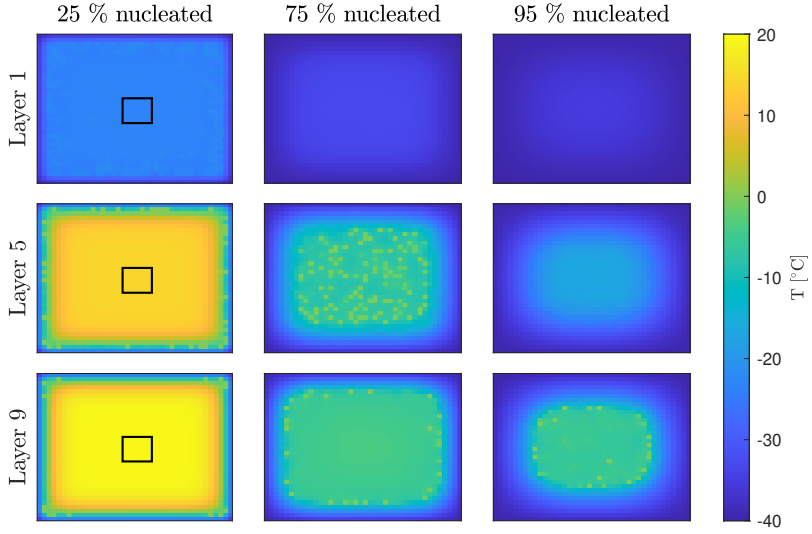

Figure 8.9 Thermal evolution for all vials in three of the 18 vertical layers at three selected points in time, identified based on the fraction of nucleated vials in the pallet, for a storage temperature of -40°C. Layer 1 indicates the top layer of the pallet, which is in direct contact with the exterior. Layer 9 denotes the central, innermost layer in the core of the pallet. Each tile corresponds to a vial. The black rectangle in the left column indicates the position of the vials that are included into the populations shown in Figure 8.10.

Figure 8.10(a) illustrates the distribution of nucleation times for the three studied layers. As anticipated, vials nucleated earlier, the closer they were

to the exterior. For high storage temperatures, the nucleation times for the individual positions strongly overlap with each other, indicating that at any given time vials in several layers are nucleating and solidifying. Under colder conditions, less overlap was observed, indicating a layer-wise freezing process from the outside to the core. Independent of storage temperature, the innermost layer 9 exhibited the broadest distribution of nucleation times. We attribute this behavior to the formation of the stationary phase, which comprises most of the process duration, and during which nucleation events may occur.

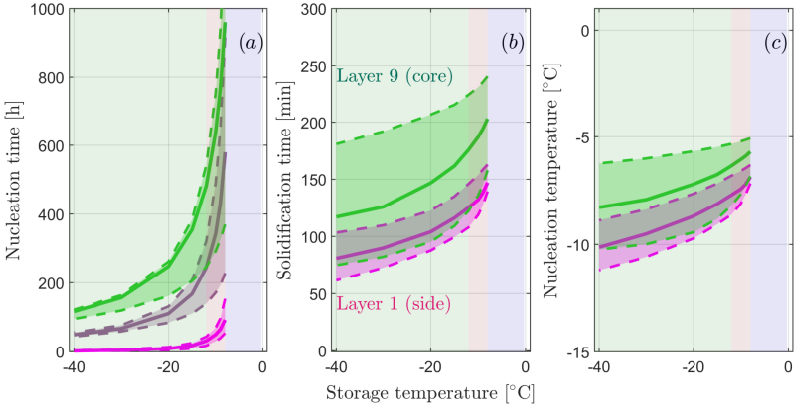

Figure 8.10 Dependency of the three characteristic quantities on storage temperature. (a) Nucleation time, shown for vials in layers 1 (pink), 5 (grey) and 9 (green). (b) Solidification time, shown for vials in layers 1 and 9. (c) Nucleation temperatures, shown for vials in layers 1 and 9. The solid lines indicate the median value of the characteristic quantity, while the dotted lines denote the 10% and 90% quantiles of the distribution. The shaded regions in the background correspond to the freezing regimes discussed in Section 8.3.4.

Figure 8.10(b) shows the distribution of solidification times. The median solidification time increased by about 75% at all positions when increasing T_{ext} from -40°C to -8°C. This is in contrast to the solidification behavior of the single vial, where the solidification time scales with the difference between storage temperature and equilibrium freezing temperature, as discussed in Section 8.5.3. For the pallet, we attribute the reduced dependency of solidification times on storage temperature in comparison to nucleation times to the thermal interaction with the neighboring vials, which governs the local heat transfer.

Independent of storage temperature, vials solidify slower with increasing distance from the exterior. For example, the median solidification times of the innermost layer 9 were about 40% higher than those of layer 1. In addition to variability due to a vial's position, we observe variability among vials in the same position. Within layer 9, vials at the 10% quantile of the distribution exhibit 40% (at $T_{ext} = -8°C$) to 60% (at $T_{ext} = -40°C$) shorter solidification times than those at the 90% quantile. Furthermore, the variability within layer 9 is more pronounced than the one within layer 1. A more detailed characterization of the position-dependent freezing behavior is provided in Section 8.5.6, which revealed that the large variability within layer 9 stems from the more pronounced variability in nucleation times and the connected change in thermal environment over time. Vials that nucleated later in time, were found to exhibit shorter solidification times, since most of their neighbors were already completely frozen; the heat of ice formation is absorbed faster by the neighborhood, thus accelerating solidification.

Finally, we discuss the distributions of nucleation temperatures, illustrated in Figure 8.10(c). The median nucleation temperatures increased with increasing storage temperatures. However, the extent of this effect is limited compared to the other two quantities, since the range of feasible nucleation temperatures is governed by the nucleation kinetics. On the one hand, nucleation cannot occur at too high temperatures, because of the low nucleation rate. On the other hand, very low nucleation temperatures are unlikely to ever be reached. With respect to position-dependency, the same trends are observed as for the solidification times, and for the same reasons.

To summarize, we find that pallet freezing naturally results in strong batch heterogeneity in all three characteristic quantities due to spatial differences in heat transfer, thermal interaction among vials and the inherent stochasticity of ice nucleation. We observed a position-dependency and intra-layer variability among vials independent of storage temperature in both the thermal evolution profiles, and in nucleation and solidification behavior. Furthermore, only limited control over the median values and the variability of solidification times and of nucleation temperatures can be exerted by the choice of the storage temperature, in comparison to nucleation times. Thus, in case a drug product requires a tight control over solidification times or nucleation temperatures, additional process variables have to be investigated, such as different packaging configurations and scenarios involving faster heat transfer.

8.4 CONCLUDING REMARKS

We have presented a modeling framework for the simulation of freezing processes involving an arbitrary number of densely packed vials up to pallet scale. Instantiations of this model qualitatively predict all experimental trends observed in the engineering run data of the Janssen COVID-19 vaccine. The findings imply that stochastic ice nucleation is an essential aspect of the freezing process and that a mechanistic description of it is required in order to fully understand, and eventually optimize, the process.

We applied the model to characterize the observed trends in detail, revealing that thermal spikes occur due to the release of latent heat induced by nucleation events both in the monitored vials and in their neighborhood. The emergence of a *stationary phase* was explained by the interplay between the heat generated by ice formation, governed by nucleation, and the heat removed via external cooling. The model also confirmed the position-dependency of the thermal evolution, where vials freeze in average later the closer they are to the core of the pallet. In addition, it revealed a yet unknown, but potentially relevant batch heterogeneity among vials in equivalent positions that could not be inferred from the thermal monitoring; this variability results from the interplay of stochastic nucleation and thermal interaction among vials. Since it may affect the stability of the frozen drug product, it should be considered in drug development and in freezing process design: the model provides information on the variability in the nucleation and solidification behavior among vials, and thus may inform the stability analysis to ensure that quality requirements are met for the entire range of predicted values.

The main application for the presented model lies in the quantification of the process duration for a wide range of freezing settings in industry. We revealed that freezing in vials may occur in three regimes, the boundaries of which depend on the nucleation kinetics of the formulation. Knowledge of the kinetics thus is required to predict the process duration and to choose suitable packaging configurations and storage temperatures. Given that typical freezers in industry operate between -20°C and -40°C, while nucleation temperatures of lower than -20°C are commonly reported in literature, stochastic ice nucleation indeed governs the process behavior under practically relevant process conditions.

Since process design currently is carried out experimentally without considering ice nucleation, this work aims to provide professionals in industry and academia with the means to conduct a more rational, model-informed process design. For this reason, we provide open access to the model and the source files in the form of a python package.[73] To provide practitioners with a simple rule-of-thumb, we further developed a simplified version of the model,

for which all model parameters can be inferred from a single engineering run at low temperature.

Finally, we understand this work as starting point towards rational process design of pallet freezing. The use of the model as *digital twin* in a quantitative manner is planned for the future, paving the path towards fully optimized processes with respect to process duration and batch heterogeneity.

8.5 SUPPLEMENTARY INFORMATION

8.5.1 Pallet packaging geometries

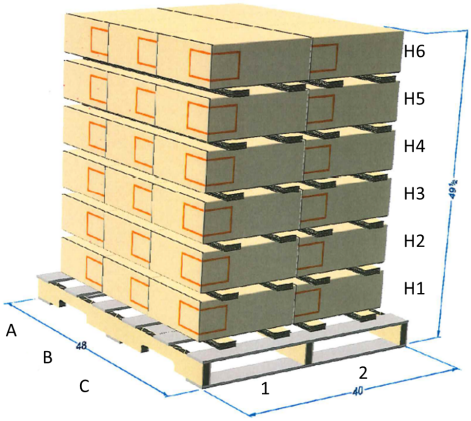

Figure 8.11 Packaging configuration A-1, as used in engineering runs 1-3.

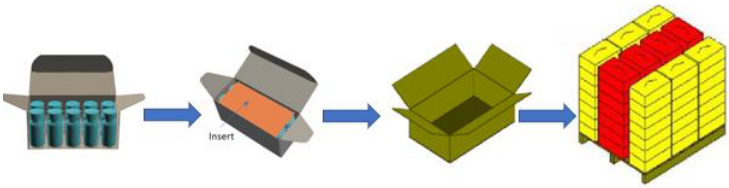

Figure 8.12 Packaging configuration B, as used in engineering run 5.

8.5.2 List of simulation parameters

Quantity	Abbreviation	Unit	Value
Vial volume	V	m^3	10^{-6}
Vial surface area	A	m^2	10^{-4}
Mass of formulation	m_v	kg	0.001
Solute mass fraction	w_0	%	5
Heat capacity water	$c_{p,w}$	$J\,K^{-1}kg^{-1}$	4187
Heat capacity ice	$c_{p,i}$	$J\,K^{-1}kg^{-1}$	2108
Heat capacity sucrose	$c_{p,s}$	$J\,K^{-1}kg^{-1}$	1240
Molar mass sucrose	M_s	$kg\,mol^{-1}$	0.3423
Cryoscopic constant water	k_f	$K\,kg\,mol^{-1}$	1.853
Heat of fusion water	λ_w	$J\,kg^{-1}$	333550
Melting point water	T_0^{eq}	°C	0
Initial vial temperature	T_0	°C	20
Nucleation parameter 1 (fast)	b	-	12
Nucleation parameter 2 (fast)	k_b	$m^{-3}s^{-1}K^{-b}$	10^{-9}
Nucleation parameter 1 (slow)	b	-	23
Nucleation parameter 2 (slow)	k_b	$m^{-3}s^{-1}K^{-b}$	10^{-26}
Batch size pallet	$M \times N \times P$	-	$40 \times 36 \times 18$
Batch size box	$M \times N \times P$	-	$20 \times 12 \times 3$
Time step	dt	s	5
Vial to vial HT coefficient	k_{int}	$\frac{W}{m^2K}$	5-20
Vial to exterior HT coefficient	k_{ext}	$\frac{W}{m^2K}$	10

Table 8.2 List of model parameters that were used in the simulations presented in this work.

8.5.3 Supplementary simulations: isolated vials

The stochasticity in the time of nucleation results in variability in all three characteristic quantities, as shown in Figure 8.13 that presents the simulated distributions for four values of the storage temperature, i.e., −8°C, −10°C, −20°C and −40°C. For all three quantities, the distributions were found to be highly sensitive with respect to the storage temperature. The distributions of nucleation temperatures (panel (b)) generally shift towards lower values for lower storage temperatures. Between −20°C and −40°C, only a minor

shift in nucleation temperatures is observed, while the distribution appears highly sensitive to the storage temperature in the range of −8°C and −10°C. The reason for this lies in the temperature-dependency of the nucleation rate. Nucleation events become rarer with increasing vial temperature, which explains the strongly increasing nucleation times in Figure 8.13 (a). Since the temperature-dependency of nucleation is highly non-linear, nearly no nucleation events are observed above a certain temperature, while faster rates are observed for lower storage temperatures. Thus, for low storage temperatures, most nucleation events take place early in the process during the initial cooling towards the storage temperature. For −10°C and −8°C, however, most nucleation events occur after vials have reached the vicinity of the storage temperature, thus explaining why the distribution in Figure 8.13 (b) narrows down in these cases. Such behavior may be inferred from Figure 8.5 (b-c) as well, that clearly shows that for a storage temperature of −10°C some vials nucleate after reaching the storage temperature, while all vials nucleate during the initial cooling in the case of −20°C.

Given that freezing occurs at constant storage temperature, the stochasticity of nucleation only leads to a variability in the initial mass of ice formed upon nucleation; thus only little variability in solidification times is observed for single vials, as implied by Figure 8.13 (c). This initial amount only accounts for about 10% to 20% of the total ice, as can be seen e.g. in Figure 8.1(b) in the main body of this work. The remaining water is frozen after nucleation in a deterministic manner, at a rate that is governed solely by the storage temperature. Solidification times, therefore, decrease nearly inversely proportional with decreasing the storage temperature with respect to the equilibrium freezing temperature.

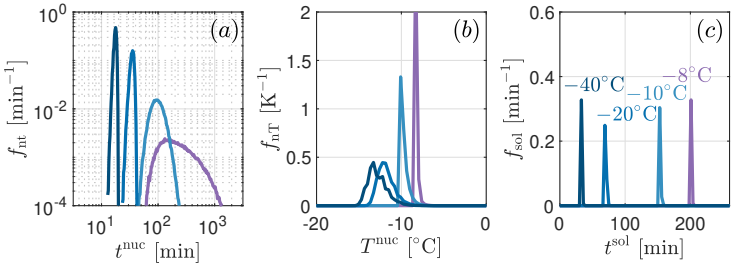

Figure 8.13 Distributions of (a) nucleation times, of (b) nucleation temperatures, and of (c) solidification times, for four storage temperatures each. 80,000 repetitions of the process were simulated per storage temperature. The scale of the nucleation time distribution is logarithmic to account for the strong effect of the external temperature on this quantity.

8.5.4 Supplementary simulations: interacting vials

When moving from the single vial towards larger systems, thermal interaction among vials becomes a relevant mechanism of heat transfer. To understand how the freezing behavior is affected by such interaction, we have conducted a sensitivity analysis considering a system of $2 \times 2 \times 2$ vials and various values of the thermal interaction coefficient k_{int} while keeping $k_{\text{ext}} = 10\ \text{Wm}^{-2}\text{K}^{-1}$. We have chosen a batch geometry of $2 \times 2 \times 2$ vials, because all eight vials are in equivalent position, with three sides facing other vials and the remaining three interacting with the exterior. This enables the study of thermal interaction without the effect of position-dependency, which will further enhance batch heterogeneity in larger systems. We investigate a total of six settings, namely two storage temperatures of -10°C (nucleation-limited regime) and of -20°C (cooling-limited regime) with three values of k_{int} each ($5\text{Wm}^{-2}\text{K}^{-1}$, $10\ \text{Wm}^{-2}\text{K}^{-1}$, $20\ \text{Wm}^{-2}\text{K}^{-1}$).

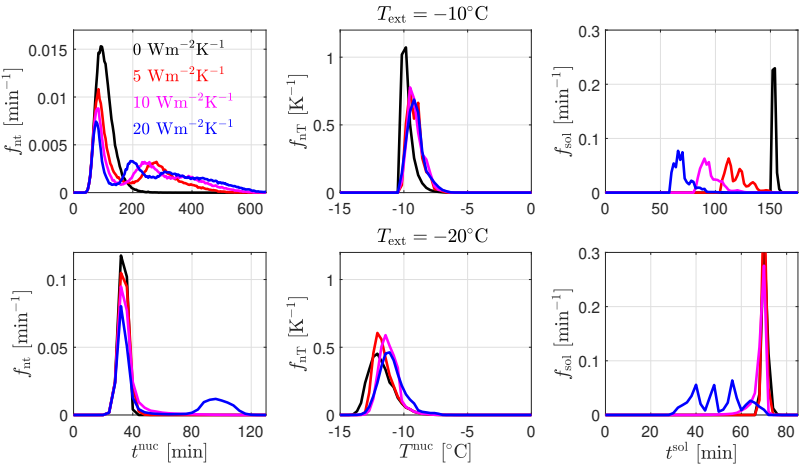

Figure 8.14 Characteristic distributions for the system with $2 \times 2 \times 2$ vials for external temperatures of -10°C (top) and -20°C (bottom) for varying values of the interaction coefficient k_{int}.

Figure 8.14 illustrates the various characteristic distributions for all studied cases. Thermal interaction leads to a decrease in solidification times due to the heat exchange with neighboring vials: Vials solidify faster, the stronger they thermally interact with their neighbors. On the other hand, the variability in nucleation times becomes more pronounced: while the time of the first

nucleation event is not affected by thermal interaction, subsequent nucleation events are increasingly delayed in time with increasing interaction. This is especially true in the nucleation-limited regime, i.e. at -10°C: Here, the heat received from the early nucleating vials may heat up the neighboring vials towards the metastable regime, basically preventing nucleation events until complete solidification of the early nucleating vials. Nucleation temperatures, finally are affected to a smaller extent than the two other quantities, with values being slightly increased compared to the single vial system. This increase again is a consequence of the vials spending more time in the metastable, supercooled state due to heat received from their neighbors.

8.5.5 Supplementary simulations: box of vials

Within this section, we present the model predictions for the freezing of a box comprising $20 \times 12 \times 3$ vials. The additional complexity compared to the $2 \times 2 \times 2$ system lies in the position-dependency of freezing.

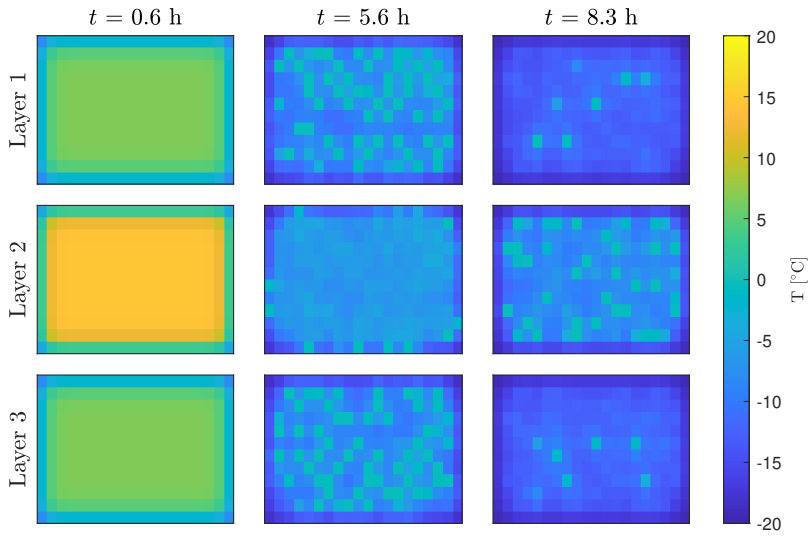

Figure 8.15 Thermal evolution for all vials at three selected points in time, selected based on the fraction of nucleated vials, for a storage temperature of -20°C. Each tile denotes a vial.

For a system of this size, it is not helpful to plot the thermal evolution of all vials when aiming at understanding the process. Instead, we prefer to show the temperature of all vials at a few points in time in the form of heatmap snapshots to achieve a system-scale understanding of the process. Figure 8.15 illustrates such evolution for three points in time and a storage temperature of −20°C. Figure 8.15 shows that corner and edge vials cool down and nucleate faster than their inner counterparts; bright spots indicate vials that are solidifying at the specific time shown in the figure. Vials in the central layer nucleate later than those in the top and bottom layers. It is noteworthy that with this type of representation, thermal interaction can be studied in a direct manner; one indeed observes that some vials are *hot spots* in the system and heat up their neighbors.

A more comprehensive analysis of the position-dependency in freezing is carried out by generating distributions of the characteristic quantities for position-specific populations of vials. Figure 8.16 shows the distributions of nucleation times, nucleation temperatures, and of solidification times for four populations of vials at a storage temperature of −20°C. The populations are defined based on the number of sides that face the exterior. Corner vials have three such sides, edge vials have two, side vials have one, and core vials have none. For this study at −20°C, we observe a strong position-dependency for all three distributions. On average, vials nucleate later the less contact they have with the environment, in line with the observations made for the thermal evolution. Solidification was found to be faster the closer a vial was to the environment, although side vials (one side in contact with exterior) and core vials (no contact with exterior) experienced similar solidification times.

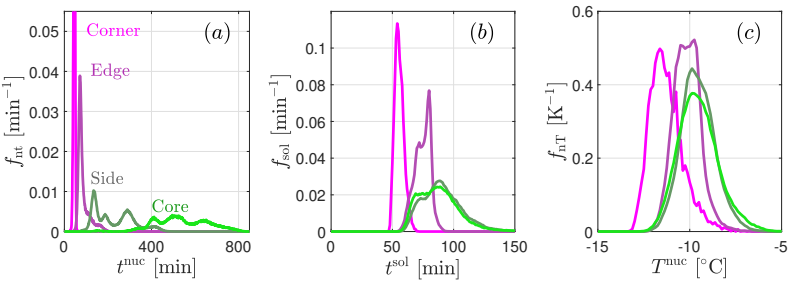

Figure 8.16 Distributions of the three characteristic quantities for the freezing process of the box ($20 \times 12 \times 3$ vials) at an external temperature of −20°C. The color-coding indicates the position of the vials in the box, ranging from corner vials in pink to core vials in green.

Figure 8.16 also demonstrates the limitations of visualizing the distributions as probability density functions; since the four populations contain different numbers of vials, the level of noise differs as well. The effect is particularly pronounced for corner vials, of which only eight exist. We therefore opt for a different visualization, i.e. the cumulative distribution, when assessing the impact of the external temperature on the freezing behavior.

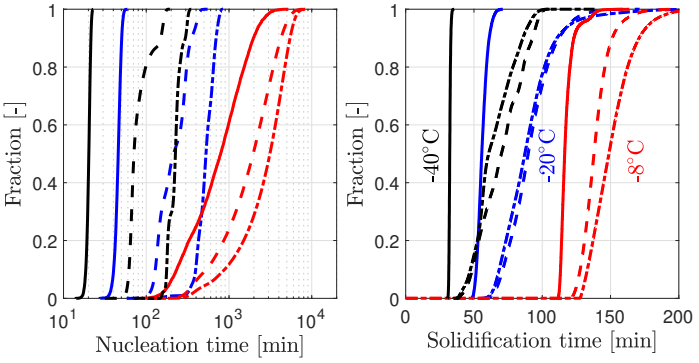

Figure 8.17 Cumulative distributions of nucleation times and of solidification times. The color coding indicates the storage temperature, the line style the population: Full lines refer to corner vials, dashed lines to side vials and dash-dotted lines to core vials. Edge vials were excluded for the sake of clarity; their behavior generally was found to be between corner and side vials.

Figure 8.17 shows these cumulative distributions for the nucleation and solidification times. As expected, both increase with increasing storage temperature. For the nucleation times, this increase occurs over several orders of magnitude and we also find that the broadness of the distributions increases with temperature; for -8°C, the distributions span more than one order of magnitude in time, while only little variability is observed at -40°C due to the more pronounced cooling. At -40°C, freezing occurs sequentially from the outside towards the core and the individual populations do not overlap; this is a direct consequence of operating in the cooling-limited regime. On the other hand, at -8°C, freezing takes place in the nucleation limited-regime, and significant overlap between the populations is observed.

These findings for the temperature-dependency of the nucleation times cannot be translated directly to the solidification times. While we again observe an increase in time with increasing temperature, this increase appears to scale linearly with the temperature difference between the equilibrium freezing

temperature of the solution and the storage temperature. For example, the median solidification time for corner vials was found to increase from 32.7 min at −40°C to 58.2 min at −20°C and 138.4 min at −8°C. With respect to variability, no clear trend could be found for its dependency on temperature. While the distributions for corner and edge vials appear narrow at all temperatures, significant variability for side and core vials was found independent of temperature. We also note that while side and core vials solidify at similar times at −20°C, side vials solidified faster at −8°C: at such high temperature the capability of the neighboring vials to receive heat is limited. The opposite was found for −40°C; here, core vials solidified faster than side vials and they do so as a consequence of the enhanced position-dependency: At the time, when the side vials solidify, the core vials are still at relatively high temperature in the liquid state and unable to receive the heat of nucleation of the side vials. However, when the core vials solidify, the remaining system already is completely frozen and thus capable to receive heat, leading to faster solidification.

8.5.6 Supplementary simulations: pallet of vials

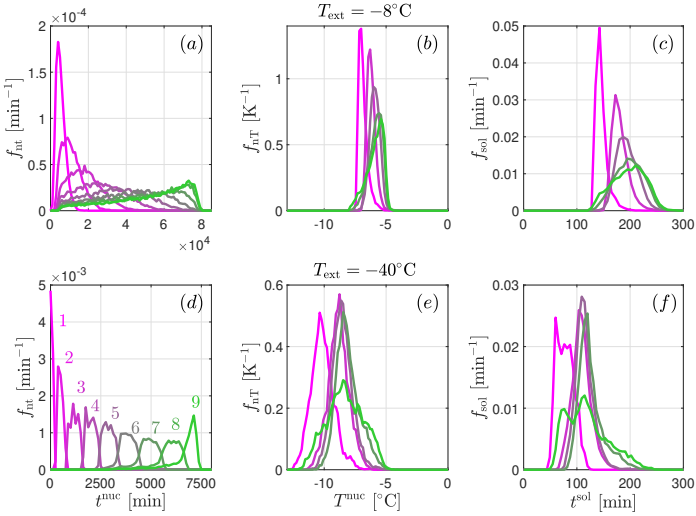

Figure 8.18 Characteristic distributions for the pallet with 40x36x18 vials for storage temperatures of −8°C (top) and −40°C (bottom). The color indicates the layers in vertical direction: the pallet comprises 18 layers in total, leading to 9 populations.

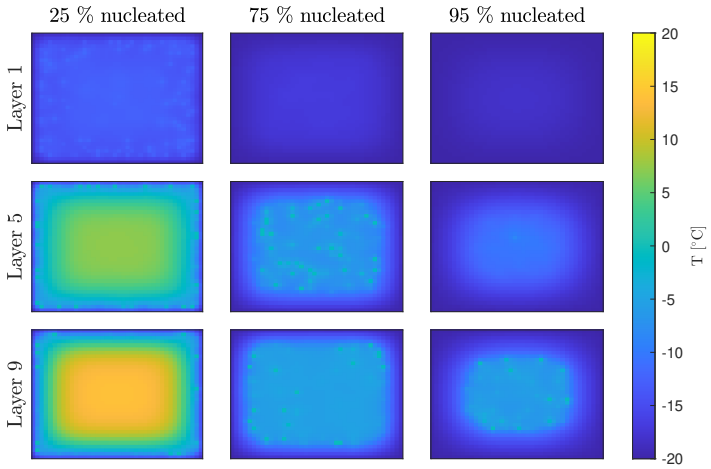

Figure 8.19 Thermal evolution for all vials in three of the 18 layers at three selected points in time for a storage temperature of −20°C. Layer 1 indicates the top layer of the pallet, layer 9 the central, innermost layer. Each tile denotes a vial.

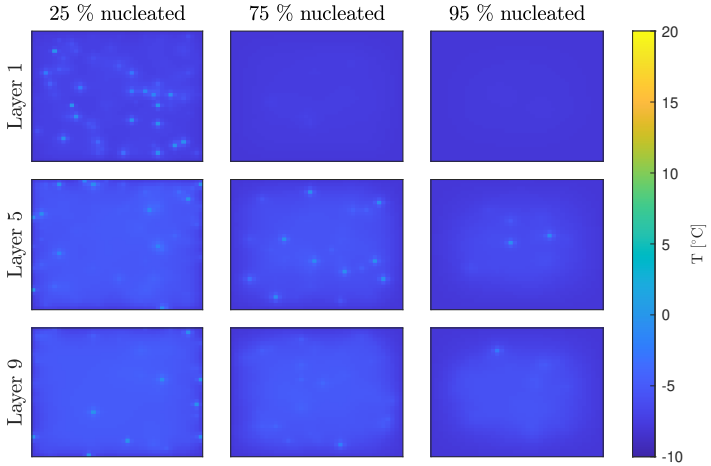

Figure 8.20 Thermal evolution for all vials in three of the 18 layers at three selected points in time for a storage temperature of −8°C.

Freezing of the innermost vials

The exceptionally large variability observed within the innermost population motivated a more detailed analysis. To do so, we analyze the tri-variate distribution (green) and the three bi-variate distributions (grey) of the characteristic quantities of freezing, as shown in Figure 8.21 for this population. The tri- and bi-variate distributions shown enable an analysis of correlations among the characteristic quantities. For each distribution, three iso-surfaces for the probability density were drawn that denote the regions in the space of nucleation and solidification properties that were increasingly frequently observed for the freezing vials. The region limited by the largest iso-surface each comprises a level of 3% compared to the maximum observed probability density; the inner surfaces correspond to levels of 10% and 30%, thus denoting the regions in which vials were most likely to nucleate and solidify.

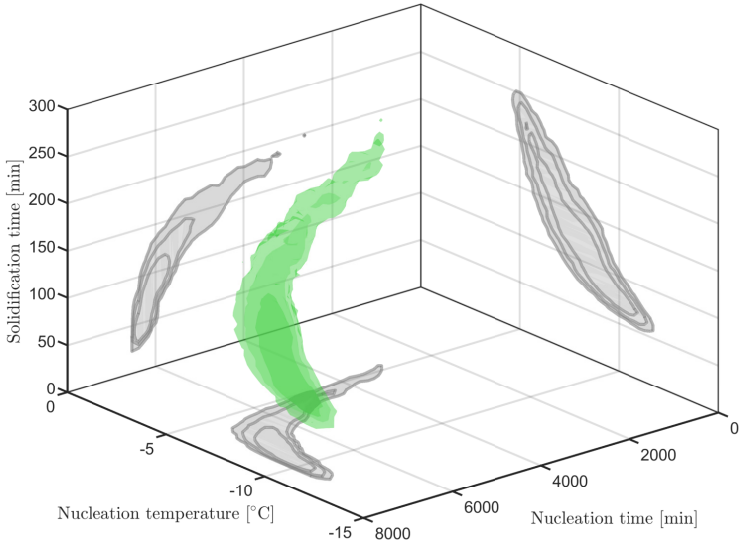

Figure 8.21 Tri-variate distribution of the characteristic quantities of freezing for the pallet with 40x36x18 vials for a storage temperature of −40°C. Only the innermost population 9/10 is shown. The three marginal bi-variate distributions are shown in the three planes of the plot.

We may draw several conclusions from this analysis. The tri-variate distribution exhibits a *banana-like* shape, corresponding to two regions in nucleation time. For short nucleation times, few nucleation events occur, predominantly at high nucleation temperatures and long solidification times. For larger nucleation times, close to the completion of freezing, the frequency of nucleation events increases. This is indicated by the position of the innermost iso-surface. Here, we observe lower nucleation temperatures and shorter nucleation times. This observation of two regimes is in line with the findings presented in Figure 8.4, where the thermal evolution for a core vial in the innermost layer was shown; such core vial spends a long time in the supercooled state, before a final cool-down at the end of the process. Vials nucleating during the stationary phase naturally exhibit long solidification times and a relatively narrow distribution of nucleation temperatures around the value of the stationary temperature. The faster solidification process later on stems from an acceleration in heat transfer at the end of the stationary phase, when nearly all vials are already completely frozen. Since vials in the core may nucleate either during the long, stationary phase, or during the cool-down in the end, we observe an enhanced heterogeneity for the core part of the system.

9 MODELING THE FREEZING PROCESS OF AQUEOUS SOLUTIONS CONSIDERING THERMAL GRADIENTS AND STOCHASTIC ICE NUCLEATION

Despite its importance to multiple scientific fields and industries, the freezing process of aqueous solutions is not yet completely understood. In particular, the relationship between temperature gradients within a solution and the occurrence of stochastic ice nucleation remains elusive. To address this knowledge gap, we have derived a novel stochastic spatial freezing model from first principles. The model predicts with quantitative accuracy how temperature gradients affect the stochastic ice nucleation of sucrose solutions in vials. This motivated a detailed study of the freezing-stage in freeze-drying. In particular, the model enabled a mechanistic assessment of vacuum-induced surface freezing, an emerging approach towards optimized freeze-drying processes. Model predictions revealed both the stochastic nature of this freezing method, and its performance limitations in case highly concentrated solutions are frozen. To ensure that both researchers and practitioners benefit from this modeling work, we provide open source access to it within our python package *ethz-snow*.

9.1 INTRODUCTION

Many biopharmaceuticals exhibit limited stability in the liquid state and require a freezing treatment to ensure sufficiently long shelf life.[8,14,16,17] Biopharmaceutical formulations comprising the active pharmaceutical ingredient (API) and excipients are typically filled under sterile conditions into vials that contain a single or a few doses of the drug product and then frozen or

The results presented in this chapter have been reported in: Deck, L.-T.; Košir, A.; Mazzotti, M. Modeling the freezing process of aqueous solutions considering thermal gradients and stochastic ice nucleation. *Chem. Eng. J.* **2024**, 483, 148660. There are two major differences between this chapter and the journal article. First, the article does not include the results on vacuum-induced surface freezing (VISF) that are shown here. Second, for the sake of brevity, supplementary information that accompanies the journal article and focuses on the numerical aspects of the model has been excluded from this chapter.

freeze-dried in large batches.[41,170] Under these conditions, aqueous solutions experience pronounced supercooling during freezing,[28,43,76] meaning that they cool down in the liquid state significantly below the equilibrium freezing temperature before the first ice crystals are formed.

Freezing comprises two phenomena, namely ice nucleation, which consists of the random formation of ice crystals from the liquid, and solidification, which is the formation of ice due to growth of these nuclei.[21,40,74] Ice nucleation is an activated process and therefore it is stochastic.[22,27,66,76] Hence, vials that contain the same product and are frozen under identical process conditions may undergo nucleation at different times. Such variability is regarded as one of the main challenges in the design of pharmaceutical freezing and freeze-drying processes, since it may translate into variability in critical material attributes of the final product.[20,28,41,75,170] Despite its relevance, stochastic ice nucleation remains poorly understood in the context of pharmaceutical freezing. While a large number of experimental studies acknowledge the variability in nucleation time among vials within a batch,[28,43,170] the stochasticity of ice nucleation traditionally has not been considered in models and theoretical works in the context of pharmaceutical manufacturing,[19,20,28,212] until very recently.[40,62,74]

To simulate the stochastic freezing process of an arbitrarily sized batch of thermally interacting vials in a mechanistic manner, we have recently developed a model termed *Stochastic Nucleation of Water (SNOW)*.[73,74,186] We have applied the SNOW model to the freezing process of the Janssen COVID-19 vaccine, where the model correctly predicted all relevant experimental trends, and where we could highlight the importance of an accurate description of stochastic ice nucleation for process understanding, design, and optimization.[75] In addition, we have developed a robust methodology to estimate the kinetic parameters for ice nucleation from experimental data.[76]

To keep the computational costs of process-scale simulations reasonably low, *SNOW* does not consider thermal gradients within individual vessels.[74] Such simplification is accurate for freezing in vials with small fill volumes and at sufficiently small cooling rates, as is the case in pallet freezing and in shelf-ramped freezing.[74,75] Conversely, *SNOW* may be limited in describing freezing processes where large thermal gradients occur, e.g., when freezing in large containers,[32,39] or when applying very large cooling rates such as in vacuum-induced surface freezing (VISF).[176,212,213] VISF is a technical modification of the freezing stage in freeze-drying that aims at controlling the nucleation behavior by rapidly cooling down the formulation through surface evaporation.[20,176] While VISF has been shown to positively affect product attributes compared to conventional freezing techniques, its design and optimization remain challenging due to the large number of process

parameters involved,[178,213,214] and ultimately due to the lack of a mechanistic model.

To accurately model such process, the effects of thermal gradients on the stochastic occurrence of nucleation have to be considered. No model available in the literature is able to do so, which motivates us to develop this capability by incorporating thermal gradients into the *SNOW* methodology. This extended model is termed *SNOWing* (for *SNOW* - INternal Gradients) and available to researchers and practitioners for free as part of the open-source python package *ethz-snow*.[73,186]

This work is structured as follows: In Section 9.2 we derive the *SNOWing* modeling framework and we discuss how to interpret the model predictions. We assess the role of thermal gradients in detail in Section 9.3, where we also compare model predictions with experimental data. Having confirmed the predictive performance of the model, we study the freezing stage in freeze-drying in Section 9.3. We consider both shelf-ramped freezing in Section 9.4.1 and vacuum-induced surface freezing in Section 9.4.2. Finally, we draw the relevant conclusions in Section 9.5.

9.2 METHODS

In this section, we present the modeling framework for the simulation of freezing processes in a single vial considering both thermal gradients and stochastic ice nucleation. We provide in Section 9.2.1 the derivation for the spatial description of freezing in a single vessel of arbitrary geometry. The freezing processes studied in this work involve two-dimensional (2D) cylindrical and one-dimensional (1D) slab geometries; the corresponding sets of balance equations for these geometries, as well as the numerical solution approach, are provided in the Supplementary Information of the associated journal article.[79] Finally, we outline how to characterize freezing based on model predictions in Section 9.2.2.

9.2.1 Modeling framework

Freezing comprises first a cooling phase, where the solution within the vessel is in the liquid state, and second a solidification phase, during which ice is formed. The transition between the two phases is initiated by a single stochastic ice nucleation event. These phases are discussed individually in the following sections. We start the derivation by introducing the relevant assumptions.

Model assumptions

The model describes the freezing process in a vessel that contains an aqueous solution of mass m_v, which comprises water, m_w, and solutes, m_s; the mass both of the water and of the solutes remains constant during freezing. Water may be present either as liquid (with mass m_ℓ) or as ice (with mass m_i), whereby no ice is present at the beginning of the process. Physically, growing ice crystals incorporate only little solute in their structure. During solidification, the solute concentration in the remaining solution thus increases. The solution co-exists with the ice crystals, forming a partially frozen state consisting of two interwoven phases. The model describes this state as a homogeneous phase: every point within the volume to be frozen is considered to comprise ice, with mass fraction w_i, and a solution comprising liquid water with mass fraction w_ℓ and solute with mass fraction w_s. No ice is present in the beginning ($w_i = 0$), and as soon as ice is formed, the mass fraction of ice increases and that of liquid water decreases. Similar assumptions are common in models that describe porous media.[40] The effective thermal properties for such system are defined as

$$c_{p,\text{eff}} = c_{p,s} w_s + c_{p,\ell} w_\ell + c_{p,i} w_i \tag{9.1}$$

$$k_{\text{eff}} = k_s w_s + k_\ell w_\ell + k_i w_i \tag{9.2}$$

whereby $c_{p,\text{eff}}$ denotes the specific heat capacity and k_{eff} the thermal conductivity. Both properties are assumed to depend on solution composition, but not on temperature. The increase in solute concentration in the liquid phase, due to the exclusion of solutes from the growing ice crystals, lowers its equilibrium freezing temperature, T^{eq}. The initial equilibrium freezing temperature, i.e., when no ice is present yet, is termed T_ℓ^{eq}. The depression of the freezing point of a solvent due to the presence of solutes is described in this work based on the law by Blagden:[98]

$$T^{\text{eq}} = T_m - \frac{k_f}{M_s} \frac{w_s}{w_\ell} \tag{9.3}$$

whereby T_m denotes the freezing temperature of pure water and k_f its cryoscopic constant. The molar mass of the solute present with mass fraction w_s is M_s. Finally, the following assumptions are made with respect to mass and heat transfer, and to the kinetics of the process:

1. The model describes only the volume of the solution to be frozen; the surrounding vessel is not explicitly modeled. Its contribution to heat transfer is accounted for by defining appropriate boundary conditions (see Section 9.2.1).

2. The density change associated with the transition from liquid water to solid ice is considered negligible.
3. The simulated volume is stagnant; internal heat transfer is considered to occur through thermal conduction only.
4. The mass of water remains constant during freezing: in case of heat transfer through evaporation, we neglect the associated mass loss, after verifying that this is indeed negligible.
5. Crystallization of the solute during freezing is neglected, the solute remains in solution during the entire process.

These assumptions were made in line with the relevant literature on modeling of freezing in small volumes such as vials.[19,40,171,212]

Cooling phase

During the cooling phase the system consists only of the solution (liquid water and solute). Introducing the thermal diffusivity $\alpha_{\text{eff}} = k_{\text{eff}}/(c_{\text{p,eff}}\rho)$, which depends on the specific heat capacity $c_{\text{p,eff}}$, on the heat conductivity k_{eff}, and on the density ρ of the solution, the enthalpy balance for the evolution of the system during the cooling phase can be written:

$$\frac{\partial T}{\partial t} = \alpha_{\text{eff}} \nabla^2 T \tag{9.4}$$

The enthalpy balance can be solved for given sets of initial and boundary conditions. In this work, we impose as initial condition that all positions $\mathbf{x}$ belonging to the simulated volume V are at a given initial temperature, i.e., $T(\mathbf{x}, t = 0) = T_0$. The definition of the boundary conditions is subject to the applied technical variation of the freezing process. Boundary conditions for a number of industrially relevant freezing processes are presented in Section 9.2.1.

Stochastic ice nucleation

The temperature in the vessel decreases due to cooling, eventually approaching the equilibrium freezing temperature of the solution T_ℓ^{eq}. Upon further cooling, the solution enters a liquid, super-cooled state, in which nucleation may occur. Nucleation is described as an inhomogeneous Poisson process, following a large body of literature,[22,25,40,66] whereby a single nucleation event occurs at the time of nucleation t^{nuc}.[27,74,76] We define the time-dependent

domain of nucleation $D_\mathrm{n}(t) \subseteq V \subset \mathbb{R}^3$ as the super-cooled region of the volume of interest:

$$D_\mathrm{n}(t) = \begin{cases} \left\{ \mathbf{x} \in V | T(\mathbf{x},t) < T_\ell^\mathrm{eq} \right\} & ; \quad t \leq t^\mathrm{nuc} \\ \emptyset & ; \quad t > t^\mathrm{nuc} \end{cases} \tag{9.5}$$

The literature widely uses the terms *local supercooling* when nucleation occurs at a time where only parts of the volume are supercooled (i.e., $D_\mathrm{n}(t^\mathrm{nuc}) \subset V$), and *global supercooling* when the entire volume is supercooled (i.e., $D_\mathrm{n}(t^\mathrm{nuc}) = V$).[43] The model is capable of simulating both cases. To quantify the occurrence of nucleation events, we define the time-dependent nucleation frequency $K_\mathrm{v}(t)$ that represents the expected number of nucleation events per unit time in the domain of nucleation $D_\mathrm{n}(t)$:

$$K_\mathrm{v}(t) = \int_{D_\mathrm{n}(t)} J(\mathbf{x},t) \, \mathrm{d}^3\mathbf{x} \; = \int_{D_\mathrm{n}(t)} k_\mathrm{b} \left(T_\ell^\mathrm{eq} - T(\mathbf{x},t) \right)^b \mathrm{d}^3\mathbf{x} \tag{9.6}$$

whereby $J(\mathbf{x},t)$ denotes the rate of nucleation per unit volume at an arbitrary position $\mathbf{x}$ within the domain of nucleation D_n. J is expressed as a function of the supercooling, which is the difference between the equilibrium freezing temperature of the solution and the actual temperature at the relevant position.[40,62,74,76,88] The parameters b and k_b may be obtained experimentally following the procedure that was developed earlier;[76] they are considered temperature-independent, but may depend on manufacturing conditions such as the concentration of particulate impurities. By defining the nucleation rate in terms of supercooling, effects of solution composition are inherently accounted for: more concentrated solutions exhibit a lower equilibrium freezing temperature and hence nucleate at lower temperatures than less concentrated ones. This quantitatively matches experimental findings.[79,88] In particular, we recently demonstrated that a single set of kinetic parameters accurately describes nucleation in aqueous solutions of ten different compositions containing sucrose, trehalose, and sodium chloride at different concentration levels.

It is worth noting that significant differences in the nucleation kinetics among vials that contained solutions of identical composition were observed experimentally.[76,79,159] This was attributed to the heterogeneous nature of nucleation; i.e., ice nucleation is rate-controlled by the availability of impurities such as dust particles, and their number and activity may vary among vials. To this end, a vial-dependency of the pre-factor k_b has been introduced: for a specific vial v, the vial-specific pre-factor $k_\mathrm{b,v}$ is defined as $-\log_{10}(k_\mathrm{b,v}) = a + \xi_\mathrm{v} c$. Here, a and c are two kinetic parameters, while ξ_v is a number randomly drawn from the standard normal distribution. This vial-dependent approach was shown to provide both a closer fit to experimental data, and to

exhibit a superior predictive performance compared to the vial-independent approach,[76,79] which is why we use it in this work as well.

Having discussed how to compute the nucleation frequency $K_v(t)$, we note that integrating it over the duration of the cooling phase yields the expected number of nuclei formed, called $E(N_v)(t)$:

$$E(N_v)(t) = \int_0^t K_v(t')\, dt' \tag{9.7}$$

The cumulative density function (CDF) $F_{nt}(t^{nuc})$ for the probability that nucleation occurred at or before time t^{nuc} is defined as[66,76]

$$F_{nt}(t^{nuc}) = 1 - \exp\left\{ - E(N_v)(t^{nuc}) \right\} \tag{9.8}$$

Accordingly, the probability density function (PDF) $f(t^{nuc})$ is

$$f(t^{nuc}) = \frac{dF_{nt}}{dt^{nuc}} = K_v(t^{nuc}) \exp\left\{ - \int_0^{t^{nuc}} K_v(t') dt' \right\}. \tag{9.9}$$

In addition to the density functions above, it is of interest to identify the time of nucleation in individual realizations of the freezing process. We do so by drawing a randomly generated number from the uniform distribution in [0,1]. This number is inserted for F_{nt} in Eq. 9.8, hence obtaining an implicit expression for the nucleation time..[22,76,215]

Next, we consider how the nucleation event initiates the transition from the cooling phase to the solidification phase. The chosen modeling approach implies that a single nucleation event triggers the transition to the solidification phase in the entire volume of interest, in line with experimental observations.[20,76] The literature reports that ice grows from a single point in space, called the *origin of freezing*, which constitutes the position of the nucleation event. In diluted, super-cooled solutions, the growth rate of ice crystals is in the order of centimetres per second.[69] Hence, a single nucleus initiates ice growth throughout the super-cooled volume and depletes the supercooling in a time span considerably shorter than the cooling and solidification phases. Accordingly, we define the time-dependent domain of solidification $D_s(t) \subset V$:

$$D_s(t) = \begin{cases} \emptyset & ; \quad t < t^{nuc} \\ D_n(t^{nuc}) & ; \quad t = t^{nuc} \\ \{\mathbf{x} | w_i(\mathbf{x}, t) > 0\} \cup \left\{ \mathbf{x} | w_i(\mathbf{x}, t) = 0 \wedge T(\mathbf{x}, t) < T_\ell^{eq} \right\} & ; \quad t > t^{nuc} \end{cases} \tag{9.10}$$

The domain is empty before nucleation occurred and it equals the domain of nucleation at the time of nucleation. In case of local supercooling (i.e.,

$D_n(t^{nuc}) \subset V$), some positions are not supercooled at the time of nucleation; they will continue to cool down until they eventually supercool (at a time termed t^{s0}), and then start to solidify as well.

Solidification phase

During solidification, both temperature and ice mass fraction depend on time and position, and are unknown. The enthalpy balance for solidification accounts both for thermal conduction and for the release of latent heat λ_w:

$$c_{p,eff}\rho\frac{\partial T}{\partial t} = \nabla\cdot(k_{eff}\nabla T) + \lambda_w\rho\frac{\partial w_i}{\partial t} \tag{9.11}$$

As discussed in Section 9.2.1, ice crystal growth in diluted solutions is a rapid process; therefore it is rate-limited by the heat transfer with the surroundings, and the supercooling is practically depleted during solidification, i.e., $T^{eq} - T = 0$ within D_s. Since T^{eq} is a function of the ice mass fraction, Equation 9.11 forms with the expression for the freezing point depression (Equation 9.3) a system of two equations with two unknowns. When combining the two equations and solving for the temperature, we obtain:

$$c_{p,eff}\rho\frac{\partial T}{\partial t}\left(1+\frac{\beta}{(T-T_m)^2}\right) = \nabla\cdot(k_{eff}\nabla T) \tag{9.12}$$

whereby we introduce the term $\beta(\mathbf{x},t)$:

$$\beta(\mathbf{x},t) = \begin{cases} \frac{\lambda_w k_f w_s}{M_s c_{p,eff}} & ; \quad \mathbf{x}\in D_s(t) \\ 0 & ; \quad \text{otherwise} \end{cases} \tag{9.13}$$

The quantity β can be understood as an apparent heat capacity term that describes the liquid-to-solid phase transition in the domain of solidification. Conversely, in the part of the vial that does not solidify (yet), it assumes a value of zero. In this way, the model is capable of simulating solidification in a system that experiences local supercooling at the time of nucleation.

Initial and boundary conditions are required to solve the enthalpy balance. Boundary conditions are discussed in detail in the next Section 9.2.1, whereas we consider the initial conditions here. Solidification at a position $\mathbf{x}$ starts when this position enters the domain of solidification at time $t^{s0}(\mathbf{x})$; this time equals the nucleation time t^{nuc} for those positions that are supercooled at nucleation (see Equation 9.10). At t^{s0}, the enthalpy associated with the rise in temperature from the value T^{s0} to the equilibrium value T^{eq} corresponds to the enthalpy released by the formation of ice:

$$\lambda_w w_i(\mathbf{x},t) = \left(T^{eq}(\mathbf{x},t) - T^{s0}(\mathbf{x})\right)c_{p,eff} \qquad \text{for} \quad t = t^{s0}(\mathbf{x}) \tag{9.14}$$

Consequently the set of initial conditions $T^{\mathrm{eq}}(\mathbf{x}, t), w_{\mathrm{i}}(\mathbf{x}, t)$ at time t^{s0} is obtained by solving Equation 9.14 together with the expression for the freezing-point depression (Equation 9.3).

Technical variations of the freezing process

Various types of freezing processes find widespread use in the manufacture of bio-pharmaceuticals,[14,16] and beyond. One may distinguish between the freezing of large volumes for the purpose of storage and transport, and the freezing in vials. Freezing in vials is relevant first as standalone process for drug products that are stored in the frozen state; this is for example the case for most commercially available COVID-19 vaccines where large numbers of vials are frozen in pallet configurations.[75] Second, freezing in vials is the first step in freeze-drying, which is the most common process to stabilize biopharmaceuticals.[20,41,171]

Knowledge of the type of freezing process is essential for process modeling, since the boundary conditions have to account for the relevant process-specific types of heat transfer. In this work, we study three common freezing processes, which are described below, and which are also illustrated in Table 9.1. The table provides the equations that define the relevant boundary conditions.

Jacket-ramped freezing (JRF): In this process, the temperature in the vials is controlled by a jacket, which cools the vials at both the sides and the bottom. Heat transfer at the bottom occurs directly with the jacket, while the one at the sides is slowed down due to a small air gap between vial and jacket. The top of the vials is insulated. This process has been used in an earlier work to generate large sets of experimental nucleation temperature data,[76] which are compared with the predictions of the model developed here.

Shelf-ramped freezing (SRF): This is the predominant type of freezing used in freeze-drying, where vials are placed on a shelf with time-dependent temperature $T_{\mathrm{sh}}(t)$.[41,43,170] The shelf is in contact with the bottom of the vial, which facilitates fast heat transfer. Furthermore, heat transfer may occur through both the top and the sides of the vial, either by means of natural convection due to the surrounding gas at temperature $T_{\mathrm{g}}(t)$, or by means of thermal radiation.

Vacuum-induced surface freezing (VISF): This is a modification of shelf-ramped freezing, where ice nucleation is induced by rapid evaporative cooling at low pressure.[176,178] First, vials are pre-cooled on a shelf to a set temperature close to 0°C; then, vacuum is applied, hence lowering the temperature at the top surface of the liquid. Heat transfer during vacuum differs from SRF, as there is an additional heat flux due to evaporative cooling at the top surface of the vial.[212,216,217]

Jacket-ramped freezing (JRF): Section 9.3	
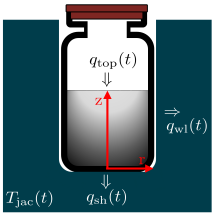	$-k_{eff}\frac{\partial T}{\partial z}\Big\|_{t,z=0,r} = q_{sh}(t) = K_{sh}\left(T_{jac}(t) - T\Big\|_{t,z=0,r}\right)$ $-k_{eff}\frac{\partial T}{\partial z}\Big\|_{t,z=H,r} = q_{top}(t) = h_g\left(T_g(t) - T\Big\|_{t,z=H,r}\right) = 0$ $-k_{eff}\frac{\partial T}{\partial r}\Big\|_{t,z,r=R} = q_{wl}(t) = K_{wl}\left(T_{jac}(t) - T\Big\|_{t,z,r=R}\right)$ $\frac{1}{K_{wl}} = \frac{1}{K_{sh}} + \frac{d_{air}}{k_{air}}$ $\frac{\partial T}{\partial r}\Big\|_{t,z,r=0} = 0$
Shelf-ramped freezing (SRF): Section 9.4.1	
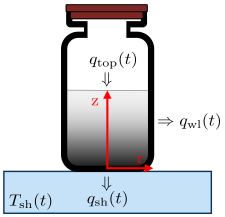	$-k_{eff}\frac{\partial T}{\partial z}\Big\|_{t,z=0,r} = q_{sh}(t) = K_{sh}\left(T_{sh}(t) - T\Big\|_{t,z=0,r}\right)$ $-k_{eff}\frac{\partial T}{\partial z}\Big\|_{t,z=H,r} = q_{top}(t) = h_g\left(T_g(t) - T\Big\|_{t,z=H,r}\right) = 0$ $-k_{eff}\frac{\partial T}{\partial r}\Big\|_{t,z,r=R} = q_{wl}(t) = h_g\left(T_g(t) - T\Big\|_{t,z,r=R}\right) = 0$ $\frac{\partial T}{\partial r}\Big\|_{t,z,r=0} = 0$
Vacuum-induced surface freezing (VISF): Section 9.4.2	
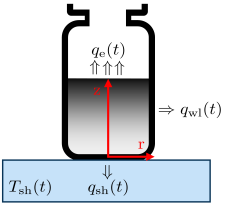	$-k_{eff}\frac{\partial T}{\partial z}\Big\|_{t,z=0,r} = q_{sh}(t) = K_{sh}\left(T_{sh}(t) - T\Big\|_{t,z=0,r}\right)$ $-k_{eff}\frac{\partial T}{\partial z}\Big\|_{t,z=H,r} = q_e(t) = N_w(t)\Delta H_e$ $N_w(t) = \frac{2\kappa}{2-\kappa}\sqrt{\frac{M}{2\pi R}}\left[\frac{p_v^*}{\sqrt{T_l(t)}} - \frac{p_{vac}}{\sqrt{T_v(t)}}\right]$ $-k_{eff}\frac{\partial T}{\partial r}\Big\|_{t,z,r=R} = q_{wl}(t) = h_g\left(T_g(t) - T\Big\|_{t,z,r=R}\right) = 0$ $\frac{\partial T}{\partial r}\Big\|_{t,z,r=0} = 0$

Table 9.1 The table visualizes the three technical variations of freezing considered in this work along with the relevant boundary conditions.

We limit this work to the aforementioned three processes for the sake of brevity; the modeling framework, however, can be applied to any arbitrary freezing process that relies on boundary conditions involving conduction, convection, radiation or evaporation.

Numerical approach

The three freezing processes studied in this work (see Section 9.2.1) involve radial-symmetric 2D cylindrical and 1D slab geometries; the corresponding sets of balance equations for these geometries, as well as the numerical approach to the solution, are provided in the Supplementary Information of the associated journal article.[79] In these sections, an overview of the numerical methods, which are used to solve the model equation, is provided, along with a brief discussion of their features, such as stability, accuracy and convergence.

Two methods have been considered, implemented, and tested for the numerical solution, following the literature:[218–222] the finite difference method (FDM) and the finite volume method (FVM). The model predictions obtained with the two methods quantitatively agreed with each other, hence verifying their correct implementation. In the following, we show the results obtained through the finite difference method only.

We provide an open source implementation of the model in the form of a python package published on pypi under the MIT license.[186] The model is part of the package *Stochastic Nucleation of Water*,[73] which in its first version comprised the two process-scale models for the freezing process of a large number of vials that were presented in earlier works.[74,75] All versions of the python package starting from v2.0.0 contain the spatial freezing model that has been developed in this work. Future extensions of the freezing model will be integrated into this package as well.

9.2.2 Characterizing the freezing process

The model presented in this work enables the fully stochastic simulation of a freezing process comprising cooling, ice nucleation, and solidification. Hence, it may be used to characterize a number of essential aspects of freezing, such as *batch* heterogeneity and *spatial* heterogeneity.

Batch heterogeneity denotes the variability in product attributes among vials frozen within the same batch, or within different batches. This variability is attributed both to the stochasticity of ice nucleation, and to the variability in heat transfer among positions of the vials in the batch.[28,43,84,199] Recently, we showed that thermal interaction among vials acts as a third mechanism of batch heterogeneity in freezing by enhancing the first two.[74,75]

The model can be used to characterize batch heterogeneity by carrying out a large number of stochastic simulations, hence capturing the variability in time and temperature of the nucleation event, as well as its effect on solidification.

We define the probability density functions $f_{\mathrm{nt}}(t)$ for the nucleation time t^{nuc}, $f_{\mathrm{fr}}(t)$ for the time of complete freezing t^{fr}, and $f_{\mathrm{sol}}(t)$ for the solidification time t^{sol}. In line with our earlier works,[74,75] freezing is considered complete when 90% of the total water in the vessel has solidified, i.e., when $m_{\mathrm{i}}(t^{\mathrm{fr}})/m_{\mathrm{w}} = 0.9$; however, we note that the endpoint of freezing may be defined using a different threshold. The solidification time t^{sol} is defined as the time elapsed between nucleation and complete freezing. By definition, $f_{\mathrm{nt}}(t)\mathrm{d}t$ provides the fraction of nucleation events that take place between t and $t + \mathrm{d}t$; $f_{\mathrm{fr}}(t)\mathrm{d}t$ the fraction of vials that freezes completely between t^{fr} and $t^{\mathrm{fr}} + \mathrm{d}t$; $f_{\mathrm{sol}}(t)\mathrm{d}t$ is the fraction of freezing processes with solidification times between t and $t + \mathrm{d}t$. The capital letter F with appropriate subscript denotes the corresponding cumulative distribution.

This methodology closely resembles the one that we introduced in the earlier, process-scale freezing model *SNOW*.[74,75] The difference is that *SNOW* was developed to simulate the freezing process of a batch of vials that thermally interact with each other. The model presented here (called *SNOWing*), is not tailored towards process-scale simulations, but considers individual vessels. In turn, *SNOWing* provides spatial information of freezing, which goes beyond the scope of *SNOW*. The two models provide complementary information and can be applied together to achieve a comprehensive, multi-scale understanding of freezing.

Spatial heterogeneity is directly observed in the evolution profiles both of temperature and of ice mass fraction. Of special interest is the temperature profile at the time of nucleation $T(t^{\mathrm{nuc}})$; due to temperature gradients, different positions in the vessel exhibit different temperatures at this point in time. The process-scale model *SNOW*, however, provides only a single value for the nucleation temperature, termed $T_{0\mathrm{D}}^{\mathrm{nuc}}$. To compare the predictions of the two models, we define the kinetic mean temperature $\bar{T}_{\mathrm{kin}}^{\mathrm{nuc}}$ that represents the temperature at which a volume in the absence of thermal gradients exhibits the same nucleation frequency as the one with thermal gradients:

$$\bar{T}_{\mathrm{kin}}^{\mathrm{nuc}} = \frac{1}{K_{\mathrm{v}}(t^{\mathrm{nuc}})} \int_{D_{\mathrm{n}}(t^{\mathrm{nuc}})} T(\mathbf{x}, t^{\mathrm{nuc}}) J(\mathbf{x}, t^{\mathrm{nuc}}) \, \mathrm{d}^3\mathbf{x} \tag{9.15}$$

If the difference between $T_{0\mathrm{D}}^{\mathrm{nuc}}$ and $\bar{T}_{\mathrm{kin}}^{\mathrm{nuc}}$ is sufficiently small, the effect of thermal gradients on nucleation may be neglected and the process-scale freezing model may be considered accurate. We carry out such comparison in Section 9.4.1 for shelf-ramped freezing.

As reference system for all simulations, a vial containing 1 mL of 20 wt% aqueous sucrose solution is considered; the freezing in this system has been studied previously.[76] The kinetic parameters for stochastic ice nucleation have been estimated for this solution, thus ensuring that the simulations presented

here are physically meaningful. A list of all simulation parameters is provided in the Supplementary Information of the associated journal article.[79]

9.3 THE ROLE OF THERMAL GRADIENTS

In this section, we study the role of thermal gradients during freezing and we assess the capability of the presented model to describe them. We simulate a cylindrical vessel with a fill height of 1.38 cm and a radius of 0.48 cm (fill volume of 1 mL, Figure 9.1) and a scaled-up cylindrical vessel with a fill height of 13.8 cm and a radius of 4.8 cm (fill volume of 1 L, Figure 9.2). We compare model predictions with a large set of experimental freezing data recently reported.[76] The data comprises thousands of freezing experiments in vials containing 1 mL of 20 wt% aqueous sucrose solution. The heat transfer of the vials is well-controlled; they are surrounded by a jacket that cools them both from the sides and from the bottom (see Section 9.2.1).[76]

In a first step, we confirmed that the predicted thermal evolution profiles from this work closely resemble the experimental ones (measured with a thermocouple).[76] Figure 9.1 (a) reports three experimentally measured evolution curves (black) for vials that exhibited different nucleation temperatures at a cooling rate of 0.6 K min^{-1}. Moreover, one simulated temperature profile, corresponding to the median nucleation time, t_{50}^{nuc}, and to the position of the thermocouple, is shown in blue. In both experiments and simulations, the temperature decreases linearly during the cooling phase, and rises very rapidly close to the equilibrium value of the solution upon nucleation. It remains for some time at a value close to the equilibrium freezing temperature of the unfrozen system, indicating that the solution solidifies. Eventually, the temperature decreases again. The similarity among simulation and experiments underlines that the model is capable to predict realistic thermal evolution profiles. In fact, the model is capable to do more than that: in experiments, the temperature is only measured at a single spot (see Figure 9.1 (b)), whereas the simulations provide spatial information on both temperature and ice mass fraction. Panels (b-d) show for three points in time, i.e., t_1, t_2 and t_3, both the temperature field (top) and the ice mass fraction field (bottom). At time t_1, the vial is still in the cooling phase and no ice is present; the entire volume is supercooled, indicating *global supercooling*. At times t_2 and t_3, different stages of solidification are observed. Nucleation has occurred just before time t_2 and has induced the formation of ice throughout the volume. Hence, temperatures close to T_ℓ^{eq} are observed throughout the entire volume. During further solidification, i.e., at time t_3, additional ice has formed, predominantly

close to the bottom of the vial and to its sides. These positions are colder than the center of the vial, because heat is removed through the jacket.

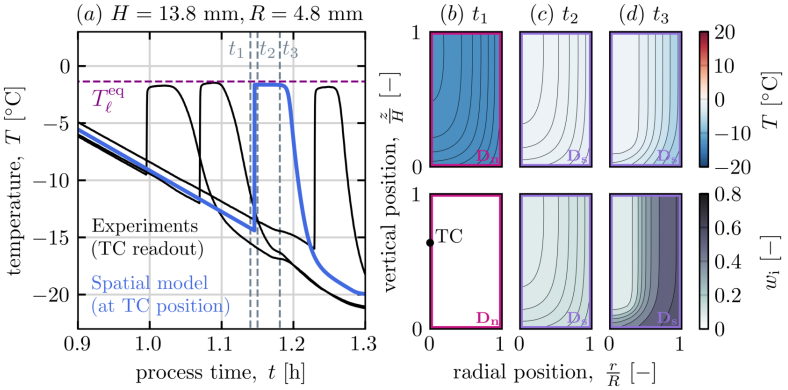

Figure 9.1 (a) Validated thermal evolution of the product: simulations performed with the spatial model (blue) for cooling rate γ = 0.6 K min^{-1} and compared to experiments (black), (b) temperature field (top) and ice mass fraction field (bottom) at time t_1 before nucleation, (c) same for time t_2 after nucleation and (d) t_3.

Even though we did not carry out experiments at larger scales, it is worth considering the model predictions for the freezing in larger volumes. Figure 9.2 shows model predictions for a system in which both radius and height were increased by one order of magnitude compared to the vial. This amounts to a fill volume of 1 L, which is a typical size in the pharmaceutical industry when freezing pharmaceutical solutions for the purpose of storage and transport. Panel (a) shows the temperature profiles for three different positions in the vessel, labelled A, B and C. Position A is at the same relative position as the thermocouple in the vial of Figure 9.1. Position B is at the bottom center, which is the coldest spot in the vessel, whereas position C is at the bottom side of the vessel. Panels (b-d) show the temperature and ice mass fraction fields for three points in time. There are some aspects worth mentioning:

First, the thermal evolution profiles for the three positions strongly differ; this indicates the presence of large thermal gradients within the vessel. These gradients are shown more explicitly in panels (b-d). Second, the nucleation temperature depends on position. If a thermocouple were placed in position A, it would indicate a temperature larger than 0°C at the time of nucleation. In positions B and C, however, supercooling occurs before nucleation, and a clear spike in the thermal evolution profile is visible. We discuss this issue in more detail in Section 9.4.1. Finally, nucleation occurs under local supercooling:

as indicated before, point A is not supercooled at the time of nucleation. Panel (b) shows the domain of nucleation, which covers about half of the vessel's volume just before the nucleation event. Consequently, solidification is initiated only in the volume that belongs to the domain of nucleation. The core of the vessel starts to solidify at later times. This is shown by the inward movement of the domain of solidification from t_2 to t_3.

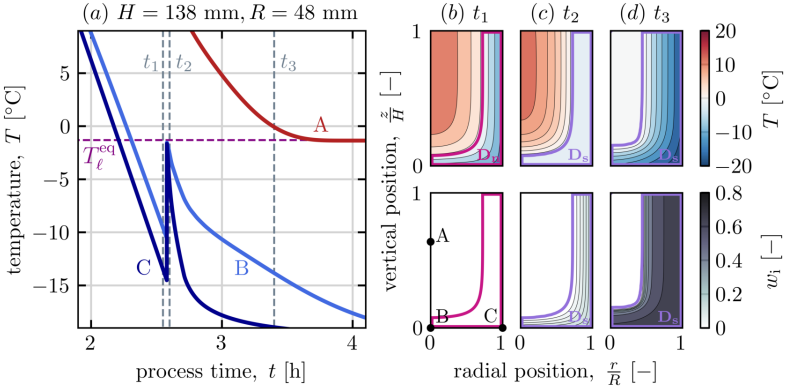

Figure 9.2 Similar to Fig. 9.1, but for a vessel with height and radius increased by a factor of ten compared to the vial: (a) temperature evolution in positions A, B and C (potential thermocouple locations), (b) temperature field (top) and ice mass fraction field (bottom) at time t_1, (c) t_2 and (d) t_3.

While thermal gradients increase with vessel size, they are already present at the vial-scale. Hence, we further probe the model predictions by assessing the model's capability to accurately predict the nucleation temperature distribution for the vial. For this, we rely on the cooling rate analysis in our earlier work,[76] where we have measured the experimental nucleation temperature distributions for cooling rates of 0.2 K min^{-1} and of 0.6 K min^{-1}, as shown in Figure 9.3. We estimated the nucleation kinetics for both cooling rates separately using a lumped freezing model (violet). Then, we used the estimated parameters to simulate the freezing process at the second cooling rate, and compared the predictions with experimental data. Here, we extend this procedure to the new spatial model (black). Figure 9.3 (a) shows the experimental distribution of nucleation temperatures (blue) for the cooling rate of 0.2 K min^{-1}, as well as the lumped model fit (violet), which was used to parameterize the model. The parameters in the nucleation rate equation (Eq. 9.6) were estimated to be: $a = 29.0$, $b = 29.3$, $c = 1.00$.[76] However, these parameter values were estimated assuming that no thermal gradients

are present. For the spatial model, a close fit to the 0.2 K min^{-1} experimental data is obtained when slightly adjusting parameter a to a value of 29.25; the resulting fit is shown in Figure 9.3 (a). Furthermore, Figure 9.3 (b) shows the model predictions for 0.6 K min^{-1}, as well as the experimental measurements (red). As it can be seen, and as discussed in our earlier work,[76] the lumped model fits well the data at 0.2 K min^{-1}, but underestimates the nucleation temperatures at the cooling rate of 0.6 K min^{-1} by about 0.5 K. The predictions of the new spatial model, on the other hand, quantitatively agree with the experimental data.

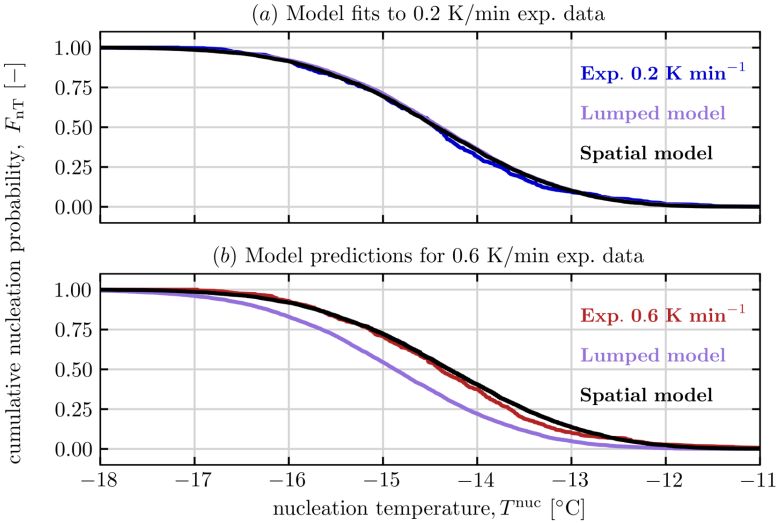

Figure 9.3 (a) Lumped and spatial model fits for experimental data obtained at 0.2 K min^{-1} using nucleation kinetics estimated based on the same experimental data with the lumped model. (b) Lumped and spatial model predictions for experimental data obtained at 0.6 K min^{-1}, when using parameters estimated with the lumped model based on 0.2 K min^{-1} experimental data; all experimental data taken from previous work[76].

This implies that an accurate description of thermal gradients is required for a quantitative description of stochastic ice nucleation in case large thermal gradients occur. The spatial model is therefore well-suited to study freezing processes where this is the case, such as either shelf-ramped freezing with large volumes or at high cooling rates (see Section 9.4.1), or vacuum-induced surface freezing (see Section 9.4.2). The lumped model, on the other hand, may be applied with reasonable accuracy to freezing processes that involve

only small thermal gradients, such as pallet freezing or shelf-ramped freezing in small volumes or at low cooling rates.

9.4 ON THE FREEZING STAGE IN FREEZE-DRYING

In this section, we study freezing as part of the freeze-drying process. We simulate a cylindrical vessel with a fill height of 1 cm and a radius of 0.56 cm, amounting to a fill volume of 1 mL. For shelf-ramped freezing (SRF, see Section 9.4.1), heat transfer occurs only at the vessel bottom, i.e., through the shelf. For vacuum-induced surface freezing (VISF, see Section 9.4.2), surface evaporation at the top of the vial is considered as well. In both cases, the spatial model simplifies into a 1D model, since we do not consider heat transfer through the sides of the vial.

Let us first consider the role of the shelf temperature profile $T_{sh}(t)$, which represents the main design parameter for the freezing stage in freeze-drying. Figure 9.4 presents three scenarios typically applied in pharmaceutical freeze-drying.[21,41] In scenario (1), $T_{sh}(t)$ (blue) decreases at a constant rate γ to a final temperature T_{sh}^{end}, which is the base case in shelf-ramped freezing. In scenarios (2) and (3), a holding step is integrated during which the shelf temperature remains constant.

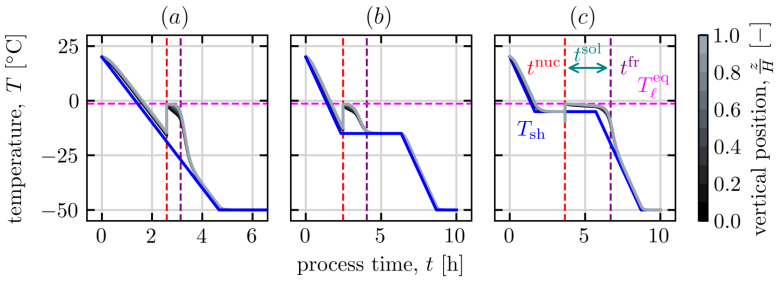

Figure 9.4 Spatial temperature evolution for a single vial when (a) no holding steps are used, (b) a 4 h ad-nucleation holding step is added at a temperature of $T = -15$°C and (c) both a 2 h pre-nucleation and a 2 h post-nucleation holding step are added at $T = -5$°C in combination with vacuum.

Scenario (1) is discussed in more detail in Section 9.4.1, where we assess the effect of cooling rate, solute concentration and vial fill volume on freezing. Scenario (2) corresponds to a process where nucleation occurs at constant temperature during the holding step. This leads to a narrower distribution

of nucleation temperatures, and to longer solidification times, which are considered beneficial in freeze-drying.[20] For the sake of brevity, we do not discuss the design of such holding step in detail in this work, and we refer to our earlier process-scale modeling work.[74] Importantly, both the existing process-scale freezing model and the new spatial freezing model can be used to simulate holding steps; together they provide a comprehensive picture of the effect of holding on freezing.

In scenario (3), finally, we report a typical temperature profile for vacuum-induced surface freezing. The temperature is hold for 2 h at $T = -5°C$, before vacuum is applied. The ensuing evaporative cooling leads to rapid nucleation. After nucleation, the shelf remains for two more hours at $-5°C$ to ensure slow, but complete solidification. We study the design of such vacuum-induced surface freezing process in detail in Section 9.4.2.

9.4.1 Shelf-ramped freezing

In the following, we study scenario (1) in detail, which comprises cooling at a constant rate without holding steps. We assess the effect of three process parameters, namely the cooling rate (cases A), the solute mass fraction (cases B), and the fill height (cases C), on the freezing behavior. A total of ten cases have been studied, as summarized in Tables 9.2 and 9.3.

Case	γ [K min^{-1}]	H [cm]	w_s [%]
R	1.0	1.0	20
A1	0.1	1.0	20
A2	2.0	1.0	20
A3	∞	1.0	20
B1	1.0	1.0	0
B2	1.0	1.0	10
B3	1.0	1.0	60
C1	1.0	0.5	20
C2	1.0	2.0	20
C3	1.0	5.0	20

Table 9.2 List of the operating conditions for the ten simulated cases for shelf-ramped freezing. The reference case is denoted with *R*. Cases (A1-3) correspond to different cooling rates, (B1-3) to different solute mass fractions, and eventually (C1-3) to different fill heights.

Table 9.3 provides the following information for all cases: first, the median nucleation time t_{50}^{nuc} and the median solidification time t_{50}^{sol}. And second, two temperature values at the median nucleation time: the minimum temperature in the vial, T_{min}^{nuc}, and its mean temperature, $\bar{T}^{nuc}$. We observe the following:

Nucleation time: Shorter nucleation times are obtained with faster cooling rates (see cases A1-3,R) due to the faster decrease in shelf temperature. The solute mass fraction has only little effect on the nucleation time (see cases B1-3,R). This is because it influences the nucleation time through two opposing mechanisms. On the one hand, solutions with higher solute concentrations nucleate later (as seen in case B3), since lower temperatures are required to initiate nucleation due to freezing-point depression. On the other hand, the effective heat capacity of the solution is smaller when the sucrose mass fraction is higher. This means that the vial reaches lower temperature levels earlier, which is directly shown in Figure 9.5 (B). As a consequence, no major effect of solute mass fraction on nucleation time is observed. With respect to fill height (see cases C1-3,R), nucleation occurs later, the higher the vial. This is because more heat must be removed from larger vials to cool to the range of temperatures where nucleation is likely to occur.

Case	t_{50}^{nuc} [min]	$\bar{T}^{\mathrm{nuc}}$ [°C]	$T_{\mathrm{min}}^{\mathrm{nuc}}$ [°C]	t_{50}^{sol} [min]
R	47.9	-12.9	-16.5	23.8
A1	357.0	-14.1	-14.5	59.4
A2	28.4	-10.7	-16.9	20.2
A3	7.3	-6.3	-17.2	20.6
B1	48.1	-11.7	-15.1	21.5
B2	47.9	-12.2	-15.7	20.4
B3	51.3	-19.4	-23.4	26.6
C1	42.2	-15.3	-16.2	12.3
C2	54.3	-5.5	-16.4	40.9
C3	56.8	8.3	-15.9	151.8

Table 9.3 List of the freezing characteristics for the ten simulated cases for shelf-ramped freezing. The reference case is denoted with *R*. The mean and minimum nucleation temperatures correspond to the median nucleation time t_{50}^{nuc}.

Solidification time: Solidification times decrease with increasing cooling rate (see cases A1-3,R), and eventually approach a limit in the case of the pre-cooled shelf (case A3). With respect to the solute mass fraction (see cases B1-3,R), no clear trend can be observed, because two opposing effects cancel each other out. First, a higher solute mass fraction implies that solidification should be faster, since there is less water present to solidify. Second, high solute mass fractions are associated with significant freezing point depression, which means that the vial must reach low temperatures to solidify completely. For the fill height (see cases C1-3,R), the solidification time increases approximately linearly with height; this is expected, as the absolute amount of heat to remove scales with volume.

Nucleation temperature: The temperature at the vial bottom at the median nucleation time (termed $T_{\mathrm{min}}^{\mathrm{nuc}}$) decreases for faster cooling (see cases A1-3,R). This is expected, since there is less time for nucleation to occur at a certain temperature when cooling faster. Further, a higher solute mass fraction leads to a lower nucleation temperature due to freezing-point depression (see cases B1-3,R). This effect outweighs that of the cooling rate for high solute concentrations (e.g., case B3). For the fill height (see cases C1-3,R), perhaps surprisingly, no significant effect on $T_{\mathrm{min}}^{\mathrm{nuc}}$ was found in the range of 0.5 cm to 5.0 cm. To appreciate this behavior, let us consider the mean temperature in the vial at nucleation $\bar{T}^{\mathrm{nuc}}$. Its value strongly increases from -15.3°C for a vial height of 0.5 cm to $+8.3$°C for a height of 5.0 cm. A value larger than 0°C indicates that a part of the vial fill volume is not supercooled at the time of nucleation. In these cases, nucleation is driven by local supercooling at the bottom of the vial. For small fill heights, however, global supercooling occurs. This finding underlines the importance of thermal gradients when describing stochastic nucleation.

We continue this analysis by studying the role of internal gradients in detail. To this end, Figure 9.5 reports the spatial evolution of temperature (top rows) and of ice mass fraction (bottom rows) for all ten studied cases. The color-coding denotes the vertical position; the bottom is indicated with black, whereas the top is shown in light grey.

First, we note that thermal gradients become more prominent when cooling faster (cases A1-3,R). This is especially pronounced for the pre-cooled shelf (A3), where relevant gradients are present at all times. Similarly, gradients in the ice mass fraction are more pronounced for faster cooling. However, even for the smallest cooling rate (0.1 K min^{-1}, A1), significant gradients are still observed during solidification. In general, solidification proceeds from the bottom (black) to the top (light grey), so that more ice is present at the bottom at any given time than at the top. For the pre-cooled shelf (A3), the bottom region is nearly completely frozen before relevant amounts of ice are formed at the top.

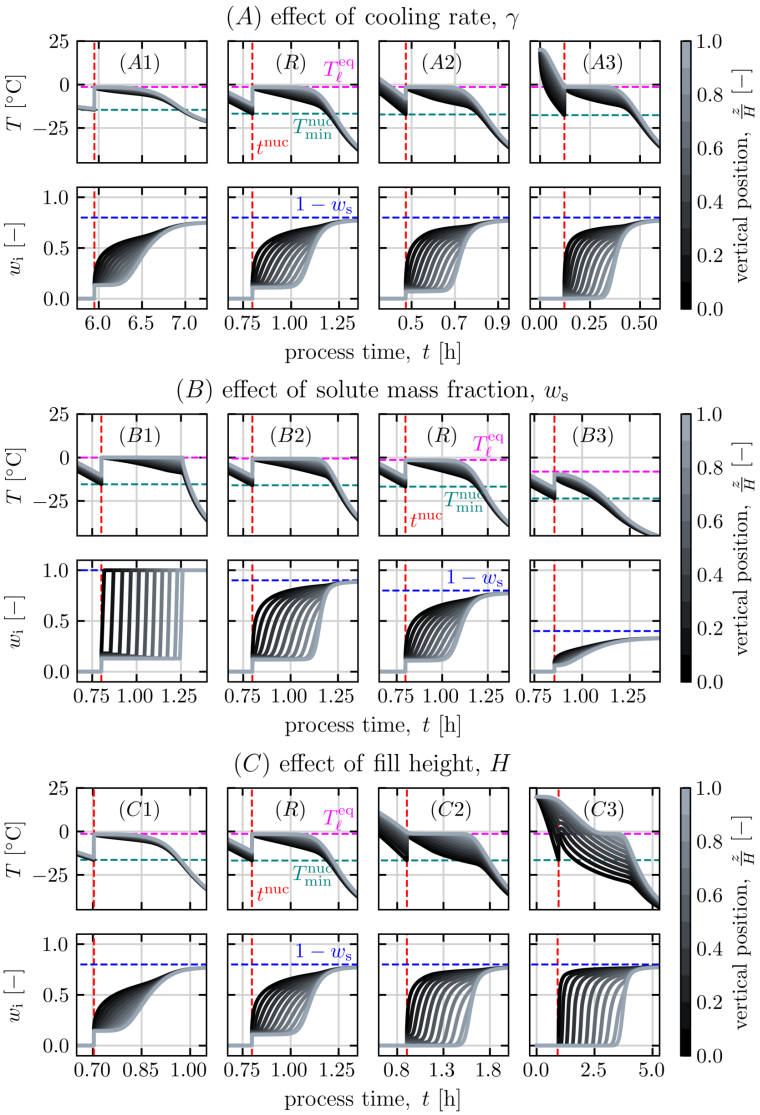

Figure 9.5 Effect of cooling rate (R, A1-3), solute content (R, B1-3) and fill height (R, C1-3) on the product temperature (top) and ice mass fraction evolution (bottom) at different positions (greyscale); the cases correspond to the results presented in Table 9.2. Case (A3), corresponds to a pre-cooled shelf: the simulation starts at a shelf temperature of −50°C, which is the final temperature in the other cases.

Next, we assess the effect of the solute mass fraction (cases B1-3,R). In the case of pure water (B1), the thermal evolution shows a sharp decrease at the end of solidification. At the top position, the temperature remains constant until freezing is completed at lower positions; if solute is present (cases R,B2,B3), the temperature at the top decreases already earlier; this is more pronounced for higher solute concentrations. The behavior is explained when considering the ice mass evolution: for pure water (case B1), the ice mass increases asymptotically, i.e., the freezing process exhibits a sharp freezing front, since the system does not experience any freezing point depression. Hence, there is a region in the bottom of the vessel that is completely frozen, while in the top no ice has been formed besides some initial one at the time of nucleation. If solute is present (cases R,B2,B3), the evolution profiles exhibit a slope that decreases with increasing solute content. This implies that there is a region, instead of a sharp front, in which ice is formed at any given time. This is because the equilibrium freezing temperature is decreasing due to the increase in solute concentration upon ice growth. The formation of such broad freezing region is therefore a direct consequence of the solidification kinetics of the system in the presence of solutes. We underline that such region of freezing has been broadly observed in freezing experiments in vials.[19,171]

Finally, we assess the effect of fill height on internal gradients (cases C1-3,R). Both the gradients in temperature and in ice mass scale with fill height: for the smallest system (case C1), solidification at the bottom is not completed before a significant amount of ice is formed also at the top. Conversely, for the largest system (case C3), freezing is completed in most of the vessel, before ice is formed at the top. We also recognize local supercooling in the evolution profiles: in the small systems (cases C1,R), ice is present at all positions at the time of nucleation, thus indicating global supercooling. For the second-largest system (case C2), only the bottom part of the vial is supercooled. Intriguingly, we observe dissolution of some ice after nucleation, i.e., for dimensionless vertical positions of about 0.4. This is because the ice present in the system dissolves to cool down the remaining, not yet-supercooled part of the system. In the largest system (case C3), ice is only formed at the very bottom at the time of nucleation; the top regions remain for an extended time at a temperature above the equilibrium value despite the formation of a significant amount of ice in the bottom.

These observations are closely connected to the discussion of the nucleation temperatures shown in Table 9.2, where we highlighted the increase in the mean temperature at the time of nucleation, $\bar{T}^{\mathrm{nuc}}$, with fill height: for the largest system (C3), a mean temperature larger than 0°C is obtained, thus indicating that most of the volume is not supercooled when nucleation occurs. Therefore the occurrence of global and local supercooling is primarily

governed by fill volume: in vials with small fill heights, global supercooling occurs in most cases, and local supercooling can only be achieved with very high cooling rates. In large volumes, however, local supercooling is the norm rather than the exception. The transition between these regimes occurs at fill heights on the order of a few centimetres, as shown here. Since this corresponds to typical heights used in pharmaceutical freeze-drying,[41,213] the case of local supercooling should indeed be considered in process design and development. If modeling is to inform process design, local supercooling has to be accounted for, as we do here.

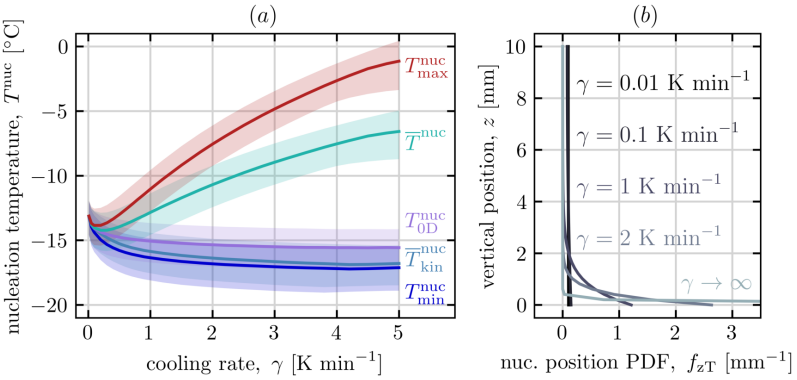

Figure 9.6 (a) Temperature at the time of nucleation versus cooling rate. The shaded regions denote the 10% and 90% quantiles of the nucleation temperature distributions. (b) Localization of nucleation as a function of cooling rate. Simulations were generated using the nucleation parameters a = 29.0, b = 29.3, c = 1.00, estimated directly from experimental data on sucrose solutions reported in Chapter 2.

To conclude this section, we assess in more detail the temperature at the nucleation time. So far, the temperature at the bottom of the vial $T^{\mathrm{nuc}}_{\mathrm{min}}$ and the mean temperature $\bar{T}^{\mathrm{nuc}}$ have been discussed, both evaluated at the median nucleation time. Since different trends in the two quantities were observed for the ten simulated cases, we carried out an additional sensitivity study shown in Figure 9.6. The figure reports the simulated nucleation behavior for a vial with reference parameters as a function of cooling rate (0.01 K min^{-1} $\leq \gamma \leq$ 5 K min^{-1}). Panel (a) shows the temperature field $T^{\mathrm{nuc}}(\mathbf{x})$ at the time of nucleation: the solid lines indicate the median values, and the shaded regions the variability, i.e., the region between the 10% and 90% quantiles of the distribution. The colors indicate five different definitions of the nucleation temperature: the minimum temperature (blue, $T^{\mathrm{nuc}}_{\mathrm{min}}$) at the bottom, the maximum temperature (red, $T^{\mathrm{nuc}}_{\mathrm{max}}$) at the top, and the mean temperature

(green, $\bar{T}^{\mathrm{nuc}}$) in the vial, as well as the kinetic mean (light blue, $\bar{T}^{\mathrm{nuc}}_{\mathrm{kin}}$, defined in Equation 9.15) and, for comparison, the predictions of the lumped model (magenta, $T^{\mathrm{nuc}}_{\mathrm{0D}}$).

Let us first consider the minimum temperature (blue, $T^{\mathrm{nuc}}_{\mathrm{min}}$). It monotonously decreases with increasing cooling rate, and eventually reaches a plateau; the plateau corresponds to the case when nucleation occurs at a time when the shelf has already reached its final temperature. In shelf-ramped freezing, the minimum temperature generally is at the bottom. This is also where the temperature is typically measured in experimental studies when inserting thermocouples.[102] Hence, it is no surprise to find that various experimental studies indeed confirm that faster cooling leads to lower nucleation temperatures.[19,43]

Both the maximum temperature (red, $T^{\mathrm{nuc}}_{\mathrm{max}}$) and the mean temperature (green, $\bar{T}^{\mathrm{nuc}}$), however, behave differently. For sufficiently slow cooling, the nucleation temperature decreases with increasing cooling rate; for faster cooling, the trend reverses and the temperature increases with cooling rate. Such effect is due to temperature gradients formed in the vial that scale with the cooling rate, as illustrated in Figure 9.6 (b). This panel shows the spatial probability density for nucleation to occur at a certain vertical position. A vertical line is obtained in the case of slow cooling rates of 0.1 K min^{-1} and below (black), which means that nucleation may occur throughout the fill volume with similar probability. For 1 K min^{-1}, however, a higher probability of nucleation is observed in the bottom of the vial; this effect is even more pronounced in the case of 2 K min^{-1} (grey). Hence, for sufficiently fast cooling, nucleation is dominated by the coldest bottom part of the vial and neither the maximum temperature nor the mean temperature serve as useful indicators for nucleation.

Next, we assess the kinetic mean nucleation temperature (light blue, $\bar{T}^{\mathrm{nuc}}_{\mathrm{kin}}$), which represents the uniform temperature at which the vial would exhibit the same nucleation frequency. Its value is close to the minimum temperature, which confirms that nucleation is dominated by the bottom part of the vessel. The kinetic mean temperature may also be used to compare the predictions of the lumped freezing model (magenta, $T^{\mathrm{nuc}}_{\mathrm{0D}}$) with the newly developed spatial model. We note that neither the minimum, nor the maximum, nor the mean of the spatial nucleation temperature field $T^{\mathrm{nuc}}(\mathbf{x})$ can be used for such comparison, as they insufficiently describe the spatial effects on nucleation. As it can be seen in Figure 9.6, both the kinetic mean and the lumped model predictions assume similar values and follow the same trend. This confirms that the lumped model correctly captures the nucleation behavior, with quantitative accuracy in the case of sufficiently low cooling rates. Moreover, it supports our earlier analysis, where we had concluded that thermal gradients

may be neglected without loss of accuracy when modeling the shelf-ramped freezing in vials with 1 mL fill volume.[74] Conversely, thermal gradients become more prominent for systems with larger volumes and faster cooling. When simulating such systems, the predictions of both spatial and lumped models should be compared to assess whether a spatial resolution is beneficial or not. Perhaps the most extreme process with respect to thermal gradients is the case of vacuum-induced surface freezing, which is discussed in the following.

9.4.2 Vacuum-induced surface freezing

In this section, we expand the assessment of the freezing stage in freeze-drying to vacuum-induced surface freezing. We first consider the evolution profiles of shelf temperature, vial temperature, and of ice mass fraction, as shown in Figure 9.7. The findings motivate a sensitivity study on surface evaporation, which is illustrated in Figure 9.8. Finally, the times required to induce nucleation and their dependency on vacuum parameters are discussed with reference to Figure 9.9.

Figure 9.7 reports a typical setting for vacuum-induced surface freezing that comprises six stages. Panel (a) illustrates the thermal evolution of both shelf (blue) and vial (shades of grey). After the initial ramp (stage 1), the shelf temperature is held at a pre-defined temperature (pre-hold, stage 2). In stage 3, the pressure is lowered to a value of p_{vac} for a certain amount of time t_{vac} that should suffice to induce nucleation in all vials. Both the cooling due to evaporation and the post-nucleation temperature rise are clearly visible in the thermal evolution of the vial. Panel (b) shows a zoom-in of the process that highlights these phenomena: the temperature at the top of the vial drastically decreases within seconds, while the bottom temperature remains nearly constant. This means that large temperature gradients form in a short time, which implies that surface evaporation is an effective method to rapidly cool-down and nucleate an aqueous solution. Concerning the practical implementation of such process, we note that an instantaneous decrease to a pre-defined vacuum pressure level as simulated here is not feasible;[178,213] if the capabilities of the freeze-drying apparatus are known, however, the boundary conditions of the model may be adjusted to match the experimentally accessible pressure profiles.

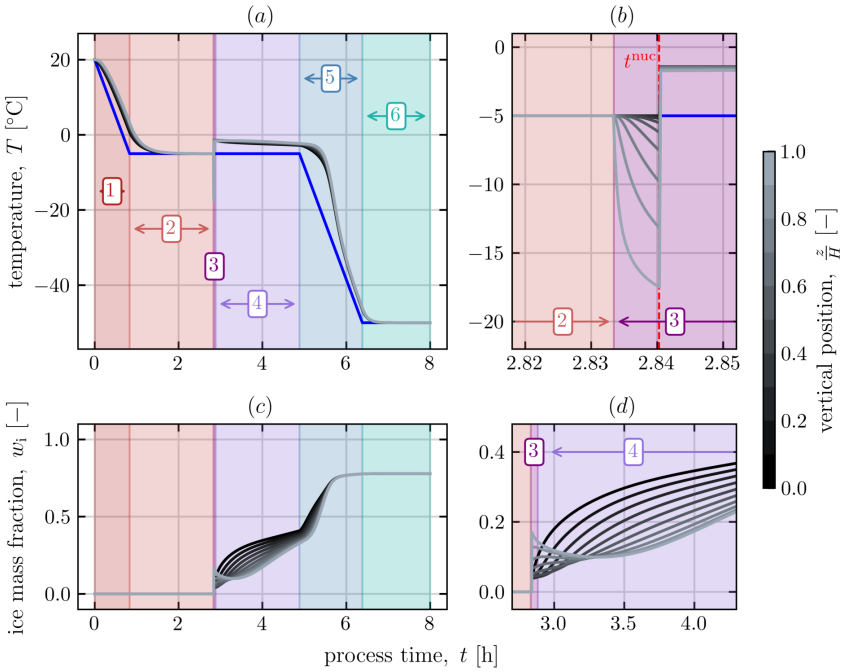

Figure 9.7 (a) Shelf temperature (blue) and product temperature at different positions (greyscale) profile during VISF, colored regions represent different process stages: (1) first ramp, (2) pre-hold, (3) vacuum, (4) post-hold, (5) ramp and (6) minimum shelf temperature stage; (b) zoom-in the temperature profile at time of nucleation; (c) ice mass fraction evolution; (d) zoom-in at the initial part of solidification.

After the vacuum stage, a second holding step follows at higher pressure to ensure complete solidification in all vials (post-hold, stage 4). This is visualized in panels (c,d), which report the ice mass fraction profile in the vial. At the time of nucleation, the largest ice fraction is observed at the top of the vial. Intriguingly, some of the ice formed at the very top during nucleation melts again to cool down the lower parts of the vial. In general, ice grows from the bottom due to the heat transfer with the shelf. Since nucleation is induced in a short amount of time, most of the solidification takes place in this stage; the solidification time can be adjusted by changing the temperature of the holding step. Finally, the temperature is ramped down to the final, minimum value of the shelf temperature (stages 5 and 6). To design an optimal vacuum-induced surface freezing process, the process parameters have to be chosen carefully, especially for the vacuum stage.

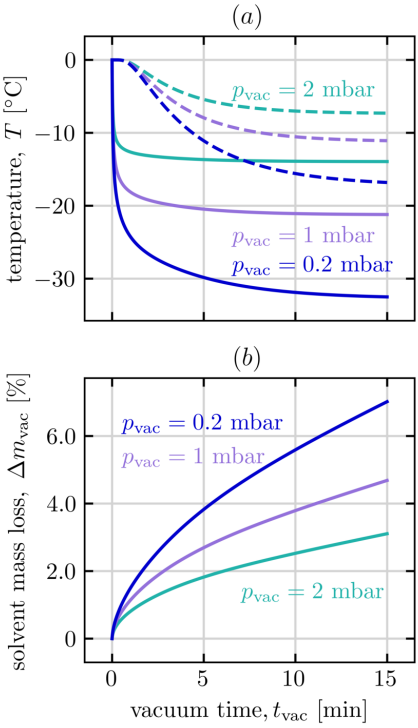

Figure 9.8 (a) Effect of vacuum pressure on the product temperature at the top of the vial (solid) and at the bottom of the vial (dashed); (b) cumulative solvent mass loss (dotted) due to the evaporative vapour flux.

The time t_{vac} and pressure p_{vac} of the vacuum are of great interest; additionally, the temperature of the shelf during stages 3 and 4 should be chosen high enough that vials do not nucleate spontaneously before vacuum is applied. Given the nucleation kinetics of the sucrose solution, a value of -5°C is chosen. Figure 9.8 shows the effects of the vacuum parameters on both thermal evolution (panel a) and evaporated mass Δm_{vac} (panel b). We consider the mass loss due to evaporation Δm_{vac} an important process attribute for two reasons. First, it provides a definite time limit to the process, given that only a finite amount of water is present. Second, the evaporation of water increases the concentration in the remaining solution, which may be detrimental to product quality. Such increase in concentration would lead to slightly slower nucleation due to the additional depression of the freezing point. To keep computational costs low, this is not considered in the model. Given that the

process is supposed to operate under conditions where the mass loss is small, this is a reasonable assumption that has also been made in earlier modeling works.[212] With respect to temperature (Figure 9.8 (a)), we note that lower pressures lead to a faster decrease in temperature, and to a lower final value of the temperature. For all studied pressure levels, eventually a steady state temperature profile is obtained. This is because the heat removed through evaporation at the top will eventually balance the heat provided through the shelf.

Similar effects are observed concerning the evaporated mass (Figure 9.8 (b)): more mass is lost in a specific amount of time, the lower the pressure. However, there is no steady state: in principle all water can evaporate. Hence, the process must be designed with the objective of limiting the evaporation of water to a reasonable extent. In practice, further operational challenges such as the possible boiling of the solution have to be accounted for as well.[213,214]

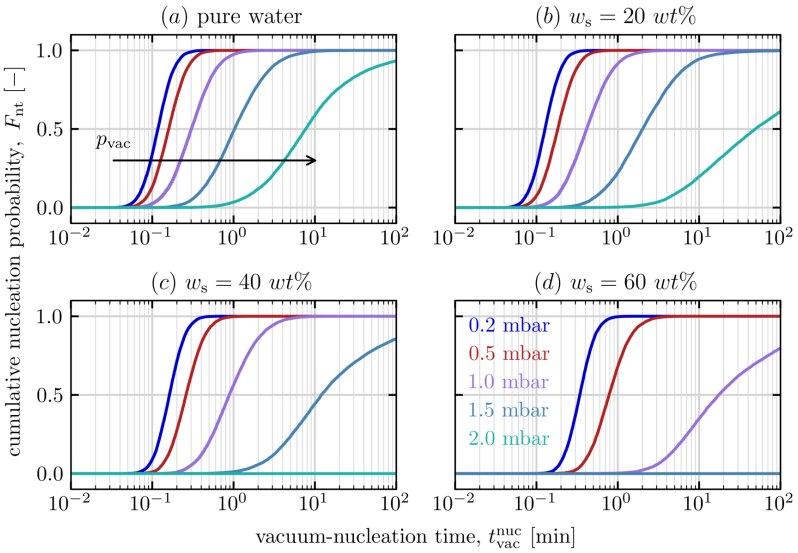

Figure 9.9 Cumulative density function of nucleation times for a VISF process subject to different solution compositions: (a) pure water, (b) 20 wt%, (c) 40 wt% and (d) 60 wt% sucrose solution. All simulations start at an initial temperature of −5°C in the vials. The shelf temperature is set to −5°C throughout the entire simulation. Different vacuum pressures are applied; in some cases, the applied vacuum pressure is incapable of inducing nucleation, hence the missing distributions, e.g., in panels (c) and (d).

Let us next assess the effect of the vacuum on the nucleation behavior. Figure 9.9 shows the nucleation time distributions obtained for four different solute concentrations (four panels) at five pressure levels each (colors). The most fundamental, and perhaps most relevant, observation is that the nucleation times are randomly distributed. While surface evaporation promotes nucleation, it does not affect its stochastic nature; rather, the rapid cooling narrows down the range of likely nucleation times. Traditionally, vacuum-induced surface freezing is considered as a deterministic technique that enables a control of the nucleation temperature.[20,178] However, this is not the case, as our simulations predict, and as recent experimental evidence has confirmed.[213,214] With respect to the nucleation temperature, we underline that the notion of a single value may be of little relevance due to the large thermal gradients; the literature typically refers to the temperature reached by the vials during the pre-hold as nucleation temperature.[62] However, as shown in Figure 9.8, the actual temperature at nucleation may be significantly lower and exhibit a strong dependency on position.

Next, we investigate the effect of pressure and solute concentration on the nucleation times (Figure 9.9). Independent of solution composition, nucleation occurs earlier when the pressure is lower. With increasing concentration, nucleation occurs later; this is because lower temperatures are required to achieve the same nucleation rates (see Eq. 9.6). For the highest concentrations, pressure levels of 1 mbar and above are unable to induce nucleation in a short amount of time, i.e., before a significant amount of water has evaporated. Importantly, this concentration-dependency of the nucleation times is in line with recent experimental observations.[213] We further note that in experimental studies involving vacuum-induced surface freezing, the pressure is continuously decreased down to a value of zero. When doing so, nucleation was reported to occur in diluted solutions in the range from 1.3 mbar down to 0.7 mbar.[214] Our simulations for pure water indicate that almost all vials nucleate at a pressure of 1 mbar within one minute, in accordance with these experimental observations. It is worth emphasizing this finding, since the simulations rely on nucleation parameters that have been estimated from jacket-ramped freezing experiments, i.e., from a different freezing process. This implies that the model provides sound predictions across different freezing processes thanks to its mechanistic character. To do so, it only requires the information on the nucleation kinetics of the formulation to be frozen and of the vacuum capabilities of the equipment.

9.5 CONCLUDING REMARKS

In this work we present a model to simulate the freezing process in a vessel, which accounts for the stochastic nature of ice nucleation and considers thermal gradients. We compared the model predictions with the largest experimental data set for freezing in vials available to date,[76] where we found a quantitative agreement between the fitted and predicted nucleation temperature distributions. With respect to pharmaceutical freezing and to freeze-drying, the following findings are of obvious relevance:

Stochasticity of nucleation: We here achieve a quantitative description of the experimentally measured nucleation behavior for freezing in vials. Doing so will promote the use of mechanistic freezing models for process design and development in pharmaceutical freezing and freeze-drying. Comparable models that consider stochastic nucleation have found widespread use in related fields such as industrial crystallization[22,66] and atmospheric sciences[27,82] already during the past decade. Most existing pharmaceutical freezing models, however, describe nucleation in a deterministic manner.[19,28,171] The models that consider stochastic nucleation[40,62] do it in a manner inconsistent with its underlying physical principles, so that they are unable to predict physically meaningful nucleation temperature (or time) distributions.[76] Hence, the mechanistic spatial model presented here, together with our earlier contributions on process-scale modeling,[74,75] provides insights into freezing that go beyond the capabilities of the existing models.

Definition of the nucleation temperature: The spatial freezing model demonstrates that the nucleation temperature as commonly referred to in the literature is an ill-defined quantity: a broad range of temperatures may be present at different positions in the vessel at the time of nucleation. Further, different positions and definitions of the nucleation temperature exhibit different trends, as shown in Section 9.4.1. Experimental studies hence should follow best practices and standardize the positions where temperatures are measured; this is commonly done in the bottom center of the vessel,[43,102] although some authors also measure the temperature at the side wall at half height,[19] or at the top.[213] Recently, non-invasive means for temperature monitoring have been used to monitor the freezing stage in pharmaceutical freeze-drying, which enable a spatially distributed measurement of the nucleation temperature;[200,203] their further use will be beneficial for scientists and practitioners in the field.

Local and global supercooling: Modeling works on freezing in the pharmaceutical context typically focus either on small volumes where global supercooling dominates,[19,28,171] or on large volumes, where local supercooling dominates.[39] Some attributes of the freezing process, such as the ice crystal

size in the frozen materials, strongly depend on the type of supercooling.[20,43] Thus, there is a need for mechanistic models that are capable of describing freezing in both cases within a single mathematically sound framework, as we do here.

Vacuum-induced surface freezing (VISF): We present the first mechanistic assessment of this emerging freezing technique that accounts for its underlying stochastic nature. We show how vacuum pressure, solute concentration, and nucleation kinetics affect the distribution of nucleation times, thus obtaining a design space for the process. We clearly demonstrate the limitations of VISF towards formulations that nucleate slowly, such as highly concentrated sucrose solutions. Hence, this study provides novel insights into how to design and to conceptualize the VISF process in a rational manner. Practitioners may use these information to identify suitable process conditions, while also considering additional challenges such as the possible boiling of the solution.[213,214]

Finally, we highlight that some of the observations reported here deviate from the commonly accepted understanding of nucleation in the pharmaceutical freezing and freeze-drying literature. For example, it has been argued that nucleation temperatures are lower when cooling faster, and that this leads to smaller mean ice crystal sizes.[20,43,223] In contrast, this contribution shows, in line with our earlier works,[74–76] that the trends of the nucleation behavior are rather complex. While it is true that faster cooling leads to lower temperatures measured at the bottom of the vial, such effect is relatively small. If the spatial distribution of temperatures is considered, the trend may reverse: the mean temperature at the time of nucleation increases when cooling faster under conditions of practical relevance. Importantly, this behavior has been observed in our earlier experimental work as well,[76] and it is quantitatively predicted by the model presented here. Hence, additional factors have to be considered in order to explain the behavior of the crystal sizes and of their distribution with respect to pharmaceutical freeze-drying.

To conclude, this work provides researchers and practitioners with novel insights into the role of stochastic ice nucleation in freezing, and it reports a systematic framework to inform process design and optimization for various freezing processes widely used in the pharmaceutical industry. The model may be connected to our earlier process-scale models of freezing,[74,75] and we provide open source access to it in the form of a python package termed *ethz-snow*.[73,186]

Part III

CRYSTALLIZATION SYSTEMS

10 CONCEPTUAL VALIDATION OF STOCHASTIC AND DETERMINISTIC METHODS TO ESTIMATE CRYSTAL NUCLEATION RATES

This work presents a generalized framework to assess the accuracy of methods to estimate primary and secondary nucleation rates from experimental data. The crystallization process of a well-studied model compound was simulated by means of a novel stochastic modeling methodology. Nucleation rates were estimated from the simulated data through multiple methods and were compared with the true values. For primary nucleation, no method considered in this work was able to estimate the rates accurately under general conditions. Two deterministic methods that are widely used in the literature were shown to over-predict rates in the presence of secondary nucleation. This behavior is shared by all methods that extract rates from deterministic process attributes, as they are insensitive to primary nucleation if secondary nucleation is sufficiently fast. Two stochastic methods were found to be accurate independent of whether secondary nucleation is present, but they underestimated rates in case a large number of primary nuclei are formed. We hence proposed a criterion to probe the accuracy of stochastic methods for arbitrary data sets, thus providing the theoretical foundations required for their rational use. Finally, we showed how both primary and secondary nucleation rates can be inferred from the same set of detection time data by combining deterministic and stochastic considerations.

10.1 INTRODUCTION

The role of nucleation in crystallization processes remains elusive due to various issues related to the measurement of nucleation rates.[22,45,70,97] Accurate knowledge of the nucleation rates is required for the rational design and

The work presented in this chapter has been reported in: Deck, L.-T.; Mazzotti, M. Conceptual Validation of Stochastic and Deterministic Methods to Estimate Crystal Nucleation Rates. *Cryst. Growth Des.* **2023**, 23, 2, 899–914.

optimization of industrial crystallization processes. Three types of nucleation may occur in stirred crystallizers, namely primary homogeneous nucleation (HON), primary heterogeneous nucleation (HEN), and secondary nucleation (SN). Numerous methods have been proposed to measure the rates of these phenomena; some of them correlate nucleation either with the first point in time when crystals are detected,[224,225] or with the evolution of the crystal size distribution and features derived therefrom,[97,226–229] or with the observation of the inherent variability of the process.[22,66,68]

Nucleation is an activated process and therefore it is stochastic.[22,64,66,76,230] Repetitions of a crystallization experiment under identical conditions hence exhibit a certain degree of variability. Conceptually, one may infer the primary nucleation kinetics by linking the experimental variability to the inherent stochasticity of nucleation.[22,66,68,231] During a crystallization process, all crystals nucleate in a stochastic manner, whereby earlier nucleation events affect later ones in two ways: first, nuclei deplete supersaturation *via* crystal growth, and second, they provide active sites for secondary nucleation. Such secondary nucleation may occur through various mechanisms, which are discussed elsewhere in detail.[71,232–235] Similar to primary nucleation, multiple types of secondary nucleation are activated processes, and their inherent stochasticity hence may contribute to the experimental variability. Thus, an accurate description of the inherent variability of a crystallization process is difficult to achieve.[66,74,215] Therefore, all widely applied stochastic methods to estimate primary nucleation are based on a strong simplification: they impose that only the first nucleus is formed in a stochastic manner so that the variability in time of the first nucleation event equals the variability in detection time.[22,68,231]

However, recent literature suggests that stochastic methods underestimate primary nucleation rates compared to more established methods based on deterministic process attributes: for *p*-aminobenzoic acid in ethanol, an underprediction of $5-6$ orders of magnitude was reported,[97] and for paracetamol in ethanol one of $2-3$ orders of magnitude.[236] Thus, some researchers argue that estimates obtained from stochastic methods should not be used in process design.[70,97,236,237] Evidence collected in this work, however, challenges this view. We find that the estimates of the stochastic method are accurate under a broad range of conditions, whereas deterministic methods over-predict rates under the same conditions due to neglecting or misinterpreting secondary nucleation.

To arrive at this conclusion, we assessed multiple methods to measure isothermal nucleation rates by means of a newly developed modeling framework, which we refer to as *stochastic particle balance model*. The model is derived in Section 10.2, together with methods to estimate nucleation rates. In Section

10.3 we simulate the crystallization of *p*-aminobenzoic acid, a compound for which some of the largest deviations in nucleation rates among measurement methods have been reported. The kinetic parameters are estimated from literature data reported by Cedeno et al[97]. In Section 10.4 we compare and assess methods to estimate nucleation rates from the simulated data sets and we critically assess their accuracy. Finally, we generalize our findings and draw the relevant conclusions in Section 10.5.

10.2 THREE ASPECTS OF NUCLEATION

In this section, we derive the stochastic modeling framework that is used to simulate a crystallization process comprising stochastic primary nucleation, stochastic secondary nucleation and deterministic crystal growth. Doing so requires a consistent description of at least three different aspects of nucleation. We first discuss phenomenological aspects in Section 10.2.1, before outlining deterministic aspects in Section 10.2.2 and stochastic aspects in Section 10.2.3. We conclude with the methodology to probe methods for the estimation of crystal nucleation rates in Section 10.2.4.

10.2.1 Phenomenological aspect

Nucleation is characterized by the nucleation frequency K, which denotes the number of nuclei formed per unit time.[22,45] The overall nucleation frequency in a process is the sum of the contributions of all relevant types:

$$K = K_{\mathrm{HON}} + K_{\mathrm{HEN}} + K_{\mathrm{SN}} = K_{\mathrm{PN}} + K_{\mathrm{SN}} \tag{10.1}$$

Homogeneous and heterogeneous rates commonly are grouped together in a single term that comprises the total frequency of primary nucleation (PN). In addition, one may define a rate of nucleation per unit volume, i.e., $B = K/V$.[22,45,238] Nucleation is an activated process, since an energy barrier has to be overcome in order to form a nucleus.[45,64,215] Thus, K may be interpreted as the product of three contributions, namely

$$K = \begin{pmatrix} \text{number of} \\ \text{sites} \end{pmatrix} \begin{pmatrix} \text{frequency of} \\ \text{attempts per site} \end{pmatrix} \begin{pmatrix} \text{probability of success} \\ \text{per attempt} \end{pmatrix} \tag{10.2}$$

Importantly, the value of each contribution may change during a crystallization process. The number of active sites for secondary nucleation may increase due to the nucleation and growth of crystals; for heterogeneous primary nucleation it may change due to the occurrence of impurities or due to deactivation. The

frequency of attempts depends on the temperature, the hydrodynamics within the reactor, and on the solution properties such as solute diffusivity.[45,65] Further, both the probability of success and the frequency of attempts are strong functions of supersaturation. Let us consider in detail what this entails for a crystallization process. The primary nucleation frequency K_{PN} in a volume V is given as:

$$K_{\mathrm{PN}} = \int_0^V J_{\mathrm{PN}}(V')\mathrm{d}V' \approx J_{\mathrm{PN}}V \tag{10.3}$$

where J_{PN} is the local primary nucleation rate defined at each location V' within the reactor. We note that the formulation of a local rate implicitly assumes that nucleation is an infinitely divisible process, i.e., that a nucleation event may occur within an infinitesimally small volume. Under the assumption of uniform conditions within the reactor volume, this expression simplifies and J_{PN} may be defined as the volume-averaged rate of primary nucleation. It is this quantity that is typically reported in the literature. We highlight that such averaging is potentially inaccurate under two conditions. First, in case of heterogeneous nucleation, nucleation events are enabled by nucleation sites on external surfaces.[68,239] These sites, however, may be distributed arbitrarily within the system.[76,240] Since external surfaces such as reactor walls may also act as nucleation sites, the primary nucleation frequency may not scale linearly with volume in real processes.[104,241] Second, process conditions may vary within the volume; thermal gradients and hydrodynamic variabilities may be present and may alter the local nucleation rate.[76,242]

Primary nucleation is commonly interpreted in the context of the classical nucleation theory (CNT).[45,65] The functional form used in this work is the one used in the experimental reference work,[97] namely

$$K_{\mathrm{PN}} = VA_{\mathrm{PN}}S\exp\left\{-\frac{B_{\mathrm{PN}}}{\ln(S)^2}\right\} \tag{10.4}$$

where A_{PN}, B_{PN} are parameters with physical meaning as discussed elsewhere.[45,65] The supersaturation level S is approximated as

$$S = \frac{c}{c^*(T)} \tag{10.5}$$

where $c^*(T)$ is the equilibrium concentration of the solute at temperature T and c the actual solute concentration.

Secondary nucleation may occur through different mechanisms, among which the dominating ones are typically not known *a priori*.[71] Potential underlying mechanisms are discussed elsewhere.[71,232–235] For simplification, it is common practice to describe secondary nucleation with power laws

that scale with either the surface area or the volume of the crystals.[45,215,228] The frequency of secondary nucleation events may be defined for a system comprising a total number of N crystals with characteristic lengths L_i as

$$K_{SN} = VB_{SN} = k_a \mu_2 V J_{SN} = k_a \left(\sum_{i=1}^{N} L_i^2 \right) J_{SN} = k_a \left(\sum_{i=1}^{N} L_i^2 \right) k_{SN,a} (S-1)^{s_a} \tag{10.6}$$

in case secondary nucleation scales with the surface area of the crystals, or as

$$K_{SN} = VB_{SN} = k_v \mu_3 V J_{SN} = k_v \left(\sum_{i=1}^{N} L_i^3 \right) J_{SN} = k_v \left(\sum_{i=1}^{N} L_i^3 \right) k_{SN,v} (S-1)^{s_v} \tag{10.7}$$

in case it scales with their volume. k_v and k_a denote the shape factors for crystal volume and surface area, respectively.[45] We applied both equations to fit secondary nucleation rates to experimental data,[97] whereby a closer agreement was observed for Equation 10.6. Thus, this expression is considered in the following.

10.2.2 Deterministic aspect

This section outlines how to mathematically describe nucleation within a crystallization process in a deterministic manner. In Section 10.2.2, we present the deterministic population balance model, before discussing deterministic methods to measure nucleation rates in Section 10.2.2.

Population balance model

Crystallization processes are characterized by the evolution of the crystal population over time. If the population is sufficiently large, it may be described by a continuous crystal size distribution $n(L)$;[45,243] $n(L)\mathrm{d}L$ is the number of crystals with a characteristic length between L and $L + \mathrm{d}L$ per unit volume of the crystallizer. The moments μ_j of such distribution are defined as

$$\mu_j = \int_0^\infty L^j n(L) \mathrm{d}L \tag{10.8}$$

A batch crystallization process comprising nucleation and growth may be simulated by tracking the evolution of the first four moments together with that of the solute concentration (see Equation 10.10):

$$\frac{\mathrm{d}\mu_0}{\mathrm{d}t} = B \tag{10.9a}$$

$$\frac{\mathrm{d}\mu_1}{\mathrm{d}t} = G\mu_0 \tag{10.9b}$$

$$\frac{\mathrm{d}\mu_2}{\mathrm{d}t} = 2G\mu_1 \tag{10.9c}$$

$$\frac{\mathrm{d}\mu_3}{\mathrm{d}t} = 3G\mu_2 \tag{10.9d}$$

Importantly, these equations are independent of the type of nucleation occurring: they hold for any arbitrary form of the volumetric nucleation rate B, whereby the size of newly formed nuclei is assumed to be zero. The evolution of the solute mass concentration in solution c over time relates to the evolution of the third moment as

$$c(t) = c_0 - k_\mathrm{v}\rho_\mathrm{c}\mu_3(t). \tag{10.10}$$

where ρ_c denotes the mass density of the crystals. The crystal growth rate G is assumed to be size-independent and to follow a power law of the thermodynamic driving force

$$G = k_\mathrm{g}(S-1)^g \tag{10.11}$$

where k_g and g are compound-specific temperature-dependent parameters. Such mathematical description of growth was chosen for the sake of simplicity, but without loss of generality. A plethora of alternate growth rate expressions have successfully been implemented in population balance models reported in the literature.[45,215]

The evolution of the crystallization process may be simulated by solving the set of moment equations coupled with the solute mass balance. Methods that estimate nucleation rates based on evolution profiles are referred to as *direct deterministic* methods. Both primary and secondary nucleation rates have been estimated in the literature by minimizing the difference between the experimental evolution of process attributes, and predictions of the population balance model.[227–229]

A simple direct method that does not require solving the population balance is to extract the primary nucleation rate from the linearized particle count profile (corresponding to μ_0), imposing that the evolution is governed by primary nucleation. We refer to this as **Method 1**.[97,236] In this work, we linearize the profile by measuring the time elapsed between reaching 25% and

75% of the final number of crystals detected at the end of the process ($\Delta t_{25,75}$), and the total number of detected crystals (N_{tot}):

$$J_{PN} = \frac{N_{tot}}{2V\Delta t_{25,75}} \tag{10.12}$$

The value of N_{tot} is subject to the sensitivity of the sensing equipment. In line with the experimental reference work,[97] we assume that all crystals larger than a size of $L_{det} = 5\mu$m are detected, whereas smaller ones are not. As pointed out recently,[244] such approach may be considered simplistic, and more advanced analytical techniques capable of detecting smaller crystals may benefit the accuracy of the method.

Deterministic view on detection times

The experimental effort required to quantitatively monitor the process evolution has motivated the development of indirect deterministic methods to estimate nucleation rates. These methods do not rely on evolution profiles, but on alternative process attributes such as the detection time (also termed induction time in the literature).[225,237] The detection time t_{det} denotes the first point in time when crystals are detected from a clear solution. t_{det} is commonly defined as the time at which a critical volume fraction of crystals, α, is reached:

$$\alpha = \frac{V_c(t_{det})}{V} = k_v \mu_3(t_{det}) \tag{10.13}$$

The value of α generally depends on the sensing equipment; a value of 10^{-4} is used as reference, as recommended by the literature.[22,215] To study the effect of α, we carry out a sensitivity study considering both larger and smaller values (see Section 10.4.1). Analytical expressions for detection times may be obtained under two conditions; namely that crystallization occurs under isothermal conditions and that the change in supersaturation before detection is negligible (i.e., S is constant). In the following, we derive detection times for two different expressions of B.

Method 2: Dominant primary nucleation (PBE-PN)

The detection time for the limiting case that only primary nucleation occurs is obtained for $B = J_{PN}$ (no secondary nucleation). Since no crystals are present at the beginning of the process ($t = 0$), the initial conditions for the moment equations are $\mu_0(0) = \mu_1(0) = \mu_2(0) = \mu_3(0) = 0$. The equations can be solved explicitly, and the evolution of the third moment is given as

$$\mu_3(t) = \frac{t^4}{4} G^3 J_{PN}. \tag{10.14}$$

Crystals are detected, when the condition of detection is met (see Equation 10.13), i.e., at:

$$t_{\mathrm{det}} = \left(\frac{4\alpha}{k_{\mathrm{v}} G^3 J_{\mathrm{PN}}} \right)^{\frac{1}{4}}, \tag{10.15}$$

which is an expression that has found widespread use in both academic literature and industrial applications.[45,70,239,245]

Method 3: Dominant secondary nucleation (PBE-SN)

If secondary nucleation occurs, the detection time is the sum of t_{n1}, which is the time required for the first nucleus to form, and of a growth time t_{g}, which denotes the period in time that is required to reach the volume fraction of detection:[215]

$$t_{\mathrm{det}} = t_{\mathrm{n1}} + t_{\mathrm{g}}. \tag{10.16}$$

Despite its rather misleading name, t_{g} comprises contributions not only of growth, but also of nucleation. In the limiting case of infinitely slow primary nucleation, only secondary nucleation and growth occur during the growth time, and an explicit expression can be derived: we do so by solving the moment equations subject to $B = k_{\mathrm{a}} \mu_2 J_{\mathrm{SN}}$. At time $t = 0$ one nucleus of zero size is present, hence the initial conditions are $\mu_0(0) = \frac{1}{V}, \mu_1(0) = \mu_2(0) = \mu_3(0) = 0$. Through the explicit solution, one obtains for $\mu_3(t)$:

$$\begin{aligned} \mu_3(t) = \frac{G}{k_{\mathrm{a}} J_{\mathrm{SN}} V} \Bigg[& \exp\left\{ (k_{\mathrm{a}} 2 G^2 J_{\mathrm{SN}})^{\frac{1}{3}} t \right\} \\ & + 2 \exp\left\{ -\frac{1}{2} (k_{\mathrm{a}} 2 G^2 J_{\mathrm{SN}})^{\frac{1}{3}} t \right\} \cos\left(\frac{\sqrt{3}}{2} (k_{\mathrm{a}} 2 G^2 J_{\mathrm{SN}})^{\frac{1}{3}} t \right) - 3 \Bigg] \end{aligned} \tag{10.17}$$

and, accordingly, the growth time t_{g} is found by imposing

$$\alpha = k_{\mathrm{v}} \mu_3(t_{\mathrm{g}}). \tag{10.18}$$

Equation 10.17 reveals an exponential relationship between crystalline volume and time, which is not the case for primary nucleation (as implied by Equation 10.15). Thus, secondary nucleation may be interpreted phenomenologically in a similar way as an autocatalytic chemical reaction.[246] Finally, we note that alternative expressions for t_{g} may be derived for seeded crystallization processes by adjusting the initial conditions accordingly.

10.2.3 Stochastic aspect

This section is dedicated to the stochastic nature of nucleation. We first derive the statistical framework for the stochasticity of a single nucleation

event in Section 10.2.3. We then generalize the statistical framework to a crystallization process comprising an arbitrary number of stochastic nucleation events in Section 10.2.3.

Stochasticity of the first nucleation event

The first nucleus in a crystallization process randomly forms at time t_{n1}. This time is a random variable with mean $E(t_{n1})$ and variance $Var(t_{n1})$. The process can exhibit two states, namely state (0), where nucleation did not take place, and state (1), where it did.[74] The probability to be in either state is $P^{(0)}(t) + P^{(1)}(t) = 1$ at any time, whereby the time evolution is governed by the Master equation according to[66]

$$\frac{dP^{(0)}}{dt} = -K(t)P^{(0)}. \tag{10.19}$$

For an initial condition of $P^{(0)}(0) = 1$, the solution of the differential equation is

$$P^{(0)}(t) = \exp\left\{-\int_0^t K(t')dt'\right\} \tag{10.20a}$$

$$P^{(1)}(t) = 1 - \exp\left\{-\int_0^t K(t')dt'\right\}. \tag{10.20b}$$

where $P^{(1)}(t_{n1})$ corresponds to the cumulative distribution function (CDF) $F(t_{n1})$ of the first nucleation time t_{n1}:

$$F(t_{n1}) = P^{(1)}(t_{n1}) \tag{10.21}$$

The probability density function (PDF) $f(t_{n1})$ is obtained via

$$f(t_{n1}) = \frac{dF}{dt_{n1}} = K(t_{n1}) \exp\left\{-\int_0^{t_{n1}} K(t')dt'\right\}. \tag{10.22}$$

Mean and variance of the random variable are inferred from the moments of the PDF:

$$E(t_{n1}) = \int_0^\infty t' f(t')dt' = \int_0^\infty t' K(t') \exp\left\{-\int_0^{t'} K(s)ds\right\} dt' \tag{10.23a}$$

$$Var(t_{n1}) = \int_0^\infty (t')^2 K(t') \exp\left\{-\int_0^{t'} K(s)ds\right\} dt' - E(t_{n1})^2 \tag{10.23b}$$

Both expressions can be solved explicitly in the case of an isothermal process at constant supersaturation until detection, i.e., $K(t) = K_{\mathrm{PN}}$ = constant:

$$\mathrm{E}(t_{\mathrm{n1}}) = \frac{1}{K_{\mathrm{PN}}} \tag{10.24a}$$

$$\mathrm{Var}(t_{\mathrm{n1}}) = \frac{1}{K_{\mathrm{PN}}^2} \tag{10.24b}$$

The nucleation frequency for such processes may be inferred directly from both mean and variance of the distribution. Specifically, we use Equation 10.24a in this work to estimate the rate of primary nucleation and refer to it as **Method 4**; this equation has found widespread adoption in the literature.[45,70,245] It is commonly termed *mono-nucleus method (MNM)*, since it imposes the immediate detection of crystallization upon formation of the first nucleus.

Practically, it is not possible to instantaneously detect the first nucleation event due to the small size of the nucleus. Detection occurs when a certain amount of crystalline matter has been formed, characterized by the critical volume fraction α. As discussed in Section 10.2.2, such detection time t_{det} comprises two contributions, namely the time of the first nucleation event t_{n1} and the growth time t_{g}. Since multiple crystals are present in most crystallization processes at detection, further nucleation events take place during the growth time; thus, t_{g} and t_{det} are random variables as well. It holds that

$$\mathrm{E}(t_{\mathrm{det}}) = \mathrm{E}(t_{\mathrm{n1}}) + \mathrm{E}(t_{\mathrm{g}}) \tag{10.25a}$$

$$\mathrm{Var}(t_{\mathrm{det}}) = \mathrm{Var}(t_{\mathrm{n1}}) + \mathrm{Var}(t_{\mathrm{g}}) + 2\,\mathrm{Cov}(t_{\mathrm{n1}}, t_{\mathrm{g}}). \tag{10.25b}$$

For an isothermal process, the expression for the variance simplifies: under this condition, t_{n1} and t_{g} are not correlated and their covariance becomes zero. Thus, the following system of equations is obtained:

$$\mathrm{E}(t_{\mathrm{det}}) = \frac{1}{K_{\mathrm{PN}}} + \mathrm{E}(t_{\mathrm{g}}) \tag{10.26a}$$

$$\mathrm{Var}(t_{\mathrm{det}}) = \frac{1}{K_{\mathrm{PN}}^2} + \mathrm{Var}(t_{\mathrm{g}}) \tag{10.26b}$$

Since $\mathrm{E}(t_{\mathrm{det}})$ and $\mathrm{Var}(t_{\mathrm{det}})$ can be estimated from a sufficiently large set of detection times, Equations 10.26 form a system of two equations in the three unknowns K_{PN}, $\mathrm{E}(t_{\mathrm{g}})$ and $\mathrm{Var}(t_{\mathrm{g}})$. With the information of detection times alone it is thus *not* possible to infer primary nucleation rates in general. Methods that do so have to rely on an additional assumption, namely:

$$\mathrm{Var}(t_{\mathrm{g}}) = 0 \tag{10.27}$$

This leads to a system of two equations in the two unknowns K_{PN} and $E(t_g) = t_g$, whereby K_{PN} is governed solely by $Var(t_{det})$. The cumulative distribution for the detection times of this system assuming isothermal conditions and constant supersaturation until detection is

$$F(t_{det}) = 1 - \exp\left\{ - K_{PN}(t_{det} - t_g) \right\}. \tag{10.28}$$

The estimation of K_{PN} based on Equation 10.28 is termed **Method 5** in this work; it is known in the literature as single-nucleus *mechanism* (SNM),[67,68,91,95] due to the similarity of Equations 10.20a and 10.28. We prefer the term single-nucleus *assumption* to highlight that the underlying assumption has been motivated by necessity, not by mechanistic considerations. Since further stochastic nucleation events may occur during the growth time, non-zero values of $Var(t_g)$ are to be expected in most crystallization processes. To date, it has not been studied how large $Var(t_g)$ is, and how its value depends on the process conditions; hence, there is a lack of validation as to whether the estimated nucleation rates are accurate. This is even more true for Method 4 that entirely neglects the growth time. We address this gap in Section 10.4 of this work.

A detailed explanation of the experimental methodology to obtain statistically relevant sets of detection times is provided in the literature.[23,24,67,68,91,101] Generally, large data sets are required due to both the measurement uncertainty and the inherent variability induced by the stochasticity.[23,91,99] This necessitates the use of experimental setups with parallelized reactors and repetitive cycles, whereby experiments are commonly carried out in stirred microvials or micro-droplets.[66–68,90] We summarize how to infer nucleation rates from such data sets in Section 10.6.1.

Stochasticity of batch crystallization (Method 6)

The statistical analysis in Section 10.2.3 focused on the nucleation of the first crystal. During a real crystallization process in a stirred vessel, millions or billions of crystals may nucleate, and all of them do so in a stochastic manner.[22,215] However, this does not necessarily imply that process attributes exhibit variability among repetitions under identical conditions. In order to observe relevant variability, a second condition has to be met, which is that nucleation has to be a *rare event*.[22,66,215] This is supported by Equation 10.24a, which states that the first nucleation time is less variable when the frequency of primary nucleation is larger.

The variability of an unseeded batch crystallization process is dominated by its early phase, when the number of crystals still is small. This is because early

crystals have more time to grow until detection and hence they contribute more to the detected crystalline mass. The random formation of the first nucleus contributes the most to it, followed by the one of the second nucleus and so on. It is worth noting that already the second nucleus has a chance to be formed through secondary nucleation instead of primary nucleation. When no crystals are present, the rate of secondary nucleation by definition is zero. It thus constitutes a rare event, like primary nucleation, at least during this early phase. As the crystal surface area increases during the process, the rate of secondary nucleation increases as well; eventually, it may become large enough to be considered as deterministic in later phases. Therefore, the contributions of both primary and secondary nucleation have to be considered in the stochastic description of an unseeded crystallization process.

Typically, secondary nucleation is not explicitly considered in the literature on stochastic nucleation, with two exceptions. Maggioni and Mazzotti[215] developed a methodology that comprises stochastic primary nucleation and deterministic secondary nucleation in the framework of a population balance model, while Unno and Hirasawa[247] studied fully stochastic systems exhibiting both stochastic primary and secondary nucleation. The model presented here builds on these works and extends them; we use it for two purposes. First, to estimate kinetic parameters for secondary nucleation and for crystal growth from experimental data,[97] which is referred to as **Method 6**. Second, to simulate a large number of crystallization processes to generate synthetic data sets that are used to estimate nucleation rates through Methods 1–5 (see Section 10.2.4).

Let us consider a time interval $[t_i, t_{i+1}]$ with $t_{i+1} = t_i + \Delta t$ during a crystallization process. The expected number of nuclei $\mathrm{E}(N_i)$ that are formed during the interval is given by

$$\mathrm{E}(N_i) = \int_t^{t+\Delta t} K(t')\mathrm{d}t' \tag{10.29}$$

where N_i is a discrete random variable, since only an integer number of nuclei can be formed. If the following three conditions hold, N_i follows a Poisson distribution:

1. In the limit of an infinitesimally short time interval either zero or one nuclei are formed. This implies first that a nucleation event may physically occur in infinitesimally short time, and second that each successful nucleation event leads to the formation of exactly one nucleus.
2. Within the time interval, nucleation events occur independently from each other. The random formation of a nucleus does not affect the probability that other nuclei are formed.

3. Within the time interval, the nucleation frequency is not affected by the number of nuclei formed. The deterministic value of the nucleation frequency computed at the beginning of the interval solely governs the probability distribution of the number of nuclei formed.

The first two conditions are subject to the molecular mechanisms of nucleation, and the literature predominantly considers them to be valid independent of Δt.[22,66,215,230,247,248] The third condition, however, is quantitatively accurate only for an infinitesimally short time interval, since the formation of a nucleus inherently affects the evolution of the nucleation frequency. Thus, the stochasticity of a crystallization process goes beyond the stochasticity of a single Poisson process. Crystallization has to be described as a step-wise inhomogeneous Poisson process comprising a large number of sufficiently short time intervals. This is commonly referred to as self-exciting point process.[22,74,75,215]

The probability that k nuclei form during a time interval follows a Poisson distribution and is

$$P_i^{(\mathrm{k})} = \frac{\mathrm{E}(N_i)^{\mathrm{k}}}{k!} \exp\left\{-\mathrm{E}(N_i)\right\}. \tag{10.30}$$

The actual number of nuclei N_i formed during the interval is obtained by drawing a random number from the corresponding Poisson distribution. Since $\mathrm{E}(N_i)$ depends on the nucleation frequency, Equation 10.30 is coupled with the constitutive equations for crystal growth, nucleation rates, and the solute mass balance (cf. Section 10.2.2). Together, these equations form a fully stochastic model for crystallization. Since it is grounded on the absolute number of crystals to form, which is an extensive and discrete property, we refer to it as a *particle balance model*; this highlights the difference to the inherently intensive and continuous deterministic *population balance model*, which is unable to depict stochasticity.

As a final note, numerical aspects of the modeling framework are discussed in more detail in Section 10.6.2, which also includes a table with all parameter values that were used in the simulations.

10.2.4 Estimating crystal nucleation rates

This work aims at probing methods to estimate the crystal nucleation rates in isothermal batch crystallization processes. Various methods have been reported for this purpose, whereby a major experimental challenge lies in the separation between primary and secondary nucleation.[45,231,245] Multiple methods have been derived and are assessed in this work, as summarized

in Table 10.1. These methods are used as follows: The stochastic particle balance model derived in Section 10.2.3 is applied to generate *in-silico* large sets of detection times and of particle count evolution profiles. Since this model considers the stochastic formation of all nuclei, it constitutes the most mechanistically grounded modeling framework of crystallization for this purpose available to date. The simulated data sets are used to estimate crystal nucleation parameters according to Methods 1, 2, 3, 4 and 5. In doing so, we conceptually validate these methods for an idealized crystallization process comprising primary nucleation, secondary nucleation, and crystal growth.

Method/Model	Underlying model	Considered phenomena	Explained in
1.Direct method for PN (direct)	Deterministic population balance with dominant PN	PN at constant S	Section 10.2.2
2.Deterministic method for PN (PBE-PN)	Deterministic population balance with dominant PN	Deterministic PN and crystal growth at constant S	Section 10.2.2
3.Deterministic method for SN (PBE-SN)	Deterministic population balance with dominant SN	Single stochastic PN event followed by deterministic SN and crystal growth at constant S	Section 10.2.2
4.Mono-nucleus method for PN (MNM)	Mono-nucleus assumption (no growth time)	Single stochastic PN event with immediate detection	Section 10.2.3
5.Single-nucleus method for PN (SNM)	Single-nucleus assumption (constant growth time)	Same as for Method 3	Section 10.2.3
6.Stochastic simulation of crystallization	Stochastic particle balance	Stochastic PN and SN, and deterministic crystal growth at time-dependent S	Section 10.2.3

Table 10.1 Summary of the six modeling methods used in this work. Methods 1, 2, 3, 4, 5 are applied to estimate nucleation kinetics from data sets generated *in-silico* by Method 6.

To ensure that this validation is of practical relevance, physically meaningful values have to be chosen for the kinetic parameters in the stochastic particle balance model. We select para-aminobenzoic acid as model compound due to the broad literature available on its crystallization behavior,[249,250] and because of the widely diverging primary nucleation parameters reported in the literature.[97] Importantly, the unseeded isothermal batch crystallization process of this compound has been characterized in great detail experimentally by Cedeno et al.[97] in a solvent mixture of water and ethanol; we use this data to estimate the kinetic parameters for primary nucleation through Method 5, and the kinetics for secondary nucleation and crystal growth trough Method 6. This is discussed in detail in Section 10.6.3.

10.3 STOCHASTIC SIMULATIONS OF CRYSTALLIZATION

In this section, we present stochastic simulations of the crystallization of para-aminobenzoic acid in water/ethanol generated *via* the stochastic particle balance model derived in Section 10.2.3 (Method 6). Simulations comprise primary nucleation, secondary nucleation, and crystal growth; a similar set of simulations in the absence of secondary nucleation is presented in Section 10.6.4. To accurately capture the variability of the process, 16384 independent simulations of the system were carried out. Such large number was required to generate figures with smooth probability distributions. Figure 10.1 shows the time evolution of the number of detected crystals (panel (a)) as well as of all crystals (panel (b)) formed. When considering such evolution profiles, crystals are considered to be detected when they reach a critical size of $L_{\text{det}} = 5\mu\text{m}$.[97] Figure 10.2 highlights the variability in three process attributes. Figure 10.3 finally shows the absolute number of primary nuclei formed for this system.

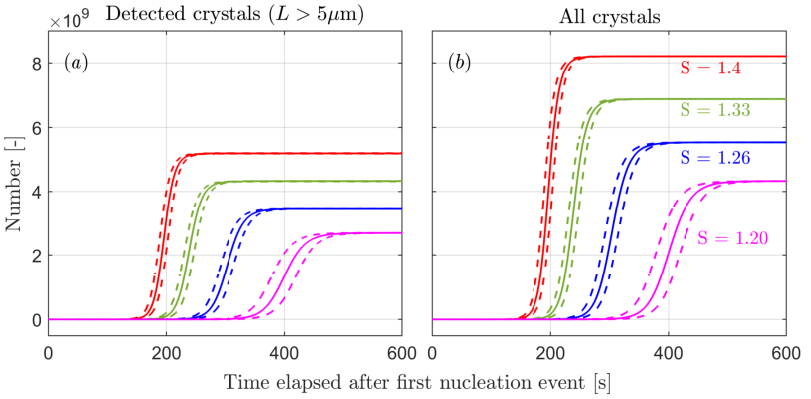

Figure 10.1 Characterization of the reference system: Evolution of the system after the first nucleation event. (a) Total number of detected crystals, i.e., of those with a size larger than $L_{\text{det}} = 5\mu\text{m}$. (b) Total number of crystals, i.e., including those smaller than the detection threshold. The colors indicate the four supersaturation levels studied by Cedeno et al.[97]: S = 1.40 (red), S = 1.33 (green), S = 1.26 (blue), and S = 1.20 (magenta). The solid lines indicate the simulation corresponding to the median detection time, while the dashed lines show the profiles for the simulations corresponding to the 10% and 90% quantiles of the detection time distribution.

Let us first consider the evolution of the process, as shown in Figure 10.1. The figure illustrates the total number of detected crystals and of all crystals *vs.* time elapsed after the first nucleation event. The solid lines

correspond to the simulation that exhibited the median detection time; the dashed lines correspond to the simulations with the 10% and 90% quantiles of the detection time distribution. For all supersaturation levels, variability due to the stochasticity of nucleation is observed; more so for the lower supersaturation levels. Importantly, the variability shown in the figure is the one due to stochastic nucleation events *after* the first one. Such variability is commonly neglected in the literature, and it is worth underlining that the stochastic particle balance model is capable of quantifying it; this is a prerequisite to assess the accuracy of stochastic methods for the estimation of primary nucleation rates (cf. Section 10.4).

With respect to the shape of the evolution profile, one clearly observes a lag time, the duration of which becomes shorter with increasing supersaturation. This is because both crystal growth and nucleation are faster at higher supersaturation. Furthermore, the total number of crystals present increases with supersaturation, up to a total value of about five billions of detected crystals for the highest supersaturation. While the lag time clearly exhibits stochasticity, both the total number of crystals formed and the slope of the profile can be considered deterministic. This finding agrees with the theoretical considerations made in Section 10.2.3: the lag time is governed by the early phase of the process, where nucleation still is a rare event; the other attributes are governed by later stages of the process, where nucleation is not rare anymore and thus deterministic.

Next, we investigate the variability of the process in detail. Figure 10.2 shows the variability in three characteristic times in the form of probability density functions: namely the induction/detection time (left), the first nucleation time (center), and the growth time (right). A value of $\alpha = 10^{-4}$ is considered as condition of detection. As discussed in Section 10.2.3, the detection time is the sum of first nucleation time and of growth time. With respect to detection times, we notice a broad distribution for the lowest supersaturation (magenta), and narrower ones with increasing supersaturation. This is indeed in line with the observations made in the literature,[97] and with the theory derived in Section 10.2.3. Since both mean and variance of the detection time depend on the primary nucleation frequency, both values are to decrease with increasing supersaturation. This effect can be observed even more clearly in the first nucleation times (center). Here, the typical shape of the exponential distribution is obtained for all supersaturation levels, and both mean and variance decrease with supersaturation. With respect to the growth time (right), we also observe shorter times and less variability for higher supersaturation levels. However, the supersaturation-dependency of the growth time is weaker than the one of the first nucleation time; this is due to secondary nucleation being less dependent on supersaturation than primary nucleation. As a

consequence, the growth time contributes considerably to the variability in detection times, especially at high supersaturation levels.

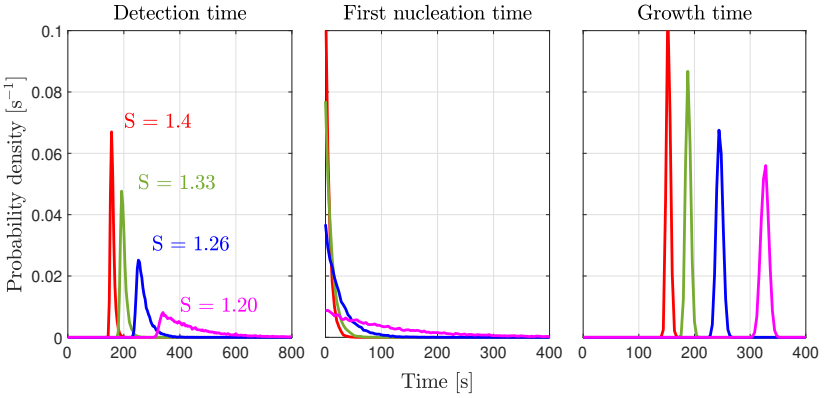

Figure 10.2 Characterization of the reference system: Distribution of the detection times (left), and of its components, i.e., of the first nucleation times (center) and of the growth times (right). A total of 16384 crystallization processes were simulated to generate the distributions. The colors indicate the four supersaturation levels studied by Cedeno et al.[97]: S = 1.40 (red), S = 1.33 (green), S = 1.26 (blue), and S = 1.20 (magenta).

Here, we have to highlight one important feature of the stochastic particle balance model: it provides information on the number of crystals formed by each type of nucleation, which is an information that is inaccessible through experiments. Figure 10.3 shows the number of primary nuclei formed. The dashed lines indicate the number of primary nuclei at the end of the process, whereas the solid lines denote the number present at the detection time. We posit that the latter is more insightful, since the methods to measure nucleation discussed in this work are based on detection times. At all supersaturation levels more than one primary nucleus is formed, and the number increases with supersaturation. The overall number of primary nuclei is small; below 50 in all simulations. Since Figure 10.1 shows that billions of crystals are formed during the process, secondary nucleation can be considered the dominant mechanism of nucleation.

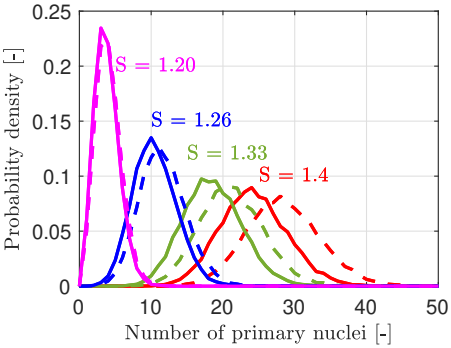

Figure 10.3 Characterization of the reference system: Number of primary nuclei formed in the 100 mL system. A total of 16384 crystallization processes were simulated to generate the distributions. The dashed lines indicate the number of crystals formed by primary nucleation at the end of the process, the solid lines show the number at the detection time. The colors indicate the four supersaturations studied: S = 1.40 (red), S = 1.33 (green), S = 1.26 (blue), and S = 1.20 (magenta).

To conclude this section, we compare the number of nuclei formed (Figure 10.3) with the detection times shown in Figure 10.2; we find that the variability in detection times decreases with increasing number of primary nuclei. For the highest supersaturation ($S = 1.40$), about 25 primary nuclei are present at detection in average and the variability in detection times is practically negligible. For the lowest supersaturation ($S = 1.20$), about 3 primary nuclei are formed in average and a pronounced variability in detection times can be observed. It follows that a crystallization process has to comprise a small absolute number of primary nucleation events in order to exhibit relevant variability. This is in line with the general understanding that nucleation has to occur as a *rare event* to observe variability. Intriguingly, only the number of primary nucleation events is small, whereas billions of crystals are formed through secondary nucleation. As discussed in the following sections, the number of primary nuclei governs the extent of variability present, and in turn it is related to the accuracy of various methods to infer nucleation rates from experimental data.

10.4 ASSESSING METHODS TO MEASURE NUCLEATION RATES

In this section, we assess the methods to estimate nucleation rates that were derived in Section 10.2: we first compare four methods to estimate the rate of

primary nucleation in Section 10.4.1. The study considers the effect of multiple process conditions, i.e., of crystallizer volume, supersaturation level, condition of detection, and with/without secondary nucleation. The findings motivated a more detailed characterization of deterministic methods (Methods 1 and 2) in Sections 10.4.2 and 10.4.3 and of the more accurate stochastic method (SNM, Method 5) in Section 10.4.4.

For every process condition, 4096 simulations were carried out. We underline that experimental data sets typically comprise only about 80–120 data points, which is considered large enough to estimate the variability in detection times with sufficient accuracy;[68,70] however, some experimental uncertainty remains at this data set size.[23,24] Hence, we simulate larger data sets to be able to quantitatively compare sets of simulations generated under different process conditions without relevant error due to the limited size of the data set.

10.4.1 Comparison of the methods

Figure 10.4 reports the computed primary nucleation rates estimated using Methods 1, 2, 4, and 5 for a broad range of crystallizer volumes at a supersaturation of $S = 1.40$. We limit this study to a single supersaturation level, since similar trends were obtained at all levels in the range of $1.20 < S < 1.40$, i.e., in the range that was studied experimentally by Cedeno et al[97]. We carried out two sets of simulations, one with secondary nucleation (Figure 10.4 (a,c)), and one without it (Figure 10.4 (b,d)). The color-coding corresponds to the condition of detection. Method 1 depends on the size L_{det} at which crystals are detected, for which values of $L_{\mathrm{det}} = 5\mu$m (red, reference) and $L_{\mathrm{det}} = 0$ (dark red) have been studied. Methods 2,4 and 5 depend on α, i.e., the critical volume fraction required for detection. Four values have been considered: 10^{-2} (dark blue), 10^{-3} (light blue), 10^{-4} (red, reference), and 10^{-5} (yellow). We observe the following:

Method 1 (direct): In the presence of secondary nucleation, this method strongly over-predicts the rate of primary nucleation (true value, black) in all volumes; this is because the particle count evolution that is used to estimate the rate does not distinguish between primary and secondary nucleation. All crystals that are detected are interpreted as primary nuclei; hence the method overestimates the rate of primary nucleation more, the faster secondary nucleation is. With respect to the condition of detection, a lower nucleation rate is obtained for the larger value of L_{det}. This implies that a relevant fraction of crystals does not grow beyond the critical size of $L_{\mathrm{det}} = 5\mu$m. The corresponding evolution profiles shown in Figure 10.1 confirm this behavior. Hence, a small value of L_{det} is required to ensure that no crystals are missed when esti-

mating the nucleation rate. We must note, however, that the underestimation due to a non-zero value of L_{det} is small compared to the overestimation due to secondary nucleation.

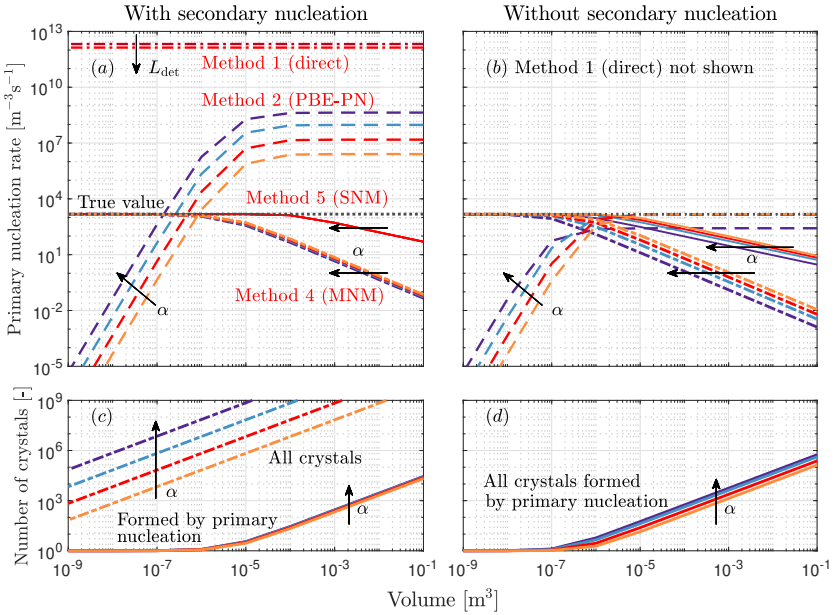

Figure 10.4 Estimating primary nucleation rates by means of deterministic (Methods 1 and 2) and stochastic methods (Methods 4 and 5) for the supersaturation level of S = 1.40. The black line indicates the true value of the primary nucleation rate, i.e., the one used to generate the simulations. Panel (a) shows the rates estimates for a process comprising primary nucleation and secondary nucleation, as presented in Section 10.3. Panel (b) shows the estimates for a simplified crystallization process in which only primary nucleation, but no secondary nucleation occurs. Panels (c,d) show the mean number of crystals present at the detection time, which depends on the value of α. Note that all crystals are formed through primary nucleation, if secondary nucleation is absent. The colors indicate the four values of the detection threshold α (Methods 2,4 and 5): 10^{-2} (dark blue), 10^{-3} (light blue), 10^{-4} (red, reference value), and 10^{-5} (yellow). For Method 1, they denote the value of the detection threshold L_{det}: 5μm (red, reference value) and 0 (dark red).

In the absence of secondary nucleation, quantitatively accurate primary nucleation rates were obtained for both values of L_{det}. They are not shown in Figure 10.4 (b), because the lines would completely overlap with other lines. It is worth noting that the method was not applied to volumes smaller

than 10 mL, since the number of crystals formed was too small to define a meaningful evolution profile (see Figure 10.4 (d)). Without secondary nucleation, quantitative accuracy of the method was expected, at least for $L_{\text{det}} = 0$. The method remains accurate for $L_{\text{det}} = 5\mu\text{m}$, because the primary nucleation rate is a stronger function of the supersaturation than the growth rate: at the time, when the last crystal nucleates, the supersaturation level is still high enough to ensure that this crystal can grow to a size of $L_{\text{det}} = 5\mu\text{m}$. These findings imply that the method can be used to estimate the primary nucleation rate accurately and in a robust manner, if no secondary nucleation occurs. Otherwise, the method should not be used, as the true will be strongly overestimated.

Method 2 (PBE-PN): Similar to Method 1, Method 2 overestimates rates in the presence of secondary nucleation (Figure 10.4 (a)), and it is accurate in its absence (Figure 10.4 (b)). However, the over-prediction is limited to large volumes, where the estimates are about four orders of magnitude too large, compared to nine orders of magnitude for Method 1. The reason for this is that the detection times used in Method 2 are more sensitive to primary nucleation than the slope of the particle count evolution used in Method 1. With respect to the value of α, we find that the method is more accurate for smaller values: this is especially prominent in the case of $\alpha = 10^{-2}$ in the absence of secondary nucleation, where rates are underestimated in all volumes. This is because the supersaturation is depleted considerably *before* detection occurs. Since such depletion is not considered by the method, rates are underestimated. Let us now consider the behavior in small volumes where the estimates increase with volume: a transition to this regime occurs at a volume of about 100 mL in the presence of secondary nucleation and of 10 mL in its absence. A comparison with Figure 10.4 (c,d) reveals that this corresponds to the transition from a regime where only a single primary nucleus is formed to a regime with a large number of primary nuclei. Since the method is derived from the deterministic population balance, it is based on the underlying assumption that the population of crystals is large enough that it can be described as a continuous entity. Hence it is unable to correctly interpret processes where only a single primary nucleus is formed. In this regime, a decrease in volume leads to an increase in detection time (see Section 10.6.6). The model cannot capture this, and instead predicts smaller and smaller rates with decreasing volume.

Method 5 (SNM): This stochastic method was found to be accurate in small volumes independent of whether secondary nucleation is present or not. It becomes inaccurate in large volumes, where a large number of primary nuclei are formed. This implies two things. First, that the stochastic formation of primary nuclei after the first one creates relevant variability in detection times:

ignoring it leads to the observed under-prediction. Second, that the stochastic formation of secondary nuclei does not contribute to the overall variability to a relevant extent: in the volume-range, where only a single primary nucleus forms, the method is accurate independent of how many secondary nuclei are formed. Secondary nucleation, however, does have some effect on the accuracy of the method: for the same number of primary nuclei formed, the method is slightly more accurate in the presence of secondary nucleation than in its absence. These aspects are discussed in Section 10.4.4. Finally, we note that the rate estimates are practically independent of the volume fraction of detection α: in the presence of secondary nucleation, the effect of α is sufficiently small that the corresponding lines overlap. This is because an earlier or later detection of crystals is accounted for by the method in the value of the growth time. A larger value of α results in longer growth times and in a larger number of crystals present at detection (Figure 10.4 (c,d)), but it affects the estimated nucleation rate only slightly.

Method 4 (MNM): This method exhibits similar trends as Method 5 (SNM), but it underestimates the rate more strongly in large volumes. The threshold volume for accuracy is smaller than for Method 5, because the underlying mono-nucleus assumption is more stringent than the single-nucleus assumption used to derive Method 5. The single-nucleus assumption imposes that the growth time after the first nucleation event is constant, whereas the mono-nucleus assumption imposes that it is zero. Method 4 is thus accurate only in the limiting case that $t_{n1} \gg t_g$. Since no growth time is considered, the estimates depend more on the value of α than those of Method 5. Small values of α are beneficial, since they correspond to conditions where the actual growth time is short; hence neglecting it has a smaller effect on the accuracy.

Having studied the accuracy of the four methods, we find that none of them is accurate under all conditions; that is, both with and without secondary nucleation and independent of volume. In sufficiently small volumes, the stochastic Method 5 (SNM) should be considered as the method of choice, since it is not affected by the presence of secondary nucleation unlike the deterministic Methods 1 and 2. Furthermore, it is in general more accurate than Method 4 (MNM). In large volumes, however, no method was accurate in the presence of secondary nucleation. Thus, we study three questions in the following: first, we investigate whether one could conceive an alternative deterministic method for primary nucleation that is not affected by secondary nucleation (Section 10.4.2). Then, we consider whether deterministic methods such as Method 3 may be used to estimate the rate of secondary nucleation in Section 10.4.3. Finally, we study in detail why the stochastic Method 5 is inaccurate in large volumes in Section 10.4.4.

10.4.2 Deterministic methods for primary nucleation

The deterministic methods (Methods 1 and 2) were found to over-predict the rate of primary nucleation in case secondary nucleation is present. Stochastic methods are still able to provide accurate estimates in the limit of small volumes, i.e., when only a few primary nuclei are formed in average (cf. Section 10.4.1). In large volumes, however, there is a need for an alternative method that is accurate. We thus investigate whether such method may be derived from deterministic considerations.

To this end, we carried out the sensitivity study illustrated in Figure 10.5, focusing on the process behavior in case primary nucleation were faster. The slowest case (solid lines) corresponds to the reference kinetics, and we compare the particle count evolution with systems exhibiting 10^2 times (dashed lines), 10^4 times (dotted lines), 10^6 times (dash-dotted lines), 10^8 times (solid lines), and 10^{10} times (dashed lines) faster primary nucleation kinetics, simulated by a corresponding increase in the value of the pre-exponential parameter A_{PN}.

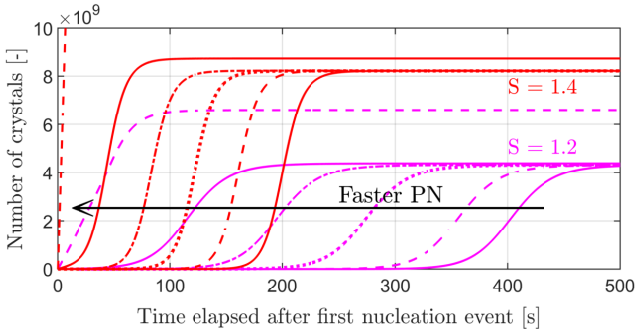

Figure 10.5 Effect of the primary nucleation rate on process behavior. Six sets of increasingly fast primary nucleation are shown for two supersaturation levels: $S = 1.40$ (red) and $S = 1.20$ (magenta). The slowest primary nucleation kinetics (solid lines) corresponds to the reference values, while faster kinetics have been evaluated by using larger values of the pre-exponential parameter A_{PN}: 10^2 times larger (dashed lines), 10^4 times larger (dotted lines), 10^6 times larger (dash-dotted lines), 10^8 times larger (solid lines), and 10^{10} times larger (dashed lines).

An increase of up to six orders of magnitude in primary nucleation rate does not significantly affect the process behavior with respect to deterministic attributes such as the shape of the evolution profile or the final number of crystals. When increasing the primary nucleation rate by eight orders of magnitude, a minor change in process behavior is observed for the supersaturation

of $S = 1.40$, i.e., a larger number of crystals. For $S = 1.20$, an increase in ten orders of magnitude is required to induce a relevant change. While this analysis focuses on the particle count profile, similar observations were made for alternative process attributes such as the shapes of the evolution profiles for concentration and particle size distribution (not explicitly shown). We conclude that most process attributes are governed predominantly by secondary nucleation in case it is present at a relevant rate, and not by primary nucleation. From a mathematical point of view, any parameter estimation method based on such attributes is thus bound to fail. The detection time is the only attribute sensitive to primary nucleation, i.e., it is shorter when primary nucleation is faster. The reason for this is that primary nucleation has a stronger effect on the early phases of crystallization, when the rate of secondary nucleation is small, compared to later phases. However, as discussed before, the deterministic method based on detection times (i.e., Method 2) is unable to yield accurate primary nucleation rates.

Therefore, we generalize these observations by arguing that deterministic methods to measure primary nucleation rates generally should not be applied to systems in which secondary nucleation dominates. While such statement may appear to be obvious, we emphasize two points: First, deterministic methods are still predominantly used in the literature to estimate primary nucleation rates, even from unseeded batch experiments.[70,228,251–253] Second, in general it is not known *a priori*, which type of nucleation dominates in a crystallization process. For example, Cedeno et al.[97] assumed that primary nucleation dominates in the reference work and extracted primary nucleation rates directly from the particle count evolution with a method similar to Method 1. This highlights the need for a simple and robust experimental approach to probe whether relevant secondary nucleation takes place. We discuss in Section 10.6.7 that experiments based on single-crystal seeding may provide this information.

If secondary nucleation dominates, and the volume is too large for an accurate application of the stochastic Methods 4 and 5, primary nucleation rates cannot be estimated accurately. Hence, process conditions have to be modified to enable accurate estimates; the volume of the crystallizer may be decreased to apply a stochastic method, or the rate of secondary nucleation may be decreased by adjusting operating conditions such as the intensity of stirring.

10.4.3 Deterministic methods for secondary nucleation

Deterministic methods for primary nucleation rates have been found to be inaccurate in the presence of secondary nucleation. Here, we study whether

the rate of secondary nucleation may be estimated in a deterministic manner. Let us first consider the method based on detection times (Method 3). Figure 10.6 (a) shows the obtained nucleation rates for all four supersaturation levels in different volumes. Figure 10.6 (b) reports the same data plotted *vs.* the mean number of primary nuclei formed instead of *vs.* volume.

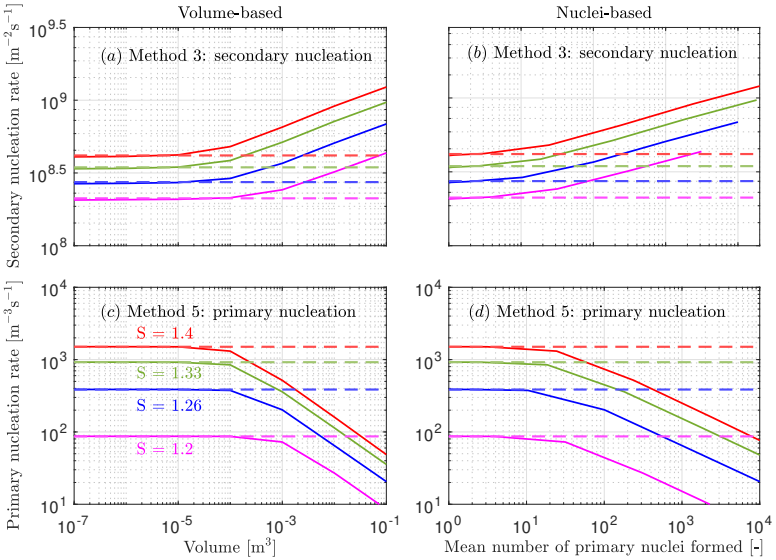

Figure 10.6 (a,b) Secondary nucleation rates obtained using the deterministic expression for the growth time (cf. Equation 10.18), Method 3. (c,d) Primary nucleation rates obtained through the stochastic Method 5. The colors indicate the four supersaturations studied: S = 1.40 (red), S = 1.33 (green), S = 1.26 (blue), and S = 1.20 (magenta). The dashed lines denote the true values of the nucleation frequency. (a,c) Plotted versus crystallizer volume. (b,d) Plotted versus mean number of primary nuclei formed.

Accurate rates are obtained at all supersaturation levels in sufficiently small volumes. Rates are over-predicted, however, in large volumes. The threshold shifts towards smaller volumes for increasing supersaturation levels. The reason for this lies in the number of nuclei formed: in the limit of a single primary nucleus, rates are estimated accurately independent of supersaturation, since the crystallization process is well described by the underlying assumptions of the method. The more primary nuclei formed, the stronger the over-prediction. This implies that the number of primary nuclei is a more useful measure of the accuracy of the nucleation rate estimate than the system's volume, as illustrated in Figure 10.6(b). Figure 10.6 (c,d) provide for comparison the

estimated rates of primary nucleation using the stochastic Method 5 for the same supersaturation levels. Intriguingly, Methods 3 and 5 exhibit the same range of accuracy, implying that they can be combined to obtain a complete understanding of nucleation in the limit of a single primary nucleus. To the best of our knowledge, such combined estimate from detection times has not yet been proposed in the literature. We thus consider it a promising avenue for future work.

In case multiple primary nuclei form, alternative deterministic methods may be applied to estimate the kinetics of secondary nucleation. As discussed in Section 10.4.2, process attributes are dominated by secondary nucleation if it occurs at a relevant rate. For example, the evolution of the particle count may be fitted to predictions of either the deterministic population balance model or of the stochastic particle balance model (Method 6). This, however, requires prior knowledge of the primary nucleation kinetics, e.g., obtained through the stochastic method (Method 5) in a smaller volume where only one primary nucleus is formed. This combination of Methods 5 and 6 is the approach that we have chosen to extract the reference kinetic parameters from the experimental data reported in the literature.[97] We describe the procedure in more detail in Section 10.6.3.

10.4.4 Stochastic methods for primary nucleation

The stochastic Methods 4 and 5 enable an accurate estimation of the primary nucleation rate in the presence of secondary nucleation, i.e., under conditions where deterministic methods fail (see Figures 10.4 and 10.6). However, their accuracy is limited to small volumes, and this section is dedicated to investigate this behavior. We focus on Method 5, since it is more accurate than Method 4. We first consider the accuracy of the predicted nucleation rates at different supersaturation levels in Figure 10.6 (c,d). The behavior closely mirrors the one of Method 3 for secondary nucleation: nucleation rates are accurately estimated in the limit of small volumes. They increasingly deviate from the true value with increasing volume, and with increasing supersaturation. At all supersaturation levels, accurate rates are estimated when only a single primary nucleus forms. We also studied the accuracy of the primary nucleation parameters estimated from these rates, where we observed the same volume-dependency of the accuracy (see Section 10.6.5).

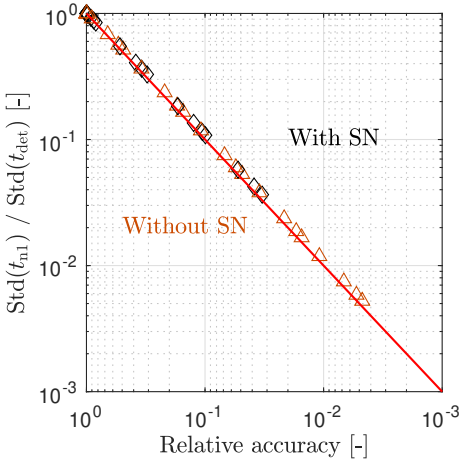

Figure 10.7 Scatter plot comprising all process conditions studied in this work, i.e., nine volumes, four supersaturation levels, and with/without secondary nucleation. For each condition, both the value of the standard deviation ratio and the relative accuracy are shown. The relative accuracy was computed as the ratio of the estimated value for the nucleation rate and the true value. The red line indicates the diagonal.

We continue this analysis by quantifying the conditions for accuracy of the method. The relative accuracy of Method 5, termed $j_{\mathrm{PN}}^{\mathrm{M5}}$, may be defined as follows:

$$j_{\mathrm{PN}}^{\mathrm{M5}} = \frac{J_{\mathrm{PN}}^{\mathrm{M5}}}{J_{\mathrm{PN}}^{\mathrm{true}}} = \frac{K_{\mathrm{PN}}^{\mathrm{M5}}}{K_{\mathrm{PN}}^{\mathrm{true}}} = \left(\frac{\mathrm{Var}(t_{\mathrm{n1}})}{\mathrm{Var}(t_{\mathrm{det}})}\right)^{0.5} = \frac{\mathrm{Std}(t_{\mathrm{n1}})}{\mathrm{Std}(t_{\mathrm{det}})} \tag{10.31}$$

Here, $J_{\mathrm{PN}}^{\mathrm{M5}}$ denotes the estimated value of the nucleation rate through Method 5, and $J_{\mathrm{PN}}^{\mathrm{true}}$ its true value. The relations between nucleation frequency and variance are given by Equations 10.26 and 10.27. To confirm the validity of Equation 10.31, Figure 10.7 reports the relative accuracy (computed as $\frac{J_{\mathrm{PN}}^{\mathrm{M5}}}{J_{\mathrm{PN}}^{\mathrm{true}}}$) and the standard deviation ratio $\frac{\mathrm{Std}(t_{\mathrm{n1}})}{\mathrm{Std}(t_{\mathrm{det}})}$ for all process conditions that were studied in this work. The two quantities are strongly correlated, confirming that the accuracy of the stochastic Method 5 can be probed quantitatively through the standard deviation ratio: the method is accurate if it assumes a value of one, and it underestimates the true nucleation rate in case it is smaller.

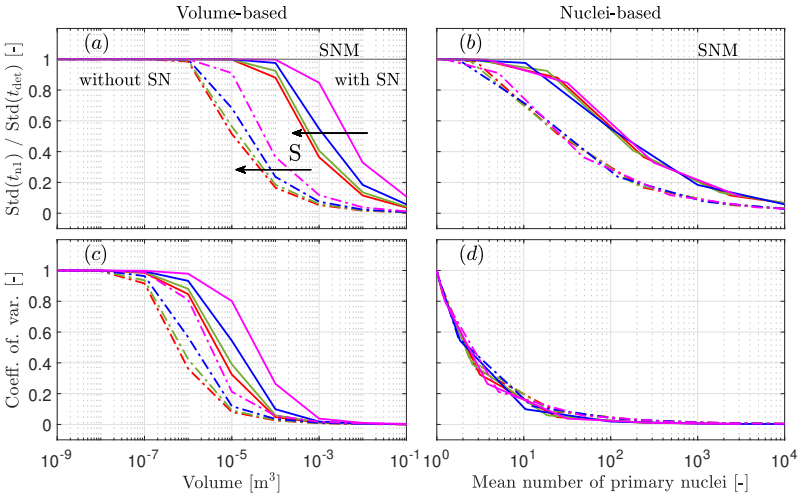

Figure 10.8 (a,b) Standard deviation ratio of first nucleation time and of detection time for nine volumes and four supersaturation levels. Simulations were carried out both in the presence and in the absence of secondary nucleation. (c,d) Coefficient of variation for the same data sets. (a,c) Volume-based plots. (b,d) Number of nuclei-based plots. The solid black line at a value of one indicates the theoretical value corresponding to the single-nucleus assumption (SNM).

To this end, Figure 10.8 reports the standard deviation ratio as a function of crystallizer volume (panel (a)) and of the mean number of primary nuclei formed (panel (b)); the colors indicate the studied supersaturation levels, and the line type the presence (solid) or absence (dash-dotted) of secondary nucleation. A value of one is observed in sufficiently small volumes and for sufficiently small numbers of nuclei in all cases, in line with the behavior observed in Figure 10.6. In larger volumes and for a large number of primary nuclei, the ratio approaches a value of zero in all cases, underlining the limitations of the method. For a given volume or number of nuclei, the standard deviation ratio is larger in the presence of secondary nucleation than in its absence. With respect to the effect of supersaturation, the lines for all levels overlap if the standard deviation ratio is plotted as a function of the number of nuclei. This again confirms that the number of primary nuclei formed is a more useful predictor of the method's accuracy than the volume. For a given number of primary nuclei, the standard deviation ratio is larger in the presence of secondary nucleation than in its absence. To appreciate this effect, one needs to consider that within an experiment early primary nuclei contribute more to the observed variability in detection times than later ones

(cf. Section 10.2.3). In the presence of secondary nucleation, early primary nuclei are even more dominant, since their daughter crystals compete with the later primary nuclei in depleting the supersaturation. Even if many primary nuclei form in the presence of secondary nucleation, the early ones retain a dominant effect on the overall variability. In turn, the stochastic Method 5 is more accurate in the presence of secondary nucleation for a given number of primary nuclei. For this reason, the standard deviation ratio in the absence of secondary nucleation may be considered as a robust *worst case* predictor of the method's accuracy.

However, we note that both the standard deviation ratio and the number of primary nuclei formed are accessible only through simulations, but not through experiments. In order to probe the method's accuracy when applying it to experimental data, an experimentally accessible validation criterion is required. Specifically, such criterion has to be based on features of the detection time distribution, since no information on the first nucleation time are available. Hence, we studied whether the coefficient of variation of detection times can be used as validation criterion. It is defined as

$$\text{Coeff. of var.} = \frac{\text{Std}(t_{\text{det}})}{\text{E}(t_{\text{det}})} = \frac{\sqrt{\text{Var}(t_{\text{n1}}) + \text{Var}(t_{\text{g}})}}{\text{E}(t_{\text{n1}}) + \text{E}(t_{\text{g}})} = \frac{\sqrt{K_{\text{PN}}^{-2} + \text{Var}(t_{\text{g}})}}{K_{\text{PN}}^{-1} + \text{E}(t_{\text{g}})} \tag{10.32}$$

assuming isothermal conditions. Conceptually, the coefficient is to approach a value of one in sufficiently small volumes and for small numbers of primary nuclei formed: this is because under this condition, the detection time is dominated by the features of the first nucleation time. In the limit of large volumes and of large numbers of primary nuclei, the coefficient approaches a value of zero. In this case, all quantities are to approach zero except the mean value of the growth time in the denominator, which is volume-independent (see Section 10.6.6). To this end, Figure 10.8 (c) shows the coefficient as a function of crystallizer volume, and Figure 10.8 (d) as a function of the mean number of primary nuclei formed. In both cases, the trends for the coefficient are in line with expectations. We further note that the lines for all process conditions overlap if the coefficient is plotted vs. the number of primary nuclei formed. This if of great relevance, since it provides strong evidence that the coefficient of variation may be used to probe the mean number of primary nuclei formed in a way that is independent of the actual crystallization kinetics of the system. As a consequence, the coefficient of variation may be used as a measure for the accuracy of the method. As reported in Figure 10.8 (b), a standard deviation ratio of about 0.9 is obtained when about 5 primary nuclei form in the absence of secondary nucleation. Hence, we consider the method to be accurate when 5 or fewer primary nuclei form. According to Figure

10.8 (d), this corresponds to a coefficient of variation of about 0.25, which we define as experimental criterion for quantitative accuracy. To conclude, we recommend that future studies involving any of the Methods $2-5$ report the value of the coefficient of variation. This will aid both practitioners and readers to assess the accuracy of the reported nucleation rates.

10.5 DISCUSSION AND CONCLUSIONS

10.5.1 Best-practice recommendations

According to the literature, different methods to estimate primary nucleation rates from unseeded batch crystallization experiments may provide values that differ by several orders of magnitude.[70,97,236,237] This work revealed that the following four factors contribute to this divergence:

1. Deterministic methods (e.g., Methods 1, 2) require knowledge on the relevant type of nucleation. This is the case because all process attributes that were studied in this work were found to be governed by secondary nucleation in case it occurs at relevant rate. Hence primary nucleation rates should be estimated from such attributes only, if secondary nucleation is negligible.
2. Deterministic methods that are derived from the population balance model (e.g., Methods 2 and 3) are unable to accurately describe crystallization processes in which a small absolute number of (primary) nuclei are present; in this case, the underlying assumption of a continuous population is not valid.
3. Deterministic methods are more sensitive to the condition of detection than stochastic methods. Specifically, if the supersaturation is depleted considerably before detection, the deterministic Method 2 may underestimate the primary nucleation rate considerably.
4. Stochastic methods (e.g., Methods 4 and 5) underestimate nucleation rates in case the underlying single-nucleus or mono-nucleus assumptions do not apply. The criterion derived in Section 10.4.4 may be used to probe the accuracy of the more accurate Method 5 for a given set of data.

Based on these findings, we developed best-practice recommendations for the measurement of nucleation rates in crystallization processes. We distinguish four cases based on two pieces of information that have to be obtained before any method is applied: first, it has to be determined whether

relevant variability is present (i.e., if the coefficient of variation is larger than 0.25) or not. To do so, a sufficiently large number of repetitions of the experiment has to be carried out. Second, one has to assess whether relevant secondary nucleation is present or not. We studied single-crystal seeding (cf. Section 10.6.7) and confirmed that this type of experiment is capable to provide such information: If a sufficiently small seed leads to a significant decrease in detection times, secondary nucleation can be considered relevant. The four cases are categorized as follows:

1. Relevant variability and relevant secondary nucleation: The primary nucleation rate can be estimated accurately with the stochastic method (Method 5), since the single-nucleus assumption applies. The secondary nucleation rate can be estimated deterministically from the detection times (Method 3), or by fitting the particle count evolution to either the deterministic population balance model or the stochastic particle balance model derived here (Method 6).
2. Relevant variability and no secondary nucleation: The primary nucleation rate can be estimated accurately with the stochastic method (Method 5), as in the first case.
3. No variability and relevant secondary nucleation: The primary nucleation rate cannot be estimated accurately, since both stochastic and deterministic methods fail under these conditions. Process conditions have to be adjusted, e.g., by decreasing volume until relevant variability is observed. The secondary nucleation rate can be estimated accurately if the primary nucleation rate is known. This is done by fitting the particle count evolution to a deterministic population balance model or the stochastic particle balance model (Method 6).
4. No variability and no secondary nucleation: The primary nucleation rate can be estimated through any deterministic method, e.g., Methods 1 and 2 that were studied in this work. In general, Method 2 is to be preferred, since it is less sensitive to over-predictions in the presence of secondary nucleation. It should be considered, however, that Methods 1 and 2 require different types of experimental data; for Method 1, the particle count evolution has to be measured accurately. For Method 2, both the limit of detection and the crystal growth rate have to be determined in separate experiments.

We especially underline the third case, where secondary nucleation occurs at a relevant rate and where no relevant variability is observed. Here, accurate rates of primary nucleation *conceptually* cannot be obtained, and different methods were confirmed to provide widely diverging values for the primary

nucleation rate. Recent experimental evidence indicates that secondary nucleation may be the dominant type of nucleation in unseeded batch processes for a wide variety of compounds, implying that this case is of practical relevance in industrial crystallization.[105,215,228,254] As demonstrated in Section 10.4.1, deterministic methods in this case over-predict primary nucleation rates, while stochastic ones under-predict them. Importantly, this conceptual finding is supported by a number of recent experimental studies in the literature, which observed that stochastic methods predicted smaller primary nucleation rates than deterministic methods for the same system.[70,97,237] These literature studies, however, were not able to identify the underlying reasons for this behavior; as we show in this work, this difference naturally arises because stochastic and deterministic methods are accurate under different conditions.

10.5.2 Concluding remarks

This work reports novel insights into how accurate measurements of nucleation rates are to be carried out: it provides practitioners with the conceptual framework to identify and apply appropriate methods for the estimation of crystal nucleation rates under general conditions. To this end, various commonly used stochastic and deterministic approaches to estimate primary and secondary nucleation rates from isothermal crystallization experiments have been studied and compared.

To carry out this assessment, we have developed a novel modeling methodology termed *stochastic particle balance* for the simulation of a crystallization process comprising stochastic primary nucleation, stochastic secondary nucleation, and deterministic crystal growth. We used the model to simulate the crystallization of a well-studied model compound, for which diverging primary nucleation rates have been reported for different methods of measurement.[97,236] Nucleation rates were estimated from the simulated data through multiple methods and were compared with the true values. For primary nucleation, no method considered in this work was able to estimate the kinetics accurately under general conditions. Deterministic methods (Methods 1 and 2) were shown to over-predict rates in the presence of secondary nucleation. Stochastic methods (Methods 4 and 5) were found to be unaffected by the presence of secondary nucleation, which is advantageous when compared to the deterministic ones. Furthermore, their estimates were shown to depend less on the condition of detection than the ones of the deterministic Method 2. However, they under-predicted rates in case a large number of primary nuclei are formed.

Based on these observations, we have studied the accuracy of the stochastic method based on the single-nucleus assumption (Method 5) in detail. We have

proposed a criterion to verify its applicability for arbitrary experimental data sets, thus providing the theoretical foundations required for its rational use. Furthermore, we have developed a method to estimate the rate of secondary nucleation from detection times (Method 3), which can be applied together with the stochastic method (Method 5). This novel approach significantly increases the amount of information that can be inferred from detection times.

Finally, we consider this work as a starting point for a more rational use of methods to estimate crystal nucleation rates in general. While we focus on isothermal conditions, the underlying methodology can be extended to more complex polythermal methods, as well as to crystallization processes of polymorphic or chiral compounds.

10.6 SUPPLEMENTARY INFORMATION

10.6.1 Parameter estimation via Method 5

In this section, we discuss how to estimate primary nucleation parameters from sets of detection times obtained through either experiments or simulations. First, the M_{det} measured detection times obtained from a total of M_{tot} measurements are sorted in ascending order:

$$\boldsymbol{t} = [t_1, t_2, ..., t_{\text{M}_{\text{det}}}]^T : 0 < t_1 < t_2 < ... < t_{\text{M}_{\text{det}}} < \infty. \tag{10.33}$$

The empirical cumulative distribution function (eCDF), $F^*(t_{\text{det}})$, for these times is defined as

$$F^*(t_{\text{det}}) = \frac{1}{M_{\text{tot}}+1} \int_0^{t_{\text{det}}} \sum_{i=1}^{M_{\text{det}}} \delta(\tau - t_{\text{i}}) \text{d}\tau \tag{10.34}$$

where δ is the Dirac delta function. Importantly, this definition of $F^*(T)$ differs from those provided in the literature in one aspect, i.e., it contains a division by $M_{\text{tot}}+1$, whereas literature expressions generally involve a division by M_{tot}.[23,24,67,68,97] As discussed elsewhere, a division by M_{tot} results in a biased distribution:[76] it assigns a physically and mathematically not meaningful value of 1 to the highest measured detection time, assuming all experiments nucleated.

According to the Glivenko-Cantelli theorem,[99] the empirical distribution approaches the theoretical one in the limit of an infinitely large data set:

$$\lim_{M_{\text{tot}} \to \infty} F^*(t_{\text{det}}) = F(t_{\text{det}}) \tag{10.35}$$

Similarly, the measured values of the mean detection time $\bar{t}_{\mathrm{det}}$ and its variance σ^2_{det} approach the theoretical values $\mathrm{E}(t_{\mathrm{det}})$ and $\mathrm{Var}(t_{\mathrm{det}})$ for infinite large data sets. However, it is worth highlighting that in some experimental studies, not all vials nucleate, so that mean and variance cannot be computed accurately.[68,91]

Thus, parameters K and t_{g} for a set of detection times are generally obtained by minimizing the difference between empirical and theoretical distributions,[23,24,68,91] which was shown to be a robust method even for incomplete data sets.[91] The literature also reports a modification of this method, where t_{g} is interpreted as the shortest measured detection time;[91,97] this procedure is motivated by the observation that the fitting of t_{g} yielded negative, and thus non-physical values in some studies. We discuss this issue in more detail in the following.

We first highlight that the model-based study on the stochastic method by Vetter and co-workers[91] observed no relevant difference among the two methods to estimate the growth time and found no explanation for the emergence of negative values. The authors studied the stochastic method under the assumptions that (1) only a single primary nucleation event occurs during the crystallization process and that (2) detection occurs when this nucleus has grown to an arbitrary, pre-defined size.[91] These assumptions are significantly stronger than those used in the stochastic particle balance model that we derived in this work. For this reason, we compared both methods to estimate the growth time based on the simulated sets of detection times. However, similar to Vetter and co-workers[91], we did not observe relevant differences between the two methods; this implies that negative growth times are caused by factors not considered in the simulations. For this reason, we only show the rates obtained by means of combined fitting of growth time and nucleation frequency in the main body of this work.

To understand where negative values for the growth time can come from, let us consider again the governing equations of the single-nucleus assumption (see also Section 10.2.3 in the main body):

$$K_{\mathrm{PN}} = \frac{1}{\mathrm{Var}(t_{\mathrm{det}})^{0.5}} \tag{10.36a}$$

$$t_{\mathrm{g}} = \mathrm{E}(t_{\mathrm{det}}) - \frac{1}{K_{\mathrm{PN}}} \tag{10.36b}$$

These two expressions may be solved exactly for any arbitrary combination of $\mathrm{E}(t_{\mathrm{det}})$ and $\mathrm{Var}(t_{\mathrm{det}})$: first, the nucleation frequency is obtained directly from $\mathrm{Var}(t_{\mathrm{det}})$. Second, t_{g} is computed based on the obtained value of the nucleation frequency and on $\mathrm{E}(t_{\mathrm{det}})$. Let us now consider how the value of t_{g} changes when the detection times are affected by experimental error. For

the sake of simplicity, we assume that such error increases the variance of the detection times by a value of σ^2_{error}, but does not affect their expected value, so that

$$\text{Var}(\hat{t}_{\text{det}}) = \text{Var}(t_{\text{det}}) + \sigma^2_{\text{error}} \tag{10.37}$$

whereby $\hat{t}_{\text{det}}$ denotes the detection times affected by the error. Such type of error may occur for example due to practical limitations in ensuring identical temperature profiles among parallelized crystallizers within an experimental series.[23,24,76] Considering Equations 10.36, it is apparent that the error leads to smaller values of both nucleation frequency and growth time. In the limit of an infinitely large experimental error, the nucleation frequency approaches zero, and the growth time approaches negative infinity. The presence of significant experimental errors therefore has to be regarded as a potential cause for negative growth times.

When the fitting of the growth time yields a negative value, one may utilize the alternative interpretation of the growth time as shortest detection time. The corresponding estimate for the nucleation frequency is to be more accurate; this is, because the shortest detection time in any case assumes a non-negative value, which is a physically more meaningful estimator for the growth time than a negative value. Setting a non-negative value for the growth time hence limits the under-prediction of the growth time due to the error, and in turn yields a more accurate nucleation frequency.

10.6.2 Numerical aspects of Method 6

In this section, we discuss several numerical aspects relevant to the implementation of the stochastic particle balance model (Method 6). First, we notice that the accuracy of the model is subject to the choice of the time interval. Therefore, numerical verification has to be carried out, which was done by comparison with the deterministic, analytical solutions of the population balance model derived in Section 10.2.2. Second, it has to be acknowledged that in case secondary nucleation is dominant, the nucleation frequency will change strongly throughout the process and may be very small initially. To avoid a large number of time steps without any formation of nuclei in the beginning of the simulation, the simulation is initiated with the presence of a single primary nucleus with zero size. The value of t_{n1} in turn is obtained by inserting a randomly generated number drawn from the uniform distribution in [0,1] into the expression for the cumulative distribution provided by Equation 10.20a.[22,76]

Now let us consider the implementation of the constitutive equations. A discrete number of nuclei N_{i} forms at time t_{i}, which denotes the beginning

of the time interval $[t_i, t_i + \Delta t)$. Information on the discrete crystal size distribution is stored in two vectors **L** and **N**, defined as

$$\mathbf{N} = [N_0, N_1, N_2, ..., N_{\text{end}}] \tag{10.38}$$

and

$$\mathbf{L} = [L_0, L_1, L_2, ..., L_{\text{end}}] \tag{10.39}$$

respectively. Note that elements in **N** are computed only once, namely at the corresponding time step. The elements in **L**, on the other hand, may change due to growth at any time step. The first entry in both vectors corresponds to the initial primary nucleation event that occurs at time $t_{\text{n1}}^{\text{PN}} = t_0$ where $L_0 = 0$ and $N_0 = 1$. The moments of the crystal size distribution then read

$$\mu_{\text{j}} = \frac{\mathbf{L}^{\text{j}} \cdot \mathbf{N}}{V} \tag{10.40}$$

Importantly, not only the moments are obtained with this stochastic modeling approach, but the entire crystal size distribution and its evolution over time. Furthermore, we highlight the capability of the method to track subpopulations of crystals; nuclei can be classified readily into primary and secondary ones, which was done in this work. Furthermore, the model allows for studies of chiral crystallization by assigning primary nuclei a random chirality and assuming that secondary nucleation is enantiospecific. This can be done in two ways: first, the absolute number of primary nuclei that form during a time step N_{i}^{PN} is obtained from the Poisson distribution; the number of primary nuclei of a certain chirality is obtained by drawing a number of the Binomial distribution subject to N_{i}^{PN} trials and a success probability of 0.5. Second, for both chiralities the number of nuclei formed is directly obtained from the Poisson distribution when applying an expected value that is half the one for the entirety of primary nucleation.

Finally, to simulate the variability of the process, multiple repetitions of the simulations were carried out subject to different seeds of the random number generator to ensure independence. For this purpose, the model was implemented in a way that allowed for parallelization, typically employing sixteen workers. Table 10.2 provides an overview over all model parameters. The model as well as all methods to estimate nucleation parameters have been implemented in MATLAB R2021a.

Quantity	Symbol	Unit	Value
Primary nucleation parameter	A_{PN}	$m^{-3}s^{-1}$	3.3×10^3
Primary nucleation parameter	B_{PN}	-	0.127
Secondary nucleation parameter	$k_a \times k_{SN,a}$	$m^{-2}s^{-1}$	10^9
Secondary nucleation power	s_a	-	0.98
Crystal growth parameter	k_g	$m\ s^{-1}$	$10^{-5.4}$
Crystal growth power	g	-	1.05
Equilibrium concentration	c^*	g / kg	40.6
Crystal density	ρ_c	$kg\ m^{-3}$	1380
Solvent density	ρ_s	$kg\ m^{-3}$	953.8
Crystal shape factor	k_v	-	0.0144
Crystallizer volume	V	m^3	10^{-9} to 10^{-1}
Supersaturation	S	-	1.20 to 1.40
Crystal detection size	L_{det}	m	5×10^{-6}
Seed crystal size	L_{seed}	m	0 to 10^{-2}
Detection volume fraction	α	-	10^{-5} to 10^{-2}
Time step	dt	s	0.1
Process duration (with SN)	t_{end}	s	1000
Process duration (without SN)	t_{end}	s	10000
Number of simulations	N	-	4096

Table 10.2 List of model parameters that were used in the simulations presented in this work. In case specific studies employed different parameter values, this is highlighted in the corresponding sections.

10.6.3 Properties of the reference system

Cedeno et al.[97] discuss their experimental methodology in detail in two works,[97,236] so that we limit this section to a summary. Cedeno et al.[97] studied the crystallization of para-aminobenzoic acid in ethanol/water via two types of isothermal experiments.

First, they measured induction times in microvials using a Crystal16 instrument, following the methodology widely used in the literature.[68] A total of 112 induction times were measured per experiment, by carrying out seven repetitions in sixteen vials. Experiments at four supersaturation levels were conducted to estimate the primary nucleation kinetics with multiple variations of the stochastic method. In this work, we use the reported parameter values for primary nucleation based on linear regression, i.e., those provided in Table

S3 in the Supplementary Information of Cedeno et al.[97] The growth time was interpreted as shortest detection time, in line with the discussion in Section 10.6.1.

The second experiment comprises measurements of the particle count evolution via optical reflectance measurement (ORM). A reactor comprising 100 mL solution was crash-cooled to the desired temperature at the beginning of the experiment; it was held at constant temperature, until no change in the particle count was observed anymore. With this method, the authors obtained a detection rate of crystals, assuming that particles are detected as soon as they reach a critical size of $L_{\text{det}} = 5\mu\text{m}$. Experiments at different stirring rates were conducted with the aim of characterizing the effect of hydrodynamics on nucleation. In this work, we analyze the data provided in the Figures 7 and 8 of Cedeno et al.[97], i.e., for a stirring rate of 700 rpm. The relevant information were digitally extracted from the figures and are reported in Table 10.3.

With respect to the kinetics of the system, we assume that the primary nucleation kinetics obtained via the stochastic method is correct. We thus use the reported primary nucleation parameters to estimate the secondary nucleation and crystal growth parameters from the particle count evolution in the 100 mL experiments. Optimal parameters were identified by minimizing an objective function using the MATLAB routine *patternsearch*, which applies a direct search algorithm. The objective function is

$$\Psi = \sum_{j=1}^{J} \sum_{h=1}^{H} \vartheta_{\text{j,h}} \tag{10.41}$$

where $\vartheta_{\text{j,h}}$ is the term related to characteristic quantity j at supersaturation level h. $\vartheta_{\text{j,h}}$ is defined as

$$\vartheta_{\text{j,h}} = \left(\frac{\theta_{\text{j,h}}^{\text{exp}} - \theta_{\text{j,h}}^{\text{sim}}}{\theta_{\text{j,h}}^{\text{exp}} + \theta_{\text{j,h}}^{\text{sim}}} \right)^2 \tag{10.42}$$

whereby $\theta_{\text{j,h}}$ is the actual value of the characteristic quantity, obtained from experimental data ($\theta_{\text{j,h}}^{\text{exp}}$) and from stochastic simulations ($\theta_{\text{j,h}}^{\text{sim}}$). Two quantities were incorporated into the objective function, namely the total number of particles formed and the duration elapsed between reaching 25% and 75% of the final particle count at the end of the process. Additional quantities were considered, but ultimately not included: the optimized parameter values already provided a sufficiently accurate representation of the experimental data.

Supersaturation	N_{tot} [-]	$\Delta t_{25,75}$ [s]
1.40	5.1×10^9	20
1.32	4.5×10^9	25
1.25	3.4×10^9	28
1.20	2.6×10^9	37

Table 10.3 Data obtained for the PABA system.

10.6.4 Simulations without secondary nucleation

In this section, we present stochastic simulations of the crystallization of para-aminobenzoic acid in water/ethanol based on the stochastic particle balance model derived in Section 10.2.3. The simulations are carried out in the absence of secondary nucleation, i.e., only primary nucleation and crystal growth are considered. This section complements the simulations shown in Section 10.3 in the main body of this work, where secondary nucleation was considered as well.

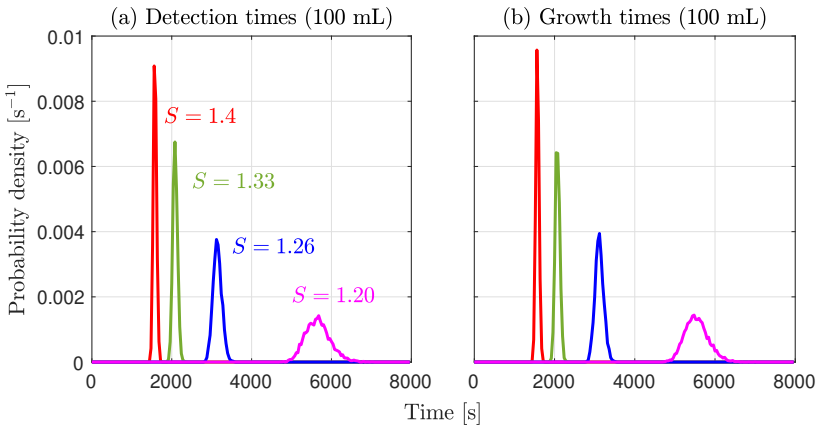

Figure 10.9 Characterization of the reference system in the absence of secondary nucleation: Distribution of the induction/detection times (left), and of its components, i.e. the first nucleation time (center) and the growth time (right). A total of 4096 crystallization processes were simulated to generate the distributions. The colors indicate the four supersaturation levels studied by Cedeno et al.[97]: S = 1.40 (red), S = 1.33 (green), S = 1.26 (blue), and S = 1.20 (magenta).

Figure 10.9 presents the detection times (panel (a)) and growth times (panel (b)). Since no secondary nuclei form, supersaturation is depleted only by

the nuclei formed through primary nucleation. We show in Figure 10.10 the number of nuclei that form; in the 100 mL system (panel (a)), about 50 to 250 nuclei form in average for the different supersaturation levels. These numbers are about one order of magnitude higher than those obtained in the presence of secondary nucleation (see panel (b)). This implies that the rapid occurrence of secondary nucleation limits the time in which primary nuclei can form.

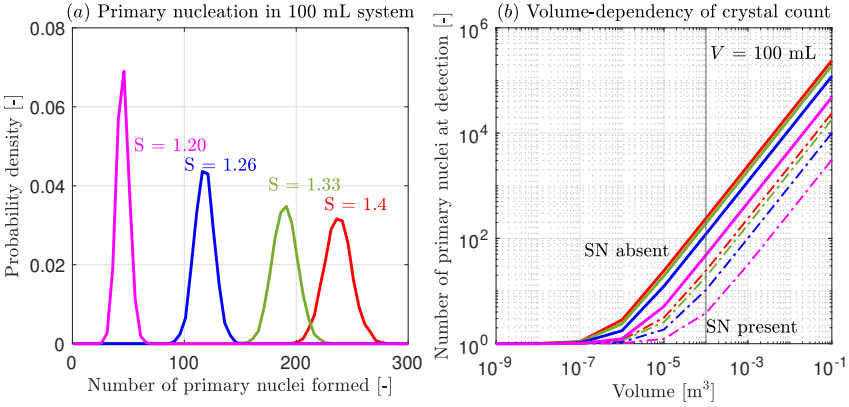

Figure 10.10 Characterization of the model system in the absence of secondary nucleation: (a) Number of primary nuclei formed in 100 mL. A total of 4096 crystallization processes were simulated to generate the distributions. (b) Mean number of primary nuclei in the absence of secondary nucleation (solid) and in the presence of secondary nucleation (base case, see Figure 10.3, dashed lines) present at the detection time for different volumes. The colors indicate the four supersaturations studied: S = 1.40 (red), S = 1.33 (green), S = 1.26 (blue), and S = 1.20 (magenta).

To conclude this section, we consider the particle count evolution in the absence of secondary nucleation as shown in Figure 10.11. As expected, the particle count increases initially in a linear manner with time. Over time, the supersaturation is depleted and the nucleation rate decreases; this leads to a decrease in the slope of the evolution profile, until a plateau is reached eventually. This behavior is very far from the one observed in the presence of secondary nucleation (cf. Figure 10.1), where an exponential increase in particle count was observed after a pronounced lag phase.

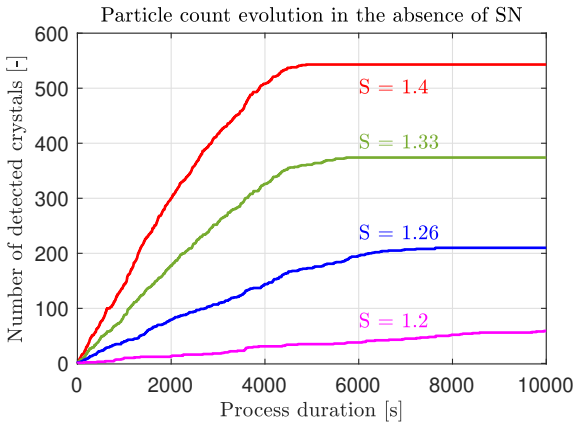

Figure 10.11 Characterization of the reference system: Evolution of the system after the first nucleation event. (a) Total number of detected crystals. (b) Total number of crystals, i.e. including those smaller than the detection threshold. The colors indicate the four supersaturation levels studied by Cedeno et al.[97]: S = 1.40 (red), S = 1.33 (green), S = 1.26 (blue), and S = 1.20 (magenta).

10.6.5 Estimation of primary nucleation parameters

The knowledge of nucleation rates *vs.* supersaturation is a prerequisite to compute the parameters in the kinetic rate equation. Figure 10.12 shows the values of the parameters A_{PN} and B_{PN} appearing in the expression for the primary nucleation frequency, $K_{\mathrm{PN}} = VA_{\mathrm{PN}}S\exp\left\{-\frac{B_{\mathrm{PN}}}{\ln(S)^2}\right\}$. The black lines correspond to the parameter values obtained from the rates shown in Figure 10.6. Further, we studied cases for faster (orange) and slower (purple) primary nucleation, corresponding to a pre-exponential factor A^{PN} increased and decreased by one order of magnitude.

For all three sets of primary nucleation kinetics, the stochastic method provided quantitatively accurate parameter values for small volumes. For larger volumes, the pre-exponential parameter A^{PN} is under-predicted, and the under-prediction increases with increasing volume. The same effect already observed in Figure 10.6 appears here as well, namely a threshold at lower volume under conditions of faster primary nucleation. With respect to the exponential parameter, B_{PN}, we similarly find a quantitative agreement for small volumes, and an under-prediction at larger ones. However, the extent of the under-prediction becomes approximately constant for sufficiently large volumes.

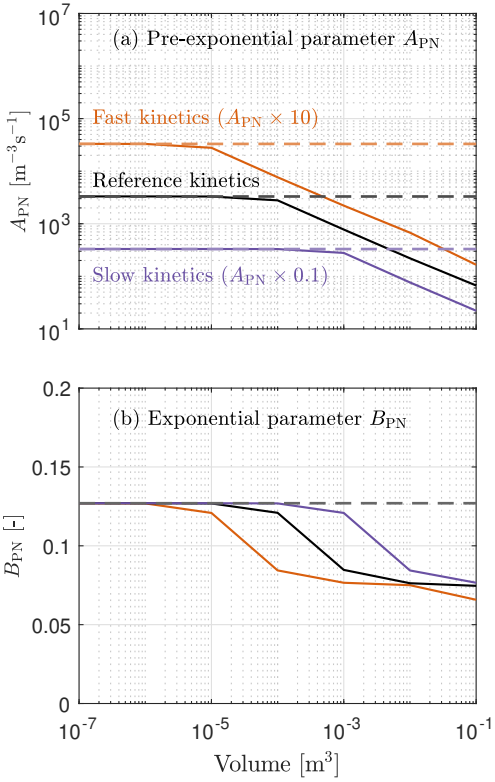

Figure 10.12 Measured nucleation parameters through the stochastic method for different volumes. (a) Pre-exponential parameter A_{PN}. (b) Exponential parameter B_{PN} (b). The dashed lines indicate the true values for the nucleation parameters. Note that three values for A_{PN} were studied to investigate the sensitivity of the methods towards the values of the kinetics. The reference set of primary nucleation kinetics corresponds to the nucleation rates shown in Figure 10.6.

10.6.6 On the characteristic times

In this section, we study in detail the volume-dependency of the three characteristic times, i.e., the first nucleation time, the growth time, and the detection time in the presence of secondary nucleation. Figure 10.13 shows

how the mean values for the three characteristic times depend on crystallizer volume.

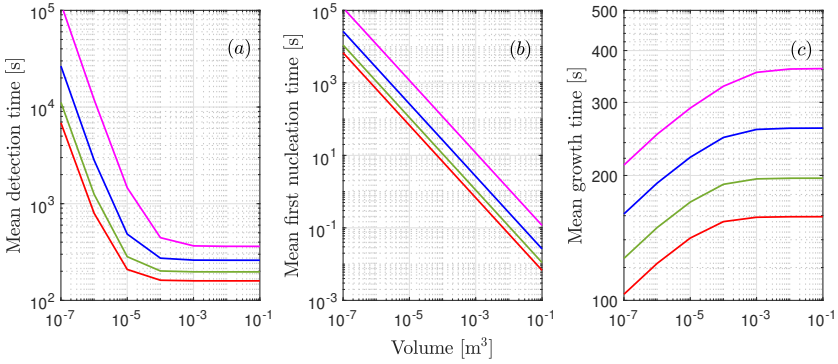

Figure 10.13 Characterization of the reference system: Effect of volume on the mean value of the three characteristic times. (a) Detection time. (b) First nucleation time. (c) Growth time. The colors indicate the four supersaturation levels studied: S = 1.40 (red), S = 1.33 (green), S = 1.26 (blue), and S = 1.20 (magenta).

Detection times (panel (a)) exhibit two regimes: for small volumes, the times exponentially increases with size; for large volumes, a nearly constant value is observed. This is due to the behavior of its constituents: The first nucleation times (panel (b)) decrease inversely proportional with increasing volume. Thus, for sufficiently small systems, the first nucleation time dominates the detection time. The growth time, on the other hand, depends only weakly on system size and eventually reaches a plateau; this is due to the exponential growth in crystalline matter due to secondary nucleation (cf. Section 10.2.2). As discussed in Section 10.4, the ratio of primary to secondary nucleation becomes scale-independent in large volumes. As a consequence, the growth time becomes scale-independent as well: an increase in volume is accounted for by a proportional increase in the number of both primary and secondary nuclei. In the limit of small volumes, where only a single primary nucleus is formed, growth times decrease with volume. Here, a decrease in volume implies that less material has to be formed via secondary nucleation of the single primary nucleus. Thus, growth times become shorter in this case.

10.6.7 Single-crystal seeding

Figure 10.14 (a) shows the effect of inserting a single seed with different sizes on the time evolution of detected crystals. The solid line indicates seeding with size zero, which corresponds to the unseeded case, since nuclei are assumed to form with size zero. Independent of supersaturation, the insertion of a seed significantly accelerates the evolution of the system. This implies that secondary nucleation due to the presence of the seed crystal is faster than primary nucleation in the unseeded system. If such behavior is observed for a sufficiently small seed, secondary nucleation should be considered dominant. If the seed crystal were found not to affect the evolution of the process (i.e., a so-called inert seed), primary nucleation could be considered dominant.

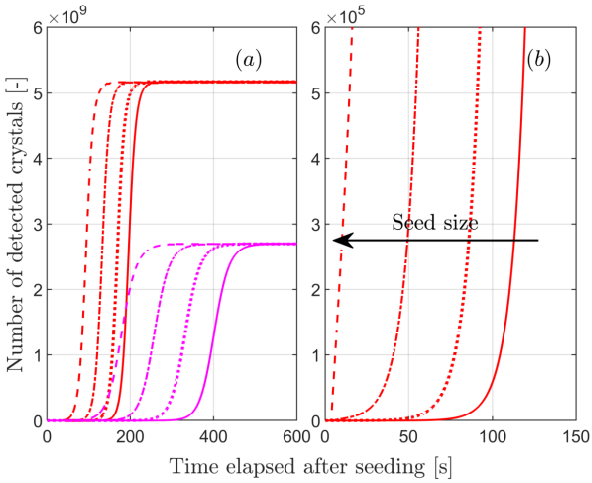

Figure 10.14 Effect of seed size on particle count evolution. Four sizes were studied: $L_{\text{seed}} = 0$ (solid lines), $L_{\text{seed}} = 10^{-4}$m (dotted lines), $L_{\text{seed}} = 10^{-3}$m (dash-dotted lines) and $L_{\text{seed}} = 10^{-2}$m (dashed). The colors indicate the two supersaturations studied: S = 1.40 (red) and S = 1.20 (magenta).

The shape of the evolution curves is nearly unaffected by the seed; a 10,000 times magnification (panel (b)) is required to observe some deviation of the exponential shape for the largest size of $L_{\text{seed}} = 10^{-2}$m. This indicates that the secondary nuclei created by the seed rapidly dominate the total nucleation frequency. While this single-crystal seeding study for the model system is purely *in silico*, we highlight that the predicted trends in Figure 10.14 qualitatively agree with observations made in recent experimental studies.[238]

11 GENERAL STABILITY ANALYSIS OF THE STEADY STATES IN THE CONTINUOUS MIXED-SUSPENSION CRYSTALLIZER

11.1 INTRODUCTION

The mathematical description of continuous mixed-suspension crystallizers was developed in the 1960s and 1970s,[45,243,255] thus enabling the widespread use of that concept across industries. In the framework of quality-by-design initiatives, interest in continuous crystallization recently has emerged also in the pharmaceutical industry.[50] Continuous crystallization promises enhanced control over polymorphism, which is a critical property of solid active pharmaceutical ingredients,[256,257] while avoiding or at least decreasing the batch-to-batch variability observed in traditional batch manufacturing.[50,258,259] Polymorphism, or more generally the existence of multiple solid forms for a chemical compound, poses a major challenge to pharmaceutical manufacturing. This is because different polymorphs exhibit different physicochemical properties across the spectrum of what is relevant, including processability and bio-availability.[260,261] The capability of a mixed suspension crystallizer to maintain stable steady states for metastable (i.e., thermodynamically unfavorable) polymorphs has therefore received great attention, particularly during the past decade.[49,258,262–264] In contrast, in batch crystallizers the thermodynamically stable polymorph is the natural long-term outcome, because metastable crystals are converted into stable ones via solvent-mediated transformation.[45,265]

However, understanding and leveraging this remarkable feature of the mixed suspension crystallizer is far from trivial, and it requires a mathematical model of its behavior and a model-based analysis of its steady states.

The results presented in this chapter have been reported in: Deck, L.-T.; Mazzotti, M. General stability analysis of the steady states in the continuous mixed-suspension crystallizer. *Chem. Eng. J.* **2024**, 483, 148721.

To this end, Farmer et al.[258,266] carried out a linear stability analysis of a bi-polymorphic system by transforming the governing population balance equation into a set of ordinary differential equations through the method of moments. While their original analysis focused on mixed suspension crystallizers with mixed product removal, commonly abbreviated as MSMPR, extensions have been proposed.[259,263,267–269]

Even though such stability analysis represented a big step forward in understanding the steady-state behavior of MSMPR-type crystallizers, it was not general for at least three reasons. First, the earlier mathematical methodology is applicable only to simplified systems, e.g., where crystal growth and withdrawal are size-independent. Second, the stability analysis applies specifically to the selected functional forms for the rate of crystal growth and nucleation, which are very simple, though still relevant for real systems. Finally, the literature has focused on systems with only one or two polymorphs,[258,259,266,270] and it remains unclear how to characterize the stability of steady states in systems where an arbitrary number of different solid forms may exist.

In this context, we have revisited the mathematical description of the mixed suspension crystallizer, and derived a general framework both to determine the possible steady states and to assess their stability. The paper is organized as follows: we first provide a general description for the mixed suspension crystallizer in Section 11.2; then we apply it to a set of relevant applications in Section 11.3; finally, we draw conclusions in Section 11.4.

11.2 MODELLING A MIXED SUSPENSION CRYSTALLIZER

The mixed suspension crystallizer is defined in this work as a well-mixed vessel with classified product removal at the outlet, in line with the relevant literature.[258,259] Its steady-state depends on the inlet concentration c_0, the temperature T, the expected residence time of the fluid τ, the energy dissipation intensity in the crystallizer ϵ, and the kinetics of the relevant set of crystallization phenomena. It is characterized by the concentration of the solute in solution c, termed c_{ss} if the crystallizer operates at steady-state, the particle size distribution inside the crystallizer $f(L)$, and those in the inlet and outlet streams, $f^{in}(L)$ and $f^{out}(L)$. This is illustrated in Fig. 11.1. The distributions $f(L)$, $f^{in}(L)$ and $f^{out}(L)$ are number density functions, i.e., $f(L)\mathrm{d}L$ denotes the number of crystals with sizes between L and $L + \mathrm{d}L$ per unit volume. The expected residence time is defined as $\tau = V/Q$, with V the suspension volume and Q the volumetric flow rate in and out the crystallizer. Similarly, $\tau/\xi(L)$ is the expected size-dependent residence time of a crystal of size L defined through the withdrawal factor $\xi(L) = f^{out}(L)/f(L)$.[271] The

withdrawal factor $\xi(L)$ is used to account for classified or non-representative product withdrawal.[269,271,272] Following its definition, if $\xi < 1$, the outgoing suspension is diluted and the crystals spend more time in the crystallizer than the fluid; if $\xi > 1$, the outgoing suspension is concentrated, as crystals leave the crystallizer preferentially compared to the fluid; under ideal conditions, $\xi = 1$ for all crystal sizes. For the sake of brevity, we describe a solution-fed crystallizer in this section, so that $f^{\text{in}}(L) = 0$, and we refer to the appendix (Section 11.5.3) for a discussion of a suspension-fed crystallizer. Crystallization is assumed to comprise two phenomena, namely crystal growth and secondary nucleation. Secondary nucleation, in contrast to primary nucleation, describes the formation of new crystals triggered by existing ones, and it is well-established that it is the dominant type of nucleation in continuous crystallizers.[45,243] Recent literature suggests that even in unseeded batch crystallization a majority of crystals is formed through secondary nucleation, with only a few formed via primary nucleation.[78,105,273,274]

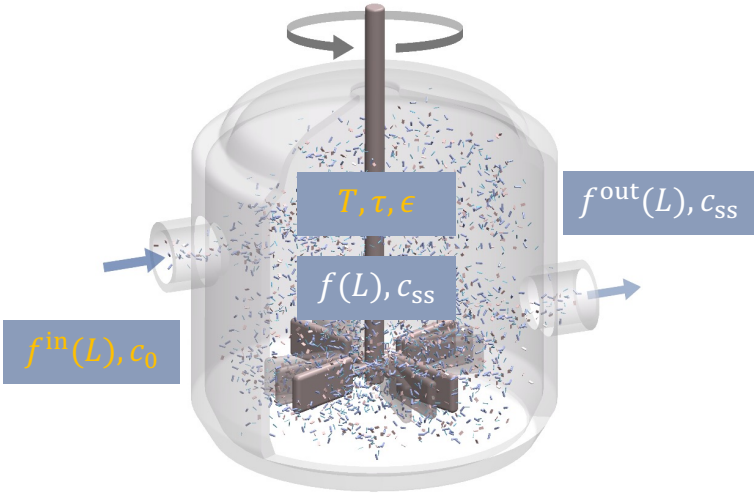

Figure 11.1 Schematic of a continuous mixed suspension crystallizer that shows all relevant physical quantities except for the crystallization kinetics. Quantities in orange are design parameters that can be chosen freely within physically meaningful and technically feasible ranges, whereas those in white denote the corresponding steady-state properties.

In the derivation that follows, we will first establish the relevant expressions for the particle size distributions using both the well-known population balance approach (Section 11.2.1) and an equivalent, but less established ap-

proach based on the residence time distribution (Section 11.2.2). In Section 11.2.3, we introduce several concepts that facilitate a general mathematical treatment of the steady state, namely a new single crystal-based definition of secondary nucleation, and the so-called birth rate function. The latter expresses the number of daughter nuclei that a crystal forms during its lifetime in the crystallizer. It determines the occurrence and stability of the steady states in the crystallizer, as discussed in Section 11.2.4.

11.2.1 Population balance approach

Following the aforementioned assumptions, a mixed-suspension crystallizer at steady-state is mathematically described through a population balance equation coupled with a material balance:

$$\frac{\mathrm{d}(f(L)G(L))}{\mathrm{d}L} = -\frac{1}{\tau}f^{\mathrm{out}}(L) = -\frac{\xi(L)}{\tau}f(L) \tag{11.1}$$

$$c_0 = c_{\mathrm{ss}} + k_{\mathrm{v}}\rho_{\mathrm{c}}n_3^{\mathrm{out}} = c_{\mathrm{ss}} + c_{\mathrm{c}} \tag{11.2}$$

with the initial condition $f(0) = B/G(L=0)$ where B is the nucleation rate, i.e., the number of nuclei formed per unit time and per unit volume. Moreover, n_3^{out} is the third moment of the PSD $f^{\mathrm{out}}(L)$, and $G(L)$ is the crystal growth rate, which may depend on crystal size L.[275–277] Finally, ρ_{c} is the density of a crystal, k_{v} its volume shape factor, and c_{c} the suspension density. Newly formed crystals are generated with size $L = 0$ through secondary nucleation.

The general solution of the PBE is obtained by multiplying and dividing the right hand side by $G(L)$, and then by integrating upon separation of variables to obtain $f(L)G(L)$; one obtains:

$$f(L) = \frac{B}{G(L)}\exp\left(-\int_0^L \frac{\xi(\lambda)}{\tau G(\lambda)}\mathrm{d}\lambda\right) \tag{11.3}$$

From this, $f^{\mathrm{out}}(L)$ follows, as:

$$f^{\mathrm{out}}(L) = \xi(L)f(L) = \frac{B\xi(L)}{G(L)}\exp\left(-\int_0^L \frac{\xi(\lambda)}{\tau G(\lambda)}\mathrm{d}\lambda\right) \tag{11.4}$$

The j-th moments of the two distributions are defined as follows:

$$n_j = \int_0^\infty L^j f(L)\mathrm{d}L, \qquad n_j^{\mathrm{out}} = \int_0^\infty L^j f^{\mathrm{out}}(L)\mathrm{d}L = \int_0^\infty L^j \xi(L) f(L)\mathrm{d}L \tag{11.5}$$

It is worth noting that transforming the PBE of Eq. 11.1 into the moment equations, and considering the steady-state equation for the zero-th order moment yields the following relationship:

$$Qn_0^{\text{out}} = VB \tag{11.6}$$

whose important physical meaning is that the rate of crystals generated in the crystallizer must equal the rate of crystals withdrawn from the crystallizer.

11.2.2 Residence time approach

The solutions for the particle size distributions may also be obtained using a second approach that relies on the concept of residence time and on its distribution. To this aim, we introduce the age a of a crystal, i.e., the time the crystal has spent inside the crystallizer since its birth.[270,272] During its lifetime within the well-mixed crystallizer at steady state a crystal experiences constant conditions, i.e., in terms of temperature, and concentration; what changes is its size $L(a)$, hence the rate of processes that depend on the crystal size L, e.g., in the context of this work its growth rate $G(L)$, the rate at which a crystal triggers the birth of secondary nuclei, and the withdrawal rate defined through $\xi(L)$. A crystal that has reached age a may either still reside inside the crystallizer, or might have already been washed out; we define the probability of the former as $P(a)$ and call it the residence probability. The probability of the latter is $P^{\text{out}}(a) = 1 - P(a)$. As a crystal ages, i.e., as a increases, its residence probability $P(a)$ decreases, according to the following ordinary differential equation:

$$\mathrm{d}P = -P(a)\xi(L(a))\frac{\mathrm{d}a}{\tau} \tag{11.7}$$

whereby the differential change of the crystal's residence probability $\mathrm{d}P$ between ages a and $a + \mathrm{d}a$ is given by the product of two probabilities: (i) the residence probability $P(a)$ at age a, and (ii) the probability that a crystal of age a is withdrawn from the crystallizer in the differential age interval $\mathrm{d}a$. For the withdrawal of a fluid element, such probability equals $Q\mathrm{d}a/V = \mathrm{d}a/\tau$, whereas for the crystal it is $\xi(L(a))\mathrm{d}a/\tau$, taking into account the size-dependent withdrawal factor $\xi(L)$. We note that the link between the size of a crystal and its age follows directly from $\mathrm{d}L = G(L)\mathrm{d}a$, so that:

$$\int_0^L \frac{\mathrm{d}\lambda}{G(\lambda)} = a \tag{11.8}$$

which simplifies to $L = Ga$ if the growth rate is size-independent. The solution to the differential equation 11.7 for the initial condition $P(a = 0) = 1$ (newborn crystals are in the crystallizer) is:

$$P(a) = \exp\left(-\int_0^a \frac{\xi(L(a'))}{\tau}\mathrm{d}a'\right) = \exp\left(-\int_0^L \frac{\xi(\lambda)}{\tau G(\lambda)}\mathrm{d}\lambda\right) = P_\mathrm{L}(L) \quad (11.9)$$

where P can be expressed equivalently in terms of both age a and size L using Eq. 11.8. Note that when approaching infinite age and size the residence probability P approaches zero, i.e., no crystal can live for ever and grow indefinitely.

The function $P^{\mathrm{out}}(a) = 1 - P(a)$ is a cumulative density function that defines the fraction of crystals that have been withdrawn from the crystallizer before reaching the age a. Its derivative, $p^{\mathrm{out}}(a)$, is a probability density function (PDF), so that $p^{\mathrm{out}}(a)\mathrm{d}a$ is the fraction of crystals that is withdrawn between ages a and $a + \mathrm{d}a$:

$$p^{\mathrm{out}}(a) = \frac{\xi(L(a))}{\tau}\exp\left(-\int_0^a \frac{\xi(L(a'))}{\tau}\mathrm{d}a'\right) = \frac{\xi(L(a))}{\tau}P(a) \quad (11.10)$$

Likewise, $p_\mathrm{L}^{\mathrm{out}}(L)$ is the PDF associated to the cumulative density function $P_\mathrm{L}^{\mathrm{out}}(L) = 1 - P_\mathrm{L}(L)$:

$$p_\mathrm{L}^{\mathrm{out}}(L) = \frac{\xi(L)}{\tau G(L)}\exp\left(-\int_0^L \frac{\xi(\lambda)}{\tau G(\lambda)}\mathrm{d}\lambda\right) = \frac{\xi(L)}{\tau G(L)}P_\mathrm{L}(L) \quad (11.11)$$

The two PDFs above are equivalent, i.e., they fulfill the condition $p^{\mathrm{out}}(a)\mathrm{d}a = p_\mathrm{L}^{\mathrm{out}}(L)\mathrm{d}L$. They can be interpreted either as normalized crystal age distribution of the withdrawn suspension in the case of $p^{\mathrm{out}}(a)$, or as normalized crystal size distribution of the withdrawn suspension in the case of $p_\mathrm{L}^{\mathrm{out}}(L)$. The latter interpretation establishes the link to the particle size distribution, which is a number density function, as follows:

$$f^{\mathrm{out}}(L) = p_\mathrm{L}^{\mathrm{out}}(L)n_0^{\mathrm{out}} = \frac{\xi(L)n_0^{\mathrm{out}}}{\tau G(L)}\exp\left(-\int_0^L \frac{\xi(\lambda)}{\tau G(\lambda)}\mathrm{d}\lambda\right) \quad (11.12)$$

This equation matches the one obtained through the population balance approach outlined before (i.e., Eq. 11.4), since $n_0^{\mathrm{out}} = B\tau$, as to Eq. 11.6, confirming the equivalence of the two approaches.

These observations allow using the material balance of Eq. 11.2 to express the nucleation rate prevailing in the crystallizer, B, in terms of the CDF of Eq. 11.9, as

$$B = (c_{\mathrm{ss}} - c_0)\left(k_\mathrm{v}\rho_\mathrm{c}\int_0^\infty L^3\frac{\xi(L)}{G(L)}P_\mathrm{L}(L)\mathrm{d}L\right)^{-1} \quad (11.13)$$

making use of both the solution of the PSD (Eq. 11.3) and the definition of its moments (Eq. 11.5). Due to the c_{ss}-dependence of the nucleation rate B, for any given constitutive relationship defining such rate, this is an implicit equation for c_{ss}, whose solution depends on c_0. To demonstrate properties of the crystallizer's steady state, it seems necessary to specify the constitutive equation defining the secondary nucleation rate, B. Interestingly, a number of steady state properties can be derived for rather general expressions of the nucleation rate, B, as we show in the following.

11.2.3 Secondary nucleation and birth rate

In general, the nucleation rate B is a function of concentration c (c_{ss} at steady state), of temperature T, of the energy dissipation intensity in the crystallizer, ϵ, and of some integral properties of the PSD, typically one of its moments, n_j, with j an integer number, often either 2 or 3;[45,46] by exploiting this observation $B(c, T, \epsilon)$ can be written as:

$$B(c, T, \epsilon) = b(c, T, \epsilon) n_j = b(c, T, \epsilon) \int_0^\infty L^j f(L) \mathrm{d}L \tag{11.14}$$

Defining the *secondary nucleation frequency* $K(c, T, \epsilon, L) = b(c, T, \epsilon) L^j$ and writing for simplicity $K(L) = bL^j$ yields

$$B = \int_0^\infty K(L) f(L) \mathrm{d}L \tag{11.15}$$

where $K(L)$ represents the number of secondary nuclei generated per unit time by a single parent crystal of size L. With this definition in mind, the last equation represents a rather natural and physically intuitive definition of the rate of secondary nucleation over a population of crystals with PSD $f(L)$.

A property of special interest and closely related to the secondary nucleation frequency, is the *birth rate* of a crystal, i.e., the expected number of nuclei formed during its lifetime in the crystallizer. We call such property ν and observe that the differential birth rate of a crystal of age a must equal the differential number of nuclei formed in the differential age interval, $K(L(a))\mathrm{d}a$, multiplied by its residence probability $P(a)$ (a withdrawn crystal cannot form nuclei in the crystallizer anymore), so that $\mathrm{d}\nu = P(a)K(L(a))\mathrm{d}a$. ν is obtained by integrating over all ages, as to

$$\nu(c, T, \tau, \epsilon) = \int_0^\infty K(L(a), c, T, \epsilon) P(a, c, T, \tau) \mathrm{d}a \tag{11.16}$$

$$= \int_0^\infty \frac{K(L, c, T, \epsilon)}{G(L, c, T)} P_{\mathrm{L}}(L, c, T, \tau) \mathrm{d}L \tag{11.17}$$

where the second equality is obtained by changing integration variables, from crystal age to crystal size. Through the definitions of $K(L, c, T, \epsilon)$, $G(L, c, T)$, and $P_L(L, c, T, \tau)$, the birth rate $\nu(c, T, \tau, \epsilon)$ is a function of concentration, residence time, temperature, and energy dissipation intensity; to keep the notation concise, we drop these dependencies where appropriate. Let us now again consider the right hand side of Eq. 11.15. Substituting first the right hand side of Eq. 11.9 into Eq. 11.3, then substituting the latter into the right hand side of Eq. 11.15, dividing the resulting relationship by B, and finally introducing the birth rate yields the following expression:

$$\nu(c_{ss}, T, \tau, \epsilon) = 1 \tag{11.18}$$

which is an implicit equation in the steady state concentration, hence defining the value of $c_{ss}(T, \tau, \epsilon)$ as a function of the operating conditions (T, τ, ϵ). This equation plays a central role in this work, and due to its importance, it deserves, together with the birth rate, a few clarification remarks.

11.2.4 Stability of the steady states

The concept of the birth rate together with the steady state condition given by Eq. 11.18 provide a general path to compute the concentration and to analyze the stability of the steady state. This is true for arbitrary expressions of the withdrawal factor $\xi(L)$, of the secondary nucleation frequency $K(L)$, and of the crystal growth rate $G(L)$.

Eq. 11.18 enforces the condition that the birth rate at steady state must be one: for the crystallizer to be at steady state, each crystal during its lifetime inside the crystallizer must in average give birth to exactly one new crystal. This is physically intuitive, because if $\nu > 1$, each generation of crystals would be more numerous than their predecessor generation. For $\nu < 1$, every generation of crystals would be smaller than their predecessor generation. Neither case is compatible with stationary operation, only for $\nu = 1$ a suspension can attain a stationary state.

To assess the stability of the steady state, it is indispensable to study how the birth rate depends on concentration. The following three properties hold true in the entire physically meaningful range of operating conditions (T, τ, ϵ):

$$\nu(c) > 0 \tag{11.19}$$

$$\lim_{c \to c_{eq}} \nu(c) = 0 \tag{11.20}$$

$$\lim_{c \to \infty} \nu(c) \to \infty \tag{11.21}$$

which requires that both the rate of crystal growth and the secondary nucleation frequency approach zero at the equilibrium concentration c_{eq}, are larger than zero at $c > c_{eq}$, and that they approach infinity when $c \to \infty$. This applies to all commonly used rate expressions for $G(L)$ and $K(L)$. Given these properties of the birth rate function, there is an odd number of concentration levels that meets the steady state condition $\nu(c_{ss}) = 1$. If $\nu(c)$ increases monotonically with concentration, there is a unique solution. This requires first that $G(L)$ and $K(L)$ monotonically increase with concentration (which is physically meaningful and virtually always true) and second that $\xi(L)$ is either size-independent or monotonically decreasing with crystal size L. Hence, a non-monotonic behavior of ν and thus steady state multiplicity are limited to the case where $\xi(L)$ increases with crystal size L; we refer to Section 11.3.2 for a detailed discussion on size-dependent withdrawal.

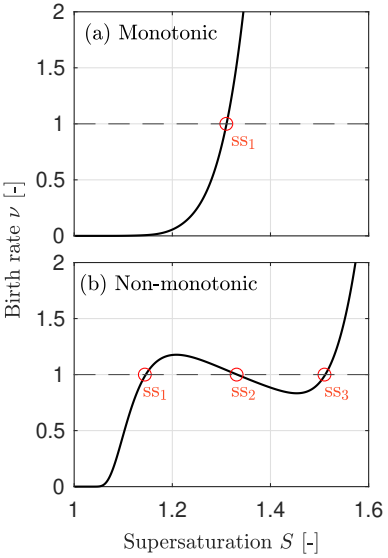

Figure 11.2 Birth rate ν as a function of supersaturation in the crystallizer. Panel (a) shows a case with size-independent withdrawal where the birth rate monotonically increases with concentration. Panel (b) illustrates size-dependent withdrawal, where larger crystals preferentially exist the crystallizer. This results in a non-monotonic birth rate function with three potential steady states.

Fig. 11.2 shows the birth rate as a function of supersaturation for two cases, first in panel (a) with a unique steady state, and second in panel (b)

with three steady states, enumerated in the order of increasing concentration/supersaturation. To assess the stability of these possible steady states, we consider their behavior with respect to a perturbation. The addition of crystals to a steady state depletes the supersaturation in the crystallizer because of their growth. If at steady state $\mathrm{d}\nu/\mathrm{d}c > 0$, which is true for all odd-numbered states, the birth rate ν would drop below 1 due to this perturbation and some crystals would be washed out until the original steady state were recovered. If on the other hand, some crystals were removed, the supersaturation would increase and the birth rate ν would become larger than 1; as a consequence more crystals would be formed to compensate for those removed until the original steady state were recovered. This proves that if at steady state $\mathrm{d}\nu/\mathrm{d}c > 0$, then the steady state is stable.

On the contrary, if $\mathrm{d}\nu/\mathrm{d}c < 0$, similar considerations prove that the steady state is unstable, and perturbations are amplified until the system approaches a different, stable steady state of either lower or higher concentration depending on whether crystals are added or removed. This holds true for steady state 2 in Fig. 11.2 (b). If multiple stable steady states exist (e.g., states 1 and 3 in panel (b)), the initial conditions during the startup of the crystallizer decide, which one is attained.

Finally, we note that the conditions $\nu(c_{\mathrm{ss}}) = 1$ and $\mathrm{d}\nu/\mathrm{d}c > 0$ are only necessary, but not sufficient to identify a stable steady-state. This is because they are independent of the mass balance, i.e., they do not consider the inlet concentration c_0. A stable steady state with crystals must maintain a suspension density $c_{\mathrm{c}} = c_0 - c_{\mathrm{ss}}$ larger than zero. Practically, this means that a stable steady state with crystals can be obtained in general, for any set of the operating conditions T, τ, and ϵ, by choosing a value of c_0 larger than c_{ss}; a concentration $c_0 < c_{\mathrm{ss}}$ however would result in a steady state without crystals, which we refer to as *trivial* steady state.

11.3 CHARACTERIZING STEADY-STATES

In the following, we show how to solve the steady-state equations derived in Section 11.2 for a process with size-independent crystal growth and crystal withdrawal (Section 11.3.1) as well as for processes with size-dependent withdrawal and multiple steady state solutions (Section 11.3.2). Then, we assess the steady-states for systems with multiple solid forms, namely for polymorphic (Sections 11.3.3 and 11.3.4) and for chiral compounds (Section 11.3.5). Further extensions to systems with growth rate dispersion (Section 11.5.1), size-dependent crystal growth (Section 11.5.2) or a suspension-fed crystallizer (Section 11.5.3) are discussed in the appendix.

11.3.1 Size-independent crystal growth and withdrawal

This section considers the crystallization of compounds with size-independent growth rate, G, and with size-independent withdrawal factor, ξ, possibly different than 1. The expression for $P_{\mathrm{L}}(L)$ in Eq. 11.9 simplifies to:

$$P_{\mathrm{L}}(L) = \exp\left(-\frac{L\xi}{G\tau}\right) = \exp\left(-\frac{L}{G\hat{\tau}}\right). \tag{11.22}$$

where $\hat{\tau} = \tau/\xi$ is the expected residence time of the crystals. To compute the steady state, information on G and $K(L)$ are required. G may be defined using the following generic functional form

$$G(c,T) = k_{\mathrm{g},0}\exp\left(-\frac{E}{RT}\right)\left(\frac{c}{c_{\mathrm{eq}}(T)}-1\right)^{g} = k_{\mathrm{g}}(T)\left(\frac{c}{c_{\mathrm{eq}}(T)}-1\right)^{g} \tag{11.23}$$

where both the growth rate constant (through an Arrhenius-like term) and the solubility depend on temperature. The term $S(c,T) = c/c_{\mathrm{eq}}(T)$ is called the saturation ratio, and when assuming that the ratio between the activity coefficients at saturation and at supersaturation is approximately one, $(S-1)$ represents the thermodynamic driving force. The dependency of the growth rate on $(S-1)$ is given through an empirical power law.

The nucleation rate B is defined as in Eq. 11.14, hence the secondary nucleation frequency $K(L) = b(c,T,\epsilon)L^{j}$, where $b(c,T,\epsilon)$ contains the temperature- and supersaturation-dependent terms of the nucleation kinetics. It is defined as power law of the thermodynamic driving force:

$$b(c,T) = k_{\mathrm{sh}}k_{\mathrm{b}}(T)\left(\frac{c}{c_{\mathrm{eq}}(T)}-1\right)^{b} \tag{11.24}$$

where k_{sh} is a crystal shape factor, which is called k_{v} if $j = 3$ and k_{a} if $j = 2$, and where we neglect the dependency on energy dissipation, ϵ, for simplicity. Numerous mechanistic expressions for $b(c,T)$ have been reported in the literature as well, and we refer to an earlier contribution for a summary of the relevant mechanisms.[278] Substituting the last equation in the birth rate definition of Eq. 11.17 and using the well-known relation $\int_0^\infty L^{j}\exp\left(-L/(G\hat{\tau})\right)\mathrm{d}L = (G\hat{\tau})^{j+1}\Gamma(j+1)$ yields (note that $j \geq 0$):

$$\nu(c,T,\hat{\tau}) = \Gamma(j+1)\hat{\tau}^{j+1}k_{\mathrm{b}}(T)k_{\mathrm{sh}}k_{\mathrm{g}}^{j}(T)\left(\frac{c}{c_{\mathrm{eq}}(T)}-1\right)^{jg+b} \tag{11.25}$$

where $\Gamma(j+1)$ is the gamma function, which equals $j!$ if j is an integer. For the two common cases where nucleation scales either with volume ($j = 3$) or with surface area ($j = 2$) of the crystals, one obtains

$$\nu(c, T, \hat{\tau}) = 6\hat{\tau}^4 k_b(T) k_v k_g^3(T) \left(\frac{c}{c_{eq}(T)} - 1 \right)^{3g+b}; \quad \text{for } j = 3 \tag{11.26}$$

$$\nu(c, T, \hat{\tau}) = 2\hat{\tau}^3 k_b(T) k_a k_g^2(T) \left(\frac{c}{c_{eq}(T)} - 1 \right)^{2g+b}; \quad \text{for } j = 2 \tag{11.27}$$

Imposing $\nu(c_{ss}, T, \hat{\tau}) = 1$ and re-arranging yields the following explicit expressions for the steady state concentration:

$$c_{ss}(T, \hat{\tau})/c_{eq}(T) = 1 + \left(6\hat{\tau}^4 k_b(T) k_v k_g^3(T) \right)^{-\frac{1}{3g+b}}; \quad \text{for } j = 3 \tag{11.28}$$

$$c_{ss}(T, \hat{\tau})/c_{eq}(T) = 1 + \left(2\hat{\tau}^3 k_b(T) k_a k_g^2(T) \right)^{-\frac{1}{2g+b}}; \quad \text{for } j = 2 \tag{11.29}$$

Eqs. 11.28 and 11.29 demonstrate that c_{ss} depends on temperature through both the solubility $c_{eq}(T)$ and through the crystallization kinetics. It further depends on residence time, whereby longer times lead to smaller values of c_{ss}; this is relevant in the context of polymorphic steady states, where longer residence times favor the thermodynamically stable polymorph (see Section 11.3.3). It is worth noting that Eqs. 11.28 and 11.29 may also be obtained when applying the method of moments to the population balance equation, as often done in the literature;[45,243,270] however, the method of moments is not generally applicable to arbitrary functional forms for $P_L(L)$, $K(L)$, and $G(L)$, unlike the approach presented here. We discuss an example of such a case in the next section.

11.3.2 Size-dependent withdrawal

Size-dependent, or classified, crystal withdrawal commonly occurs in mixed suspension crystallizers and has been studied as early as in the 1960s'.[271,272] The possible occurrence of multiple steady states had been identified earlier as well,[270,279] focusing on the role of the nucleation rate expression in causing it. Here we combine and expand these concepts and show how size-dependent withdrawal leads to steady state multiplicity.

To this aim, we consider the following empirical expression for the size-dependent withdrawal factor ξ:

$$\xi(L) = \frac{1 + a_0 L^2}{1 + a_1 L^2} \tag{11.30}$$

where a_0 and a_1 are two positive constants.[271] According to this expression, small particles are withdrawn ideally, i.e., at the same rate as the fluid ($\xi \to 1$ as $L \to 0$), whereas larger and larger particles are withdrawn with a withdrawal factor ξ approaching a_0/a_1: if $a_0 > a_1$ or $a_0 < a_1$ crystals are withdrawn more or less likely than the fluid, respectively. Substituting the last equation in the birth rate definition of Eq.11.17 yields:

$$\nu(c, T, \tau, a_0, a_1) = \frac{b(c,T)}{G(c,T)} \int_0^\infty L^j \exp\left(-\frac{1}{\tau G(c,T)}\left(\frac{(a_1 - a_0)}{a_1^{1.5}} \arctan(\sqrt{a_1}L) + \frac{a_0}{a_1}L\right)\right) \mathrm{d}L \tag{11.31}$$

assuming for simplicity that $G(c,T)$ is size-independent. Of particular interest is the case $a_0 > a_1$, i.e., where large particles preferentially leave the crystallizer. In this case, the monotonic behavior of $\nu(c)$ with c is not guaranteed, and the equation $\nu(c_{ss}) = 1$ may have multiple solutions. Figure 11.3 (a) shows the birth rate function for a scenario where three concentration levels fulfil $\nu(c_{ss}) = 1$.

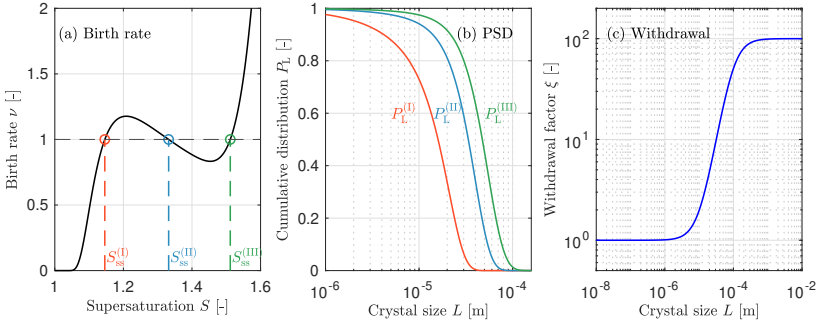

Figure 11.3 Example for a system with multiple steady-states. (a) Non-monotonic birth rate with three steady-state supersaturation levels (orange, blue, green). (b) Corresponding cumulative distributions for the three steady states. (c) Withdrawal factor as function of the crystal size, with $a_0/a_1 = 100$).

This scenario was constructed in three steps. First, by taking values for the kinetic parameters and solubility from the literature[280] for the α polymorph of L-glutamic acid, which by themselves lead to a monotonic birth rate. Second, by enforcing a particularly strong size-dependency of the withdrawal ($a_0/a_1 = 100$, see panel (c)), which leads to a locally non-monotonic behavior of the birth rate; and third, by appropriately adjusting the kinetic parameters for

nucleation and growth to ensure that the non-monotonic region includes the value $\nu = 1$. Obviously, the particle size distributions that correspond to the three steady states are different, whereby higher steady-state concentrations correspond to larger crystal sizes with a narrower distribution, as shown in panel (b).

Given the rather specific and unrealistic conditions required to obtain steady state multiplicity, this case is of little practical relevance. In the following, we hence implicitly assume that the birth rate function increases monotonically with concentration, thus leading to a unique steady state.

11.3.3 Polymorphic steady states

Experimental studies have demonstrated that continuous mixed suspension crystallizers are capable of operating stable and pure steady states for both metastable and stable polymorphs,[49,262] which was explained using a linear stability analysis based on the method of moments.[258,266] These earlier studies established that the crystallization of a polymorphic compound may lead to three types of steady states: (i) a trivial steady state in which no crystals exist, (ii) a pure steady state containing crystals of one polymorph only, either the stable one or a metastable one. And (iii), a mixed steady state where crystals of multiple polymorphs are present. We here generalize this analysis using the birth rate approach.

All $i = 1, 2..., N$ polymorphs of a compound have distinct properties, i.e., solubility, crystallization kinetics, and withdrawal factor, so that they may exhibit distinct birth rates ν_i and thus steady state concentration levels $c_{\mathrm{ss,i}}$ for any given set of operating conditions (i.e., T, τ). Figure 11.4 (a) shows the birth rates for a bi-polymorphic system for operating conditions where $c_{\mathrm{ss},1} < c_{\mathrm{ss},2}$. As discussed in Section 11.2.4, the value of the inlet concentration c_0 must be known to identify the steady state, hence there are three potential cases: first, that $c_0 < c_{\mathrm{ss},1} < c_{\mathrm{ss},2}$, which leads to a trivial steady state without crystals as neither polymorph can maintain a positive suspension density. Second, that $c_{\mathrm{ss},1} < c_0 < c_{\mathrm{ss},2}$. In this case, a pure steady state at $c_{\mathrm{ss},1}$ is obtained, because only polymorph 1 can maintain a positive suspension density, whereas crystals of polymorph 2, if inserted, would be washed out.

The third case, $c_{\mathrm{ss},1} < c_{\mathrm{ss},2} < c_0$, requires a more detailed analysis, because if they were alone, both polymorphs could maintain a stable steady state with a positive suspension density. The stability of these states depends on what happens when perturbing them by adding crystals of the other polymorph (or in general, with crystals of all other polymorphs). Only when perturbations with crystals of all other polymorphs lead to the recovery of the original state,

a pure steady state is stable. Making use of the birth rates, the pure steady state of polymorph i is stable when at the given value of $c_{ss,i}$ the birth rates of all other polymorphs j are $\nu_{j\neq i}(c_{ss,i}) < 1$. Let us consider again Figure 11.4 (a): at $c_{ss,2}$, it holds that $\nu_1(c_{ss,2}) > 1$, so the pure steady state of polymorph 2 is unstable with respect to the appearance of polymorph 1. Conversely, if crystals of polymorph 2 were to be added to a pure steady state of polymorph 1, they would be washed out over time due to $\nu_2(c_{ss,1}) < 1$. Hence, the pure steady state of polymorph 1 is stable.

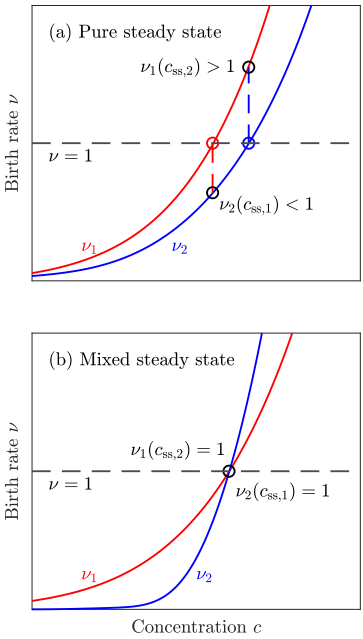

Figure 11.4 Birth rates ν_1 (red) and ν_2 (blue) as a function of concentration in the crystallizer for a given set of operating conditions T and τ. The horizontal dashed line indicates $\nu = 1$, the condition for the steady-state concentrations. (a) Scenario of a pure steady state, i.e., where $c_{ss,2} > c_{ss,1}$. (b) Scenario of a mixed steady-state, i.e., where $c_{ss,2} = c_{ss,1}$.

In fact, it is not a coincidence that the stable steady state in this example is the one with the smallest steady state concentration; such behavior is a

direct consequence of the monotonicity of the birth rates, and hence can be considered as a general rule. Note that this is independent of the number of polymorphs, i.e., it applies also to compounds with three or more polymorphs, which is the case for many or most industrially relevant compounds (consider e.g., mannitol and calcium carbonate).

A mixed steady state that contains crystals of multiple polymorphs is a special case of the pure steady state where multiple polymorphs share the lowest steady state concentration level (see panel b). One can identify the set of operating conditions (T, τ) that lead to such mixed state: temperature and residence time provide two degrees of freedom, one of which is exploited by the condition $c_{\mathrm{ss},1}(T,\tau) = c_{\mathrm{ss},2}(T,\tau)$, so that the residence time $\tau_{\mathrm{mix}}(T)$ at which the mixed state occurs can be expressed as a function of temperature, and vice versa. This is practically useful, because the mixed steady state represents the frontier of the regions in the (T,τ) plane corresponding to the pure steady states: if $\tau > \tau_{\mathrm{mix}}$, the pure state of one polymorph is obtained, and for $\tau < \tau_{\mathrm{mix}}$, the one of the other polymorph.

To conclude this section, we assess the implications of this analysis for the polymorphic design space, i.e., the polymorphic outcome of the crystallization process as function of the operating conditions (T, τ). Figure 11.5 illustrates the design space for the bi-polymorphic compound L-glutamic acid, computed using the kinetic parameters and solubility values reported in the literature,[280] and assuming ideal withdrawal ($\xi = 1$) and that no cross-nucleation between the polymorphs takes place. This design space has been simulated recently by solving the transient population balance equation for a large number of operating conditions.[259] Our analysis quantitatively agrees with the previous one, but it is based on the newly introduced birth rate approach, which leads to orders of magnitude lower computational costs (run time $<$ 1s to generate the figure on a M1 MacBook Pro).

Figure 11.5 shows three lines, which divide the (T, τ) plane into six regions. The black line corresponds to the mixed steady state, i.e., the condition $c_{\mathrm{ss},\alpha}(T,\tau) = c_{\mathrm{ss},\beta}(T,\tau)$, as discussed before. The $N = 2$ colored lines indicate the relationships $c_{\mathrm{ss,i}}(T,\tau) = c_0$, which means that they represent the frontier between the pure steady state of the i-th polymorph (red for α, blue for β) and the trivial steady state without crystals. All three lines intersect at a single point, which fulfils the condition $c_{\mathrm{ss},\alpha}(T,\tau) = c_{\mathrm{ss},\beta}(T,\tau) = c_0$, in this case $c_0 = 29\mathrm{g/kg_s}$. When decreasing the value of c_0, this point would shift on the black line towards larger residence times, hence enlarging the two regions in which the stable steady state is the trivial one without crystals. The opposite is true when increasing the value of c_0.

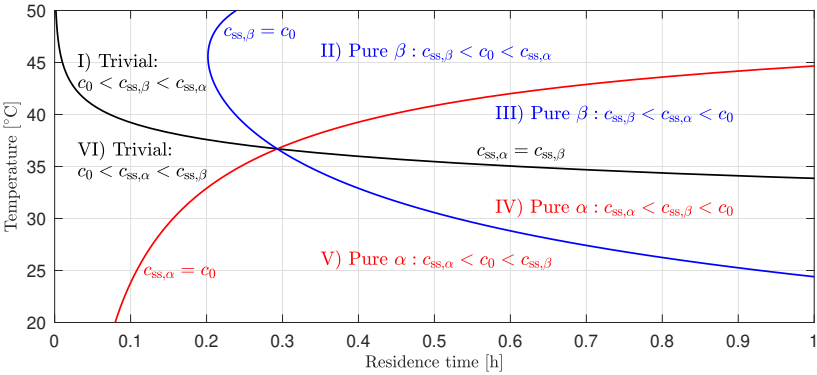

Figure 11.5 Polymorphic design space for the bi-polymorphic compound L-glutamic acid. The kinetic parameters for secondary nucleation and growth as well as the solubility values were taken from the literature.[280] The polymorphic outcome is governed by three lines, which represent the condition $c_{ss,\alpha}(T,\tau) = c_{ss,\beta}(T,\tau)$ (black) and $c_{ss,i}(T,\tau) = c_0$ (red for α, blue for β).

The stable steady state attained in each of the six regions is identified using the analysis done before, i.e., it is governed by which value out of c_0 and the two steady-state concentration levels is the smallest. In regions I) and VI), this is c_0, so that the stable steady state is a trivial one without crystals. In regions II) and III), $c_{ss,\beta}$ is the smallest, hence the pure steady state of the β polymorph is stable. Likewise, in regions IV) and V), $c_{ss,\alpha}$ is the smallest, and the pure steady state of the α polymorph is stable.

11.3.4 Cross-nucleation of polymorphs

The previous section considered polymorphic systems where each polymorph forms secondary nuclei of the same polymorph only. Such behavior is in line with the general understanding of secondary nucleation, even though for some systems cross-nucleation of polymorphs has been observed experimentally:[259,268,281,282] this means that crystals of one polymorph form secondary nuclei not only of the same polymorph, but also of others. For a detailed discussion of this phenomenon, we refer to an earlier contribution,[259] which has revealed that steady states in the presence of cross-nucleation are in general mixed; however, no theoretical analysis has been carried out. Here we show how to generalize the birth rate concept to cross-nucleating systems.

The total nucleation rate B and the total particle size distribution $f(L)$ for a system with N cross-nucleating polymorphs comprise the contributions of all polymorphs so that:

$$B = \sum_{i=1}^{N} B_i, \qquad f(L) = \sum_{i=1}^{N} f_i(L) \tag{11.32}$$

where $f_i(L)$ is defined through the properties of the i-th polymorph, as

$$f_i(L) = \frac{B_i}{G_i(L)} \exp\left(- \int_0^L \frac{\xi_i(\lambda)}{\tau G_i(\lambda)} \mathrm{d}\lambda \right) = \frac{B_i}{G_i(L)} P_{\mathrm{L},i}(L) \tag{11.33}$$

Because crystals of all N polymorphs may nucleate crystals of polymorph i, the nucleation rate B_i is written as

$$B_i = \sum_{j=1}^{N} B_{ij} = \sum_{j=1}^{N} \int_0^{\infty} K_{ij}(L) f_j(L) \mathrm{d}L \tag{11.34}$$

whereby the secondary nucleation frequency K_{ij} used in Eq. 11.34 denotes the rate at which crystals of polymorph j nucleate crystals of polymorph i. Similarly, the birth rate ν_{ij} for cross-nucleating systems is defined as

$$\nu_{ij}(c, T, \tau) = \int_0^{\infty} K_{ij}(L(a), c, T) P_j(a, c, T, \tau) \mathrm{d}a = \int_0^{\infty} \frac{K_{ij}(L, c, T)}{G_j(L, c, T)} P_{\mathrm{L},j}(L, c, T, \tau) \mathrm{d}L \tag{11.35}$$

where ν_{ij} gives the expected number of crystals of polymorph i nucleated by a crystal of polymorph j during its lifetime. Dividing Eq. 11.34 by the nucleation rate B, introducing the expression for $f_i(L)$ given by Eq. 11.33, and defining the nucleation fraction $\alpha_i = B_i/B$ leads to

$$\alpha_i = \sum_{j=1}^{N} \int_0^{\infty} \alpha_j \frac{K_{ij}(L)}{G_j(L)} P_{\mathrm{L},j}(L) \mathrm{d}L = \sum_{j=1}^{N} \alpha_j \nu_{ij} \tag{11.36}$$

where the second equality follows when considering the birth rate given in Eq. 11.35. The relation $\sum_{i=1}^{N} \alpha_i = 1$ and the N Eqs. 11.36 form a system of $N+1$ equations in $N+1$ unknowns, namely the value of the steady state concentration, and N values of the nucleation fractions α_i. For a bi-polymorphic system, one obtains:

$$\alpha_1 = \alpha_1 \nu_{11} + \alpha_2 \nu_{12} \tag{11.37}$$

$$\alpha_2 = \alpha_1 \nu_{21} + \alpha_2 \nu_{22} \tag{11.38}$$

Combining the two equations and considering $\alpha_1 + \alpha_2 = 1$ yields the relation

$$(1 - \nu_{11})(1 - \nu_{22}) = \nu_{12} \nu_{21} \tag{11.39}$$

where the four birth rates all depend on the steady-state concentration c_{ss} as the sole unknown. With c_{ss} known, the nucleation fractions α_i are computed from either Eq. 11.37 or 11.38, and the absolute value of B is found through the material balance.

Let us consider Eq. 11.39 in detail: at a sufficiently small concentration, all birth rates are zero, hence the l.h.s. equals one, and the r.h.s equals zero. An increase in concentration leads to an increase in all birth rates (given they are monotonic), so that the value of the l.h.s decreases, and the one of the r.h.s. increases. Thus, there is a unique solution for c_{ss}. Finally, Eq. 11.39 applies also if no cross-nucleation were to take place. In this case, the birth rates ν_{12} and ν_{21} would be zero at all concentration levels, and the equation is met for $\nu_{11} = 1$ and for $\nu_{22} = 1$, which agrees with the earlier discussion in Section 11.3.3.

11.3.5 Chiral steady states

In this section we study a crystallizer fed with a racemic solution of the two enantiomers of a chiral compound; given the rising demand for the crystallization of enantiopure drug products in the pharmaceutical industry, continuous chiral crystallization is increasingly studied in the literature.[105,283–285] Not accounting for potential polymorphism or solid solutions, a racemic solution of a chiral compound may crystallize into two solid forms:[53] first, a racemic crystal that contains both enantiomers in a 1:1 ratio in a regular lattice (termed DL crystal), and second, a conglomerate of enantiopure crystals that contain molecules of only one of the two enantiomers (termed D and L crystals). Since enantiomers exhibit identical physicochemical properties except for how they interact with other chiral entities, the D and L crystals behave identically also in the crystallizer, thus leading to a number of symmetric situations, among which there is the fact that $c_{ss,L} = c_{ss,D}$ under all operating condition (T, τ, ϵ). Conversely, the solubility, the crystallization kinetics, and the withdrawal behavior of the racemic DL crystal differ from those of the enantiopure D and L crystals.

Chiral conglomerate-forming compound: Let us consider a chiral compound that forms a conglomerate, i.e., one that forms D and L crystals only. Since all relevant properties of the two enantiomers are identical, their birth rates are identical as well, and hence the stable steady state must contain both types of crystals in equal amounts, i.e., it must be racemic. This follows when considering an enantiopure state where only a single type of crystals (say L) is in suspension. Since the growth of these L crystals depletes the concentration of L in solution only, but not that of D, it must hold for such state that $c_D = c_{0,D} > c_{ss,L}$. This means that $\nu_D(c_D) > 1$ so that if D crystals

were added, their population were to amplify itself until a racemic state with $c_L = c_{ss,L} = c_{ss,D} = c_D$ is attained. This racemic state remains stable even if there were a racemization reaction in solution, as commonly studied in the context of solid-state deracemization.[285,286]

Achiral conglomerate-forming compound: Some compounds such as the inorganic salts sodium bromate or sodium chlorate are achiral in solution, but form two types of enantiopure crystals. This is different from the previous case, because there is only one solute in solution, not two. Given the identical kinetics of the enantiopure D and L crystals and that they both contain the same solute, their birth rates must equal each other under all operating conditions. The stability of the steady state hence is independent of its handedness, i.e., it is marginally stable with respect to perturbations. This again follows when considering an enantiopure state of L, and assessing its behavior when perturbing it with D crystals: such perturbation would neither grow, nor would the original state be recovered. This finding of marginal stability well explains recent experimental studies that have shown that an enantiopure state of sodium bromate obtained through seeding can be maintained over multiple residence times in an MSMPR crystallizer before slowly losing enantiopurity (e.g., through primary or cross-nucleation).[105,284]

Racemic crystal-forming compound: Finally, we study a compound that forms not only the enantiopure D and L crystals, but also the racemic DL crystal; this applies to about 90% of all chiral compounds.[53] The solubility of the racemic crystal is given in terms of a temperature-dependent solubility product $\kappa_{DL}(T)$, and its supersaturation as[53]

$$S_{DL}(T) = \sqrt{\frac{c_L c_D}{\kappa_{DL}(T)}}. \tag{11.40}$$

Since S_{DL} depends on the concentration of both enantiomers, its birth rate $\nu_{DL}(c_D, c_L)$ is a function of both as well. Consequently, there is a group of concentration levels that fulfils $\nu(c_D, c_L) = 1$. We limit the stability analysis to the case of a racemic feed where $c_L = c_D$, so that there is a unique value for the steady-state concentration of the DL crystal. The stability analysis of such system is identical to the one of a bi-polymorpic compound (see Section 11.3.3), but with the racemic DL crystal and the racemic conglomerate of D and L crystals as the two attainable solid forms.

11.4 CONCLUDING REMARKS

In this work we have revisited the mathematical description of the continuous mixed suspension crystallizer and introduced a general framework to

assess the stability of its steady states. The analysis is based on the birth rate ν, which denotes the expected number of daughter crystals born by a parent crystal throughout its lifetime in the crystallizer. A stable steady state with crystals is defined through the following three conditions: (i) $\nu(c_{ss}) = 1$, i.e., the birth rate at the steady state concentration level must equal one at all operating conditions. (ii) $d\nu/dc > 0$, i.e., the derivative of the birth rate at the value of the steady state concentration must be positive, as to be stable against perturbations. (iii) $c_0 > c_{ss}$, i.e., the steady state must maintain a positive suspension density. This set of conditions enables the steady state analysis for a general mixed suspension crystallizer, applicable to arbitrary kinetic rate expressions for crystal growth and secondary nucleation, to size-dependent crystal growth and crystal withdrawal, and to growth rate dispersion.

The application of this theory to compounds with multiple solid forms, i.e., polymorphic and chiral compounds, is of particular interest. The analysis of the polymorphic steady states generalizes the existing approaches and is in agreement with the relevant literature.[258,259,263] Concerning chiral systems, enantiopure steady states for racemic feeds are found to be inherently unstable with respect to the appearance of the second enantiomer. This explains why the enantiopure continuous crystallization of chiral compounds is particularly challenging.

Thus summarizing, the insights obtained through the new mathematical framework presented here promise to further facilitate implementation of mixed suspension crystallizers across industries. The generalized steady-state analysis provides practitioners with the opportunity to study the process behavior of complex systems in detail without the need to resort to computationally much more expensive numerical simulations.

11.5 ADDITIONAL SCENARIOS

This section contains three derivations that illustrate how to apply the birth rate analysis to specific scenarios. We consider growth rate dispersion in Section 11.5.1, size-dependent crystal growth in Section 11.5.2, and a suspension-fed crystallizer in Section 11.5.3.

11.5.1 Growth rate dispersion

Growth rate dispersion describes the phenomenon that crystals of the same size and shape grow at different rates. It is widely observed in experimental studies,[254,287–289] and its effect on the behavior of an MSMPR crystallizer

has been studied theoretically already in the 1980s.[255,290,291] In line with the relevant literature, growth rate dispersion is described as random variability in the growth rate pre-factor among crystals, termed $k_{g,0}$ in Eq. 11.23. $k_{g,0}$ follows the distribution p_g where $p_g(k_{g,0})\mathrm{d}k_{g,0}$ is the fraction of crystals with values of the growth pre-factor between $k_{g,0}$ and $k_{g,0} + \mathrm{d}k_{g,0}$. The distribution itself may be of arbitrary shape, but must be normalized as probability density function, so that

$$\int_0^\infty p_g(k_{g,0})\mathrm{d}k_{g,0} = 1. \tag{11.41}$$

Such distribution in $k_{g,0}$ complicates the link between the size of a crystal and its time spent in the crystallizer. Conceptually, one may interpret growth rate dispersion as the presence of infinitely many infinitesimally small sub-populations of crystals, with identical secondary nucleation frequency $K(L)$ and withdrawal factor $\xi(L)$, but with distinct growth rates $G(L, k_{g,0})$ and hence distinct residence probabilities $P_L(L, k_{g,0})$:

$$P_L(L, k_{g,0}) = \exp\left\{-\int_0^L \frac{\xi(\lambda)}{G(\lambda, k_{g,0})\tau}\mathrm{d}\lambda\right\} \tag{11.42}$$

All sub-populations contribute to the overall birth rate ν of the suspension, to the overall nucleation rate B and to the overall particle size distribution $f(L)$. The birth rate expression hence is obtained by expanding Eq. 11.17 as follows

$$\nu(c, T, \tau) = \int_0^\infty p_g(k_{g,0}) \int_0^\infty P_L(L, k_{g,0}, c, T, \tau)\frac{K(L, c, T)}{G(L, k_{g,0}, c, T)}\mathrm{d}L\ \mathrm{d}k_{g,0} \tag{11.43}$$

and it is used to compute the steady state concentration level as discussed in Section 11.2.4. The overall nucleation rate B is found when considering the sub-populations in the mass balance (Eq. 11.13), as to

$$B = (c_0 - c_{ss})\left(\rho_c k_v \int_0^\infty p_g(k_{g,0}) \int_0^\infty \frac{L^3\xi(L)}{G(L, k_{g,0})}P_L(L, k_{g,0})\mathrm{d}L\ \mathrm{d}k_{g,0}\right)^{-1} \tag{11.44}$$

where we impose that both the crystal density ρ_c and the volume shape factor k_v are identical for all sub-populations. The overall particle size distribution $f(L)$ is obtained when integrating over all sub-populations:

$$f(L) = B\int_0^\infty p_g(k_{g,0})\frac{P_L(L, k_{g,0})}{G(L, k_{g,0})}\mathrm{d}k_{g,0} \tag{11.45}$$

Hence, if the growth rate distribution p_g is known, all properties of the steady state can be computed following the approach presented in the main body. To conclude, we emphasize that the theoretical approach developed in this

work applies to systems with growth rate dispersion as well; growth rate dispersion does not change the underlying behavior of the crystallizer, but merely influences the precise values of the relevant properties of the steady state such as the steady state concentration level.

11.5.2 Size-dependent growth

Size-dependent growth describes the phenomenon that the growth rate $G(L)$ depends on crystal size L, whereby larger crystals typically grow faster than smaller ones.[275,277] There are different reasons for such behavior, including (1) the notion that particles of different sizes behave different in a flow field,[276] (2) the effect of the size-dependent surface curvature on a crystal's solubility (Gibbs-Thomson effect),[275] and (3) the misinterpretation of alternative crystallization phenomena such as crystal agglomeration or growth rate dispersion.[290,292,293] Hence, from a practical point of view, a size-dependent growth rate provides a useful tool to empirically account for a plethora of effects that may be relevant but too complex for a more rigorous mathematical treatment.

In this section, we show how to characterize the steady-state for a system with size-dependent growth, using the following expression for the size-dependent growth rate:[293]

$$\frac{\mathrm{d}L}{\mathrm{d}a} = G_0(c,T)\left(1+\frac{L}{\alpha}\right) \tag{11.46}$$

where $G_0(c,T)$ is the growth rate of a crystal of zero size, and α is an empirical positive constant that can be fitted to experimental data. Solving this equation subject to the initial condition $L(0)=0$ gives the size of a crystal as a function of its age:

$$L(a) = \alpha\left(\exp\left(\frac{G_0 a}{\alpha}\right)-1\right) \tag{11.47}$$

Considering size-independent crystal withdrawal ($\hat{\tau}=\tau/\xi$), the birth rate ν can be expressed as

$$\nu(c,T,\hat{\tau}) = b(c,T)\int_0^\infty L(a)^j \exp\left(-\frac{a}{\hat{\tau}}\right)\mathrm{d}a \tag{11.48}$$

The integral converges if the size-dependency is sufficiently small. Assuming that secondary nucleation scales with crystal surface area ($j=2$), this holds true for values $\alpha > 2G_0\hat{\tau}$, leading to the following expression for the birth rate:

$$\nu(c,T,\hat{\tau}) = \alpha^2 b(c,T)\hat{\tau}\left[\frac{\alpha}{\alpha-2G_0(c,T)\hat{\tau}} - \frac{2\alpha}{\alpha-G_0(c,T)\hat{\tau}} + 1\right] \tag{11.49}$$

ν may be computed analytically using this expression, making the computation of the steady-state concentration straightforward. The particle size distribution $f(L)$ is obtained by inserting the expression for $G(L)$ into Eq. 11.3:

$$f(L) = \frac{B}{G(L)} \exp\left(-\int_0^L \frac{1}{G(\lambda)\tilde{\tau}} \mathrm{d}\lambda\right) = \frac{n_0^{\mathrm{out}}}{G_0 \tau} \left(1 + \frac{L}{\alpha}\right)^{-\left(1+\frac{\alpha}{G_0\tilde{\tau}}\right)} \tag{11.50}$$

where B is obtained as discussed in Section 11.2. Similar derivations can be carried out for different expressions of the size-dependent growth rate; the main conclusion of this case study is that size-dependent growth only affects the relationship between the size of a crystal and its age, but it does not change the general behavior of the steady state.

11.5.3 Suspension-fed crystallizer

In this section, we model a crystallizer fed with a suspension of known particle size distribution $f^{\mathrm{in}}(L) = n_0^{\mathrm{in}} p^{\mathrm{in}}(L)$. During their lifetime in the crystallizer, the fed particles will both grow and generate secondary nuclei. The secondary nuclei, similarly will grow and generate additional secondary nuclei. Hence, the description of such system is more complex than that of the solution-fed crystallizer. Nevertheless, one can still apply the birth rate approach, as we do in the following.

To facilitate the mathematical treatment, the populations of fed particles (termed seeds) and of nucleated particles are treated separately, i.e.,

$$f(L) = f_{\mathrm{seed}}(L) + f_{\mathrm{nuc}}(L), \quad f^{\mathrm{out}}(L) = f_{\mathrm{seed}}^{\mathrm{out}}(L) + f_{\mathrm{nuc}}^{\mathrm{out}}(L). \tag{11.51}$$

For the nucleated particles, the mathematical description initially derived in Section 11.2 applies, so that

$$f_{\mathrm{nuc}}^{\mathrm{out}}(L) = \frac{n_{0,\mathrm{nuc}}^{\mathrm{out}} \xi(L)}{G(L)\tau} \exp\left(-\int_0^L \frac{\xi(\lambda)}{\tau G(\lambda)} \mathrm{d}\lambda\right) \tag{11.52}$$

as well as the usual definition of the birth rate, here called ν_{nuc}. To describe the behavior of the fed particles, we first formulate the residence probability $P_{\mathrm{L_0}}(L, L_0)$ and the associated PDF in the outlet stream $p_{\mathrm{L_0}}^{\mathrm{out}}(L, L_0)$ for a *monodisperse* population of seeds with initial size L_0:

$$P_{\mathrm{L_0}}(L, L_0) = \exp\left(-\int_{L_0}^L \frac{\xi(\lambda)}{\tau G(\lambda)} \mathrm{d}\lambda\right) \tag{11.53}$$

$$p_{\mathrm{L_0}}^{\mathrm{out}}(L, L_0) = \frac{\xi(L)}{\tau G(L)} \exp\left(-\int_{L_0}^L \frac{\xi(\lambda)}{\tau G(\lambda)} \mathrm{d}\lambda\right) \tag{11.54}$$

Next, by imposing that the PDF of the seeds' crystal size distribution at the inlet, $p^{\text{in}}(L_0)$, is known (as one can measure it before feeding it), one can compute the corresponding one in the outlet, $p^{\text{out}}_{\text{seed}}(L)$, by integrating over all initial sizes L_0

$$p^{\text{out}}_{\text{seed}}(L) = \int_0^L p^{\text{in}}(L_0) p^{\text{out}}_{\text{L}_0}(L, L_0) \mathrm{d}L_0 = \int_0^L p^{\text{in}}(L_0) \frac{\xi(L)}{\tau G(L)} P_{\text{L}_0}(L, L_0) \mathrm{d}L_0 \tag{11.55}$$

which is related to the outlet PSD of the seeds, $f^{\text{out}}_{\text{seed}}(L)$, through $f^{\text{out}}_{\text{seed}}(L) = n^{\text{in}}_0 p^{\text{out}}_{\text{seed}}(L)$, as the number density of the seed particles in the outlet stream must equal the one in the inlet stream at steady state. The mass balance can be re-formulated using these definitions as

$$\frac{c_0 - c_{\text{ss}}}{\rho_{\text{c}} k_{\text{v}}} = \int_0^\infty L^3 n^{\text{in}}_0 \left(p^{\text{out}}_{\text{seed}}(L) - p^{\text{in}}(L) \right) \mathrm{d}L + \int_0^\infty L^3 n^{\text{out}}_{0,\text{nuc}} p^{\text{out}}_{\text{nuc}}(L) \mathrm{d}L \tag{11.56}$$

considering the contributions of both the nucleated and of the seeded crystals. We next introduce the birth rate, first for a mono-disperse seed population of size L_0, then to the poly-disperse one with the given PDF $p^{\text{in}}(L_0)$:

$$\nu_{\text{L}_0}(L_0) = \int_{L_0}^\infty \frac{K(L)}{G(L)} P_{\text{L}_0}(L, L_0) \mathrm{d}L \tag{11.57}$$

$$\nu_{\text{seed}} = \int_0^\infty p^{\text{in}}(L_0) \nu_{\text{L}_0}(L_0) \mathrm{d}L_0 \tag{11.58}$$

The birth rate of the crystallizer, ν, is obtained by inserting the expression for $f(L)$ derived in this section into Eq. 11.15, dividing by B, using the zero-th moment equation $B\tau = n^{\text{out}}_{0,\text{nuc}}$, and introducing ν_{seed} and ν_{nuc}, as to

$$\nu = \nu_{\text{nuc}} + \frac{n^{\text{in}}_0}{n^{\text{out}}_{0,\text{nuc}}} \nu_{\text{seed}} = 1 \tag{11.59}$$

where the second equality holds at steady state. The mass balance (Eq. 11.56) and the birth rate equation (Eq. 11.59) form a system of two equations and two unknowns, namely c_{ss} and $n^{\text{out}}_{0,\text{nuc}}$. Even though numerical approaches are required to solve this system, some general remarks are worth making.

First, it holds that $\nu_{\text{seed}} >> \nu_{\text{nuc}}$ given that the secondary nucleation frequency $K(L)$ strongly increases with crystal size, so that a seed crystal in average generates more secondary nuclei than a nucleated crystal.

Second, if only growth occurs, but no secondary nucleation, the only unknown is c_{ss}, which is obtained by solving the mass balance, since by definition $n^{\text{out}}_{0,\text{nuc}} = 0$. Such growth-dominated crystallizers are commonly used in the industry as part of crystallizer cascades;[50,243] in a cascade, multiple crystallizers are connected in series. Nuclei are predominantly formed in the first

one, which are then grown to larger sizes at low levels of supersaturation in the subsequent ones.

Third, the pure steady state of a suspension-fed crystallizer may be unstable with respect to the formation of another polymorph. This holds true if the birth rate of such polymorph assumes a value larger than one at the steady-state concentration level computed through solving Eq. 11.56 and Eq. 11.59, in line with the theory derived in the main body. In such case, a mixed steady-state is obtained that comprises both the fed crystals and the secondary nuclei of the first polymorph, as well as the nucleated crystals of the second polymorph.

12 EXACT AND UBIQUITOUS CONDITION FOR SOLID-STATE DERACEMIZATION IN VITRO AND IN NATURE

Solid-state deracemization is the amplification of an enantiomeric excess in suspensions of conglomerate-forming chiral compounds. Although numerous chemical and biochemical compounds deracemize, its governing mechanism has remained elusive. We introduce a novel formulation of the classical population-based model of deracemization through temperature cycles to prove that suspensions deracemize whenever a simple and ubiquitous condition is met: crystal dissolution must be faster than crystal growth. Such asymmetry is a known principle of crystallization, hence explaining the generality of deracemization. Through both experiments and a theoretical analysis, we demonstrate that this condition applies even for very small temperature cycles, and for random temperature fluctuations. These findings establish solid-state deracemization as attractive route to the manufacture of enantiopure products and as plausible pathway towards the emergence of homochirality in nature.

12.1 INTRODUCTION

Solid-state deracemization refers to the amplification of an enantiomeric excess in suspensions of conglomerate-forming compounds, in the presence of racemization in solution.[55,56,294,295] It is an attractive route to the manufacture of enantiopure products, and a possible pathway to the emergence of homochirality on Earth,[55,56,296] which is linked to the origin of life.[297,298] It has been demonstrated by various methods of manipulating the crystalline suspension, namely isothermal grinding or milling,[55,56] the application of ultrasound,[283,299] temperature-cycling in a single[57,300] or in two coupled vessels,[301,302] high-pressure homogenization,[303] and solvent-cycling.[304,305]

The results presented in this chapter have been reported in: Deck, L.-T.; Hosseinalipour, M.S.; Mazzotti, M. Exact and ubiquitous condition for solid-state deracemization in vitro and in nature. *J. Am. Chem. Soc.*. **2024**, 11, 6552–6559.

Numerous compounds have been shown to deracemize, including many of biological relevance,[306–308] which suggests the existence of a general governing mechanism.[55–57,283,295,299,300,303–305,309,310] Yet pinning down such mechanism has been difficult, controversial, and not conclusive.[311–314] In this work, we introduce a simplified formulation of the classical population balance model of deracemization through temperature cycles to prove an exact condition under which deracemization occurs: crystal dissolution must be faster than crystal growth. Such kinetic asymmetry is a fundamental principle of crystallization,[47,315,316] which explains the general success of the deracemization experiments reported in the literature.

The analysis that follows comprises theory, numerical simulations, and experiments. In Section 12.2, the mechanism of solid-state deracemization by temperature-cycling is conceptualized, which serves as starting point for the derivation of an exact condition for deracemization reported in Section 12.3. Comprehensive numerical simulations presented in Section 12.4 confirm that this condition applies not only to deracemization with periodic temperature-cycling, but to processes with arbitrarily oscillating temperature profiles. These findings are validated experimentally: Section 12.5 reports the results of deracemization experiments with the chiral compound N-(2-methylbenzylidene)-phenylglycine amide (NMPA) carried out using periodic temperature cycles, uncontrolled ambient thermal conditions, and a tightly controlled constant temperature level. Finally, conclusions are drawn and implications for the emergence of homochirality in nature are discussed in Section 12.6.

12.2 CONCEPTUAL ANALYSIS

We model solid-state deracemization using population balance equations, an approach widely applied in industrial crystallization and related fields.[45,46,243] Through numerical simulations, our group has successfully described deracemization for both temperature-cycling and isothermal process variations (the latter commonly termed Viedma ripening).[313,317–319] These earlier models attribute deracemization to the interplay between enantioselective crystal agglomeration (yielding a larger crystal by the merge of two smaller ones)[45], crystal breakage and attrition, and crystal ripening (the preferential dissolution of smaller crystals due to size-dependent solubility)[46,320,321]. Even though the overall mechanism to deracemization remains elusive, most contributions agree that both crystal agglomeration and ripening play pivotal roles in it.[311–314]

The mechanistic character of population balance-based models implies that they comprise numerous parameters, some of which are neither accessible through experiments nor predictable through theory. The identification of accurate rate expressions for crystal agglomeration, breakage and ripening, as well as the ensuing estimation of the kinetic parameters from experimental data have been found to be particularly challenging. For this reason it has not yet been possible to conclusively demonstrate which mechanisms control solid-state deracemization. Here we tackle this challenge by reducing the complexity of the underlying population balance model: we eliminate all elements that we prove are not essential to deracemization, thus enabling the derivation of an analytical solution and the design of ad-hoc experiments to confirm the theoretical findings.

In the general model we consider deracemization through periodic temperature cycling in a well-stirred batch crystallizer ($i = 1, 2$ and $j = 3 - i$), where the target (major) enantiomer is $i = 1$, and the undesired (minor) enantiomer is $i = 2$. The racemization reaction between the two enantiomers (E_1, E_2) in solution is described as a reversible first order chemical reaction

$$E_1 \underset{}{\overset{k_r}{\rightleftharpoons}} E_2 \tag{12.1}$$

where the temperature-dependent reaction rate constant, $k_r(T)$, is the same in both directions because of symmetry; therefore at equilibrium the concentration of the two enantiomers is obviously the same. The material balance is:

$$\frac{dc_i}{dt} + \frac{dn_i}{dt} = -k_r(c_i - c_j) \tag{12.2}$$

where c_i and n_i denote the mass of solute per unit mass solvent in solution and in the solid phase, respectively, and $k_r(T)$ is the temperature-dependent rate constant of racemization. The quantity n_i is given in terms of the particle size distribution of the i-th enantiomer crystals, f_i (PSD), as:

$$n_i = \rho_c \int_0^\infty v_c(L) f_i(L) dL \tag{12.3}$$

where ρ_c is the crystal density and $v_c(L) = k_v L^3$ is the volume of a crystal of characteristic size L and volume shape factor k_v. It is worth noting that, in the model system, enantiomers are present either as molecular species in solution (i.e., monomers) or as building blocks of enantiopure crystals, but not as chiral clusters (i.e., oligomers), as proposed in other studies.[311,314]

Eqs. 12.2 are coupled to the population balance equations that determine the two PSDs $f_i(t, L)$; these are transient integro-differential equations that account in general for crystal agglomeration and breakage (both through integral terms), and for crystal growth and dissolution (through a differential

term). In the context of deracemization, nucleation is neglected for two reasons. First, the classical inclusion of nucleation through the boundary condition on the population balance equation at $L = 0$ is incompatible with a model accounting for size-dependent solubility, unless master equations are used that lead to an excessive computational burden.[322] Second, experiments are typically carried out under conditions where little to none nucleation takes place; in particular, the use of slow cooling rates and of large solid loadings prevents the suspension from attaining the large supersaturation levels that would trigger nucleation.[57,300]

The temperature in the crystallizer is assumed to be precisely controlled undergoing periodic cycles, each consisting of a cooling ramp from high temperature, T_d, to low temperature, T_g, a holding period, t_g, at T_g (termed growth step), a heating ramp, and a holding period, t_d, at T_d (termed dissolution step). In the following, ramps are replaced by step changes, without loss of generality. Such cycle is associated to a solubility difference $\Delta c_\infty = c^*(T_d) - c^*(T_g)$, where $c^*(T)$ is the solubility of a crystal of infinite size, i.e., the value that is used when the size-dependency of solubility is neglected.

To assess whether deracemization occurs or not, different indicators can be used, either the change of crystal mass of the two enantiomers over one cycle, or the extent of conversion reaction from the minor to the major enantiomer during one cycle. The change in mass of the major enantiomer crystals per unit mass of solvent throughout a single cycle, Δn_{cyc} is defined as:

$$\Delta n_{cyc} = \int_g k_r(T_g)(c_2 - c_1)\mathrm{d}t + \int_d k_r(T_d)(c_2 - c_1)\mathrm{d}t \tag{12.4}$$

whereby the boundaries of the integrals (g,d) refer to the growth and dissolution steps, respectively. Note that $\Delta n_{cyc} > 0$ is required for successful deracemization. This is illustrated in Figure 12.1, whose three panels illustrate process simulations of temperature cycling (see Section 12.7.1) for different relative rates of dissolution and growth, all other model parameters being identical. Note that, in order to highlight the mechanisms that are prerequisite for deracemization, neither crystal agglomeration, nor breakage or attrition, nor ripening have been included. Moreover, for the sake of simplicity but without loss of generality heating and cooling ramps have been substituted by step changes between temperature levels. The upper row shows the evolution of the enantiomer concentrations c_1 (blue, major enantiomer) and c_2 (red, minor enantiomer), as well as the value of the solubility c^* (black) during a single temperature cycle. The lower row shows the evolution of the crystal mass suspended, n_i, for both crystal populations.

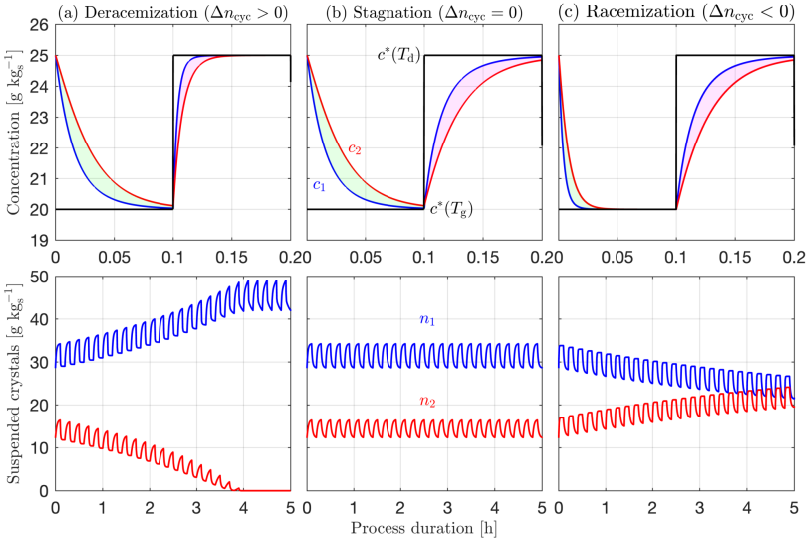

Figure 12.1 Simulations of temperature cycling-induced deracemization for three cases with different process behavior. Top row: Evolution of concentrations in solution during a single cycle. Bottom row: Evolution of suspended crystal density during the entire process. The three simulations were generated using identical model parameters except for the relative rates of growth and dissolution. Growth is either slower than, panel (a), as fast as (b), or faster than (c) dissolution.

Crystals grow at low temperature and dissolve at high temperature. During both steps, a difference in concentration between the enantiomers emerges (shaded areas), which drives the racemization reaction (see Eqs. 12.2) and governs the process performance. Deracemization happens when the net effect of the racemization reaction throughout a temperature cycle favors the major enantiomer (i.e., when $\Delta n_{cyc} > 0$, see Eq. 12.4). To enable a visual analysis of deracemization, we neglect the temperature-dependency of $k_r(T)$ in Figure 12.1, so that the shaded areas are proportional to the amount of reacted material (the integrals in Eq. 12.4). In panel (a), where model parameters are such that dissolution is fast and growth is slow (in general terms, that will be made more precise in the next section), the green area (proportional to the extent of conversion of the minor enantiomer into the major enantiomer) is larger than the red area (proportional to the extent of conversion of the major enantiomer into the minor enantiomer); hence the net effect during the whole cycle favors the major enantiomer and deracemization occurs ($\Delta n_{cyc} > 0$). In panel (c) on the contrary, where growth is fast and dissolution is slow, the

red area is larger than the green one hence temperature-cycling racemizes the suspension ($\Delta n_{\mathrm{cyc}} < 0$). In panel (b), where dissolution and growth have similar rates, both areas are of equal size and temperature-cycling does not alter the handedness of the suspension ($\Delta n_{\mathrm{cyc}} = 0$).

It follows that deracemization is successful if and only if dissolution is faster than growth (in general terms), even in the absence of crystal agglomeration, crystal breakage or attrition, and crystal ripening. This is a novel and simple criterion for deracemization, which is demonstrated rigorously in the next section and whose consequences are presented and demonstrated in the sections after the next.

12.3 EXACT CONDITION FOR DERACEMIZATION

The model used in the previous section, i.e., with neither breakage nor agglomeration, nor size-dependent solubility, has been further simplified for the analysis that follows. First, the area of the active surface of the crystals is assumed to remain constant as their volume changes. This would be the case for rods that grow and dissolve only in the length direction; it would also apply to arbitrary crystal geometries if the actual surface area change through a temperature cycle is small. Second, the growth and dissolution rate of crystals of type i is given by a temperature-dependent rate constant, $k_{\mathrm{m}}(T_{\mathrm{m}})$ (the subscript $\mathrm{m} = \mathrm{g}$ or $\mathrm{m} = \mathrm{d}$ indicates the growth or dissolution phase, respectively), multiplied by the linear driving force $x_i = c_i - c^*(T_{\mathrm{m}})$. Thorough numerical simulations have proven that these two assumptions can be relaxed without changing the main conclusions below (see SI Section 12.8.2).

Under these assumptions, the model reduces to two linear ODEs that can be written in vector notation (see methods Section 12.7.2 for the detailed derivation) as:

$$\begin{bmatrix} \frac{\mathrm{d}x_1}{\mathrm{d}\tau_{\mathrm{m}}} \\ \frac{\mathrm{d}x_2}{\mathrm{d}\tau_{\mathrm{m}}} \end{bmatrix} = \begin{bmatrix} -(a_{\mathrm{m}}+1) & 1 \\ 1 & -(a_{\mathrm{m}}\xi+1) \end{bmatrix} \begin{bmatrix} x_1 \\ x_2 \end{bmatrix} \tag{12.5}$$

where the matrix of coefficients of the linear system is called $\underline{\underline{A}}_{\mathrm{m}}$, and $\tau_{\mathrm{m}} = t k_{\mathrm{r}}(T_{\mathrm{m}})$ is a dimensionless time. The dimensionless parameter $a_{\mathrm{m}} = 3\rho_{\mathrm{c}} k_{\mathrm{v}} m_{2,1} k_{\mathrm{m}}(T_{\mathrm{m}})/k_{\mathrm{r}}(T_{\mathrm{m}})$ is proportional to the ratio of the rate constant of growth or dissolution and of the racemization reaction (at the relevant temperature); $m_{2,i}$ denotes the second moment of the i-th PSD, which scales with the population's surface area per unit mass of solvent; the quantity $\xi = m_{2,2}/m_{2,1} < 1$ characterizes the asymmetry between the enantiomers (the

simplest case is where the two crystal populations are similar in size and shape, but the amount of the minor enantiomer crystals is smaller than that of the major enantiomer crystals). Implementing temperature cycles implies solving the system above for $0 \leq \tau \leq \tau_g = k_r(T_g)t_g$ for an initial solution composition x_i^0, typically racemic, so as x_i becomes x_i^g; then switching to the dissolution temperature level and setting $x_i^0 = x_i^g - \Delta c_\infty$ (so as to account for the change in solubility) and solving the new version of the system above for $0 \leq \tau \leq \tau_d = k_r(T_d)t_d$; finally switching back to T_g and setting $x_i^0 = x_i^d + \Delta c_\infty$. In this way the evolution of the solution composition is obtained, depending on the six model parameters a_g, a_d, Δc_∞, ξ, τ_g, and τ_d.

Independent of the initial state, the solution composition reaches a cyclic steady state, as long as the surface areas of crystals and thus the parameter ξ do not change (see SI Section 12.8.2). The net amount of minor enantiomer converted into the major enantiomer in Eq. 12.4, Δn_{cyc}, can be calculated in closed form as:

$$\Delta n_{cyc} = \frac{\xi\left(a_d - a_g\right)\left(\Delta x_2 - \xi \Delta x_1\right)}{\det\left(\underline{\underline{A}}_d\right)\det\left(\underline{\underline{A}}_g\right)} = \eta \Delta c_\infty \tag{12.6}$$

where the matrices $\underline{\underline{A}}_d$ and $\underline{\underline{A}}_g$ are implicitly defined through Eq. 12.5, and Δx_i is the change in concentration of enantiomer i during the dissolution step given in closed form by:

$$\begin{bmatrix} \Delta x_1 \\ \Delta x_2 \end{bmatrix} = \left(\exp(\tau_d\,\underline{\underline{A}}_d) - \underline{\underline{I}}\right)\left(\underline{\underline{I}} - \exp(\tau_g\,\underline{\underline{A}}_g)\exp(\tau_d\,\underline{\underline{A}}_d)\right)^{-1}\left(\exp(\tau_g\,\underline{\underline{A}}_g) - \underline{\underline{I}}\right)\begin{bmatrix} \Delta c_\infty \\ \Delta c_\infty \end{bmatrix} \tag{12.7}$$

where $\exp(\tau\,\underline{\underline{A}}_m)$ is the matrix exponential and $\underline{\underline{I}}$ is the unitary matrix. The second equality in Eq. 12.6 introduces the cycle efficiency, η, which is the ratio between Δn_{cyc} and the solubility difference Δc_∞, i.e., the maximum value of Δn_{cyc} that a single cycle enables; η is independent of the amplitude of the temperature cycles because Δx_i scales with Δc_∞ as to Eq. 12.7. The two determinants in Eq. 12.6 are always positive, as also ξ obviously is ($\xi = 0$ corresponds to an enantiopure suspension). We found that also the term $(\Delta x_2 - \xi \Delta x_1)$ in the numerator of Eq. 12.6 is *always* positive, by evaluating it for a huge number of combinations of model parameters, selected randomly within broad ranges of values.

Therefore, we conclude that the cycle efficiency η is positive and deracemization occurs if and only if

$$a_d > a_g \tag{12.8}$$

or, as to the relevant definitions, if and only if

$$k_d(T_d)/k_r(T_d) > k_g(T_g)/k_r(T_g). \tag{12.9}$$

Remarkably, this condition is independent of the duration of the dissolution and growth phases, τ_d and τ_g, of the enantiomeric asymmetry, ξ, and of the solubility difference, Δc_∞. This implies that the amplitude of the temperature oscillations leading to successful deracemization may even be extremely small (see Section 12.5 where the reported successful deracemization experiments at a controlled temperature exhibit a standard deviation of 0.02°C), and that the result above applies not only to deracemization by temperature cycling, but also to isothermal Viedma ripening, where minimal temperature fluctuations may certainly be caused by intense stirring or by grinding. It is also worth noting that the analysis above applies also when temperature cycling is replaced by periodic removal and re-addition of the solvent at constant temperature, as proposed in recent experimental studies.[304,305]

Note that in practice and under rather general conditions crystal dissolution is faster than growth for the same thermodynamic driving force and at the same temperature.[47,315,316] This is because the crystal shape evolves during growth towards a steady-state shape dominated by the slowest-growing crystal facets.[47,323,324] Yet the opposite occurs during dissolution, when the crystal shape evolves away from the steady-state shape, thus exposing fast dissolving facets. Data reported in the literature indicate that for instance $k_d/k_g = 4$ for sodium chlorate,[316] and $k_d/k_g > 2.5$ for paracetamol[315] (consider Snyder et al.[47] for a detailed discussion of the asymmetry between growth and dissolution).

Note also that although a strong temperature dependence of the racemization rate constant may in theory switch the sign of the inequality in Eq. 12.9, in practice this is very unlikely given the relatively small amplitudes of temperature cycles used in experiments (order of 5–20°C),[57,300,325] if not at all impossible when considering the very small-amplitude temperature-cycling experiments presented in this work (see Section 12.5).

Finally it is worth noting that the condition derived above holds true no matter how slow (or fast) the chemical reaction is (see Figure 12.4 in the SI). This is an important remark, because most chiral compounds do not racemize easily. For example, amino acids in solution racemize very slowly at ambient temperature and neutral pH, i.e., with a characteristic time on the order of thousands of years.[326,327] The amount of material that reacts in such a case during a temperature-cycle with characteristic times for growth and dissolution on the order of minutes to hours is very small, and deracemization consequently proceeds only very slowly. From an industrial manufacturing perspective, the implementation of solid-state deracemization

is particularly interesting for compounds with fast racemization, e.g., for N-(2-methylbenzylidene)-phenylglycine amide (NMPA) that racemizes in the presence of non-nucleohilic bases within timescales of ten minutes to an hour[56,328] (see Section 12.5).

Based on the considerations above, we argue that the condition in Eqs. 12.8 and 12.9 is met for most chiral species that crystallize as conglomerates and that racemize, in a broad range of temperatures. Thus, solid-state deracemization is based on a simple and ubiquitous growth-dissolution mechanism that requires neither grinding, nor agglomeration, nor ripening.

12.4 EXTENSION TO NEARLY ISOTHERMAL CONDITIONS

While the exact condition above was derived for deracemization through temperature-cycles that induce a periodic change of solubility, here we assess through simulations carried out using the PBE model presented in Section 12.7.1 to what extent such condition and the underlying growth-dissolution mechanism applies also to cases such as isothermal deracemization, i.e., to Viedma ripening, as conjectured in the previous section.

Figure 12.2 shows the outcome of simulations of two processes with $a_d/a_g = 4$ and different values of ξ_0. In the first case the suspension undergoes temperature cycles where the solubility changes by 1%, corresponding to a temperature differential of about 0.2°C for the compound used in the experiments reported below. In the second case the suspension is subject to random temperature fluctuations generated through a random walk constrained within the same range of solubilities; the mean rate of temperature change equals that of the periodic cycling. Similar to Figure 12.1, the top panels illustrate the evolution of the concentration levels in solution, and the center ones those of the crystals in suspension; in addition, the bottom panels indicate the evolution of the enantiomeric excess in the suspension, which is defined as $ee = (n_1 - n_2)/(n_1 + n_2)$, and quantifies enantiopurity.

Notably, deracemization is achieved in both types of simulations, whereby it is faster for periodic temperature cycles than for random fluctuations. In all simulations the temporal evolution of the enantiomeric excess exhibits an acceleration over time. Such *autocatalytic* behavior has been observed in several experimental studies on Viedma ripening in the literature;[56,325,329] it has been argued that non-linear phenomena such as crystal agglomeration are required to explain both deracemization and the mentioned acceleration.[55,295,311–314]

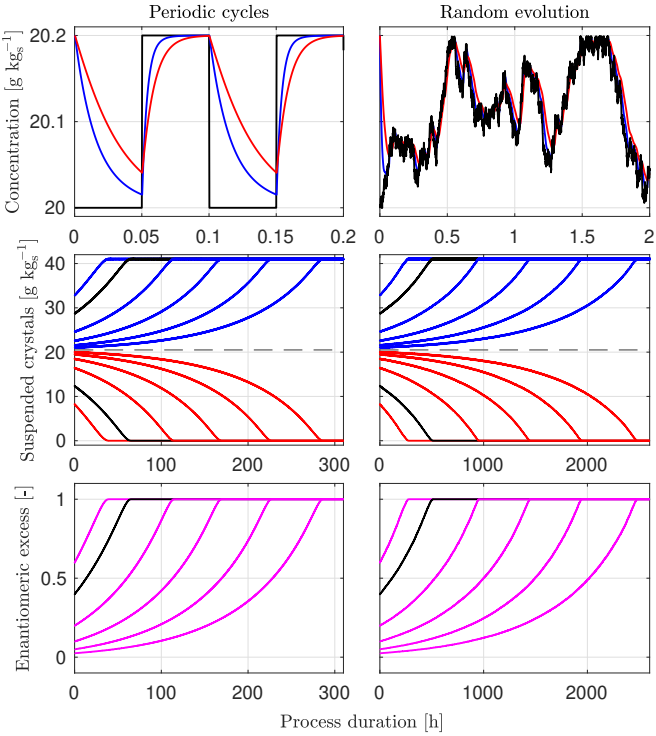

Figure 12.2 Simulations of nearly isothermal deracemization processes with different initial values of ξ. The left column shows small periodic temperature cycles, and the right one randomly generated temperature profiles, generated as random walk constrained between the solubilities used in the periodic cycles. The top row shows the concentration in solution for the simulation with $\xi = 0.43$, as in the experiments. The center panel shows the corresponding evolution of the crystalline mass, and the bottom one that of the enantiomeric excess (black lines correspond to $\xi = 0.43$).

Here we offer a completely different explanation. First, we crucially conjecture that any supposedly isothermal experiment still exhibits arbitrary temperature fluctuations, particularly when a suspension is subject to intense stirring or grinding as in Viedma ripening experiments; therefore, the random temperature fluctuation simulations presented here are indeed representative of Viedma ripening conditions. Second, such simulations demonstrate that deracemization, both in the temperature-cycling case and in the Viedma ripening case, is achieved without including any non-linear phenomenon, whilst

the acceleration in the evolution towards deracemization is due to the fact that the enantiomeric ratio ξ decreases over time because of the conversion of the minor enantiomer into the major one caused by the growth-dissolution mechanism; this leads to an increase over time of the cycle efficiency, η, until the deracemization rate becomes controlled by the irreversible disappearance of crystals of the minority enantiomer during the dissolution steps (see SI Section 12.8.1).

12.5 EXPERIMENTAL EVIDENCE

To provide experimental evidence to the theoretical results above, we carried out deracemization experiments with the conglomerate-forming species N-(2-methylbenzylidene)-phenylglycine amide **(NMPA)**, in the presence of the base 1,8-Diazabicyclo[5.4.0]undec-7-en **(DBU)** that catalyzes its racemization in solution, using 10 mL glass vials (see details in Section 12.7.3). The evolution of the enantiomeric excess during these experiments is shown in Figure 12.3.

The first set of experiments (top panel) consists of temperature cycling with very small amplitudes, i.e., of 2°C, 1°C, and 0.5°C, using a magnetic bar for stirring, and with an initial asymmetry of $\xi_0 = 0.43$ (corresponding to $ee_0 = 0.40$); complete deracemization is achieved in ca. 55, 80, and 160 cycles, respectively (i.e., between one and two days). This is consistent with the model-based analysis above. The number of cycles must in fact scale with the reciprocal of Δn_{cyc} in Eq. 12.4; and therefore, with the reciprocal of the solubility difference, Δc_∞ – which is proportional to the temperature difference for small temperature amplitudes, and with the reciprocal of the cycle efficiency, η – which is by and large independent of the solubility difference. To confirm this, we computed the value of η following the approach outlined in Section 12.8.1 not only for these three experiments where we found $0.12 \leq \eta \leq 0.18$, but also for a large set of earlier NMPA temperature-cycling experiments with similar operating conditions and an amplitude up to 21°C where we found $0.08 \leq \eta \leq 0.13$[330] (see Section 12.8.1 for the details, as well as for consistent results obtained for two other chiral compounds).

Then we carried out two sets of deracemization experiments in the same equipment, whose outcome is shown in the bottom panel of Figure 12.3. The first was operated at 26°C in a tightly controlled manner (the average temperature was 25.97°C, with a standard deviation of 0.02°C). The second was operated under uncontrolled conditions, i.e., with no temperature control, thus allowing for temperature fluctuations caused by the varying room conditions in the lab. The uncontrolled experiments deracemized faster than the controlled ones (about 8 days instead of more than 15 days), which is justified

by the presence of larger temperature fluctuations mostly between 28°C and 30°C; in fact, the 24-hour period of day-night temperature fluctuations can be easily recognized in the associated temperature profile.

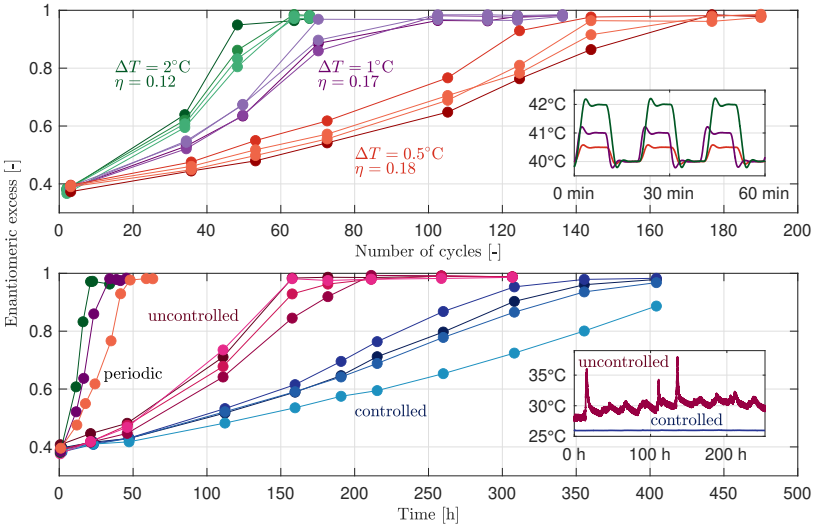

Figure 12.3 Evolution of enantiomeric excess for deracemization experiments using NMPA with an initial enantiomeric excess of 0.4 ($\xi = 0.43$); all repetitions of each experiment are shown. Top panel: temperature cycling experiments with small amplitude, i.e., of 2°C (green), 1°C (violet), and 0.5°C (orange) plotted in terms of number of cycles. Bottom panel: controlled (constant temperature, blue) and uncontrolled (random temperature fluctuations, red) experiments plotted in terms of time; one representative experiment for each of the periodic temperature cycling experiment is shown for comparison. In both panels, the insets show the thermal evolution for the relevant experiments, as indicated.

A few remarks are worth making. First, the experiments with small-amplitude periodic oscillations confirm the conclusions derived from the theoretical approach above. Second, the controlled experiments confirm that Viedma ripening, i.e., deracemization attained at constant temperature typically by continuously grinding the suspension, is explained by the same growth/dissolution mechanism of deracemization via temperature cycles, when the unavoidable random temperature fluctuations are accounted for.

Third, the uncontrolled experiments, with random temperature fluctuations as illustrated in the bottom panel of Figure 12.3, have obvious implications

on theories about the emergence of homochirality in nature: if tiny, random temperature fluctuations enable deracemization any kind of arbitrary temperature profiles experienced by pre-biotic systems (because of daily and seasonal temperature variability) may have led to deracemization and to homochirality.

12.6 CONCLUDING REMARKS

This work introduces and validates a general mechanism for solid-state deracemization based on growth and dissolution driven by temperature cycling, either periodically or randomly, even with very small temperature amplitudes. Through the derivation of an analytical solution we obtained an exact condition for deracemization: suspensions of conglomerate crystals in the presence of a racemization reaction in solution deracemize when crystal dissolution is faster than crystal growth in the terms discussed above. Such condition is ubiquitous,[47,315,316] hence solid-state deracemization of conglomerate-forming chiral compounds provides both a convenient route towards enantiopure products, e.g., in the pharmaceutical sector where this is a major challenge, and a *natural* pathway to amplify asymmetries in enantiomeric composition all the way to homochirality.

Numerous bio-relevant compounds such as the amino acids threonine and asparagine crystallize as conglomerates[306] and hence are candidates for solid-state deracemization. Amino acids in solution racemize even at ambient temperature and neutral pH, albeit slowly (order of thousands of years), and they do so many orders of magnitude faster at high temperatures and low pH.[326,327] Since even small, random temperature fluctuations (or the natural day-night cycle) enable deracemization, homochiral suspensions of these compounds may well have emerged in pre-biotic environments. This is in stark contrast to the main competing theoretical mechanism for chiral amplification, i.e., asymmetric autocatalysis, for which only a single example (in fact with no pre-biotic relevance) has ever been found experimentally.[331,332] The initial asymmetry required to kick-off deracemization may have been generated in multiple ways,[333] yet a certain asymmetry is intrinsic to crystallization due to the inherent stochasticity of the underlying micro-physical phenomena such as nucleation.[78,294,334] Based on the simple and ubiquitous mechanism demonstrated in this work, we argue that solid-state deracemization may indeed have played a pivotal role in the origin of homochirality on Earth.

12.7 MATERIALS AND METHODS

Here we present the general Population Balance Equation (PBE) model (Section 12.7.1), the simplified model and the analytical derivation of the exact condition for deracemization (Section 12.7.2), and the experimental methods (Section 12.7.3).

12.7.1 General PBE model

Model equations

We model deracemization in a well-stirred batch crystallizer ($i = 1, 2$, $j = 3 - i$), where the target (major) enantiomer is $i = 1$, and the undesired (minor) enantiomer is $i = 2$. The material balance is

$$\frac{\mathrm{d}c_i}{\mathrm{d}t} + \frac{\mathrm{d}n_i}{\mathrm{d}t} = -k_\mathrm{r}(c_i - c_j) \tag{12.10}$$

with c_i and n_i the mass of solute per unit mass solvent in solution and in the solid phase, hence

$$n_i = \rho_\mathrm{c} \int_0^\infty v_\mathrm{c}(L) f_i(L) \mathrm{d}L = \rho_\mathrm{c} k_\mathrm{v} m_{3,i} \tag{12.11}$$

and k_r is the temperature-dependent rate constant of racemization and $v_\mathrm{c}(L) = k_\mathrm{v} L^3$ is the volume of an individual crystal of size L and volume shape factor k_v. Eqs. 12.10 are coupled to the population balance equations of the two populations. The k-th moment of the particle size distributions of enantiomer i is defined as

$$m_{k,i} = \int_0^\infty L^k f_i(L) \mathrm{d}L. \tag{12.12}$$

Numerical simulations

We have numerically implemented the generalized model presented in Section 12.7.1 using Matlab R2022b. All simulations were carried out for monodisperse populations with crystals of size $L_i(t)$. This is for two reasons; first, the effect of polydispersity on deracemization has been studied extensively in an earlier contribution to which we refer the interested reader.[319] Second, the newly introduced deracemization mechanism is largely independent of the shape of the particle size distribution, hence little insights can be obtained from the analysis of more complex polydisperse systems. The k-th moment of the PSDs of enantiomer i thus is

$$m_{k,i} = L_i^k N_i. \tag{12.13}$$

where N_i is the number of crystals of enantiomer i per mass of solvent. Since here we neither consider agglomeration, breakage, nor nucleation, this number is constant throughout the entire process, until homochirality is reached and the population of enantiomer 2 dissolves, at which point $N_2 = 0$. The initial state of the suspension is characterized through initial sizes $L_{0,i}$ and numbers $N_{0,i}$ of the two enantiomers. All simulations employ $N_{0,2} < N_{0,1}$ as source of the initial asymmetry and $L_0 = L_{0,1} = L_{0,2}$, and they start with a growth step. We consider an equal initial size for two reasons: first, in actual experiments the initial crystal sizes of both enantiomers are rather similar. Second, a difference in mean crystal size is primarily relevant in the context of crystal ripening (which is faster for smaller crystals), but this is a phenomenon not essential to the new mechanism. Thanks to the monodispersity, the model reduces to a set of four ODEs that describe the evolution of c_1, c_2, L_1, and L_2:

$$\frac{\mathrm{d}L_i}{\mathrm{d}t} = M_i(c_i) \tag{12.14}$$

$$\frac{\mathrm{d}c_i}{\mathrm{d}t} = -\rho_\mathrm{c} k_\mathrm{v} N_i \frac{\mathrm{d}}{\mathrm{d}t}(L_i^3) + k_\mathrm{r}(c_j - c_i) \tag{12.15}$$

where M_i equals G_i during growth steps and D_i during dissolution steps and $\frac{\mathrm{d}}{\mathrm{d}t}(L_i^3) = 3L_i^2 \frac{\mathrm{d}L_i}{\mathrm{d}t}$ (termed 3D-growth). For simulations carried out under the assumption also used in the analytical solution that the second moment of the PSD remains constant during temperature-cycling, we impose $\frac{\mathrm{d}}{\mathrm{d}t}(L_i^3) = 3L_0^2 \frac{\mathrm{d}L_i}{\mathrm{d}t}$ (termed 1D-growth). In this case, the system simplifies into a set of two ODEs (see Section 12.7.2). In terms of the kinetic rate expressions for crystallization, we consider the following two cases:

$$G_i = k_\mathrm{g}(c_i - c^*)^g \tag{12.16}$$

$$G_i = k_\mathrm{g} \ln(S)^g \tag{12.17}$$

whereby the dissolution rates are defined analogously. Note that the dimension of the rate constant depends on both the choice of the driving force and on the value of the exponent. The saturation ratio S_i is defined as (neglecting activity coefficients):

$$S_i(T) = c_i / c^*(T) \tag{12.18}$$

From a thermodynamic point of view, the logarithmic expression of the driving force is the most accurate. Yet given that the typical operating conditions of deracemization experiments do not involve particularly large super- or undersaturation levels, we consider it adequate to linearize the logarithm when deriving the analytical solution, which yields a driving force based on the concentration difference. We confirmed the applicability of this assumption by comparing numerical simulations carried out using both linear and logarithmic driving forces, as presented in Section 12.8.2.

A complete list of simulation parameters is provided in Table 12.1. In general, parameter values were chosen to match the behavior of the model compound NMPA, which has been studied extensively in earlier contributions on deracemization through both temperature-cycling[300,328,330] and high pressure homogenization.[303]

For the generation of Figure 12.1, cases were simulated in which growth and dissolution occur at similar rates (panels b) and where growth is faster than dissolution (panels c). In case (b), it holds that $k_g(T_g) = k_d(T_d) = 10^{-4.699}$ m $s^{-1}kg^{-1}kg_s$, whereas in case (c) it holds that $k_g(T_g) = 4 \times 10^{-4.699}$ m $s^{-1}kg^{-1}kg_s$ and $k_d(T_d) = 10^{-4.699}$ m $s^{-1}kg^{-1}kg_s$.

Parameter	Symbol	Values [unit]
Crystal density	ρ_c	1300 [kg m^{-3}]
Solvent density	ρ_s	786 [kg m^{-3}]
Volume shape factor	k_v	$\pi/4$ [-]
Growth rate exponent	g	1 [-]
Dissolution rate exponent	d	1 [-]
Growth pre-factor (Δc)	$k_g(T_g)$	$10^{-4.699}$[m $s^{-1}kg^{-1}kg_s$]
Growth pre-factor ($\ln(S)$)	$k_g(T_g)$	$10^{-6.398}$ [m s^{-1}]
Growth/dissolution ratio	$k_d(T_g)/k_g(T_g)$	4 [-]
Reaction rate constant at T_g	$k_r(T_g)$	0.2 [min^{-1}]
Temp.-dep. of dissolution	$k_d(T_d)/k_d(T_g)$	1 [-]
Temp.-dep. of reaction	$k_r(T_d)/k_r(T_g)$	1 [-]
Solubility at T_g	$c^*(T_g)$	20 [g kg_s^{-1}]
Solubility at T_d	$c^*(T_d)$	20.2 or 25 [g kg_s^{-1}]
Number density of crystals	$N_0 = N_{0,1} + N_{0,2}$	10^8 [kg_s^{-1}]
Initial crystal size	$L_0 = L_{0,1} = L_{0,2}$	10^{-4} [m]
Initial enantiomeric ratio	ξ_0	0.43 [-]
Time of growth step	t_g	variable
Time of dissolution step	t_d	variable
Initial concentration	$c_0 = c_{0,1} = c_{0,2}$	$c^*(T_d)$
Simulation time step	t_{step}	1 [s]
Process duration	t_{tot}	variable, until $N_2 = 0$

Table 12.1 List of simulation parameters, grouped into physicochemical quantities, process conditions and numerical parameters. The reported parameter values represent the base case, if specific simulations use different values, this is indicated elsewhere. Note that an initial enantiomeric ratio of $\xi_0 = 0.43$ corresponds to an initial enantiomeric excess of $ee_0 = 0.40$, which was also used in most of the experiments.

12.7.2 Simplified model

Simplified model equations

The expressions for n_i and its derivative simplify when assuming no nucleation and a linear driving force for growth and dissolution as follows:

$$n_i = \rho_c k_v m_{3,i} \tag{12.19}$$

$$\frac{dn_i}{dt} = \rho_c k_v \dot{m}_{3,i} = 3\rho_c k_v M_i m_{2,i} \tag{12.20}$$

where M_i is the rate of growth or dissolution (depending on the step) of enantiomer i, for which we assume a linear driving force:

$$G_i = k_g(c_i - c^*) \tag{12.21}$$

$$D_i = k_d(c_i - c^*) \tag{12.22}$$

We discuss the effect of a non-linear driving force in Section 12.8.2. c^* is the solubility at the relevant temperature, and k_m is the rate constant of either growth or dissolution. Note that both solubility and crystallization kinetics are identical for both enantiomers, and that the solubility of each enantiomer is assumed to be independent of the concentration of the second enantiomer, i.e., that the solution is ideal.

We next introduce the assumption that the second moments of the PSDs do not change during temperature-cycling, i.e., that the crystals' active surface area remains constant as their volume changes, so that the model reduces to two linear ordinary differential equations:

$$\frac{dc_i}{dt} + 3\rho_c k_v m_{2,i} k_m (c_i - c^*) = -k_r(c_i - c_j) \tag{12.23}$$

Such assumption corresponds for example to the crystallization of rod-like particles where the rod cross section remains unchanged during growth and dissolution and crystals grow only in the length direction. It is however accurate for arbitrary geometries in case the actual change of the second moment during an individual cycle is small. We verified the validity of the assumption through a broad set of numerical simulations that are presented in the SI Section 12.8.2.

Introducing the following new variables and parameters (the condition that $m_{2,1} > m_{2,2}$ introduces the asymmetry needed to trigger deracemization):

$$\tau_m = k_r(T_m)t \tag{12.24}$$
$$x_i = c_i - c^* \tag{12.25}$$
$$a_m = 3\rho_c k_v m_{2,1} k_m(T_m)/k_r(T_m) = a \tag{12.26}$$
$$\xi = m_{2,2}/m_{2,1} < 1 \tag{12.27}$$
$$a_1 = a \tag{12.28}$$
$$a_2 = a\xi \tag{12.29}$$

yields the following pair of ODEs (we indicate the derivative of a variable with respect to the dimensionless time τ with a dot above the variable itself):

$$\dot{x}_i = -a_i x_i - (x_i - x_j) \tag{12.30}$$

The system can conveniently be written in vector notation, with $\underline{x} = [x_1, x_2]^T$ and the matrix of coefficients, $\underline{\underline{A}}$, defined below:

$$\dot{\underline{x}} = \begin{bmatrix} -(a+1) & 1 \\ 1 & -(a\xi+1) \end{bmatrix} \underline{x} = \underline{\underline{A}}\,\underline{x} \tag{12.31}$$

Note that $\det(\underline{\underline{A}}) = a(a\xi + \xi + 1) > 0$.

Before studying the solution of this system, let us introduce the following parameter, which is bounded between 0 and 1:

$$\alpha = \frac{1}{2}\left(\sqrt{a^2(1-\xi)^2 + 4} - a(1-\xi)\right) \tag{12.32}$$

The two eigenvalues of the matrix $\underline{\underline{A}}$ are:

$$\lambda_1 = -\alpha - a - 1 \tag{12.33}$$
$$\lambda_2 = \alpha - a\xi - 1 \tag{12.34}$$

with $\lambda_1 < \lambda_2 < 0$. The matrix $\underline{\underline{A}}$ can be decomposed according to $\underline{\underline{A}} = \underline{\underline{Z}}\,\underline{\underline{\Lambda}}\,\underline{\underline{Z}}^{-1}$, whereby the eigenvectors of $\underline{\underline{A}}$ are used as columns to define the orthogonal matrix $\underline{\underline{Z}}$:

$$\underline{\underline{Z}} = \frac{1}{\sqrt{1+\alpha^2}} \begin{bmatrix} -1 & \alpha \\ \alpha & 1 \end{bmatrix} = \underline{\underline{Z}}^{-1} \tag{12.35}$$

Note that $\underline{\underline{Z}}$ has been constructed such that it is symmetric as indicated by the second equality. $\underline{\underline{\Lambda}}$ is a diagonal matrix, whose diagonal elements are λ_i. Thus, the solution of the system of linear ODEs (12.31) can be written for a generic initial condition $\underline{x}_0$ as:

$$\underline{x}(\tau) = \exp(\tau\,\underline{\underline{A}})\underline{x}_0 = \underline{\underline{Z}}\exp(\tau\,\underline{\underline{\Lambda}})\underline{\underline{Z}}^{-1}\underline{x}_0 = \underline{\underline{Z}}\exp(\tau\,\underline{\underline{\Lambda}})\underline{\underline{Z}}\underline{x}_0 \tag{12.36}$$

where $\exp(\tau\,\underline{\underline{A}})$ is the matrix exponential, that can be calculated using the matrix $\underline{\underline{Z}}$ and the diagonal matrix $\exp(\tau\,\underline{\underline{\Lambda}})$, whose diagonal elements are $\exp(\tau\lambda_i)$.

Temperature cycles

Temperature cycles consist of alternate time periods spent by the system first at low temperature, T_g, and then at high temperature, T_d, i.e., at conditions first where the solution is supersaturated ($x_i > 0$) and crystals grow, and then where the solution is undersaturated ($x_i < 0$) and crystals dissolve, respectively. The transition from T_g to T_d and back occurs instantaneously, i.e., contrary to standard temperature cycles there are neither heating nor cooling ramps. Since in practice ramps are instrumental to minimize nucleation, the idealized model above, that does not include nucleation, is consistent with practice. The time periods spent at T_g and at T_d are $t_g = \tau_g / k_r(T_g)$ and $t_d = \tau_d / k_r(T_d)$, respectively.

The general discussion above is specialized to the two operation modes through the following definitions.

- During growth, at T_g:

$$\begin{aligned} \tau &= k_r(T_g)t \\ x_i &= c_i - c^*(T_g) > 0 \\ a &= a_g = 3\rho_c k_v m_{2,1} k_g(T_g)/k_r(T_g) \\ \underline{\underline{A}}_g &= \underline{\underline{A}} \end{aligned} \tag{12.37}$$

- During dissolution, at T_d:

$$\begin{aligned} \tau &= k_r(T_d)t \\ x_i &= c_i - c^*(T_d) < 0 \\ a &= a_d = 3\rho_c k_v m_{2,1} k_d(T_d)/k_r(T_d) \\ \underline{\underline{A}}_d &= \underline{\underline{A}} \end{aligned} \tag{12.38}$$

Iterating the solution given by Eq. 12.36 through the idealized temperature cycles, the system attains a cyclic steady state, where each cycle consists of alternate periods of growth and of dissolution (see SI Section 12.8.2 for a set of illustrative numerical simulations). Between the two modes the values of x_i must be converted to account for the change of temperature hence of reference solubility; to this aim, we introduce the vector $\underline{s}$, whose elements are

the solubility difference $\Delta c_\infty = c^*(T_d) - c^*(T_g)$. Using vector notation and starting from the initial state of growth, called $\underline{x}_g^0$, one obtains:

$$\begin{aligned} \underline{x}_g(\tau) &= \exp(\tau\, \underline{\underline{A}}_g)\underline{x}_g^0 \\ \underline{x}_g &= \exp(\tau_g\, \underline{\underline{A}}_g)\underline{x}_g^0 \\ \underline{x}_d^0 &= \underline{x}_g - \underline{s} \\ \underline{x}_d(\tau) &= \exp(\tau\, \underline{\underline{A}}_d)\underline{x}_d^0 \\ \underline{x}_d &= \exp(\tau_d\, \underline{\underline{A}}_d)\underline{x}_d^0 \\ \underline{x}_g^0 &= \underline{x}_d + \underline{s} \end{aligned} \tag{12.39}$$

where the last equation enforces the condition for the attainment of the cyclic steady state. Combining the equations above, and solving for $\underline{x}_d^0$ yields an explicit equation for this state vector:

$$\underline{x}_d^0 = (\underline{\underline{I}} - \exp(\tau_g\, \underline{\underline{A}}_g)\exp(\tau_d\, \underline{\underline{A}}_d))^{-1}(\exp(\tau_g\, \underline{\underline{A}}_g) - \underline{\underline{I}})\underline{s} \tag{12.40}$$

where $\underline{\underline{I}}$ is the unitary matrix. The vector $\underline{x}_d^0$ is the fixed point of the transformation defined by the sequence of Equations 12.39, whose existence is demonstrated by the fact that we can obtain an explicit expression for it, i.e., Equation 12.40. From the last equation one can also calculate the following explicit expression for the change in state vector during dissolution:

$$\underline{\Delta x}_d = (\exp(\tau_d\, \underline{\underline{A}}_d) - \underline{\underline{I}})(\underline{\underline{I}} - \exp(\tau_g\, \underline{\underline{A}}_g)\exp(\tau_d\, \underline{\underline{A}}_d))^{-1}(\exp(\tau_g\, \underline{\underline{A}}_g) - \underline{\underline{I}})\underline{s} \tag{12.41}$$

It is worth noting that the two components of this last vector are positive, as concentrations increase during dissolution, and that $\underline{\Delta x}_g = -\underline{\Delta x}_d$, as one can easily verify using the equations above.

Exact condition for deracemization

We formalize the conditions for deracemization based on two considerations. First, in a process that reaches cyclic steady state such conditions must be valid for each individual cycle. Secondly, effective deracemization can be characterized in different ways, e.g., by looking at the evolution of the two populations of crystals (that of the target enantiomer must increase in number and size, and vice versa) or by considering the solution: we follow the latter approach, and recognize that the system deracemizes if and only if the net direction of the deracemization reaction during one entire cycle is from the minor to the major enantiomer. Such condition can be formalized as

follows, where we use the following property of the matrix exponential, i.e., $\int \exp(\tau\ \underline{\underline{A}})\mathrm{d}\tau = \underline{\underline{A}}^{-1}(\exp(\tau\ \underline{\underline{A}}) - \underline{\underline{I}})$:

$$\begin{aligned}
\Delta n_{\mathrm{cyc}} &= \int_{\mathrm{g}} k_{\mathrm{r}}(T_{\mathrm{g}})(c_2(t) - c_1(t))\mathrm{d}t + \int_{\mathrm{d}} k_{\mathrm{r}}(T_{\mathrm{d}})(c_2(t) - c_1(t))\mathrm{d}t \\
&= \int_0^{\tau_{\mathrm{g}}} (x_{2,\mathrm{g}}(\tau) - x_{1,\mathrm{g}}(\tau))\mathrm{d}\tau + \int_0^{\tau_{\mathrm{d}}} (x_{2,\mathrm{d}}(\tau) - x_{1,\mathrm{d}}(\tau))\mathrm{d}\tau \\
&= [-1\ \ 1]\left(\int_0^{\tau_{\mathrm{g}}} \underline{x}_{\mathrm{g}}(\tau)\mathrm{d}\tau + \int_0^{\tau_{\mathrm{d}}} \underline{x}_{\mathrm{d}}(\tau)\mathrm{d}\tau\right) \\
&= [-1\ \ 1]\left(\int_0^{\tau_{\mathrm{g}}} \exp(\tau\ \underline{\underline{A}}_{\mathrm{g}})\underline{x}_{\mathrm{g}}^0\mathrm{d}\tau + \int_0^{\tau_{\mathrm{d}}} \exp(\tau\ \underline{\underline{A}}_{\mathrm{d}})\underline{x}_{\mathrm{d}}^0\mathrm{d}\tau\right) \\
&= [-1\ \ 1]\left(\underline{\underline{A}}_{\mathrm{g}}^{-1}(\exp(\tau_{\mathrm{g}}\ \underline{\underline{A}}_{\mathrm{g}}) - \underline{\underline{I}})\underline{x}_{\mathrm{g}}^0 + \underline{\underline{A}}_{\mathrm{d}}^{-1}(\exp(\tau_{\mathrm{d}}\ \underline{\underline{A}}_{\mathrm{d}}) - \underline{\underline{I}})\underline{x}_{\mathrm{d}}^0\right) \\
&= [-1\ \ 1]\left(\underline{\underline{A}}_{\mathrm{g}}^{-1}\underline{\Delta x}_{\mathrm{g}} + \underline{\underline{A}}_{\mathrm{d}}^{-1}\underline{\Delta x}_{\mathrm{d}}\right) \\
&= [-1\ \ 1]\left((\underline{\underline{A}}_{\mathrm{d}}^{-1} - \underline{\underline{A}}_{\mathrm{g}}^{-1})\underline{\Delta x}_{\mathrm{d}}\right) \qquad (12.42)
\end{aligned}$$

The last expression can be transformed and simplified, so as the condition for deracemization ($\Delta n_{\mathrm{cyc}} > 0$) reduces to the following inequality, written in vector notation first and then using scalar quantities:

$$\begin{aligned}
0 &< \frac{\xi(a_{\mathrm{g}} - a_{\mathrm{d}})}{\det(\underline{\underline{A}}_{\mathrm{d}})\det(\underline{\underline{A}}_{\mathrm{g}})}[\xi\ \ -1]\underline{\Delta x}_{\mathrm{d}} \\
&= \frac{\xi}{\det(\underline{\underline{A}}_{\mathrm{d}})\det(\underline{\underline{A}}_{\mathrm{g}})}(a_{\mathrm{d}} - a_{\mathrm{g}})(\Delta x_{2,\mathrm{d}} - \xi\Delta x_{1,\mathrm{d}}) \qquad (12.43)
\end{aligned}$$

In the last expression, the fraction consists of positive quantities; the factor $(a_{\mathrm{d}} - a_{\mathrm{g}})$ may be positive or negative; the last factor, i.e., $(\Delta x_{2,\mathrm{d}} - \xi\Delta x_{1,\mathrm{d}})$, appears to be ambiguous. But this is the most remarkable result of this derivation, namely that the last term is always positive, whatever the (positive) values of the six parameters that characterize the system, namely a_{g}, a_{d}, ξ, τ_{g}, τ_{d}, and $c^*(T_{\mathrm{d}}) - c^*(T_{\mathrm{g}})$. As a consequence, the difference $(a_{\mathrm{d}} - a_{\mathrm{g}})$ must also be positive to fulfill the conditions for deracemization, which can be simply written as:

$$a_{\mathrm{d}} > a_{\mathrm{g}}. \qquad (12.44)$$

12.7.3 Experimental

General protocol

All experiments were conducted with the conglomerate-forming compound N-(2-methylbenzylidene)-phenylglycine amide (NMPA). NMPA was synthe-

sized following the protocol outlined in our earlier work.[303] NMPA racemizes in the presence of non-nucleophilic bases such as 1,8-diazabicyclo[5.4.0]undec-7-ene (DBU).[56] We used a mixture of 95/5 (w/w) isopropanol (IPA) and acetonitrile (ACN) as solvent, and tert-butyl methyl ether as anti-solvent to wash crystals after filtration, all in line with earlier work.[300,328] Both DBU and the solvents were purchased from Sigma-Aldrich with a purity of 99 % and used without further purification.

Saturated solutions of NMPA were prepared in an EasyMax 102 apparatus (Mettler Toledo) by adding an excess amount of NMPA to 100 g of the solvent mixture and stirring for 8 h to allow for equilibration at the target temperature of the experiment. For each deracemization experiment, 5 g (5.032 ± 0.0035 g) of saturated solution was transferred into 10 mL cylindrical glass vials (2 cm diameter and 10 cm height) using a syringe equipped with a hydrophilic syringe filter (PTFE, 0.22 μm, pk.100) before DBU (6 μL g_s^{-1}) was added to each vial. In all experiments, the resulting mixture was stirred using a magnetic stirring bar with 1000 rpm. An initial suspension density of 40.0 g kg_s^{-1} was used, amounting to a mass of 0.2 g for each vial. 0.201 ± 0.0005 g of crystals were added to the crystallizers and the temperature evolution was recorded through inserted K-type thermocouples. A single batch of NMPA crystals was prepared with initial enantiomeric excess of 0.4 using the protocol explained in our earlier work,[300] and was used in all experiments reported here.

Samples were taken throughout each experiment by extracting 80 μL of suspension using a precision pipette. Crystals were collected from the suspension by vacuum filtration using a Büchner funnel and a MS PTFE membrane filter with pore size of 0.45µm. The crystals were then washed with few droplets of anti-solvent to remove potential residual of DBU. The dried samples were dissolved in acetonitrile and analysed with HPLC according to the protocol reported earlier.[328]

Temperature-cycling experiments

Three sets of temperature-cycling experiments were carried out with four vials each in the EasyMax 102 apparatus using the three temperature amplitudes of 2°C, 1°C, and 0.5°C and an initial enantiomeric excess of $ee_0 = 0.4$. The lower temperature of the cycle, i.e., the temperature of the growth step, was set to $T_g = 40$°C in all experiments, hence the dissolution temperatures were $T_d = 42$°C, $T_d = 41$°C, and $T_d = 40.5$°C, respectively. The cycles were designed such that dissolution and growth steps are of equal duration and that the total cycle time was 20 min (three cycles per hour); note that the actual cycle times as measured by the thermocouple turned out slightly longer for

the experiments with 0.5°C and 2°C amplitudes, with values on the order of 21 min. Heating and cooling rates were set to 1.0 K min^{-1} for the experiments with 2°C and 1°C amplitude, and to 0.3 K min^{-1} for the 0.5°C experiment. We chose slower ramps for the 0.5°C experiments to mitigate the issue of temperature overshooting. One vial per experiment was equipped with a thermocouple. Cycle efficiencies were computed for all temperature-cycling experiments as discussed in the SI in Section 12.8.1.

Isothermal experiments

Two sets of isothermal experiments were performed with four vials each. In the first, the temperature of the jacket surrounding the vials was controlled at 26°C, and in the second, the temperature was not controlled, and hence subject to the ambient conditions in the laboratory. For the controlled experiments, the vials were placed in the EasyMax 102 apparatus (jacket temperature set to 26°C), in the second case vials were placed on a magnetic stirring plate next to the window of the laboratory to allow for direct contact with sunlight. In the controlled experiments, one out of four vials was equipped with a thermocouple, in the uncontrolled ones, all vials were equipped with a thermocouple each.

12.8 SUPPORTING INFORMATION

Section 12.8.1 explains the methodology used to compute experimental cycle efficiencies from experimental data, and presents the values obtained for experiments reported earlier.[330] These values are discussed within the framework of the analytical solution derived in the main body of this work. Section 12.8.2 reports additional considerations related to the assumptions made in deriving the analytical solution; namely the effect of a non-linear driving force for crystal growth and dissolution, the occurrence of the cyclic steady state, and the effect of more complex cycle configurations.

12.8.1 Experimental cycle efficiencies

Methodology

Here we explain how to obtain estimates of the cycle efficiency η for experimental temperature-cycling data. We first discuss the general approach, which we apply to a set of literature data, before estimating η for the experiments carried out in this work.

Breveglieri et al.[330] designed temperature profiles such that a certain fraction of the minority enantiomer dissolves in the first cycle. This is quantified by the dissolution factor δ_0:

$$\delta_0 = \frac{\rho_0(1 - ee_0)}{2\Delta c_\infty} \tag{12.45}$$

whereby the enantiomeric excess in the suspension is $ee = \frac{n_1 - n_2}{n_1 + n_2}$. Its value at the beginning of the experiment is $ee_0 = ee(t = 0)$ and may be converted into an initial enantiomeric ratio ξ_0 (defined on a surface-basis) assuming that the initial particle size distributions of both enantiomers. ρ_0 denotes the total mass density of crystals in the suspension at the beginning, i.e., $\rho_0 = n_1(t = 0) + n_2(t = 0)$. The dissolution factor δ_0 is useful for this work, because it is linked to the total amount of material that must react towards enantiomer 1 to achieve homochirality, termed Δn_{tot}. All of enantiomer 2 except for the part that anyways dissolves during every cycle upon heating must be converted, so that $\Delta n_{\text{tot}} = n_2(t = 0) - \Delta c_\infty$. We further assume that every cycle converts the same amount of material, so that $\Delta n_{\text{tot}} = \Delta n_{\text{cyc}} \times n_c$. This enables the definition of the experimental cycle efficiency η:

$$\eta = \frac{\delta_0 - 1}{n_c} \tag{12.46}$$

This approach provides an easily accessible estimate of η from experimental data that just requires the values of n_c and δ_0. It is worth noting that this approach only considers the initial properties of the suspension; naturally, the value of ξ changes throughout the process as more and more material deracemizes. This is not considered here, nor is it taken account in the computation of η using the analytical solution (which provides η for a process that achieves cyclic steady-state at a constant value of ξ). In fact, the decrease in ξ over time leads to an acceleration of the deracemization process, as shown in Figure 12.2 in the main body of this work. Given the large initial asymmetry used ($ee_0 = 0.4$) in the experiments, such effect is only of limited relevance and the estimated values of η can be considered as accurate determinants of the experimental deracemization performance.

Results

Here we compute the values of the cycle efficiency following the approach outlined in Section 12.8.1. We first do so for for experiments involving the three model compounds N-(2-methylbenzylidene)-phenylglycine amide **(NMPA)**, 2- (benzylideneamino)-2-(2-chlorophenyl) acetamide **(CPG)** and 3,3-dimethyl-2-((naphthalen-2-ylmethylene)amino) butanenitrile **(tLEU)** reported previously.[330] All three compounds racemize in the presence of the

non-nucleophilic base 1,8-Diazabicyclo[5.4.0]undec-7-en **(DBU)**. The overall suspension density, ρ_0, lies between 10 and 60 g/kg solvent, with ee_0 values of 0.4 in most experiments, corresponding to $\xi_0 = 0.43$. η was found to predominantly lie between 0.08 and 0.13 for all three model compounds.

Exp.	Δc_∞ [g kg_s^{-1}]	ρ_0 [g kg_s^{-1}]	n_c [-]	δ_0 [-]	ee_0 [-]	η [-]
n1, NMPA	2.0	10	5	1.5	0.4	0.10
n2, NMPA	2.0	13	11	2	0.4	0.09
n3, NMPA	4.0	27	9	2	0.4	0.11
n4, NMPA	6.0	40	8	2	0.4	0.13
n5, NMPA	2.0	23	20	3.5	0.4	0.13
n6, NMPA	2.0	33	53	5	0.4	0.08
n7, NMPA	6.0	40	2	1.4	0.6	0.20
n8, NMPA	8.0	56	4	1.4	0.6	0.10
n9, NMPA	6.0	40	4	1.4	0.6	0.10
n10, NMPA	2.0	10	5	1.5	0.4	0.20
n11, NMPA	2.0	13	11	2	0.4	0.09
n12, NMPA	4.0	27	9	2	0.4	0.11
n13, NMPA	2.0	23	25	3.5	0.4	0.10
c1, CPG	2.0	10	16	1.5	0.4	0.03
c2, CPG	2.0	13	20	2	0.4	0.05
c3, CPG	4.0	27	10	2	0.4	0.10
c5, CPG	2.0	23	26	3.5	0.4	0.10
c11, CPG	2.0	13	15	2	0.4	0.07
c13, CPG	2.0	23	24	3.5	0.4	0.10
c14, CPG	4.0	47	18	3.5	0.4	0.14
t1, tLEU	2.0	10	5	1.5	0.4	0.10
t2, tLEU	2.0	13	9	2	0.4	0.11
t3, tLEU	4.0	27	7	2	0.4	0.14
t11, tLEU	2.0	13	10	2	0.4	0.10
t12, tLEU	4.0	27	12	2	0.4	0.08
t15, tLEU	4.0	20	5	1.5	0.4	0.10
t16, tLEU	4.0	20	7	1.5	0.4	0.07

Table 12.2 Analysis of experimental data reported by Breveglieri et al.[330]; the enumeration of the experiments equals the one of the referenced work. The model compounds studied are NMPA, CPG, and tLEU. The values of the initial enantiomeric excess, ee_0, of 0.4 and 0.6 correspond to values of the enantiomeric ratio ξ_0 of 0.43 and 0.25, respectively.

Next, we estimate the cycle efficiency η for the temperature cycling experiments carried out in this work, which involve small temperature amplitudes of 2°C, 1°C, and 0.5°C. The corresponding dissolution factors were computed

as outlined by Breveglieri et al.[330], and are 7.5, 15.2, and 30.7, i.e., much larger than those in the literature study.

For 2°C, all experiments exhibited complete deracemization after about 55 cycles; for 1°C, after 80 cycles; and for 0.5°C, after 160 cycles. This corresponds to cycle efficiencies of 0.12, 0.17, and 0.18, respectively. In all cases only little variability was observed among the four vials used in each experiment.

Discussion

To understand whether the experimental values of the cycle efficiency computed in Section 12.8.1 are attainable through the newly identified mechanism, we evaluated the analytical solution of η for different values of the three parameters a_d, a_g, and ξ, as shown in Figure 12.4.

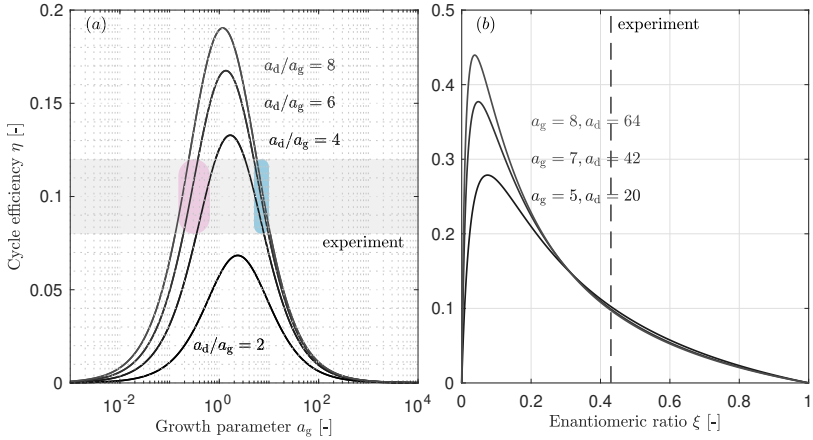

Figure 12.4 Values for the cycle efficiency given by the analytical solution in the limit of long step durations where η depends only on the three parameters a_g, a_d, and ξ. (a) η as a function of a_g with $\xi = 0.43$. The lines represent different values of the ratio a_d/a_g. (b) η as a function of ξ. The lines represent combinations of a_g, a_d that lead to model predictions that match the experimental value of η.

This analysis focuses on the model compound NMPA, which has been studied intensely by our group,[300,328,330] and by others,[56,325] over the past decade. Motivated by the observation[330] that longer steps did not have a major effect on the cycle efficiency of NMPA temperature cycling experiments, we assume that the step durations t_d and t_g are sufficiently long that the

concentration levels of the enantiomers in solution approach the equilibrium values, i.e., the solubility, before the steps end. In this case, η is independent of t_d and t_g. The lines shown in panel (a) correspond to different values of the ratio a_d/a_g and to the experimental value of $\xi_0 = 0.43$. Even though the precise crystallization kinetics of the model compounds are not known, one can identify the space of parameter values where the analytical solution and experiments match each other in terms of η (colored regions, corresponding to the cycle efficiencies observed in the literature experiments). The red region that corresponds to small values of a_g can be ruled out, because a previous study has shown that an increase in the reaction rate (which would decrease the values of a_d and a_g) increases the deracemization rate and hence η.[328] Consequently, the relevant parameter space is given by the blue region.

From a physical point of view, it is well plausible that the actual parameter values associated to the literature experiments lie within the identified space: first, the required values of the ratio $a_d/a_g \geq 4$ agree with the ratios of growth and dissolution rates reported in the literature for different compounds, including sodium chlorate ($k_d/k_g = 4$),[316] and paracetamol ($k_d/k_g > 2.5$)[315]. Second, given a characteristic time of the racemization reaction on the order of 10 min to an hour, and that crystallization is complete in step durations on the order of 10 min, it must hold that $a_g > 1$.

Considering the identified parameter space, one can explain the recent observation by Belletti et al.[325] that temperature-cycling experiments involving NMPA showed slower deracemization in some cases when they were combined with grinding. Grinding decreases the mean crystal size in the suspension, hence increasing the values of a_d and a_g, which in turn leads to smaller values of η under the relevant conditions. This experimental observation in fact cannot be explained when considering alternative deracemization mechanisms based on crystal ripening, since ripening becomes more pronounced the smaller the crystal size. That grinding accelerates isothermal deracemization processes, on the other hand, may be due to the fact that the grinding process enhances the naturally occurring temperature fluctuations. Obviously, such enhancement is of little relevance in temperature cycling processes which are dominated by the periodic temperature variations.

Finally, 12.4 panel (b) illustrates the dependency of the cycle efficiency η on the enantiomeric ratio ξ for sets of realistic parameter values. η generally increases when decreasing ξ, except when ξ becomes very small values, i.e., under conditions where the suspension is already nearly homochiral. Keeping in mind that ξ decreases with every cycle during a successful deracemization process, it follows that deracemization is to accelerate throughout the process. This is the reason why the numerical simulations of solid-state deracemization

reported in Figure 12.2 show an acceleration in the increase of the enantiomeric excess over time.

12.8.2 Additional considerations

In this section, we assess how the predicted deracemization performance changes when relaxing the assumptions made in deriving the analytical solution. We consider the role of the linear driving force for crystal growth and dissolution in Section 12.8.2, the emergence of the cyclic steady state in Section 12.8.2, and more complex cycle configurations such as those including temperature ramps in Section 12.8.2.

Relaxing the linear driving force

In this section, we discuss the effect of a non-linear driving force for crystal growth and dissolution on deracemization. To this end, we numerically solved the general model as outlined in Section 12.7.1 for values of the exponents $g = d = 1$ (termed 3D, ln(S)). We further solved two simplified systems, one comprising 3D growth and the linearized driving force (termed 3D, Δc), and one comprising 1D growth and the linearized driving force (termed 1D, Δc); the latter corresponds to the assumptions made in the derivation of the analytical solution. In particular, 1D growth refers to the assumption that the surface area of the crystals does not change as their volume changes, and 3D growth to the general case where the surface area does change. Figure 12.5 compares the predictions for the cycle efficiency η as a function of the parameter ratio a_d/a_g obtained through the analytical solution and the three sets of numerical simulations. The values for η that belong to the simulations were obtained by simulating a single temperature cycle subject to sufficiently long step duration that the concentration levels of the enantiomers in solution approach the equilibrium values.

Panel (a) shows the result for cycling between the equilibrium concentrations of 20 g kg_s^{-1} and 25 g kg_s^{-1}, whereas panel (b) shows the outcome for cycling between 20 g kg_s^{-1} and 20.2 g kg_s^{-1}. All simulations were generated for a constant value of the growth parameter $a_g = 5.15$ and for the surface area ratio $\xi_0 = 0.43$, while changing the value of the dissolution parameter.

All four solutions in both panels indicate that an increase in the ratio a_d/a_g leads to a more positive value of the cycle efficiency. The exact solution (black dashed line) and the corresponding numerical solution (Sim. 1D, Δc, green) quantitatively agree with each other; this verifies the accuracy of the numerical implementation of the three numerical solutions. When comparing the exact

solution with the numerical solution for 3D growth (Sim. 3D, Δc, violet), only minor differences are observed. Importantly, the root of η lies exactly at $a_d/a_g = 1$, hence the choice of 3D or 1D growth does not affect the condition for deracemization. The minor difference in the values of η results from the change in surface area of the crystals during growth and dissolution within a cycle that is considered in the 3D growth simulation, but not in the exact solution. Finally, the line corresponding to the solution with the non-linear driving force (Sim. 3D, $\ln(S)$, blue) exhibits a similar shape as the one for the linear driving force, but it is shifted towards the right, i.e., deracemization requires $a_d/a_g > 1$.

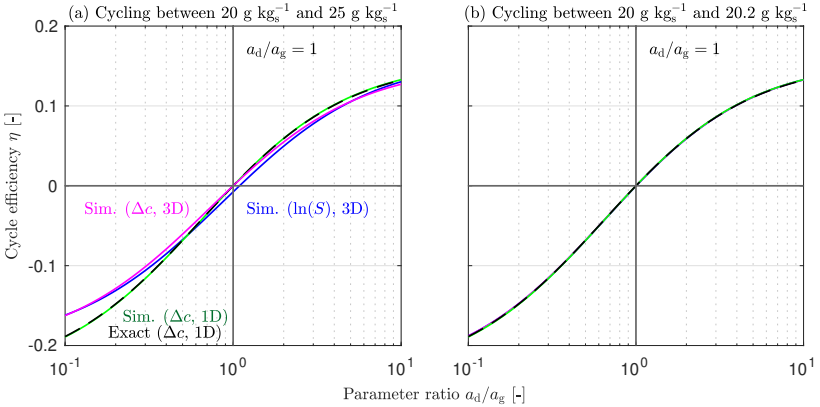

Figure 12.5 Comparison of the exact (black dashed lines) and three numerical solutions to temperature cycling-induced deracemization for two cases. The numerical solutions correspond (i) to the general case with logarithmic driving force and 3D growth (blue lines), (ii) to a simplified version considering 3D growth and the linear driving force (magenta line), and (iii) to the conditions of the analytical solution with 1D growth and linear driving force (green line). Panel (a): Cycling between solubilities of 20 g kg$_s^{-1}$ and 25 g kg$_s^{-1}$. Panel (b): Cycling between solubilities of 20 g kg$_s^{-1}$ and 20.2 g kg$_s^{-1}$. All simulations were generated for a constant value of the growth parameter $a_g = 5.15$ and for the initial enantiomeric ratio $\xi_0 = 0.43$, while changing the value of a_d.

This is because the logarithm introduces additional asymmetry to the system, since it is not symmetric around $S = 1$. Such asymmetry becomes more prevalent the larger the levels of super- and undersaturation at the beginning of the growth and dissolution steps. Panel (a), which shows an experimentally realistic case of temperature-cycling, highlights that such effect is small enough to be of limited practical relevance, i.e., the root of η lies at $a_d/a_g = 1.10$. In the case of a cycle with a small solubility difference, as

illustrated in panel (b), all simulations perfectly overlap, as expected. Hence, the conclusions using the assumptions made in deriving the analytical solution can be generalized to systems with non-linear driving force and 3D growth.

The cyclic steady state

The analytical solution was derived under the assumption of a cyclic steady state, i.e., that the evolution of the concentration during a cycle is periodic, so that the concentration at the beginning of a cycle matches the one at the end. Such behavior is obvious for the case of sufficiently long growth and dissolution steps, where the concentration at the beginning of each step equals the solubility value of the step before. For short step durations, the situation is more complex and we show through numerical simulations (1D growth, Δc driving force) that a cyclic steady state emerges.

Figure 12.6 shows four sets of simulations: the top left panel shows simulations for sufficiently long cycles so that the concentration levels of the enantiomers (blue and red) approach the solubility (black) at the end of each cycle. This is similar to the simulations shown in Figure 12.1 in the main body of this work. The top right panel shows the evolution of the re-scaled concentration vector $\underline{x}$ with $x_i = c_i - c^*$: a value of [0 0] indicates that both concentration levels are at equilibrium. As initial condition, where the concentration levels are at 25 g kg_s^{-1} and the solubility at 20 g kg_s^{-1}, the vector assumes values of [5 5], corresponding to the right top corner of the panel. During the growth step, the supersaturation depletes and the concentration levels approach 20 g kg_s^{-1}, corresponding to a value of [0 0]. When the dissolution step starts, the solubility changes, so that $\underline{x}$ =[-5 -5]. During dissolution, the undersaturation is depleted and the concentrations again approach [0 0]; with the start of a new growth step, the solubility changes, leading to [5 5]. As can be seen clearly, the concentrations rapidly approach a cyclic steady state.

In the case that the dissolution step is short (row b), a similar behavior emerges, however, the value of $\underline{x}$ at the end of the dissolution step does not reach [0 0], but rather a value of [-1.8 -3.1]; the growth step hence starts at a value of [3.2 1.9]. Still, the growth step is sufficiently long that the equilibrium value of [0 0] is approached at its end. Just as in the first case, a cyclic steady state emerges here as well, and already between the second and third cycles no relevant difference in the concentration levels is observed. The same holds true in case the growth step is short, and dissolution is long (row c).

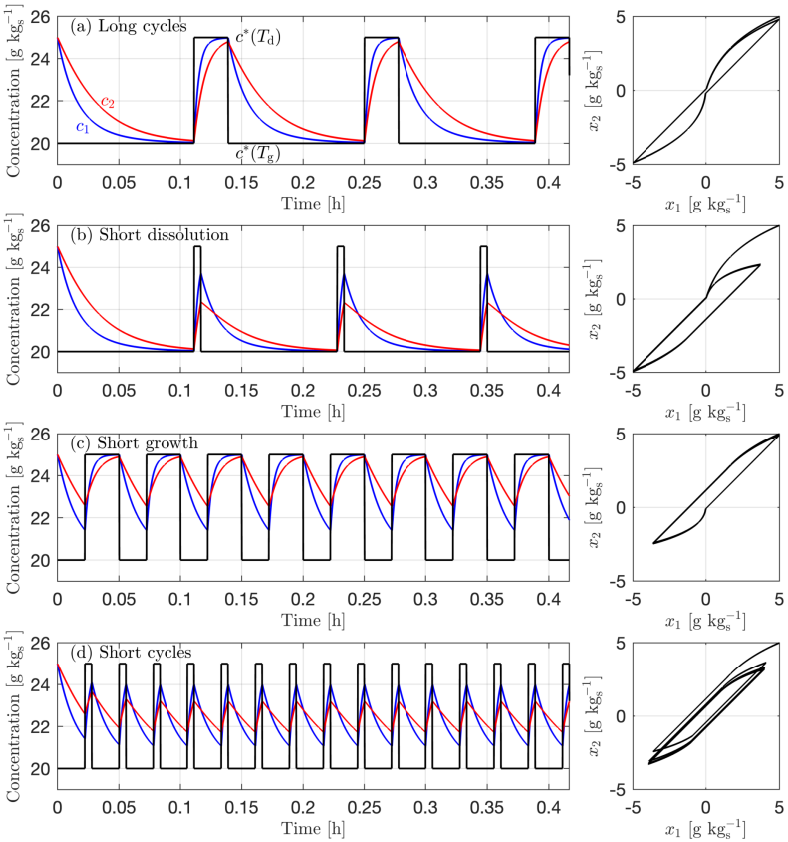

Figure 12.6 Numerical simulations for deracemization using four different step durations (a-d). The left panels illustrate the evolution of the concentration levels of both enantiomers in solution (red and blue), and the one of the solubility (black). The right panels show the cyclic evolution of the rescaled concentration vector $\underline{x}$ with $x_i = c_i - c^*$.

The final case that both steps are too short to approach the equilibrium is shown in the bottom row (d). Again, a cyclic steady state is reached, even though more slowly as in cases (b) and (c). These simulations clearly illustrate the emergence of the cyclic steady state independent of the values of the step durations. Hence it is safe to contend that the assumption of such steady state

in the derivation of the analytical solution is valid. Note that, while not shown explicitly, a similar behavior is observed when simulating the process using 3D growth and the logarithmic driving force.

Effect of more complex cycle configurations

We proved $a_d > a_g$ as exact condition for solid-state deracemization under the set of assumptions made to derive the analytical solution in Section 12.3, and we generalized this condition to systems with 3D growth and non-linear driving force for crystal growth and dissolution in Section 12.8.2.

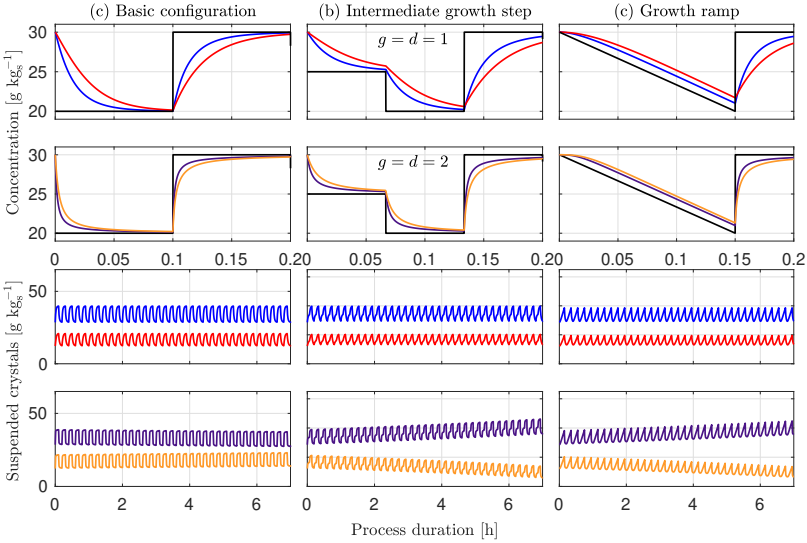

Figure 12.7 Numerical solution for temperature cycling-induced deracemization. Th red and blue lines show the evolution of concentration in the case of $g = d = 1$, the violet and yellow lines for $g = d = 2$. Three process configurations are considered (columns): (a) Basic cycle with one growth and one dissolution step. (b) Cycle with intermediate growth step. (c) Cycle with growth ramp and constant dissolution step. We note that for $g = d = 2$, configurations (b) and (c) enable deracemization; this is remarkable, since $a_d = a_g$, and hence the analytical solution would predict no change in the handedness of the suspension. The simulation parameters for the case $g = d = 2$ are reported in Table 12.3.

Here, we show that deracemization becomes feasible for $a_d \leq a_g$ when relaxing some further assumptions; namely when considering more complex

cycle configurations combined with values of the exponents g and d in the expressions for the driving force that differ from 1. Figure 12.7 illustrates the deracemization performance for six simulations with $a_d = a_g$, i.e., for three cycle configurations with $g = d = 1$ (top row), and with $g = d = 2$ (second row). The columns report the cycle configurations; (a) is the base configuration with two steps connected through temperature jumps, (b) includes a third intermediate step for growth, and (c) shows a cycle comprising a dissolution step and a ramped growth step. To enable a fair comparison, the duration of a single cycle has been chosen to be the same in all three configurations, namely 12 min. While one may extend this study to an arbitrary number of cycle configurations, the three chosen ones sufficiently highlight the main effects.

Following the exact condition for deracemization, the simulations should neither lead to deracemization nor to racemization. For $g = d = 1$, this is indeed the case for all three cycle configurations. For $g = d = 2$, however, the configurations with intermediate growth step and with growth ramp lead to deracemization. In these two cases, growth takes place at a lower value of the driving force than dissolution in average. For $g > 1$ this creates an additional asymmetry that shifts the process towards deracemization. This effect is most pronounced for a ramped step, where growth occurs at low, nearly constant supersaturation over the entire step duration. While not shown explicitly, similar effects are observed for configurations where dissolution occurs at lower values of the driving force than growth, which favors racemization.

It is worth underlining the practical relevance of this finding. The ratio a_d/a_g is hard to control in practice, as it depends on the physicochemical properties of the compound that is crystallizing, and on the temperature-dependency of the racemization reaction. In contrast, the manipulation of the cycle configuration provides an accessible means of improving the deracemization performance in the rather relevant scenario that at least one of the exponents g and d is unequal one.

Parameter	Symbol	Values [unit]
Growth rate exponent	g	2 [-]
Dissolution rate exponent	d	2 [-]
Growth pre-factor at T_g (Δc)	$k_g(T_g)$	$10^{-1.699}$[m s^{-1}kg^{-2}kg$_s^2$]
Growth/dissolution ratio	$k_d(T_g)/k_g(T_g)$	4 [-]
Time of growth step	t_g	variable
Time of dissolution step	t_d	variable
Simulation time step	t_{step}	0.05 [s]
Process duration	t_{tot}	until $N_2 = 0$

Table 12.3 Set of parameter values used in the simulations for $g = d = 2$. Note that these simulations required a shorter time step due to the non-linearity introduced by the values of the exponents.

13 | CONCLUDING REMARKS

The preceding chapters provided detailed insights into the research activities carried out within this thesis. This chapter aims to synthesize the main achievements and to indicate potential avenues for future investigations. Its structure mirrors that of the thesis as a whole, whereby the following three sections are related to the three parts of the thesis. I close the thesis with a personal perspective on the broader research field of pharmaceutical manufacturing.

13.1 PART I: NUCLEATION OF ICE

The limited understanding of ice nucleation in the commercial freezing process of the Janssen COVID-19 vaccine was a main motivation for this thesis. Chapters 2–5 report experimental studies that shed light on the fundamentals of this elusive phenomenon and its relevance to the freezing process of pharmaceuticals. In Chapter 2, I developed an experimental methodology to monitor ice nucleation in vials filled with aqueous solution at mid-throughput. I further showed how to estimate the kinetic parameters in the nucleation rate expression and their uncertainty from the collected experimental data.

This first study aimed to establish a robust measurement methodology for ice nucleation and hence experiments focused on a single solution composition, namely 20 wt% sucrose solution. Next, I carried out a large experimental campaign comprising solutions of ten different compositions that contained sucrose, trehalose and sodium chloride at various concentration levels, as reported in Chapter 3. The objective of this study was to quantify the effect of solution composition on the rate of ice nucleation; and as the experimental data indicated, such an effect mirrors that of the solution's thermodynamic properties (i.e., the melting point) on its composition. Three nucleation rate expressions based on the supercooling, on the water activity difference, and on the chemical potential difference were shown to accurately describe the effect of solution composition: when estimating the kinetic parameters in these expressions for all ten compositions studied, no significant differences were observed among the compositions. This finding is of immediate relevance to the pharmaceutical industry, as it demonstrates that nucleation rates do not

have to be measured for all formulations individually; rather, it is sufficient to measure them for a single formulation of a specific composition and then to extrapolate to different compositions.

In addition to solution composition, particulate impurities are of key interest to the freezing of pharmaceuticals. This is because drug products prepared under manufacturing conditions must be particulate-free, whereas those prepared under standard laboratory conditions are contaminated with dust particles. Therefore, Chapter 4 reports a detailed investigation on the effect of particulates on ice nucleation. Samples prepared under standard conditions were compared first with particulate-free ones prepared at Janssen, and second with samples spiked with silver iodide particles, which are known to promote ice nucleation. As expected, and now quantified with statistical relevance, the particulate-free samples nucleated significantly slower than the less clean samples. This finding highlights that nucleation rates should be measured under conditions that are representative for the manufacturing process. The effect of particulates on ice nucleation is also relevant to the freeze-drying process of pharmaceuticals in vials where scale-up issues between particulate-free manufacturing conditions and less clean laboratory conditions are widely reported.

Chapters 2–4 focus on the freezing process in vials. This was done to match the conditions of industrial processes, where vials are used as well. However, it is also true that a certain volume, on the order of tens of milli-liters, is required to measure the nucleation kinetics at the vial-scale, which may be expensive and hard to acquire during early stages of drug development. To this end, I explored in collaboration with the research groups of Prof. Dr. Ulrike Lohmann (Atmospheric Physics) and Prof. Dr. Andrew deMello (Biochemical Engineering), both at ETH Zurich, the use of droplet microfluidics to monitor the freezing process of aqueous solutions in pico-liter volumes at high throughput. Initially focusing on ice nucleation, the main achievement of this study was the discovery that droplet microfluidics allows for the direct visualization of the maximally freeze-concentrated state that represents the endpoint of solidification. We applied this technique to extract the critical temperature and composition of this state, which are relevant to the design of pharmaceutical freeze-drying processes. This demonstrates that the use of miniaturized setups is beneficial for pharmaceutical applications and should be explored further.

I conclude this section by emphasizing that the experimental studies reported in Part I focus on binary solutions that consist of water and either sucrose, trehalose, or sodium chloride. These three solutes indeed are of pharmaceutical relevance, as they are common excipients in biopharmaceuticals. Yet, one may wonder whether actual drug products that comprise a multitude

of excipients and – often rather complex – active ingredients, nucleate in a similar manner or if they show a more complex nucleation behavior. While not explicitly reported in this thesis, the nucleation behavior of the Janssen COVID-19 vaccine was studied in the context of Chapter 4, and no major differences were observed between the vaccine and the particulate-free sucrose solutions. As a next step, it would be very interesting to generalize these findings and to measure the ice nucleation rate in samples of all relevant classes of biopharmaceuticals – such as those based on macro-molecules (peptides, proteins, RNA, etc.), on nano-particles, on viral vectors, and so on. Such a study could also establish links to the literature on so-called antifreeze-proteins,[335] which are proteins known to inhibit ice nucleation, and that are abundant in different organisms that live in cold environments.

13.2 PART II: FREEZING OF PHARMACEUTICALS

While the first part of this thesis focuses on fundamental aspects of freezing, the second part utilizes these insights for the rational design and understanding of pharmaceutical processes that involve freezing. Chapters 6–9 report the development of mechanistic models for different types of freezing processes and the comparison of model predictions with experimental data. In Chapter 6, I introduce a process-scale freezing model that accounts for the stochastic nature of ice nucleation, and I apply it to simulate the freezing stage in a freeze-drying process. In such a process, numerous vials are densely packed in two dimensions on a temperature-controlled shelf, and frozen together. A key finding of this modeling study was that vials thermally interact with each other as a consequence of their dense packing, and that such interactions significantly enhance batch heterogeneity. Such heterogeneity among vials is undesired and represents a major challenge to the design and optimization of pharmaceutical freeze-drying processes.

To validate these model predictions, I designed an experimental setup that enables for the first time the monitoring of nucleation times, nucleation temperatures, and solidification times for all vials in a batch of up to one hundred vials. This setup relies on infrared thermography, as reported in Chapter 7, and experiments carried out with the setup placed in a laboratory-scale freeze-dryer confirmed the trends predicted by the model. In particular, the experiments corroborated the key role that thermal interactions among vials play in freeze-drying and elucidated the effect of loading configurations on the extent of these interactions. In line with model predictions, high cooling rates and fast heat transfer with the shelf were found to mitigate thermal interactions, and hence to reduce batch heterogeneity.

The two-dimensional model for the freezing stage in freeze-drying served as a starting point for the development of a three-dimensional model for the commercial freezing process of the Janssen COVID-19 vaccine, as reported in Chapter 8. In this process, tens of thousands of vials are stacked in three dimensions on a pallet and frozen over several days in a cold storage room. Engineering runs, however, revealed that after multiple days at −20°C, the drug product in many vials remained liquid, whereas in others ice formed. Temperature sensors located in the pallet reported complex thermal evolution profiles with numerous unexpected features such as thermal spikes that were not understood at the time of process design. With the help of the mechanistic freezing model, however, all these trends could be explained and were traced back to the phenomenon of ice nucleation. In particular, I found that the ice nucleation kinetics of the vaccine were too slow at the given temperature for nucleation to happen in all vials in the given time frame; the use of lower freezing temperatures and less dense packing configurations ensured that the drug product in all vials freezes in a reasonably short amount of time.

To assess the accuracy of a key assumption in these process-scale models, namely that temperature and composition in each vial are spatially uniform, I developed a third freezing model that simulates the spatial evolution of freezing in a single vessel, which is reported in Chapter 9. Given that the walls of the vessel are cooled during freezing, the regions in the vicinity of these walls are colder than the center of the vessel, and therefore nucleation should be more likely to happen there than. The spatial freezing model correctly predicted this behavior, and further revealed that thermal gradients strongly influence the time of nucleation in case of freezing in large vessels (tens of mL and above) or at high cooling rates. Thermal gradients affect the interplay between the distribution of nucleation temperatures and the cooling rate, and hence the model was validated using experimental nucleation data in vials generated at two different cooling rates. When applied to the conditions used in pallet freezing and in the freezing stage of freeze-drying, the model predicted no relevant effects of thermal gradients, thus confirming that such gradients can be neglected at the process-scale without loss of accuracy.

The three freezing models have been made available to the public in the form of a Python package termed *SNOW*, short for *Stochastic Nucleation of Water*.[73] Considering potential avenues for future work, there are several promising opportunities how to expand these models. In particular, it may be worthwhile to explore how to integrate the shelf-scale freezing model presented in Chapter 6 with a mechanistic model for drying, to obtain a complete model for the freeze-drying process of pharmaceuticals. Such a model must be able to predict the properties of the micro-structure that forms during freezing, because it is this micro-structure that affects the dynamics of

drying. This promises to be challenging, as the mechanisms that govern the formation of this micro-structure are not entirely understood.

To validate such a freeze-drying model, one should carry out an experimental campaign where aqueous solutions are frozen under different process conditions and then dried under vacuum afterward. By monitoring both freezing and drying of all vials on the shelf using the setup introduced in Chapter 7, one can experimentally quantify the link between the two stages of the process. The micro-structure in dried samples can be analyzed using scanning electron microscopy (SEM), whereby pores in the dried material represent regions of pure ice in the formerly frozen product. Alternatively, one could use μ-computed tomography, which provides three-dimensional images of the micro-structure. This technique avoids issues that arise during sample preparation for SEM, which involves cutting the fragile dried product. During the early stages of my doctorate, I conducted preliminary experiments using μ-computed tomography, where I could confirm the feasibility of this technique for the analysis of freeze-dried products.

13.3 PART III: CRYSTALLIZATION SYSTEMS

The third and final part of this thesis comprises Chapters 10–12 and focuses on complex systems related to crystallization. Originally, I envisioned to focus my thesis research entirely on freezing and freeze-drying, however, when investigating these processes in detail I learned to appreciate the similarities with crystallization. In particular, nucleation plays a central role in both freezing and crystallization, and its limited understanding represents a major hurdle for rational process design in both cases. Intriguingly, one of the main methods to measure nucleation rates in crystallization from solution relies on the same principles as the one I developed for ice nucleation during freezing in vials. Both methods assume that a single nucleus randomly forms in the vessel and extract the nucleation rate from the statistics of this random event. In the case of crystallization, one also accounts for the time that this nucleus requires to grow to a detectable size. In the case of freezing, ice crystal growth is rapid and quickly penetrates the entire vial, so that the first nucleus is detected immediately after its formation, as observed many times during the studies reported in Part I. In crystallization, however, there is still a major debate around this *detection delay* and the general notion of forming only a single (primary) nucleus in a vessel. I therefore studied in Chapter 10 how the interplay of primary nucleation, secondary nucleation and crystal growth results in the formation of detectable crystalline matter. I assessed the accuracy

of different methods for the estimation of nucleation rates and formulated recommendations for their correct application.

In Chapter 11, I investigated secondary nucleation in more detail. The rate of secondary nucleation dominates that of primary nucleation at low supersaturation levels,[50,105] which is relevant to the design of continuous crystallization processes that rely predominantly on secondary nucleation. Such continuous crystallizers operate at steady state, and an open question in the field was how to rigorously describe the stability of the steady state. I conceived a general mathematical framework for this purpose, which is grounded on the notion that at steady state a crystal must on average promote the formation of one secondary nucleus during its lifetime in the crystallizer. This framework confirmed the findings of earlier studies,[258,259] and provided a set of necessary and sufficient conditions to characterize the stability of systems with size-dependent crystal growth, size-dependent crystal withdrawal, growth rate dispersion, and cross-nucleation. It is particularly useful to characterize the steady state of systems that form multiple types of crystals such as polymorphic or chiral compounds, which are of immediate interest to the pharmaceutical industry.

The crystallization of chiral compounds is also the topic of Chapter 12. To summarize it, I quote one of the anonymous reviewers of the associated journal publication:[80] *The authors make a landmark contribution to an important scientific and technological phenomenon that has occupied the minds of many scholars since the late twentieth century. The phenomenon is this, when a racemic mixture of crystals is stirred in solution or ground (e.g., in a mortar and pestle) in the solid state it is found experimentally that the crystals transform to one particular enantiomorph. They all become L- or they all become D- crystals. When this phenomenon was first reported there was general disbelief that it was real, but after many confirming experiments from many laboratories the phenomenon became accepted but mysterious. During the last 25 years there have been several explanations offered to account for the phenomenon, but they are all mysteriously complex until now. In this manuscript, Mazzotti and co-workers offer a simple, believable, and very general explanation that is validated by theory, simulation, and experiment. The explanation is that deracemization occurs when the crystal dissolution rate is faster than the crystal growth rate. Their proof is beyond doubt, their simulations are in excellent agreement with theory, and the experiments agree with both theory and simulation. There is nothing more to say on this topic in my opinion, except well done.*

This phenomenon, called solid-state deracemization, is relevant both to the industry in the context of chiral resolution, and to the fundamental sciences in the context of how homochirality emerged on Earth. Given that chemical reactions with achiral starting materials yield chiral products as racemates, it is an open question how it happened that chiral molecules in

nature such as carbohydrates or amino acids nowadays occur in homochiral form, i.e., as only one of the two enantiomers. Two phenomena are known to enable the amplification of a given enantiomeric excess, which are solid-state deracemization and asymmetric autocatalysis. While the newly identified mechanism for solid-state deracemization is ubiquitous and many different chiral compounds have successfully been deracemized in the past, only a single class of chemical reactions, without biological relevance, has been found to undergo asymmetric autocatalysis.[332] This supports the notion that solid-state deracemization has contributed to the emergence of homochirality. These results open up several exciting paths for future research concerning the crystallization of chiral compounds, both in the context of the emergence of homochirality on Earth and related to the industrial implementation of solid-state deracemization.

13.4 PERSPECTIVE

The study of the physical and chemical foundations of manufacturing processes is of immediate interest not only to industry but also to the fundamental sciences and to society as a whole. Despite many decades of successful implementation in the pharmaceutical industry, the mechanistic understanding of the three processes studied in this thesis – freezing, freeze-drying, and crystallization – is not yet sufficient for model-based process design. While the predominant use of trial and error in industrial process design may yield acceptable results under *normal* circumstances, it became a major issue in the context of the COVID-19 pandemic and the associated accelerated manufacturing timelines.

There are many lessons to be learned from the pandemic, and one of them is that drug products can be brought to the market significantly faster than done in the past. To avoid becoming a bottleneck in the overall drug development timeline, the way how processes are designed must change. In this context, process models will become more relevant as they help to reduce the necessary number of time-consuming experiments. Such models may rely on mechanistic considerations as is the case for those presented in this thesis, or instead on data-driven approaches. Mechanistic models are particularly useful if there is at least some basic understanding of the relevant fundamental phenomena involved in the process, such as crystal nucleation in case of freezing and crystallization.

The work in this area greatly benefits from collaborations between academia and industry, as is exemplified by the fruitful interactions I had during my doctorate with my collaborators at The Janssen Pharmaceutical Companies

of Johnson & Johnson. This is for several reasons, and the most important one is that academia and industry are two very different environments with distinct ways of working. The rather slow-paced nature of academia allows researchers to deeply dive into specific topics without too many external constraints, hence nurturing the discovery of fundamental advances. The pace in industry is much faster, even more so in the future, so that there may be only little time for fundamental studies dedicated to the mechanistic understanding of processes. Therefore, by supporting academic research, pharmaceutical companies can promote the generation of relevant knowledge that they may find difficult to obtain on their own.

A lot of work remains to be done, and I would not be surprised to see more and more such collaborations in the future (and perhaps to be involved in some of them). Indeed, one may argue that freezing and crystallization represent rather *basic* processes in the field of pharmaceutical manufacturing because they have been around for a long time. It is quite remarkable that even for these processes there is a substantial lack of process understanding. And while I am confident that the results of my thesis filled some of the gaps, I also acknowledge that there are many more issues to address in the future. Various processes of industrial relevance do not have such a long history, consider for instance the manufacture of mRNA-based drug products. How to design and optimize the manufacturing processes for these products will remain a topic of great relevance for a long time, as mechanistic investigations have only just begun.

BIBLIOGRAPHY

(1) AboulFotouh, K.; Cui, Z.; Williams, R. O. Next-Generation COVID-19 Vaccines Should Take Efficiency of Distribution into Consideration. *AAPS PharmSciTech* **2021**, *22*, 126 (cit. on pp. 1, 5, 58, 72, 145, 175).

(2) Fahrni, M. L. et al. Management of COVID-19 vaccines cold chain logistics: a scoping review. *Journal of Pharmaceutical Policy and Practice* **2022**, *15*, 16 (cit. on pp. 1, 145).

(3) Uddin, M. N.; Roni, M. A. Challenges of Storage and Stability of mRNA-Based COVID-19 Vaccines. *Vaccines* **2021**, *9*, 1033 (cit. on p. 1).

(4) Pambudi, N. A.; Sarifudin, A.; Gandidi, I. M.; Romadhon, R. Vaccine Cold Chain Management and Cold Storage Technology to Address the Challenges of Vaccination Programs. *Energy Reports* **2022**, *8*, 955–972 (cit. on pp. 1, 58, 145, 175).

(5) Erassa, T. E.; Bachore, B. B.; Faltamo, W. F.; Molla, S.; Bogino, E. A. Vaccine Cold Chain Management and Associated Factors in Public Health Facilities and District Health Offices of Wolaita Zone, Ethiopia. *Journal of Multidisciplinary Healthcare* **2023**, *16*, 75–84 (cit. on p. 1).

(6) Capelle, M. A. et al. Stability and suitability for storage and distribution of Ad26.ZEBOV/MVA-BN®-Filo heterologous prime-boost Ebola vaccine. *European Journal of Pharmaceutics and Biopharmaceutics* **2018**, *129*, 215–221 (cit. on p. 1).

(7) Custers, J. et al. Vaccines based on replication incompetent Ad26 viral vectors: Standardized template with key considerations for a risk/benefit assessment. *Vaccine* **2021**, *39*, 3081–3101 (cit. on p. 1).

(8) Bhatnagar, B. S.; Bogner, R. H.; Pikal, M. J. Protein Stability During Freezing: Separation of Stresses and Mechanisms of Protein Stabilization. *Pharmaceutical Development and Technology* **2007**, *12*, 505–523 (cit. on pp. 3, 5, 85, 175, 215).

(9) Fang, R.; Bogner, R. H.; Nail, S. L.; Pikal, M. J. Stability of Freeze-Dried Protein Formulations: Contributions of Ice Nucleation Temperature and Residence Time in the Freeze-Concentrate. *Journal of Pharmaceutical Sciences* **2020**, *109*, 1896–1904 (cit. on pp. 3, 162, 175, 176, 184).

(10) Privalov, P. L. Cold Denaturation of Protein. *Critical Reviews in Biochemistry and Molecular Biology* **1990**, *25*, 281–306 (cit. on pp. 3, 175, 176).

(11) Lopez, C. F.; Darst, R. K.; Rossky, P. J. Mechanistic Elements of Protein Cold Denaturation. *The Journal of Physical Chemistry B* **2008**, *112*, 5961–5967 (cit. on pp. 3, 175, 176).

(12) Arsiccio, A.; Pisano, R. The Ice-Water Interface and Protein Stability: A Review. *Journal of Pharmaceutical Sciences* **2020**, *109*, 2116–2130 (cit. on pp. 3, 4, 175, 176).

(13) Strambini, G.; Gabellieri, E. Proteins in frozen solutions: evidence of ice-induced partial unfolding. *Biophysical Journal* **1996**, *70*, 971–976 (cit. on pp. 3, 175, 176).

(14) Authelin, J.-R. et al. Freezing of Biologicals Revisited: Scale, Stability, Excipients, and Degradation Stresses. *Journal of Pharmaceutical Sciences* **2020**, *109*, 44–61 (cit. on pp. 3, 72, 175, 176, 215, 223).

(15) Muralidhara, B. K.; Wong, M. Critical considerations in the formulation development of parenteral biologic drugs. *Drug Discovery Today* **2020**, *25*, 574–581 (cit. on pp. 3, 175).

(16) Rathore, N.; Rajan, R. Current Perspectives on Stability of Protein Drug Products during Formulation, Fill and Finish Operations. *Biotechnology Progress* **2008**, *24*, 504–514 (cit. on pp. 3, 176, 215, 223).

(17) Radmanovic, N.; Serno, T.; Joerg, S.; Germershaus, O. Understanding the Freezing of Biopharmaceuticals: First-Principle Modeling of the Process and Evaluation of Its Effect on Product Quality. *Journal of Pharmaceutical Sciences* **2013**, *102*, 2495–2507 (cit. on pp. 3, 176, 215).

(18) Bjelošević, M.; Pobirk, A. Z.; Planinšek, O.; Grabnar, P. A. Excipients in freeze-dried biopharmaceuticals: Contributions toward formulation stability and lyophilisation cycle optimisation. *International Journal of Pharmaceutics* **2020**, *576*, 119029 (cit. on pp. 3, 176).

(19) Nakagawa, K.; Hottot, A.; Vessot, S.; Andrieu, J. Modeling of freezing step during freeze-drying of drugs in vials. *AIChE Journal* **2007**, *53*, 1362–1372 (cit. on pp. 3, 5, 7, 10, 22, 48, 58, 63, 76, 82, 108, 109, 122, 124, 146, 176, 184, 216, 219, 236, 238, 244).

(20) Assegehegn, G.; de la Fuente, E. B.; Franco, J. M.; Gallegos, C. The Importance of Understanding the Freezing Step and Its Impact on Freeze-Drying Process Performance. *Journal of Pharmaceutical Sciences* **2019**, *108*, 1378–1395 (cit. on pp. 3, 7, 21–24, 48, 57, 58, 72, 76, 82, 85, 98, 111, 146, 162, 176, 179, 183, 216, 221, 223, 232, 243, 245).

(21) Kasper, J. C.; Friess, W. The freezing step in lyophilization: Physico-chemical fundamentals, freezing methods and consequences on process performance and quality attributes of biopharmaceuticals. *European Journal of Pharmaceutics and Biopharmaceutics* **2011**, *78*, 248–263 (cit. on pp. 3, 4, 6, 7, 22, 48, 58, 59, 72, 82, 85, 98, 107, 146, 150, 176, 183, 216, 231).

(22) Maggioni, G. M.; Mazzotti, M. Modelling the stochastic behaviour of primary nucleation. *Faraday Discussions* **2015**, *179*, 359–382 (cit. on pp. 3, 12, 23, 25, 29, 31, 33, 43, 64, 109, 115, 116, 176, 178, 182, 216, 219, 221, 244, 249–251, 255, 259, 261, 283).

(23) Maggioni, G. M.; Bosetti, L.; dos Santos, E.; Mazzotti, M. Statistical Analysis of Series of Detection Time Measurements for the Estimation of Nucleation Rates. *Crystal Growth & Design* **2017**, *17*, 5488–5498 (cit. on pp. 3, 22, 23, 25–28, 30, 32, 49, 115, 151, 164, 176, 178, 182, 259, 267, 281–283).

(24) Maggioni, G. M.; Mazzotti, M. Stochasticity in Primary Nucleation: Measuring and Modeling Detection Times. *Crystal Growth & Design* **2017**, *17*, 3625–3635 (cit. on pp. 3, 23, 28, 30, 32, 33, 164, 176, 259, 267, 281–283).

(25) Kubota, N. Random distribution active site model for ice nucleation in water droplets. *CrystEngComm* **2019**, *21*, 3810–3821 (cit. on pp. 3, 22, 25, 33, 176, 178, 182, 219).

(26) Kaufmann, L.; Marcolli, C.; Luo, B.; Peter, T. Refreeze experiments with water droplets containing different types of ice nuclei interpreted by classical nucleation theory. *Atmospheric Chemistry and Physics* **2017**, *17*, 3525–3552 (cit. on pp. 3, 22, 89, 176, 182).

(27) Isenrich, F. N. et al. The Microfluidic Ice Nuclei Counter Zürich (MINCZ): A platform for homogeneous and heterogeneous ice nucleation. *Atmospheric Measurement Techniques Discussions* **2022**, *2022*, 1–24 (cit. on pp. 3, 22, 58, 68, 72, 83, 97, 102, 103, 176, 216, 219, 244).

(28) Capozzi, L. C.; Pisano, R. Looking inside the 'black box': Freezing engineering to ensure the quality of freeze-dried biopharmaceuticals. *European Journal of Pharmaceutics and Biopharmaceutics* **2018**, *129*, 58–65 (cit. on pp. 3, 5, 22, 24, 48, 72, 76, 108, 109, 122, 124, 129, 146, 176, 183, 184, 216, 225, 244).

(29) Kubota, N. Effect of sample volume on metastable zone width and induction time. *Journal of Crystal Growth* **2012**, *345*, 27–33 (cit. on pp. 3, 176, 178).

(30) Van den Berg, L.; Rose, D. Effect of freezing on the pH and composition of sodium and potassium phosphate solutions: the reciprocal system KH2PO4-Na2HPO4-H2O. *Archives of Biochemistry and Biophysics* **1959**, *81*, 319–329 (cit. on pp. 4, 176).

(31) Murase, N.; Franks, F. Salt precipitation during the freeze-concentration of phosphate buffer solutions. *Biophysical Chemistry* **1989**, *34*, 293–300 (cit. on pp. 4, 176).

(32) Bluemel, O. et al. The effect of mAb and excipient cryoconcentration on long-term frozen storage stability – Part 1: Higher molecular weight species and subvisible particle formation. *International Journal of Pharmaceutics: X* **2022**, *4*, 100108 (cit. on pp. 4, 162, 176, 184, 216).

(33) Bluemel, O. et al. The effect of mAb and excipient cryoconcentration on long-term frozen storage stability – part 2: Aggregate formation and oxidation. *International Journal of Pharmaceutics: X* **2022**, *4*, 100109 (cit. on pp. 4, 176).

(34) Hottot, A.; Vessot, S.; Andrieu, J. Freeze drying of pharmaceuticals in vials: Influence of freezing protocol and sample configuration on ice morphology and freeze-dried cake texture. *Chemical Engineering and Processing: Process Intensification* **2007**, *46*, 666–674 (cit. on pp. 4, 22, 48, 108, 176).

(35) Rathore, A. S.; Winkle, H. Quality by design for biopharmaceuticals. *Nature Biotechnology* **2009**, *27*, 26–34 (cit. on pp. 5, 176).

(36) Yu, L. X. et al. Understanding Pharmaceutical Quality by Design. *The AAPS Journal* **2014**, *16*, 771–783 (cit. on pp. 5, 176).

(37) Arsiccio, A.; Giorsello, P.; Marenco, L.; Pisano, R. Considerations on Protein Stability During Freezing and Its Impact on the Freeze-Drying Cycle: A Design Space Approach. *Journal of Pharmaceutical Sciences* **2020**, *109*, 464–475 (cit. on pp. 5, 176, 183, 184).

(38) Roessl, U.; Jajcevic, D.; Leitgeb, S.; Khinast, J. G.; Nidetzky, B. Characterization of a Laboratory-Scale Container for Freezing Protein Solutions with Detailed Evaluation of a Freezing Process Simulation. *Journal of Pharmaceutical Sciences* **2014**, *103*, 417–426 (cit. on pp. 5, 176).

(39) Geraldes, V.; Gomes, D. C.; Rego, P.; Fegley, D.; Rodrigues, M. A. A New Perspective on Scale-Down Strategies for Freezing of Biopharmaceutics by Means of Computational Fluid Dynamics. *Journal of Pharmaceutical Sciences* **2020**, *109*, 1978–1989 (cit. on pp. 5, 176, 184, 216, 244).

(40) Colucci, D.; Fissore, D.; Barresi, A. A.; Braatz, R. D. A new mathematical model for monitoring the temporal evolution of the ice crystal size distribution during freezing in pharmaceutical solutions. *European Journal of Pharmaceutics and Biopharmaceutics* **2020**, *148*, 148–159 (cit. on pp. 5, 23, 26, 27, 31, 53, 108, 109, 116, 122, 176, 216, 218–220, 244).

(41) Tang, X. C.; Pikal, M. J. Design of Freeze-Drying Processes for Pharmaceuticals: Practical Advice. *Pharmaceutical Research* **2004**, *21*, 191–200 (cit. on pp. 5, 6, 21, 22, 28, 59, 72, 82, 83, 108, 118, 119, 135, 146, 157, 176, 183, 194, 216, 223, 231, 237).

(42) Patel, S. M. et al. Lyophilized Drug Product Cake Appearance: What Is Acceptable? *Journal of Pharmaceutical Sciences* **2017**, *106*, 1706–1721 (cit. on p. 6).

(43) Searles, J. A.; Carpenter, J. F.; Randolph, T. W. The ice nucleation temperature determines the primary drying rate of lyophilization for samples frozen on a temperature-controlled shelf. *Journal of Pharmaceutical Sciences* **2001**, *90*, 860–871 (cit. on pp. 7, 22, 25, 28, 33, 45, 48, 58, 72, 76, 82, 108, 133, 146, 216, 220, 223, 225, 238, 244, 245).

(44) Pisano, R.; Arsiccio, A.; Nakagawa, K.; Barresi, A. A. Tuning, measurement and prediction of the impact of freezing on product morphology: A step toward improved design of freeze-drying cycles. *Drying Technology* **2019**, *37*, 579–599 (cit. on pp. 7, 108).

(45) Kashchiev, D., *Nucleation: Basic Theory with Applications*; Butterworth-Heinemann: 2000 (cit. on pp. 8, 11, 12, 14, 57, 64, 72, 88, 249, 251–254, 256, 258, 261, 293, 295, 299, 304, 320).

(46) *Crystallization Technology Handbook*; Mersmann, A., Ed.; CRC Press: 2001 (cit. on pp. 8, 11, 299, 320).

(47) Snyder, R. C.; Doherty, M. F. Faceted crystal shape evolution during dissolution or growth. *AIChE Journal* **2007**, *53*, 1337–1348 (cit. on pp. 8, 320, 326, 331).

(48) Variankaval, N.; Cote, A. S.; Doherty, M. F. From form to function: Crystallization of active pharmaceutical ingredients. *AIChE Journal* **2008**, *54*, 1682–1688 (cit. on p. 8).

(49) Lai, T.-T. C.; Ferguson, S.; Palmer, L.; Trout, B. L.; Myerson, A. S. Continuous Crystallization and Polymorph Dynamics in the L-Glutamic Acid System. *Organic Process Research & Development* **2014**, *18*, 1382–1390 (cit. on pp. 8, 293, 306).

(50) Eren, A.; Civati, F.; Ma, W.; Gamekkanda, J. C.; Myerson, A. S. Continuous crystallization and its potential use in drug substance Manufacture: A review. *Journal of Crystal Growth* **2023**, *601*, 126958 (cit. on pp. 8, 14, 293, 317, 358).

(51) Nguyen, L. A.; He, H.; Pham-Huy, C. Chiral drugs: an overview. *International journal of biomedical science: IJBS* **2006**, *2*, 85 (cit. on p. 9).

(52) Klug, S. et al. Embryotoxic effects of thalidomide derivatives in the non-human primateCallithrix jacchus: 5. Lack of teratogenic effects of phthalimidophthalmide. *Archives of Toxicology* **1994**, *68*, 203–205 (cit. on p. 9).

(53) Jacques, J.; Collet, A.; Wilen, S. H., *Enantiomers, racemates, and resolutions*; Wiley: 1981 (cit. on pp. 9, 311, 312).

(54) Pasteur, L. On the relationships between the crystalline form, chemical composition and the direction of optical rotation. *Annales Chimie Phys.* **1848**, *24*, 442–459 (cit. on p. 9).

(55) Viedma, C. Experimental evidence of chiral symmetry breaking in crystallization from primary nucleation. *Journal of Crystal Growth* **2004**, *261*, 118–121 (cit. on pp. 9, 319, 320, 327).

(56) Noorduin, W. L. et al. Emergence of a Single Solid Chiral State from a Nearly Racemic Amino Acid Derivative. *Journal of the American Chemical Society* **2008**, *130*, 1158–1159 (cit. on pp. 9, 319, 320, 327, 340, 344).

(57) Suwannasang, K.; Flood, A. E.; Rougeot, C.; Coquerel, G. Using Programmed Heating–Cooling Cycles with Racemization in Solution for Complete Symmetry Breaking of a Conglomerate Forming System. *Crystal Growth & Design* **2013**, *13*, 3498–3504 (cit. on pp. 9, 319, 320, 322, 326).

(58) Koop, T.; Luo, B.; Tsias, A.; Peter, T. Water Activity as the Determinant for Homogeneous Ice Nucleation in Aqueous Solutions. *Nature* **2000**, *406*, 611–614 (cit. on pp. 10, 58, 61, 63, 67, 82, 88).

(59) Zobrist, B.; Marcolli, C.; Peter, T.; Koop, T. Heterogeneous Ice Nucleation in Aqueous Solutions: the Role of Water Activity. *The Journal of Physical Chemistry A* **2008**, *112*, 3965–3975 (cit. on pp. 10, 58, 61, 63, 67, 72).

(60) Knopf, D. A.; Alpert, P. A. Atmospheric Ice Nucleation. *Nature Reviews Physics* **2023**, *5*, 203–217 (cit. on pp. 10, 58, 61, 63, 64, 67, 82).

(61) Corti, H. R. et al. Empirical and Theoretical Models of Equilibrium and non-Equilibrium Transition Temperatures of Supplemented Phase Diagrams in Aqueous Systems (IUPAC Technical Report). *Pure and Applied Chemistry* **2010**, *82*, 1065–1097 (cit. on pp. 10, 61).

(62) Harguindeguy, M.; Stratta, L.; Fissore, D.; Pisano, R. Combining Mathematical Modeling and Thermal Infrared Data in the Freezing of Pharmaceutical Liquid Formulations. *Industrial & Engineering Chemistry Research* **2022**, *61*, 4379–4389 (cit. on pp. 10, 23, 26, 31, 58, 63, 216, 220, 243, 244).

(63) Langer, H.; Offermann, H. On the solubility of sodium chloride in water. *Journal of Crystal Growth* **1982**, *60*, 389–392 (cit. on p. 11).

(64) Debenedetti, P. G., *Metastable Liquids: Concepts and Principles*; Princeton University Press: 2021 (cit. on pp. 12, 57, 72, 82, 86, 88, 146, 250, 251).

(65) Erdemir, D.; Lee, A. Y.; Myerson, A. S. Nucleation of Crystals from Solution: Classical and Two-Step Models. *Accounts of Chemical Research* **2009**, *42*, 621–629 (cit. on pp. 12, 252).

(66) Goh, L. et al. A Stochastic Model for Nucleation Kinetics Determination in Droplet-Based Microfluidic Systems. *Crystal Growth & Design* **2010**, *10*, 2515–2521 (cit. on pp. 12, 22, 58, 64, 76, 115, 146, 178, 182, 216, 219, 221, 244, 250, 257, 259, 261).

(67) Jiang, S.; ter Horst, J. H. Crystal Nucleation Rates from Probability Distributions of Induction Times. *Crystal Growth & Design* **2011**, *11*, 256–261 (cit. on pp. 13, 259, 281).

(68) Kadam, S. S.; Kramer, H. J. M.; ter Horst, J. H. Combination of a Single Primary Nucleation Event and Secondary Nucleation in Crystallization Processes. *Crystal Growth & Design* **2011**, *11*, 1271–1277 (cit. on pp. 13, 22, 24, 25, 30, 33, 49, 97, 250, 252, 259, 267, 281, 282, 285).

(69) Wahl, M. S.; Aasen, A.; Hjelme, D. R.; Øivind Wilhelmsen Ice formation and growth in supercooled water–alcohol mixtures: Theory and experiments with dual fiber sensors. *Fluid Phase Equilibria* **2020**, *522*, 112741 (cit. on pp. 13, 24, 221).

(70) Devos, C.; Gerven, T. V.; Kuhn, S. A Review of Experimental Methods for Nucleation Rate Determination in Large-Volume Batch and Microfluidic Crystallization. *Crystal Growth & Design* **2021**, *21*, 2541–2565 (cit. on pp. 14, 26, 49, 178, 249, 250, 256, 258, 267, 272, 278, 280).

(71) Agrawal, S. G.; Paterson, A. H. J. Secondary Nucleation: Mechanisms and Models. *Chemical Engineering Communications* **2015**, *202*, 698–706 (cit. on pp. 14, 250, 252).

(72) Bosetti, L.; Ahn, B.; Mazzotti, M. Secondary Nucleation by Interparticle Energies. I. Thermodynamics. *Crystal Growth & Design* **2022**, *22*, 87–97 (cit. on p. 14).

(73) Deck, L.-T.; Ochsenbein, D. R.; Mazzotti, M. SNOW – Stochastic Nucleation of Water, http://doi.org/10.5905/ethz-1007-520, 2021 (cit. on pp. 15, 22, 48, 117, 142, 175, 177, 182, 183, 203, 216, 217, 225, 245, 356).

(74) Deck, L.-T.; Ochsenbein, D. R.; Mazzotti, M. Stochastic Shelf-Scale Modeling Framework for the Freezing Stage in Freeze-Drying Processes. *International Journal of Pharmaceutics* **2021**, 121276 (cit. on pp. 17, 21–23, 25–27, 29, 43, 48, 58, 72, 76, 82, 146, 147, 163, 166, 172, 173, 176–179, 183–185, 216, 219, 220, 225, 226, 232, 239, 244, 245, 250, 257, 261).

(75) Deck, L.-T.; Ochsenbein, D. R.; Mazzotti, M. Stochastic ice nucleation governs the freezing process of biopharmaceuticals in vials. *International Journal of Pharmaceutics* **2022**, *625*, 122051 (cit. on pp. 17, 21–23, 29, 48, 58, 63, 72, 76, 147, 216, 223, 225, 226, 244, 245, 261).

(76) Deck, L.-T.; Mazzotti, M. Characterizing and measuring the ice nucleation kinetics of aqueous solutions in vials. *Chemical Engineering Science* **2023**, *272*, 118531 (cit. on pp. 17, 58, 60, 64, 65, 68, 69, 72, 73, 76, 89, 97, 146, 150–152, 156, 164, 167, 216, 219–221, 223, 226, 227, 229, 230, 244, 245, 250, 252, 281, 283).

(77) Deck, L.-T.; Košir, A.; Mazzotti, M. Modeling the freezing process of aqueous solutions considering thermal gradients and stochastic ice nucleation. *Chemical Engineering Journal* **2024**, *483*, 148660 (cit. on pp. 17, 76, 161, 163, 169).

(78) Deck, L.-T.; Mazzotti, M. Conceptual Validation of Stochastic and Deterministic Methods To Estimate Crystal Nucleation Rates. *Crystal Growth & Design* **2022**, *23*, 899–914 (cit. on pp. 17, 30, 97, 295, 331).

(79) Deck, L.-T.; Wittenberg, L.; Mazzotti, M. Thermodynamics Explains How Solution Composition Affects the Kinetics of Stochastic Ice Nucleation. *The Journal of Physical Chemistry Letters* **2023**, 5993–6000 (cit. on pp. 17, 72, 74, 76, 77, 88, 89, 97, 156, 164, 217, 220, 221, 225, 227).

(80) Deck, L.-T.; Hosseinalipour, M. S.; Mazzotti, M. Exact and Ubiquitous Condition for Solid-State Deracemization in Vitro and in Nature. *Journal of the American Chemical Society* **2024**, DOI: 10.1021/jacs.3c11332 (cit. on pp. 17, 358).

(81) Deck, L.-T.; Mazzotti, M. General stability analysis of the steady states in the continuous mixed-suspension crystallizer. *Chemical Engineering Journal* **2024**, *483*, 148721 (cit. on p. 17).

(82) Murray, B. J.; O'Sullivan, D.; Atkinson, J. D.; Webb, M. E. Ice nucleation by particles immersed in supercooled cloud droplets. *Chem. Soc. Rev.* **2012**, *41*, 6519–6554 (cit. on pp. 22, 25, 26, 33, 58, 64, 69, 82, 89, 244).

(83) Ickes, L.; Welti, A.; Hoose, C.; Lohmann, U. Classical nucleation theory of homogeneous freezing of water: thermodynamic and kinetic parameters. *Phys. Chem. Chem. Phys.* **2015**, *17*, 5514–5537 (cit. on pp. 22, 25, 26, 58, 72).

(84) Ehlers, S.; Schroeder, R.; Friess, W. Trouble With the Neighbor During Freeze-Drying: Rivalry About Energy. *Journal of Pharmaceutical Sciences* **2021**, *110*, 1219–1226 (cit. on pp. 22, 23, 72, 130, 146, 176, 185, 225).

(85) Perepezko, J.; Wilde, G. Melt undercooling and nucleation kinetics. *Current Opinion in Solid State and Materials Science* **2016**, *20*, Recent Advances in Solidification Microstructure- Experiments and Computational Analysis, 3–12 (cit. on p. 22).

(86) Marcolli, C.; Gedamke, S.; Peter, T.; Zobrist, B. Efficiency of immersion mode ice nucleation on surrogates of mineral dust. *Atmospheric Chemistry and Physics* **2007**, *7*, 5081–5091 (cit. on pp. 22, 25, 33, 58, 64, 67, 69, 82, 89, 97).

(87) Shardt, N. et al. Homogeneous freezing of water droplets for different volumes and cooling rates. *Physical Chemistry Chemical Physics* **2022**, *24*, 28213–28221 (cit. on pp. 22, 83, 87, 89, 94, 101, 102).

(88) Consiglio, A. N.; Lilley, D.; Prasher, R.; Rubinsky, B.; Powell-Palm, M. J. Methods to stabilize aqueous supercooling identified by use of an isochoric nucleation detection (INDe) device. *Cryobiology* **2022**, *106*, 91–101 (cit. on pp. 22, 58, 67, 72, 74, 220).

(89) Bilbao-Sainz, C. et al. Isochoric freezing and isochoric supercooling as innovative postharvest technologies for pomegranate preservation. *Postharvest Biology and Technology* **2022**, *194*, 112072 (cit. on p. 22).

(90) Dos Santos, E. C.; Maggioni, G. M.; Mazzotti, M. Statistical Analysis and Nucleation Parameter Estimation from Nucleation Experiments in Flowing Microdroplets. *Crystal Growth & Design* **2019**, *19*, 6159–6174 (cit. on pp. 23, 33, 259).

(91) Xiao, Y.; Tang, S. K.; Hao, H.; Davey, R. J.; Vetter, T. Quantifying the Inherent Uncertainty Associated with Nucleation Rates Estimated from Induction Time Data Measured in Small Volumes. *Crystal Growth & Design* **2017**, *17*, 2852–2863 (cit. on pp. 23, 28, 151, 259, 282).

(92) Scutellà, B. et al. 3D mathematical modelling to understand atypical heat transfer observed in vial freeze-drying. *Applied Thermal Engineering* **2017**, *126*, 226–236 (cit. on pp. 23, 113, 146).

(93) Harguindeguy, M.; Stratta, L.; Fissore, D.; Pisano, R. Investigation of the Freezing Phenomenon in Vials Using an Infrared Camera. *Pharmaceutics* **2021**, *13*, 1664 (cit. on pp. 23, 27, 130, 141, 150).

(94) Kubota, N.; Kawakami, T.; Tadaki, T. Calculation of supercooling temperature for primary nucleation of potassium nitrate from aqueous solution by the two-kind active site model. *Journal of Crystal Growth* **1986**, *74*, 259–274 (cit. on pp. 25, 33, 48, 58, 64, 69, 72, 86).

(95) Brandel, C.; ter Horst, J. H. Measuring induction times and crystal nucleation rates. *Faraday Discuss.* **2015**, *179*, 199–214 (cit. on pp. 25, 26, 33, 48, 259).

(96) Kulkarni, S. A.; Kadam, S. S.; Meekes, H.; Stankiewicz, A. I.; ter Horst, J. H. Crystal Nucleation Kinetics from Induction Times and Metastable Zone Widths. *Crystal Growth & Design* **2013**, *13*, 2435–2440 (cit. on pp. 25, 33, 48).

(97) Cedeno, R.; Maosoongnern, S.; Flood, A. Direct Measurements of Primary Nucleation Rates of p-Aminobenzoic Acid and Glutamic Acid and Comparison with Predictions from Induction Time Distributions. *Industrial & Engineering Chemistry Research* **2018**, *57*, 17504–17515 (cit. on pp. 26, 30, 32, 49, 249–255, 260, 262–265, 267, 272, 274, 278, 280–282, 285–287, 289).

(98) Blagden, C. XVIII. Experiments on the effect of various substances in lowering the point of congelation in water. *Philosophical Transactions of the Royal Society of London* **1788**, *78*, 277–312 (cit. on pp. 29, 60, 112, 179, 218).

(99) Kosorok, M. R., *Introduction to Empirical Processes and Semiparametric Inference*; Springer-Verlag: New York, 2008 (cit. on pp. 30, 259, 281).

(100) Lagarias, J. C.; Reeds, J. A.; Wright, M. H.; Wright, P. E. Convergence Properties of the Nelder–Mead Simplex Method in Low Dimensions. *SIAM Journal on Optimization* **1998**, *9*, 112–147 (cit. on p. 31).

(101) dos Santos, E. C.; Ładosz, A.; Maggioni, G. M.; Rudolf von Rohr, P.; Mazzotti, M. Characterization of shapes and volumes of droplets generated in PDMS T-junctions to study nucleation. *Chemical Engineering Research and Design* **2018**, *138*, 444–457 (cit. on pp. 33, 259).

(102) Nail, S. et al. Recommended Best Practices for Process Monitoring Instrumentation in Pharmaceutical Freeze Drying—2017. *AAPS PharmSciTech* **2017**, *18*, 2379–2393 (cit. on pp. 45, 58, 72, 187, 191, 194, 238, 244).

(103) Jiang, X. et al. A non-invasive multipoint product temperature measurement for pharmaceutical lyophilization. *Scientific Reports* **2022**, *12*, 12010 (cit. on p. 45).

(104) Dela Cruz, I. J. C.; Perez, J. V.; Alamani, B. G.; Capellades, G.; Myerson, A. S. Influence of Volume on the Nucleation of Model Organic Molecular Crystals through an Induction Time Approach. *Crystal Growth & Design* **2021**, *21*, 2932–2941 (cit. on pp. 49, 252).

(105) Hoffmann, J. et al. The unexpected dominance of secondary over primary nucleation. *Faraday Discussions* **2022**, *235*, 109–131 (cit. on pp. 49, 280, 295, 311, 312, 358).

(106) Koop, T.; Luo, B.; Biermann, U. M.; Crutzen, P. J.; Peter, T. Freezing of $HNO_3/H_2SO4/H_2O$ Solutions at Stratospheric Temperatures: Nucleation Statistics and Experiments. *The Journal of Physical Chemistry A* **1997**, *101*, 1117–1133 (cit. on pp. 58, 64, 72).

(107) Morris, G. J.; Acton, E. Controlled Ice Nucleation in Cryopreservation – A review. *Cryobiology* **2013**, *66*, 85–92 (cit. on pp. 58, 72, 82).

(108) Geidobler, R.; Winter, G. Controlled Ice Nucleation in the Field of Freeze-Drying: Fundamentals and Technology Review. *European Journal of Pharmaceutics and Biopharmaceutics* **2013**, *85*, 214–222 (cit. on p. 58).

(109) Knopf, D. A.; Forrester, S. M. Freezing of Water and Aqueous NaCl Droplets Coated by Organic Monolayers as a Function of Surfactant Properties and Water Activity. *The Journal of Physical Chemistry A* **2011**, *115*, 5579–5591 (cit. on p. 58).

(110) Rigg, Y. J.; Alpert, P. A.; Knopf, D. A. Immersion Freezing of Water and Aqueous Ammonium Sulfate Droplets Initiated by Humic-like Substances as a Function of Water Activity. *Atmospheric Chemistry and Physics* **2013**, *13*, 6603–6622 (cit. on p. 58).

(111) Tarn, M. D.; Sikora, S. N. F.; Porter, G. C. E.; uk Shim, J.; Murray, B. J. Homogeneous Freezing of Water Using Microfluidics. *Micromachines* **2021**, *12*, 223 (cit. on p. 58).

(112) Koop, T.; Zobrist, B. Parameterizations for Ice Nucleation in Biological and Atmospheric Systems. *Physical Chemistry Chemical Physics* **2009**, *11*, 10839–10850 (cit. on pp. 58, 67).

(113) Knopf, D. A.; Alpert, P. A. A Water Activity Based Model of Heterogeneous Ice Nucleation Kinetics for Freezing of Water and Aqueous Solution Droplets. *Faraday Discussions* **2013**, *165*, 513–534 (cit. on pp. 58, 67).

(114) Knopf, D. A.; Alpert, P. A.; Zipori, A.; Reicher, N.; Rudich, Y. Stochastic Nucleation Processes and Substrate Abundance Explain Time-Dependent Freezing in Supercooled Droplets. *npj Climate and Atmospheric Science* **2020**, *3*, DOI: 10.1038/s41612-020-0106-4 (cit. on pp. 58, 72).

(115) Young, F. E.; Jones, F. T. Sucrose Hydrates. The Sucrose–Water Phase Diagram. *The Journal of Physical and Colloid Chemistry* **1949**, *53*, 1334–1350 (cit. on pp. 60, 69, 78, 92, 95).

(116) Bodnar, R. Revised Equation and Table for Determining the Freezing Point Depression of H2O-Nacl Solutions. *Geochimica et Cosmochimica Acta* **1993**, *57*, 683–684 (cit. on pp. 60, 69).

(117) Alpert, P. A.; Knopf, D. A. Analysis of Isothermal and Cooling-Rate-Dependent Immersion Freezing by a Unifying Stochastic Ice Nucleation Model. *Atmospheric Chemistry and Physics* **2016**, *16*, 2083–2107 (cit. on p. 64).

(118) Barahona, D. On the Ice Nucleation Spectrum. *Atmospheric Chemistry and Physics* **2012**, *12*, 3733–3752 (cit. on p. 64).

(119) Rasmussen, D. H. Thermodynamics and Nucleation Phenomena — A Set of Experimental Observations. *Journal of Crystal Growth* **1982**, *56*, 56–66 (cit. on p. 67).

(120) Kanno, H.; Soga, M.; Kajiwara, K. Linear Relation Between T_H (Homogeneous Ice Nucleation Temperature) and T_m (Melting Temperature) for Aqueous Solutions of Sucrose, Trehalose, and Maltose. *Chemical Physics Letters* **2007**, *443*, 280–283 (cit. on p. 67).

(121) Cheng, L.; Sun, D.-W.; Zhu, Z.; Zhang, Z. Emerging techniques for assisting and accelerating food freezing processes: A review of recent research progresses. *Critical Reviews in Food Science and Nutrition* **2015**, *57*, 769–781 (cit. on pp. 72, 82).

(122) You, Y.; Kang, T.; Jun, S. Control of Ice Nucleation for Subzero Food Preservation. *Food Engineering Reviews* **2020**, *13*, 15–35 (cit. on pp. 72, 82).

(123) Jiang, S.; Nail, S. L. Effect of process conditions on recovery of protein activity after freezing and freeze-drying. *European Journal of Pharmaceutics and Biopharmaceutics* **1998**, *45*, 249–257 (cit. on p. 72).

(124) Pisano, R. et al. Freeze-drying of pharmaceuticals in vials nested in a rack system—Part I: Freezing behaviour. *Pharmaceutics* **2023**, *15*, 635 (cit. on pp. 72, 166).

(125) Holden, M. A. et al. High-speed imaging of ice nucleation in water proves the existence of active sites. *Science Advances* **2019**, *5*, DOI: 10.1126/sciadv.aav4316 (cit. on p. 72).

(126) Wood, G. R.; Walton, A. G. Homogeneous Nucleation Kinetics of Ice from Water. *Journal of Applied Physics* **1970**, *41*, 3027–3036 (cit. on pp. 72, 76).

(127) Patel, S. M.; Pikal, M. J. Emerging Freeze-Drying Process Development and Scale-up Issues. *AAPS PharmSciTech* **2011**, *12*, 372–378 (cit. on p. 72).

(128) Vonnegut, B. The Nucleation of Ice Formation by Silver Iodide. *Journal of Applied Physics* **1947**, *18*, 593–595 (cit. on p. 72).

(129) Fletcher, N. H. Size Effect in Heterogeneous Nucleation. *The Journal of Chemical Physics* **1958**, *29*, 572–576 (cit. on p. 72).

(130) Marcolli, C.; Nagare, B.; Welti, A.; Lohmann, U. Ice nucleation efficiency of AgI: review and new insights. *Atmospheric Chemistry and Physics* **2016**, *16*, 8915–8937 (cit. on p. 72).

(131) Kanji, Z. A. et al. Overview of Ice Nucleating Particles. *Meteorological Monographs* **2017**, *58*, 1.1 –1.33 (cit. on p. 82).

(132) Kalita, A. et al. Microstructure and crystal order during freezing of supercooled water drops. *Nature* **2023**, *620*, 557–561 (cit. on p. 82).

(133) Miller, A. J. et al. Development of the drop Freezing Ice Nuclei Counter (FINC), intercomparison of droplet freezing techniques, and use of soluble lignin as an atmospheric ice nucleation standard. *Atmospheric Measurement Techniques* **2021**, *14*, 3131–3151 (cit. on p. 82).

(134) David, R. O. et al. Development of the DRoplet Ice Nuclei Counter Zurich (DRINCZ): validation and application to field-collected snow samples. *Atmospheric Measurement Techniques* **2019**, *12*, 6865–6888 (cit. on p. 82).

(135) Acker, J. P.; McGann, L. E. Protective effect of intracellular ice during freezing? *Cryobiology* **2003**, *46*, 197–202 (cit. on p. 82).

(136) Mazur, P. Principles of cryobiology. *Life in the frozen state* **2004**, 29–92 (cit. on p. 82).

(137) Karlsson, J. O. Effects of solution composition on the theoretical prediction of ice nucleation kinetics and thermodynamics. *Cryobiology* **2010**, *60*, Special Issue: Thermodynamic aspects of Cryobiology, 43–51 (cit. on p. 82).

(138) Prickett, R. C.; Marquez-Curtis, L. A.; Elliott, J. A.; McGann, L. E. Effect of supercooling and cell volume on intracellular ice formation. *Cryobiology* **2015**, *70*, 156–163 (cit. on pp. 82, 95).

(139) Powell-Palm, M. J.; Koh-Bell, A.; Rubinsky, B. Isochoric conditions enhance stability of metastable supercooled water. *Applied Physics Letters* **2020**, *116*, 123702 (cit. on p. 82).

(140) Chew, P. Y.; Reinhardt, A. Phase diagrams—Why they matter and how to predict them. *The Journal of Chemical Physics* **2023**, *158*, 030902 (cit. on p. 82).

(141) DeMott, P. J. et al. Resurgence in ice nuclei measurement research. *Bulletin of the American Meteorological Society* **2011**, *92*, 1623–1635 (cit. on p. 82).

(142) Arsiccio, A. et al. Impact of controlled vacuum induced surface freezing on the freeze drying of human plasma. *International Journal of Pharmaceutics* **2020**, *582*, 119290 (cit. on pp. 82, 119).

(143) Pansare, S. K.; Patel, S. M. Practical Considerations for Determination of Glass Transition Temperature of a Maximally Freeze Concentrated Solution. *AAPS PharmSciTech* **2016**, *17*, 805–819 (cit. on pp. 82, 84, 85, 94, 95).

(144) Chieng, N.; Rades, T.; Aaltonen, J. An overview of recent studies on the analysis of pharmaceutical polymorphs. *Journal of pharmaceutical and biomedical analysis* **2011**, *55*, 618–644 (cit. on p. 82).

(145) Her, L.-M.; Nail, S. L. Measurement of glass transition temperatures of freeze-concentrated solutes by differential scanning calorimetry. *Pharmaceutical research* **1994**, *11*, 54–59 (cit. on pp. 82, 94).

(146) Passot, S.; Fonseca, F.; Alarcon-Lorca, M.; Rolland, D.; Marin, M. Physical characterisation of formulations for the development of two stable freeze-dried proteins during both dried and liquid storage. *European Journal of Pharmaceutics and Biopharmaceutics* **2005**, *60*, 335–348 (cit. on p. 82).

(147) Meister, E.; Gieseler, H. Freeze-Dry Microscopy of Protein/Sugar Mixtures: Drying Behavior, Interpretation of Collapse Temperatures and a Comparison to Corresponding Glass Transition Data. *Journal of Pharmaceutical Sciences* **2009**, *98*, 3072–3087 (cit. on p. 82).

(148) Blanshard, J. M. V.; Muhr, A. H.; Gough, A. In *Water Relationships in Foods*; Springer US: 1991, 639–655 (cit. on pp. 83, 100).

(149) Kim, A. I.; Akers, M. J.; Nail, S. L. The Physical State of Mannitol after Freeze-Drying: Effects of Mannitol Concentration, Freezing Rate, and a Noncrystallizing Cosolute. *Journal of Pharmaceutical Sciences* **1998**, *87*, 931–935 (cit. on p. 83).

(150) Roos, Y. H.; Drusch, S. In *Phase Transitions in Foods (Second Edition)*, Roos, Y. H., Drusch, S., Eds., Second Edition; Academic Press: San Diego, 2016, pp 79–113 (cit. on p. 84).

(151) Sacha, G. A.; Nail, S. L. Thermal Analysis of Frozen Solutions: Multiple Glass Transitions in Amorphous Systems. *Journal of Pharmaceutical Sciences* **2009**, *98*, 3397–3405 (cit. on pp. 84, 85).

(152) Zobrist, B.; Marcolli, C.; Pedernera, D. A.; Koop, T. Do atmospheric aerosols form glasses? *Atmospheric Chemistry and Physics* **2008**, *8*, 5221–5244 (cit. on p. 84).

(153) Gayle, F. W.; Cocks, F. H.; Shepard, M. L. The H2O–NaCl–sucrose phase diagram and applications in cryobiology. *Journal of Applied Chemistry and Biotechnology* **1977**, *27*, 599–607 (cit. on pp. 84, 85, 92).

(154) Seifert, I.; Bregolin, A.; Fissore, D.; Friess, W. Method development and analysis of the water content of the maximally freeze concentrated solution suitable for protein lyophilisation. *European Journal of Pharmaceutics and Biopharmaceutics* **2020**, *153*, 36–42 (cit. on pp. 85, 94, 95).

(155) Krämer, B. et al. Homogeneous nucleation rates of supercooled water measured in single levitated microdroplets. *The Journal of Chemical Physics* **1999**, *111*, 6521–6527 (cit. on p. 88).

(156) Stöckel, P.; Weidinger, I. M.; Baumgärtel, H.; Leisner, T. Rates of Homogeneous Ice Nucleation in Levitated H2O and D2O Droplets. *The Journal of Physical Chemistry A* **2005**, *109*, 2540–2546 (cit. on p. 88).

(157) Miyata, K.; Kanno, H. Supercooling behavior of aqueous solutions of alcohols and saccharides. *Journal of Molecular Liquids* **2005**, *119*, 189–193 (cit. on p. 89).

(158) Vali, G. Interpretation of freezing nucleation experiments: singular and stochastic; sites and surfaces. *Atmospheric Chemistry and Physics* **2014**, *14*, 5271–5294 (cit. on p. 89).

(159) Consiglio, A. N.; Ouyang, Y.; Powell-Palm, M. J.; Rubinsky, B. An extreme value statistics model of heterogeneous ice nucleation for quantifying the stability of supercooled aqueous systems, 2023 (cit. on pp. 89, 220).

(160) Blond, G.; Simatos, D.; Catté, M.; Dussap, C. G.; Gros, J. B. Modeling of the water–sucrose state diagram below o C. *Carbohydrate Research* **1997**, *298*, 139–145 (cit. on pp. 92, 95).

(161) Elliott, J.; Prickett, R.; Elmoazzen, H.; Porter, K.; McGann, L. A multisolute osmotic virial equation for solutions of interest in biology. *The Journal of Physical Chemistry B* **2007**, *111*, 1775–1785 (cit. on pp. 95, 96).

(162) Chen, C. Effective molecular weight of aqueous solutions and liquid foods calculated from the freezing point depression. *Journal of food science* **1986**, *51*, 1537–1539 (cit. on pp. 95, 96).

(163) McMillan Jr, W. G.; Mayer, J. E. The statistical thermodynamics of multicomponent systems. *The Journal of Chemical Physics* **1945**, *13*, 276–305 (cit. on p. 95).

(164) Hill, T. L. Theory of Solutions. I. *Journal of the American Chemical Society* **1957**, *79*, 4885–4890 (cit. on p. 95).

(165) Zielinski, M. W.; McGann, L. E.; Nychka, J. A.; Elliott, J. A. Comparison of non-ideal solution theories for multi-solute solutions in cryobiology and tabulation of required coefficients. *Cryobiology* **2014**, *69*, 305–317 (cit. on p. 95).

(166) Roos, Y.; Karel, M Phase transitions of amorphous sucrose and frozen sucrose solutions. *Journal of Food Science* **1991**, *56*, 266–267 (cit. on p. 96).

(167) Foerst, P. et al. Estimation of mass transfer rate and primary drying times during freeze-drying of frozen maltodextrin solutions based on x-ray -computed tomography measurements of pore size distributions. *Journal of Food Engineering* **2019**, *260*, 50–57 (cit. on pp. 98, 108).

(168) Schremb, M.; Tropea, C. Solidification of supercooled water in the vicinity of a solid wall. *Physical Review E* **2016**, *94*, 052804 (cit. on p. 100).

(169) Rambhatla, S.; Ramot, R.; Bhugra, C.; Pikal, M. J. Heat and mass transfer scale-up issues during freeze drying: II. Control and characterization of the degree of supercooling. *AAPS PharmSciTech* **2004**, *5*, 54–62 (cit. on pp. 108, 146, 194).

(170) Pikal, M.; Rambhatla, S.; Ramot, R. The impact of the freezing stage in lyophilization: Effects of the ice nucleation temperature on process design and product quality. *Am. Pharm. Rev.* **2002**, *5*, 48–52 (cit. on pp. 108, 146, 216, 223).

(171) Arsiccio, A.; Barresi, A. A.; Pisano, R. Prediction of Ice Crystal Size Distribution after Freezing of Pharmaceutical Solutions. *Crystal Growth & Design* **2017**, *17*, 4573–4581 (cit. on pp. 108, 122, 219, 223, 236, 244).

(172) Pikal, M. J.; Bogner, R.; Mudhivarthi, V.; Sharma, P.; Sane, P. Freeze-Drying Process Development and Scale-Up: Scale-Up of Edge Vial Versus Center Vial Heat Transfer Coefficients, K v. *Journal of Pharmaceutical Sciences* **2016**, *105*, 3333–3343 (cit. on p. 108).

(173) Scutellà, B.; Passot, S.; Bourlés, E.; Fonseca, F.; Tréléa, I. C. How Vial Geometry Variability Influences Heat Transfer and Product Temperature During Freeze-Drying. *Journal of Pharmaceutical Sciences* **2017**, *106*, 770–778 (cit. on pp. 108, 114).

(174) Rambhatla, S.; Ramot, R.; Bhugra, C.; Pikal, M. J. Heat and mass transfer scale-up issues during freeze drying: II. Control and characterization of the degree of supercooling. *AAPS PharmSciTech* **2004**, *5*, 54–62 (cit. on p. 109).

(175) Oddone, I.; Bockstal, P.-J. V.; Beer, T. D.; Pisano, R. Impact of vacuum-induced surface freezing on inter- and intra-vial heterogeneity. *European Journal of Pharmaceutics and Biopharmaceutics* **2016**, *103*, 167–178 (cit. on pp. 109, 121, 122).

(176) Kramer, M.; Sennhenn, B.; Lee, G. Freeze-drying using vacuum-induced surface freezing. *Journal of Pharmaceutical Sciences* **2002**, *91*, 433–443 (cit. on pp. 109, 216, 223).

(177) Konstantinidis, A. K.; Kuu, W.; Otten, L.; Nail, S. L.; Sever, R. R. Controlled nucleation in freeze-drying: Effects on pore size in the dried product layer, mass transfer resistance, and primary drying rate. *Journal of Pharmaceutical Sciences* **2011**, *100*, 3453–3470 (cit. on p. 109).

(178) Pisano, R. In *Lyophilization of Pharmaceuticals and Biologicals: New Technologies and Approaches*, Ward, K. R., Matejtschuk, P., Eds.; Springer New York: New York, NY, 2019, pp 79–111 (cit. on pp. 109, 217, 223, 239, 243).

(179) Passot, S. et al. Effect of Controlled Ice Nucleation on Primary Drying Stage and Protein Recovery in Vials Cooled in a Modified Freeze-Dryer. *Journal of Biomechanical Engineering* **2009**, *131*, DOI: 10.1115/1.3143034 (cit. on p. 109).

(180) Akyurt, M.; Zaki, G.; Habeebullah, B. Freezing phenomena in ice–water systems. *Energy Conversion and Management* **2002**, *43*, 1773–1789 (cit. on pp. 111, 179).

(181) Venkatesh, P. B.; Back, C.; Liberman, A.; Pourpoint, T. L. In *53rd AIAA/SAE/ASEE Joint Propulsion Conference*, American Institute of Aeronautics and Astronautics: 2017 (cit. on p. 112).

(182) Ontsouka, C.; Bruckmaier, R.; Blum, J. Fractionized Milk Composition During Removal of Colostrum and Mature Milk. *Journal of Dairy Science* **2003**, *86*, 2005–2011 (cit. on p. 112).

(183) Nail, S. L.; Jiang, S.; Chongprasert, S.; Knopp, S. A. In *Pharmaceutical Biotechnology*; Springer US: 2002, pp 281–360 (cit. on p. 112).

(184) Burridge, H. C.; Linden, P. F. Questioning the Mpemba effect: hot water does not cool more quickly than cold. *Scientific Reports* **2016**, *6*, DOI: 10.1038/srep37665 (cit. on p. 115).

(185) Kuhs, M.; Zeglinski, J.; Rasmuson, Å. C. Influence of History of Solution in Crystal Nucleation of Fenoxycarb: Kinetics and Mechanisms. *Crystal Growth & Design* **2014**, *14*, 905–915 (cit. on p. 115).

(186) Python Package Index - PyPI (cit. on pp. 117, 182, 216, 217, 225, 245).

(187) Liu, J.; Viverette, T.; Virgin, M.; Anderson, M.; Dalal, P. A Study of the Impact of Freezing on the Lyophilization of a Concentrated Formulation with a High Fill Depth. *Pharmaceutical Development and Technology* **2005**, *10*, 261–272 (cit. on p. 119).

(188) Vollrath, I.; Friess, W.; Freitag, A.; Hawe, A.; Winter, G. Comparison of ice fog methods and monitoring of controlled nucleation success after freeze-drying. *International Journal of Pharmaceutics* **2019**, *558*, 18–28 (cit. on pp. 121, 122, 136).

(189) Goshima, H.; Do, G.; Nakagawa, K. Impact of Ice Morphology on Design Space of Pharmaceutical Freeze-Drying. *Journal of Pharmaceutical Sciences* **2016**, *105*, 1920–1933 (cit. on p. 122).

(190) Scutellà, B.; Trelea, I. C.; Bourlès, E.; Fonseca, F.; Passot, S. Determination of the dried product resistance variability and its influence on the product temperature in pharmaceutical freeze-drying. *European Journal of Pharmaceutics and Biopharmaceutics* **2018**, *128*, 379–388 (cit. on p. 122).

(191) Kurz, W.; Fisher, D. J., *Fundamentals of Solidification*; Trans Tech Publications: Switzerland: 1992 (cit. on p. 123).

(192) Pikal, M. J., *Mechanisms of Protein Stabilization During Freeze-Drying Storage: The Relative Importance of Thermodynamic Stabilization and Glassy State Relaxation Dynamics*; Informa Healthcare, London: 2010 (cit. on p. 124).

(193) Deck, L.-T.; Ferru, N.; Košir, A.; Mazzotti, M. Visualizing and understanding batch heterogeneity during freeze-drying using shelf-scale infrared thermography. *ChemRxiv* **2024**, DOI: 10.26434/chemrxiv-2024-41r63 (cit. on p. 145).

(194) Desai, K. G.; Colandene, J. D.; Adams, M. Comprehensive temperature excursion management program for the commercial distribution of biopharmaceutical drug products. *Journal of Pharmaceutical Sciences* **2020**, *109*, 2131–2144 (cit. on p. 145).

(195) Hansen, L. J.; Daoussi, R.; Vervaet, C.; Remon, J. P.; De Beer, T. R. Freeze-drying of live virus vaccines: A review. *Vaccine* **2015**, *33*, 5507–5519 (cit. on p. 146).

(196) Ghaemmaghamian, Z.; Zarghami, R.; Walker, G.; O'Reilly, E.; Ziaee, A. Stabilizing vaccines via drying: Quality by design considerations. *Advanced Drug Delivery Reviews* **2022**, *187*, 114313 (cit. on p. 146).

(197) Meulewaeter, S. et al. Continuous freeze-drying of messenger RNA lipid nanoparticles enables storage at higher temperatures. *Journal of Controlled Release* **2023**, *357*, 149–160 (cit. on p. 146).

(198) Zhang, C.; Berg, A.; Joe, C. C. D.; Dalby, P. A.; Douglas, A. D. Lyophilization to enable distribution of ChAdOx1 and ChAdOx2 adenovirus-vectored vaccines without refrigeration. *npj Vaccines* **2023**, *8*, DOI: 10.1038/s41541-023-00674-2 (cit. on p. 146).

(199) Matejčíková, A.; Tichý, E.; Rajniak, P. Experimental investigation of inhomogeneities of primary drying during lyophilization: Impact of the vials packing density. *Journal of Drug Delivery Science and Technology* **2022**, *74*, 103550 (cit. on pp. 146, 225).

(200) Emteborg, H. et al. Infrared Thermography for Monitoring of Freeze-Drying Processes: Instrumental Developments and Preliminary Results. *Journal of Pharmaceutical Sciences* **2014**, *103*, 2088–2097 (cit. on pp. 148, 166, 244).

(201) Emteborg, H.; Charoud-Got, J.; Seghers, J. Infrared Thermography for Monitoring of Freeze Drying Processes—Part 2: Monitoring of Temperature on the Surface and Vertically in Cuvettes during Freeze Drying of a Pharmaceutical Formulation. *Pharmaceutics* **2022**, *14*, 1007 (cit. on p. 148).

(202) Lietta, E.; Colucci, D.; Distefano, G.; Fissore, D. On the Use of Infrared Thermography for Monitoring a Vial Freeze-Drying Process. *Journal of Pharmaceutical Sciences* **2019**, *108*, 391–398 (cit. on pp. 148, 149, 157, 166).

(203) Colucci, D.; Maniaci, R.; Fissore, D. Monitoring of the freezing stage in a freeze-drying process using IR thermography. *International Journal of Pharmaceutics* **2019**, *566*, 488–499 (cit. on pp. 148, 150, 244).

(204) Colucci, D.; Prats-Montalbán, J. M.; Fissore, D.; Ferrer, A. Application of multivariate image analysis for on-line monitoring of a freeze-drying process for pharmaceutical products in vials. *Chemometrics and Intelligent Laboratory Systems* **2019**, *187*, 19–27 (cit. on p. 148).

(205) Brewster, M. Q., *Thermal radiative transfer and properties*; John Wiley & Sons: 1992 (cit. on p. 150).

(206) Patel, S. M.; Doen, T.; Pikal, M. J. Determination of End Point of Primary Drying in Freeze-Drying Process Control. *AAPS PharmSciTech* **2010**, *11*, 73–84 (cit. on p. 157).

(207) Kasper, J. C.; Wiggenhorn, M.; Resch, M.; Friess, W. Implementation and evaluation of an optical fiber system as novel process monitoring tool during lyophilization. *European Journal of Pharmaceutics and Biopharmaceutics* **2013**, *83*, 449–459 (cit. on p. 166).

(208) Ashok, A.; Brison, M.; LeTallec, Y. Improving cold chain systems: Challenges and solutions. *Vaccine* **2017**, *35*, 2217–2223 (cit. on p. 175).

(209) Oddone, I.; Fulginiti, D.; Barresi, A. A.; Grassini, S.; Pisano, R. Non-Invasive Temperature Monitoring in Freeze Drying: Control of Freezing as a Case Study. *Drying Technology* **2015**, *33*, 1621–1630 (cit. on p. 187).

(210) Parvis, M.; Grassini, S.; Fulginiti, D.; Pisano, R.; Barresi, A. A. In *2014 IEEE International Instrumentation and Measurement Technology Conference (I2MTC) Proceedings*, 2014, pp 1465–1470 (cit. on p. 187).

(211) Smith, G.; Arshad, M. S.; Polygalov, E.; Ermolina, I. Factors Affecting the Use of Impedance Spectroscopy in the Characterisation of the Freezing Stage of the Lyophilisation Process: the Impact of Liquid Fill Height in Relation to Electrode Geometry. *AAPS PharmSciTech* **2014**, *15*, 261–269 (cit. on p. 187).

(212) Pisano, R.; Capozzi, L. C. Prediction of product morphology of lyophilized drugs in the case of Vacuum Induced Surface Freezing. *Chemical Engineering Research and Design* **2017**, *125*, 119–129 (cit. on pp. 216, 219, 223, 242).

(213) Wenzel, T.; Gieseler, M.; Gieseler, H. Design of Vacuum-Induced Freezing Protocols for High Fill Volume Formulations in Freeze-Drying: A Strategic Approach. *Journal of Pharmaceutical Sciences* **2020**, *109*, 3035–3044 (cit. on pp. 216, 217, 237, 239, 242–245).

(214) Regis, F.; Arsiccio, A.; Bourlès, E.; Scutellà, B.; Pisano, R. Surface Treatment of Glass Vials for Lyophilization: Implications for Vacuum-Induced Surface Freezing. *Pharmaceutics* **2021**, *13*, 1766 (cit. on pp. 217, 242, 243, 245).

(215) Maggioni, G. M.; Mazzotti, M. A Stochastic Population Balance Equation Model for Nucleation and Growth of Crystals with Multiple Polymorphs. *Crystal Growth & Design* **2019**, *19*, 4698–4709 (cit. on pp. 221, 250, 251, 253–256, 259–261, 280).

(216) Murphy, D. M.; Koop, T. Review of the vapour pressures of ice and supercooled water for atmospheric applications. *Quarterly Journal of the Royal Meteorological Society* **2005**, *131*, 1539–1565 (cit. on p. 223).

(217) Marek, R.; Straub, J. Analysis of the evaporation coefficient and the condensation coefficient of water. *International Journal of Heat and Mass Transfer* **2001**, *44*, 39–53 (cit. on p. 223).

(218) Özişik, M.; Orlande, H.; Colaço, M.; Cotta, R., *Finite Difference Methods in Heat Transfer (2nd ed.)* CRC Press: London, 2017 (cit. on p. 225).

(219) Capozzi, L. C.; Trout, B. L.; Pisano, R. From Batch to Continuous: Freeze-Drying of Suspended Vials for Pharmaceuticals in Unit-Doses. *Industrial & Engineering Chemistry Research* **2019**, *58*, 1635–1649 (cit. on p. 225).

(220) Gan, K. H.; Bruttini, R.; Crosser, O. K.; Liapis, A. I. Heating Policies during the Primary and Secondary Drying Stages of the Lyophilization Process in Vials: Effects of the Arrangement of Vials in Clusters of Square and Hexagonal Arrays on Trays. *Drying Technology* **2004**, *22*, 1539–1575 (cit. on p. 225).

(221) Hussain, M.; Dincer, I. Two-dimensional heat and moisture transfer analysis of a cylindrical moist object subjected to drying: A finite-difference approach. *International Journal of Heat and Mass Transfer* **2003**, *46*, 4033–4039 (cit. on p. 225).

(222) LeVeque, R. J., *Finite Volume Methods for Hyperbolic Problems*; Cambridge University Press: 2002 (cit. on p. 225).

(223) Gruber, S. et al. The Influence of Local Microstructure Inhomogeneities on Local Drying Kinetics during Freeze-Drying. *Pharmaceutics* **2022**, *14*, 2132 (cit. on p. 245).

(224) Nývlt, J. Kinetics of nucleation in solutions. *Journal of Crystal Growth* **1968**, *3-4*, 377–383 (cit. on p. 250).

(225) Camacho Corzo, D. M. et al. Nucleation mechanism and kinetics from the analysis of polythermal crystallisation data: methyl stearate from kerosene solutions. *CrystEngComm* **2014**, *16*, 974–991 (cit. on pp. 250, 255).

(226) Kee, N. C. S.; Arendt, P. D.; May Goh, L.; Tan, R. B. H.; Braatz, R. D. Nucleation and growth kinetics estimation for l-phenylalanine hydrate and anhydrate crystallization. *CrystEngComm* **2011**, *13*, 1197–1209 (cit. on p. 250).

(227) Gherras, N.; Fevotte, G. On the use of process analytical technologies and population balance equations for the estimation of crystallization kinetics. A case study. *AIChE Journal* **2011**, *58*, 2650–2664 (cit. on pp. 250, 254).

(228) Li, H.; Kawajiri, Y.; Grover, M. A.; Rousseau, R. W. Modeling of Nucleation and Growth Kinetics for Unseeded Batch Cooling Crystallization. *Industrial & Engineering Chemistry Research* **2017**, *56*, 4060–4073 (cit. on pp. 250, 253, 254, 272, 280).

(229) Worlitschek, J.; Mazzotti, M. Model-Based Optimization of Particle Size Distribution in Batch-Cooling Crystallization of Paracetamol. *Crystal Growth & Design* **2004**, *4*, 891–903 (cit. on pp. 250, 254).

(230) Toschev, S; Milchev, A; Stoyanov, S On some probabilistic aspects of the nucleation process. *Journal of Crystal Growth* **1972**, *13-14*, Third International Conference on Crystal Growth, 123–127 (cit. on pp. 250, 261).

(231) Cedeno, R. et al. Nucleation in sessile saline microdroplets: induction time measurement via deliquescence–recrystallization cycling. *Faraday Discuss.* **2022**, *235*, 183–197 (cit. on pp. 250, 261).

(232) Bosetti, L.; Mazzotti, M. Population Balance Modeling of Growth and Secondary Nucleation by Attrition and Ripening. *Crystal Growth & Design* **2020**, *20*, 307–319 (cit. on pp. 250, 252).

(233) Ahn, B.; Bosetti, L.; Mazzotti, M. Secondary Nucleation by Interparticle Energies. III. Nucleation Rate Model. *Crystal Growth & Design* **2022**, *22*, 3625–3636 (cit. on pp. 250, 252).

(234) Denk, E. G.; Botsaris, G. D. Fundamental studies in secondary nucleation from solution. *Journal of Crystal Growth* **1972**, *13-14*, Third International Conference on Crystal Growth, 493–499 (cit. on pp. 250, 252).

(235) Qian, R.-Y.; Botsaris, G. D. Nuclei breeding from a chiral crystal seed of NaClO3. *Chemical Engineering Science* **1998**, *53*, 1745–1756 (cit. on pp. 250, 252).

(236) Maosoongnern, S.; Flood, A. Validation of Models Predicting Nucleation Rates from Induction Times and Metastable Zone Widths. *Chemical Engineering & Technology* **2018**, *41*, 2066–2076 (cit. on pp. 250, 254, 278, 280, 285).

(237) Sangwal, K. On the linear and integral models for metastable zone width determined by solution cooling method. *Journal of Crystal Growth* **2021**, *576*, 126377 (cit. on pp. 250, 255, 278, 280).

(238) Briuglia, M. L.; Sefcik, J.; ter Horst, J. H. Measuring Secondary Nucleation through Single Crystal Seeding. *Crystal Growth & Design* **2019**, *19*, 421–429 (cit. on pp. 251, 292).

(239) Lindenberg, C.; Mazzotti, M. Effect of temperature on the nucleation kinetics of α l-glutamic acid. *Journal of Crystal Growth* **2009**, *311*, 1178–1184 (cit. on pp. 252, 256).

(240) Kubota, N. Modeling of nucleation time distribution using Laplace transform of activity density function – Stochastic heterogeneous nucleation –. *Journal of Crystal Growth* **2022**, *587*, 126638 (cit. on p. 252).

(241) Steendam, R. R. E. et al. Effects of Scale-Up on the Mechanism and Kinetics of Crystal Nucleation. *Crystal Growth & Design* **2018**, *18*, 5547–5555 (cit. on p. 252).

(242) Achermann, R.; Adams, R.; Prasser, H.-M.; Mazzotti, M. Characterization of a small-scale crystallizer using CFD simulations and X-ray CT measurements. *Chemical Engineering Science* **2022**, *256*, 117697 (cit. on p. 252).

(243) Randolph, A. D.; Larson, M. A., *Theory of Particulate Processes*; Elsevier: 1971 (cit. on pp. 253, 293, 295, 304, 317, 320).

(244) Ahn, B.; Chen, M.; Mazzotti, M. Online Monitoring of the Concentrations of Amorphous and Crystalline Mesoscopic Species Present in Solution. *Crystal Growth & Design* **2022**, *22*, 5071–5080 (cit. on p. 255).

(245) Kashchiev, D.; Verdoes, D.; van Rosmalen, G. Induction time and metastability limit in new phase formation. *Journal of Crystal Growth* **1991**, *110*, 373–380 (cit. on pp. 256, 258, 261).

(246) Arosio, P.; Knowles, T. P. J.; Linse, S. On the lag phase in amyloid fibril formation. *Phys. Chem. Chem. Phys.* **2015**, *17*, 7606–7618 (cit. on p. 256).

(247) Unno, J.; Hirasawa, I. Parameter Estimation of the Stochastic Primary Nucleation Kinetics by Stochastic Integrals Using Focused-Beam Reflectance Measurements. *Crystals* **2020**, *10*, DOI: 10.3390/cryst10050380 (cit. on pp. 260, 261).

(248) Unno, J.; Hirasawa, I. Numerical Simulations of Seeded Batch Crystallization Demonstrating the Effect of Stochastic Nucleation on Crystal Product Quality. *Journal of Chemical Engineering of Japan* **2021**, *54*, 380–386 (cit. on p. 261).

(249) Turner, T. D. et al. The influence of solution environment on the nucleation kinetics and crystallisability of para-aminobenzoic acid. *Phys. Chem. Chem. Phys.* **2016**, *18*, 27507–27520 (cit. on p. 262).

(250) Sullivan, R. A. et al. Revealing the Roles of Desolvation and Molecular Self-Assembly in Crystal Nucleation from Solution: Benzoic and p-Aminobenzoic Acids. *Crystal Growth & Design* **2014**, *14*, 2689–2696 (cit. on p. 262).

(251) Karthika, S.; Radhakrishnan, T. K.; Kalaichelvi, P. Crystallization and Kinetic Studies of an Active Pharmaceutical Compound Using Ethyl Lactate As a Green Solvent. *ACS Sustainable Chemistry & Engineering* **2020**, *8*, 1527–1537 (cit. on p. 272).

(252) Zhao, Y. et al. Primary Nucleation of Benzoic Acid in Aqueous Ethanol Solution. *Industrial & Engineering Chemistry Research* **2020**, *59*, 484–490 (cit. on p. 272).

(253) Kim, S.; Yeol Lee, S.; Woong Chang, J.; Ryook Yang, D. Evaluation of the kinetics of unseeded batch cooling crystallization using population balance modeling: sucrose and KNO_3 case studies. *Journal of Industrial and Engineering Chemistry* **2022**, DOI: https://doi.org/10.1016/j.jiec.2022.11.038 (cit. on p. 272).

(254) McDonald, M. A.; Bommarius, A. S.; Grover, M. A.; Rousseau, R. W. Direct Observation of Growth Rate Dispersion in the Enzymatic Reactive Crystallization of Ampicillin. *Processes* **2019**, *7*, 390 (cit. on pp. 280, 313).

(255) Larson, M. A.; White, E. T.; Ramanarayanan, K. A.; Berglund, K. A. Growth rate dispersion in MSMPR crystallizers. *AIChE Journal* **1985**, *31*, 90–94 (cit. on pp. 293, 314).

(256) Llinàs, A.; Goodman, J. M. Polymorph control: past, present and future. *Drug Discovery Today* **2008**, *13*, 198–210 (cit. on p. 293).

(257) Blagden, N.; de Matas, M.; Gavan, P.; York, P. Crystal engineering of active pharmaceutical ingredients to improve solubility and dissolution rates. *Advanced Drug Delivery Reviews* **2007**, *59*, 617–630 (cit. on p. 293).

(258) Farmer, T. C.; Carpenter, C. L.; Doherty, M. F. Polymorph selection by continuous crystallization. *AIChE Journal* **2016**, *62*, 3505–3514 (cit. on pp. 293, 294, 306, 313, 358).

(259) Achermann, R.; Košir, A.; Bodák, B.; Bosetti, L.; Mazzotti, M. Process Performance and Operational Challenges in Continuous Crystallization: A Study of the Polymorphs of *L*-Glutamic Acid. *Crystal Growth & Design* **2023**, *23*, 2485–2503 (cit. on pp. 293, 294, 308, 309, 313, 358).

(260) Chemburkar, S. R. et al. Dealing with the Impact of Ritonavir Polymorphs on the Late Stages of Bulk Drug Process Development. *Organic Process Research & Development* **2000**, *4*, 413–417 (cit. on p. 293).

(261) Wieckhusen, D. The Development of API Manufacturing Processes – Targets and Strategies. *CHIMIA* **2006**, *60*, 598 (cit. on p. 293).

(262) Lai, T.-T. C. et al. Control of Polymorphism in Continuous Crystallization via Mixed Suspension Mixed Product Removal Systems Cascade Design. *Crystal Growth & Design* **2015**, *15*, 3374–3382 (cit. on pp. 293, 306).

(263) Li, Y.; O'Shea, S.; Yin, Q.; Vetter, T. Polymorph Selection by Continuous Crystallization in the Presence of Wet Milling. *Crystal Growth & Design* **2019**, *19*, 2259–2271 (cit. on pp. 293, 294, 313).

(264) Gong, W.; Wu, Y.; Lin, M.; Rohani, S. Polymorphism control of l-Glutamic acid in a single-stage and a two-stage MSMPR crystallizer by different seeding strategies. *Chemical Engineering Research and Design* **2021**, *170*, 23–33 (cit. on p. 293).

(265) Kitamura, M. Strategy for control of crystallization of polymorphs. *CrystEngComm* **2009**, *11*, 949–964 (cit. on p. 293).

(266) Farmer, T. C.; Schiebel, S. K.; Chmelka, B. F.; Doherty, M. F. Polymorph Selection by Continuous Precipitation. *Crystal Growth & Design* **2018**, *18*, 4306–4319 (cit. on pp. 294, 306).

(267) Lin, M.; Wu, Y.; Rohani, S. Identifying the Polymorphic Outcome of Hypothetical Polymorphs in Batch and Continuous Crystallizers by Numerical Simulation. *Crystal Growth & Design* **2020**, *20*, 7312–7319 (cit. on p. 294).

(268) Köllges, T.; Vetter, T. Polymorph Selection and Process Intensification in a Continuous Crystallization–Milling Process: A Case Study on l-Glutamic Acid Crystallized from Water. *Organic Process Research & Development* **2019**, *23*, 361–374 (cit. on pp. 294, 309).

(269) Achermann, R.; Wiedmeyer, V.; Hosseinalipour, M. S.; Güngör, S.; Mazzotti, M. Model-based design of pressure-driven product removal from stirred suspensions. *Chemical Engineering Research and Design* **2021**, *174*, 57–70 (cit. on pp. 294, 295).

(270) Tavare, N. S.; Garside, J. Multiplicity in continuous MSMPR crystallizers. Part I: Concentration multiplicity in an isothermal crystallizer. *AIChE Journal* **1985**, *31*, 1121–1127 (cit. on pp. 294, 297, 304).

(271) Bourne, J.; Zabelka, M. The influence of gradual classification on continuous crystallization. *Chemical Engineering Science* **1980**, *35*, 533–542 (cit. on pp. 294, 295, 304, 305).

(272) Han, C. D.; Shinnar, R. The steady state behavior of crystallizers with classified product removal. *AIChE Journal* **1968**, *14*, 612–619 (cit. on pp. 295, 297, 304).

(273) Kim, Y.; Kawajiri, Y.; Rousseau, R. W.; Grover, M. A. Modeling of Nucleation, Growth, and Dissolution of Paracetamol in Ethanol Solution for Unseeded Batch Cooling Crystallization with Temperature-Cycling Strategy. *Industrial & Engineering Chemistry Research* **2023**, *62*, 2866–2881 (cit. on p. 295).

(274) Cashmore, A. et al. Rapid Assessment of Crystal Nucleation and Growth Kinetics: Comparison of Seeded and Unseeded Experiments. *Crystal Growth & Design* **2023**, *23*, 4779–4790 (cit. on p. 295).

(275) McCabe, W. L. Crystal Growth in Aqueous Solutions: I—Theory. *Industrial & Engineering Chemistry* **1929**, *21*, 30–33 (cit. on pp. 296, 315).

(276) Abegg, C. F.; Stevens, J. D.; Larson, M. A. Crystal size distributions in continuous crystallizers when growth rate is size dependent. *AIChE Journal* **1968**, *14*, 118–122 (cit. on pp. 296, 315).

(277) Garside, J.; Phillips, V. R.; Shah, M. B. On Size-Dependent Crystal Growth. *Industrial & Engineering Chemistry Fundamentals* **1976**, *15*, 230–233 (cit. on pp. 296, 315).

(278) Ahn, B.; Bosetti, L.; Mazzotti, M. Secondary Nucleation by Interparticle Energies. III. Nucleation Rate Model. *Crystal Growth & Design* **2022**, *22*, 3625–3636 (cit. on p. 303).

(279) Lakatos, B. G.; Sapundzhiev, T. J.; Garside, J. Stability and dynamics of isothermal CMSMPR crystallizers. *Chemical Engineering Science* **2007**, *62*, 4348–4364 (cit. on p. 304).

(280) Hermanto, M. W.; Kee, N. C.; Tan, R. B. H.; Chiu, M.-S.; Braatz, R. D. Robust Bayesian estimation of kinetics for the polymorphic transformation of *L*-glutamic acid crystals. *AIChE Journal* **2008**, *54*, 3248–3259 (cit. on pp. 305, 308, 309).

(281) Chen, S.; Xi, H.; Yu, L. Cross-Nucleation between ROY Polymorphs. *Journal of the American Chemical Society* **2005**, *127*, 17439–17444 (cit. on p. 309).

(282) Nicoud, L.; Licordari, F.; Myerson, A. S. Polymorph Control in MSMPR Crystallizers. A Case Study with Paracetamol. *Organic Process Research & Development* **2019**, *23*, 794–806 (cit. on p. 309).

(283) Rougeot, C.; Hein, J. E. Application of Continuous Preferential Crystallization to Efficiently Access Enantiopure Chemicals. *Organic Process Research & Development* **2015**, *19*, 1809–1819 (cit. on pp. 311, 319, 320).

(284) Steendam, R. R. E.; ter Horst, J. H. Continuous Total Spontaneous Resolution. *Crystal Growth & Design* **2017**, *17*, 4428–4436 (cit. on pp. 311, 312).

(285) Bodák, B.; Mazzotti, M. Solid-State Deracemization via Temperature Cycles in Continuous Operation: Model-Based Process Design. *Crystal Growth & Design* **2022**, *22*, 1846–1856 (cit. on pp. 311, 312).

(286) Bodák, B.; Breveglieri, F.; Mazzotti, M. On the model-based design and comparison of crystallization-based deracemization techniques. *Chemical Engineering Science* **2022**, *254*, 117595 (cit. on p. 312).

(287) Janse, A. H.; Jong, E. J. D. In *Industrial Crystallization*; Springer US: 1976, pp 145–154 (cit. on p. 313).

(288) Garside, J.; Ristić, R. Growth rate dispersion among ADP crystals formed by primary nucleation. *Journal of Crystal Growth* **1983**, *61*, 215–220 (cit. on p. 313).

(289) Ochsenbein, D. R. et al. Modeling the facet growth rate dispersion of l-glutamic acid—Combining single crystal experiments with nD particle size distribution data. *Chemical Engineering Science* **2015**, *133*, 30–43 (cit. on p. 313).

(290) Berglund, K. A.; Larson, M. A. Modeling of growth rate dispersion of citric acid monohydrate in continuous crystallizers. *AIChE Journal* **1984**, *30*, 280–287 (cit. on pp. 314, 315).

(291) Zumstein, R. C.; Rousseau, R. W. Growth rate dispersion by initial growth rate distributions and growth rate fluctuations. *AIChE Journal* **1987**, *33*, 121–129 (cit. on p. 314).

(292) Ulrich, J. Growth rate dispersion — a review. *Crystal Research and Technology* **1989**, *24*, 249–257 (cit. on p. 315).

(293) Srisanga, S. et al. Crystal Growth Rate Dispersion versus Size-Dependent Crystal Growth: Appropriate Modeling for Crystallization Processes. *Crystal Growth & Design* **2015**, *15*, 2330–2336 (cit. on p. 315).

(294) Kondepudi, D. K.; Kaufman, R. J.; Singh, N. Chiral Symmetry Breaking in Sodium Chlorate Crystallization. *Science* **1990**, *250*, 975–976 (cit. on pp. 319, 331).

(295) Viedma, C. Chiral Symmetry Breaking During Crystallization: Complete Chiral Purity Induced by Nonlinear Autocatalysis and Recycling. *Physical Review Letters* **2005**, *94*, 065504 (cit. on pp. 319, 320, 327).

(296) Ozturk, S. F.; Liu, Z.; Sutherland, J. D.; Sasselov, D. D. Origin of biological homochirality by crystallization of an RNA precursor on a magnetic surface. *Science Advances* **2023**, *9*, eadg827 (cit. on p. 319).

(297) Gujarro, A; Yus, M, *The origin of chirality in the molecules of life: a revision from awareness to the current theories and perspectives of this unsolved problem*; RCS Publishing, Cambridge: 2009 (cit. on p. 319).

(298) Chen, Y.; Ma, W. The origin of biological homochirality along with the origin of life. *PLOS Computational Biology* **2020**, *16*, ed. by Morozov, A. V., e1007592 (cit. on p. 319).

(299) Xiouras, C. et al. Applications of ultrasound to chiral crystallization, resolution and deracemization. *Ultrasonics Sonochemistry* **2018**, *43*, 184–192 (cit. on pp. 319, 320).

(300) Breveglieri, F.; Maggioni, G. M.; Mazzotti, M. Deracemization of NMPA via Temperature Cycles. *Crystal Growth & Design* **2018**, *18*, 1873–1881 (cit. on pp. 319, 320, 322, 326, 334, 340, 344).

(301) Suwannasang, K.; Flood, A. E.; Coquerel, G. A Novel Design Approach To Scale Up the Temperature Cycle Enhanced Deracemization Process: Coupled Mixed-Suspension Vessels. *Crystal Growth & Design* **2016**, *16*, 6461–6467 (cit. on p. 319).

(302) Rehman, G. u.; Vetter, T.; Martin, P. A. Investigation of Temperature Cycling with Coupled Vessels for Efficient Deracemization of NMPA. *Crystal Growth & Design* **2023**, *23*, 5428–5436 (cit. on p. 319).

(303) Iggland, M.; Fernández-Ronco, M. P.; Senn, R.; Kluge, J.; Mazzotti, M. Complete solid state deracemization by High Pressure Homogenization. *Chemical Engineering Science* **2014**, *111*, 106–111 (cit. on pp. 319, 320, 334, 340).

(304) Intaraboonrod, K.; Flood, A. E. A Novel Strategy for Deracemization Using Periodic Fluctuations of Concentration. *Chemical Engineering & Technology* **2023**, *46*, 2310–2315 (cit. on pp. 319, 320, 326).

(305) Van Dongen, S. W. et al. Rapid deracemization through solvent cycling: proof-of-concept using a racemizable conglomerate clopidogrel precursor. *Chemical Communications* **2023**, *59*, 3838–3841 (cit. on pp. 319, 320, 326).

(306) Addadi, L. et al. Resolution of conglomerates by stereoselective habit modifications. *Nature* **1982**, *296*, 21–26 (cit. on pp. 320, 331).

(307) Anastasi, C.; Crowe, M. A.; Powner, M. W.; Sutherland, J. D. Direct Assembly of Nucleoside Precursors from Two- and Three-Carbon Units. *Angewandte Chemie International Edition* **2006**, *45*, 6176–6179 (cit. on p. 320).

(308) Hein, J. E.; Tse, E.; Blackmond, D. G. A route to enantiopure RNA precursors from nearly racemic starting materials. *Nature Chemistry* **2011**, *3*, 704–706 (cit. on p. 320).

(309) Tsogoeva, S.; Wei, S.; Freund, M.; Mauksch, M. Generation of Highly Enantioenriched Crystalline Products in Reversible Asymmetric Reactions with Racemic or Achiral Catalysts. *Angewandte Chemie International Edition* **2009**, *48*, 590–594 (cit. on p. 320).

(310) Viedma, C.; Cintas, P. Homochirality beyond grinding: deracemizing chiral crystals by temperature gradient under boiling. *Chemical Communications* **2011**, *47*, 12786–12788 (cit. on p. 320).

(311) Uwaha, M. A Model for Complete Chiral Crystallization. *Journal of the Physical Society of Japan* **2004**, *73*, 2601–2603 (cit. on pp. 320, 321, 327).

(312) Noorduin, W. L. et al. The Driving Mechanism Behind Attrition-Enhanced Deracemization. *Angewandte Chemie* **2010**, *122*, 8613–8616 (cit. on pp. 320, 327).

(313) Iggland, M.; Mazzotti, M. A Population Balance Model for Chiral Resolution via Viedma Ripening. *Crystal Growth & Design* **2011**, *11*, 4611–4622 (cit. on pp. 320, 327).

(314) Uwaha, M.; Katsuno, H. Mechanism of chirality conversion of crystals by Viedma ripening and temperature cycling. *Journal of Crystal Growth* **2022**, *598*, 126873 (cit. on pp. 320, 321, 327).

(315) Lovette, M. A.; Muratore, M.; Doherty, M. F. Crystal shape modification through cycles of dissolution and growth: Attainable regions and experimental validation. *AIChE Journal* **2011**, *58*, 1465–1474 (cit. on pp. 320, 326, 331, 345).

(316) Fytopoulos, A. A. et al. Crystal Growth, Dissolution, and Agglomeration Kinetics of Sodium Chlorate. *Industrial & Engineering Chemistry Research* **2021**, *60*, 7367–7384 (cit. on pp. 320, 326, 331, 345).

(317) Iggland, M.; Mazzotti, M. Population Balance Modeling with Size-Dependent Solubility: Ostwald Ripening. *Crystal Growth & Design* **2012**, *12*, 1489–1500 (cit. on p. 320).

(318) Bodák, B.; Maggioni, G. M.; Mazzotti, M. Population-Based Mathematical Model of Solid-State Deracemization via Temperature Cycles. *Crystal Growth & Design* **2018**, *18*, 7122–7131 (cit. on p. 320).

(319) Bodák, B.; Maggioni, G. M.; Mazzotti, M. Effect of Initial Conditions on Solid-State Deracemization via Temperature Cycles: A Model-Based Study. *Crystal Growth & Design* **2019**, *19*, 6552–6559 (cit. on pp. 320, 332).

(320) Wagner, C. Theorie der Alterung von Niederschlägen durch Umlösen (Ostwald-Reifung). *Zeitschrift für Elektrochemie, Berichte der Bunsengesellschaft für physikalische Chemie* **1961**, *65*, 581–591 (cit. on p. 320).

(321) Lifshitz, I.; Slyozov, V. The kinetics of precipitation from supersaturated solid solutions. *Journal of Physics and Chemistry of Solids* **1961**, *19*, 35–50 (cit. on p. 320).

(322) Vetter, T.; Iggland, M.; Ochsenbein, D. R.; Hänseler, F. S.; Mazzotti, M. Modeling Nucleation, Growth, and Ostwald Ripening in Crystallization Processes: A Comparison between Population Balance and Kinetic Rate Equation. *Crystal Growth & Design* **2013**, *13*, 4890–4905 (cit. on p. 322).

(323) Chernov, A. The kinetics of the growth forms of crystals. *Sov. Phys. Crystallogr* **1963**, *7*, 728–730 (cit. on p. 326).

(324) Frank, F. C. On the Kinematic Theory of Crystal Growth and Dissolution Processes, II. *Zeitschrift für Physikalische Chemie* **1972**, *77*, 84–92 (cit. on p. 326).

(325) Belletti, G. et al. Combining Viedma Ripening and Temperature Cycling Deracemization. *Crystal Growth & Design* **2022**, *22*, 1874–1881 (cit. on pp. 326, 327, 344, 345).

(326) Bada, J. L. Kinetics of racemization of amino acids as a function of pH. *Journal of the American Chemical Society* **1972**, *94*, 1371–1373 (cit. on pp. 326, 331).

(327) Yamada, S.; Hongo, C.; Yoshioka, R.; Chibata, I. Method for the racemization of optically active amino acids. *The Journal of Organic Chemistry* **1983**, *48*, 843–846 (cit. on pp. 326, 331).

(328) Breveglieri, F.; Mazzotti, M. Role of racemization kinetics in the deracemization process via temperature cycles. *Crystal Growth & Design* **2019**, *19*, 3551–3558 (cit. on pp. 327, 334, 340, 344, 345).

(329) Viedma, C.; Ortiz, J. E.; de Torres, T.; Izumi, T.; Blackmond, D. G. Evolution of Solid Phase Homochirality for a Proteinogenic Amino Acid. *Journal of the American Chemical Society* **2008**, *130*, 15274–15275 (cit. on p. 327).

(330) Breveglieri, F.; Bodák, B.; Mazzotti, M. Deracemization via Periodic and Non-periodic Temperature Cycles: Rationalization and Experimental Validation of a Simplified Process Design Approach. *Organic Process Research & Development* **2021**, *25*, 2551–2565 (cit. on pp. 329, 334, 341–344).

(331) Frank, F. On spontaneous asymmetric synthesis. *Biochimica et Biophysica Acta* **1953**, *11*, 459–463 (cit. on p. 331).

(332) Soai, K.; Shibata, T.; Morioka, H.; Choji, K. Asymmetric autocatalysis and amplification of enantiomeric excess of a chiral molecule. *Nature* **1995**, *378*, 767–768 (cit. on pp. 331, 359).

(333) Buhse, T. et al. Spontaneous Deracemizations. *Chemical Reviews* **2021**, *121*, 2147–2229 (cit. on p. 331).

(334) McBride, J. M.; Carter, R. L. Spontaneous Resolution by Stirred Crystallization. *Angewandte Chemie International Edition in English* **1991**, *30*, 293–295 (cit. on p. 331).

(335) Eskandari, A.; Leow, T. C.; Rahman, M. B. A.; Oslan, S. N. Antifreeze Proteins and Their Practical Utilization in Industry, Medicine, and Agriculture. *Biomolecules* **2020**, *10*, 1649 (cit. on p. 355).